

Investigation of Middle Atmospheric Wave Dynamics during Sudden Stratospheric Warming

A thesis submitted in partial fulfilment of the requirements
for the degree of

Doctor of Philosophy

by

Gourav Mitra

(Roll No. 19330008)

Under the supervision of

Dr. Amitava Guharay

Space and Atmospheric Sciences Division

Physical Research Laboratory, Ahmedabad, India



Discipline of Physics

Indian Institute of Technology Gandhinagar, India

2024

To
My Family and Teachers

Declaration

I declare that this written submission represents my ideas in my own words, and where others' ideas or comments have been included, I have adequately cited and referenced the sources. I also declare that I have adhered to all academic honesty and integrity principles and have not misrepresented, fabricated, or falsified any idea/data/fact/source in my submission. I understand that any violation of the above will cause disciplinary action by the Institute and can also evoke penal action from the sources which have thus not been appropriately cited or from whom proper permission has not been taken when needed.

Signature

Name: Gourav Mitra

(Roll No: 19330008)

Date: 24.12.2024

CERTIFICATE

It is certified that the work in the thesis titled “**Investigation of Middle Atmospheric Wave Dynamics during Sudden Stratospheric Warming**” by Mr. Gourav Mitra (Roll No. 19330008) has been carried out under my supervision and has not been submitted elsewhere for a degree.

I have read this dissertation, and in my opinion, it is fully adequate in scope and quality as a dissertation for the degree of Doctor of Philosophy.

Dr. Amitava Guharay

(Thesis Supervisor)

Associate Professor

Space and Atmospheric Sciences Division,

Physical Research Laboratory,

Ahmedabad, India.

Date: 24.12.2024

Acknowledgements

In the grand tapestry of life, this journey of intellectual pursuit has been one of the most intricate and profound. As I reach the culmination of my PhD journey, I am filled with immense gratitude towards the many individuals who have supported, inspired, and guided me through this voyage of discovery and growth.

First and foremost, my deepest appreciation goes to my esteemed supervisor, Dr. Amitava Guharay. His unwavering support, insightful guidance, and boundless patience have been the pillars of this thesis. His intellectual rigor and profound knowledge have constantly inspired me to push the boundaries of my understanding. I thank him wholeheartedly for believing in me and for his invaluable mentorship throughout this journey.

I extend my heartfelt thanks to the members of my Doctoral Studies Committee (DSC), Dr. Harish Gadhavi, Dr. Narendra Ojha, and Dr. Manash Samal. Their critical insights, constructive feedback, and encouragement have significantly enriched this work. I am deeply grateful for their time, effort, and dedication in helping me refine and enhance my research.

A special note of gratitude to SCOSTEP for awarding me the SCOSTEP Visiting Scholarship (SVS) in 2022. This prestigious recognition enabled me to spend three enriching months at the Leibniz Institute of Atmospheric Physics (IAP) in Kuhlungsborn, Germany. I am incredibly thankful to Prof. Jorge Chau (Koki) and Dr. Fede Conte for their kind supervision and unwavering support during my stay at IAP. To Siva Da, Priyanka Di, Tarique, Kesava, Hari, Sunil, Teri, Sony, and the Radar Remote Sensing Group, your companionship and assistance during my SVS visit were invaluable, making my time in Kuhlungsborn memorable and enriching.

I am sincerely thankful to the Department of Science and Technology, Science and Engineering Research Board, Government of India, for their kind support in awarding me the international travel grant to attend and present my research at the 16th International Workshop and School on Technical and Scientific Aspects of iMST Radar and Lidar (MST16) in Germany. I also appreciate the generous assistance from the iMST3/MST16

organizers, who covered the registration fees for the workshop and school and provided accommodation during my stay. This support has been invaluable to my experience and learning journey.

I am profoundly grateful to Prof. P. P. Batista from the Instituto Nacional de Pesquisas Espaciais (INPE) and Prof. R. A. Buriti from the Universidade Federal de Campina Grande (UFCG) for providing valuable resources and feedback that were instrumental in the completion of my thesis. Additionally, I acknowledge the support from my collaborators at the British Antarctic Survey.

My journey would not have been possible without the unwavering support from the Physical Research Laboratory (PRL). I extend my heartfelt thanks to the Department of Space, Government of India, for providing the research grant that supported my tenure at PRL. My gratitude to Prof. A. Bharadwaj (Director), Prof. D. Pallamraju (Dean), Prof. R. D. Deshpande (Registrar), and Prof. D. Chakrabarty (Head of Space and Atmospheric Sciences Division) for their steadfast support and encouragement throughout my research. I am grateful to the Academic Committee members for their insightful comments and suggestions that greatly improved the quality of my research. I express my sincere thanks to the colleagues of the SPASC division: Prof. S. Ramachandran, Prof. L. K. Sahu, Prof. S. Sharma, Dr. R. P. Singh, Dr. T. A. Rajesh, Dr. K. Venkatesh, Mr. S. Venkataramani, Sneha Di, Mr. M. Bhavsar, Mr. T. K. Sunilkumar, Aaditya, Malaidevan, Shashank, Rahul, Pankaj, Chitra, Pradip, Vishnu, Mohit, Dheeraj, Aryan, and Hemangir, for providing me with such a pleasant working ambiance.

Leading the SPASC Volleyball team to glory for three consecutive years was a highlight of my time at PRL. To my cherished volleyball team members Kamran, Sunil, Bijoy, Kshitiz, R. P. Sir, Dharmendra, Subarna, Sandip, Shivam, Nitin, and others, our victories were a testament to our teamwork and dedication. Together, we excelled on the court, showcasing exceptional performance and unity, achieving an incredible hat-trick of championships with unmatched determination and spirit.

I have cherished the interactions with seniors and juniors from the SPASC division: Dupinder Paaji, Kuldeep Bhaiya, Sumanjit Da, Subir Da, Subarna Da, Suman Da, Sandeep Paaji, Sovan Da, Ankit Bhaiya, Yogesh, Meghna, Mansi, Akhanksha, Kiran, Harithashree, Komal, and

Ankita. Your wisdom and camaraderie have been a constant source of motivation. Representing our division in football, tug of war, and drama (Hindi Pakwada) further enriched my experience at PRL, adding layers of joy and fulfillment. To our lunch group members—Akash, Anil Bhai, Jacob, Abhishek, Aniket, Maanyash, and others—their humor and engaging discussions turned our lunchtimes into delightful and intellectually stimulating moments. I am grateful to have a wonderful office space, Room 654, and cherish the good moments with office mates Kshitiz and Sandip.

I cherished the delightful lunch and dinners with Amitava sir and Subarna Da, where we celebrated festive occasions and our academic triumphs, creating memories that brightened my scholarly journey.

I am also thankful to my friends from the 2019 batch: Bijoy, Saurabh, Bharathi, Swagatika, Kimi, Vineet, Birendra, Soumya, Ajayeta, Santunu, Rithvik, Neha, Tanya, Vardaan, Kshitiz, Yogesh, Satyam, Sandipan, and Jiban. I have good memories of us preparing for the freshers' performance. My lobbymates Bijoy and Saurabh, and our late-night discussions over tea with Bharathi—these moments are etched in my memory. I fondly remember the vibrant sports community, particularly volleyball in Navrangpura hostel, including Guru, Debasish, Siddhartha Da, Supriyo Da, Atif Bhai, Pandey Ji, Parveen Bhai, Praveen Bhai, Madhu Da, Priyank Bhai, Milan Bhai, Ranjan and others. Playing football at Vikramnagar with Sovan Da, Soumya, Aravind, Gautam Sir, Arvind Sir, Rohit, Dibyendu, Soumik, and others was always exhilarating. I enjoyed participating in festive decorations, celebrations, birthday gatherings, and get-togethers at the Navrangpura hostel with Sarika Di, JT, Lobby B, Aishwarya, Rahul, Malika, Chandrima, Monika Di, Indrajit, and others. Thanks to Aditya, Wafikul, Trinesh, Goldy, and others from Thaltej Hostel for their cherished, fun-filled moments. I also cherish the beautiful moments spent in my abode E201, PRL Navrangpura Hostel.

My thanks extend to the Library (Dr. Nistha, Dr. Pragya, and the team), Head of Academic Services (Dr. B. Vaishnav), Medical Facility (Dr. S. Dani and Dr. S. Patel), Computer Centre team (CNIT), Canteen facility, Administrative staff (Richa Maam), CISF, housekeeping staff, and Ganesh Bhai for their indispensable support. I also acknowledge the support from Academic and Administrative personnel at IITGN for providing necessary resources and smooth processing of official formalities.

I am profoundly grateful to my family, Maa, Baba, Dada, and Boudi, for their unconditional love, support, and encouragement. To my parents, Maa and Baba, thank you for instilling the values of perseverance, curiosity, and resilience in me. Your sacrifices and unwavering belief in my abilities have been my guiding light. To Dada, your constant encouragement and understanding have meant the world to me. To Lopa, the best person who has stood by me through thick and thin, your presence has been a source of strength and joy.

Finally, I acknowledge myself for staying strong and resilient, tackling challenges with unwavering determination, and cheering myself on through every high and low. In moments of quiet reflection, on the sports field, during travels to new horizons, and while crafting culinary delights, I found joy and kept the positive vibes flowing, enriching my journey beyond research.

With deep gratitude and heartfelt thanks,

Gourav

Abstract

The Earth's atmosphere is divided into four regions based on vertical temperature profiles: the troposphere, stratosphere, mesosphere, and thermosphere. This thesis focuses on the middle atmosphere, covering the stratosphere, mesosphere, and lower thermosphere, extending from 30 to 110 km altitude. Atmospheric waves largely control the middle atmospheric dynamics. These waves, generated mainly in the lower atmosphere, increase in amplitude as they propagate upward, conserving energy and coupling different atmospheric layers by transporting energy and momentum. The present thesis examines planetary-scale waves, specifically tides, and PWs, with horizontal scales comparable to the Earth's circumference. Tides, with periods of integral subharmonics of a solar day, and PWs, with periods of 2-20 days, are pivotal to affect and control global atmospheric dynamics.

A significant phenomenon driven by PWs in the middle atmosphere is the Sudden Stratospheric Warming (SSW). SSWs occur due to enhanced PW activity, disrupting the polar vortex and causing rapid polar stratospheric warming and deceleration of the zonal mean westerlies. This thesis aims to investigate the global middle atmospheric dynamics during SSW events, with a special focus on the relatively less explored and least understood rare Southern Hemisphere (SH) SSWs. The thesis is divided into nine chapters.

Chapter 1 sets the stage by outlining the Earth's atmospheric layers and emphasizing the role of atmospheric waves in the middle atmosphere, identifying gaps in the current understanding of wave dynamics during SSW events.

Chapter 2 details the instruments and observational datasets used for this study and various spectral analysis techniques essential for extracting wave dynamical information from observational data.

Chapter 3 investigates the dynamics of low-latitude middle atmospheric PWs during the September 2019 SH minor SSW, using meteor radar observations and reanalysis data. Significant findings include the presence of a quasi-16-day wave (Q16DW) before the SSW and a quasi-6-day wave (Q6DW) after the warming event and their plausible generation

mechanism. This chapter provides insights into the low-latitude middle atmospheric dynamics during this minor but robust SSW event.

Chapter 4 examines tidal variability in the mesosphere and lower thermosphere (MLT) during the 2019 SH minor SSW, utilizing meteor radar wind observations from multiple locations in the SH and global reanalysis data. The study identifies notable short-term variability in specific zonal wavenumber components of diurnal and semidiurnal tides, emphasizing the complex processes involved in tidal responses to SSW events.

Chapter 5 compares the impacts of rare SH SSWs on middle atmospheric circulation. The study reveals distinct dynamical signatures of SSW events by isolating the seasonal transition effects. It also suggests a potential tropical precursor to SH SSWs based on deseasoned winds in the stratosphere.

Chapter 6 investigates non-linear interactions of planetary-scale waves during two major NH SSWs, revealing the first observational evidence of a two-step non-linear interaction associated with zonally symmetric PWs.

Chapter 7 discusses the unusual enhancement of the zonally symmetric semidiurnal tide (S_0) observed during SSW in the stratosphere and explains the plausible generation mechanisms. The potential role of non-linear interaction and unique distribution of source species in S_0 enhancement is investigated.

Chapter 8 discusses the modulation of the quasi-2-day wave (Q2dw) with a quasi-16-day period during the 2019 boreal summer, highlighting the role of Q2dw modes in interhemispheric coupling and carrying the Q16dw signature from winter to summer hemispheres.

Chapter 9 summarizes the findings from Chapters 3 to 8 and proposes future research directions to understand middle atmospheric dynamics during SSW events further.

This thesis provides a comprehensive investigation of the global impact of SSW on middle atmospheric dynamics, focusing on planetary-scale waves. It examines various aspects, including low latitude PW dynamics, global tidal variability, and non-linear interactions

between planetary-scale waves in both hemispheres during SSW events. The research reveals the mechanisms behind the enhancement of zonally symmetric waves and the interhemispheric coupling processes through PW modulation, underscoring the complexity of atmospheric processes during SSW events and their far-reaching effects on the global middle atmospheric system.

Keywords: Middle atmosphere; Tides; Planetary waves; Non-linear interaction; Circulation; Dynamics

Contents

Abstract	10
List of Figures	17
List of Abbreviations.....	26
Chapter 1.....	30
Introduction	30
1.1. The Earth's atmosphere	30
1.2. Middle atmosphere dynamics	33
1.3. Atmospheric waves	36
1.4. Wave parameters	37
1.5. Internal Gravity Waves	39
1.5.1. Brunt-Väisälä frequency and static stability	40
1.6. Atmospheric tides	42
1.6.1. Migrating tides	45
1.6.2. Non-migrating tides	45
1.7. Planetary waves	45
1.7.1. Phase speed of planetary waves	47
1.8. Sudden Stratospheric Warming	49
1.8.1. Generation mechanism	49
1.8.2 Classification	51
1.8.3. Global Impact.....	53
1.9. Summary	54
1.10. Aim of the thesis	55
1.11. Scope of the thesis	56
Chapter 2.....	60
Instruments, Dataset and Methodology	60
2.1. Introduction	60
2.2. Meteor Radar	61
2.2.1. Meteors	61
2.2.2. Working principle	62
2.2.3. The RADAR equation	64
2.2.4. Calculation of wind	66
2.3. Reanalysis Data	71
2.3.1. Purpose	72
2.3.2. Classification	72

2.3.3. Working scheme.....	74
2.3.4. ERA5	77
2.3.5. MERRA2	78
2.3.6. NCEP-DOE Reanalysis 2	78
2.4. Time series analysis.....	79
2.4.1. Fourier transform	79
2.4.2. Lomb-Scargle Periodogram	80
2.4.3. Wavelet transform	81
2.4.4. Least-square fitting.....	83
2.5. Summary	83
Chapter 3.....	85
Impact of SSW on Low-latitude Planetary Wave Dynamics	85
3.1. Introduction	85
3.2. Results	86
3.2.1. Background Dynamical Conditions	86
3.2.2. Low-latitude Traveling Planetary Wave Dynamics	89
3.2.3. Direction of Zonal Propagation	94
3.2.4. Stationary Planetary wave activity	99
3.2.5. Meridional air-mass mixing and instability	101
3.2.6. Q6DW and Q16DW Flux Propagation and Source	102
3.3. Discussion.....	105
3.4. Summary and Conclusions	110
Chapter 4.....	112
Tidal Variability during 2019 minor SSW.....	112
4.1. Introduction	112
4.2. Results	113
4.2.1. Background state	113
4.2.2. Local tidal variability	115
4.2.3. Variability of global tidal modes.....	118
4.2.4. Tidal sources.....	120
4.3. Discussion.....	128
4.4. Summary and Conclusions	130
Chapter 5.....	132
Middle Atmospheric Circulation during SSW	132
5.1. Introduction	132
5.2. Analysis method.....	133

5.3. Results	138
5.3.1. Altitude-time variability of the zonal mean background conditions	138
5.3.2. Latitude-time distribution of zonal mean flow	140
5.3.3. Distribution of winds in the SH at various phases of SSW	145
5.4. Discussion.....	154
5.5. Summary and conclusions	156
Chapter 6.....	158
Nonlinear Interaction between Planetary-scale waves	158
6.1. Introduction	158
6.2. Results and Discussions.....	159
6.2.1. ST and PW spectra in the specular meteor radar winds	160
6.2.2. Temporal evolution of interacting wave components	162
6.2.3. Dominant zonal wavenumber components of primary waves	165
6.2.4. Possible forcing mechanism of 20dw0.....	167
6.3. Summary and conclusions	170
Chapter 7.....	172
Enhancement of zonally Symmetric Semidiurnal Tide during SSW	172
7.1. Introduction	172
7.2. Results and Discussions.....	173
7.2.1. Enhancement in S0 during SSW	173
7.2.2. S0 component in Ozone variability	176
7.2.3. Vertical profile of S0 at maximum.....	179
7.3. Summary and Conclusions	182
Chapter 8.....	184
Interhemispheric coupling via Q2DW modulation during pre-warming	184
8.1. Introduction	184
8.2. Results and Discussions.....	185
8.2.1. Q2DW activity in the MLT	186
8.2.2. Quasi-16-day modulation in the summer MLT winds	188
8.2.3. Zonal wavenumber diagnosis.....	190
8.2.4. Origin of modulation	192
8.3. Summary and Conclusions	199
Chapter 9.....	200
Summary and Future Plans	200
9.1. Summary	200
9.2. Broader Implication.....	208

9.3. Future Scope	209
References.....	211
List of Publications Included in Thesis.....	230
Publications In Refereed Journals	230
Under preparation	230
List of Publications Outside Thesis.....	231
Publications In Refereed Journals	231
Under Review.....	231

List of Figures

Figure 1. 1. Vertical temperature profile of the Earth's atmosphere over Ahmedabad (23.0° N, 72.5° E) on 19 July 2019 using NRL (Naval Research Laboratory) MSIS (mass spectrometer and incoherent scatter radar) 2.0 model available at https://ccmc.gsfc.nasa.gov/models/NRLMSIS~2.0/	31
Figure 1. 2. Schematic picture of meridional circulation in the middle atmosphere during the solstice (left) and equinox (right) condition.....	34
Figure 1. 3. Schematic of lower and middle atmosphere showing thermal and dynamical structure. The relative temperatures are represented by colours, with red being warmer and dark blue being cooler. The wind directions are also shown with westerly (eastward) and easterly (westward) using solid and dashed lines, respectively. Ray path of gravity waves and planetary waves are also shown along with the circulation in the region (From Meriwether & Gerrard, 2004).....	35
Figure 1. 4. Classification of waves based on the time period, horizontal scale and restoring forces.....	36
Figure 1. 5. An illustration of wave fronts and wave vectors for a two-dimensional wave. The wave fronts are perpendicular to the wave vector. The negative values of phase angle ϕ indicate that these wave fronts passed a stationary observer earlier than the following fronts (Nappo, 2013).	37
Figure 1. 6. Signature of gravity waves in clouds as viewed from the top.	39
Figure 1. 7. Buoyancy oscillation of a disturbed air parcel.	41
Figure 1. 8. Lomb-Scargle periodograms of the hourly zonal and meridional wind at 90 km for the years (a) 2005, (b) 2006, (c) 2007 and (d) 2008 over a Brazilian equatorial station using meteor radar observations (From Guharay et al., 2013).	43
Figure 1. 9. Schematic representation of DW1 (migrating) and DE3 (non-migrating) structures in longitude-time domain. A is the amplitude.	44
Figure 1. 10. Signature of planetary waves in the meandering jet stream (courtesy: NASA GSFC).	46
Figure 1. 11. Conservation of absolute vorticity as air parcel moves along with the flow.....	47

Figure 1. 12. Schematic of wave mean flow interaction resulting in weakening of the polar vortex (courtesy: National Oceanic and Atmospheric Administration (NOAA)).....	50
Figure 1. 13. Time series of (a) temperature (K) at 90° S and 10 hPa and (b) zonal-mean zonal wind (m s^{-1}) at 60° S and 10 hPa, from 1 June to 31 October. Climatological values (blue) from 2002 (green) to 2019 (red) are represented with one standard deviation shown by error bars (From Liu et al., 2022).	52
Figure 1. 14. Illustration of the coupling processes and atmospheric variability present during SSW events. Red ovals represent warming areas, while blue ovals indicate cooling regions (From Pedatella et al., 2018).....	53
Figure 2. 1. The geometry of backscattering for a meteor trail exhibiting specular reflections (From Stober, 2009).	63
Figure 2. 2. Radar echo from a (a) underdense echo and (b) long overdense echo (From Wislez, 1996).	64
Figure 2. 3. The Jones configuration is a common setup employed in specular meteor radars (From Hocking et al., 2001).....	66
Figure 2. 4. Position of i^{th} meteor in a spherical coordinate system.	68
Figure 2. 5. Locations of meteor wind radars (red star) utilized in the thesis.	70
Figure 2. 6. Schematic representation of peak power, average power, pulse length and pulse repetition time of a signal (not drawn to scale).....	70
Figure 2. 7. Data Assimilation Scheme (From Dole, 2008)	74
Figure 2. 8. A graphical depiction of the time and frequency resolutions for Fourier, STFT, and wavelet transforms. It's noticeable that for the wavelet transform, time resolution increases with increasing frequency.....	81
Figure 2. 9. Morlet wavelet function.	82
Figure 3. 1. (a) Difference between the zonal mean temperature and temporal mean of zonal mean temperature ($\text{ZMT} - \text{TMZMT}$) during August-October 2019 (DOY 213 ~ 1 August) and (b) zonal mean zonal wind (ZMU) plotted during the same period at 10 hPa pressure level using ERA5. Altitudinal profiles ($\sim 0\text{-}80$ km) of ($\text{ZMT} - \text{TMZMT}$) are shown at (c) 60°S, (e) 22.7°S (CP latitude) and (g) 7.4°S (CA latitude). Similarly, altitudinal profiles ($\sim 0\text{-}$	

80 km) of ZMU are shown at (d) 60°S, (f) 22.7°S (CP latitude) and (h) 7.4 S (CA latitude). The white bold curves represent zero value in all the plots, and the bold black curve represents a value of 25 K in Figure 3.1a. Region between two vertical lines shows warming period for the present and all the following figures. Please note the change of scale in the colorbars corresponding to each subplot while comparing.....89

Figure 3. 2. Wavelet power spectra at 90 km of (a) U, and (e) V using meteor radar. Wavelet spectra of U at (b) 0.02 hPa, (c) 1 hPa, (d) 10 hPa, and V at (f) 0.02 hPa, (g) 1 hPa, (h) 10 hPa at CP using ERA5. Bold white curves in each plot represent 95% confidence level. Please note the change of scale in the colorbars corresponding to each subplot while comparing. ...90

Figure 3. 3. Similar to Figure 3.2, but shown for CA.91

Figure 3. 4. The meteor radar derived representative amplitude of the (a) Q6DW and (b) Q16DW in U at CP. The same for the (c) Q6DW and (d) Q16DW in U at CA. The same for the (e) Q6DW and (f) Q16DW in V at CP. The same for the (g) Q6DW and (h) Q16DW in V at CA. Please note the change of scale in the colorbars while comparing.....93

Figure 3. 5. Period vs zonal wavenumber spectra in U at (a) 0.02 hPa (b) 1 hPa, (c) 10 hPa and V at (d) 0.02 hPa (e) 1 hPa, (f) 10 hPa at CP latitude (22.7°S) using ERA5. Please note the change of scale in the colorbars corresponding to each subplot while comparing.95

Figure 3. 6. Similar to Figure 3.5, but at CA latitude (7.4°S).96

Figure 3. 7. The representative amplitude of the Q6DWW1 (blue curve) and Q16DWW1 (red curve) using ERA5 U at (a) 0.02 hPa, (b) 1 hPa and (c) 10 hPa at CP latitude (22.7° S). The same at (e) 0.02 hPa, (f) 1 hPa and (h) 10 hPa, but at CA latitude (7.4° S).98

Figure 3. 8. Latitudinal-temporal variation of SPW1 at (a) 0.02 hPa (b) 1 hPa, (c) 10 hPa and SPW2 at (d) 0.02 hPa (e) 1 hPa, (f) 10 hPa estimated using ERA5 U. Please note the change of scale in the colorbars while comparing. 100

Figure 3. 9. Temporal evolution of PV averaged within 35-45°W with latitudes using ERA5 at (a) 1 hPa and (b) 10 hPa in Potential vorticity unit PVU ($1 \text{ PVU} = 10^{-6} \text{ K m}^2 \text{ kg}^{-1} \text{ s}^{-1}$). The blue contour represents negative value of meridional gradient of PV averaged within 35-45°W at (c) 1 hPa and (d) 10 hPa in PVU per degree latitude. Please note the change of scale in the colorbars while comparing. 101

Figure 3. 10. EP flux cross-section of the Q6DW in the meridional plane for prior, during and post warming periods shown for various days. The arrows Indicate the EP flux F. The contour value represents wave driving, D in $\text{ms}^{-1} \text{ day}^{-1}$. The white bold curve represents zero value of D..... 103

Figure 3. 11. Similar to Figure 3.10, but for the Q16DW. 105

Figure 4. 1. (a) Altitudinal profile of difference between the zonal mean temperature at 90° S and 60° S during August-October 2019 (DOY 213 ~ 1 August). (b) Latitudinal profile of the zonal mean zonal wind at 10 hPa during the same period. (c) Latitudinal profile of the difference between zonal mean temperature and the temporal mean of zonal mean temperature at 0.01 hPa. (d) Latitudinal profile of the zonal mean zonal wind at 0.01 hPa. The bold white line represents zero value in the present figure and all the following figures, and the bold black curve represents a value of 20 K in Figure 1a. The vertical black solid line and the dashed line represent the SSW onset date and the PWD, respectively, for the present and all the following figures. Please note the change of scale in the color bars while comparing. 114

Figure 4. 2. Temporal variation in the DT amplitude in ms^{-1} at (a) RO (67.6°S, 68.1°W), (b) KE (54.3°S, 36.5°W), (c) CP (22.7°S, 45°W), and (d) CA (7.4°S, 36.5°W) using V from meteor radar (80-100 km altitude) and MERRA2 (50-75 km altitude). Same for the ST amplitude in ms^{-1} at (e) RO, (f) KE, (g) CP, and (h) CA. Please note the change of scale in the colorbars while comparing. 116

Figure 4. 3. Temporal variation in the DW1 amplitude in ms^{-1} in the mesosphere (50-75 km altitude) at (a) 67.5° S (RO latitude), (b) 54.5° S (KE latitude), (c) 22.5° S (CP latitude) and (d) 7.5° S (CA latitude) estimated using MERRA-2 V. Same for the DE3 amplitude in ms^{-1} at (e) 67.5° S (RO latitude), (f) 54.5° S (KE latitude), (g) 22.5° S (CP latitude) and (h) 7.5° S (CA latitude), and for the SW2 amplitude in ms^{-1} at (i) 67.5° S (RO latitude), (j) 54.5° S (KE latitude), (k) 22.5° S (CP latitude) and (l) 7.5° S (CA latitude). Please note the change of scale in the color bars while comparing. 119

Figure 4. 4. Temporal variation in the zonal mean TPWV (blue curve) in Kg m^{-2} and zonal mean OLR in Wm^{-2} (red curve) at (a) 67.5° S (RO latitude), (b) 54.5° S (KE latitude), (c) 22.5° S (CP latitude) and (d) 7.5° S (CA latitude). Temporal variation in the zonal mean columnar ozone (black curve) in Dobsons and ZMU (averaged over 50-75 km altitude) in ms^{-1} (magenta curve) at (a) 67.5° S (RO latitude), (b) 54.5° S (KE latitude), (c) 22.5° S (CP latitude) and (d) 7.5° S (CA latitude). The thin curve represents the daily value, and the bold curve indicates the moving average. 122

Figure 4. 5. Temporal variation in the composite seasonal mean amplitudes of the DW1 in ms^{-1} in the mesosphere (50-75 km altitude) at (a) 67.5° S (RO latitude), (b) 54.5° S (KE latitude), (c) 22.5° S (CP latitude) and (d) 7.5° S (CA latitude) estimated using meridional wind data from MERRA-2. Same for the DE3 in ms^{-1} at (e) 67.5° S (RO latitude), (f) 54.5° S (KE latitude), (g) 22.5° S (CP latitude) and (h) 7.5° S (CA latitude), and for the SW2 in ms^{-1} at (i) 67.5° S (RO latitude), (j) 54.5° S (KE latitude), (k) 22.5° S (CP latitude) and (l) 7.5° S (CA latitude). Please note the change of scale in the colorbars while comparing. 124

Figure 4. 6. Temporal variation in the DW1d in ms^{-1} in the mesosphere (50-75 km altitude) at (a) 67.5° S (RO latitude), (b) 54.5° S (KE latitude), (c) 22.5° S (CP latitude) and (d) 7.5° S (CA latitude) estimated from MERRA-2 data. Same for the DE3d in ms^{-1} at (e) 67.5° S (RO latitude), (f) 54.5° S (KE latitude), (g) 22.5° S (CP latitude) and (h) 7.5° S (CA latitude), and for the SW2d amplitude in ms^{-1} at (i) 67.5° S (RO latitude), (j) 54.5° S (KE latitude), (k) 22.5° S (CP latitude) and (l) 7.5° S (CA latitude). The white contour line denotes statistically significant region. Please note the change of scale in the color bars while comparing..... 126

Figure 4. 7. Latitudinal-temporal variation of the (a) DW1, (b) DE3, and (c) SW2 amplitude at 0.01 hPa estimated from the MERRA-2 data set. Same for the (d) DW1d, (e) DE3d, and (f) SW2d at 0.01 hPa. The white contour line denotes statistically significant region. Please note the change of scale in the color bars while comparing. 127

Figure 5. 1. Altitude-time section of the (a) ZMU, (b) SMS, and (c) dZMU at 60° S during the 2002 observational days. (d, e, f) represent the same as (a, b, c), but during 2019. The solid vertical line represents the peak warming day (PWD). 133

Figure 5. 2. The latitude time section of (a) ZMU, (b) SMS, and (c) dZMU at 10 hPa during the 2002 observational days. (d, e, f) represent the same as (a, b, c), but during the 2019 observational days..... 136

Figure 5. 3. Altitude-time section of the zonal mean zonal wind at 60° S during (a) 2001, (b) 2002, (c) 2003, (d) 2018, (e) 2019, and (f) 2020 observational days (1 August – 31 October). The white curve represents the zero-wind value..... 138

Figure 5. 4. Time-height section of (a) T at 90°S, (e) ZMU at 60°S, and (i) ZMV at 60°S during 2002 observational days and (b) T at 90°S, (f) ZMU at 60°S, and (j) ZMV at 60°S during 2019 observational days. Same for (c) dT at 90°S, (g) dZMU at 60°S, and (k) dZMV at 60°S during 2002 observational days and (d) dT at 90°S, (h) dZMU at 60°S, and (l) dZMV at 60°S during 2019 observational days. The solid vertical line represents the PWD. The white bold curves represent zero values in all the plots. Please note the change of scale in the colorbars corresponding to each subplot while comparing. Also, consider the difference in colorbar used to represent actual and deseasoned variability. 139

Figure 5. 5. Latitude-time section of ZMU at (a) 10 hPa, (e) 1 hPa, and (i) 0.01 hPa and dZMU at (c) 10 hPa, (g) 1 hPa, and (k) 0.01 hPa °S during 2002 observational days. Same during 2019 observational days for ZMU at (b) 10 hPa, (f) 1 hPa, and (j) 0.01 hPa and dZMU at (d) 10 hPa, (h) 1 hPa, and (l) 0.01 hPa °S. Please note the change of scale in the colorbars corresponding to each subplot while comparing. Also, consider the difference in colorbar used to represent actual and deseasoned variability..... 142

Figure 5. 6. Latitude-time section of ZMV at (a) 10 hPa, (e) 1 hPa, and (i) 0.01 hPa and dZMV at (c) 10 hPa, (g) 1 hPa, and (k) 0.01 hPa °S during 2002 observational days. Same

during 2019 observational days for ZMV at (b) 10 hPa, (f) 1 hPa, and (j) 0.01 hPa and dZMV at (d) 10 hPa, (h) 1 hPa, and (l) 0.01 hPa °S. Please note the change of scale in the colorbars corresponding to each subplot while comparing. Also, consider the difference in colorbar used to represent actual and deseasoned variability..... 144

Figure 5. 7. Latitude-longitude section of U at 10 hPa during 2002 (a) Pre-W (e) W, and (i) Post-W and dU during 2002 (c) Pre-W (g) W, and (k) Post-W at 10 hPa. Same for U during 2019 (b) Pre-W (f) W, and (j) Post-W and dU during 2019 (d) Pre-W (h) W, and (l) Post-W. Please note the change of scale in the colorbars corresponding to each subplot while comparing. Also, consider the difference in colorbar used to represent actual and deseasoned variability. 146

Figure 5. 8. Same as Figure 5.7, but at 1 hPa. 148

Figure 5. 9. Same as Figure 5.8, but at 0.01 hPa. 149

Figure 5. 10. Latitude-longitude section of V at 10 hPa during 2002 (a) Pre-W (e) W, and (i) Post-W and dV during 2002 (c) Pre-W (g) W, and (k) Post-W at 10 hPa. Same for V during 2019 (b) Pre-W (f) W, and (j) Post-W and dV during 2019 (d) Pre-W (h) W, and (l) Post-W. Please note the change of scale in the colorbars corresponding to each subplot while comparing. Also, consider the difference in colorbar used to represent actual and deseasoned variability. 150

Figure 5. 11. Same as Figure 5.10, but at 1 hPa..... 152

Figure 5. 12. Same as Figure 5.10, but at 0.01 hPa. 153

Figure 6. 1. (a) Evolutionary Lomb Scargle amplitude spectra (semidiurnal tide period range) and (b) wavelet amplitude spectra (PW period range) of the U at 90 km, and (c) wavelet spectra of the instantaneous ST amplitude at 90 km using meteor radar observations at Andenes (69.3° N, 16° E), from 1 November 2008 until 31 March 2009. (d, e, f) represent the same as (a, b, c) but during 2012-13. The solid vertical line represents the PWD and the thin tilted line represents the cone of influence (COI). The white curve in the wavelet spectra represents the 95 % confidence level. Please note the change of scale in the colorbars corresponding to each subplot while comparing. The letters N, D, J, F, and M in the x axis denote November, December, January, February, and March; the subsequent number indicates the day of the given month. 161

Figure 6. 2. (a) Altitude profile of the wavelet amplitude spectra of the 20dw, ELS amplitude spectra of (b) LSB, (c) ST, and (d) USB using meteor radar derived U at Andenes (69.3° N, 16° E) during the 2008-09 observational days. (e, f, g, h) represents the same as (a, b, c, d) but during 2012-13. Please note the change of scale in the colorbars for each subplot while comparing. 163

Figure 6. 3. Schematic of the energy exchange among the nonlinear interacting triad (20dw, LSB, ST or 20dw, ST, USB) following the Manley Rowe energy exchange relationship (Details of the relationship can be found in He et al., 2017). 164

Figure 6. 4. Period versus zonal wavenumber spectra in the period range (a) 4 to 30 days, and (b) 11 to 13 hours utilizing U at 0.01 hPa, 70 ° N from MERRA-2 during 2008-09 SSW. (c) Temporal variability of different zonal wavenumber components of (c) 20dw, and (d) ST during the 2008-09 observational days. (e, f, g, h) represent the same as (a, b, c, d) but during 2012-13. Positive/ Negative zonal wavenumber denotes westward/ eastward propagation, and zero zonal wavenumber represents the zonally symmetric component. 165

Figure 6. 5. Theoretical ZWN-period spectra of nonlinear interaction between primary waves SW2 and 20dw0, producing USB and LSB as secondary waves corresponding to ZWN 2. 167

Figure 6. 6. Altitude profile of (a) 20dw0, and (b) SPW2 at 70° N during the 2008-09 observational days. (c, d) represent the same as (a, b), but during 2012-13. Please note the change of scale in the colorbars for each subplot while comparing. 168

Figure 6. 7. Latitude profile at 10 hPa of (a) SPW2, (b) 20dwW2, (c) 20dw0, and (d) 20dwW4 during the 2008-09 observational days. (e, f, g, h) represent the same as (a, b, c, d), but during 2012-13..... 169

Figure 7. 1. Temporal variability of different ZWN components of (a) ST, (b) SPW utilizing U at 10 hPa, 70°N from MERRA 2 during 2008–2009 observational days (1 December-28 February). (c) Latitude profile at 10 hPa of S0. (d) Altitude profile at 70°N of S0. (e–h) The same as (a–d), but during 2012–2013. (i–l) The same as (a–d), but during 2002 (1 August-31 October). The solid vertical line represents the peak warming day. Please note the change of scale in the colorbars corresponding to each subplot while comparing. The letters D, J, F, and A, S, O on the x axis denote December, January, February, and August, September, October; the subsequent number indicates the day of the given month. 175

Figure 7. 2. The latitude profile of (a) TCO and (b) S0 (in TCO) in Dobson unit (DU) during 2008-09 observational days from MERRA-2 data. (c, d) represent the same as (a, b) but during 2012-13. (e, f) represent the same as (a,b), but during 2002. 177

Figure 7. 3. Latitude-time variability of zonal mean total columnar ozone (TCO) in Dobson unit (DU) from 1 January 2000 to 31 December 2003. The letters F, M, A, and N on the x-axis denote February, March, August, and November; the subsequent number indicates day of the month. 177

Figure 7. 4. The latitudinal profile of the zonal mean U (red curve) and amplitudes of the S0 in the TCO (blue curve) and U (green curve) on 23 September 2002. 179

Figure 7. 5. (a) Height-latitude section of S0 amplitude in ms^{-1} , and (b) variation in SW2 (red curve), SPW2 (blue curve), and S0 (green curve) phase as a function of height at 70°N on 20 January 2009. (c, d) represent the same as (a, b) but on 6 January 2013. The straight line in (b, d) represents the linear fit. Coefficient of determination, R^2 , is highlighted with the same colour in plots b and d. 180

Figure 7. 6. Height-latitude section of S0 amplitude in ms^{-1} on 23 September 2002. 181

Figure 8. 1. ELS amplitude spectra (4-80 hours period range) in ms^{-1} using SMR-derived V at (a) 81 km, CA (7.4°S , 36.5°W), (b) 80 km, WU (30.5°N , 114.6°E), and (c) 80 km, JU (54.6°N , 13.4°E) from 1 June to 3 October 2019. Altitude profile of the Q2DW amplitude in ms^{-1} at (d) CA, (e) WU, and (f) JU. The solid black vertical line represents the peak warming day. The letters JN, JL, A, and S in the x-axis denote June, July, August, and September; the subsequent number indicates the day of the given month. 186

Figure 8. 2. Wavelet amplitude spectra (PW period range) of (a) V, and (b) Q2DW amplitude at 80 km during the observational days, and the vertical evolution (80-98 km) of dominant waves during July in the period range (c) 4-80 hours, and (d) 4-20 days using SMR-derived V at WU. (e, f, g, h) represents the same as (a, b, c, d) but at JU. The white curve in the wavelet spectra represents the 95% confidence level. 189

Figure 8. 3. Wavelet amplitude spectra (PW period range) of the U at 80 km using SMR observations at (a) WU (30.5°N , 114.6°E) and (b) JU (54.6°N , 13.4°E). 190

Figure 8. 4. (a) Period (4-70 hours) versus ZWN amplitude spectra at 80 km (0.01 hPa), 7.5°S during July. Height-time section of the (b) Q2DWW3, (c) Q2DWW4, and (d) Q16DWE2 amplitude at the equator. Temporal variability of (e) W3 in the 4-70 hours period. Latitude-time section of (f) Q2DWW3, (g) Q2DWW4, and (h) Q16DWE2 at 50 km. Temporal variability of (i) W4 in the 4-70 hours period. (j, k, l) represent the same as (f, g, h) but at 74 km. ERA5 V and U data are utilized for Q2DW and Q16DW analysis, respectively. Dashed vertical lines mark the peak amplitude day of Q2DWW3 (black) and Q2DWW4 (magenta). 191

Figure 8. 5. The temporal variability of (a) Eastward traveling ZWN 6 (E6), (b) E5, (c) E4, (d) E3, (e) E2, (f) E1, (g) Zonally symmetric (ZWN=0), (h) Westward traveling ZWN 1 (W1), (i) W2, (j) W3, (k) W4, (l) W5, and (m) W6 in the period range 4-20 days at 50 km altitude at the equator using ERA5 U. Note the dominance of eastward traveling Q16DW corresponding to ZWN 2 (Q16DWE2) in (e). 193

Figure 8. 6. Temporal variability of Q16DW at (a) WU and (b) JU in the altitude range of 0-80 km using ERA5 U. (c, d) represent the same as (a, b) but using ERA5 V. 194

Figure 8. 7. Temporal variability of Q16DWE2 (red), Q2DWW4 (magenta), and Q2DWW3 (black) at an altitude of 50 km at the equator. The red dashed vertical line denotes the peak Q16DWE2 amplitude on 19 June. Similarly, magenta and black dashed vertical lines mark the initial peak amplitude of Q2DWW4 and Q2DWW3, respectively, on 3 July and 9 July. 196

Figure 8. 8. Height latitude section of (a) Q16DWE2 amplitude on 19 June using ERA5 U, (b) Q2DWW4 amplitude on 3 July, and (c) Q2DWW3 amplitude on 9 July using ERA5 V. (d,e,f) represent the same as (a,b,c) but of the ZMU on 19 June, 3 July, and 9 July, respectively. The magenta curve represents the critical layer of the Q16DWE2 (a,d), Q2DWW4 (b,e), and Q2DWW3 (c,f). The black curve represents the zero ZMU line. 197

Figure 9. 1. A simplified diagram depicting global middle atmospheric dynamics during SSW events, influenced by planetary-scale waves, as explored in this thesis. 208

List of Abbreviations

20dw	20-day-wave
20dw0	Zonally symmetric 20dw
AAP	Active Active Passive
AMIP	Atmospheric Model Intercomparison Project
AN	Andenes
APV	Absolute PV
CA	São João do Cariri
CFW	Combined Fourier-Wavelet
COI	Cone of influence
CP	Cachoeira Paulista
D0	Zonally Symmetric (ZWN 0) DT
DE3	DT Eastward traveling ZWN 3
DE3d	Deseasoned DE3
DOY	Day of Year
DT	Diurnal tide
DW1	DT Westward traveling ZWN 1
DW1d	Deseasoned DW1
dT	Deseasoned T
dU	Deseasoned U
dV	Deaseasoned V
dZMU	Deaseasoned ZMU
dZMV	Deaseasoned ZMV
ECMWF	European Center for Medium-Range Weather Forecast
ELS	Evolutionary Lomb-Scargle
ERA5	The fifth major global reanalysis produced by ECMWF
EUV	Extreme ultraviolet
FFT	Fast Fourier Transform
GW	Gravity wave

JMA	Japan Meteorological Agency
JU	Juliusruh
KE	King Edward Point
LS	Lomb-Scargle
LSB	Lower sideband
LT	Lower Thermosphere
MERRA-2	Modern-Era Retrospective analysis for Research and Applications version 2
MLT	Mesosphere and lower thermosphere
MRR	Manley Rowe Relationship
MSIS	Mass spectrometer and incoherent scatter radar
NASA	National Aeronautics and Space Administration
NCEP	National Center for Environmental Prediction
NH	Northern Hemisphere
NIR	Near-infrared
NOAA	National Oceanic and Atmospheric Administration
NRL	Naval Research Laboratory
OLR	Outgoing longwave radiation
PPA	Passive Passive Active
PRF	Pulse repetition frequency
PV	Potential vorticity
PW	Planetary wave
PWD	Peak warming day
Q2DW	Quasi-2-day wave
Q2DWW3	Quasi-2-day wave westward traveling ZWN 3
Q2DWW4	Quasi-2-day wave westward traveling ZWN 4
Q3DW	Quasi-3-day wave
Q6DW	Quasi-6-day wave
Q20DW	Quasi-20-day wave
Q6DWW1	Q6DW westward traveling ZWN 1
Q16DWW1	Q16DW westward traveling ZWN 1

Q16DWE2	Q16DW eastward traveling ZWN 2
Q10DW	Quasi-10-day wave
Q16DW	Quasi-16-day wave
RADAR	Radio Detection And Ranging
RO	Rothera
S0	Zonally Symmetric (ZWN 0) ST
SH	Southern hemisphere
SMS	Seasonal mean state
SMR	Specular meteor radar
SPW	Stationary planetary wave
SPW1	SPW ZWN 1
SPW2	SPW ZWN 2
SSW	Sudden stratospheric warming
ST	Semidiurnal
STFT	Short Time Fourier Transform
SW1	ST Westward traveling ZWN 1
SW2	ST Westward traveling ZWN 2
SW2d	Deseasoned SW2
T	Temperature
TCO	Total columnar ozone
TPW	Traveling planetary wave
TPWV	Total precipitable water vapor
U	Zonal wind
USB	Upper sideband
UV	Ultraviolet
V	Meridional wind
W3	Westward traveling ZWN3
W4	Westward traveling ZWN4
WU	Wuhan
ZMT	Zonal mean T

ZMU	Zonal mean U
ZMV	Zonal mean V
ZWN	Zonal wavenumber

Chapter 1

Introduction

1.1.The Earth's atmosphere

The Earth's atmosphere is essential for the existence of life on Earth as it contains oxygen. Based on the vertical temperature profile, the neutral atmosphere is generally divided into four regions, namely, the troposphere (0-15 km), stratosphere (15-50 km), mesosphere (50-90 km), and the thermosphere (90-400 km), as shown in Figure 1.1. The altitude range mentioned are typical values that may change with latitude, seasons, and other factors. The regions are separated by distinct zero temperature gradient points (turning points) called tropopause, stratopause, and mesopause.

In the troposphere, the temperature decreases with an average lapse rate of 6.5 K/km due to the decrease in the infrared radiation away from the Earth's surface. This region is generally unstable due to colder air over warmer air and, hence, convectively active. The tropopause is lowest over poles (approx. 8 km) and highest over the equator (approx. 16 km). The troposphere's thickness is determined by the amount of solar radiation and vertical mixing. Hence, the tropopause is lower over areas where the air is cold than where it is warm. The troposphere is highly variable on short time scales and is strongly affected by the Earth's surface properties such as orography, landform, vegetation, snow cover of land surface, ice cover of ocean and lake surfaces, etc.

The layer immediately above the troposphere is known as the stratosphere. As altitude increases, the temperature rise in the stratosphere is mainly caused by ozone molecules absorbing solar UV radiation. Approximately 90% of atmospheric ozone is found in the stratosphere, with the highest density of ozone occurring at around 25 km. Furthermore, stratospheric ozone shields the Earth's surface from damaging UV rays, contributes significantly to heating the stratosphere through solar radiation, and exhibits considerable chemical activity. Because of the positive temperature gradient, the stratosphere remains highly stable.

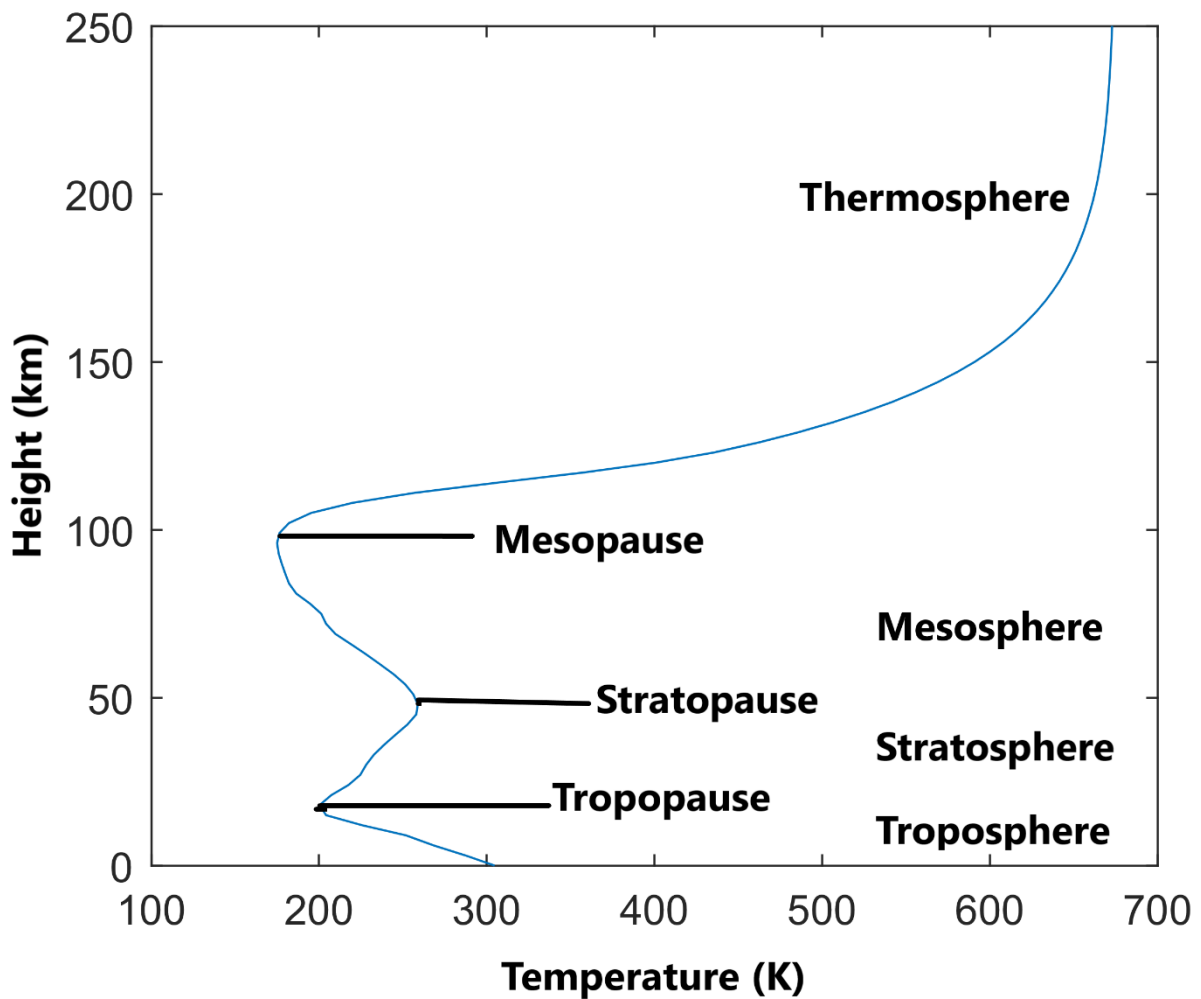


Figure 1. 1. Vertical temperature profile of the Earth's atmosphere over Ahmedabad (23.0° N, 72.5° E) on 19 July 2019 using NRL (Naval Research Laboratory) MSIS (mass spectrometer and incoherent scatter radar) 2.0 model available at <https://ccmc.gsfc.nasa.gov/models/NRLMSIS~2.0/>.

Above stratopause, the temperature decreases with height and reaches a minimum value of 180 K (approx) near the mesopause due to radiative cooling at infrared wavelengths, primarily by CO₂. In the mesosphere, dynamical forcing, due to waves and tides, becomes significant due to dissipation in the presence of inherent instability supported by negative temperature gradient.

The mesopause is the coldest part in the Earth's atmosphere. Above the mesopause, the temperature increases rapidly with height with a sharp gradient. The peak temperature attained in the thermosphere is solar activity-dependent and can vary from 600-2000 K. The

high temperature of the thermosphere (90-400 km) is caused by the absorption of solar extreme UV (EUV) radiation by molecular oxygen at 100-150 km, the absorption of ionizing EUV radiation above 150 km, dissipation of gravity and tidal waves, joule heating due to ionospheric electric current, etc. The thermosphere is nearly isothermal because of its high heat conductivity due to electrons.

Above the thermosphere lies the exosphere, where the collision between neutral particles is infrequent. The exosphere extends roughly from 600 km to interplanetary space. The ionosphere (roughly 60-500 km) is the part of the thermosphere where the medium is partially ionized with sufficient plasma density to affect radio wave propagation. The region above the ionosphere is filled with cold plasma density, mainly H^+ ions, called the plasmasphere. The magnetosphere is the space surrounding the Earth where the geomagnetic field dominates over the interplanetary magnetic field. The magnetopause is the outer terminator of the geomagnetic field at about 10 earth radii in the sunward direction.

The Earth's atmosphere can be classified into homosphere and heterosphere based on the composition. The homosphere is the atmosphere below 100 km, where the constituents are well mixed by eddy processes. The heterosphere lies above 100 km, where molecular diffusion dominates over mixing, and the constituents distribute according to their respective masses. The turbopause is the transition region between the homosphere and the heterosphere.

Nitrogen and oxygen are the major species of the Earth's middle and lower atmosphere. Together, they constitute 99% of the total by mass and volume, as shown in Table 1.1. The third most abundant gas is argon, which includes about 0.93% of the dry atmosphere's mass. The remaining mass (less than $\sim 0.1\%$) is due to atmospheric trace species. The major trace species are water vapour, carbon dioxide, and ozone. Water vapor in the lower atmosphere varies significantly due to evaporation, condensation, and sublimation processes, whereas concentrations in the stratosphere remain very low. Among the major trace species, carbon dioxide is well mixed in most of the middle atmosphere. The most important trace species in the middle atmosphere is ozone, the concentration of which reaches a maximum at around 25 km. The major radiative heat input for the middle atmosphere is due to absorption of the solar UV radiation by ozone.

Constituent Gas	By Mass (%)	By Volume (%)	Molecular Weight
Nitrogen (N ₂)	75.51	78.09	28.02
Oxygen (O ₂)	23.14	20.95	32.00
Argon (Ar)	1.3	0.93	39.94
Carbon dioxide (CO ₂)	0.05	0.03	44.01
Neon (Ne)	1.2×10^{-3}	1.8×10^{-3}	20.18
Helium (He)	8.0×10^{-4}	5.2×10^{-4}	4.00
Krypton (Kr)	2.9×10^{-4}	1.0×10^{-4}	83.7
Hydrogen (H ₂)	0.35×10^{-5}	5.0×10^{-5}	2.02
Xenon (X)	3.6×10^{-5}	0.8×10^{-5}	131.3
Ozone (O ₃)	0.17×10^{-5}	0.1×10^{-5}	48.0
Radon (Rn)	-	6.0×10^{-18}	222.0

Table 1.1 Atmospheric composition with their abundance.

1.2.Middle atmosphere dynamics

The stratosphere, mesosphere, and lower thermosphere are termed the middle atmosphere (approx. 10-110 km). The mesosphere and lower thermosphere (MLT) represents the upper part of the middle atmosphere and lies between 60 and 110 km in altitude. The middle atmosphere was referred to as the ignorosphere due to lack of study as it is too high for aircraft and balloon measurements and too low for in-situ satellite measurements. Thus, owing to the lack of direct measurements, the middle atmosphere remains one of the least explored regions of the Earth's atmosphere. Method of chaff release onboard sounding rocket provides a limited in-situ measurement of the mesosphere because it is location specific and can only give a snapshot of the atmospheric parameters. However remote sensing techniques such as lidar, meteor radar, medium frequency radars, incoherent scatter radars, mesosphere stratosphere troposphere radars, airglow instruments and satellite-based instruments provide regular observations of the middle atmosphere. Several authors have reviewed middle atmospheric dynamics in recent times. Shepherd (2000) describes some critical phenomena in the middle atmosphere. Becker (2012) delineates the processes that control the mean circulation in the middle atmosphere. The processes involved interaction between the lower middle and upper atmospheres was explained by Smith (2012). In addition to the effect on the

neutral dynamics of the middle atmosphere, the waves propagating upward into the ionosphere cause plasma irregularities (Hines, 1960).

Figure 1.2 shows the schematic picture of the meridional circulation in the middle atmosphere during solstice and equinox conditions. The meridional circulation is dominated by air mass motion from the summer polar to the winter polar region during solstice. In the stratosphere at the solstice, the horizontal temperature and pressure differences between the warm summer hemisphere and the cold winter hemisphere result in pole-to-pole gradients. As the air parcel moves from summer to winter poles, they will experience Coriolis force, which acts at a right angle to air parcel movement. A geostrophic wind arises when the Coriolis force balances the pressure gradient force. Since the Coriolis force deflects the air sample towards the right in the northern hemisphere (NH) and towards the left in the southern hemisphere (SH), the mean winds blow westward in the summer and eastward in the winter hemisphere. During the equinox, there is a poleward movement of air parcel from the warm equator, resulting in westerlies in both the hemisphere (Figure 1.2).

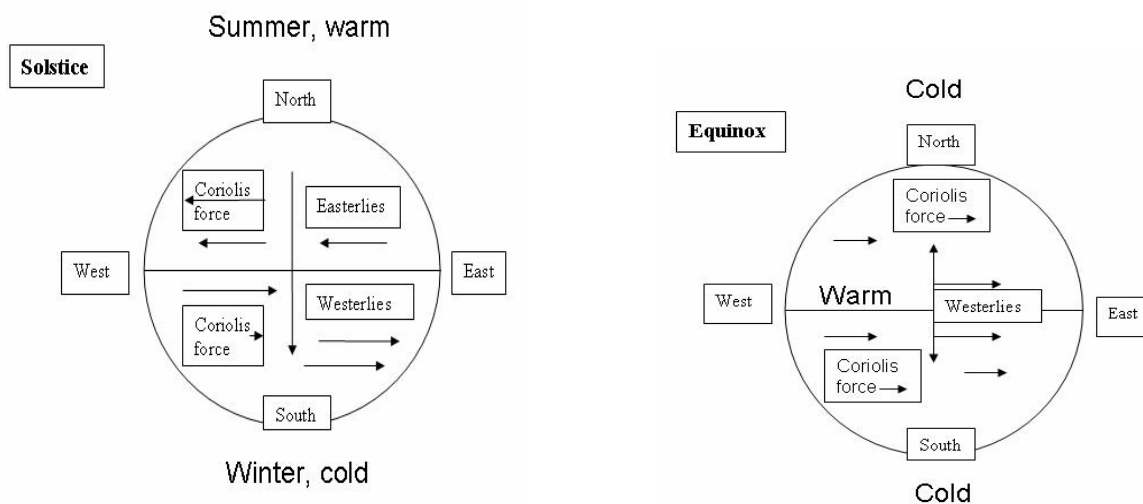


Figure 1. 2. Schematic picture of meridional circulation in the middle atmosphere during the solstice (left) and equinox (right) condition.

Figure 1.3 represents a schematic of the globally averaged lower and middle-atmosphere thermal and dynamical structure during solstices (Andrews et al. 1987). In addition to large-scale winds, as shown in Figure 1.2, the dynamics of the middle atmosphere are also dominated by atmospheric waves (Gravity waves, tides, and planetary waves) that are

generated in the lower atmosphere and propagate upward. The amplitude of these waves increases with altitude to conserve energy as density decreases with height. While propagating, these waves interact with background winds and other waves and dissipate their energy and momentum, contributing to the region's wind and temperature variability. Thus, atmospheric waves play a crucial role in transporting energy and momentum from one part to another part of the atmosphere (Forbes, 1995). The prevalent westerlies in the winter hemisphere support predominantly westward flowing atmospheric waves such as planetary waves and tides, resulting in higher wave activity than in the summer hemisphere. Hence, there is a higher chance of heating due to wave dissipation in the MLT region of the winter hemisphere, which explains the occurrence of cold summer polar mesopause and warm winter polar mesopause, as depicted in Figure 1.3.

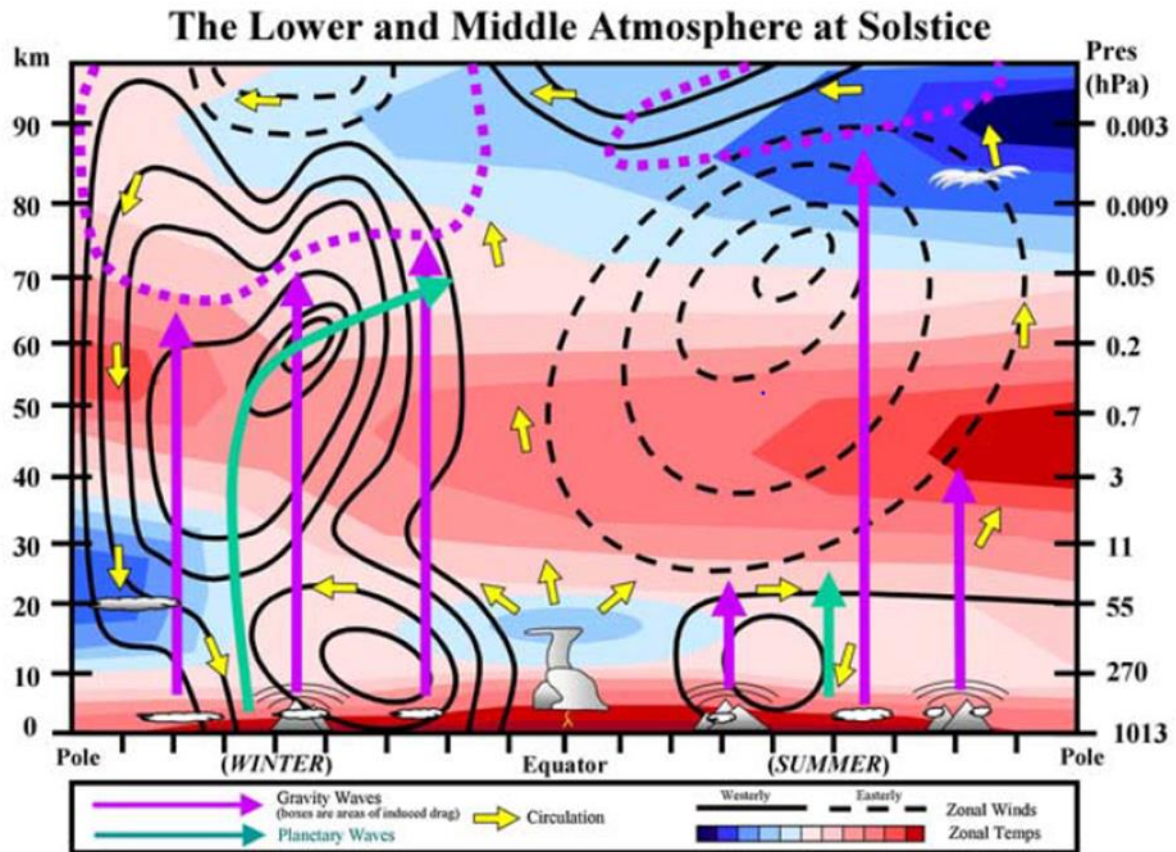


Figure 1. 3. Schematic of lower and middle atmosphere showing thermal and dynamical structure. The relative temperatures are represented by colours, with red being warmer and dark blue being cooler. The wind directions are also shown with westerly (eastward) and easterly (westward) using solid and dashed lines, respectively. Ray path of gravity waves and

planetary waves are also shown along with the circulation in the region (From Meriwether & Gerrard, 2004).

Thus, the middle atmosphere observations improved our understanding of temperature structure and general circulation. It is believed that the external forcing in the middle atmosphere from below comes from breaking atmospheric waves. Such dynamical forcing due to wave drag affects the jet associated with the pole-to-pole temperature gradient in the middle atmosphere (Andrews et al., 1987). Hence, it is essential to understand the role of wave dynamics in the middle atmosphere for a better understanding of the processes involved in various atmospheric regions. The different waves which are pertinent in the middle atmosphere are described in the next section.

1.3. Atmospheric waves

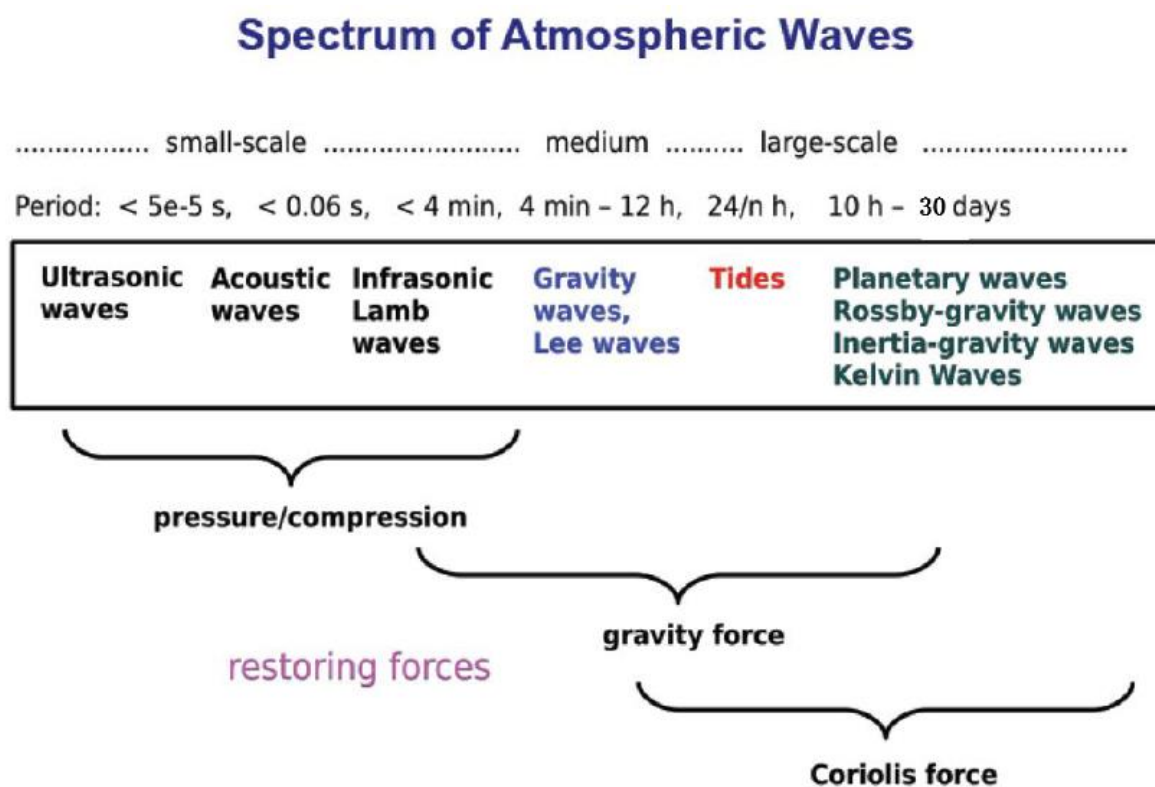


Figure 1. 4. Classification of waves based on the time period, horizontal scale and restoring forces.

Atmospheric waves are perturbations on a steady, slowly changing background, and such disturbances propagate in space and time. Wave motions are feasible in the presence of a

restoring force that opposes disturbances and, in a process, supports local oscillations in the field of atmospheric variables such as pressure, temperature, chemical species, or wind velocity. The atmosphere is capable of sustaining a large number of wave phenomena. Based on excitation source, restoring force, time period, and horizontal scale, atmospheric waves can be classified in various ways (Beer, 1974). A more detailed classification of these waves and their probable restoring forces are summarized in Figure 1.4. In general, atmospheric waves play a crucial role in the coupling processes between different layers of the Earth's atmosphere by transporting energy and momentum from the source region to the dissipation region.

The restoring forces for sound waves, gravity waves (GW), and planetary waves (PW) are the compression force, buoyancy force, and meridional variation of the Coriolis force, respectively. Restoring forces may also combine to generate mixed waves, such as inertia-gravity waves, mixed acoustic-gravity waves, and mixed Rossby-gravity waves (Lin, 2007).

1.4. Wave parameters

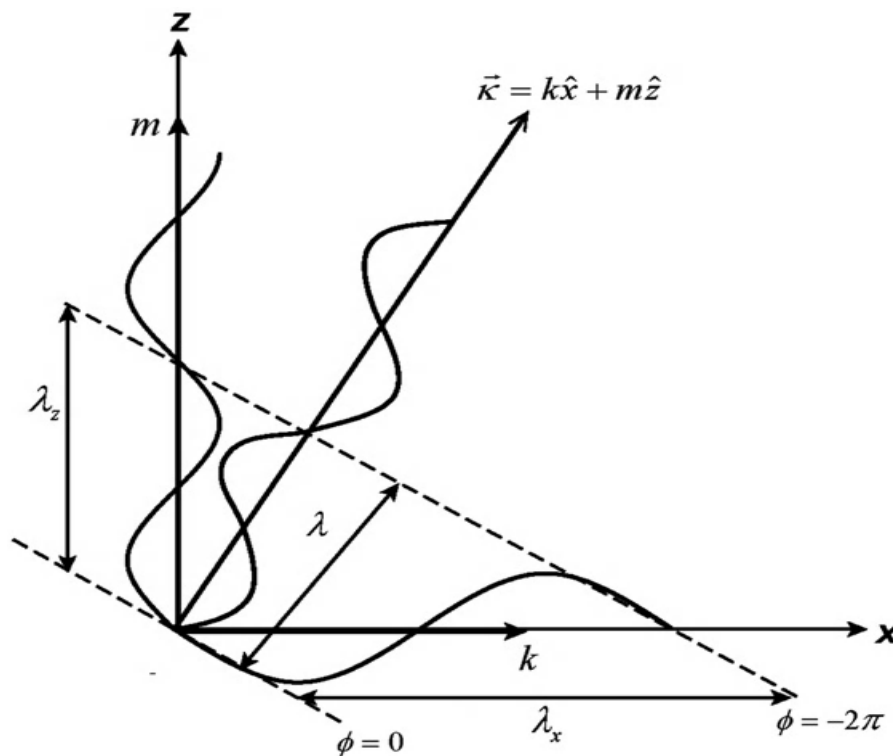


Figure 1. 5. An illustration of wave fronts and wave vectors for a two-dimensional wave. The wave fronts are perpendicular to the wave vector. The negative values of phase angle ϕ

indicate that these wave fronts passed a stationary observer earlier than the following fronts (Nappo, 2013).

The following equation can represent a wave propagating in x and z-direction.

$$\Psi(x,z,t) = Ae^{i(kx+mz-\omega t)} \quad (1.1)$$

where, A is the amplitude of the wave; t is the time; $\omega \left(= \frac{2\pi}{T} \right)$ is the wave frequency; T is the time period of oscillation; k and m are the horizontal and vertical wavenumber respectively. Wave phase is often referred to as phase angle i.e. $\varphi = \vec{K} \cdot \vec{r} - \omega t$; where wave vector $\vec{K} = k\hat{x} + m\hat{z}$; $\vec{r} = x\hat{x} + z\hat{z}$; $k = \frac{2\pi}{\lambda_x}$ and $m = \frac{2\pi}{\lambda_z}$. λ_x and λ_z are horizontal and vertical wavelength, respectively. Wavefronts or phase lines are lines of constant phase. Wave vector \vec{K} is perpendicular to the wave fronts.

The phase speed, c , of the wave is the speed at which a point of constant phase moves in the direction of the travelling wave.

The phase speed in the x direction is

$$c_x = \frac{\omega}{k} \quad (1.2)$$

Similarly, the phase speed in the z direction is

$$c_z = \frac{\omega}{m} \quad (1.3)$$

Wave phase speed is given as,

$$c = \frac{\omega}{K} = \frac{\omega}{\sqrt{k^2 + m^2}} \quad (1.4)$$

Wave phase speed c is a scalar quantity and is related to c_x and c_z as follows,

$$\frac{1}{c^2} = \frac{1}{c_x^2} + \frac{1}{c_z^2} \quad (1.5)$$

Since wave phase speed is a function of wavenumber and wave frequency, and, therefore, for a given period T , long waves will travel faster than short waves, leading to wave dispersion.

The group velocity is a vector quantity which is a measure of the rate at which the energy of the disturbance propagates and is given by the relation,

$$\vec{c}_g = c_{gx} \hat{x} + c_{gz} \hat{z} = \frac{\partial \omega}{\partial k} \hat{x} + \frac{\partial \omega}{\partial m} \hat{z} \quad (1.6)$$

As discussed above, different kinds of waves are present in the atmosphere. The three most dominant types of waves, namely, GWs, tides, and PWs, which are essential in the middle atmosphere, will be introduced in the following section.

1.5. Internal Gravity Waves

When an air parcel is initially disturbed vertically upward from hydrostatic equilibrium, it moves into a region of lower atmospheric density. Because of gravity, it comes back to its equilibrium. The air sample overshoots and moves to a denser atmosphere below the equilibrium point; now, it experiences a buoyant force from the surrounding air and again rises upward. This causes an oscillation of the parcel with a frequency known as the Brunt-Väisälä frequency. A stable stratified atmosphere can sustain such oscillation.

GW may propagate vertically as well as horizontally. For example, Figure 1.6 shows a beautiful signature of GW in clouds. GW's horizontal wavelength ranges from 10 to 1000 km, and vertical wavelength ranges from 1 to 30 km.



Figure 1. 6. *Signature of gravity waves in clouds as viewed from the top.*

The generation, propagation, and dissipation of GW depend on the thermal and wind structure of the surrounding atmosphere (Matsuoka et al., 2020). GWs are mostly generated through tropospheric activities: airflow over mountains (orographic waves), convection, wind shear, and sudden disturbances (e.g., thunder, cyclone, volcanic eruption). As the GWs propagate upward, their amplitudes (A) grow non-linearly to compensate for the exponential decrease in the atmospheric density (ρ) to conserve the energy ($E = \frac{1}{2} \rho A^2$). The GW propagation depends on the wind distribution and thermal structure, which varies markedly with season and the static stability (e.g., Brasseur & Solomon, 2006). The concept of potential temperature and static stability is explained below.

The potential temperature (θ) of a fluid parcel at pressure P and temperature T refers to the temperature the parcel would reach if it were adiabatically brought to a standard reference pressure P_s (1000 mb).

$$\theta = T \left(\frac{P_s}{P} \right)^k \quad (1.7)$$

where $k = \frac{R}{C_p} = 0.286$; R ($= 288 \text{ J kg}^{-1} \text{ K}^{-1}$) is the specific gas constant for dry air; C_p ($= 1005 \text{ J kg}^{-1} \text{ K}^{-1}$) is the specific heat capacity of dry air at constant pressure.

Using ideal gas law and hydrostatic approximation, the lapse rate of temperature and the rate of change of θ with height is related by the following equation.

$$\frac{1}{\theta} \frac{\partial \theta}{\partial z} = \frac{1}{T} (\Gamma_d - \Gamma) \quad (1.8)$$

Where, Γ_d ($= \frac{g}{C_p}$) is the dry adiabatic lapse rate of the parcel, and Γ ($= -\frac{dT}{dz}$) is the atmospheric lapse rate.

1.5.1. Brunt-Väisälä frequency and static stability

Consider an atmosphere at rest and an air parcel of mass m_p in equilibrium with its environment at height z_o as shown in Figure 1.7.

Let the parcel be displaced a small distance z' upward from z_o . The equation of motion is as follows:

Inertia force = restoring force (combined role of gravity and buoyancy force)

$$m_p \frac{d^2 z'}{dt^2} = -g(m_p - m_a) \quad (1.9)$$

Mass of air parcel: $m_p = \rho_p V_p = \frac{P V_p}{R T_p}$; Mass of displaced air: $m_a = \rho_a V_p = \frac{P V_p}{R T_a}$. (using ideal gas law, $P = \rho RT$)

We assumed the pressure within the air sample as equal to environmental pressure.

Substituting the value of m_p and m_a , equation (1.9) becomes:

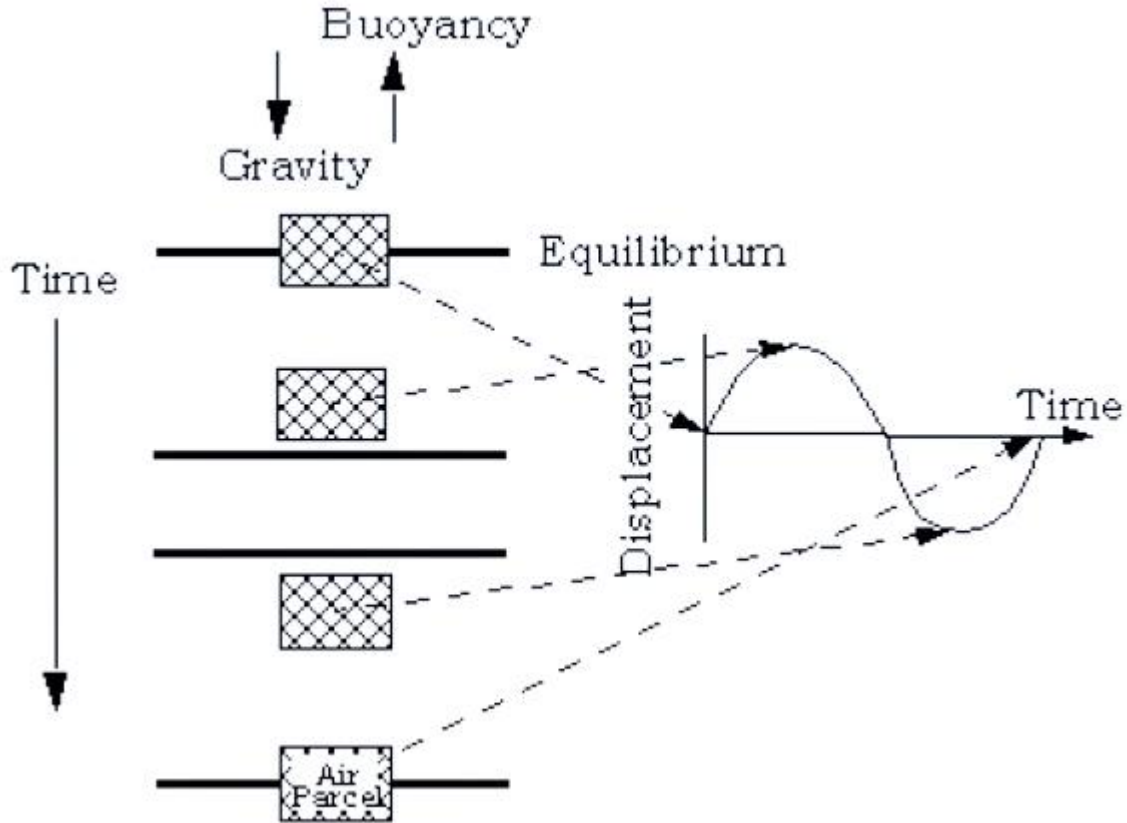


Figure 1. 7. Buoyancy oscillation of a disturbed air parcel.

$$\frac{d^2 z'}{dt^2} = -g \frac{\rho_p - \rho_a}{\rho_p} = -g \frac{T_a - T_p}{T_p} \quad (1.10)$$

Taylor expansion of T_a and T_p leads to the equation in z' :

$$\frac{d^2 z'}{dt^2} = -\frac{g}{T} (\Gamma_d - \Gamma) z' = -N^2 z' \quad (1.11)$$

The solution of z' for $N^2 > 0$ is as follow:

$$z' = A e^{iNt} + B e^{-iNt} \quad (1.12)$$

Where N is the Brunt-Väisälä frequency and is given by the following formulae:

$$N^2 = \frac{g}{\theta} \frac{\partial \theta}{\partial z} = \frac{g}{T} (\Gamma_d - \Gamma)$$

Solution given in (1.12) is valid for $N^2 > 0$, i.e. $\frac{\partial \theta}{\partial z} > 0$ (convectively stable).

If $\frac{\partial \theta}{\partial z} < 0$, solution of z' becomes:

$$z' = A e^{-Nt} + B e^{Nt} \quad (1.13)$$

Solution B represents unbounded growth of air parcel's vertical displacement, i.e. convectively unstable.

$\frac{\partial \theta}{\partial z} = 0$, signifies convectively neutral condition.

If an air parcel is displaced at an angle α to the vertical, the parcel executes a simple harmonic motion at the frequency:

$$v = N \cos \alpha \quad (1.14)$$

The range of allowed frequencies of the GWs follows the condition, Coriolis frequency ($f = 2 \Omega \sin \varphi$; φ is the latitude) \leq frequency of GW \leq Buoyancy frequency N .

1.6. Atmospheric tides

Atmospheric tides are large-scale global oscillations of the atmosphere primarily excited due to the absorption of solar near-infrared (NIR) radiation by water vapour in the troposphere, absorption of UV radiation by ozone in the stratosphere, and, in the thermosphere, molecular oxygen and nitrogen (120-170 km) contribute in heating (Chapman & Lindzen, 1970). In addition, latent heat release due to convective activity provides heating in the troposphere (Hagan et al., 2007). Additionally, the gravitational pull exerted by the moon generates lunar atmospheric tides, which are generally weaker than solar thermal tides but are found to exhibit significant amplitude at times, e. g., sudden stratospheric warming (Zhang & Forbes, 2014).

In the local (solar) time frame, the heating may be represented as:

$$\text{Heating} = Q_0 + \sum_{n=1}^N A_n \cos(n\omega t - \varphi) \quad (1.15)$$

Q_0 is the mean heating component, $\omega \left(= \frac{2\pi}{T} \right)$ is the wave frequency, t is the local time and φ is the phase. At any given height, the day-night variation in the absorbed radiation due to differential heating gives rise to periods which are integral subharmonics of a solar day: 24 hours, 12 hours, 8 hours, and so on, which are referred to as the diurnal tide ($n=1$), semidiurnal tide ($n=2$), terdiurnal tide ($n=3$), respectively. Such waves have a horizontal wavelength of several thousand km and a vertical wavelength ranging from a few km to tens of km. Tides can

be identified from oscillations of atmospheric parameters such as temperature, atmospheric winds, and pressure variables (Chapman & Lindzen, 1970). The density of the Earth's atmosphere decreases exponentially with height; thus, the amplitude of the tide increases exponentially as the tide ascends to conserve energy. Hence, at greater heights in the mesosphere, the tidal amplitude attains a significantly large value, eventually controlling the MLT dynamics. Figure 1.3 shows the significant amplitude of diurnal, semidiurnal, and terdiurnal tides in the MLT horizontal winds.

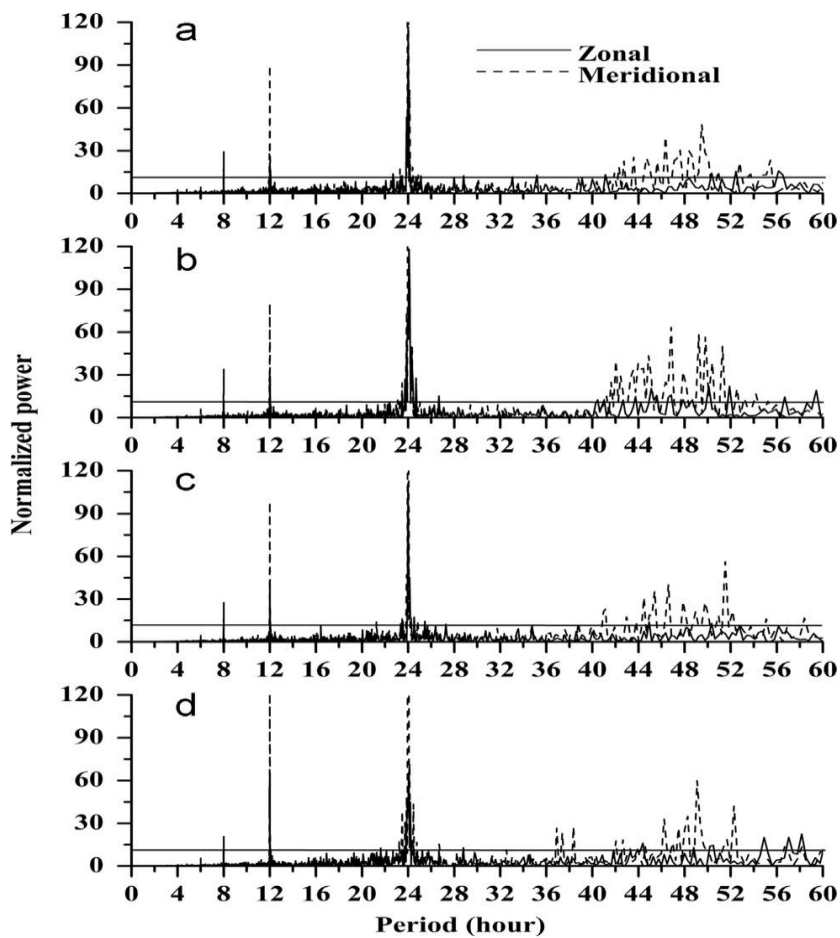


Figure 1. 8. Lomb-Scargle periodograms of the hourly zonal and meridional wind at 90 km for the years (a) 2005, (b) 2006, (c) 2007 and (d) 2008 over a Brazilian equatorial station using meteor radar observations (From Guharay et al., 2013).

In 2D longitude-time domain, the tidal amplitude corresponding to different zonal wavenumbers is represented by the following wave equation.

$$A_{n,s} \cos[2\pi (n \frac{t}{24} + s \frac{\lambda}{360}) - \varphi_{n,s}] \quad (1.16)$$

where $n = 1, 2, 3$ denotes diurnal, semidiurnal and terdiurnal components, $A_{n,s}$ is the wave's amplitude, t is the universal time and $\varphi_{n,s}$ is the wave's phase. The periodicity in longitude λ is given by the zonal wavenumber s . We use the abbreviation DWs/DEs to denote a westward/eastward propagating diurnal tide, respectively. In the case of semidiurnal and terdiurnal tide, 'D' in the above-mentioned abbreviations is replaced by 'S' and 'T', respectively. The positive, negative, and zero s values correspond to westward, eastward propagating, and zonally symmetric component, respectively. Based on the propagation direction with respect to the Sun, atmospheric tides can be further classified into migrating and non-migrating components.

Figure 1.9 shows the schematic surface of DW1 and DE3 in longitude-time domain.

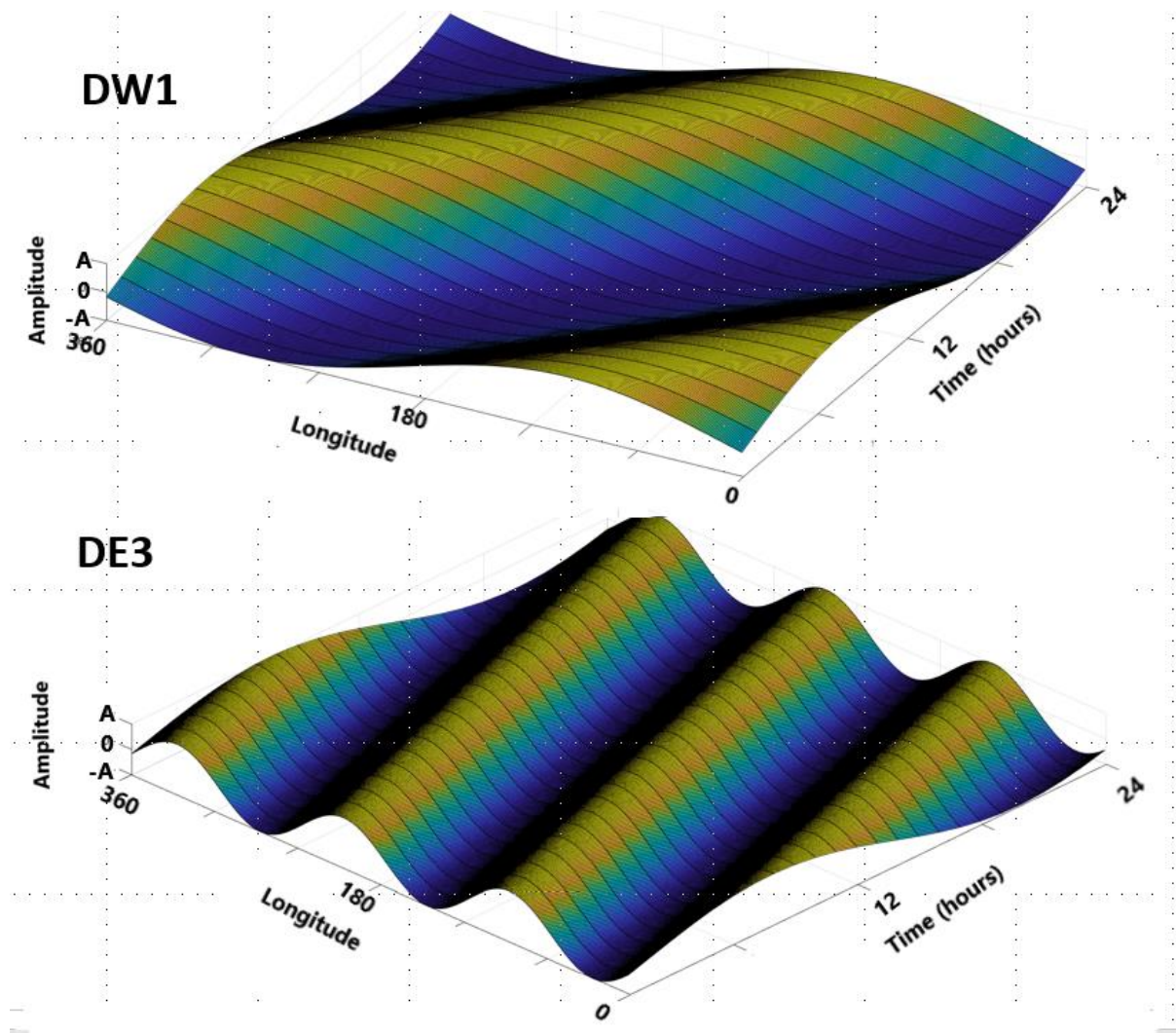


Figure 1. 9. Schematic representation of DW1 (migrating) and DE3 (non-migrating) structures in longitude-time domain. A is the amplitude.

Classical tidal theory, extensively discussed by Chapman and Lindzen (1970), offers essential insights into tidal characteristics within the lower and middle atmosphere. Equation (1.16) can be simplified further into a single equation, separable into its latitude and altitude components. The latitudinal component is represented by Laplace's tidal equation, which is solved using an orthogonal set of eigenfunctions known as Hough modes, with associated eigenvalues termed equivalent depths. A comprehensive explanation of Hough modes and the equivalent depths associated with global tidal modes is available in Oberheide et al. (2015).

1.6.1. Migrating tides

Migrating solar tides are synchronized with the apparent movement of the Sun and travel westward. Therefore, the zonal phase speed of the migrating tides equals the Earth's rotation speed ($n=s$). The primary source of migrating solar tides is the absorption of radiation by an atmosphere that is invariant along its longitude. Owing to the rotation of the Earth, this absorption is periodic in time, as seen by a ground-based observer. The resultant heating gives rise to migrating tides. In general, the DW1 and SW2 are the dominant migrating tides in the middle atmosphere (e.g., Forbes & Garrett, 1978).

1.6.2. Non-migrating tides

Non-migrating tides do not follow the Sun's motion and propagate eastward or westward or maintain zonal symmetry (i.e., $n \neq s$). These are generated by the difference in longitudinal variation in topography, ozone and water vapour concentration, and, alternate rate of latent heat release due to deep convection mainly in the equator, tide-tide nonlinear interaction and the nonlinear interaction between tides and planetary waves (e.g., Xu et al., 2014; Truskowski et al., 2014). Few examples of non-migrating tides are DE3, SW1, S0, and D0.

1.7. Planetary waves

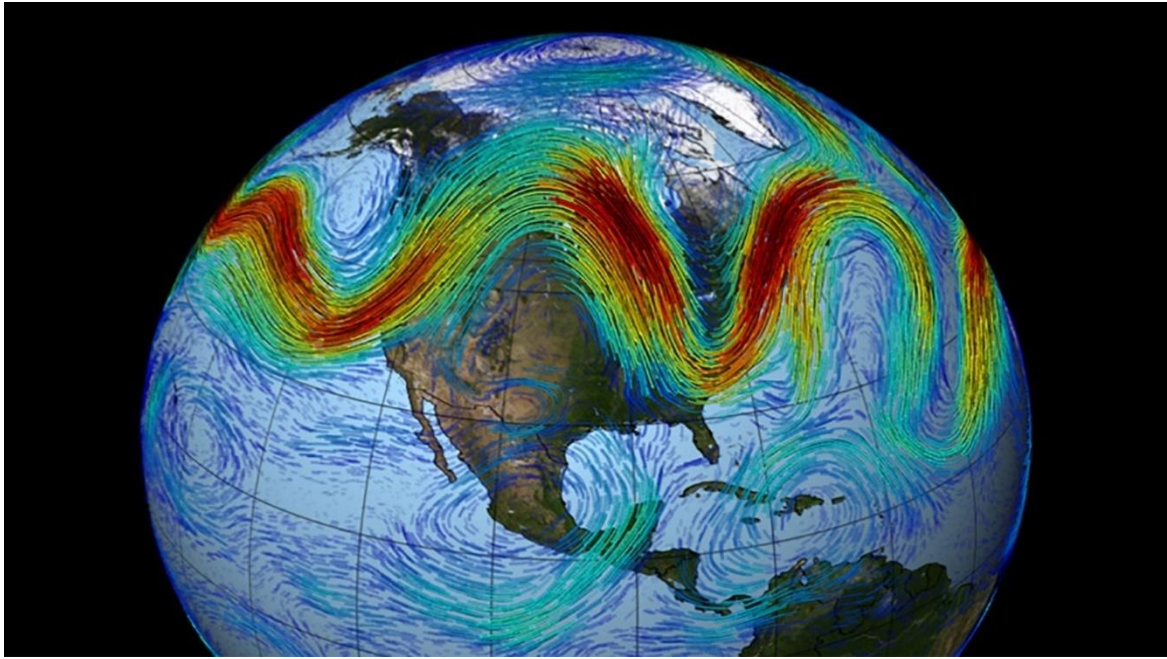


Figure 1. 10. Signature of planetary waves in the meandering jet stream (courtesy: NASA GSFC).

PWs are large-scale oscillations in the atmosphere that oscillate with the horizontal scales comparable to the Earth's circumference at any latitude. The horizontal propagation of PW can either be traveling eastwards/westwards or remain zonally symmetric with respect to the background zonal flow. Stationary PW (SPW) are forced modes, excited and maintained in the troposphere by topographic features such as mountain ranges and land/ocean heating differences. Traveling PW (TPW) are normal modes, generally have periods similar to the natural resonances of the atmosphere. The normal modes have periods that include 2-day, 5, 10, and 16-day waves.

PW is often called as Rossby wave and are generated due to airflow over mountain ranges, land-sea heating contrast, and barotropic/baroclinic instability of the wind jet. The latitudinal gradient of the Coriolis force, in conjunction with the pressure gradient force, acts as the restoring force to conserve the total angular momentum, resulting in PWs. These waves show westward phase propagation with respect to mean flow and are strongly dispersive. PWs are dominant mainly at middle- and high latitudes, although they exist at lower latitudes as well. In the middle atmosphere, similar to GWs and tides, PWs can attain large amplitudes. The vertical propagation depends on zonal flow and is governed by the wave-mean flow interactions. The majority of the traveling PW are westward propagating; therefore, they can

propagate up through the eastward winds of the winter stratosphere, ascend out of the troposphere, and reach the MLT region. However, during summer, their vertical propagation is restricted by westward winds of the summer stratosphere (e.g., Charney and Drazin, 1961). As will be described later, PW activity can cause large scale atmospheric disturbances, e. g., sudden stratospheric warmings (SSW) when it weakens/breaks down the polar vortex during winter. The distribution of continents and topography of the NH produces more PW activity than in the SH.

1.7.1. Phase speed of planetary waves

PWs are essential for large-scale atmospheric processes. PWs owe their existence to the variation of the Coriolis parameter with latitude, known as the β effect (Rossby et al., 1939).

$$\beta = \frac{\partial f}{\partial y} \quad (1.17)$$

y is along longitude.

PWs can be understood from absolute vorticity conservation by considering a closed chain of fluid parcels initially aligned along a circle of latitude. Absolute vorticity (η) is the sum of planetary vorticity (f) and relative vorticity (ζ).

$$\eta = f + \zeta \quad (1.18)$$

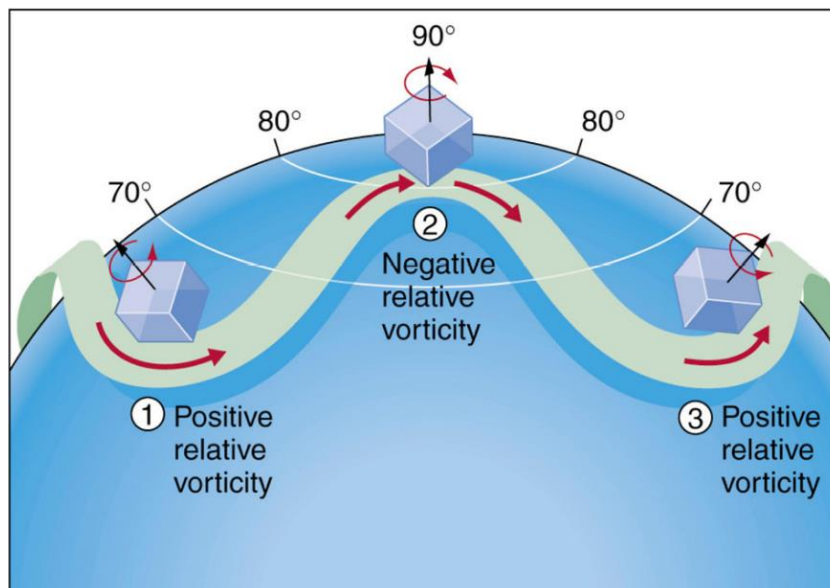


Figure 1. 11. Conservation of absolute vorticity as air parcel moves along with the flow.

Vorticity is the measure of the local spinning motion of the flow. It consists of a vector that denotes the local axis of rotation and the local magnitude of the Earth's rotation rate. Cyclonic rotation (anticlockwise) denotes positive vorticity, and anticyclonic rotation (clockwise) denotes negative vorticity. Relative vorticity ζ is the local spinning motion, excluding the rotation of the Earth.

$$\vec{\zeta} = \hat{k} \cdot (\vec{\nabla} \times \vec{u}) = \frac{\partial v}{\partial x} - \frac{\partial u}{\partial y} \quad (1.19)$$

Planetary vorticity f is the contribution to the angular momentum resulting from the Earth's rotation.

$$f = 2 \Omega \sin \varphi \quad (1.20)$$

where, $\Omega (= 7.29 \times 10^{-5} \text{ rad s}^{-1})$ is the angular speed of Earth's rotation and φ is the latitude. f increases as one moves towards the pole from the equator in the NH and in the SH, the f value becomes more negative away from the equator. Solving the horizontal equation of motion and ignoring friction, the conservation law for absolute vorticity is given as follows:

$$\frac{D}{Dt} (f + \zeta) = 0 \quad (1.21)$$

Where, $\frac{D}{Dt} = \frac{\partial}{\partial t} + \vec{u} \cdot \frac{\partial}{\partial x}$, is the convective derivative. This implies that absolute vorticity remains conserved as air parcel moves along with the horizontal wind field. ($\zeta + f = \text{constant}$) (Figure 1.11).

Figure 1.11 shows that at point 1, ζ increases (positive relative vorticity) since f decreases as fluid parcel moves downward to a lower latitude due to initial disturbances to keep the absolute vorticity constant. Similarly, at point 2, ζ decreases as the fluid parcel moves upward to higher latitude to balance the increase in f and hence, moves in a clockwise sense (negative relative vorticity). This continues as Rossby waves meander along a latitude. Assuming $\zeta = 0$ at time t_0 , and let δy is the meridional displacement of a fluid parcel from the original latitude at time t_1 .

$$\begin{aligned} \zeta(t_1) + f(t_1) &= f(t_0) \\ \zeta(t_1) &= f(t_0) - f(t_1) = -\beta \delta y \end{aligned}$$

The chain of parcels is subjected to a sinusoidal meridional displacement, which conserves η . Positive ζ (anticlockwise) for southward displacement and negative ζ (clockwise) for northward displacement to adjust with increasing and decreasing values of f , respectively.

Letting, $\delta y = a \sin[k(x - ct)]$; where a is the maximum northward displacement. Then, for one-dimensional motion, $v = \frac{D(\delta y)}{Dt} = \left(\frac{\partial}{\partial t} + \bar{u} \frac{\partial}{\partial x} \right) \delta y = ka(\bar{u} - c) \cos[k(x - ct)]$.

Assuming meridional variation in zonal velocity to be small, $\zeta = \frac{\partial v}{\partial x} = -k^2 a(\bar{u} - c) \sin[k(x - ct)]$. From the conservation of absolute vorticity, using the expression

$$\zeta(t_1) = -\beta \delta y$$

$$\text{Or, } -k^2 a(\bar{u} - c) \sin[k(x - ct)] = -\beta a \sin[k(x - ct)]$$

Canceling the common terms on both sides and the phase velocity is given as

$$c = \bar{u} - \frac{\beta}{k^2} \quad (1.22)$$

The negative sign in the dispersion relation (equation 1.22) signifies westward propagation with respect to the mean flow. Hence, Rossby waves always propagate westward relative to the mean flow. The meridional gradient of absolute vorticity acts as a restoring force by resisting meridional displacement.

1.8. Sudden Stratospheric Warming

SSW is a dramatic meteorological event in the polar region of the winter hemisphere, in which the stratospheric temperature increases by a few tens of Kelvin within a few days, affecting atmospheric dynamics on a global scale (Andrews et al., 1987). Such a large-scale event is initiated by enhanced PW activities, which causes significant deceleration of the westerlies in the middle atmosphere.

SSW was discovered by Richard Scherhag in radiosonde measured temperature above Berlin, Germany, in January 1951 (Scherhag, 1952). After years of studying SSWs, significant advancements have been achieved in understanding their dynamic nature. However, our comprehension of their impact on both surface weather and the middle and the upper atmosphere remains incomplete.

1.8.1. Generation mechanism

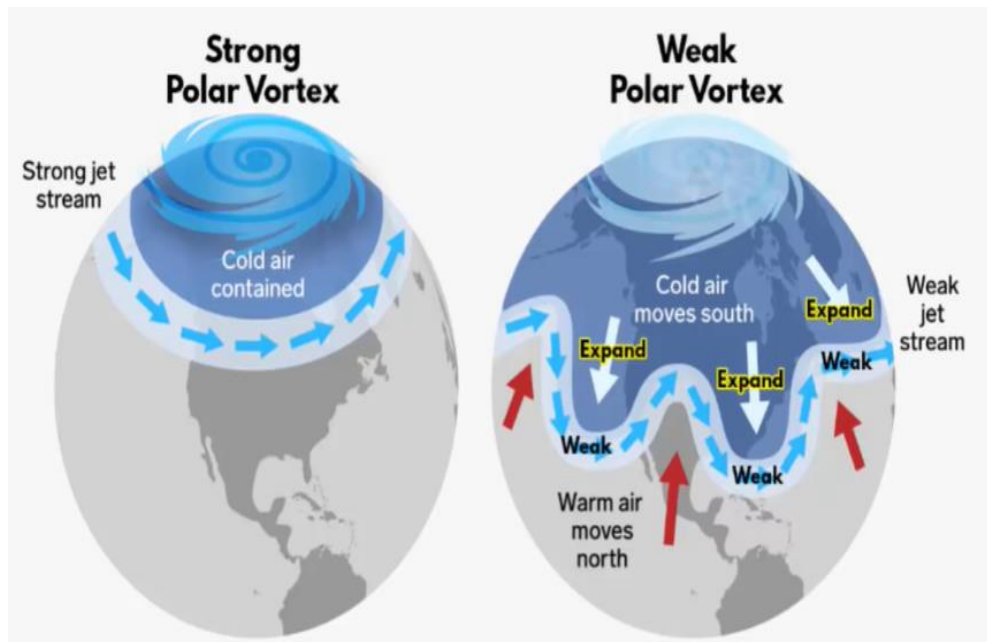


Figure 1. 12. Schematic of wave mean flow interaction resulting in weakening of the polar vortex (courtesy: National Oceanic and Atmospheric Administration (NOAA))

SSW is a fascinating fluid dynamical event that stems from unique wave-mean flow interactions, summarized as follows.

The wintertime stratospheric polar vortex is a large area of low pressure and rotating cold air around Earth's pole, formed primarily through radiative cooling. It is situated around 15 to 50 km high and forms above the tropopause where the Polar cell converges, creating a counterclockwise airflow that keeps cold air near the pole. A strong polar jet stream, situated at the interface of the Ferrel and Polar cell, maintains the stability of the polar vortex by forming a warm or polar front that prevents cold air from moving toward lower latitudes.

PWs are large-scale atmospheric waves that weaken the eastward traveling polar jet stream by inducing their westward momentum, causing it to meander and destabilize the polar vortex. Matsuno (1971) described SSW as a sudden breakdown of the stratospheric polar vortex due to upward propagating planetary waves from the troposphere. As the polar vortex becomes unstable, cold air moves towards lower latitudes, and warm air moves poleward. Further, the weakening of the polar vortex induces a downward circulation in the polar stratosphere, leading to adiabatic heating as the air in the vortex is compressed downward.

In summary, the generation of SSW involves the destabilization of the polar vortex by upward propagating PWs from the troposphere during winter, leading to a significant deceleration in westerlies, accompanied by a sudden and remarkable increase in polar stratospheric temperature.

1.8.2 Classification

According to the World Meteorological Organization, if the stratospheric temperature at the 10 hPa pressure level and poleward of 60°N rises by over 25 K within one week, it is identified as SSW (Labitzke, 1981). Major and Minor warmings are the two main categories of the SSW event. The reversal of the zonal mean temperature poleward of 60° is a signature of both major and minor events, but the reversal of zonal mean zonal wind at 60° latitude and 10 hPa pressure level is characteristic of major warming (Charlton & Polvani, 2007). Figure 1.13. exhibits the warming feature of the 2002 major and 2019 minor SSW in the SH.

Apart from distinguishing major and minor SSW events, there is also a classification based on the morphology of the event. During SSW, the polar vortex may be displaced from the pole or split into two segments. Various methods have been devised to categorize these split and displacement events (e.g., Mitchell et al., 2011; Seviour et al., 2013). The split and displaced type SSW are generally associated with PWs with zonal wavenumber 1 and 2, respectively (Shepherd, 2000).

SSWs is also classified according to their time of occurrence, such as early, mid-winter and final warming. Mid-winter warmings are generally classified into major and minor warmings. In contrast, evolution of the early winter extremes might vary from the late winter extremes. One example is Canadian Warmings, which involve amplifications of the Aleutian High in the lower and middle NH stratosphere. These warmings are the primary type seen in early boreal winter (Labitzke, 1977). Final warmings, on the other hand, mark the seasonal transition of the polar vortex from a westerly to an easterly state (e.g., Thiéblemont et al., 2019).

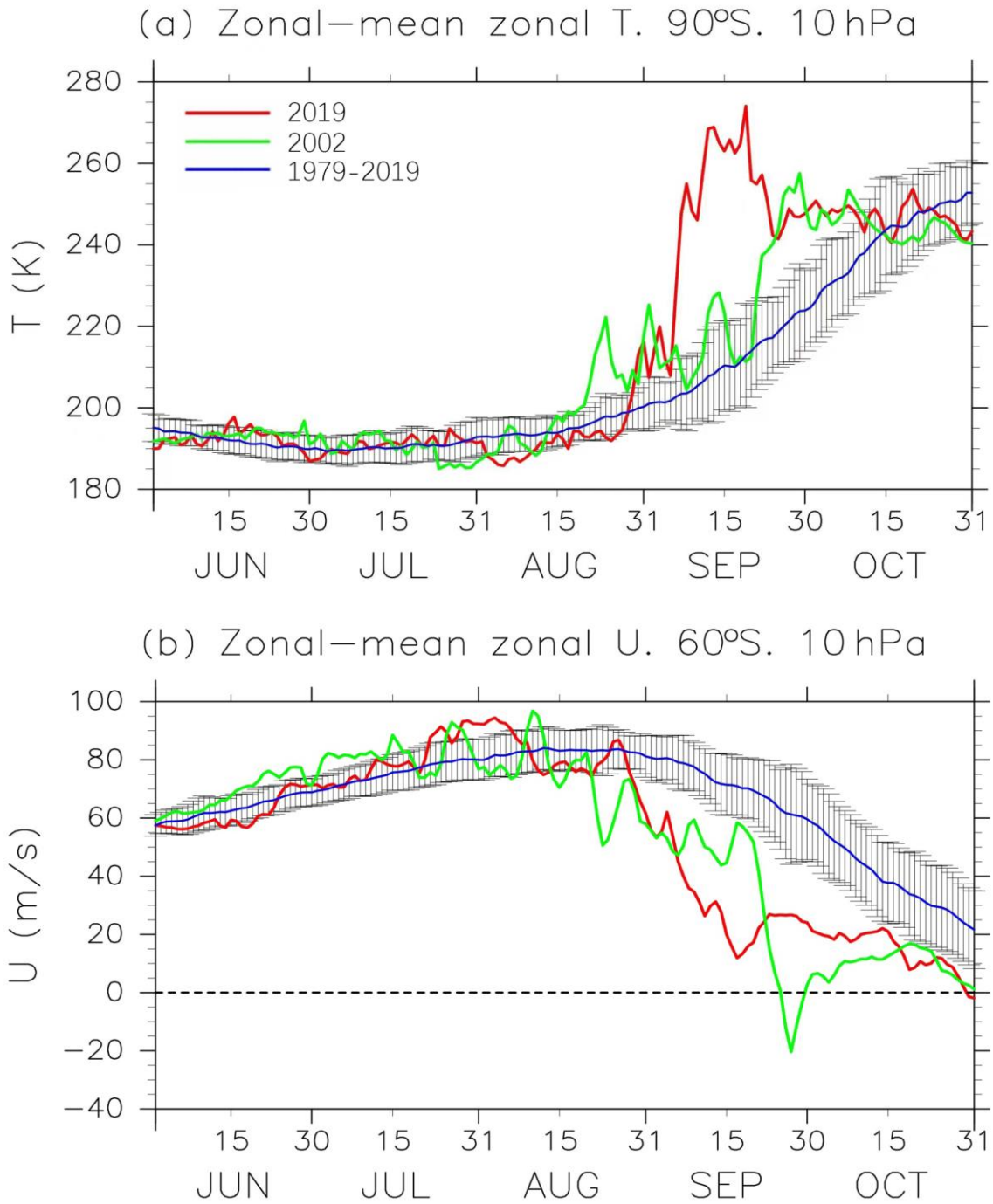


Figure 1. 13. Time series of (a) temperature (K) at 90°S and 10 hPa and (b) zonal-mean zonal wind (m s^{-1}) at 60°S and 10 hPa, from 1 June to 31 October. Climatological values (blue) from 2002 (green) to 2019 (red) are represented with one standard deviation shown by error bars (From Liu et al., 2022).

SSW events are more common in the NH than in the SH. Major SSW events occur approximately once every two years in the NH. So far only one major warming event occurred in September 2002 (Varotsos, 2002), resulting in an ozone hole nearly 40% smaller

than the average observed in the six years prior. Additionally, a minor but notable Antarctic SSW occurred in September 2019. This hemispheric difference in SSW occurrence is primarily attributed to the greater PW activity in the NH due to higher orographic disparities and land-sea variances. Furthermore, stronger polar jets in the SH also contribute to this asymmetry (Newman & Nash, 2005; Rao et al., 2020).

1.8.3. Global Impact

Variability in the stratosphere has a profound influence on surface weather as well as weather hundreds of km above. Studies show that accurately modelling stratospheric dynamics allows forecasters to extend their predictions of surface weather, especially during winter in the NH (Tripathi et al., 2015). One significant stratospheric disturbance is the SSW, in which the stratospheric temperature and wind change remarkably within a few days, further causing extensive changes throughout the Earth's atmosphere. These variations can influence atmospheric chemistry, temperatures, winds, neutral densities, electrons, and electric fields (Figure 1.14.). Such effects span from the surface to the thermosphere and encompass both hemispheres.

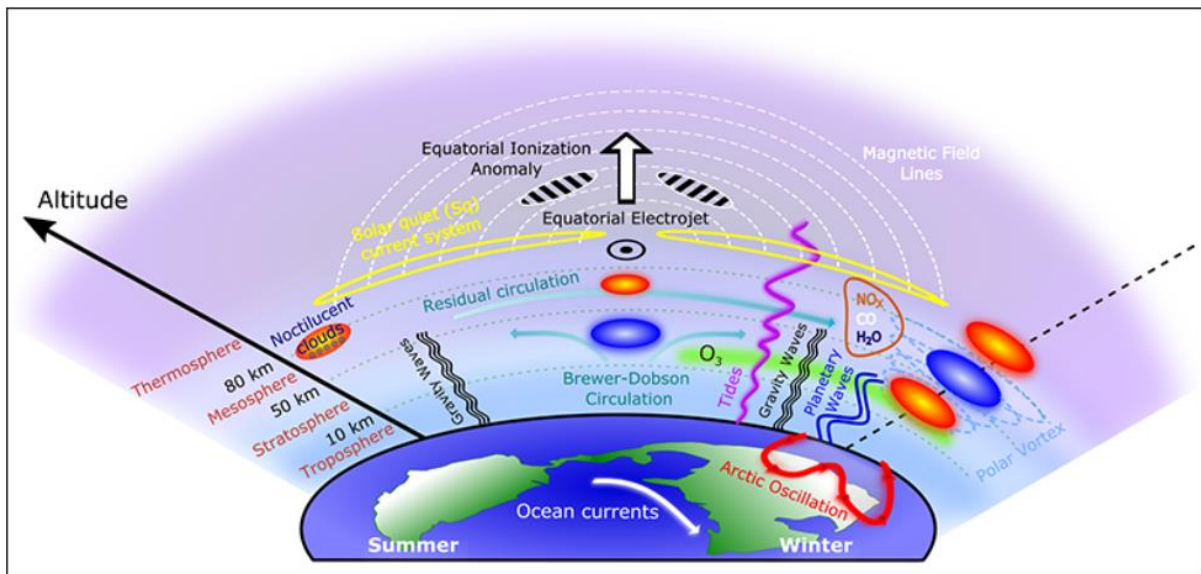


Figure 1. 14. Illustration of the coupling processes and atmospheric variability present during SSW events. Red ovals represent warming areas, while blue ovals indicate cooling regions (From Pedatella et al., 2018).

The impact of downward influence is evident in the equatorward movement of the extratropical cyclonic storm track. This leads to a higher likelihood of storms passing over specific areas of

Europe and an increased probability of cold air outbreaks in North America (Kidston et al., 2015). The impact of SSWs reaches the ocean as well, creating a sustained effect on surface winds that influence the broader patterns of ocean circulation (Reichler et al., 2012).

The stratospheric circulation alterations during SSW influence the spectrum of atmospheric waves that move upward into the mesosphere. This, in turn, causes fluctuations in the MLT temperature and winds. Additionally, changes in middle atmospheric circulation during SSWs impact atmospheric thermal and lunar tides, which are crucial for middle and upper atmospheric variability, showcasing the global impact of SSWs (e.g., Liu et al., 2014; Zhang & Forbes, 2014). The interhemispheric impact of SSWs is observed in the rise of summer polar mesosphere temperature, influencing the occurrence of polar mesospheric clouds (Körnich & Becker, 2010).

The polar vortex breakdown during SSW induces variation in the intensity of the Brewer Dobson circulation, altering the distribution of trace gas species such as stratospheric ozone (Veenus et al., 2023). Moreover, the dramatic changes in stratospheric temperature may alter the chemical reaction rate. Some SSW has also been found to facilitate the downwelling of NO_x-rich air into the stratosphere, which has further implications for ozone chemistry in the upper stratosphere.

SSW impacts the equatorial and low-latitude ionosphere by altering the equatorial ionization anomaly (Chau et al., 2012). Notably, Goncharenko et al. (2012) noted substantial variability in electron density during SSW, comparable in magnitude to a moderate geomagnetic storm. Additionally, tidal changes during SSW influence the equatorial electrojet (Siddiqui et al., 2018). SSW can also decrease thermospheric neutral density, significantly affecting satellite drag (Yamazaki et al., 2015).

Therefore, although SSW is a polar winter stratospheric phenomenon, it can influence the global atmospheric system from the troposphere to the thermosphere and across both hemispheres.

1.9. Summary

Chapter 1 provides a concise overview of Earth's atmospheric layers and thermal structure. It delves into middle atmosphere dynamics, detailing circulation patterns and the role of atmospheric waves in these dynamics. The generation mechanisms and restoring forces of various atmospheric waves like GWs, PWs, and tides are broadly elucidated, underscoring their vital role in coupling different atmospheric layers by transferring energy and momentum from source regions to dissipation regions. The chapter also introduces SSW, a significant disturbance driven by waves in the stratosphere. It discusses its potential generation mechanisms and primary types of warming, emphasizing its global impact. Subsequent chapters then detail and analyze the responses of planetary-scale waves (PWs and tides) and associated middle atmospheric dynamics during SSW.

1.10. Aim of the thesis

The thesis is primarily motivated by the quest to comprehend the dynamic variations within the middle atmosphere during infrequent SSW in the SH, particularly focusing on the less-understood influence on low latitudes. Additionally, it aims to address the intricate and unresolved temporal processes involving non-linear interactions among planetary-scale waves during short-term extreme SSW events, which have received relatively less exploration and urge further investigation for a more thorough understanding of middle atmospheric dynamics. The interhemispheric coupling associated with planetary wave breaking before SSW events also remains inadequately understood.

Therefore, this thesis endeavors to address the following key issues concerning the impact of SSWs on middle atmospheric dynamics:

- Investigation of the characteristics of middle atmospheric PW dynamics at low latitudes in response to rare SH SSW.
- Analyzing the significant variability in global tidal modes in the MLT during the minor yet robust 2019 SH SSW event.
- Examining the impact of rare SH SSWs on middle atmospheric circulation.

- Exploration of the role of nonlinear interaction between planetary-scale waves in atmospheric dynamics and the plausible generation mechanism of significantly enhanced specific tidal components associated with warming events.
- Studying interhemispheric coupling via PW modulation of the quasi-2-day wave during winter characterized by SSW.

Consequently, the focus of my PhD thesis is to fill these knowledge gaps by studying the dynamics of PWs and atmospheric tides during SSWs, with a specific emphasis on the infrequent SH SSWs. My research endeavors to analyze the behavior of these waves and assess their impact on global atmospheric dynamics during SSW events.

1.11. Scope of the thesis

This thesis work is planned to be organized into nine chapters. The prospective content of each chapter is briefly discussed below:

Chapter 1 provides an overview of the Earth's atmospheric layers, with particular emphasis on the middle atmosphere and the role of atmospheric waves therein. It discusses the generation mechanism of SSW, driven by PW, and the existing knowledge of the impact of SSW on the global atmospheric system. The extant gap area regarding understanding the middle atmospheric wave dynamics during SSW is also addressed. The first chapter sets the stage for the subsequent chapters to improve our current understanding of atmospheric wave dynamics in connection with SSW events.

Chapter 2 elaborates on the details of instruments and global reanalysis datasets, i.e., the working principle of meteor radar for horizontal wind observations and the complementing reanalysis datasets. The chapter also describes the various time series spectral analysis techniques, including Lomb Scargle, Fourier transform, wavelet transform, and least-square fitting technique. These methods are crucial for extracting wave dynamical information, such as amplitude, phase, etc., from the observational data and enhancing our understanding of atmospheric dynamics.

Chapter 3 delves into low latitude middle atmospheric PW dynamics during the September 2019 SH SSW using meteor radar wind observations from two low-latitude stations in the Brazilian sector and reanalysis data. Notable findings include the presence of a significant

quasi-16-day wave (Q16DW) prior to the SSW and a sudden burst of a quasi-6-day wave (Q6DW) after the warming event. Substantial mixing of air mass between high and low latitudes during the warming event causes barotropic/baroclinic instability, which seems to excite the Q6DW. The zonal wavenumber 1 PWs (both SPW and TPW) are found to play a significant role in preconditioning the historically rare 2019 event in the SH. Furthermore, the chapter highlights the equatorward propagation of Q6DW and Q16DW waves from mid-latitudes during the warming event. Therefore, chapter 3 provides a detailed insight into the PW-associated low-latitude middle atmospheric dynamics during a minor yet robust SSW event in the SH.

This work has been published in a peer-reviewed journal.

Mitra, G., Guharay, A., Batista, P. P., & Buriti, R. A. (2022). Impact of the September 2019 minor sudden stratospheric warming on the low-latitude middle atmospheric planetary wave dynamics. *Journal of Geophysical Research: Atmospheres*, e2021JD035538.

<https://doi.org/10.1029/2021JD035538>

Chapter 4 focuses on the variability of atmospheric tides in the MLT during the same 2019 SH SSW. Ground-based meteor radar wind observations from various latitudinal stations (high, mid, extratropical, and equatorial) and global reanalysis data are used. The research finds that the polar warming associated with the SSW event affects global tidal behavior. While diurnal and semidiurnal tides at individual sites do not exhibit substantial responses, specific zonal wavenumber components (global tidal modes), including DW1 (migrating diurnal tide), DE3 (non-migrating diurnal tide), and SW2 (migrating semidiurnal tide), exhibit notable and consistent variability during the warming event. The study also explores the influence of seasonal changes in tidal activities, emphasizing the need for further investigations into the complex processes involved in short-term tidal variability associated with warming.

This work has been published in a peer-reviewed journal.

Mitra, G., Guharay, A., Batista, P. P., Buriti, R. A., & T. Moffat-Griffin (2023). Investigation on the MLT tidal variability during September 2019 minor sudden stratospheric warming. *Advances in Space Research*, 71(1), 869-882. <https://doi.org/10.1016/j.asr.2022.08.017>

Chapter 5 uses global reanalysis data to investigate the impact of a major and a minor SH SSW on middle atmospheric circulation. So far, the SH SSWs occur around the spring

equinox, marking the seasonal transition. Hence, the present study focuses on isolating the seasonal transition effect through deseasoning, revealing weaker but distinct dynamical signatures of SSW on middle atmospheric circulation. The study shows easterly forcing around the peak warming day (PWD) during the 2002 event reaching the troposphere, contrasting with the 2019 event. It also suggests a potential tropical precursor to SH SSWs based on deseasoned winds in the stratosphere. The analysis uncovers varying horizontal flow patterns across longitudes, indicating an uneven response of the atmosphere to SSW events globally.

This work has been published in a peer-reviewed journal.

Mitra, G., & Guharay, A. (2024). Impact of sudden stratospheric warming on middle atmospheric circulation in the southern hemisphere: A comparative study. *Journal of Atmospheric and Solar-Terrestrial Physics*, 254, 106173.

<https://doi.org/10.1016/j.jastp.2024.106173>

Chapter 6 focuses on the non-linear interactions of planetary-scale waves during two major boreal SSWs. The study analyzes meteor radar-derived wind observations from a NH high latitude station and identifies evidence of non-linear interactions between the semidiurnal solar tide and the quasi-20-day wave (Q20dw). It uncovers the importance of zonal wavenumber 2 components of stationary PW in generating the Q20dw0 (zonally symmetric Q20dw) in the stratosphere and highlights the role of non-linear interaction between Q20dw0 and SW2 in producing the secondary waves in the form of upper and lower sidebands in the MLT. This research provides the first observational evidence of a two-step non-linear interaction associated with zonally symmetric PW during major SSWs.

This work has been published in a peer-reviewed journal.

Mitra, G., Guharay, A., Conte, J. F., & Chau, J. L. (2023). Signature of two-step non-linear interactions associated to zonally symmetric waves during major sudden stratospheric warmings. *Geophysical Research Letters*, 50, e2023GL104756.

<https://doi.org/10.1029/2023GL104756>

Chapter 7 discusses the unusual enhancement of the zonally symmetric semidiurnal tide (S0) observed during SSW in the stratosphere and explains the plausible generation mechanisms. The potential role of non-linear interaction and unique distribution of source species in S0 enhancement is investigated using a reanalysis dataset.

This work has been published in a peer-reviewed journal.

Mitra, G., Guharay, A., & Paulino, I. (2024). Signature of a zonally symmetric semidiurnal tide during major sudden stratospheric warmings and plausible mechanisms: a case study. *Scientific Reports*, 14(1), 23806. <https://doi.org/10.1038/s41598-024-72594-7>

Chapter 8 discusses the observation of quasi-2-day wave (Q2dw) modulation with a quasi-16-day period during the 2019 boreal summer, using meteor radar winds and global reanalysis data. It identifies the origin of modulation near the equator at 50 km altitude and links it to the presence of the dominant quasi-16-day wave (Q16dw) in the austral winter. The study highlights the crucial role of Q2dw modes in carrying the Q16dw signature from winter to summer hemispheres, with evidence of interhemispheric coupling in the upper mesosphere and lower thermosphere. The result of this chapter is under preparation and soon to be communicated to an International peer-reviewed journal.

Chapter 9 summarizes the work done in Chapters 3, 4, 5, 6, 7 and 8 of the thesis and the future direction of the present work for a comprehensive understanding of middle atmospheric dynamics during SSW.

Chapter 2

Instruments, Dataset and Methodology

2.1. Introduction

Harnessing both ground- and space-based remote sensing techniques improves the precision of middle atmosphere using atmospheric models. This, in turn, leads to enhanced weather forecasting capabilities facilitated by the dynamic interactions between various atmospheric layers (Shaw & Shepherd, 2008). These observations involve either direct physical contact through in-situ techniques like balloons (up to the stratosphere) and rockets or remote sensing via electromagnetic or sound waves, such as radar (active remote sensing), satellite observations (active or passive remote sensing), airglow observations (passive remote sensing), etc. This extensive data collection has led to the discovery of various atmospheric phenomena, which are studied to identify the underlying processes using mathematical equations in atmospheric models. Solving these equations under different conditions forms the foundation for weather and climate predictions.

Chapter 2 provides an overview of the ground-based observation and reanalysis dataset used in this thesis and the methodology employed to carry out analysis of the data. Given the focus of the thesis on the middle atmosphere variability during SSW via planetary-scale waves, emphasis is placed on probing the MLT region (80-98 km) using meteor radar winds. In addition, the global reanalysis dataset complements the meteor radar observation, providing a comprehensive picture of dynamic variability below 80 km. Moreover, it offers the opportunity to investigate the latitudinal and vertical coupling associated with the planetary-scale waves. The chapter delves into the principles of meteor radars and the techniques for deriving horizontal winds in the MLT region.

Meteor radar observations are particularly highlighted because they allow for the continuous observation and understanding of temporal variabilities over a single geographic location, which is impossible through satellite observations alone. Additionally, the chapter briefly describes reanalysis datasets providing longitudinally spaced contemporaneous datasets, which are essential in understanding the spatial features of the planetary-scale waves.

As waves travel through the atmosphere, they cause disturbances in ambient factors like density, temperature, and winds. Therefore, examining variations in these physical parameters over time provides insights into the wave dynamics across different altitude regions of the atmosphere corresponding to these observed parameters. The measurement of atmospheric parameters with time constitutes the time series data. Various methods exist for analyzing time series data, including Fourier transform, Least-square fitting of sinusoidal functions, Lomb-Scargle Periodogram, Wavelet transform, etc. Chapter 2 overviews the time series analysis methods employed in this thesis, highlighting their advantages and limitations.

2.2. Meteor Radar

RADAR stands for Radio Detection And Ranging. RADAR functions as an active remote sensing technique that emits electromagnetic radiation in the direction of target and measures the time delay t_d between the transmitted and received signal. The distance R between the radar and the target can be calculated using the following equation:

$$R = \frac{ct_d}{2} \quad (2.1)$$

Meteor wind radar makes use of the reflection of radio wave pulses by meteor trails.

2.2.1. Meteors

A meteor is formed when a particle of interplanetary material from space, known as a meteoroid, enters Earth's atmosphere and is consumed by heat. These meteoroids travel at speeds of a few dozen km s^{-1} . As the meteoroid approaches the Earth, our planet's gravity accelerates it with an additional 11 km s^{-1} (Earth's escape velocity), making it incredibly fast with speed ranging from 11 to 72 km s^{-1} . Owing to its hypersonic speed, the meteoroid compresses the air in front of it, heating it significantly. The temperature of the compressed gas can attain thousands of degree of Celsius for a few seconds. The air transfer the heat to the meteoroid and when the surface temperature of the meteoroid reaches around 1850 K , it begins to ablate, losing a significant amount of mass. This phenomenon is called a meteor. Further, if the meteoroid survives through the Earth's atmosphere and reaches the surface, it is called a meteorite.

The visible light we see from a meteor mainly comes from the excited atoms that are released from the meteoroid's surface during this process. These atoms collide with air molecules, creating an ionized trail that typically follows a cylindrical shape behind the meteoroid. Most meteors detected by radar are caused by particles smaller than 1 mm.

Meteors are generally categorized into two groups: shower meteors and sporadic meteors. Shower meteors are typically linked to the intersection of Earth's orbit with trails of dust left by cometary bodies. Consequently, these meteors often have periodic occurrences throughout the year. Additionally, during meteor showers, many meteors seem to emanate from a specific point in the sky known as the radiant. These showers are usually named after the constellations (e.g., Leonids for Leo, Geminids for Gemini, etc.) associated with their radiants. On the other hand, sporadic meteors exhibit random distributions of their radiants in the sky and occur less frequently. They also vary in mass and entry velocities without a clear pattern.

2.2.2. Working principle

The meteor radar operates as a pulsed system, transmitting short and regularly spaced pulses of radio waves to identify targets. Using high-frequency radio waves, this radar targets the transient ionized meteor trail. The received power of the reflected radiation is significantly lower than the transmitted power used for target identification. An independent array of antennas, configured as an interferometer on the ground, receives these reflections. The phase difference of the received radiation across different antennas is calculated using the interferometer setup, allowing for calculating the arrival angle of meteor echo. Combining this angle with range information enables pinpointing the meteor's position in the sky. Additionally, the Doppler shift in the received frequency caused by drifts of the meteor trail with the background wind provides information on the meteor's velocity. More detailed insights into deriving winds from radar echoes are presented in subsequent sections.

The working of the meteor radar is based on the ability of the ionized meteor trail to scatter/reflect very high frequency radio signals. In a radar setup where the transmitting and receiving antennas are colocated (monostatic), a meteor is detected solely when its plasma

tail aligns perpendicular to the line connecting the radar beam and the meteor trail (Figure 2.1). Therefore, meteor radar captures "specular reflections" from meteor trails.

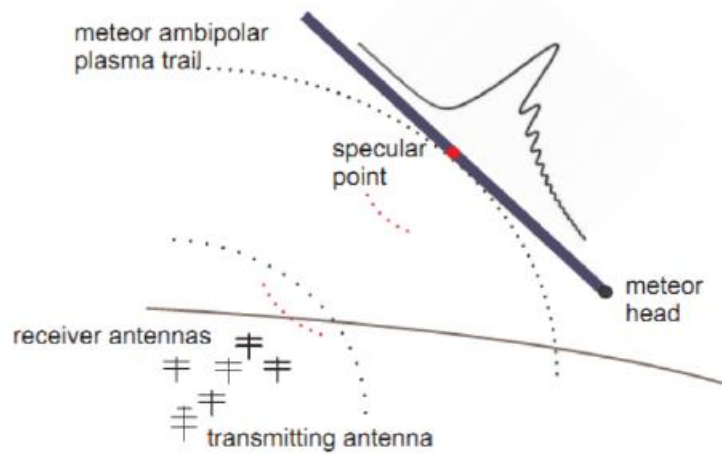


Figure 2. 1. The geometry of backscattering for a meteor trail exhibiting specular reflections (From Stober, 2009).

The structure of the ionized trail formed by the meteor depends on factors such as the entry speed, entry angle, and initial mass of the meteoroid particle. An important property controlling the radio scattering by meteors is the number of free electrons per unit length of the ionized meteor trail. Meteors are classified as underdense if their meteor trails have a line charge density lower than 10^{14} electrons per meter, while those with a higher line charge density are categorized as overdense meteors. As the meteor passes the specular reflection point, the radio echo's amplitude quickly rises to a peak, primarily reflecting signals from the first Fresnel zone. Subsequent echo behavior heavily relies on the electron line density.

In the case of underdense meteors, the radio wave penetrates the trail fully, and the received scattered signal originates from the contributions of all electrons within the trail. However, due to ambipolar diffusion, the trail's radius gradually increases over time. Within a few seconds, the radius expands enough that for typical radio wavelengths (5-10 m), destructive interference from scattering at various depths within the trail dampens the echo amplitude. Consequently, the echo's strength diminishes rapidly from its peak value. The occurrence of destructive interference imposes a constraint on detecting underdense meteors at higher altitudes using a specific radio wavelength. As the atmospheric mean free path increases with altitude, beyond a certain height, the trail radii become large enough for immediate destructive interference to occur. This phenomenon is referred to as the underdense echo

ceiling. Underdense echoes typically persist for a fraction of a second and can be identified from the distinctive pattern of a sudden rise in power followed by an exponential decay (Figure 2.2a).

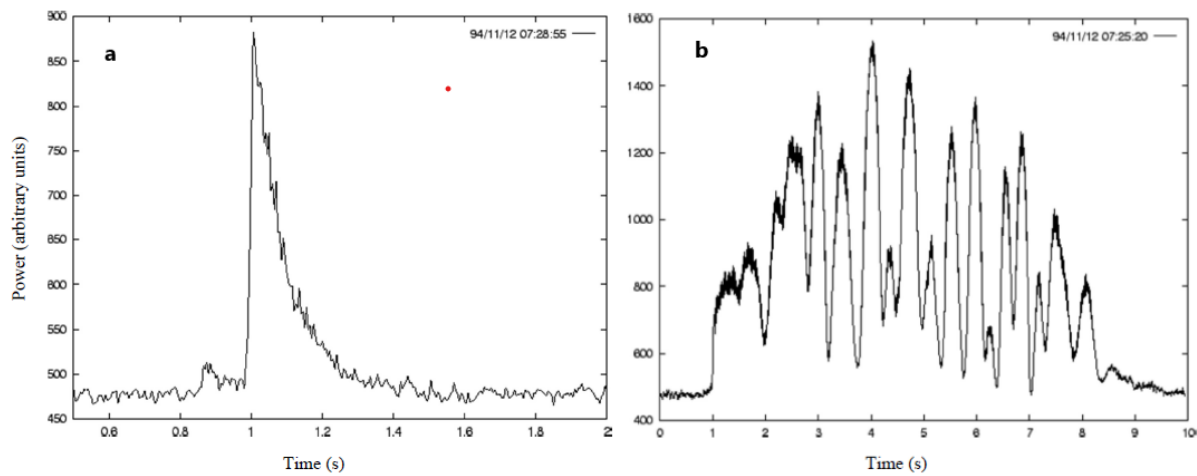


Figure 2. 2. Radar echo from a (a) underdense echo and (b) long overdense echo (From Wislez, 1996).

On the other hand, overdense echoes are less frequent. In such cases, secondary scattering between electrons becomes significant, causing the radio wave to reflect from the meteor trail's surface as if it were a metallic surface. Overdense echoes do not exhibit the rapid power decay seen in underdense echoes. Overdense echoes can persist for several seconds (Figure 2.2b), and their lifespan is determined by recombination processes that ultimately end the meteor's ionization. However, overdense echoes are less practical because their echo amplitude may fluctuate randomly due to wind shears distorting the trail. This distortion gives rise to constructive and destructive interference from multiple specular reflection points, making it more challenging to distinguish the echo from noise clearly. Additionally, such distortions may cause the specular reflection point to move along the distorted trail, resulting in an inaccurate drift velocity.

Therefore, only underdense meteor echoes are considered to determine line-of-sight velocities in the MLT region.

2.2.3. The RADAR equation

For an underdense trail, the received echo power (P_r) derived from the combined signal scattered by all electrons within the first Fresnel zone of the trail, can be expressed as described in Sugar (1964).

$$P_r = \frac{P_T G_T G_R}{32\pi^2} \left(\frac{\lambda}{R}\right)^3 (N_e r_e)^2 e^{-\left(\frac{8\pi^2 r_o^2 + 32\pi^2 D t}{\lambda^2}\right)} \quad (2.2)$$

Where,

P_T = transmitted peak power

G_T, G_R = transmitting and receiving antenna gains

N_e = electron line density (electrons/m)

r_e = classical electron radius (2.818×10^{-15} m)

r_o = initial radius of the trail (m)

D = ambipolar diffusion coefficient (m^2s^{-1})

t = time measured from the instant of specular reflection (s)

λ = operating wavelength (m)

R = Range of the specular reflection point on the trail (m)

The first term in the exponential function considers the attenuation caused by the finite initial radius of the trail, while the second term accounts for the decrease in echo intensity over time due to radial diffusion.

The ambipolar diffusion leads to decreased coherence in the scattering of radio waves by electrons within the meteor trail. Consequently, the echo amplitude experiences exponential decay over time (Herlofson, 1948). The ambipolar diffusion coefficient D depends on the surrounding temperature (T) and pressure (P) and is expressed as:

$$D = \frac{2kT}{e} \left(\frac{T}{273.16}\right) \left(\frac{1.013 \times 10^5}{P}\right) K_o \quad (2.3)$$

Where, K_o ($= 2.5 \times 10^{-4} \text{ m}^2\text{s}^{-1}$) represents a constant influenced by the characteristics of the plasma trail (Hocking et al., 1997) and ($k = 1.38 \times 10^{-23} \text{ JK}^{-1}$) is the Boltzmann constant.

The amplitude (A) of an underdense trail diminishes over time, influenced by the ambipolar diffusion coefficient, as follows.

$$A = A_o e^{-\left(\frac{16\pi^2 D t}{\lambda^2}\right)} \quad (2.4)$$

A_o is the peak amplitude. The decay constant $\tau \left(= \frac{\lambda^2}{16\pi^2 D} \right)$ represents the time required for the amplitude to decrease to $1/e^{\text{th}}$ of its original value.

Traditionally, the range of 15-70 MHz is considered optimal for meteor detection using meteor radars. At lower operating frequencies, the radar receives longer echoes, with echo duration directly proportional to the square of the radio signal wavelength (Sugar, 1964). Consequently, low-frequency systems excel at detecting brief trails at higher altitudes. However, absorption from the D region of the ionosphere becomes significant at these lower frequencies.

Conversely, higher frequency systems offer superior height resolution due to the smaller first Fresnel zone (of length $\sqrt{2R\lambda}$), which scales with the wavelength of the radio wave (Verbeeck & Wislez, 2006). Considering these factors, a frequency range of 35 ± 5 MHz is identified as the most suitable for operating meteor radars.

2.2.4. Calculation of wind

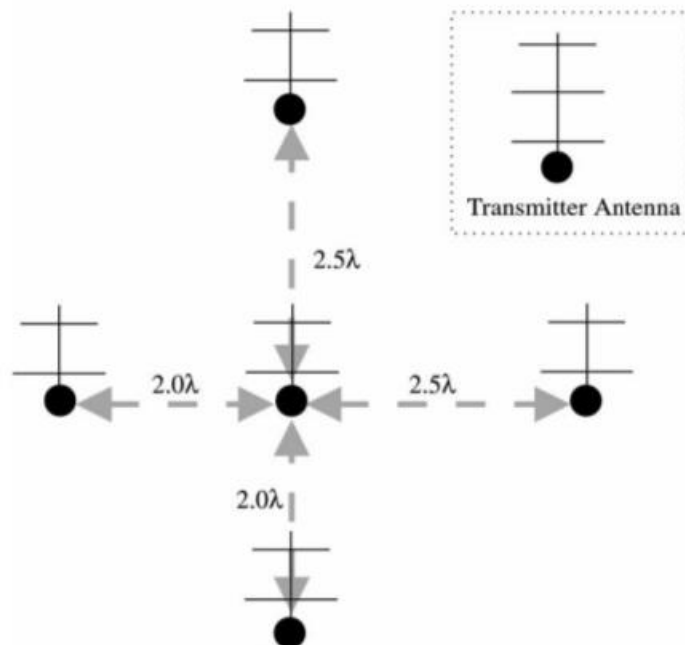


Figure 2. 3. *The Jones configuration is a common setup employed in specular meteor radars (From Hocking et al., 2001).*

The All-Sky Interferometric Meteor Wind Radar, also known as "SKiYMET" radar, is a state of art radar capable of obtaining various meteor-related parameters comprehensively and in real-time. A detailed explanation of the SKiYMET radar system is available in Hocking et al. (2001). This radar system employs a transmitter that emits short pulses (typically ranging from 1 μ s to 200 μ s) of very high-frequency radio waves (typically around 35 \pm 5 MHz), illuminating a wide area of the sky. The receiver system utilizes interferometric techniques, where phase information from different receiving antennas is used to determine the locations of meteor echoes.

The SKiYMET radar features a 5-antenna interferometer with a minimum spacing of 2 λ between receiving antennas, commonly referred to as the Jones configuration or Jones-Webster-Hocking (JWH) configuration (Jones et al., 1998). Overall, the setup includes a single Yagi antenna with three elements for transmitting and five phase-coherent Yagi antennas with two elements each for receiving. These receiving antennas are positioned along two perpendicular baselines, sharing a central antenna, to capture the echo signals from meteors. The typical configuration utilized in specular meteor radars is illustrated in Figure 2.3.

The radar echoes scattered from ionized meteor trails, which drift under the influence of neutral winds, are examined. The wind profile is derived by determining the line-of-sight Doppler velocity, range of the echo, and arrival angle. The meteor radar velocity is estimated from the line of sight Doppler velocity. The Doppler shifted frequency (f_d) is the difference between the transmitted frequency (f_t) and the received frequency (f_r) of the signal, and is related to the velocity of the target (v) as follows. In this case, the meteor trail is the moving target.

$$f_d = f_t - f_r = \frac{2v}{\lambda} = \frac{2fv}{c} \quad (2.5)$$

Where f is the operating frequency and c is the speed of radio wave (3×10^8 ms⁻¹).

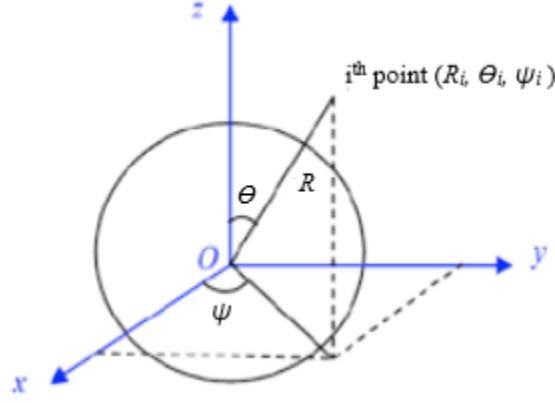


Figure 2. 4. Position of i^{th} meteor in a spherical coordinate system.

The i^{th} meteor location in a three-dimensional spherical coordinate system using R , θ , and ψ coordinates is shown in Figure 2.4. These coordinates can be converted into Cartesian coordinates, with x , y , and z axes representing eastward, northward, and vertical directions, respectively. The Doppler frequency allows for the estimation of the radial velocity (V_{Ri}) of individual scattering points as follows:

From equation (2.5),

$$V_{Ri} = \left(\frac{c}{2f} \right) f_{di} \quad (2.6)$$

Given $i = 1, 2, 3, \dots, N$, where N represents the count of scattering points identified within a specific height z and time interval Δt .

Radial velocity in vectorial form,

$$\vec{V}_{Ri} = V_{Ri} \vec{I}_{Ri} \quad (2.7)$$

Where \vec{I}_{Ri} is a unit vector representing the i^{th} position in the radial direction (line of sight), and is expressed in the cartesian coordinate as

$$\vec{I}_{Ri} = k_i \hat{i} + l_i \hat{j} + m_i \hat{k} \quad (2.8)$$

k_i , l_i and m_i denote the direction cosines for the i^{th} scattering point, given as

$$k_i = \sin \theta_i \cos \psi_i; \quad l_i = \sin \theta_i \sin \psi_i; \quad m_i = \cos \theta_i$$

The wind field \vec{U} in cartesian coordinate is described as,

$$\vec{U} = u \hat{i} + v \hat{j} + w \hat{k} \quad (2.9)$$

Where u , v and w are zonal wind, meridional wind, and vertical wind, respectively.

The measured V_{Ri} is the projection of the \vec{U} on the line of sight unit vector \vec{I}_{Ri} . Thus,

$$V_{Ri} = \vec{U} \cdot \vec{I}_{Ri} = uk_i + vl_i + wm_i \quad (2.10)$$

A least-square fitting procedure applied to the individual radial drift measurements is used to determine the wind components, i.e., u , v and w . The residual for the least-square fit is given as,

$$\chi^2 = \sum_{i=1}^N [(uk_i + vl_i + wm_i) - V_{Ri}]^2 \quad (2.11)$$

The residual is minimised by equating the derivatives of χ^2 with respect to u , v and w to zero.

$$\frac{\partial \chi^2}{\partial u} = 0; \frac{\partial \chi^2}{\partial v} = 0; \frac{\partial \chi^2}{\partial w} = 0 \quad (2.12)$$

Solving equation (2.12) yields three equations, represented in the matrix form as,

$$\begin{bmatrix} \sum k_i^2 & \sum k_i l_i & \sum k_i m_i \\ \sum k_i l_i & \sum l_i^2 & \sum l_i m_i \\ \sum k_i m_i & \sum l_i m_i & \sum m_i^2 \end{bmatrix} \begin{bmatrix} u \\ v \\ w \end{bmatrix} = \begin{bmatrix} \sum V_{Ri} k_i \\ \sum V_{Ri} l_i \\ \sum V_{Ri} m_i \end{bmatrix} \quad (2.13)$$

The equation (2.13) can be solved to determine the best estimate for the wind components (u , v and w) from the measured parameters i.e. k , l , m , and V_{Ri} . In general, w is considered to be zero based on the reasonable assumption that vertical flow velocities are significantly smaller than horizontal velocities within timeframes comparable to the achievable time resolution, which is typically around 1 hour. Consequently, the radar produces hourly estimates of u and v within the 80-100 km altitude range.

The present thesis utilizes a diverse network of meteor radar wind observations spanning high to low latitudes and encompassing both hemispheres. In total, seven meteor radars are utilized, which are located at Rothera (67.6°S, 68.1°W) (RO), King Edward Point (54.3°S, 36.5°W) (KE), Cachoeira Paulista (22.7°S, 45°W) (CP), São João do Cariri (7.4°S, 36.5°W) (CA), Wuhan (30.5° N, 114.6° E) (WU), Juliusruh (54.6°N, 13.4°E) (JU), and Andenes (69°N, 16°E) (AN). The location of the radar sites is shown in Fig 2.5. Specifications and technical details of the instrument at CA and CP, WU, AN and JU, KP, and RO are summarized in Lima et al. (2007), Zhao et al. (2005), Hoffmann et al. (2010), Mitchell (2021) and Mitchell (2019), respectively. The diverse network of meteor radar observations used in the present study provides valuable insights into global activity of planetary-scale waves in

the MLT (80-98 km).

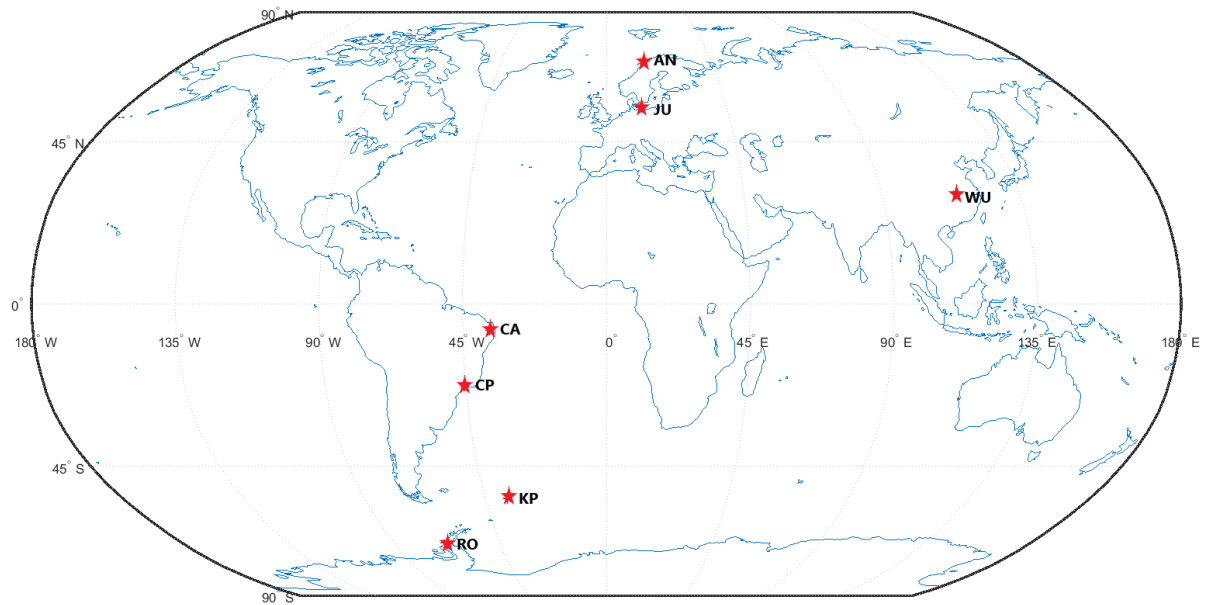


Figure 2. 5. Locations of meteor wind radars (red star) utilized in the thesis.

Specifications of a typical meteor radar is summarised in Table 2.1.

Operating frequency	25-60 MHz
Peak power	6-200 kW
Duty cycle	1-15 %
Pulse repetition frequency	200-2000 Hz

Table 2.1. Specifications of a typical meteor radar (From Mitchell, 2015).

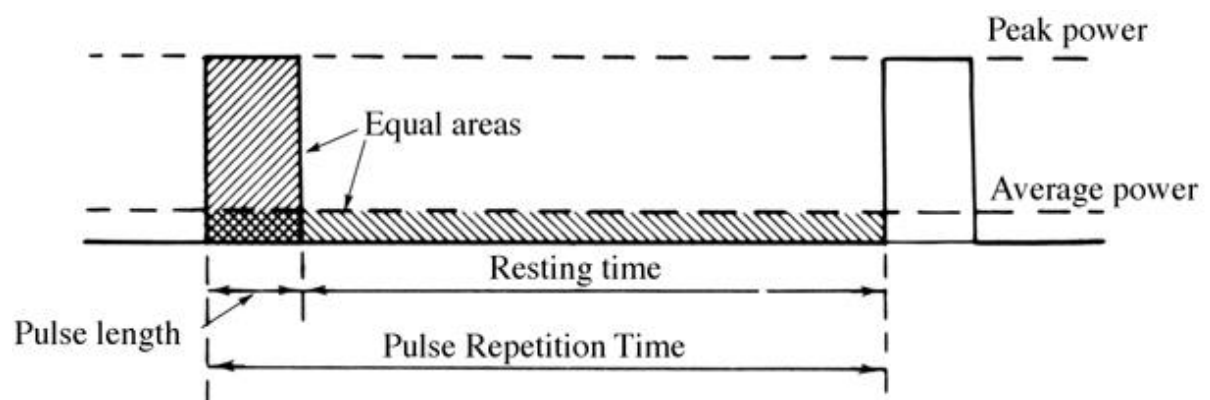


Figure 2. 6. Schematic representation of peak power, average power, pulse length and pulse repetition time of a signal (not drawn to scale).

Pulse repetition frequency (PRF) is the number of pulses transmitted per second. Pulse repetition time is the time interval between successive pulses.

$$PRF = \frac{1}{\text{Pulse repetition time}} \quad (2.14)$$

PRF determines the maximum unambiguous range (R_{unamb}), given as

$$R_{unamb} = \frac{c}{2 \times PRF} \quad (2.15)$$

Pulse length is the duration of the transmitted radar pulse, which is commonly measured in microseconds. Pulse length determines the minimum range at which a target can be detected. Duty cycle represents the ratio of pulse length and pulse repetition time.

The PRF is optimised accordingly. So that it is sufficiently high enough to capture an adequate number of samples from an underdense echo, allowing for the determination of its parameters before the echo's amplitude diminishes to the level of background noise. At the same time, higher PRF can reduce the R_{unamb} (equation 2.15).

The resolution of wind measurements from the meteor radars depends on distribution of meteors in space and time. Typically, these measurements have good height and time resolutions of around 3 km and 1 hour, respectively. Moreover, meteor radar has exceptional ability to gather continuous, high-quality data over many years, regardless of specific geomagnetic conditions, weather, or time of day. Generally, time resolution of 1 hour is good enough to investigate large scale waves such as PWs and tides. Additionally, the vertical scale sizes and wavelengths of these entities are much larger than the typical height resolution of a few kilometers, allowing meteor radars to conduct detailed studies of vertical structures across the meteor region (80-100 km).

Therefore, meteor radars are well-suited for investigating mean winds, tides, and planetary waves and have significantly helped in advancing research in this area. Their simplicity and ability to operate for extended periods with minimal maintenance make them particularly effective for prolonged observations in remote locations.

2.3. Reanalysis Data

An atmospheric reanalysis system comprises a worldwide forecast model, inputted observations, and an assimilation method that combines input observations with numerical model forecasts. These systems generate global atmospheric data, presenting the most accurate approximations (analyses) of prior atmospheric conditions. The data gathered in these analyses is then projected forward in both time and space through subsequent forecasts. Reanalysis datasets play a crucial role in climate science, meteorology, and environmental research by providing comprehensive and consistent records of atmospheric and oceanic variables over long periods.

2.3.1. Purpose

The necessity of utilization of a reanalysis dataset stems from two key reasons:

- Zonal wavenumber diagnosis: The reanalysis dataset offers a longitudinally spaced contemporaneous dataset, facilitating the analysis of the horizontal scale (zonal wavenumber) of planetary-scale waves. Ground-based observations from a single geographic location are insufficient for delineating the primary zonal wavenumber modes of a specific wave. Satellite observations, on the other hand, are sparse and necessitate sampling over several days to achieve 24-hour local time coverage. Consequently, they are not ideal for investigating temporaneous wave activity during short-term extreme events such as SSW.
- Vertical and latitudinal coupling: The reanalysis dataset complements meteor radar observations by providing a comprehensive overview of dynamic variability below 80 km. Additionally, it helps to investigate the latitudinal, vertical, and interhemispheric coupling associated with planetary-scale waves.

2.3.2. Classification

Reanalysis systems can be classified based on their observational inputs coverage into three main categories: "full input" systems, "conventional input" systems, and "surface input" systems. Additionally, some reanalysis centers offer "AMIP-type" simulations, which do not

assimilate observational data but are constrained by applying observed boundary conditions. AMIP stands for the Atmospheric Model Intercomparison Project.

- Full Input Systems: These systems assimilate both surface and upper-air conventional data as well as satellite data. They offer a comprehensive view of the atmosphere by incorporating a wide range of observational sources.
- Conventional Input Systems: These systems assimilate surface and upper-air conventional data but do not incorporate satellite data. They provide a detailed picture of atmospheric conditions based on conventional observation sources.
- Surface Input Systems: These systems assimilate surface data only, focusing specifically on surface-level atmospheric parameters. While they may lack the vertical coverage of conventional or full input systems, they are useful for certain applications that prioritize surface-level information.

In addition to these categories, there are also distinctions based on temporal coverage:

- Satellite Era Reanalyses (1979 - present): These reanalyses focus on providing data for the period from 1979 to the present, which corresponds to the era of extensive satellite observations. They utilize modern satellite data in their assimilation processes.
- Extended Reanalyses (pre-1979): Reanalyses that cover dates before January 1979 are referred to as extended reanalyses. These datasets are valuable for studying historical climate conditions and are often used to analyze long-term climate trends and variability.

The inclusion of "AMIP-type" simulations is another aspect, where simulations are based on observed boundary conditions like sea surface temperatures and sea ice without assimilating observational data directly. These simulations help understand how the atmosphere responds to observed external factors without altering the internal atmospheric state through data assimilation.

2.3.3. Working scheme

The working principle behind the reanalysis datasets involves several key components and processes:

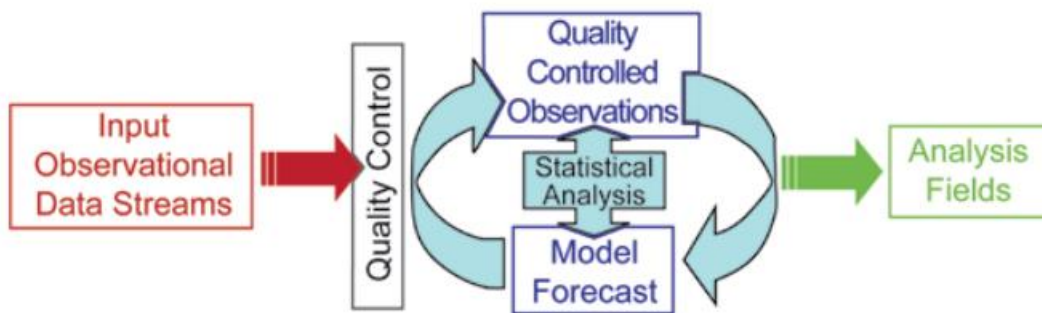


Figure 2. 7. *Data Assimilation Scheme (From Dole, 2008)*

- Input Observational Data: The process begins with collecting observational data from various sources such as weather stations, balloons, ocean buoys, rockets, satellites, radar, aircraft, etc. These data include temperature, pressure, humidity, wind speed, and other atmospheric and oceanic parameters.
- Quality Control: Prior to incorporation into reanalysis, the collected data undergoes meticulous quality control procedures aimed at eliminating errors, biases, and inconsistencies. This process is essential to ensure the reliability and accuracy of the final dataset.
- Data Assimilation: Once the observational data is quality-controlled, it is assimilated into numerical models using advanced data assimilation techniques. Data assimilation combines the observational data with model simulations to produce a consistent and coherent representation of the atmosphere and oceans (Dole, 2008). Data assimilation follows a sequential time-stepping approach, where each step involves comparing a prior model forecast with newly received observations, adjusting the model state based on the observations, initializing a new forecast, and repeating the cycle. This

updating phase is commonly known as the analysis step, while the brief model forecast utilized to generate the analysis is termed the background.

- Numerical Models: Reanalysis datasets rely on sophisticated physics-based numerical models of the Earth's atmosphere and oceans. These models solve complex mathematical equations (e.g., momentum, continuity, thermodynamic equations) to simulate the behavior of atmospheric and oceanic processes, including weather patterns, climate variability, and interactions between different Earth system components.

The reanalysis approach utilizes a fixed or frozen numerical model alongside a data assimilation scheme to construct an extensive database of geophysical parameters covering the entire globe. This database maintains uniform spatial and temporal resolutions across the data domain. The use of a frozen model guarantees that temporal changes can be unequivocally linked to changes in the atmospheric state rather than fluctuations in the model's performance (Kalnay et al., 1996).

- Temporal and Spatial Grid: Reanalysis datasets are typically generated on a regular temporal grid (e.g., hourly, daily, monthly) and a spatial grid covering the entire globe with a certain resolution (e.g., 1 degree by 1 degree). This grid structure allows researchers to analyze and compare data across different time periods and geographic regions.
- Reconstruction: By assimilating observational data into numerical models, reanalysis datasets reconstruct past weather and climate conditions over long periods, often spanning several decades or even centuries. This reconstruction provides a valuable resource for studying climate trends, variability, extreme events, and their impacts on the environment and society.
- Data Outputs: Reanalysis datasets produce various output variables such as temperature, precipitation, wind fields, atmospheric pressure, sea surface temperatures, heat fluxes, etc. These variables are available globally at different vertical levels in the atmosphere and ocean, allowing researchers to examine the entire Earth system in detail.

- Validation and Verification: Before being released to the scientific community, reanalysis datasets undergo extensive validation and verification processes to assess their accuracy, consistency, and reliability. This involves comparing reanalysis data with independent observations, field campaigns, and other datasets to ensure that they capture the true behavior of the Earth's atmospheric system.

In summary, reanalysis datasets are potent tools that integrate observational data and numerical models to provide a comprehensive and continuous record of past weather and climate conditions. They are widely used in atmospheric research, weather forecasting, environmental monitoring, and various other applications to understand and address global climate change and variability challenges.

Although reanalysis datasets are extremely useful for investigating atmospheric processes, care should be taken to check the fidelity of the dataset before utilizing it, particularly at high altitudes. Here are some possible limitations of reanalysis datasets at high altitudes:

- **Sparse Observational Data**: Reanalyses rely heavily on observational data for accuracy, but the availability of direct measurements diminishes significantly at high altitudes, leading to reduced reliability in these regions.
- **Lower Spatial Resolution**: The vertical and horizontal resolution at high altitudes is often coarser, which can smooth out finer-scale atmospheric structures and dynamics, such as gravity waves and small-scale turbulence.
- **Uncertain Model Physics**: Parameterizations and model physics for high-altitude processes (e.g., wave propagation, photochemistry) are less well-constrained, resulting in increased uncertainties in the simulations.
- **Data Assimilation Challenges**: The assimilation of satellite and other indirect measurements at high altitudes can introduce biases and inconsistencies, as the quality and type of observations may vary over time.

- **Limited Upper Boundary Constraints:** The model's upper boundary can affect simulations near the top of the reanalysis altitude range, which may lead to artificial damping of atmospheric processes or influence from extrapolated conditions.

These limitations mean that while reanalysis datasets provide useful insights, their accuracy in capturing high-altitude phenomena should be interpreted cautiously.

Different organizations like the National Center for Environmental Prediction (NCEP), National Center for Atmospheric Research (NCAR), European Center for Medium-Range Weather Forecast (ECMWF), and the National Aeronautics and Space Administration (NASA), Japan Meteorological Agency (JMA), etc have created distinct editions of reanalysis datasets, each covering extensive periods spanning multiple decades. Further information regarding the reanalysis datasets utilized in this thesis is provided below.

2.3.4. ERA5

ERA5, the fifth major global reanalysis developed by the ECMWF (Hersbach et al., 2020), represents an improved and updated version of the ERA-Interim dataset (Dee et al., 2011). ERA5 is considered superior to ERA-Interim due to its higher spatial and vertical resolution, improved data assimilation techniques, extended time period coverage, inclusion of additional variables, and enhanced handling of uncertainties.

The ERA5 database provides reanalysis data of various atmospheric parameters from 1979 to the present. The number of vertical pressure levels has increased from 37 in ERA-interim to 137 model pressure levels in ERA5, covering the vertical range 1,000–0.01 hPa (~0–80 km altitude) with a latitudinal and longitudinal grid of $0.25^\circ \times 0.25^\circ$. Temperature, zonal wind, and meridional wind data from ERA5 are employed in the current thesis. The ERA5 data is available at <https://www.ecmwf.int/en/forecasts/datasets>.

The analysis of ERA5 data set is aimed to complement the meteor radar observation for providing a holistic picture of the dynamical variability in the lower and middle atmosphere. Furthermore, the ERA5 global database offers the opportunity to investigate the latitudinal coupling between high and low latitude during such a dynamical event.

2.3.5. MERRA2

Modern-Era Retrospective analysis for Research and Applications version 2 (MERRA-2) is the most recent version of global atmospheric reanalysis during the satellite era, generated by NASA's Global Modeling and Assimilation Office (GMAO) using the Goddard Earth Observing System Model (GEOS) version 5.12.4 (Gelaro et al. 2017). This dataset spans from 1980 to the present day, with data typically becoming available approximately three weeks after the end of each month. The data can be downloaded from <https://gmao.gsfc.nasa.gov/reanalysis/MERRA-2/>.

M2I3NVASM (or inst3_3d_asm_Nv) is an instantaneous 3-dimensional 3-hourly data collection in MERRA-2. For the present investigation, we have used temperature, zonal wind, and meridional wind at 72 model pressure levels within the range 985–0.01 hPa (~0–75 km) with a latitude-longitude grid of $0.5^\circ \times 0.625^\circ$.

Additionally, the total precipitable water vapor (TPWV) and the total columnar ozone (TCO) are utilized for the present work, which are available in M2I1NXASM (or inst1_2d_asm_Nx), an instantaneous 2-dimensional hourly data collection in MERRA-2.

2.3.6. NCEP-DOE Reanalysis 2

The NCEP-Department of Energy (DOE) Reanalysis-2 represents an upgraded version of the earlier NCEP Reanalysis-1. This dataset covers the period from 1979 to the present day and offers global spatial coverage. The present thesis uses the daily outgoing longwave radiation (OLR) data as a proxy for convective activity available on a latitude-longitude grid of $2.5^\circ \times 2.5^\circ$. Access to the data is available via

<https://psl.noaa.gov/data/gridded/data.olrcdr.interp.html>. For more comprehensive information regarding the model utilized, data assimilation methods employed, improvements from Reanalysis 1, updated model physics, and rectified errors, refer to Kanamitsu et al. (2002). Liebmann and Smith (1996) provided a detailed account of a comprehensive (Interpolated) Outgoing Long-wave Radiation dataset.

2.4. Time series analysis

Time series analysis entails extracting information about the frequency, wavenumber, amplitude, and temporal occurrence of physically varying features within the data. Here, we outline several commonly employed time series analysis methods utilized in this study.

2.4.1. Fourier transform

The Fourier transform is a method of expressing any periodic function (satisfying Dirichlet conditions) in time or space using sine and cosine functions in the frequency domain. The magnitude of the Fourier transform indicates the magnitude of a specific frequency within the original time series, while the argument shows the phase shift in the sinusoidal component. Fourier transforms offer distinct advantages, as certain operations conducted in the time domain translate to simpler operations in the frequency domain. For instance, convolution in the time domain is equivalent to multiplication in the frequency domain.

The Fourier transform $F(\omega)$ of a continuous time series $f(t)$ is

$$F(\omega) = \int_{-\infty}^{+\infty} f(t)e^{-i\omega t} dt \quad (2.16)$$

where ω is the angular frequency, t is the time, and $i = \sqrt{-1}$. The inverse Fourier transform is given as

$$f(t) = \int_{-\infty}^{+\infty} F(\omega)e^{i\omega t} d\omega \quad (2.17)$$

Practically, data collected during experimental observations are represented as a discrete function of time, denoted as $f(t_n)$ where n ranges from 1 to N . The discrete Fourier transform for such functions can be expressed as follows:

$$F(\omega_k) = \frac{1}{N} \sum_{n=1}^N f(t_n)e^{-i\omega_k t} \quad (2.18)$$

Where $\omega_k = \frac{2\pi kn}{N}$; $k = 1, 2, \dots, N$ and $n = 1, 2, \dots, N$.

The normalization factor of $\frac{1}{N}$ can be applied before either the forward or inverse transform.

Alternatively, it can be expressed as $\frac{1}{\sqrt{N}}$, but it must be consistently applied in both the forward and reverse transform scenarios to ensure that the product of the two factors equals

$\frac{1}{N}$. The computation of the Discrete Fourier Transform (DFT) typically involves roughly N^2 multiplications and summations. Hence, in practice, the Fast Fourier Transform (FFT) is employed for faster calculations, requiring a maximum of $N \log N$ computations.

However, the FFT can be performed on uniformly spaced time series data. In numerous geophysical observations, the time-series data collected are irregularly spaced in time due to various practical constraints. In such instances, the least squares fitting of sine and cosine functions, or an equivalent method known as the Lomb-Scargle analysis, is employed.

2.4.2. Lomb-Scargle Periodogram

The Lomb-Scargle (LS) periodogram is a powerful tool used in signal to analyze the periodicity or periodic signals in irregularly sampled data. Unlike Fourier transform, which requires uniformly spaced data points, the Lomb-Scargle periodogram can handle unevenly spaced observations (Lomb, 1976). It calculates the power spectrum of a signal to identify dominant frequencies, making it particularly useful for detecting periodicities in time-series data with irregular sampling intervals.

LS algorithm involves sine waves of the form

$$y(t_n) = a \cos \omega(t_n - t_{ave} - \tau) + b \sin \omega(t_n - t_{ave} - \tau) \quad (2.19)$$

fitted to the time series data f_n (with zero mean) at times t_n , $n = 1, 2, \dots, N$. ω is the angular frequency and $t_{ave} = \left(\frac{t_1 + t_N}{2}\right)$. Parameter τ is defined by Scargle (1982) as,

$$\tan(2\omega\tau) = \frac{\sum_{n=1}^N \sin 2\omega(t_n - t_{ave})}{\sum_{n=1}^N \cos 2\omega(t_n - t_{ave})} \quad (2.20)$$

a and b are given as,

$$a = \frac{\sqrt{\frac{2}{N}} \sum_{n=1}^N f_n \cos \omega(t_n - t_{ave} - \tau)}{(\sum_{n=1}^N \cos^2 \omega(t_n - t_{ave} - \tau))^{\frac{1}{2}}} \quad (2.21)$$

$$b = \frac{\sqrt{\frac{2}{N}} \sum_{n=1}^N f_n \sin \omega(t_n - t_{ave} - \tau)}{(\sum_{n=1}^N \sin^2 \omega(t_n - t_{ave} - \tau))^{\frac{1}{2}}} \quad (2.22)$$

The amplitude spectra $A(\omega)$ is derived as,

$$A(\omega) = \sqrt{a^2 + b^2} \quad (2.23)$$

The periodogram is calculated at the angular frequencies

$$\omega_j = \frac{2\pi}{(t_N - t_1) of} j, j=1,2,\dots \quad (2.24)$$

of is the oversampling factor and is chosen as integer greater than 4 (Press et al., 1996). Detailed discussion on the significance of the frequency can be found in Scargle (1982). Thus the LS amplitude spectra can be calculated using equation (2.23).

2.4.3. Wavelet transform

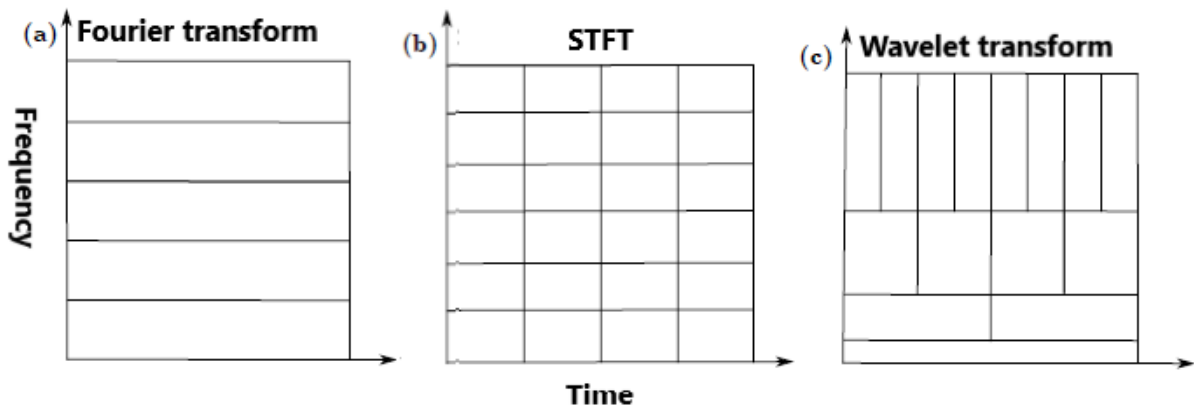


Figure 2. 8. A graphical depiction of the time and frequency resolutions for Fourier, STFT, and wavelet transforms. It's noticeable that for the wavelet transform, time resolution increases with increasing frequency.

While both the FFT and LS algorithm efficiently extracts frequency information from time domain signals, it lacks the ability to provide insight into the time localization of frequency components. This limitation is addressed by the Wavelet Transform, which utilizes short-duration waveforms with a zero average, called wavelet. Wavelets are classified as discrete when they have finite temporal extent and continuous otherwise. The Wavelet Transform involves decomposing a signal into shifted and scaled versions of a "mother" wavelet, enabling temporal localization of frequency components. This method surpasses the Short Time Fourier Transform (STFT), which employs a single window for analysis. Wavelet analysis adjusts window lengths according to frequency, using longer windows for low frequencies and shorter ones for high frequencies in the time-frequency plane (Figure 2.8). This variation in window length enhances both time and frequency resolution, facilitating localized time-frequency analysis of signals.

The continuous wavelet transform (CWT) is the convolution of time series signal $f(t)$ with a translated and scaled form of the mother wavelet $\psi(t)$, expressed as:

$$W_{t,\psi}(s, d) = \frac{1}{\sqrt{s}} \int_{-\infty}^{+\infty} f(t) \psi^* \left(\frac{t-d}{s} \right) dt \quad (2.25)$$

Where, s and d are scaling and translational parameter. $\frac{1}{\sqrt{s}}$ is the normalization factor.

Morlet wavelet is used as a mother wavelet, which is a plane sinusoidal wave modulated by Gaussian envelope, as shown in Figure 2.9.

Mathematically, Morlet wavelet is expressed as,

$$\psi_o(\eta) = \pi^{-\frac{1}{4}} e^{i\omega_o\eta} e^{-\frac{\eta^2}{2}} \quad (2.26)$$

Where η is a non-dimensional time parameter and ω_o is a non-dimensional frequency factor which has been taken as 6 to satisfy the admissibility condition (details in Farge, 1992).

The Morlet wavelet is favored as the mother wavelet due to its sinusoidal and complex characteristics, making it suitable for estimating both signal amplitude and phase, as well as identifying signal periodicity (Torrence & Compo, 1998).

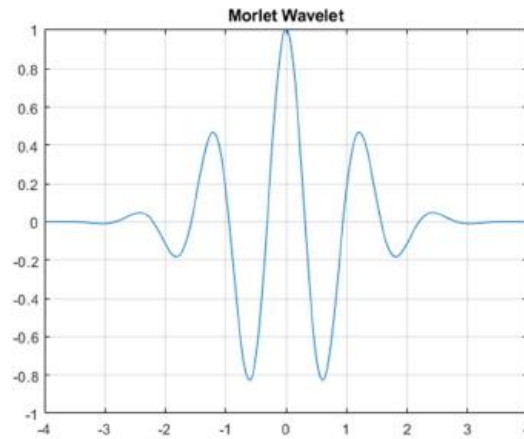


Figure 2. 9. Morlet wavelet function.

In real-world scenarios, measurements are conducted discretely over time. Let $n=0, 1, \dots, N-1$ represent the discrete time series f_n with a sampling interval δt . The wavelet transform can then be expressed as:

$$W_n(s) = \sum_{n'=0}^{N-1} f_{n'} \psi' \left[\frac{(n'-n)\delta t}{s} \right] \quad (2.27)$$

By varying the time index, n , and translating it, one can compute the wavelet coefficients. A quicker approach to calculating these coefficients involves utilizing the convolution theorem.

As per the theorem, the wavelet transform equals the inverse Fourier transform of the product of the Fourier transforms of the signal f_n and the conjugate of the mother wavelet (details in Daubechies, 1988). Torrence and Compo (1998) extensively discuss a range of wavelet basis functions, along with the estimation of significance levels, cone of influence (COI) and confidence intervals.

2.4.4. Least-square fitting

Least squares fitting aims to find the best-fitting curve that represents a set of data points by minimizing the weighted sum of the squares of the deviations χ^2 .

$$\chi^2 = \sum_{n=1}^N \left[\frac{y_i - y(x_i)}{\sigma_i} \right]^2 \quad (2.28)$$

Where y_i are measured values and $y(x_i)$ are model values. σ_i denote the uncertainties in y_i .

One of the applications of the least-square fitting in the present thesis is the estimation of daily tidal amplitudes. The tidal amplitude in winds can be estimated by the nonlinear least-squares fitting using the following wave equation.

$$Y(t) = Y_o + \sum_{n=1}^3 A_n \cos \left[\frac{2\pi n}{24} (t - \varphi_n) \right] \quad (2.29)$$

where $n = 1, 2, 3$ denotes diurnal, semidiurnal and terdiurnal components, A_n is the amplitude, t is the universal time and φ_n is the phase. $Y(t)$ is the hourly meridional/ zonal wind, and Y_o is the mean wind over the fitting window.

Least squares fitting is utilized on the data within each window, allowing for the extraction of amplitudes and phases of tidal components or PWs of known period. The data window is then progressively shifted by one day at a time to estimate daily tidal/wave parameters across the entire time series.

2.5. Summary

This chapter introduces the instruments, and datasets utilized in this thesis. Useful data from a comprehensive network of meteor radars are utilized to study planetary-scale wave activity in the MLT at altitudes ranging from 80 to 100 kilometers. The meteor phenomenon is introduced briefly, along with a detailed discussion on the operational principles of meteor

radar, including the RADAR equation for an underdense meteor trail and the wind retrieval technique. Additionally, the chapter provides an overview of reanalysis data and its working principles. It further delves into the specifics of reanalysis datasets used in this thesis, such as ERA5, MERRA2, and NCEP-DOE Reanalysis 2, highlighting their importance in understanding latitudinal and vertical coupling and diagnosing zonal wavenumber of planetary-scale waves.

Moreover, chapter 2 provides a brief overview of the time series analysis methods employed in this thesis. The Fourier transform is well-suited for identifying frequency components within evenly spaced time series. On the other hand, Lomb-Scargle serves as an equivalent method for period analysis in irregularly spaced data and is also applicable to regularly spaced data points. When analyzing temporal wave activity during short-term extreme events like SSW, the timing of this activity is often critical information. In such cases, the Wavelet transform is employed to extract both time and frequency information simultaneously. The application of least-square fitting in estimating tidal amplitude is also discussed. Additional auxiliary methods such as the 2-D least-square fitting, evolutionary Lomb-Scargle (ELS) and the combined Fourier-Wavelet (CFW) technique used for determining wave parameters will be discussed in the respective texts of the various chapters.

Chapter 3

Impact of SSW on Low-latitude Planetary Wave Dynamics

3.1. Introduction

Understanding SSW events has been a longstanding interest in atmospheric science due to their profound impact on the dynamics of the middle atmosphere. In the realm of SSW research, much attention has been devoted to the NH, where SSWs are more frequent compared to the SH due to topographic and land-sea contrast differences leading to higher PW activity. Also, the cumulative wave flux requirement to cause SSW in SH is supposed to be much larger because of the stronger SH polar jet compared to the NH counterpart (Rao et al., 2020). The abnormal changes in stratospheric temperature and zonal winds during SSWs significantly affect the dynamical variability of the middle atmosphere (e.g., Pedatella et al., 2018). While studies have explored the impact of SSWs on the MLT in NH mid and high latitudes (e.g., Whiteway & Carswell, 1994; Hoffman et al., 2002), research from SH mid and high latitudes is scarce (Dowdy et al., 2004).

The influence of SSW disturbances on the tropical atmosphere was first noted by Fritz and Soules (1970), with subsequent studies reporting stratospheric cooling in the tropics during SSW events (Andrews et al., 1987; Guharay et al., 2014). Regarding low and high-latitude coupling during SSWs, investigations have primarily focused on the NH (Sivakumar et al., 2004; Kodera, 2006; Guharay & Sekar, 2012). So far, in the Southern Hemisphere, only one major SSW event occurred in September 2002 (Dowdy et al., 2004). Hence, there is a lack of observational studies regarding the response of the tropical middle atmosphere during SSW events in the Southern Hemisphere (Guharay et al., 2014; Guharay & Batista, 2019).

Therefore, more research from low latitudes is needed to comprehend the coupling between low and high latitudes during such rare yet impactful SSW events in the SH.

The recent minor SSW event in the SH in September 2019 has drawn attention (Lim et al., 2020; Yamazaki et al., 2020), especially regarding its impact on convective activity in the tropical summer hemisphere (Noguchi et al., 2020). Additionally, this event provided an opportunity to study ionospheric variability due to lower and middle atmospheric forcing

during a period of low solar activity (Goncharenko et al., 2020). Notably, studies have explored ionospheric variability during the 2019 SSW event, such as the quasi-6-day wave (Q6DW) forcing observed by Yamazaki et al. (2020) and the non-linear interaction between Q6DW and the migrating semidiurnal tide reported by Miyoshi and Yamazaki (2020) in the ionosphere. However, during this event, the dynamic variability in the middle atmosphere, particularly at low latitudes, remains unexplored.

Therefore, the present study aims to fill this gap by investigating PW-associated dynamical variability in the equatorial and extratropical middle atmosphere during the September 2019 minor SSW event. For this purpose, meteor radar wind observations from São João do Cariri (7.4°S, 36.5°W) (CA) and Cachoeira Paulista (22.7°S, 45°W) (CP) along with ERA5 reanalysis dataset are utilized during the period centered around the minor warming episode ~ from 1 August to 31 October (2019). The present study holds significance due to the insufficient understanding of the influence of SH SSW on the dynamics of the middle atmosphere at low latitudes in the SH.

3.2. Results

For the current investigation, we utilized temperature, zonal wind (U), and meridional wind (V) data across 137 model pressure levels ranging from 1000 to 0.01 hPa (approximately 0-80 km), employing a grid resolution of 0.1° in both latitude and longitude. Specifically, the grid points closest to CP and CA are selected as (22.7°S, 45°W) and (7.4°S, 36.5°W) respectively. The analysis of the ERA5 dataset is aimed to complement the meteor radar observations to understand dynamical variability in the lower and middle atmosphere comprehensively. Moreover, the global coverage of the ERA5 database provided an opportunity to explore the latitudinal coupling between high and low latitudes during such dynamic events.

3.2.1. Background Dynamical Conditions

To identify heating and cooling patterns, we plotted differences between the zonal mean temperature (ZMT) and the temporal mean (August-October 2019) of the ZMT at the 10 hPa pressure level in the Southern Hemisphere using the ERA5 dataset. This analysis covers the

observational interval from 1 August to 31 October 2019 (Day of Year (DOY) 213 = 1 August), as depicted in Figure 3.1a.

At latitudes higher than 75°S, the temperature difference is primarily negative from DOY 213 to DOY 248. It transitions to positive, with the peak warming occurring on 18 September (DOY 261), persisting for the rest of the study period. Noteworthy warming exceeding 25 K is observed between DOY 253 and DOY 263, marking the warming period (SSW event) based on criteria of a temperature rise of at least 25 K within a week or less at any stratospheric altitude in any winter hemisphere region (defined by McInturff, 1978). This warming at mid and high latitudes corresponds to cooling in the tropical area between DOY 243 and DOY 263, which is the focal point of interest in this study. The relative cooling at 10 hPa in low latitudes ($< 30^{\circ}\text{S}$) is evident from Figure 3.1a.

Figure 3.1b illustrates the zonal mean zonal wind (ZMU) during the aforementioned period at 10 hPa. The strong eastward wind at 10 hPa, 60°S, gradually weakens by approximately 70 m/s until the end of the warming period, i.e., DOY 263, without a wind reversal.

Altitudinal profiles showing the difference between the zonal mean temperature and its temporal mean at 60°S, 22.7°S (CP latitude), and 7.4°S (CA latitude) are presented in Figures 3.1c, 3.1e, and 3.1g, respectively. Similarly, Figures 3.1d, 3.1f, and 3.1h display the altitudinal profiles of the ZMU at the same latitudes.

Key observations include:

- At 60°S (Figure 3.1c), a significant temperature increase is observed in the mid-stratosphere (20-40 km) during the warming period, persisting throughout the observation period, while there is notable cooling at mesospheric altitudes concurrent with the stratospheric warming.
- Westerly winds at 60°S (Figure 3.1d) decrease in magnitude at the onset of the warming event in the middle atmosphere, with a reversal in U in the upper stratosphere prominent during the SSW event. Thus, the current minor warming episode can be classified as high stratospheric warming (Savenkova et al., 2017).

- However, the behavior of the low-latitude middle atmosphere (Figure 3.1e and 3.1g) contrasts with that of high latitudes, showing stratospheric cooling alongside high-latitude warming and mesospheric warming concurrent with high-latitude cooling.
- The U at low latitudes (Figure 3.1f and 3.1h), particularly near 50-70 km altitude at CP, exhibits noticeable weakening with the onset of the warming. However, this effect is much weaker at lower latitudes (CA), confined to a narrow altitude region near 65 km.

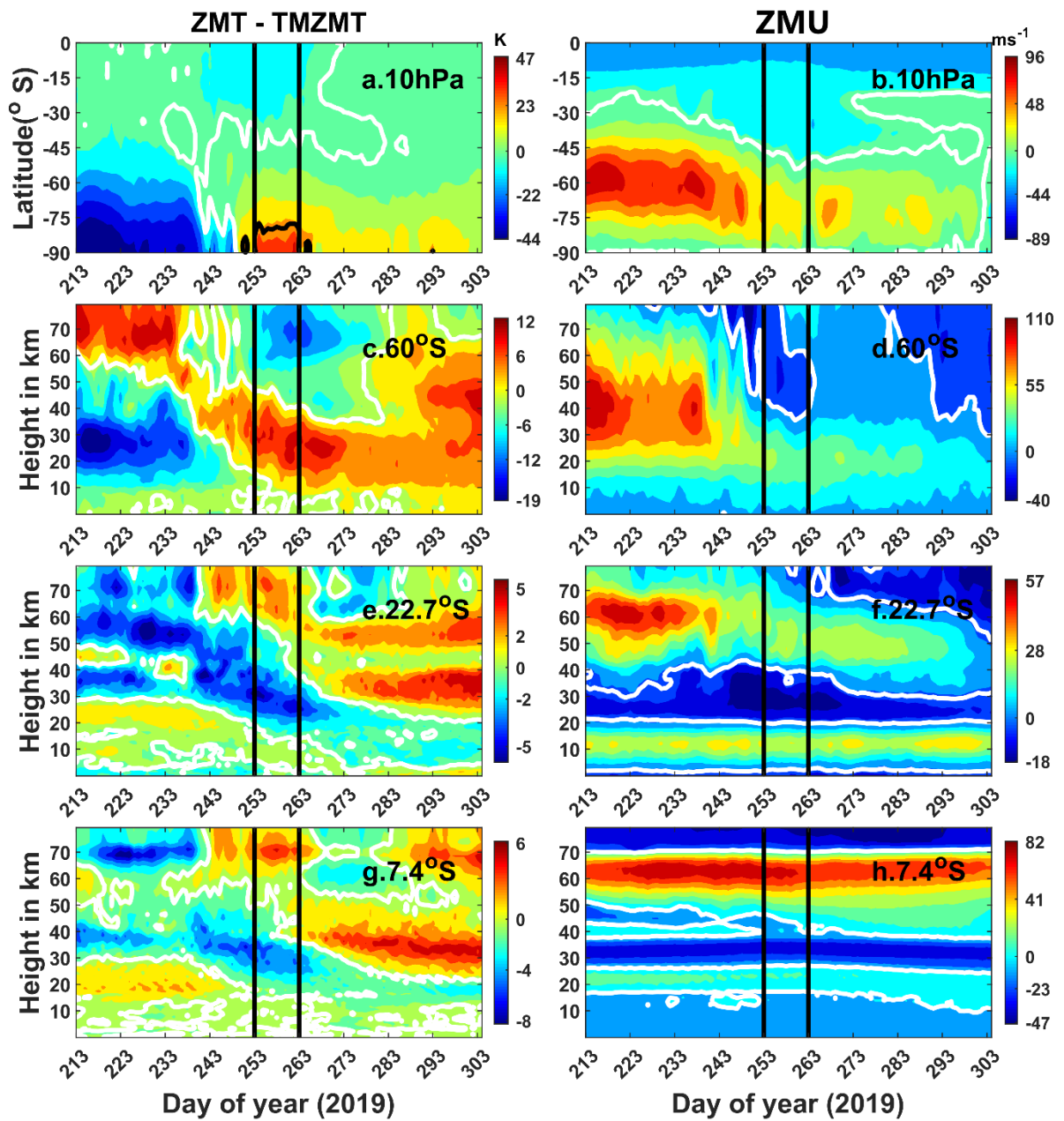


Figure 3. 1. (a) Difference between the zonal mean temperature and temporal mean of zonal mean temperature ($ZMT - TMZMT$) during August-October 2019 (DOY 213 ~ 1 August) and (b) zonal mean zonal wind (ZMU) plotted during the same period at 10 hPa pressure level using ERA5. Altitudinal profiles (~ 0 -80 km) of ($ZMT - TMZMT$) are shown at (c) $60^\circ S$, (e) $22.7^\circ S$ (CP latitude) and (g) $7.4^\circ S$ (CA latitude). Similarly, altitudinal profiles (~ 0 -80 km) of ZMU are shown at (d) $60^\circ S$, (f) $22.7^\circ S$ (CP latitude) and (h) $7.4^\circ S$ (CA latitude). The white bold curves represent zero value in all the plots, and the bold black curve represents a value of 25 K in Figure 3.1a. Region between two vertical lines shows warming period for the present and all the following figures. Please note the change of scale in the colorbars corresponding to each subplot while comparing.

3.2.2. Low-latitude Traveling Planetary Wave Dynamics

To investigate the characteristics of traveling planetary waves (TPWs) at the current low latitude locations, we conducted a wavelet analysis using Morlet as the mother wavelet for the observational period. Figures 3.2a-d display the wavelet power spectra of U at 90 km, 0.02 hPa (approximately 80 km), 1 hPa (around 48 km), and 10 hPa (about 32 km), respectively, at CP. The bold white curves in each plot represent the 95% confidence level.

Figure 3.2a reveals the emergence of a quasi-6-day wave (Q6DW) (also identified by Yamazaki et al. (2020) in the ionosphere) with periods ranging from 5 to 7 days in the mid-MLT (90 km) immediately after the warming, persisting for a few days. At 0.02 hPa (near the mesopause), the wavelet spectrum of U at CP exhibits a robust quasi-10-day wave (Q10DW) with periods ranging from 9 to 12 days before the warming event, alongside a relatively weaker Q6DW that persists during and after the warming, as shown in Figure 3.2b. In the pre-warming condition in the mesopause region (0.02 hPa), a quasi-16-day wave (Q16DW) with periodicity ranging from 14 to 20 days is observed, albeit with lesser strength. The wavelet power spectra of U indicate presence of the Q16DW at 1 hPa (upper stratosphere) before the warming event, diminishing in strength in the subsequent observational interval (Figure 3.2c). A similar pattern is observed at 10 hPa, as depicted in Figure 3.2d, with the Q16DW exhibiting greater strength at 1 hPa than at 10 hPa.

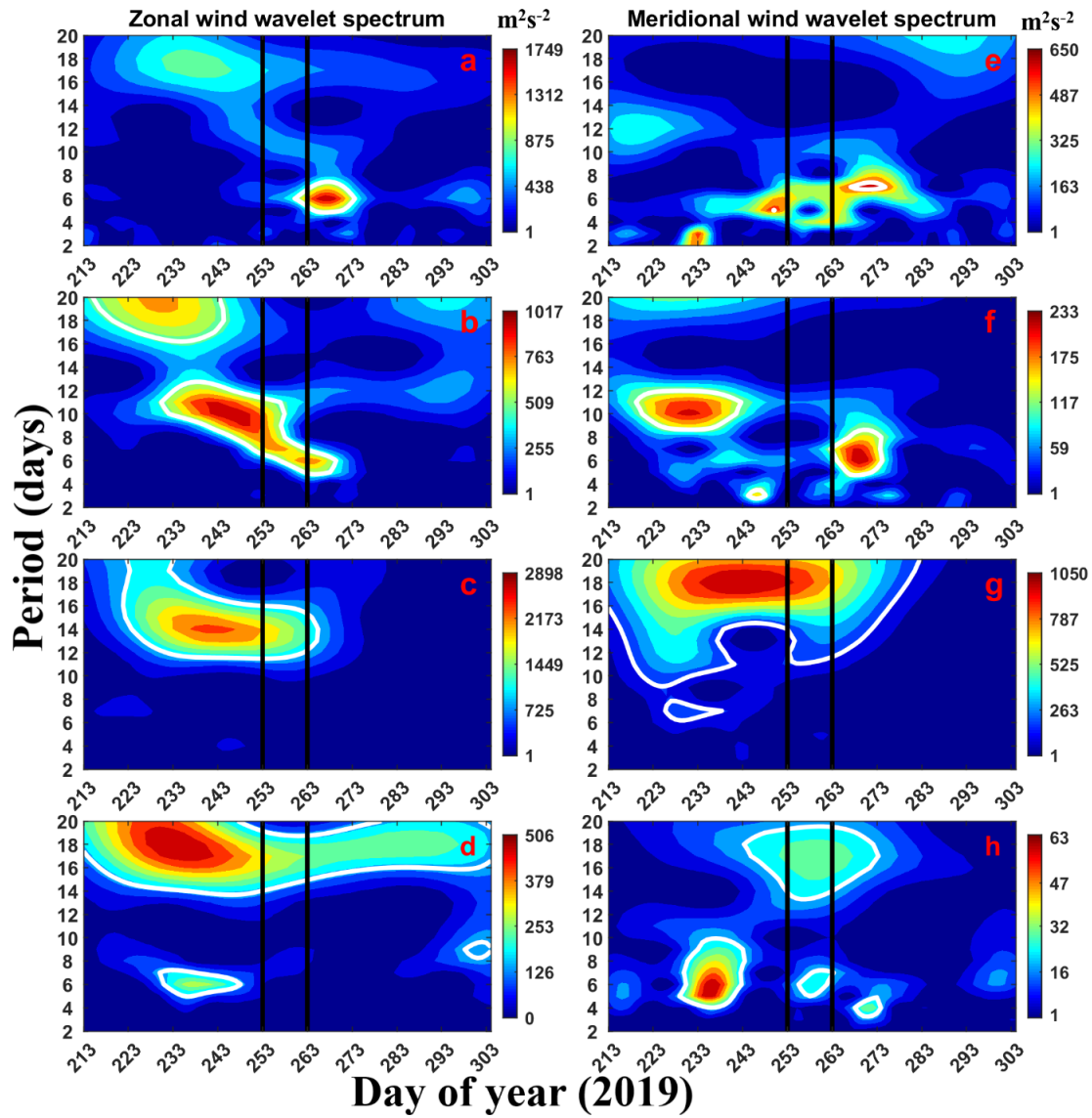


Figure 3. 2. Wavelet power spectra at 90 km of (a) U, and (e) V using meteor radar. Wavelet spectra of U at (b) 0.02 hPa, (c) 1 hPa, (d) 10 hPa, and V at (f) 0.02 hPa, (g) 1 hPa, (h) 10 hPa at CP using ERA5. Bold white curves in each plot represent 95% confidence level. Please note the change of scale in the colorbars corresponding to each subplot while comparing.

Figures 3.2e-h depict the same as Figures 3.2a-d but of V. The Q6DW is distributed around the warming days in the mid-MLT region, as seen in Figure 3.2e. At the 0.02 hPa pressure level near the mesopause (Figure 3.2f), a Q10DW is observed during the pre-warming period, followed by the appearance and intensification of a Q6DW at the end of warming, persisting until DOY 273. In the upper stratosphere at 1 hPa pressure level (Figure 3.2g), a strong Q16DW is evident before the warming episodes, weakening by the end of the warming event. At 10 hPa (Figure 2h), the Q6DW dominates for a few days before and during the warming,

while the Q16DW appears during the warming days. Additionally, a weak quasi-3-day wave (Q3DW) with a periodicity of 3-4 days is observed after the warming event for a short period. Overall, the traveling PW activities are more pronounced in wavelet spectra of U than in V.

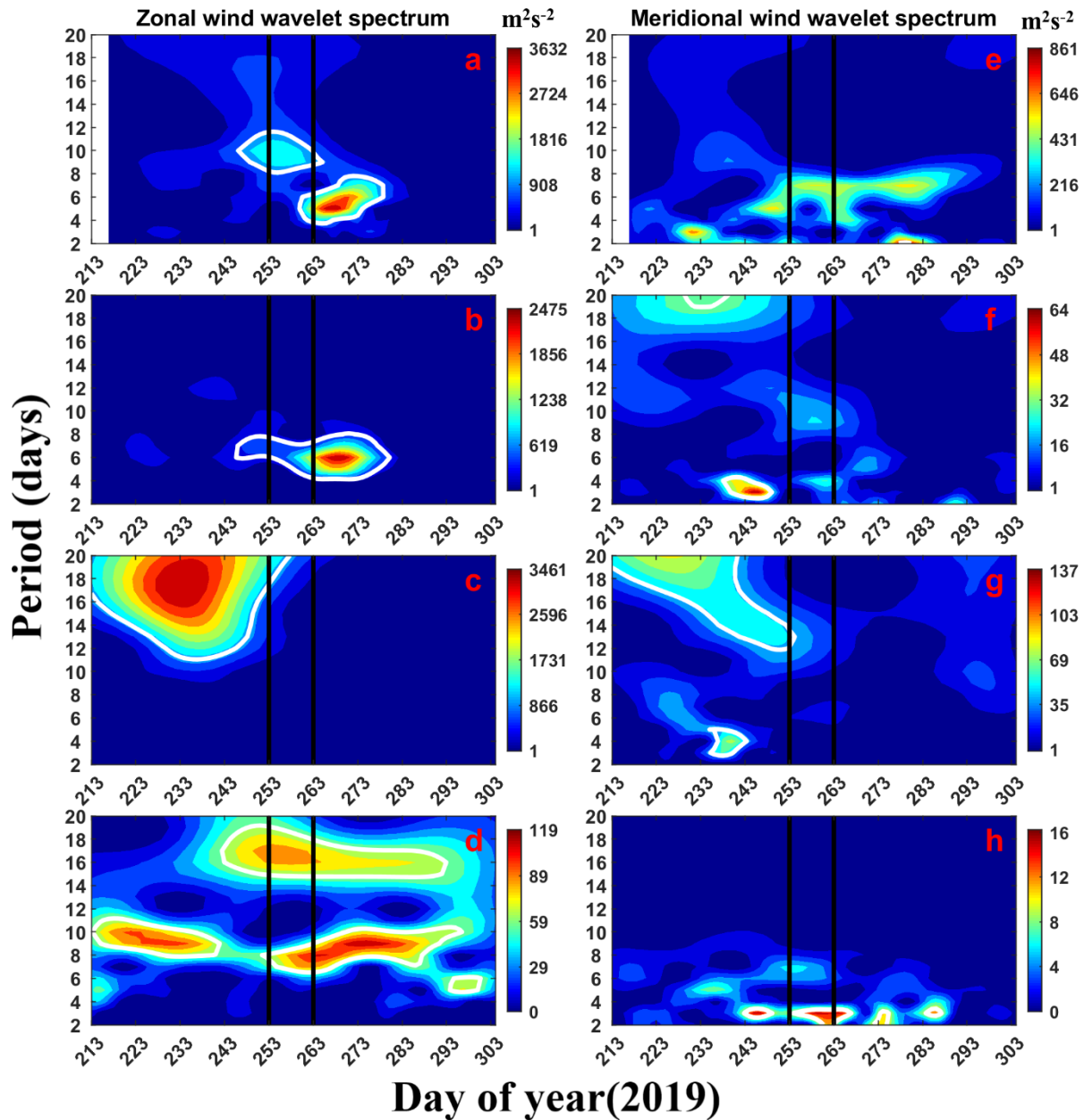


Figure 3.3. Similar to Figure 3.2, but shown for CA.

Similarly, Figures 3.3a-d present the wavelet spectra of U for CA at 90 km, 0.02 hPa, 1 hPa, and 10 hPa, respectively. The Q10DW feature is significant at 90 km during warming days, although its magnitude is lesser than the Q6DW, which is more prominent during a brief interval following the warming. Enhancement of the Q6DW in the U wavelet spectrum near the mesopause during a short interval after the warming days is evident (Figure 3.3b). The

Q16DW activity is dominant in the upper stratosphere before warming days, diminishing at the onset of the warming event (Figure 3.3c). In the mid-stratosphere, the Q10DW is present throughout the observational period except for an interval of about 10 days before the warming onset. Conversely, the Q16DW intensifies during warming days and weakens afterward (Figure 3.3d).

Figures 3.3e-h illustrate the same as Figures 3.3a-d but of V. Weak traces of the Q6DW are observed around the warming days at 90 km (Figure 3.3e). The Q3DW is present before the onset of warming at the 0.02 hPa pressure level (Figure 3.3f). In the upper stratosphere at 1 hPa, the Q16DW is prominent before the warming days, while the Q3DW becomes significant between DOY 233 and DOY 243 (Figure 3.3g). At 10 hPa pressure level (Figure 3.3h), the Q3DW is significant before, during, and after the warming event.

Since both observational sites exhibit dominant periodicities around 6 and 16 days in the wavelet spectra, we delved deeper into the vertical structure of these two wave components in both wind components in the MLT region, as depicted in Figure 3.4. To achieve this, we calculated the representative amplitudes of these waves using non-linear cosine fits with periods of 6 days and 16 days, respectively (Pancheva et al., 2018). As we are interested in looking into the pattern of spatiotemporal variability of the two wave components, consideration of specific periods in the representative amplitude estimation does not affect the interpretation.

Figure 3.4a showcases a prominent signature of the quasi-6-day wave (Q6DW) in U during the warming days at CP. Meanwhile, the Q16DW in U at CP exhibits significant activity during the pre-warming interval in the MLT region (Figure 3.4b), with another enhancement observed near the top of the MLT during the post-warming period. At CA, strong Q6DW activity during the late warming phase is spread throughout the MLT range and can be observed in U (Figure 3.4c). Prominent Q16DW activity, mostly during the pre-warming interval, is discernible in U at CA from Figure 3.4d, although an isolated patch of wave amplitude can be noted at the lower MLT during the post-warming interval.

However, the representative amplitude of the Q6DW at CP generally shows a much weaker signature in V than in U at various times throughout the observational span (Figure 3.4e). The activity of the Q16DW at CP is notable mainly during the pre-warming interval, mostly at

higher MLT altitudes in V, as evident in Figure 3.4f, with a weaker signature visible in the post-warming period. Traces of weak 6-day periodicity around the warming days can be seen in V at CA (Figure 3.4g). The weak feature of the Q16DW in the meridional wind at CA is mainly observed during the pre-warming interval and at higher MLT altitudes in the post-warming span, as seen in Figure 3.4h.

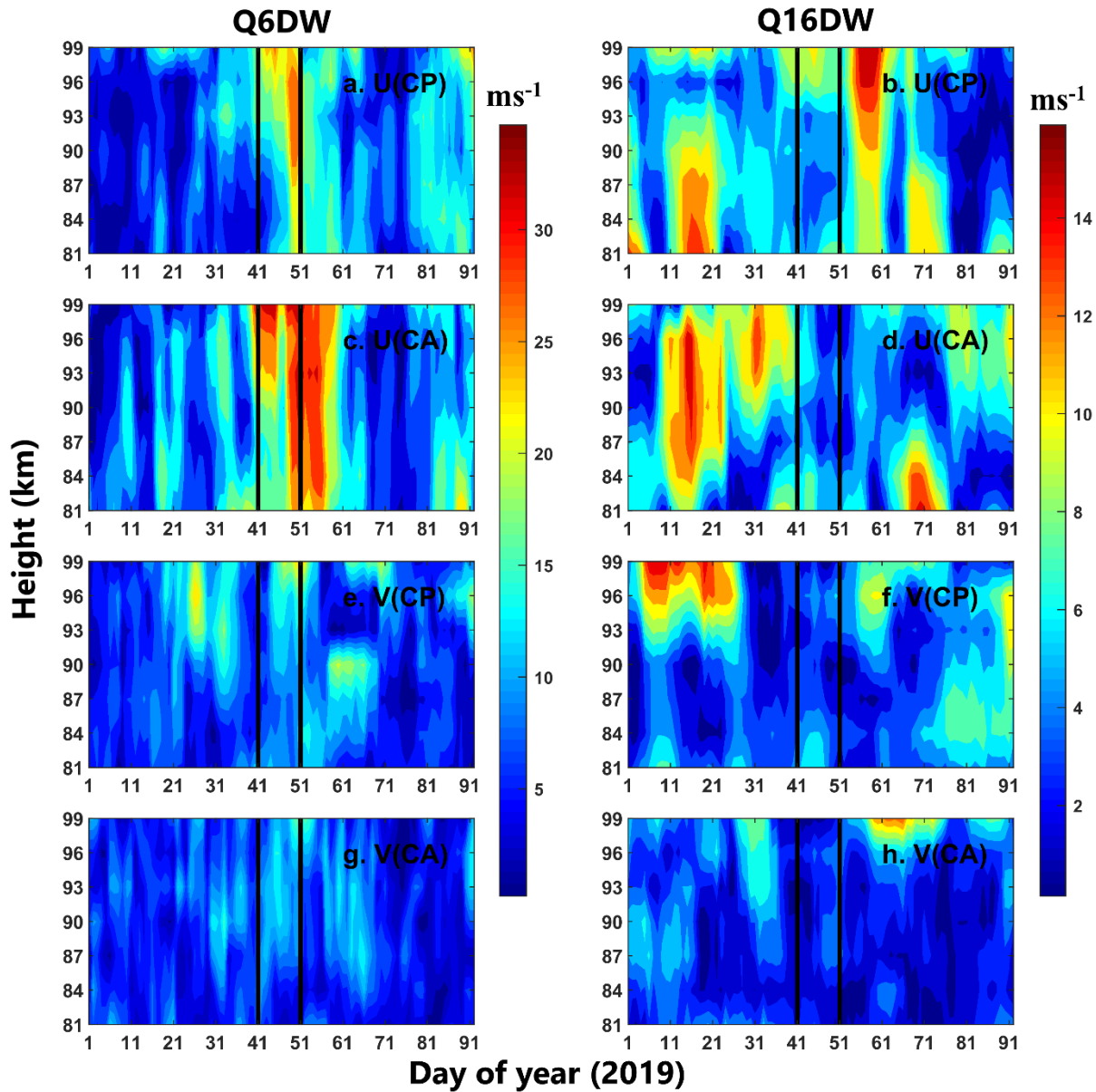


Figure 3. 4. The meteor radar derived representative amplitude of the (a) Q6DW and (b) Q16DW in U at CP. The same for the (c) Q6DW and (d) Q16DW in U at CA. The same for the (e) Q6DW and (f) Q16DW in V at CP. The same for the (g) Q6DW and (h) Q16DW in V at CA. Please note the change of scale in the colorbars while comparing.

Overall, the representative amplitude of the Q6DW is greater compared to that of the Q16DW in the MLT region. The Q16DW is generally more prominent during the pre-warming interval, while the Q6DW dominates during the post-warming interval, consistent with previous results (Figures 3.2 and 3.3) from various altitudes in the middle atmosphere.

3.2.3. Direction of Zonal Propagation

To determine the direction of propagation of traveling Planetary Waves (PWs) around the warming episode, we analyzed zonal and meridional wind data at 0.02 hPa, 1 hPa, and 10 hPa at both CP (22.7°S) and CA (7.4°S) latitudes during September 2019 using the ERA5 dataset. We estimated the amplitude of a wave with zonal wavenumber s and period T using non-linear least-square fitting with the equation:

$$A \cos[2\pi (\frac{t}{T} + s \frac{\lambda}{360}) - \phi] \quad (3.1)$$

Here, A represents the amplitude of the wave, t is the universal time, λ is the longitude, and ϕ is the phase of the wave. Positive and negative values of s correspond to westward and eastward propagating waves, respectively.

The zonal wavenumber-period spectra U over CP at 0.02 hPa, 1 hPa, and 10 hPa are shown in Figures 3.5a-c, respectively. Notable features in these spectra include:

- The zonal wavenumber (ZWN) 1 is the primary westward component of the Q16DW, Q10DW, and Q6DW in the mesopause region (0.02 hPa) (Figure 3.5a).
- The westward propagating Q16DW with ZWN 2 is dominant in U at 1 hPa pressure level (Figure 3.5b).
- In the mid-stratosphere (10 hPa), the Q16DW exhibits a strong westward ZWN 1 component and a weaker westward ZWN 2 component (Figure 3.5c).

Similarly, the ZWN-period spectra of V over CP at 0.02 hPa, 1 hPa, and 10 hPa pressure levels are shown in Figures 3.5d-f, respectively. Key observations from these spectra include:

- The Q10DW mainly consists of westward ZWN 1, whereas the Q6DW contains both westward ZWN 1 and 3 in the mesopause (0.02 hPa). Additionally, a weak feature of the Q3DW contains westward ZWN 2 (Figure 3.5d).

- The Q16DW is primarily composed of westward ZWN 2 in the upper stratosphere (Figure 3.5e).
- The Q16DW has a strong westward ZWN 2 component at 10 hPa (Figure 3.5f).

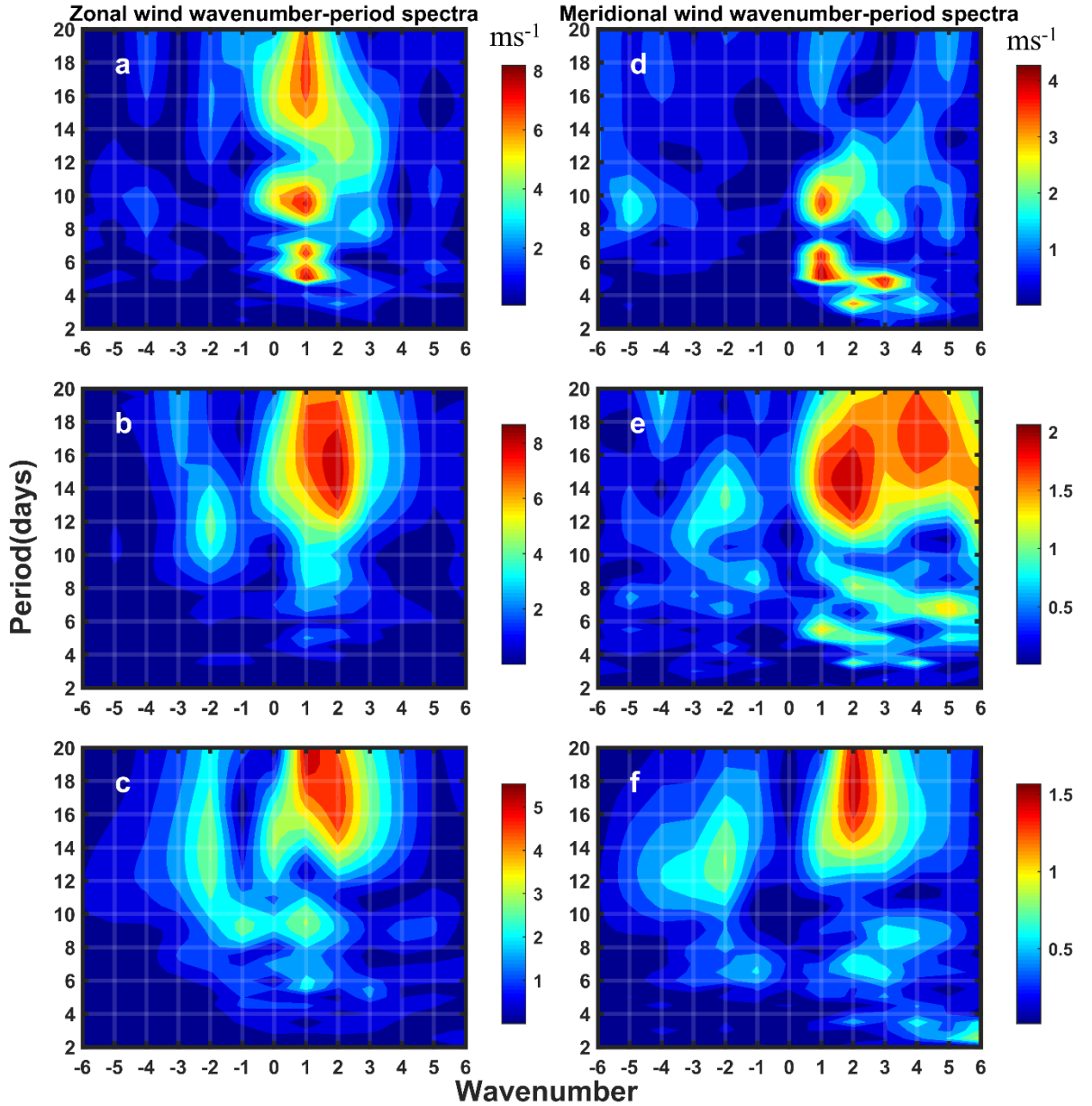


Figure 3. 5. Period vs zonal wavenumber spectra in U at (a) 0.02 hPa (b) 1 hPa, (c) 10 hPa and V at (d) 0.02 hPa (e) 1 hPa, (f) 10 hPa at CP latitude (22.7°S) using ERA5. Please note the change of scale in the colorbars corresponding to each subplot while comparing.

Moving on to CA, the ZWN-period spectra of U at 0.02 hPa, 1 hPa, and 10 hPa are illustrated in Figures 3.6a-c, respectively. Key observations include:

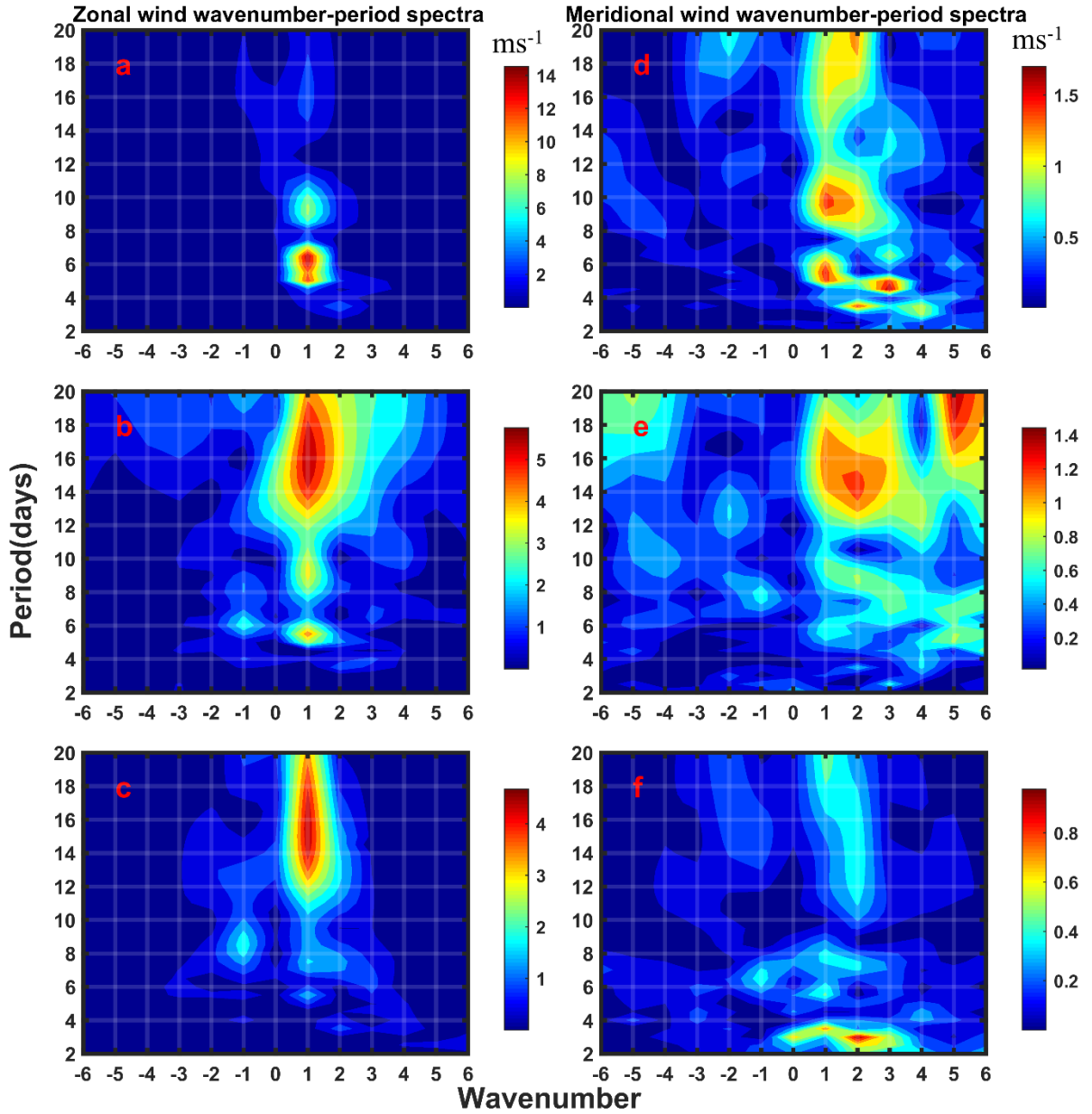


Figure 3. 6. Similar to Figure 3.5, but at CA latitude (7.4°S).

- The Q6DW observed in the U wavelet spectra at 0.02 hPa travels westward with ZWN 1 (Figure 3.6a). A weak signature of the Q10DW with westward ZWN 1 is found at 0.02 hPa.
- The westward propagating ZWN 1 component is prominent in the Q16DW at 1 hPa (upper stratosphere) (Figure 3.6b).
- In the mid-stratosphere (10 hPa), the Q16DW propagates westward with ZWN 1 (Figure 3.6c).

Finally, Figures 3.6d-f show the ZWN-period spectra of V over CA at 0.02 hPa, 1 hPa, and 10 hPa, respectively. Key features from these spectra include:

- The primary component of the Q10DW is westward ZWN 1, and that of the Q6DW is westward ZWN 1 and 3 in the mesopause (0.02 hPa). Additionally, the Q3DW contains westward ZWN 2 (Figure 3.6d).
- The Q16DW is primarily composed of westward ZWN 2 (Figure 3.6e).
- The Q3DW is primarily westward with ZWN 2 in the mid-stratosphere at 10 hPa (Figure 3.6f).

Overall, the amplitude of the wavenumber-period spectra for V is significantly less than that of U over both CP and CA. Hence, U will be considered for further analysis.

The Q6DW and Q16DW are found to be predominantly westward traveling, characterized by a zonal wavenumber 1 component, as identified in the wavenumber-period spectra.

Consequently, the temporal variability of the westward zonal wavenumber 1 component for the Q6DW (Q6DWW1) and Q16DW (Q16DWW1) is investigated utilizing U over the observational interval, depicted in Figure 3.7. The representative amplitudes of Q6DWW1 and Q16DWW1 are determined using Equation 3.1, considering periods of 6 days and 16 days, and indicated by blue and red colors, respectively. Figures 3.7a-c illustrate the representative amplitudes of Q6DWW1 and Q16DWW1 at CP latitude at 0.02 hPa, 1 hPa, and 10 hPa, respectively. Similarly, Figures 3.7d-f display the representative amplitudes of Q6DWW1 and Q16DWW1 at CA latitude at 0.02 hPa, 1 hPa, and 10 hPa, respectively.

At 0.02 hPa, Q16DWW1 exhibits nearly simultaneous enhancement with similar amplitudes prior to warming around DOY 233-243 at both locations. Another peak in the post-warming period is also evident around DOY 273 at CP and DOY 283 at CA, albeit with a smaller amplitude. The Q6DWW1 shows simultaneous amplification around DOY-268 at both locations, with an amplitude nearly double at CA compared to CP. Overall, the Q6DWW1 demonstrates significantly higher amplitudes compared to Q16DWW1.

At 1 hPa, a broad enhancement peak is observed in the Q16DWW1 amplitude at both locations during the pre-warming period, followed by a weaker feature in the post-warming period.

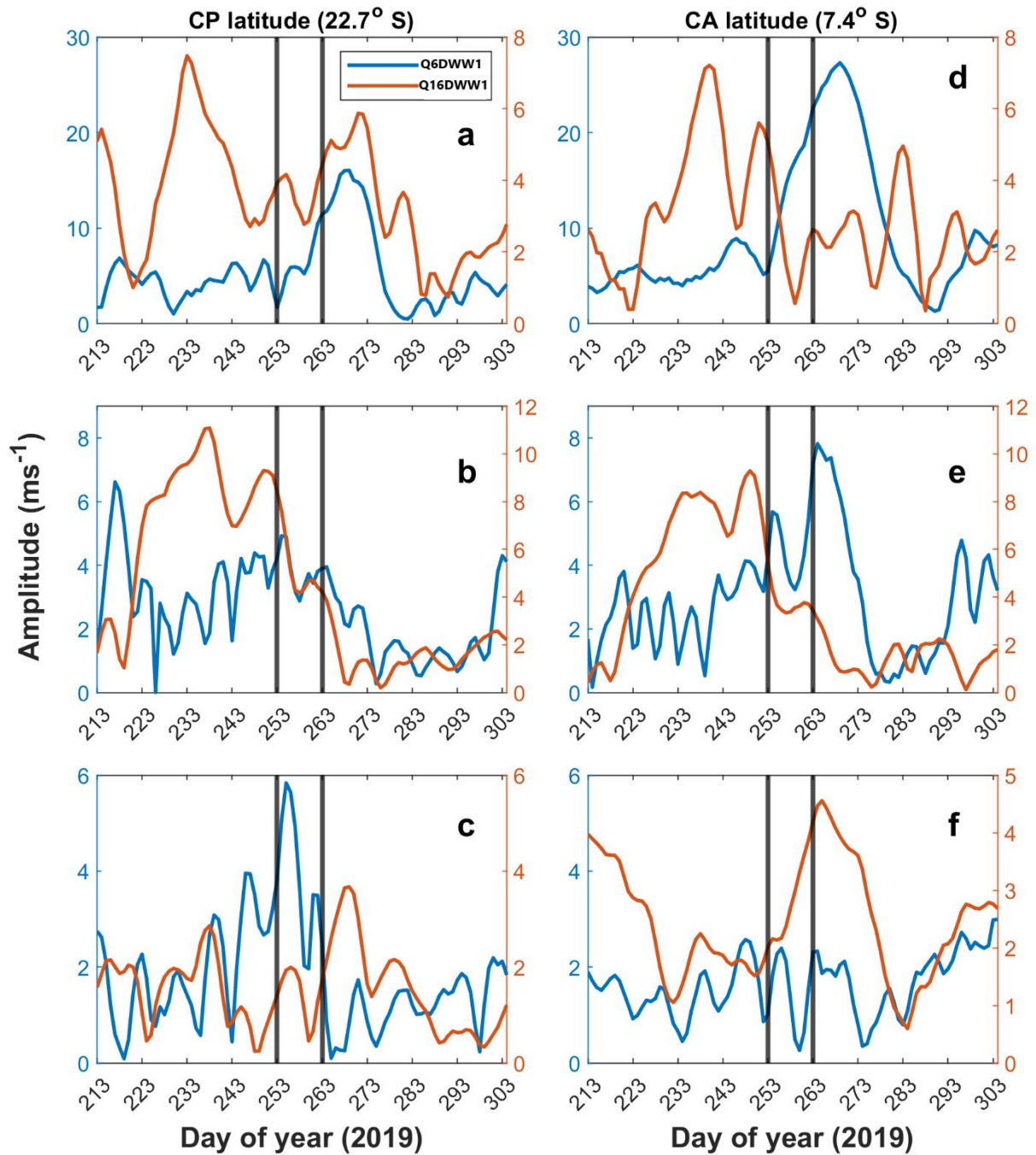


Figure 3. 7. The representative amplitude of the Q6DWW1 (blue curve) and Q16DWW1 (red curve) using ERA5 U at (a) 0.02 hPa, (b) 1 hPa and (c) 10 hPa at CP latitude (22.7° S). The same at (e) 0.02 hPa, (f) 1 hPa and (h) 10 hPa, but at CA latitude (7.4° S).

However, the Q6DWW1 does not exhibit consistent enhancement except for a sharp peak on DOY 217 at CP. Notably, a prominent enhancement in Q6DWW1 is observed on DOY 263 at CP.

CA. It's worth noting that Q6DWW1 activity decreases significantly, while Q16DWW1 enhances at 1 hPa compared to higher altitudes (0.02 hPa).

At 10 hPa, Q16DWW1 does not display notable behavior in response to warming at CP, although it seems enhanced during the warming period at CA. Conversely, Q6DWW1 amplifies during warming at CP but shows no apparent increase at CA, unlike Q16DWW1. Both wave components are considerably weaker at 10 hPa compared to higher altitudes. Consequently, Q16DWW1 dominates during the pre-warming period, while Q6DWW1 enhances during the post-warming period in both tropical and extratropical upper stratosphere and MLT, consistent with the wavelet spectra (Figure 3.2 and 3.3).

3.2.4. Stationary Planetary wave activity

In addition to analyzing TPWs, we also investigate the dynamics of stationary planetary waves (SPWs) during the observational period. To assess the variability of the primary wave components in the middle atmosphere, we estimate the amplitudes of SPW corresponding to zonal wavenumbers 1 and 2 in U using the same method as Pancheva et al. (2008a), as depicted in Figure 3.8.

The temporal changes in stationary planetary wavenumber 1 (SPW1) in the SH at 0.02 hPa, 1 hPa, and 10 hPa are shown in Figures 3.8a-c, respectively. There is a noticeable amplification of SPW1 at mid-latitudes (30° - 60°S) during the warming and post-warming phases near the mesopause (0.02 hPa), as seen in Figure 3.8a. In the upper stratosphere at the 1 hPa pressure level (Figure 3.8b), SPW1 intensifies before the warming at high latitudes, sharply declining at the start of the warming event and remaining weak thereafter. At mid-latitudes, SPW1 is active until the onset of warming, after which it weakens significantly. At 10 hPa, SPW1 shows high amplitude at polar latitudes during the warming days but becomes considerably weaker afterward. At mid-latitudes, SPW1 weakens as warming begins, as depicted in Figure 3.8c.

The stationary planetary wavenumber 2 (SPW2) amplitude at 0.02 hPa, 1 hPa, and 10 hPa are shown in Figures 3.8d-f, respectively. At 0.02 hPa, there are no notable features in SPW2 activity in response to the SSW event (Figure 3.8d). SPW2 remains active until the end of

warming at 1 hPa in mid-latitudes, as shown in Figure 3.8e, with higher amplitude than at high latitudes at 1 hPa. SPW2 activity weakens in the post-warming period at the 10 hPa pressure level, as depicted in Figure 3.8f. Overall, both components exhibit significant variability associated with the warming episode, with SPW1 being stronger than SPW2, as illustrated in Figure 3.8.

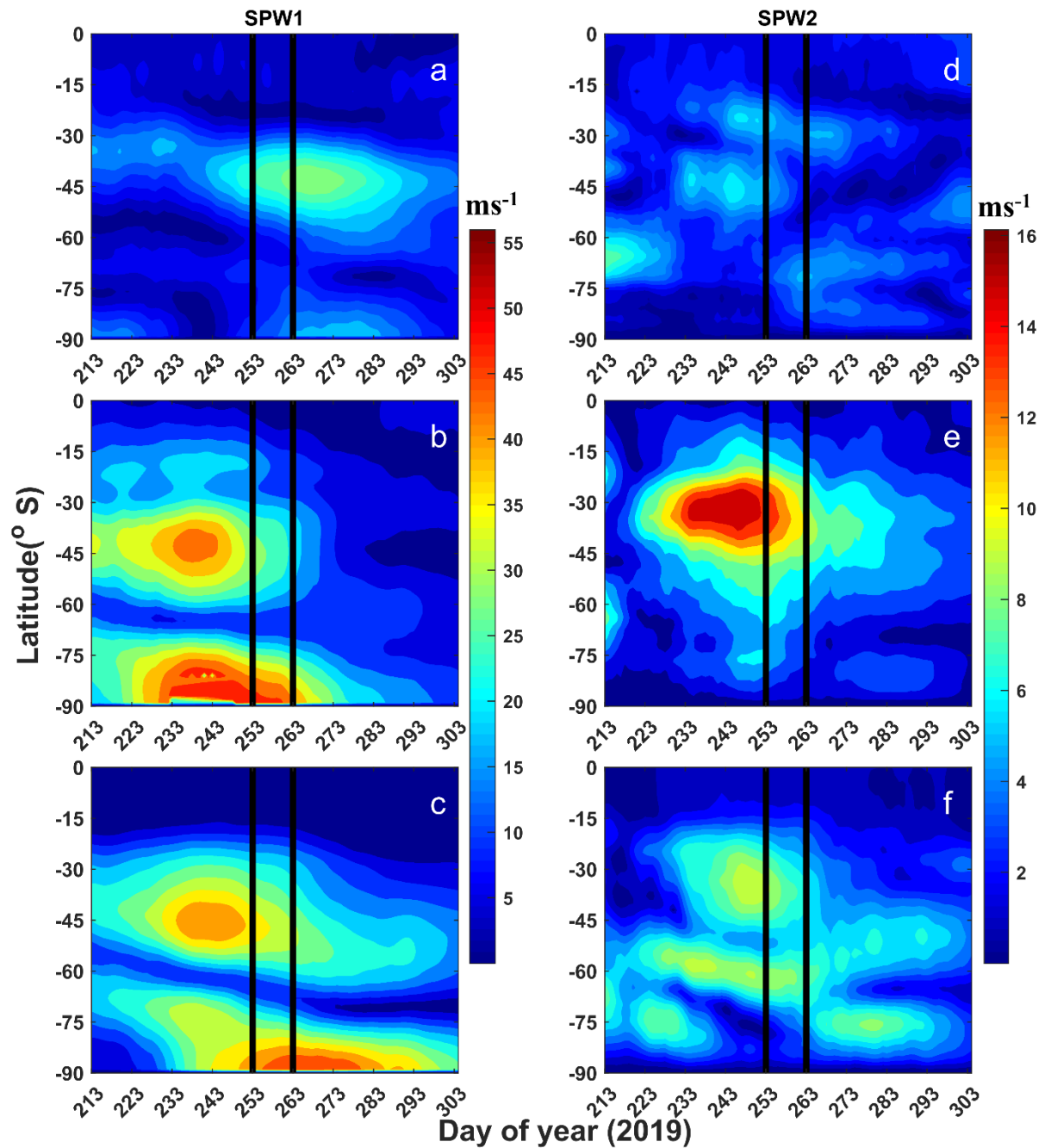


Figure 3. 8. Latitudinal-temporal variation of SPW1 at (a) 0.02 hPa (b) 1 hPa, (c) 10 hPa and SPW2 at (d) 0.02 hPa (e) 1 hPa, (f) 10 hPa estimated using ERA5 U. Please note the change of scale in the colorbars while comparing.

3.2.5. Meridional air-mass mixing and instability

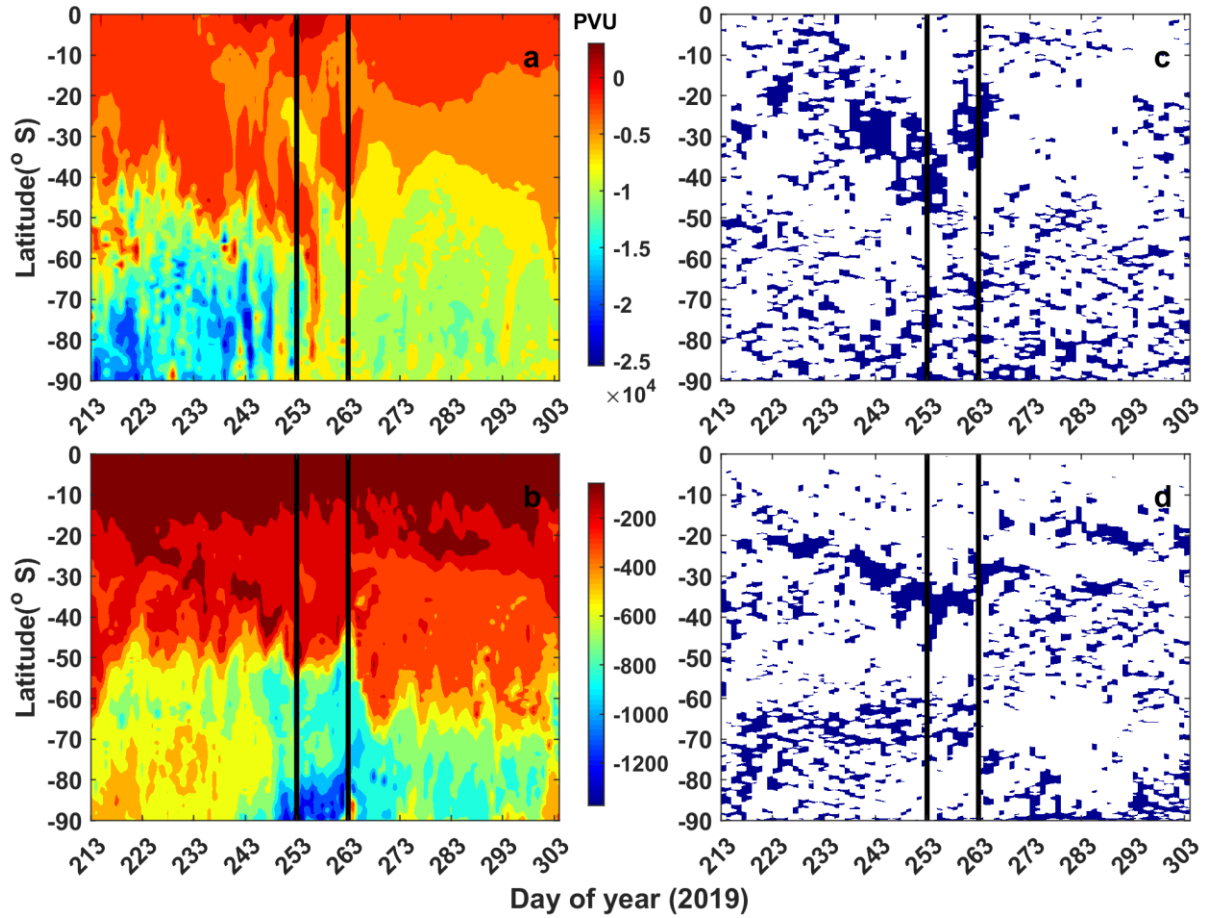


Figure 3. 9. Temporal evolution of PV averaged within 35-45°W with latitudes using ERA5 at (a) 1 hPa and (b) 10 hPa in Potential vorticity unit PVU (1 PVU = $10^{-6} \text{ K m}^2 \text{ kg}^{-1} \text{ s}^{-1}$). The blue contour represents negative value of meridional gradient of PV averaged within 35-45°W at (c) 1 hPa and (d) 10 hPa in PVU per degree latitude. Please note the change of scale in the colorbars while comparing.

The breaking of PWs results in the mixing of air masses between low and high latitudes (Abatzoglou & Magnusdottir, 2006). Utilizing Ertel's potential vorticity (PV) data available in the ERA5 database, we present the PV results up to 1 hPa from the surface. Figures 3.9a and 3.9b display the temporal changes of PV averaged over longitudes 35-45° W (including CP and CA) at 1 hPa and 10 hPa, respectively. These PV maps offer valuable insights into the temporal dynamics of meridional air mass mixing.

Figure 3.9a depicts a well-structured layer with increasing absolute PV (APV) values with latitude before the warming event at 1 hPa. During warming days, there is a noticeable intrusion of low APV values across high latitudes, persisting for the observation interval. Some patches of high APV values extend to low latitudes, possibly due to large-scale mixing during the warming event (DOY 253-263). Similarly, stratified layers of increasing APV values with latitude are evident at 10 hPa (Figure 3.9b). At this altitude, significant variability of APV is observed at high latitudes ($> 70^\circ\text{S}$) during warming, though this effect is less pronounced at low latitudes.

We also examine the presence of baroclinic/barotropic instability during the observation period, as depicted in Figures 3.9c and 3.9d. Following the Charney-Stern-Pedlosky criteria (Pedlosky, 1964), a reversal in the meridional gradient of PV in the background flow is a necessary condition, though not sufficient, for growth of wave. Therefore, we calculate the meridional gradient of PV averaged over longitudes $35\text{-}45^\circ\text{W}$ (covering CP and CA) at 1 hPa and 10 hPa. Figures 3.9c and 3.9d highlight areas with negative PV gradients at 1 hPa and 10 hPa, respectively, to identify regions of instability. Several patches of negative PV gradients are observed across all latitudes throughout the observational interval at 1 hPa. A dense patch within the $20\text{-}40^\circ\text{S}$ latitudinal domain during DOY 233 and DOY 263 in Figure 3.9c suggests considerable instability. Similar features are also noted in the mid-stratosphere at 10 hPa (Figure 3.9d).

3.2.6. Q6DW and Q16DW Flux Propagation and Source

For further exploration of the potential source, dissipation, and meridional propagation of the dominant wave components such as Q6DW or Q16DW, the Eliassen-Palm flux (EP flux F) and its divergence ($\nabla \cdot F$) are calculated (Andrews et al., 1987; Sivakumar et al., 2004). These quantities are formulated in spherical geometry under the quasi-geostrophic approximation as follows:

$$F = \{f_{(\phi)}, F(z)\} = \{-\rho_o a \cos \phi (\overline{V'U'}), f \rho_o a \cos \phi (\frac{\overline{V'\theta'}}{\theta_z})\} \quad (3.2)$$

$$\nabla \cdot F = \frac{1}{a \cos \phi} (F_{(\phi)} \cos \phi)_\phi + (F(z))_z \quad (3.3)$$

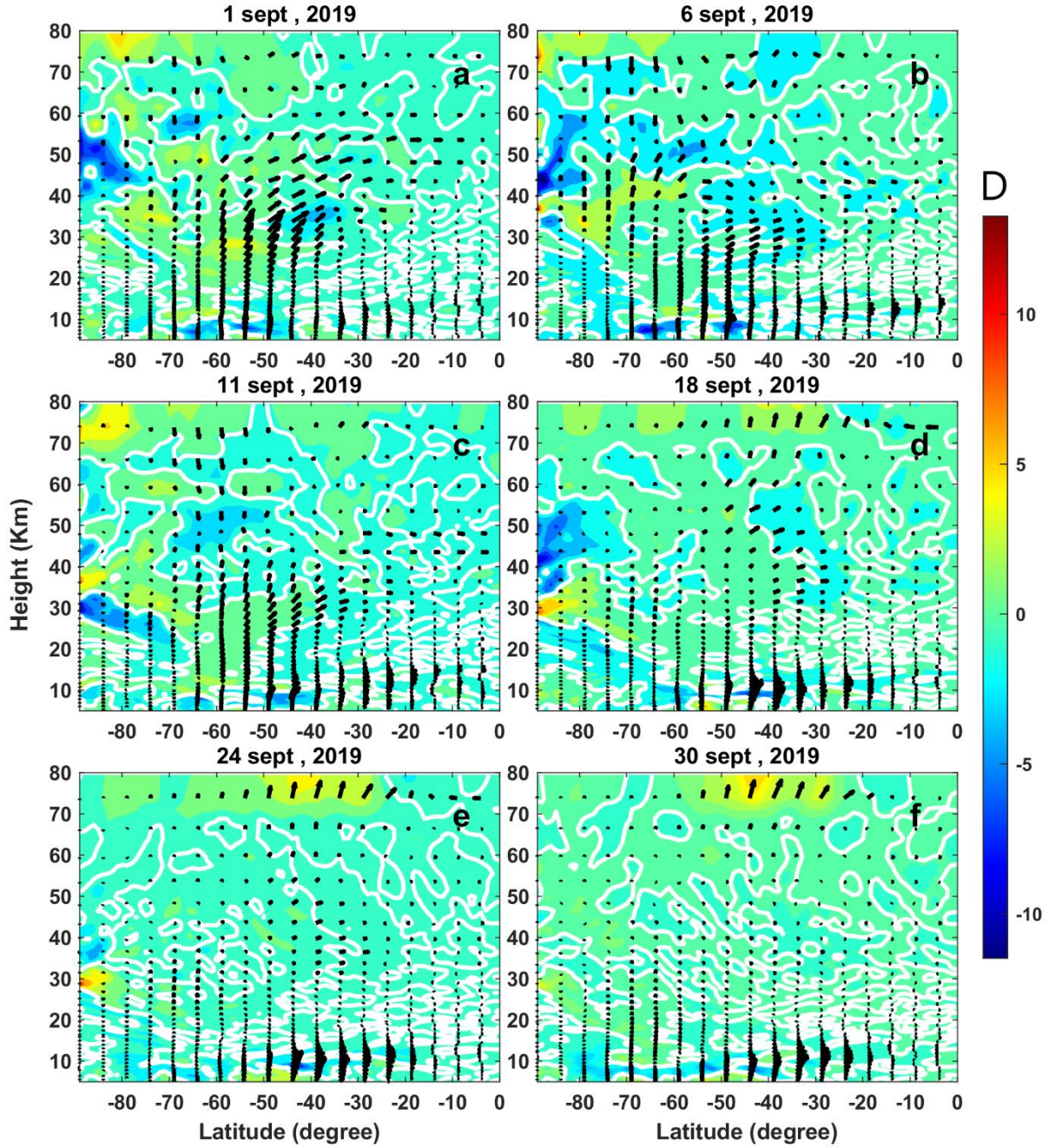


Figure 3. 10. EP flux cross-section of the Q6DW in the meridional plane for prior, during and post warming periods shown for various days. The arrows Indicate the EP flux F . The contour value represents wave driving, D in $\text{ms}^{-1} \text{day}^{-1}$. The white bold curve represents zero value of D .

Here, the overbar denotes the zonal mean, and prime signifies perturbations due to Q6DW or Q16DW, with other symbols as per Andrews et al. (1987). The perturbations (V' , U') are calculated using a bandpass filter in U , V , and potential temperature (Θ), with passbands of 5-

7 days for Q6DW and 14-20 days for Q16DW. Wave driving (D) is proportional to the EP flux divergence ($\nabla \cdot F$), as explained by Sivakumar et al. (2004):

$$D = \frac{1}{\rho_0 a \cos \phi} \nabla \cdot F \quad (3.4)$$

The EP flux (F) indicates the direction of PW propagation (Kanzawa, 1984). A negative D value signifies strong EP flux convergence, suggesting possible PW breaking and energy dissipation. Conversely, a positive D value indicates the source region. Specific days, such as pre-warming (1 and 6 September), warming (11 and 18 September), and post-warming (24 and 30 September), are chosen to depict the dynamic evolution of wave propagation and zonal wave forcing.

Figures 3.10a-f presents latitude-height cross-sections of F (arrow) and wave driving, D (contours), corresponding to Q6DW before, during, and after warming. During the pre-warming and warming phases (1-18 September), strong wave convergence occurs at polar latitudes (30-60 km), with weak divergence at higher altitudes (70-80 km). It's important to note that simultaneous divergence and equatorward wave flux begin to intensify starting from the peak warming period (18 September) at 70-80 km near 30-50°S. Another region of equatorward wave flux becomes prominent in the troposphere, particularly during the warming and post-warming phases (18-30 September), though it's confined to 20-50°S and lacks accompanying divergence. Furthermore, wave convergence/divergence at low and mid-latitudes is relatively subdued after the warming period (24-30 September). Thus, the significant equatorward propagation of Q6DW during the post-warming period in the upper mesosphere is noteworthy, potentially originating from a plausible source in the mid-latitudes.

Similarly, Figure 3.11a-f illustrates latitude-height cross-sections of F and D for Q16DW across the warming phases. The Q16DW activity, in terms of convergence/divergence, peaks in the polar region within a vertical range of 20-60 km. However, at mid-latitudes (50-60°S), the convergence zone near 50 km diminishes over time, transitioning into a divergence zone. This divergence zone serves as the origin for a noticeable equatorward Q16DW flux until 24 September, after which it notably weakens.

In summary, notable features include significant equatorward Q6DW propagation post-warming in the upper mesosphere, likely originating from mid-latitudes. Conversely, Q16DW shows gradually increasing flux in the stratosphere during warming from mid to low latitudes.

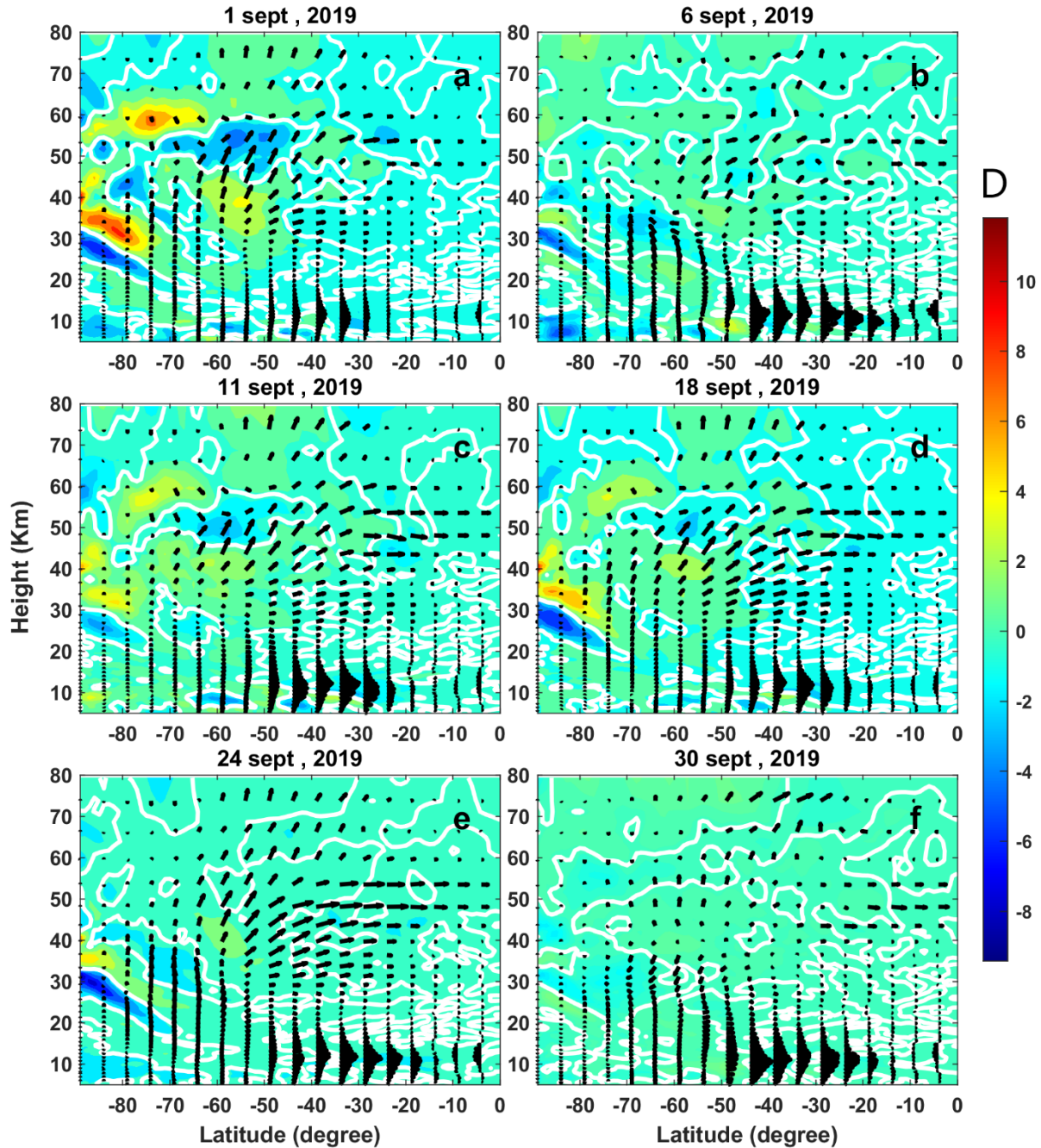


Figure 3. 11. Similar to Figure 3.10, but for the Q16DW.

3.3. Discussion

Our current investigation has highlighted key dynamical aspects of a minor SH SSW event that occurred in September 2019. This analysis is based on meteor radar wind observations from two low-latitude Brazilian stations and the ERA5 reanalysis dataset. The 2019 minor SSW event is only the second most intense warming event in the SH reported to date (Noguchi et al., 2020). This study aims to provide valuable insights into middle atmospheric dynamics, particularly regarding PW activity, especially at low latitudes during such rare occurrences.

During the warming event, mesospheric cooling is observed at 60°S from DOY 213 until DOY 263 (end of the warming period). Past studies (Schoeberl, 1978; Duck et al., 1998; Mukhtarov et al., 2007) have also reported mesospheric cooling during similar warming events. This cooling in the polar mesosphere is attributed to the upward flow of mean residual circulation (Matsuno, 1971; Liu & Roble, 2002). Concurrently, polar stratospheric warming is observed alongside stratospheric cooling at tropical latitudes in our observations. This pattern of tropical stratospheric cooling with simultaneous stratospheric warming at high latitudes has been documented in previous research (Fritz & Soules, 1970; Guharay et al., 2014). Fritz and Soules (1970), using NIMBUS III satellite observations over the northern hemisphere, proposed that tropical cooling results from eddy heat transport, driven by changes in meridional circulation from high to low latitudes. Noguchi et al. (2020) specifically studied the 2019 SH minor warming event and concluded that tropical cooling is due to enhanced Brewer-Dobson circulation. Additionally, the 2019 minor SH SSW features mesospheric warming at low latitudes concurrently with mesospheric cooling at high latitudes. The 2019 SH minor SSW event is characterized by a sudden deceleration of westerly ZMU from 90 to 10 m/s at 60°S, 10 hPa (Lim et al., 2020 and Yamazaki et al., 2020). This reduction in magnitude, occurring from late August to mid-September 2019, is comparable to the 2002 SH major SSW event, where the wind changed from about 60 to -20 m/s in late September (Guharay et al., 2014; Lim et al., 2020).

The reversal of westerly ZMU at high latitudes (60°S) initially occurred in the upper mesosphere on 2 September (DOY 245), descending to lower altitudes and reaching 36 km height on 18 September (DOY 261), consistent with recent studies by Yamazaki et al. (2020) and Miyoshi and Yamazaki (2020). Since the wind reversal at high latitudes did not occur at 10 hPa, the event is classified as minor in the SH. The ZMU at our observing latitudes is also influenced by polar warming, leading to a weakening of the eastward wind. This weakening

is notable around 65 km (mesosphere) over both the CA and CP latitudes. The decrease in the magnitude of westerly U around 65 km in low latitudes may be attributed to the induction of westward momentum to the mean flow through PW dissipation at mesospheric altitudes during the warming period.

The strong westerly wind observed before the warming event, as depicted in Figures 3.1d, 3.1f, and 3.1h, likely supports and intensifies the PW activity. PWs propagate upward provided the background wind speed remains below the Rossby critical velocity (Charney & Drazin, 1961). The wavelet spectra at both low-latitude locations show similar responses in terms of TPWs related to the warming event. The enhanced activity of Q16DW in the mid and upper stratosphere diminishes following the warming, giving way to the appearance of Q6DW in the upper mesosphere (0.02 hPa) and MLT region, persisting for about a week (Figures 3.2 and 3.3).

The Q6DW is typically observed as an equinoctial phenomenon in the MLT region over equatorial and tropical regions during April/May and Sept/Oct months (Lima et al., 2005; Kishore et al., 2004). Notably, the observed Q6DW enhancement in September 2019 stands out as exceptional, with the maximum recorded amplitude far surpassing both the climatological average and any individual amplitudes recorded from 2004 to 2018 (Yamazaki et al., 2020). The Q6DW activity in the MLT region is more pronounced in U than in V (Kishore et al., 2004). The appearance of Q6DW in U after the warming days in the tropical mesosphere could be linked to the weakening of the westerly ZMU around 65 km altitude, as indicated in Figures 3.1g and 3.1h. Although there is some indication of the Q6DW in V at CP, it is relatively weaker and insignificant at CA.

Miyoshi and Yamazaki (2020) studied the Q6DW behavior during the same warming event using simulation from the Ground-to-Topside model of Atmosphere and Ionosphere for Aeronomy (GAIA) and found similar features, supporting our present findings. Notably, the Q16DW is primarily active in the stratosphere during pre-warming conditions, while the Q6DW dominates in the upper mesosphere during and after the warming event. These observations suggest the dissipation of the Q16DW and the subsequent generation of secondary waves in the form of Q6DW at mesospheric altitudes and the MLT region.

These intriguing observations indeed suggest a potential link between Q6DW growth and instability, potentially influenced by Q16DW dissipation, which could drive instability through momentum redistribution associated with planetary wave breaking (Singh et al., 2024; Hitchman et al., 1987). However, further investigation is needed to validate this hypothesis. The occurrence of secondary PWs in the mesosphere after the 2012 minor SSW event is observed by Chandran et al. (2013). They attributed the secondary wave in the MLT after the SSW to the in situ generation of instabilities in the presence of large temperature and wind gradients. In our study, the reversal of eastward ZMU at 60°S above 10 hPa (Figure 3.1f) could be contributing to the enhancement of Q6DW. Koushik et al. (2020) proposed that significant wind reversals in the stratosphere following SSWs in the Northern Hemisphere may favor the instability mechanism for generating secondary planetary waves. The presence of PWs with periods of 6.5 days and 16 days during the same time period may suggest a relationship between them (Talaat et al., 2002).

The mesospheric warming anomaly during the SSW event at low latitudes, as seen in Figures 3.1c-d, is possibly due to the dissipation of the Q16DW, which is active mainly during pre-warming conditions in the stratosphere. Additionally, the Q10DW and Q3DW are observed at various times during the observational period but do not exhibit a significant response to the minor SSW event. Overall, there is a noticeable difference in the periodicity of traveling waves observed in V than in U. This difference could be attributed to the Doppler shift in the frequency of TPWs caused by variations in background winds (Salby, 1981; Pancheva et al., 2008b).

The present investigation into the propagation direction of TPWs such as Q16DW, Q10DW, and Q3DW over CP and CA, as depicted in Figures 3.5 and 3.6, highlights westward TPWs with zonal wavenumbers 1 and 2 as the dominant components. Specifically, Q16DW predominantly exhibits westward flow with a ZWN 1 component. Given that Q16DW is most active prior to the onset of the warming event, it likely plays a role in preconditioning the event. Furthermore, the appearance of Q6DW primarily towards the end of the warming also shows westward propagation with a ZWN 1. It's worth noting that Q6DW in the atmosphere behaves as a Rossby wave with ZWN 1 (Hirota & Hirooka, 1984), a robust feature in the middle and upper atmosphere (Hirota & Hirooka, 1984; Talaat et al., 2002; Lieberman et al., 2003; Pancheva et al., 2018). Additionally, a strong SPW1 is observed in the stratosphere (at 10 hPa and 1 hPa) of middle and high latitudes leading up to the warming event, significantly

diminishing during post-warming conditions, aligning with previous findings by Yamazaki et al. (2020). Similarly, features of SPW2 are noted at 10 hPa (Figure 3.8f) and 1 hPa (Figure 3.8e), albeit with notably lower amplitudes compared to SPW1. This underscores the significant role of PWs, particularly those with ZWN 1 (stationary and westward traveling), in preconditioning the SH 2019 minor SSW event.

The presence of barotropic/baroclinic instability is evident at the onset of the warming, as indicated by the negative meridional gradient of APV at low and mid-latitudes (Figure 3.9c and 3.9d). This instability significantly diminishes after the warming event. Such instability contributes to the growth of PW activity by extracting energy from the horizontal/vertical shear of the background flow or, equivalently, from horizontal temperature gradients (Charney et al., 1962). In the context of the generation and maintenance of the 2012/13 SSW, Xu and Liang (2017) argued that this instability involved extracting available potential energy from the vertical or meridional unstable wind structure, leading to a reversal of the polar jet.

In our study, the presence of instability is also noticeable in the ZMU, where the strong westerly jet decelerates at the beginning of the warming days, as depicted in Figures 3.1d, 3.11f, and 3.1h. Additionally, Tomikawa et al. (2012) suggested the possibility of barotropic/baroclinic growth of PW immediately after the SSW due to the reversed potential vorticity (PV) gradient, linked to the formation of an anomalous westward jet. Theoretical studies by Salby and Callaghan (2001) reported the amplification of the 6.5-day wave in an unstable background condition. Lieberman et al. (2003) and Gan et al. (2018) reported growth of the Q6DW due to baroclinic and barotropic instability during equinoxes. Limpasuvan et al. (2016) observed the generation of westward propagating secondary planetary waves during SSW due to barotropic/baroclinic jet instability.

Hence, the consistency of our findings with these previous investigations further supports a potential link between Q6DW and instability in the middle atmosphere. Furthermore, the coincidence of the zero wind line at low latitudes in Figure 3.1b and the negative PV gradient patch in Figure 3.9d at 10 hPa during DOY 213-263 suggests a potential connection between instability and the reversal of ZMU.

The EP flux analysis reveals propagation of the Q6DW and Q16DW from mid and high latitudes towards the equator in the stratosphere and lower mesosphere. The presence of an intensifying divergence zone, coupled with equatorward Q6DW flux around 70-80 km altitude within the latitudinal range of 30-50°S on the peak warming day, i.e., 18 September, and the subsequent interval, may suggest a potential source of Q6DW observed at CP and CA at 90 km and 0.02 hPa (Figures 2 and 3). The notable equatorward Q16DW flux appears active until the conclusion of the warming days but diminishes during the post-warming phase. Additionally, the presence of a divergence zone at mid and high latitudes may indicate a plausible source region for Q16DW.

Overall, the equatorward activity of Q6DW/Q16DW is prominent, extending down to latitudes as low as 20°S (near CP location). Furthermore, the impact of the warming is comparatively weaker at equatorial latitudes (near CA) compared to the extratropics, aligning with findings from prior studies (Hauchecorne & Chanin, 1988; Whiteway & Carswell, 1994).

3.4. Summary and Conclusions

The present study delves into the dynamics of PWs in the middle atmosphere during a minor but impactful SH SSW event in September 2019, as observed from two low-latitude stations in the Brazilian sector. Despite existing literature on convective activity and ionospheric variability during such events, there is a noticeable gap regarding their impact on the middle atmosphere at low latitudes. This study fills that void by shedding light on the PW dynamics during this event.

The observed features characterize the warming event as a high stratospheric warming, highlighting distinct behavior in the low-latitude middle atmosphere compared to high latitudes. Notably, cooling in the tropical stratosphere coincides with warming at high latitudes, while warming in the tropical mesosphere aligns with cooling in high latitudes, showcasing a contrasting pattern.

The study identifies a strong presence of the Q16DW before warming, diminishing significantly afterward. This is followed by a significant and short-time burst of the Q6DW in

the MLT during the initial days of the post-warming phase. Additionally, several TPW components, including Q16DW, Q10DW, Q6DW, and Q3DW, predominantly exhibit westward propagation with ZWN 1 and 2. Furthermore, the study emphasizes the significant role of SPWs with ZWN 1 in preconditioning the 2019 minor SSW event. Analysis of PV maps in the stratosphere indicates notable latitudinal mixing of the air mass, associated with instability. The growth of the Q6DW during the warming period is suggested to be linked with the baroclinic/barotropic instability.

Finally, the Eliassen-Palm (EP) flux analysis unveils propagation of the Q6DW and Q16DW from high and mid-latitudes to low latitudes associated with the SSW event. Overall, these findings enhance our understanding of PW dynamics during a rare SH SSW event, particularly at low-latitude regions, and their potential implications on the middle atmosphere.

Chapter 4

Tidal Variability during 2019 minor SSW

4.1. Introduction

Continuing our previous investigation into low-latitude PW dynamics during a rare SH SSW, we now turn our attention to atmospheric tides. Like PWs, Atmospheric tides are large-scale global perturbations, which are crucial in coupling the lower, middle, and upper atmosphere and can also influence the ionospheric processes. Significant changes in atmospheric tides are observed during NH SSWs (e.g., Goncharenko et al., 2012; Lima et al., 2012) and as well as during only major SH SSW (Guharay & Batista, 2019). The observed tidal variability during SSW may be due to the following factors.

- SSW may alter the distribution of excitation source species, such as ozone and water vapor, essential to excite the tides.
- Non-linear interaction with the enhanced PWs during SSW can lead to modulation of the tidal amplitude with the PW period.
- The significant changes in background wind influence the tidal propagation.

Past studies have enhanced our understanding of the atmospheric tidal variability in the middle atmosphere during NH SSW. For instance, Sridharan et al. (2012) observed a reduction in ST amplitude in the zonal wind at 88 km above a tropical location before a minor SSW in the Northern Hemisphere in 2011. Sassi et al. (2013) noted a decline in migrating ST amplitude due to increased westward meridional shear in the mesosphere and lower thermosphere during a 2009 SSW event. He et al. (2020) recently reported the suppression of higher-order migrating tides like the terdiurnal and quarterdiurnal tides during SSW onsets. Furthermore, a study by He & Chau (2019) observed a weakening of migrating ST components during SSW events using a zonal wavenumber constraints method. However, due to the rare occurrence of SSW in the SH, we have a limited understanding of the changes in atmospheric tides during SH SSW. For example, Guharay & Batista (2019) identified a predominant migrating DT signature during the only major SSW in the SH in 2002, which could lead to nonmigrating components through nonlinear interactions with planetary waves. In this regard, the recent 2019 SSW event in the SH offers the opportunity to enhance our

understanding of the tidal responses in the SH middle atmosphere during such short-term extreme fluid dynamical events.

Despite recent studies on convective activity (Noguchi et al., 2020), ionospheric variability (Miyoshi & Yamazaki, 2020), and planetary wave activity (Mitra et al., 2022) related to this event, the atmospheric tidal variability during such historically rare SH SSW is yet to be explored. Hence, our current study aims to explore the dynamical variability of atmospheric tides in the SH middle atmosphere during the 2019 SH minor SSW event. This study bears significance because there is a limited understanding of the impact of SH SSW on middle atmospheric tidal wave dynamics.

4.2. Results

For the present investigation, we utilized meteor radar wind data from different latitudes: São João do Cariri (7.4°S, 36.5°W) (CA) at the equator, Cachoeira Paulista (22.7°S, 45°W) (CP) at extratropical latitudes, King Edward Point (54.3°S, 36.5°W) (KE) at middle latitudes, and Rothera (67.6°S, 68.1°W) (RO) at high latitudes. Additionally, we incorporated a longitudinally spaced contemporaneous MERRA2 U and V dataset to analyze various zonal wavenumber modes of atmospheric tides during the warming event. The total precipitable water vapor (TPWV) and the total columnar ozone (TCO) data provided by MERRA2, are utilized to understand the tidal excitation sources. Further, the outgoing longwave radiation (OLR) data obtained from NCEP is used as a proxy for convective activity. The observational interval spans from 1 August to 31 October 2019.

4.2.1. Background state

Section 4.2.1 expands upon Section 3.2.1 by providing further insights into the distinct characteristics of the background dynamical state observed during the 2019 event, especially highlighting the impact of the warming event on mesospheric dynamics in the Southern Hemisphere. Eswaraiyah et al. (2020) studied the 2019 minor SH SSW event and noted its onset on 30 August, 2019 (Day of Year [DOY] 242), marked by a sudden increase in the zonal mean polar stratospheric temperature, peaking on 18 September, 2019 (DOY 261). A black solid and dashed vertical line indicates the onset and the peak warming day (PWD),

respectively, in all figures. The altitude profile (0-75 km) of the difference in ZMT between 90°S and 60°S from 1 August to 31 October 2019 (DOY 213 = 1 August), is shown in Figure 4.1a. The bold white curve represents zero value in all the plots, while the bold black curve represents a 20 K value in Figure 4.1a. The ZMT difference between 90° S and 60° S exceeding 20 K is considered as high polar warming in the present study. The ZMT difference reverses and becomes positive in the upper stratosphere (30-45 km altitude) from 30 August (DOY 242) onward, indicating polar stratospheric warming relative to mid-latitudes. A noticeable polar stratospheric warming exceeding 20 K is observed between DOY 242 and DOY 263 within the 30-45 km altitude range. Simultaneously, a negative ZMT gradient in the 60-75 km altitude band indicates polar mesospheric cooling relative to mid-latitudes, occurring concurrently with polar stratospheric warming. An intriguing observation is the apparent downward propagation of the high poleward warming from the mesosphere to the stratosphere until the PWD.

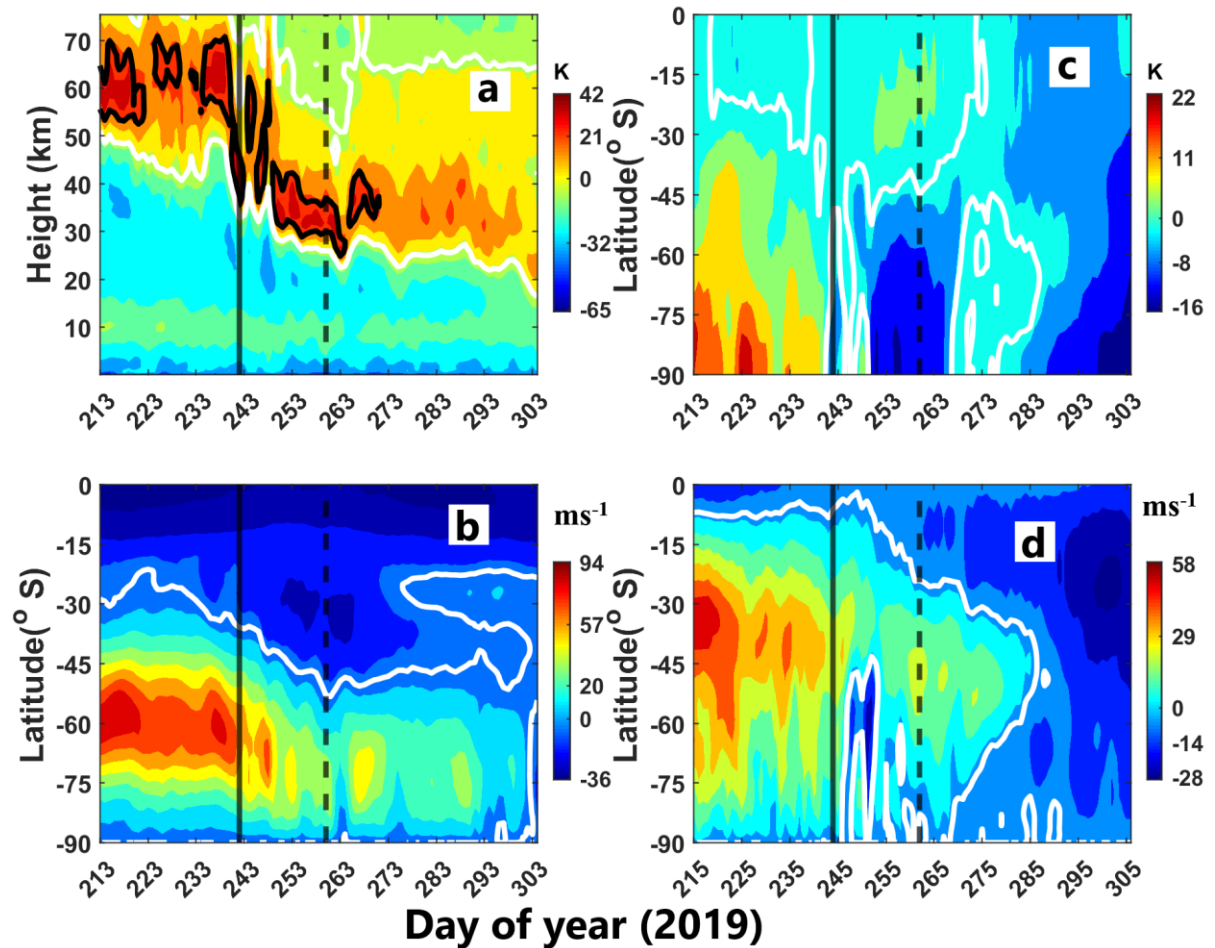


Figure 4. 1. (a) Altitudinal profile of difference between the zonal mean temperature at 90° S and 60° S during August-October 2019 (DOY 213 ~ 1 August). (b) Latitudinal profile of the zonal mean zonal wind at 10 hPa during the same period. (c) Latitudinal profile of the

difference between zonal mean temperature and the temporal mean of zonal mean temperature at 0.01 hPa. (d) Latitudinal profile of the zonal mean zonal wind at 0.01 hPa. The bold white line represents zero value in the present figure and all the following figures, and the bold black curve represents a value of 20 K in Figure 1a. The vertical black solid line and the dashed line represent the SSW onset date and the PWD, respectively, for the present and all the following figures. Please note the change of scale in the color bars while comparing.

Figure 4.1b depicts the latitudinal profile of ZMU at 10 hPa during the observational interval. The strong westerly at 10 hPa, 60°S, shows considerable deceleration around the PWD without undergoing a wind reversal. Figure 4.1c shows the latitudinal profile of the difference between ZMT and the temporal mean (August - October 2019) of ZMT at 0.01 hPa. It reveals relative mesospheric cooling at 0.01 hPa at high and mid-latitudes between the onset and PWD. However, there is contrasting behavior in the low-latitude mesosphere compared to high latitudes, with warming in the mesosphere occurring concurrently with cooling at high latitudes. Figure 4.1d displays the ZMU at 0.01 hPa, showing significant deceleration in the zonal mean westerly wind at the onset of the warming event, particularly in the 20-40°S latitudinal band. Interestingly, a wind reversal occurs at mid and high latitudes at 0.01 hPa for a few days between the onset and PWD.

4.2.2. Local tidal variability

The notable changes in the underlying dynamic conditions during the warming event prompted us to delve into the potential impact on the primary harmonics of atmospheric tides in the MLT associated with this warming event. To achieve this, the amplitude of the principal harmonics of atmospheric tides, specifically the diurnal tide (DT) and semidiurnal tide (ST) are assessed, by analyzing U and V data from RO, KE, CP, and CA. Horizontal wind data from meteor radar and MERRA-2 is employed to gain a comprehensive understanding of the dynamical changes in DT and ST in the MLT region spanning from 50 km to 100 km altitude. The tidal amplitude is estimated through non-linear least-squares fitting using the following wave equation:

$$Y(t) = Y_o + A_n \cos\left[\frac{2\pi n}{24}(t - \varphi_n)\right] \quad (4.1)$$

Here, $n = 1, 2$ represents diurnal and semidiurnal components, A_n is the amplitude, t is the universal time, and φ_n is the phase. $Y(t)$ denotes the hourly V/U , while Y_o is the mean wind over a 48-hour fitting window. The window is progressively shifted by one day (24 hours) to derive daily tidal amplitudes, as depicted in Figure 4.2.

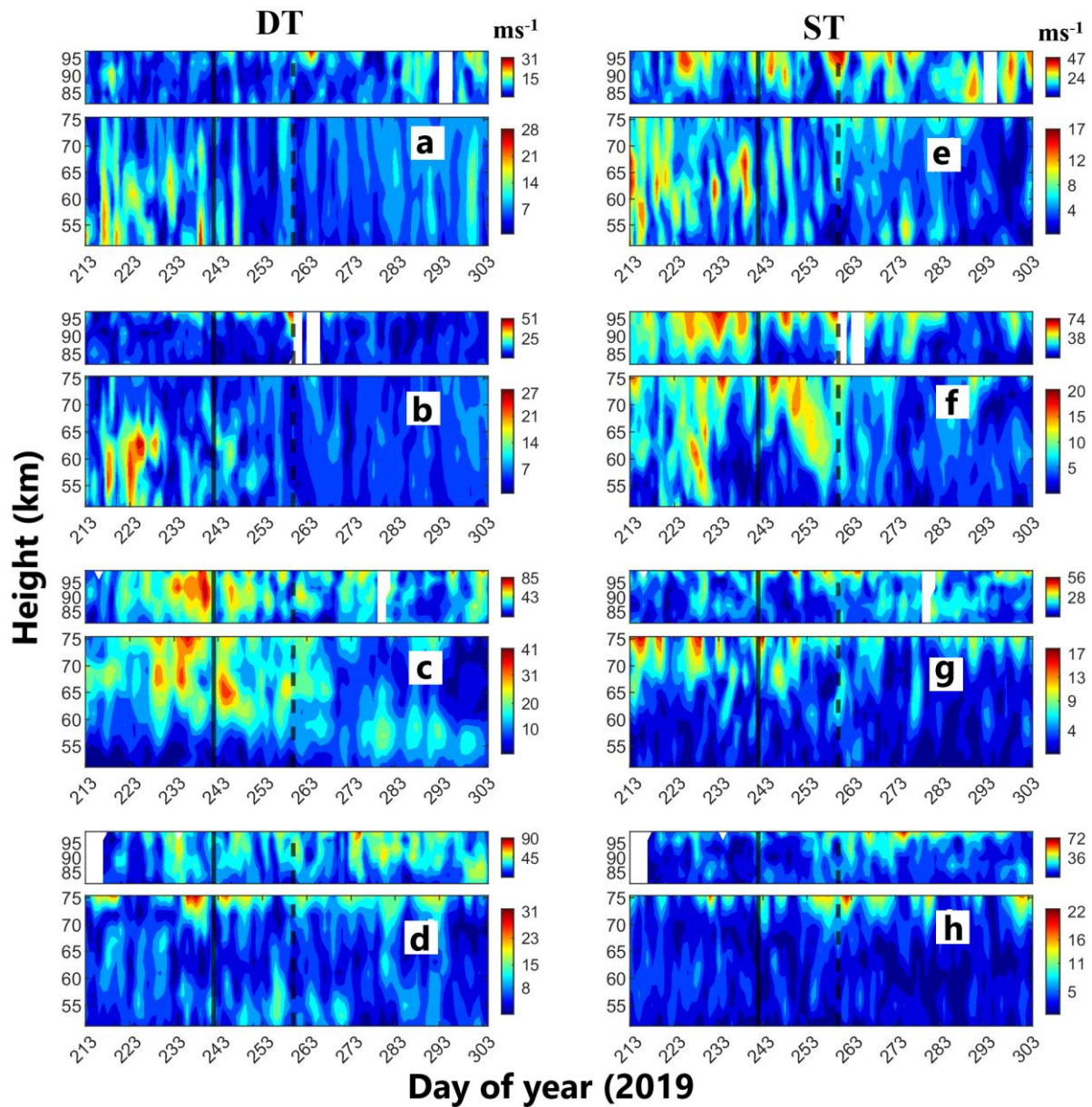


Figure 4. 2. Temporal variation in the DT amplitude in ms^{-1} at (a) RO (67.6°S, 68.1°W), (b) KE (54.3°S, 36.5°W), (c) CP (22.7°S, 45°W), and (d) CA (7.4°S, 36.5°W) using V from meteor radar (80-100 km altitude) and MERRA2 (50-75 km altitude). Same for the ST amplitude in ms^{-1} at (e) RO, (f) KE, (g) CP, and (h) CA. Please note the change of scale in the colorbars while comparing.

Overall, the DT and ST amplitude is more pronounced in V than in U across RO, KE, CP, and CA. Furthermore, the DT and ST amplitude derived from V and U show similar trends during the observational interval (figures not displayed), as we focus only on V for further analysis to avoid redundancy. The temporal changes in the DT amplitude in the MLT region (approximately 50–100 km) over RO, KE, CP, and CA are illustrated in Figures 4.2a-d, respectively. The top and bottom contour plots in each subplot of Figure 4.2 depict the DT/ST amplitude derived from meteor radar (80–100 km altitude) and MERRA-2 (50–75 km altitude), respectively. White vertical patches in the contour plot indicate missing observational data from the meteor radar. Notably, there's a considerable difference in tidal amplitudes between radar and reanalysis datasets. However, since the emphasis is on the pattern of variability rather than the absolute magnitude of amplitude, these differences do not affect our conclusions.

The DT amplitude at RO shows an overall decreasing trend in the mesosphere (50–75 km) at the Sudden Stratospheric Warming (SSW) onset, with no clear response to warming in the Lower Thermosphere (LT) (80–100 km) (Figure 4.2a). Similarly, the DT amplitude at KE doesn't exhibit notable features regarding the warming event in the LT but does show a discernible decrease in amplitude in the mesosphere leading up to the onset date (Figure 4.2b). Figure 4.2c illustrates the variability in DT amplitude at CP, where a sudden burst in amplitude is observed around the SSW onset date. However, the DT amplitude doesn't show a striking signature at CA during the warming period (Figure 4.2d).

Likewise, Figures 4.2e-h show the variability in ST amplitude in the MLT over RO, KE, CP, and CA, respectively. The ST amplitude at RO doesn't show apparent variability concerning the warming event in the LT but exhibits a gradual drop in amplitude in the mesosphere at the SSW onset (Figure 4.2e). At KE, the ST appears active during the prewarming phase and diminishes after the PWD (Figure 4.2f). The ST amplitude doesn't vary notably at CP concerning the SSW event in the LT but does show a decrease in amplitude in the mesosphere after the PWD (Figure 4.2g). The ST amplitude is significant for a few days around the PWD at CA (Figure 4.2h). While some variability is observed in specific regions and locations concerning the warming event, there's no substantial response in local DT and ST amplitudes. Next, we investigate the variability in the dominant global DT and ST components

corresponding to different zonal wavenumbers to identify any variations during the warming event.

4.2.3. Variability of global tidal modes

The tidal amplitude associated with various zonal wavenumbers is calculated using V in the mesosphere (approximately 50–75 km) from the MERRA-2 dataset. The amplitude of a wave with a zonal wavenumber s and a period T can be estimated using non-linear least-square fitting employing the following wave equation:

$$A_{n,s} \cos[2\pi (n \frac{t}{24} + s \frac{\lambda}{360}) - \varphi_{n,s}] \quad (4.2)$$

Here, $n = 1, 2$ represents diurnal and semidiurnal components, $A_{n,s}$ signifies the amplitude, t denotes universal time, and $\varphi_{n,s}$ is the phase. The periodicity in longitude λ is determined by the zonal wavenumber s . We use the abbreviations DWs/DEs to refer to westward/eastward propagating DT, respectively. For ST, 'D' in the abbreviations is replaced by 'S'. Positive, negative values or zero values of s indicate westward, eastward propagating, or zonally symmetric waves.

Given the 3-hour data resolution of MERRA-2, the daily amplitude is derived using 48 data points, i.e., a 6-day window, progressively shifted by one day. After analyzing principal zonal wavenumbers ($s = -4$ to $+4$) corresponding to DT and ST, we observe a significant response during the observational interval of the warming event in amplitude only for DW1 (migrating), DE3 (nonmigrating), and SW2 (migrating), as depicted in Figure 4.3. To derive tidal parameters from the MERRA-2 dataset using equation 4.2, we selected latitudes closest to meteor radar observational sites, specifically 67.5° S for RO, 54.5° S for KE, 22.5° S for CP, and 7.5° S for CA.

Figures 4.3a-d display the temporal variability of the DW1 at latitudes 67.5° S, 54.5° S, 22.5° S, and 7.5° S, respectively. The DW1 shows a gradual increase in amplitude starting a few days before the PWD and remains active during the post-warming phase at 67.5° S (Figure 4.3a). Similar behavior is seen at 54.5° S (Figure 4.3b). At 22.5° S, a slight decrease in DW1 amplitude is observed in the upper mesosphere (65–75 km altitude) for a few days between SSW onset and PWD, with relative enhancement at lower altitudes (50–60 km) after PWD (Figure 4.3c). Figure 4.3d shows enhanced DW1 activity after PWD at 7.5° S.

Figures 4.3e-h illustrate the temporal variability of DE3 at latitudes 67.5° S, 54.5° S, 22.5° S, and 7.5° S, respectively. DE3 shows significant enhancement during the pre-warming interval, diminishing considerably at SSW onset, and remaining weak during warming and post-warming at 67.5° S (Figure 4.3e). Similar trends are seen at 54.5° S (Figure 4.3f). At 22.5° S, a slight enhancement in DE3 activity is observed around warming onset till PWD, with a notable increase in the upper mesosphere during post-PWD interval (Figure 4.3g). Figure 4.3h shows similar features for DE3 at 7.5° S.

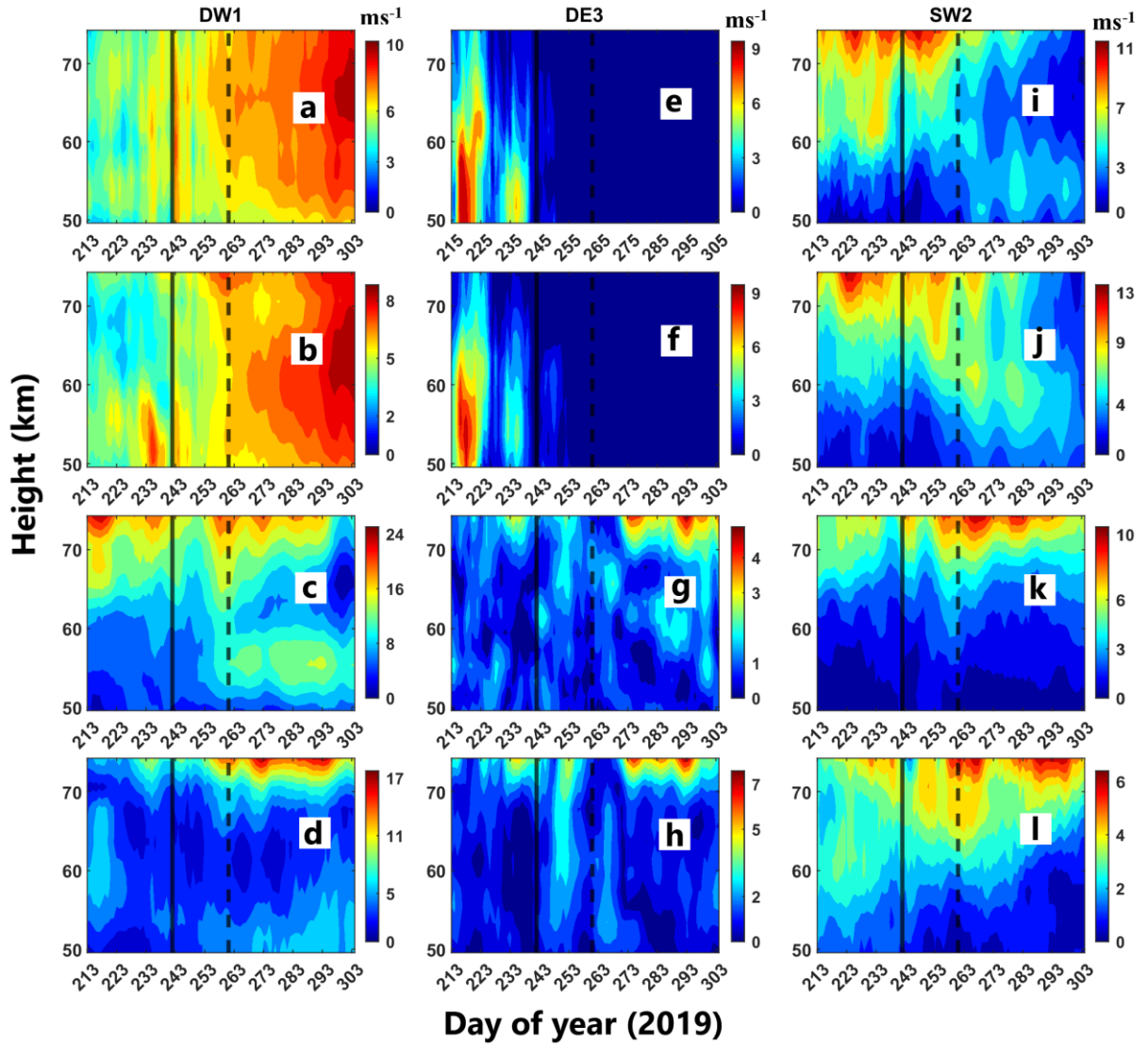


Figure 4. 3. Temporal variation in the DW1 amplitude in ms^{-1} in the mesosphere (50-75 km altitude) at (a) 67.5° S (RO latitude), (b) 54.5° S (KE latitude), (c) 22.5° S (CP latitude) and (d) 7.5° S (CA latitude) estimated using MERRA-2 V. Same for the DE3 amplitude in ms^{-1} at (e) 67.5° S (RO latitude), (f) 54.5° S (KE latitude), (g) 22.5° S (CP latitude) and (h) 7.5° S (CA latitude), and for the SW2 amplitude in ms^{-1} at (i) 67.5° S (RO latitude), (j) 54.5° S (KE

latitude), (k) 22.5° S (CP latitude) and (l) 7.5° S (CA latitude). Please note the change of scale in the color bars while comparing.

Figures 4.3i-l display SW2 amplitude variability during the observational interval at latitudes 67.5° S, 54.5° S, 22.5° S, and 7.5° S, respectively. SW2 amplitude notably decreases after PWD at 67.5° S (Figure 4.3i). At 54.5° S, SW2 remains relatively higher during pre-warming and decreases after PWD (Figure 4.3j). At 22.5° S, SW2 activity remains weak during the pre-warming interval but enhances post-PWD in the upper mesosphere (Figure 4.3k). Figure 4.3l shows enhanced SW2 amplitude post-PWD, similar to Figure 4.3k. In summary, SW2 amplitude decreases post-PWD at high latitudes (RO and KE) but increases in the low-latitude upper mesosphere (CP and CA), indicating contrasting behavior between low and high latitudes during the observational interval.

4.2.4. Tidal sources

Next, the influence of potential sources on the observed variation in DW1, DE3, and SW2 amplitudes is investigated. DW1 primarily arises from the absorption of solar near-infrared (NIR) radiation by water vapor in the lower atmosphere (Lieberman et al., 2007; Sridharan et al., 2012), while the nonmigrating DE3 is triggered by latent heat release associated with convective activity (Hagan & Forbes, 2002; Hagan et al., 2007). To explore these dynamics, we analyzed the variability in TPWV using MERRA-2 data and outgoing longwave radiation OLR from NCEP. TPWV refers to the total precipitable water vapor within a vertical column of a unit cross-section (King et al., 1992). OLR is the measure of energy emitted from Earth and its atmosphere out to space in the form of infrared thermal radiation. Higher (lower) OLR values signify suppressed (enhanced) convection, making OLR a proxy for convection in our study.

Figures 4.4a-d illustrate the fluctuations in zonal mean TPWV (blue curve) and zonal mean OLR (red curve) at latitudes 67.5° S, 54.5° S, 22.5° S, and 7.5° S, respectively. The thin curve represents daily amplitude, while the bold curve shows the moving average of amplitudes across all figures. The moving average, calculated over an 11-day sliding window, helps reveal broader trends in variability.

At 67.5° S, OLR notably increases at the onset of the warming event, while TPWV shows a noticeable peak around the same time (Figure 4.4a). At 54.5° S, both OLR and TPWV exhibit a gradual increase throughout the observational interval (Figure 4.4b). However, at 22.5° S, no apparent trend is observed in OLR variability, while TPWV shows an increasing trend starting from the SSW onset and continuing thereafter (Figure 4.4c). At 7.5° S, OLR decreases after PWD and remains low for the rest of the observational interval, whereas TPWV significantly increases following PWD (Figure 4.4d).

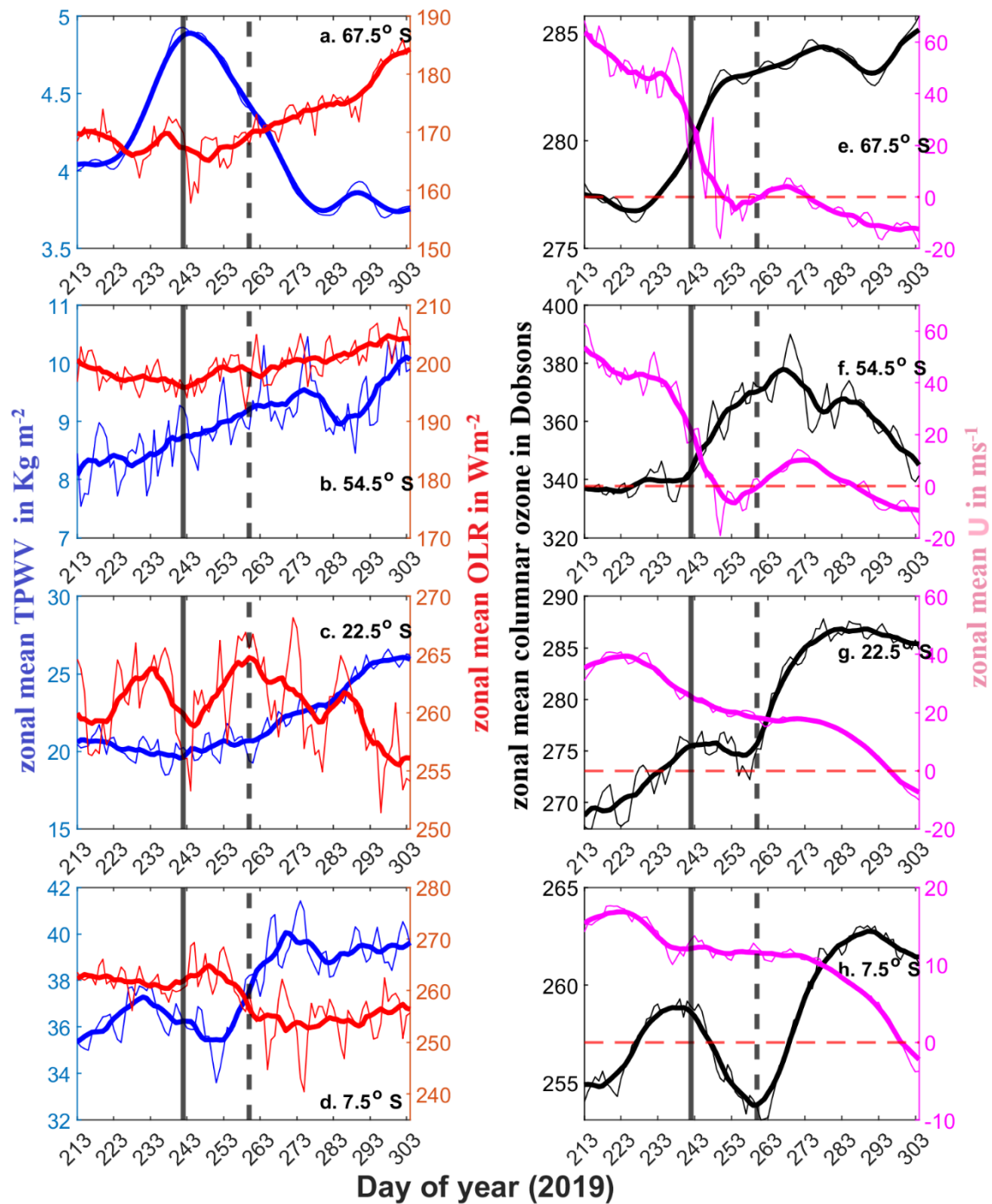


Figure 4. 4. Temporal variation in the zonal mean TPWV (blue curve) in Kg m^{-2} and zonal mean OLR in Wm^{-2} (red curve) at (a) 67.5° S (RO latitude), (b) 54.5° S (KE latitude), (c) 22.5° S (CP latitude) and (d) 7.5° S (CA latitude). Temporal variation in the zonal mean columnar ozone (black curve) in Dobsons and ZMU (averaged over 50-75 km altitude) in ms^{-1} (magenta curve) at (a) 67.5° S (RO latitude), (b) 54.5° S (KE latitude), (c) 22.5° S (CP latitude) and (d) 7.5° S (CA latitude). The thin curve represents the daily value, and the bold curve indicates the moving average.

Overall, TPWV shows an increasing trend across all latitudes except at 67.5° S , where it remains notably low compared to other latitudes. OLR decreases at low latitudes (7.5° S) and increases at mid and high latitudes (54.5° S and 67.5° S) around SSW onset and during the post-warming period. OLR values are generally higher at mid and high latitudes than at low latitudes, while TPWV is more significant at low latitudes than at high latitudes. These variations have crucial implications for the atmospheric tidal dynamics, which we will discuss in the following section.

Several previous studies attributed SW2 amplitude variability to changes in forcing due to stratospheric ozone variations (Goncharenko et al., 2012; Sridharan et al., 2012). Past studies also reported changes in tidal propagation related to zonal mean atmospheric conditions (e.g., Pedatella & Liu, 2013). The primary excitation source for SW2 tide is solar UV radiation absorption through ozone in the stratosphere and mesosphere (e.g., Lindzen & Chapman, 1969). These studies motivate us to examine the role of zonal mean columnar ozone (O_3) and zonal mean zonal wind (ZMU) (averaged over the altitude region 50-75 km) in the MLT concerning SW2 variability during the observational interval.

Figures 4.4e-h display the temporal variability in ozone (black curve) measured in Dobsons and U (magenta curve) measured in ms^{-1} at latitudes 67.5° S , 54.5° S , 22.5° S , and 7.5° S , respectively. The dashed red horizontal line in these figures represents zero wind. At 67.5° S , westerly u significantly decelerates from $\sim 20 \text{ ms}^{-1}$ at SSW onset to 0 ms^{-1} pre-PWD, followed by a brief reversal to easterly wind for a few days. Ozone begins increasing a few days before the warming event onset at 67.5° S (Figure 4.4e). The ZMU at 54.5° S behaves similarly to that at 67.5° S (Figure 4.4f).

Ozone increases at warming onset and peaks just after PWD at 54.5° S. A similar weakening trend of westerly ZMU is observed at 22.5° S (Figure 4.4g). However, the reversal from westerly to easterly occurs a month after PWD. Ozone also behaves similarly at 54.5° S, although peaking occurs a month after warming onset at 7.5° S. At 7.5° S (Figure 4.4h). ZMU exhibits variability similar to Figure 4.4g. Ozone peaks around SSW onset, followed by a minimum near PWD. Another rise in ozone is observed almost a month later at 7.5° S.

In summary, significant deceleration of westerly wind in the mesosphere (averaged over 50-75 km altitude) is observed at all latitudes studied. In general, the ozone is found to be maximum at mid latitude (54.5° S) and minimum at equatorial latitude (7.5° S). The relationship of the ozone and zonal wind with the observed tidal variability will be discussed later.

4.2.5. Deseasoned tidal variability

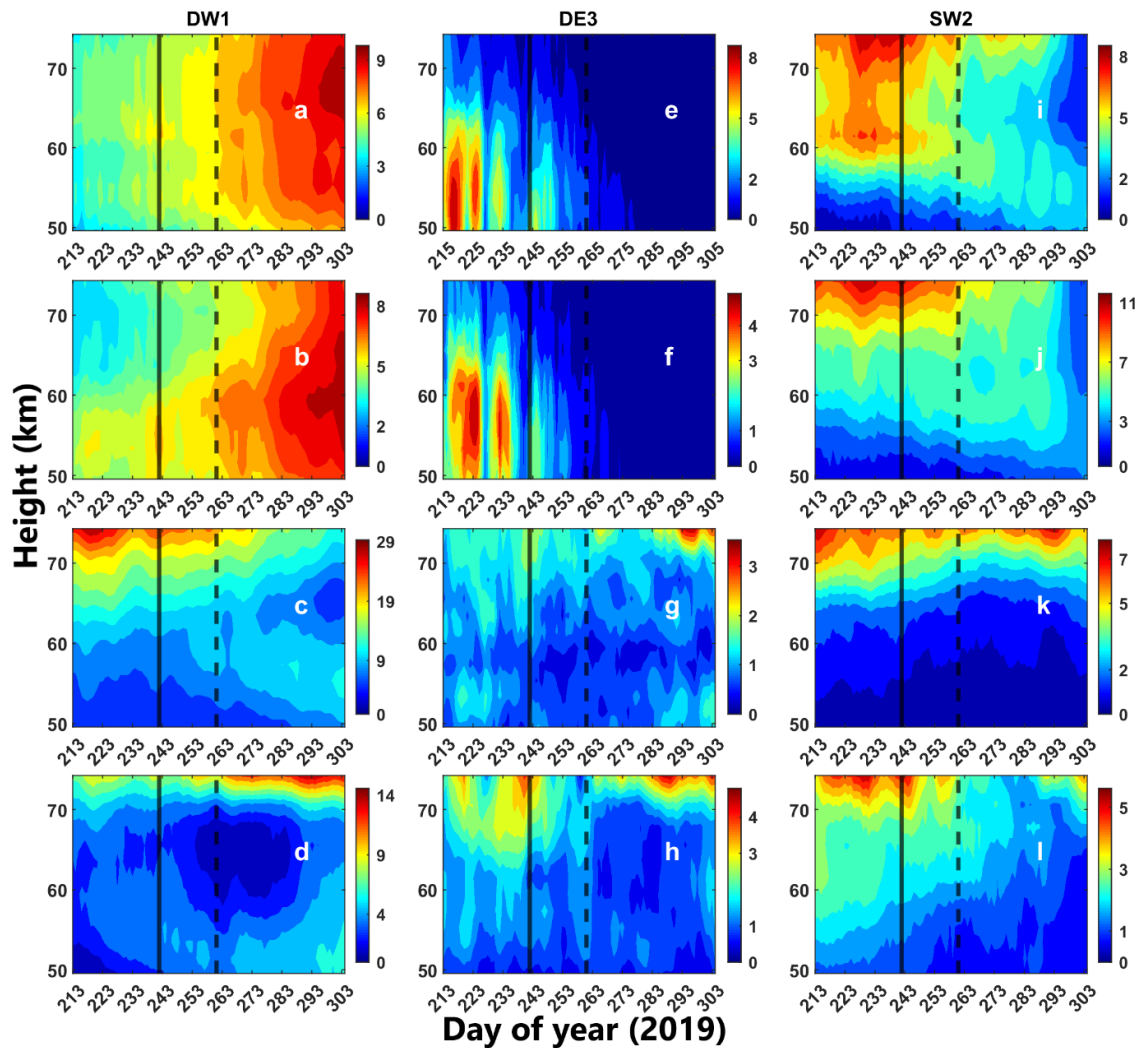


Figure 4. 5. Temporal variation in the composite seasonal mean amplitudes of the DW1 in ms^{-1} in the mesosphere (50-75 km altitude) at (a) 67.5° S (RO latitude), (b) 54.5° S (KE latitude), (c) 22.5° S (CP latitude) and (d) 7.5° S (CA latitude) estimated using meridional wind data from MERRA-2. Same for the DE3 in ms^{-1} at (e) 67.5° S (RO latitude), (f) 54.5° S (KE latitude), (g) 22.5° S (CP latitude) and (h) 7.5° S (CA latitude), and for the SW2 in ms^{-1} at (i) 67.5° S (RO latitude), (j) 54.5° S (KE latitude), (k) 22.5° S (CP latitude) and (l) 7.5° S (CA latitude). Please note the change of scale in the colorbars while comparing.

Up until now, our focus has been on understanding the variations in tidal behavior during September 2019, particularly around the spring equinox. However, given the significant influence of seasonal changes, especially during the equinox, it's crucial to discern the broader seasonal trends. To achieve this, we looked at similar timeframes in other non-SSW years, specifically from 1 August to 31 October of 2017, 2018, 2020, and 2021 (adjacent non-SSW years). Surprisingly, the seasonal composite mean of the DW1, DE3, and SW2 amplitudes of these non-SSW years (Figure 4.5) closely resembled those of 2019 (Figure 4.4). Therefore, the broad variability observed during the 2019 warming event is likely due to seasonal effects.

To isolate the specific signatures of tidal variability associated solely with SSW, we subtracted the composite seasonal mean amplitudes from the non-SSW years from the instantaneous tidal amplitudes. This process, referred to as "deseasoning" in our paper, allowed us to identify the deseasoned tidal amplitudes during the 2019 warming event. The deseasoned tidal amplitude during the observational period of the 2019 warming event are shown in Figure 4.6. The deseasoned amplitudes of the respective tides are mentioned with a "d" suffix in the rest of the paper. For instance, a positive or negative DW1d value indicates an increase or decrease in the DW1 amplitude during the 2019 SSW compared to the non-SSW years. DE3d and SW2d represent the deseasoned amplitudes for DE3 and SW2, respectively. In Figure 4.6, the bold white line denotes a 2 sigma deviation from the composite seasonal mean amplitude, and the area enclosed by this curve is considered to be statistically significant.

The DW1d consistently shows patches with positive values in the upper mesosphere around the 2019 PWD across all locations except RO. Additionally, we observed consecutive bursts

of positive DW1d around 50-60 km altitude during the post-warming period at CP (Figures 4.6a-d). The DE3d does not exhibit any distinct patches concerning the 2019 warming event at 67.5° S, 54.5° S, and 22.5° S, as shown in Figures 4.6e-g. However, DE3d is found to be significantly negative before the onset date at 7.5° S, and later switches to positive for a few days around the PWD (Figure 4.6h). SW2d is notably positive during the SSW onset for several days at 67.5° S and 54.5° S, illustrated in Figures 4.6i-j. Furthermore, Figures 4.6k-l demonstrate the positive SW2d observed at and after the PWD at 22.5° S and 7.5° S, respectively. In general, DW1d and SW2d exhibit significant enhancement (positive patches) in response to the 2019 minor warming event compared to the non-SSW years.

We also explored the relationship between deseasoned tidal amplitudes and deseasoned source parameters (TPWV, ozone, OLR, etc.), but no correlations were found, so we omitted those details here. The implications of this finding will be discussed later.

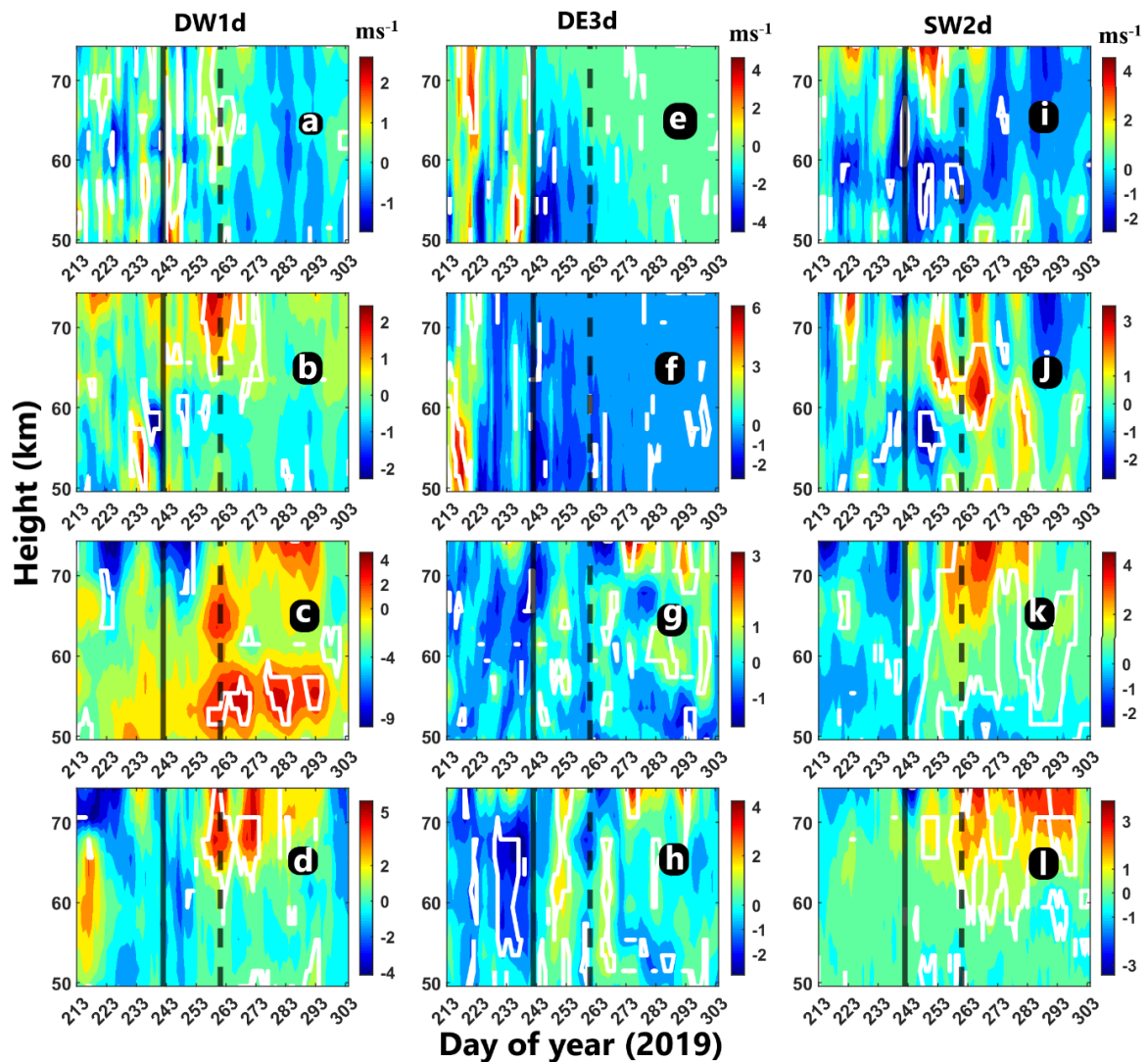


Figure 4. 6. Temporal variation in the DW1d in ms^{-1} in the mesosphere (50-75 km altitude) at (a) 67.5° S (RO latitude), (b) 54.5° S (KE latitude), (c) 22.5° S (CP latitude) and (d) 7.5° S (CA latitude) estimated from MERRA-2 data. Same for the DE3d in ms^{-1} at (e) 67.5° S (RO latitude), (f) 54.5° S (KE latitude), (g) 22.5° S (CP latitude) and (h) 7.5° S (CA latitude), and for the SW2d amplitude in ms^{-1} at (i) 67.5° S (RO latitude), (j) 54.5° S (KE latitude), (k) 22.5° S (CP latitude) and (l) 7.5° S (CA latitude). The white contour line denotes statistically significant region. Please note the change of scale in the color bars while comparing.

To gain a comprehensive understanding of the tidal dynamics surrounding the warming event, we delved deeper into the latitudinal-temporal variability of the DW1, DE3, and SW2 amplitudes at a representative altitude in the MLT, i.e., 0.01 hPa in the SH. Figures 4.7a-c depict the latitudinal-temporal sections of the DW1, DE3, and SW2 amplitude, respectively, at 0.01 hPa.

At 0.01 hPa, the DW1 appears prominently within the latitudinal band of 15° to 35° S during the pre-warming phase. However, there's a shift in the enhancement structure toward equatorial latitudes as it weakens during the post-warming phase. Additionally, a slight enhancement in the DW1 amplitude is observed at mid and high latitudes (60-90° S) during the post-warming interval (Figure 4.7a). The DE3 amplitude begins to increase at the onset of the warming event, particularly at low latitudes. However, there's a relative decrease in DE3 activity at mid and high latitudes during the SSW onset (Figure 4.7b). Figure 6c illustrates the predominant activity of SW2 at mid-latitudes until the PWD. There's also an enhancement in the SW2 amplitude at low latitudes (15-30° S) that peaks around the PWD. It's worth mentioning that similar broad variability features in the DW1, DE3, and SW2 amplitudes are observed during non-SSW years as well, although not shown here. Hence, such broad variability may not solely be attributed to the 2019 SSW, as previously observed.

To assess the impact associated with SSW, the temporal variability of DW1d, DE3d, and SW2d at 0.01 hPa in the SH is presented in Figures 4.7d-f, respectively. The white contour line signifies statistically significant regions, as mentioned earlier. DW1d exhibits positive values around the PWD at equatorial, mid, and high latitudes (Figure 4.7d). However, at extratropical latitudes, DW1d shows negative values at the SSW onset, persisting until the PWD. Figure 4.7e indicates significant DE3 activity, particularly at equatorial latitudes, with

a positive DE3d patch between the onset and PWD, followed by a negative patch shortly after the PWD for a few days. SW2d shows significant enhancement, as evidenced by positive values observed at the SSW onset until the PWD, especially at high latitudes (Figure 4.7f). At low latitudes, a significant positive SW2d can be noted around the PWD. Overall, SW2d exhibits the most significant response with enhancement to the warming event, followed by DW1d and DE3d during the observational interval.

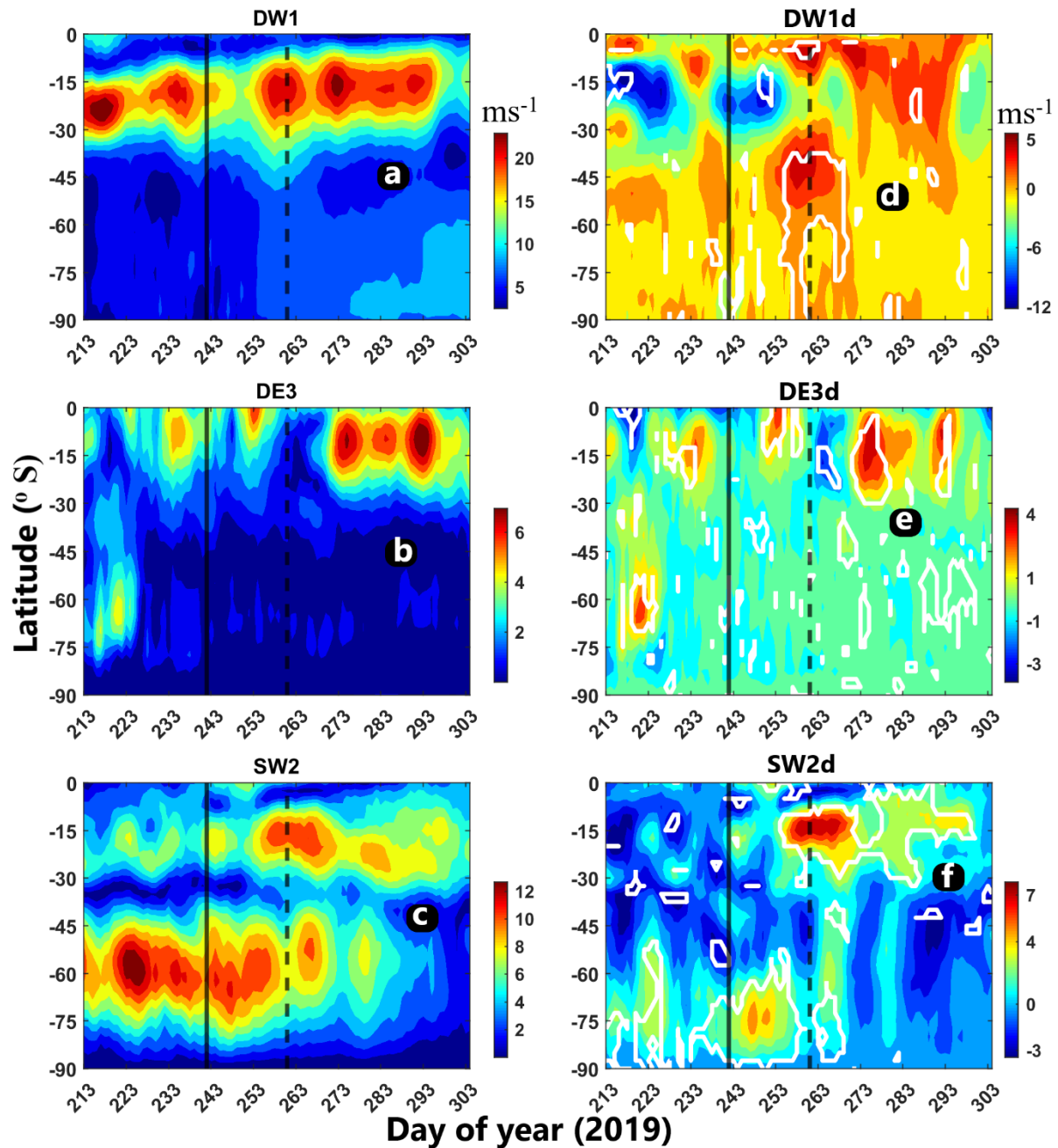


Figure 4. 7. Latitudinal-temporal variation of the (a) DW1, (b) DE3, and (c) SW2 amplitude at 0.01 hPa estimated from the MERRA-2 data set. Same for the (d) DW1d, (e) DE3d, and (f)

SW2d at 0.01 hPa. The white contour line denotes statistically significant region. Please note the change of scale in the color bars while comparing.

4.3. Discussion

The present study has uncovered intriguing and distinctive dynamic aspects of a minor SSW event in the SH during September 2019, utilizing meteor radar wind observations and the MERRA-2 reanalysis dataset. The 2019 minor SSW event is the second most robust warming event reported in the SH thus far. Our study aims to offer valuable insights into MLT dynamics, particularly regarding tidal activity during such a rare event.

The current minor warming event reveals the movement of high polar warming from the mesosphere to the stratosphere before the SSW onset, depicted in Figure 4.1a. As noted by Pedatella et al. (2018), mesospheric anomalies often, though not always, manifest initially a week or more before the peak stratospheric disturbances.). The ZMU at 0.01 hPa is also impacted, showing weakening of westerly winds and a reversal to easterly winds at mid and high latitudes before the SSW onset (Figure 4.1d) (Limpasuvan et al., 2016; Pedatella et al., 2014). This weakening of westerly winds may stem from westward momentum induction to the mean flow by dissipating westward traveling planetary waves (PW) at mesospheric altitudes during the warming period (Mitra et al., 2022).

Consequently, a noticeable and significant change in background dynamical conditions is observed during the September 2019 SH minor SSW event. However, these changes do not consistently correlate with variations in local diurnal tide (DT) and semidiurnal tide (ST) amplitudes in the MLT region over the observation period, as evidenced from individual meteor radar observational sites (RO, KE, CP, and CA) (Figure 4.2). Furthermore, in terms of various wavenumber components, global tidal modes demonstrate notable variability during the observational period (Figure 4.3).

The ground-based method from a single geographic location has a limitation in distinguishing between global and local signatures. Interactions between different zonal wavenumbers can drive longitudinal and temporal variations in locally measured tidal wind variability (Hibbins et al., 2010). Hence, any discussion on tidal variability drivers necessitates addressing each

mode separately (Hibbins et al., 2019). To tackle this issue, our study employs zonal wavenumber diagnosis utilizing the MERRA-2 global reanalysis dataset to elucidate global tidal propagation responses during the observational interval.

Interestingly, our study reveals significant global-scale tidal variability during the observational period, particularly in the DW1, DE3, and SW2 amplitudes in the MLT. We consistently observe increased DW1 amplitude around the PWD at all latitudes (Figure 4.3). Additionally, broad-scale DW1 amplitude variability during the observational period correlates with TPWV at all locations (except RO, where water vapor is generally low), as depicted in Figures 4.4a-d. Chapman & Lindzen (1970) attributed the most significant forcing of the DW1 to solar NIR absorption by water vapor in the troposphere. Lieberman et al. (2007) also noted substantial DW1 enhancement due to increased water vapor concentration. However, since DW1 amplitude variations occur similarly during the spring equinox in non-SSW years, seasonal changes may account for this variability (Figure 4.5a-d). Notably, the deseasoned component of DW1 (DW1d) significantly increases around PWD at all latitudes, indicating DW1's plausible response to the warming event (Figures 4.6a-d).

We observe contrasting DE3 amplitude behaviors at mid and high latitudes (decrease) compared to low latitudes (increase) post-2019 SSW onset. This mid-high latitude DE3 decrease may stem from reduced convective activity at similar latitudes, evidenced by increased OLR values after DOY 233 (Figures 4.3a-d). Conversely, increased convective activity at low latitudes may explain rising DE3 amplitudes. This behavior is consistent with global tidal maps at 0.01 hPa (Figure 4.7b). Previous studies (e.g., Hagan & Forbes, 2003) discussed convectively forced DE3, aligning with our interpretation. However, DE3 amplitude trends in SSW years mirror those in non-SSW years, suggesting seasonal changes may dominate this broad-scale variability (Figures 4.5e-h). Interestingly, the DE3d amplitude, a component of DE3 after seasonal variations are removed, displays a significant response to the SSW event around the CA latitude. This response is characterized by a pronounced negative patch before the onset of the SSW, transitioning to positive thereafter during the Peak Warming Day (PWD) and post-warming interval (Figure 4.6h). It is worth noting that DE3 has the potential to propagate directly into the thermosphere, influencing the E region dynamo and imprinting tropospheric convective variability onto the ionospheric plasma (Oberheide et al., 2009; Chang et al., 2013). Previous studies (Immel et al., 2006; Wan et al., 2008) have also highlighted the significant role of DE3 in generating the wavenumber 4

structure of the equatorial ionization anomaly on a global scale. Therefore, the changes observed in the DE3 amplitude at low latitudes in relation to SSW events, as demonstrated in this study, may have significant implications for ionospheric variability.

SW2 amplitude considerably decreases post-PWD at mid and high latitudes (KE and RO) but increases in the upper mesosphere at low latitudes (CP and CA) around PWD (Figure 4.3i-l). Previous studies (Lindzen & Hong, 1974; Aso et al., 1981; Pedatella & Liu, 2013; Limpasuvan et al., 2016) noted that strong westward background winds hinder SW2 propagation from the stratosphere into the MLT. Conversely, an eastward wind reversal post-SSW has been linked to SW2 weakening (Hibbins et al., 2019; Sassi et al., 2013). Additionally, ozone trends post-PWD resemble SW2 activity at low latitudes, suggesting ozone's potential influence on SW2 activity. However, broad SW2 amplitude variability in SSW years likely results from seasonal changes, as observed in non-SSW years. Notably, SW2d amplitude significantly enhances post-onset at high latitudes and in the low-latitude MLT, supported by Figures 4.7c, 4.7f, and 4.6i-l.

Despite the absence of a clear relationship between deseasoned tidal amplitudes and deseasoned source parameters in our study, unlike seasonal trends, this suggests short-term tidal component variability during SSW in seasonal transitions are not directly governed by the sources but involve complex processes related to global atmospheric disturbances. Unraveling these mechanisms necessitates further extensive investigations into such short-term tidal variability during SSW events.

4.4. Summary and Conclusions

The present study delves into the atmospheric tidal dynamics in the MLT during a minor yet impactful SSW event occurring in September 2019, as observed in the SH across various latitudes. Analysis of the DT and ST amplitudes derived from location-specific meteor radar meridional wind data reveals no substantial variability in the MLT throughout the observational interval. However, a striking and uniform variability is discernible in global tidal modes at similar latitudes, notably in the DW1, DE3, and SW2 components during the observation timeframe. Interestingly, this behavior mirrors patterns seen in non-SSW years during the same season, suggesting a link to seasonal tidal variability. The broad fluctuations

in the DW1, DE3, and SW2 amplitudes can be attributed to corresponding sources such as water vapor, convective activity, ozone, and U.

To isolate the distinct response of global tidal modes to the current warming event, we analyze deseasoned tidal amplitudes. Remarkably, deseasoned DW1 shows a significant increase for a few days around PWD across all latitudes, indicating a clear response to the warming event. Deseasoned DE3 also exhibits a notable response, particularly at equatorial latitudes. Similarly, deseasoned SW2 displays a significant enhancement around PWD. The short-term variability in dominant tidal modes concerning the SSW cannot be solely explained through sources, suggesting the involvement of complex processes in these global disturbances. Therefore, further investigations are imperative to better understand these features.

Chapter 5

Middle Atmospheric Circulation during SSW

5.1. Introduction

Building on our previous investigation into planetary waves (PWs) and tidal dynamics during the 2019 Southern Hemisphere (SH) SSW, we now focus on examining the influence of the rare SH SSW events in 2002 and 2019 on middle atmospheric circulation. As discussed in Chapter 4, the SH SSW events occurred around the spring equinox, marking the transition from late winter to early spring. During this transition, seasonal changes driven by solar radiation and enhanced PW activity play pivotal roles in weakening the polar vortex (Rao & Garfinkel, 2021). This weakening culminates in the transition from westerly to easterly circulation, known as Stratospheric Final Warming, which can occur gradually due to radiative processes or suddenly due to dynamic influences from enhanced planetary waves (Butler et al., 2015; Maury et al., 2016).

Against this backdrop, our study aims to separate the seasonal mean background state from actual winds to delve into the unique dynamical features of middle atmospheric circulation solely attributed to these rare SH SSW events. Recent work by Veenus et al. (2023) highlights the impact of the 2019 SH SSW on stratospheric circulation, affecting the transport of ozone and water vapor from the tropics to the poles. While previous studies have examined planetary wave forcing in the MLT (Vincent et al., 2022) and the role of PW activity in the evolution of the 2019 minor event (Liu et al., 2022), comprehensive comparative study of middle atmospheric circulation during SH SSW events remained untouched so far.

Thus, our study seeks to compare middle atmospheric circulation characteristics during two prominent SH SSW events, one major and one minor. For this purpose, we utilize the MERRA2 U and V datasets during the period centered around the 2002 major and 2019 SH minor warming episodes ~ from 1 August to 31 October of the year 2002 and 2019,

respectively, to explore latitudinal, altitudinal, and longitudinal variabilities associated with middle atmospheric circulation during these unusual and dramatic SH SSWs. This comparative approach aims to provide deeper insights into the dynamics and impacts of these unique and rare atmospheric phenomena in the SH.

5.2. Analysis method

Typically, the SH experiences SSW events around the September equinox, coinciding with the seasonal transition. Consequently, during SSW years, atmospheric dynamics are influenced by both factors, as discussed earlier. Thus, it is crucial to disentangle and assess the specific impact of SSW on atmospheric circulation by isolating the seasonal contribution occurring concurrently.

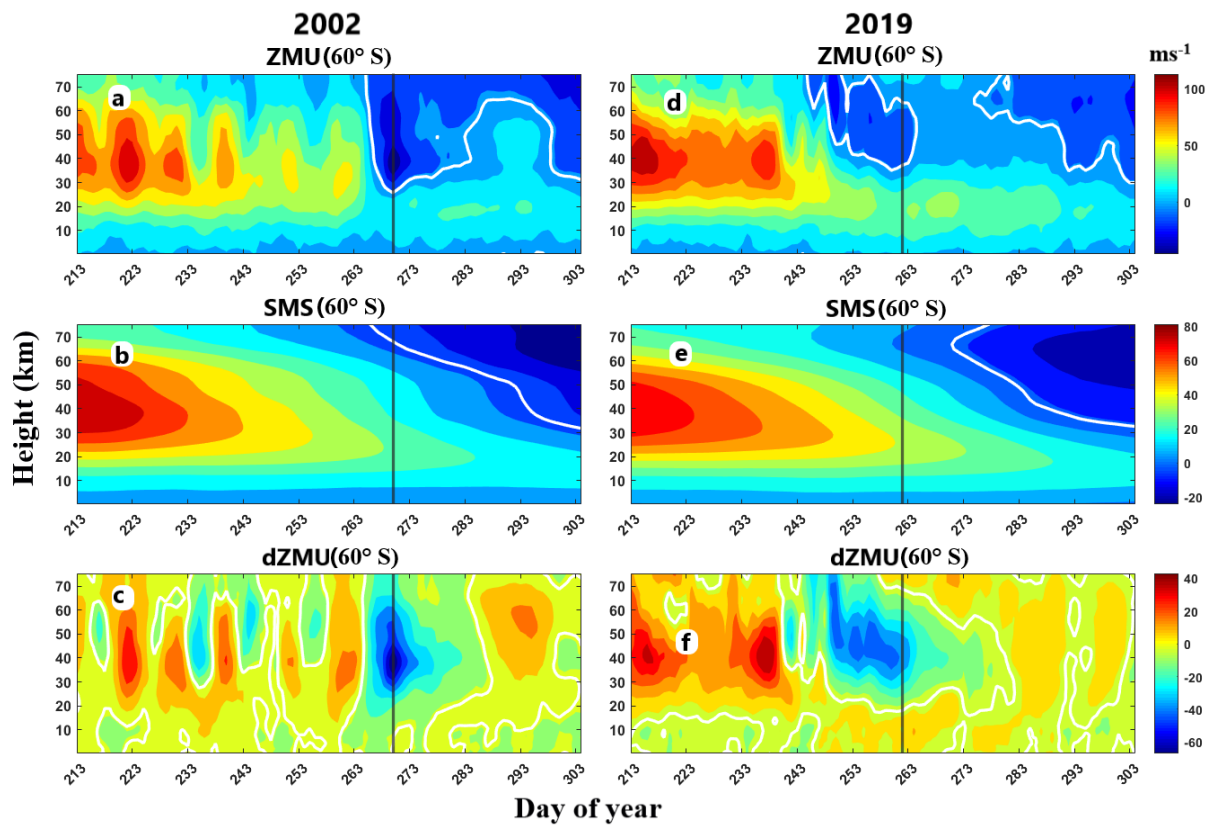


Figure 5. 1. Altitude-time section of the (a) ZMU, (b) SMS, and (c) dZMU at 60° S during the 2002 observational days. (d, e, f) represent the same as (a, b, c), but during 2019. The solid vertical line represents the peak warming day (PWD).

The primary goal of this study is to isolate and analyze the effects of SSW events in the SH by separating the seasonal contribution during the September equinox. This allows us to

discern the unique influence of SSW on atmospheric dynamics. To achieve this, we calculate deseasoned values of atmospheric parameters (temperature, zonal, and meridional winds denoted as T, U, and V, respectively) by subtracting the seasonal mean state (SMS) from instantaneous values. The SMS is represented by a 90-day central moving average during the relevant SH SSW year. Deseasoned values are denoted with a "d" prefix throughout the paper.

The relationship between the actual (A), deseasoned (d), and the seasonal mean state is as follows:

$$A = SMS + d \quad (5.1)$$

Therefore, $d = A - SMS$;

In the following Figures, the ZMU and dZMU represent the actual and deseasoned value of the ZMU, respectively. Figures 5.1a-c illustrate the variability of ZMU, SMS, and dZMU at 60°S during the observation days in 2002. Similarly, Figures 5.1d-f display the same variables for the observation days in 2019. The solid vertical line represents the peak warming day (PWD). In both years, the calculated SMS (Figures 5.1b and 5.1e) reveals a gradual shift from westerly to easterly winds in the upper stratosphere and mesosphere, driven by seasonal transitions. Additionally, the estimated dZMU (Figures 5.1c and 5.1f) clearly shows an easterly influence on ZMU during the PWD of the SSW event.

Here are the justifications for using a 90-day moving average window for estimating the seasonal mean state (SMS) and determining the SSW impact:

- Capturing the seasonal trend: The present paper highlights that the SSW event in the Southern Hemisphere (SH) generally occurs around the September equinox, coinciding with the seasonal transition when a significant change in wind direction occurs (Figures 5.1a and 5.1d). The 90-day moving average window helps to capture the general seasonal trend during this period (Figures 5.1b and 5.1e).
- Isolating the seasonal contribution: Since both the SSW event and the seasonal transition influence the atmospheric dynamics during the same time interval, it is crucial to isolate the seasonal contribution in order to determine the SSW impact. Moreover, usage of a 90-day window captures approximately three months of data,

which is the typical length of a season. This allows the identification of seasonal patterns and helps to determine the average state during any season (Figures 5.1b and 5.1e). By estimating the SMS using a 90-day moving average, the long-term average state over the concerned SH SSW year is obtained. This approach helps to separate the seasonal variations from the instantaneous values of the atmospheric parameters (T, U, and V) and provides a baseline reference for assessing the deviations attributable to the short-term disturbances, e.g., SSW (intra-seasonal time scale).

- Unveiling weak dynamical features: SSW events can induce relatively weak dynamical features in the middle atmosphere that may not be readily apparent in the actual parameters. By subtracting the SMS from the instantaneous values, the resulting residuals highlight the deviations from the SMS, specifically capturing the relatively weak dynamical features solely due to the SSW. For example, Figure 5.2a-c represents the ZMU, SMS, and dZMU variability at 10 hPa during the 2002 observational days. Similarly, Figures 5.2d-f display the same variables for the observation days in 2019. The influence of the 2002 SSW on the ZMU in terms of reversal of westerlies is clearly discernible from Figure 5.2a, but the impact of the 2019 SSW seems not to be clear from the actual ZMU variability (Figure 5.2d). The seasonal transition during 2019 masks the SSW impact on the ZMU at 10 hPa (Figure 5.2d). Figures 5.2b and 5.2e exhibit the SMS during the 2002 and 2019 observational days, representing the gradual seasonal changes in the ZMU. Further, the dZMU reveals SSW impact in terms of easterly influence on the ZMU, as shown in Figures 5.2c and 5.2f. Hence, the adopted methodology helps to identify the weak features due to the SSW for several cases in the present study.
- Removing interannual variability: Using a 90-day moving average helps to remove interannual variability in the SMS during the observational intervals which the climatological mean cannot address (elaborated later). This ensures that the focus remains on the SSW-induced effects rather than year-to-year fluctuations. Removing interannual variability enhances the clarity and consistency of the analysis, enabling a better assessment of the SSW impact.

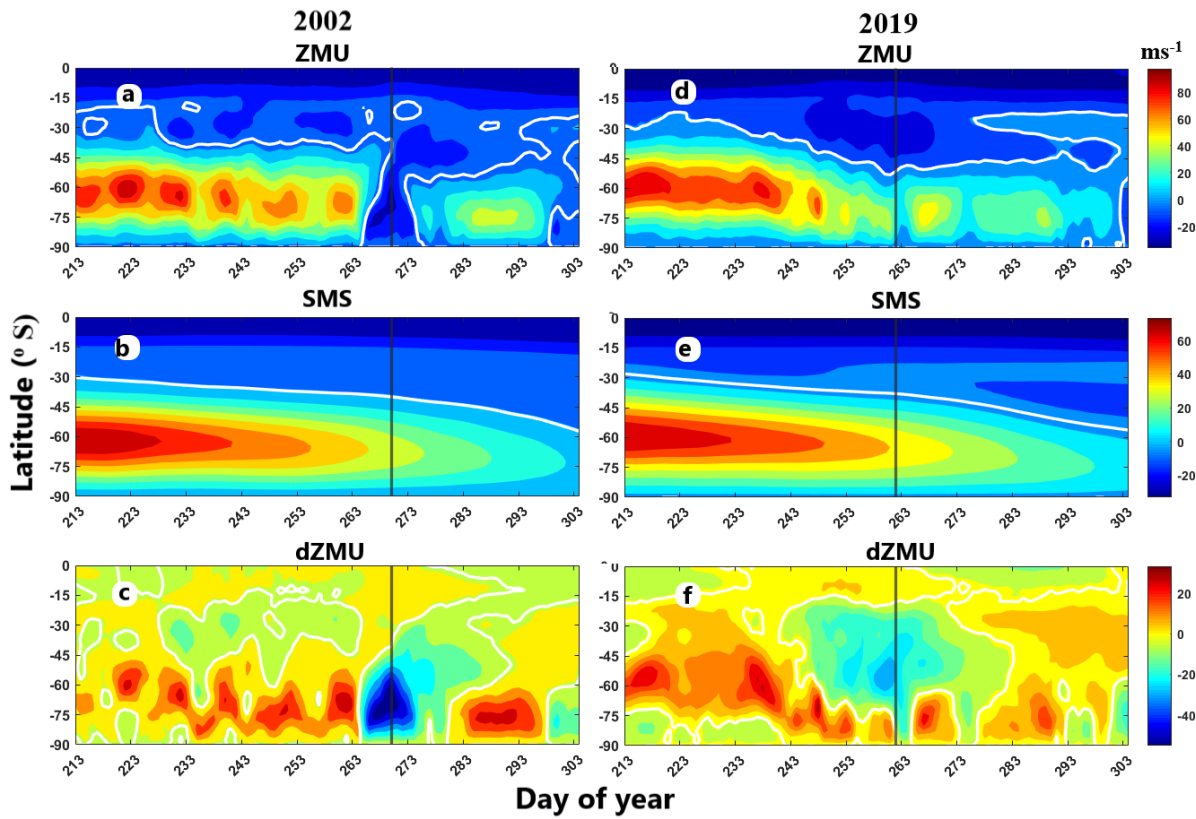


Figure 5. 2. The latitude time section of (a) ZMU, (b) SMS, and (c) dZMU at 10 hPa during the 2002 observational days. (d, e, f) represent the same as (a, b, c), but during the 2019 observational days.

In summary, employing a 90-day moving average window facilitates the isolation of the seasonal contribution and determination of the SSW impact. It captures the seasonal transition, separates the SSW-induced deviations from the instantaneous values, unveils weak dynamical features, and removes interannual variability. This approach provides a more comprehensive understanding of the atmospheric dynamics during the SSW event and allows for a focused analysis of the SSW-induced changes in the middle atmosphere.

The advantages of using SMS over climatological mean are as follows.

Figure 5.3 shows the altitude-time section of ZMU during the observational days of non-SSW years (2001, 2003, 2018, and 2020), and SSW years (2002 and 2019). The seasonal transition marked by the final reversal of westerly ZMU to easterly can be identified from the zero-wind line. The time of seasonal reversal from westerly to easterly varies significantly among the selected years, as evident in Figure 5.3. Therefore, significant interannual variability can

be expected to affect the climatological mean profile due to varied time of seasonal transition over various years. By estimating the SMS, we focus only the observational interval centered around the SSW event, allowing us to detect, the deviations associated with these events. In a nutshell, using SMS over climatological mean is justified when studying the effect of any disturbances in the time scale of intra-seasonal or smaller and removal of inter-annual variability is required.

Furthermore, it should be noted that SMS itself may vary a lot over the years. Therefore, if any year/s contain/s significant deviations from the rest, then the climatological mean profile also be affected, resulting in over/underestimation of the SSW impact to some extent. However, it is interesting to note that our adopted methodology is not influenced by such issues as we subtract the SMS each year independently.

Therefore, deseasoning serves the purpose of highlighting relatively subtle dynamical features of the middle atmosphere solely attributable to SSW, which might not be readily apparent in actual parameters. Furthermore, this analysis method helps eliminate interannual variability of the SMS during observational periods, enhancing the clarity of our findings.

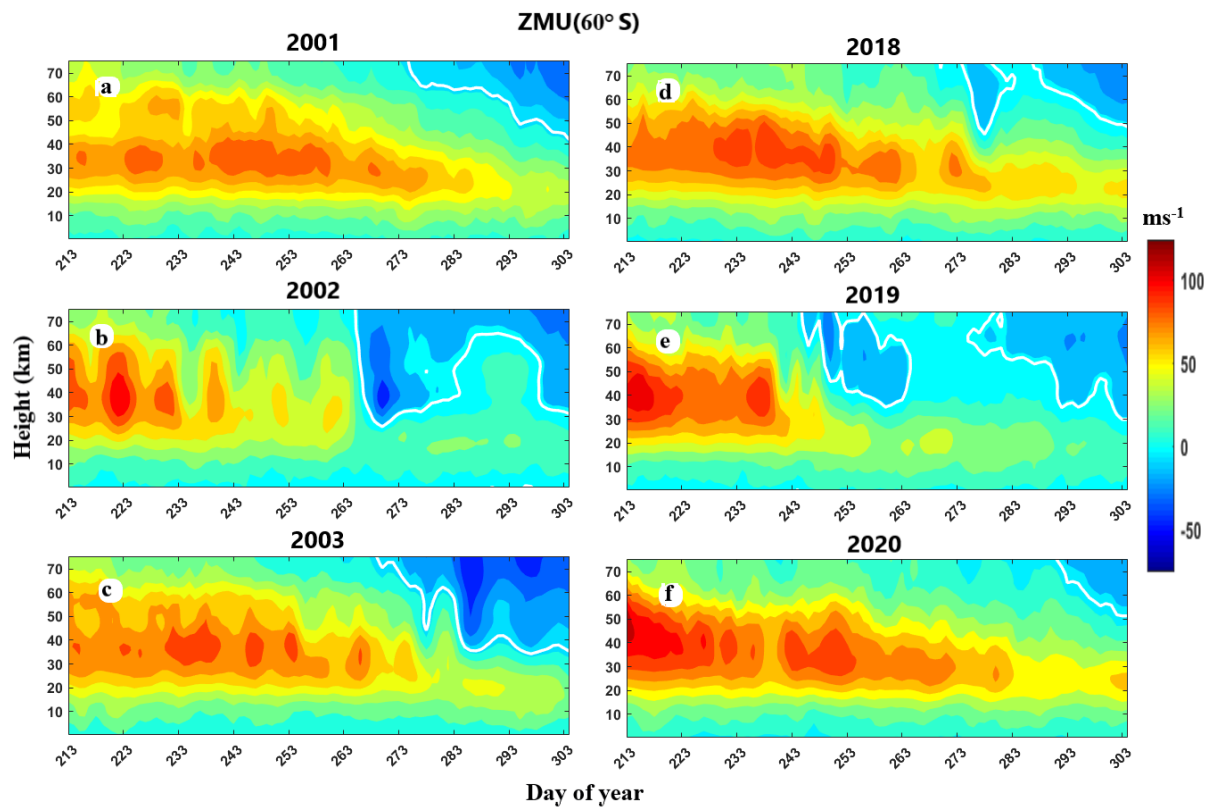


Figure 5. 3. *Altitude-time section of the zonal mean zonal wind at 60° S during (a) 2001, (b) 2002, (c) 2003, (d) 2018, (e) 2019, and (f) 2020 observational days (1 August – 31 October). The white curve represents the zero-wind value.*

5.3. Results

5.3.1. Altitude-time variability of the zonal mean background conditions

Figures 5.4a-b depict the time-height profiles of T at 90° S for the years 2002 and 2019, respectively. Maximum polar warming at 10 hPa is observed on 27 September (DOY 270) 2002, considered as the PWD for the 2002 SH major SSW. Similarly, for the minor 2019 SH SSW, the PWD is identified as 18 September (DOY 261). A black solid line in the figures represents the PWD for both events, while a white contour curve signifies zero value throughout the figures. Before the 2002 PWD, intermittent enhancements in polar T characterized by three distinct warming bursts can be seen around 40 km altitude in Figure 5.4a, with rapid downward warming propagation noticeable on the 2002 PWD to 15 km altitude. In Figure 5.4b, the warming gradually propagates to lower altitudes up to 20 km until the 2019 PWD.

Figures 5.4c-d display the time-height profiles of deseasoned polar T (dT) for the 2002 and 2019 SH SSW, respectively. The warming bursts near 40 km altitude, as observed in Figure 5.4a, are more prominent in Figure 5.4c, accompanied by noticeable polar mesospheric cooling above 40 km concurrent with polar stratospheric warming. Similarly, Figure 5.4d shows discernible stratospheric warming features during the 2019 SSW event. The dT variability indicates that warming appears to start early in the upper stratosphere and extend to lower altitudes around the 2002 and 2019 PWD, although the downward propagation of warming is more gradual in 2019 compared to 2002.

Figures 5.4e-f illustrate the time-height profiles of the ZMU at 60° S during the observational intervals of 2002 and 2019, respectively. Before the 2002 PWD, there's intermittent weakening of the zonal mean westerlies in the altitude range of 30-60 km, coinciding with warming pulses as depicted in Figure 5.4a. This weakening is followed by a sudden transition to easterlies near the PWD, as shown in Figure 5.4e. Interestingly, this wind reversal persists

throughout the upper mesosphere for the rest of the observational interval. On the other hand, during the 2019 SSW event, the westerly wind reverses to easterly before the PWD in the upper mesosphere, reaching altitudes as low as 37 km on the PWD, as demonstrated in Figure 5.4f. Following the PWD, the easterly wind then reverts back to westerly. Additionally, there is another reversal of the zonal mean westerly wind above 35 km a few days after the PWD, with an earlier reversal in the mesosphere. The reversed state of ZMU (easterly) in the mesosphere and stratosphere for a few days around the 2019 PWD is discernible from the actual variability, contrasting with 2002, where the upper mesospheric westerly winds transition to easterlies.

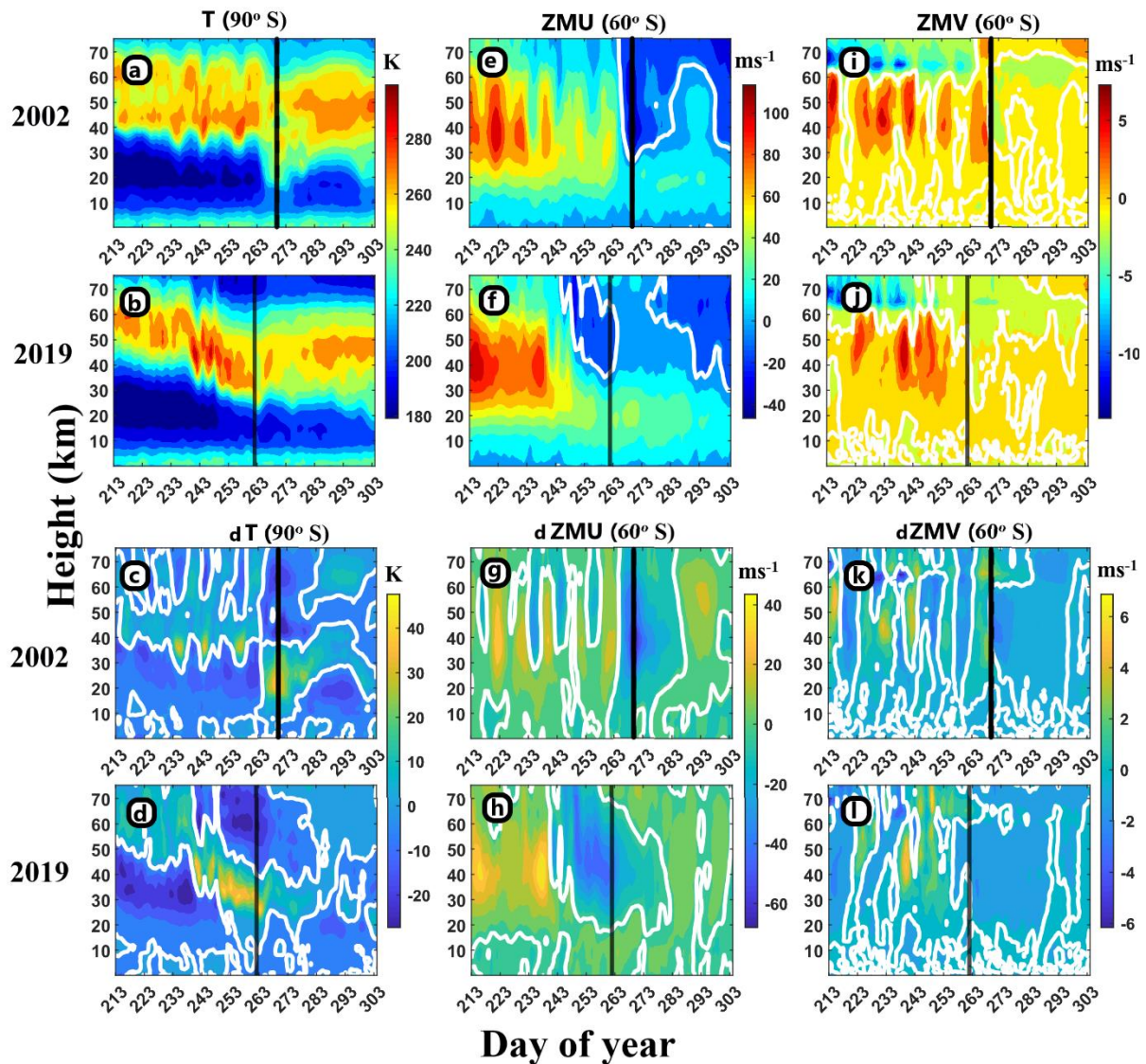


Figure 5. 4. Time-height section of (a) T at 90°S , (e) ZMU at 60°S , and (i) ZMV at 60°S during 2002 observational days and (b) T at 90°S , (f) ZMU at 60°S , and (j) ZMV at 60°S during 2019 observational days. Same for (c) dT at 90°S , (g) $dZMU$ at 60°S , and (k) $dZMV$ at

60°S during 2002 observational days and (d) dT at 90°S, (h) dZMU at 60°S, and (l) dZMV at 60°S during 2019 observational days. The solid vertical line represents the PWD. The white bold curves represent zero values in all the plots. Please note the change of scale in the colorbars corresponding to each subplot while comparing. Also, consider the difference in colorbar used to represent actual and deseasoned variability.

Figures 5.4g and 5.4h show the time-height profiles of deseasoned ZMU (dZMU) at 60° S for 2002 and 2019 SH SSW, respectively. Around the 2002 PWD, dZMU significantly diminishes in the observed altitude region (0-75 km) and reinstates to former values shortly after, as seen in Figure 5.4g. During the 2019 event, dZMU shows easterly winds from late August to early October in the stratosphere and mesosphere above 20 km centered around the PWD, as evident in Figure 5.4h. The influence of the SSW extends further towards lower altitudes in dZMU compared to ZMU. It's noteworthy that the impact of SSW appears to extend into the troposphere during 2002, a contrast from 2019, evident from the negative dZMU around the PWD. This underscores the importance of examining deseasoned variability to clarify the influence of SSW on lower altitudes. Additionally, the significant effect of SSW on the upper mesospheric dZMU in 2002 is notable, although it appears to be overshadowed by the seasonal transition in the ZMU profile.

Lastly, Figures 5.4i and 5.4j depict the time-height profiles of ZMV at 60° S for 2002 and 2019, respectively. Until the 2002 PWD, alternative weakening and strengthening of zonal mean southerlies are observed in the upper stratosphere and lower mesosphere (40-60 km) in Figure 5.4i. In contrast, in the 2019 SSW, southerly wind seems to enhance for a few days before the PWD, as seen in Figure 5.4j. The deseasoned ZMV (dZMV) for 2002 (Figure 5.4k) and 2019 SH SSW (Figure 5.4l) exhibit much extended reversed (northerly) wind conditions after the PWD compared to ZMV alone.

5.3.2. Latitude-time distribution of zonal mean flow

To grasp the features of the zonal mean circulation in the middle atmosphere during the SH SSW, we examined the latitude-time profiles of ZMU and ZMV at three specific altitudes in the SH. These representative pressure levels are 10 hPa (~ 30 km), 1 hPa (~ 45 km), and 0.01 hPa (~ 75 km).

5.3.2.1. ZMU

Figures 5.5a and 5.5b showcase the latitude-time depiction of ZMU at 10 hPa (mid-stratosphere) during two warming events. During the 2002 SSW, the robust westerly ZMU near 60° S experiences intermittent weakening before transitioning into an easterly wind around the PWD (Figure 5.5a). Conversely, in the 2019 SSW, there is a significant deceleration of the westerly ZMU near 60° S leading up to the PWD, with no wind reversal observed (Figure 5.5b). Figures 5.5c and 5.5d display the latitudinal profile of dZMU at 10 hPa for the observational intervals of 2002 and 2019, respectively. A notable deceleration is evident in the westerly wind, starting from extratropical latitudes (30-45° S) and extending to mid and high latitudes during both events, indicated by distinct negative values of dZMU (Figures 5.5c and 5.5d). Moreover, the weakening of the westerly wind during the minor SSW is clearly discernible in the corresponding dZMU profile (Figure 5.5d), a detail that seems masked in the actual variability.

Figures 5.5e-h depict similar information as Figures 5.5a-d but at 1 hPa (upper stratosphere). In both the 2002 and 2019 events, the westerly ZMU reverses into easterly winds for a brief period around the PWD in middle and high latitudes (Figures 5.5e-f). Notably, the reversal of the westerly ZMU during the 2019 warming initiates earlier at 30° S, as seen in Figure 5.5f. Interestingly, the poleward progression of the zero wind line commences early in the low latitude stratosphere, as evident from the dZMU profile in both events (Figures 5.5g-h), although there's a noticeable discontinuity in the 2002 event.

Figures 5.5i-j showcase the latitude-time section of ZMU at 0.01 hPa (upper mesosphere) during 2002 and 2019, respectively. The zonal mean westerly wind starts weakening and reverses into easterly winds a few days prior to the 2002 PWD, persisting for the remaining observational days (Figure 5.5i). Conversely, in the 2019 event, a short-lived reversal of the westerly ZMU to easterly is observed a few days before the PWD. Additionally, an almost permanent westerly to easterly reversal of ZMU, likely due to seasonal transition, is noticeable (Figure 5.5j). Consequently, no clear response to the warming episodes of ZMU at 0.01 hPa can be determined. Figures 5.5k and 5.5l show the latitudinal-temporal variability in dZMU at 0.01 hPa during 2002 and 2019, respectively. The dZMU exhibits a distinct occurrence of easterly forcing lasting for a few days around the 2002 PWD across the entire

SH (Figure 5.5k). Similarly, for the 2019 SSW, evidence of easterly forcing a few days before the PWD can be observed in Figure 5.5l. A noticeable difference between the ZMU (Figures 5.5i and 5.5j) and dZMU (Figures 5.5k and 5.5l) profiles is observed at the upper mesosphere during both events.

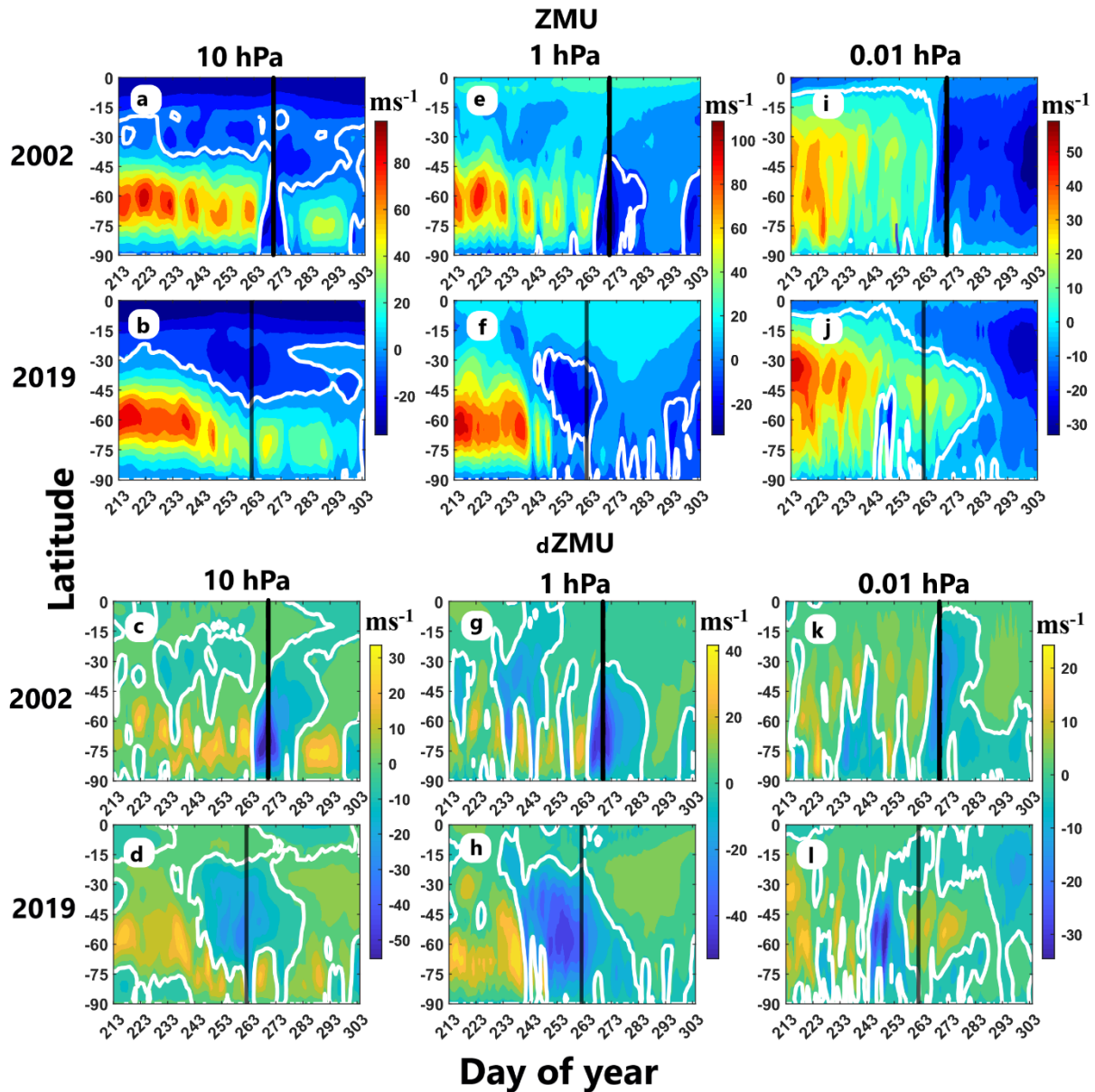


Figure 5. 5. Latitudinal-time section of ZMU at (a) 10 hPa, (e) 1 hPa, and (i) 0.01 hPa and dZMU at (c) 10 hPa, (g) 1 hPa, and (k) 0.01 hPa $^{\circ}\text{S}$ during 2002 observational days. Same during 2019 observational days for ZMU at (b) 10 hPa, (f) 1 hPa, and (j) 0.01 hPa and dZMU at (d) 10 hPa, (h) 1 hPa, and (l) 0.01 hPa $^{\circ}\text{S}$. Please note the change of scale in the colorbars corresponding to each subplot while comparing. Also, consider the difference in colorbar used to represent actual and deseasoned variability.

5.3.2.2. ZMV

In a similar manner, we have analyzed the latitudinal-temporal variability of ZMV at the mentioned representative altitudes for the two warming events. Figures 5.6a and 5.6b depict the latitudinal profile of ZMV at 10 hPa for the 2002 and 2019 SSW events, respectively. In the 2002 event, a distinct band of southerly wind centered at 60° S exhibits intermittent strengthening before the PWD, followed by a sudden decrease afterward (Figure 5.6a). On the other hand, during 2019, there is a poleward shift of southerly ZMV patches from midlatitude (60° S) until the PWD (Figure 5.6b). The latitude-time variability of dZMV at 10 hPa during these events is shown in Figures 5.6c and 5.6d. A noticeable southerly deseasoned forcing is evident around the 2002 PWD at midlatitude (Figure 5.6c). Figure 5.6d illustrates the clear poleward movement of southerly dZMV, intensifying around the PWD in 2019, similar to the corresponding ZMV profile.

Figures 5.6e and 5.6f illustrate the latitudinal-temporal variability in ZMV at 1 hPa during the 2002 and 2019 events. In 2002, intermittent strengthening in southerly ZMV centered at 60° S is observed until the PWD (Figure 5.6e). In 2019, enhanced southerly ZMV can be observed a few days before the PWD (Figure 5.6f). The dZMV profiles (Figures 5.6g and 5.6h) exhibit very similar behavior to ZMV at 1 hPa.

The latitudinal profile of ZMV at 0.01 hPa during the two events is shown in Figures 5.6i and 5.6j. The northerly ZMV shifts to southerly around the 2002 PWD and persists for the remaining observational days (Figure 5.6i). Similar features are observed during the 2019 event (Figure 5.6j), with the only difference being the delayed reversal of northerly ZMV to southerly after the 2019 PWD in the middle latitudes. The overall pattern closely resembles ZMU at 0.01 hPa (Figures 5.6i and 5.6j). Figures 5.6k and 5.6l depict the latitudinal-temporal variability of dZMV at 0.01 hPa during the 2002 and 2019 events, respectively. In 2002, a noticeable southerly deseasoned forcing is observed around the PWD, especially at low latitude (Figure 5.6k). Figure 5.6l shows southerly deseasoned forcing starting a few days before the PWD, mainly at low latitude in 2019.

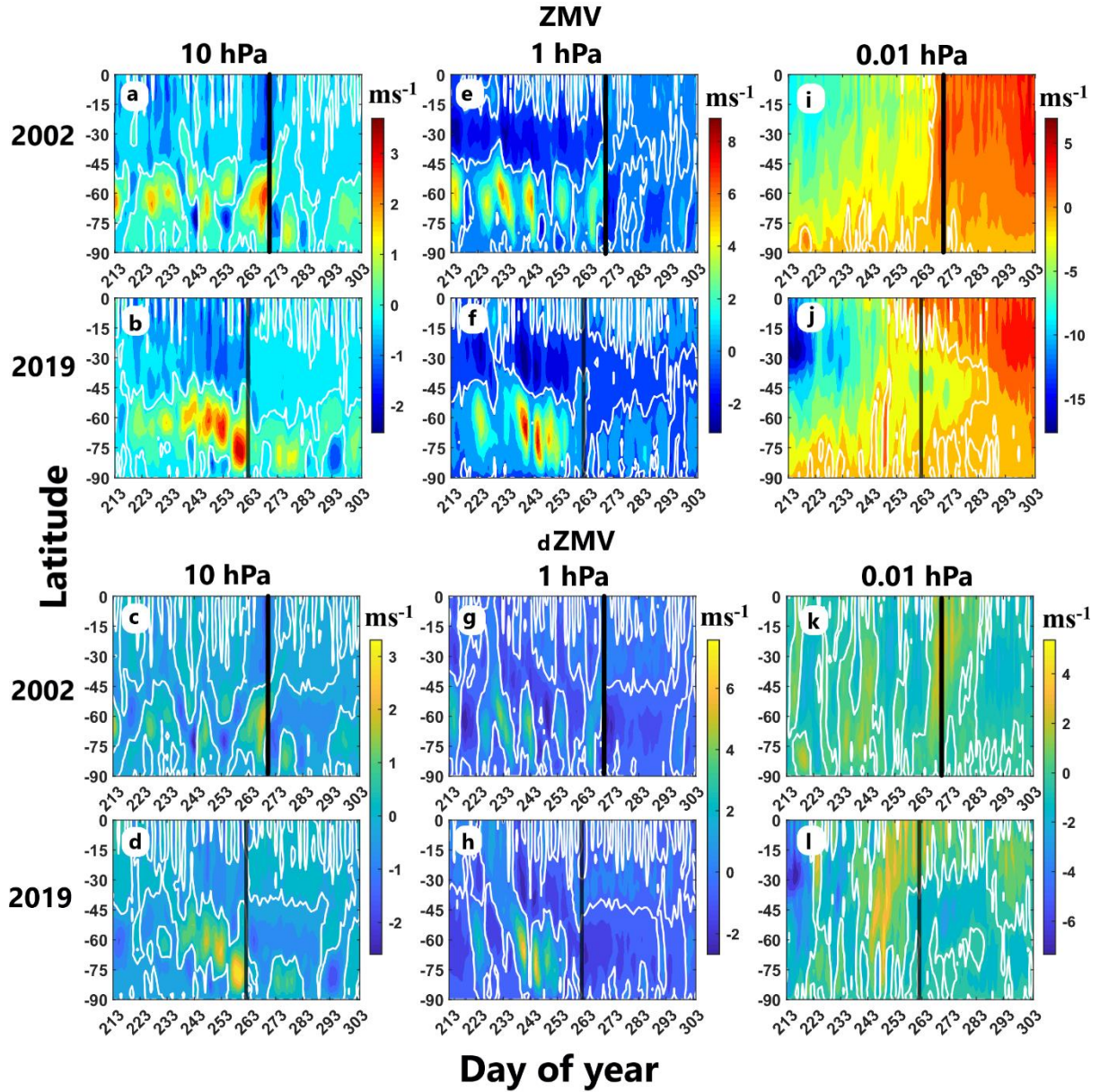


Figure 5. 6. Latitude-time section of ZMV at (a) 10 hPa, (e) 1 hPa, and (i) 0.01 hPa and dZMV at (c) 10 hPa, (g) 1 hPa, and (k) 0.01 hPa °S during 2002 observational days. Same during 2019 observational days for ZMV at (b) 10 hPa, (f) 1 hPa, and (j) 0.01 hPa and dZMV at (d) 10 hPa, (h) 1 hPa, and (l) 0.01 hPa °S. Please note the change of scale in the colorbars corresponding to each subplot while comparing. Also, consider the difference in colorbar used to represent actual and deseasoned variability.

Overall, significant differences are observed between actual and deseasoned zonal mean flow, particularly in the upper mesosphere. Therefore, the deseasoned flow provides crucial insights into the characteristics of the zonal mean horizontal wind circulation induced by the sudden global-scale disturbance, i.e., SSW.

5.3.3. Distribution of winds in the SH at various phases of SSW

To comprehend the development of horizontal wind flow and the related longitudinal variations concerning the SH SSW, we have examined the latitude-longitude section of both U and V in three distinct phases: pre-warming (pre-W), warming (W), and post-warming (post-W) relative to the SSW PWD. Here, the pre-W, W, and post-W phases are determined in relation to the PWD. A 5-day average has been applied for each phase to depict the dynamic state of the horizontal wind. For the 2002 event, the temporal average of U/V during 15-19 September, 25-29 September, and 5-9 October has been calculated to illustrate the evolution of U/V across the three phases of the 2002 SSW. A 5-day gap is selected between two consecutive phases, such as pre-W and W or W and post-W. Similarly, for the 2019 SSW, we have chosen 6-10 September, 16-20 September, and 26 September-30 September as time intervals representing the Pre-W, W, and Post-W phases.

5.3.3.1. Evolution of U

We chose altitudes of 10 hPa, 1 hPa, and 0.01 hPa in the middle atmosphere to study the evolution of the U during the Pre-W, W, and Post-W phases. Figures 5.7a and 5.7b depict the latitude-longitude section of the U at 10 hPa during the Pre-W phase for 2002 and 2019, respectively. Figures 5.7c and 5.7d show the deseasoned U (dU) at 10 hPa during the Pre-W phase for 2002 and 2019, respectively. Figures 5.7e-h and 5.7i-l represent similar comparisons but for the W and Post-W phases, respectively. The white bold curve indicates a zero value.

At 10 hPa, a strong westerly flow is found to meander across all longitudes in the mid and high latitudes during the Pre-W phases of 2002 (Figure 5.7a) and 2019 (Figure 5.7b). The characteristics seen in Figures 5.7a and 5.7b are more pronounced in the dU profiles during the Pre-W phases of 2002 (Figure 5.7c) and 2019 (Figure 5.7d).

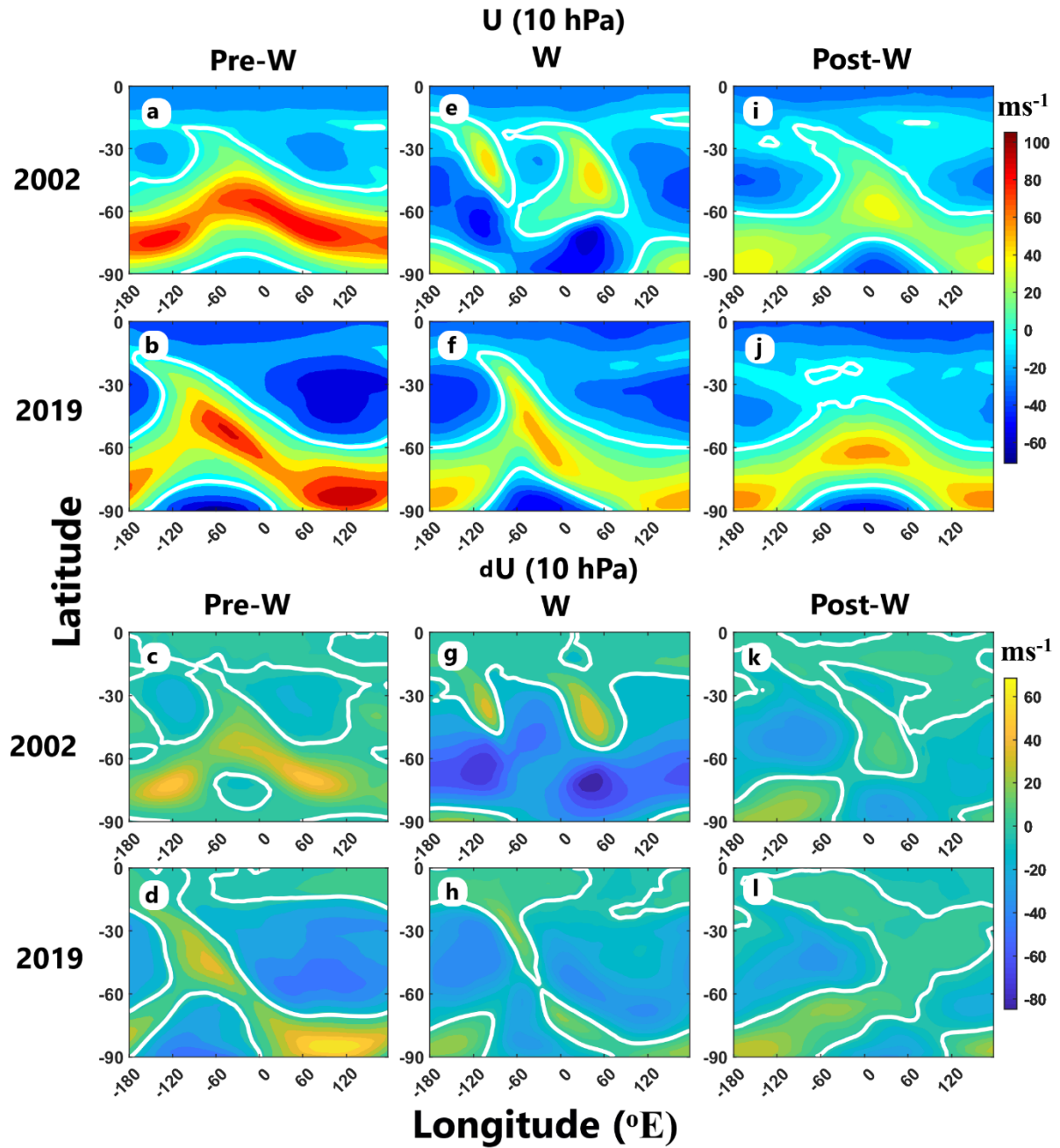


Figure 5. 7. Latitude-longitude section of U at 10 hPa during 2002 (a) Pre-W (e) W, and (i) Post-W and dU during 2002 (c) Pre-W (g) W, and (k) Post-W at 10 hPa. Same for U during 2019 (b) Pre-W (f) W, and (j) Post-W and dU during 2019 (d) Pre-W (h) W, and (l) Post-W. Please note the change of scale in the colorbars corresponding to each subplot while comparing. Also, consider the difference in colorbar used to represent actual and deseasoned variability.

During the W phase of the 2002 SSW event, two distinct patches of westerly winds between easterly zones, indicating the dominance of a zonal wavenumber 2 structure, are evident in the midlatitudes (Figure 5.7e). In 2019, the U pattern closely resembles that of the Pre-W

phase but with reduced magnitude and an eastward shift at low latitudes ($\sim 30^\circ$ S) (Figure 5.7f). The reversal in westerly winds at high latitudes and the appearance of the zonal wavenumber 2 feature in the U at midlatitudes become more apparent in the dU profile during the 2002 W phase (Figure 5.7g). Figure 5.7h shows a noticeable weakening in westerly winds during the 2019 W phase, as seen from the negative dU values at mid and high latitudes.

During the 2002 Post-W phase, the U reinstates the westerly trend at mid and high latitudes with a smaller overall magnitude compared to the Pre-W phase (Figure 5.7i). In 2019, the westerly winds at high latitudes remain weak during the Post-W phase (Figure 5.7j). According to the dU profiles during the Post-W phase, the easterly zones are suppressed by the westerly ones for both 2002 (Figure 5.7k) and 2019 (Figure 5.7l), although the patterns do not resemble those of the Pre-W phase unlike the behavior of the U.

Figure 5.8 depicts the same as Figure 5.7 but at the 1 hPa pressure level. A notable westerly wind structure is evident during the Pre-W phase of 2002 across all longitudes, centered around 60° S (Figure 5.8a). This is succeeded by a transition from westerly to easterly winds at mid and high latitudes during the 2002 W phase (Figure 5.8e), with a partial recovery of westerly winds during the 2002 Post-W days (Figure 5.8i). In contrast, during the 2019 Pre-W days, the U exhibits an opposing variation at mid and high latitudes. Interestingly, a dominant zonal wavenumber 1 structure of U in the midlatitudes is found to be in the opposite phase to the same at high latitudes, i.e., the easterly and westerly patches seem to interchange their location among the mid and high latitudes with longitude (Figure 5.8b). Similar patterns are observed during the 2019 W days, albeit with a smaller magnitude (Figure 5.8f). The westerly winds dominate during the 2019 Post-W days (Figure 5.8j), although the magnitude is much reduced compared to the previous two phases.

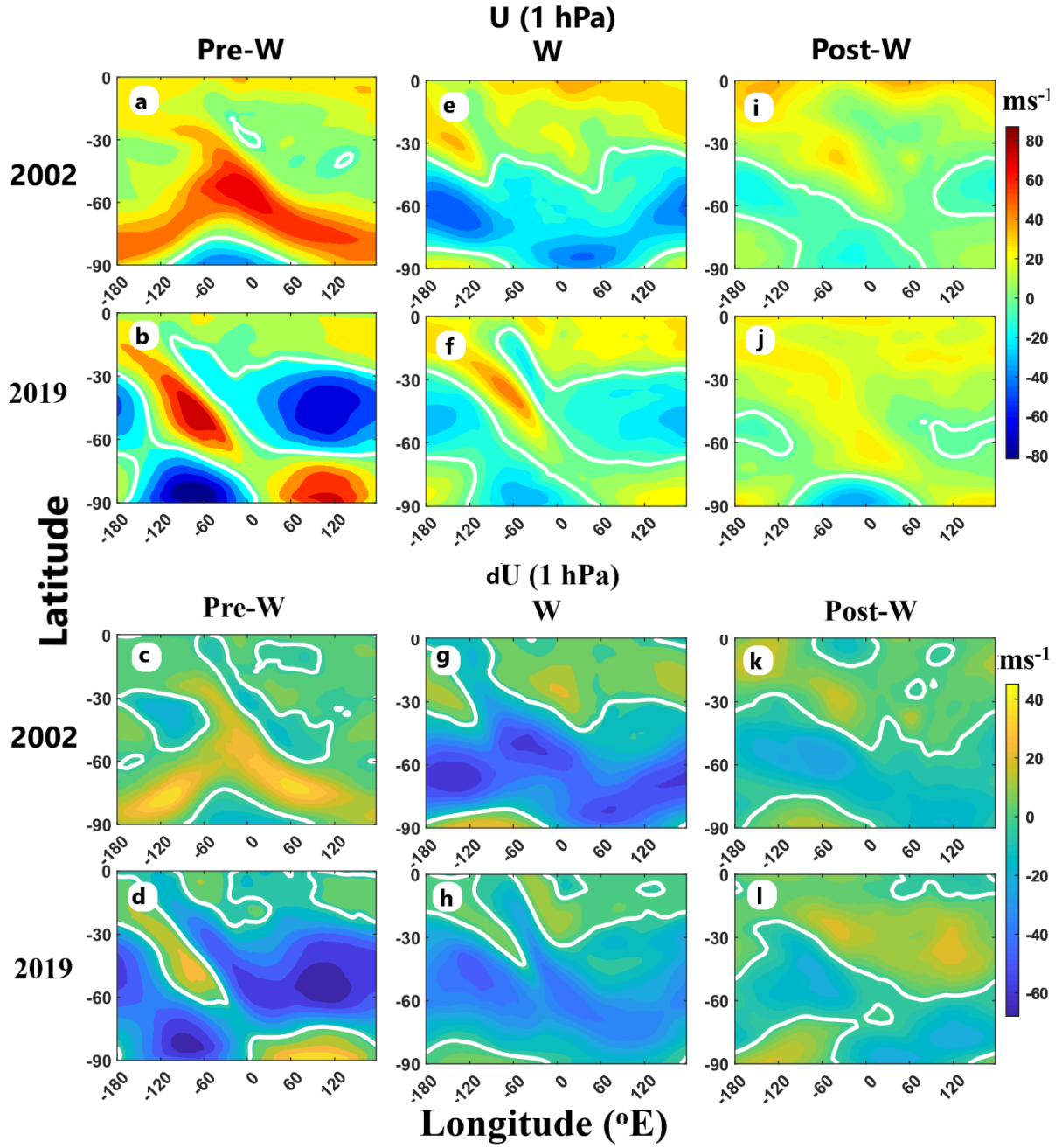


Figure 5. 8. Same as Figure 5.7, but at 1 hPa.

Figures 5.8c, 5.8g, and 5.8k highlight significant features of dU evolution concerning the 2002 event, which mirror the patterns seen in Figures 5.8a, 5.8e, and 5.8i, respectively. During the 2019 Pre-W phase, dU shows significant easterly winds at mid and high latitudes across different longitudes (Figure 5.8d), followed by an overall reduction in magnitude during the W phase (Figure 5.8h) and Post-W phase (Figure 5.8l). In the 2019 Post-W phase, westerly flow persists at lower latitudes, while easterly winds dominate at higher latitudes across most longitudes.

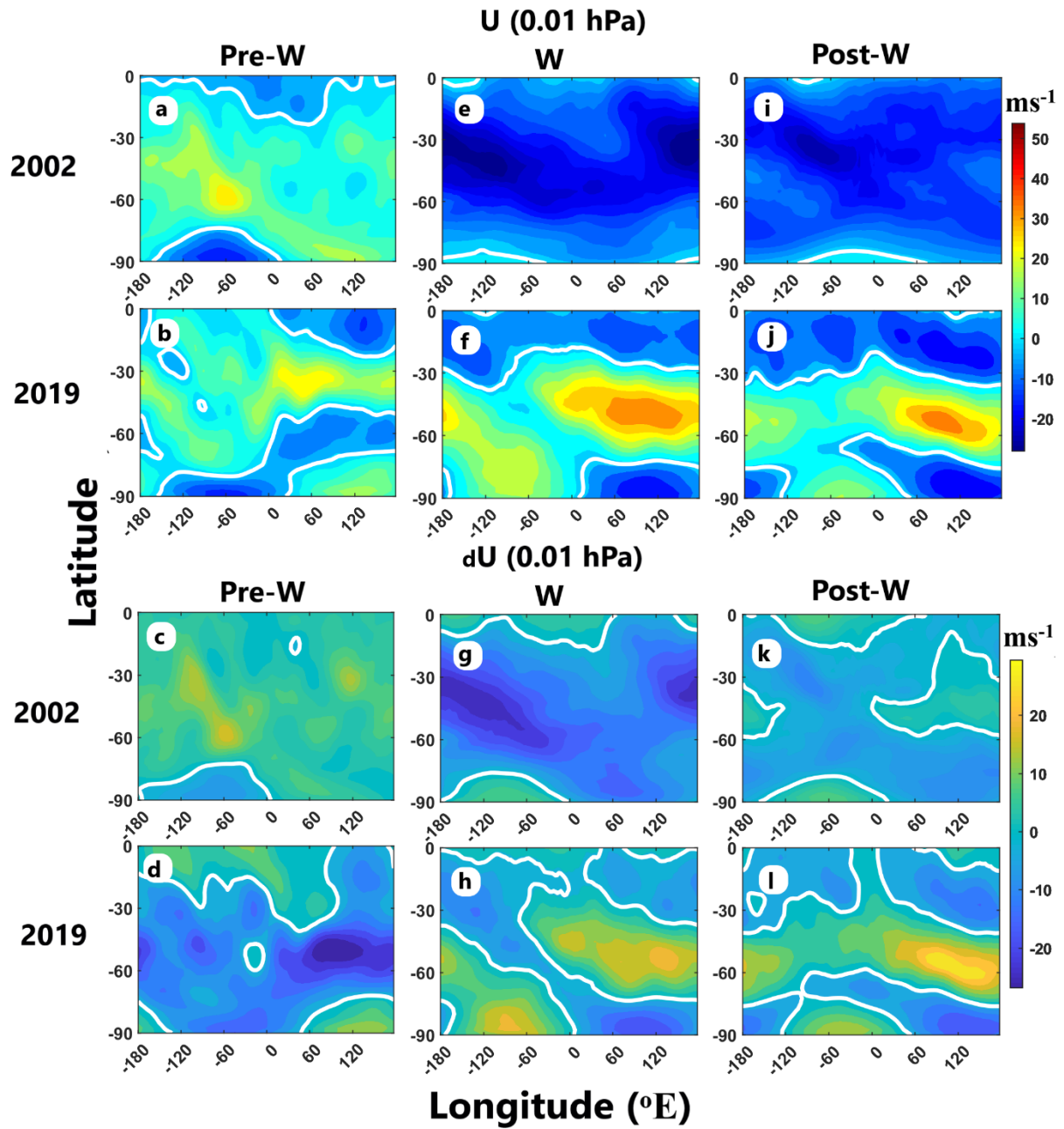


Figure 5. 9. Same as Figure 5.8, but at 0.01 hPa.

Figure 5.9 presents the same as Figure 5.7 but at the 0.01 hPa pressure level. The prevailing westerly winds during the Pre-W phase of 2002 are evident in Figure 5.9a. The reversal from westerly to easterly winds is observed during the W and Post-W phases, as illustrated in Figures 5.9e and 5.9i, respectively. Conversely, in the 2019 event, the westerly winds generally dominate during the Pre-W days (Figure 5.9b). The westerly winds appear to strengthen during the W phase in the eastern longitude sector at mid latitudes (Figure 5.9f), and this trend persists during the Post-W phase as well (Figure 5.9j). Figures 5.9c, 5.9g, and

5.9k show dU , which closely mirrors U as seen in Figures 5.9a, 5.9e, and 5.9i during the 2002 event. The variability of dU during different phases of the 2019 SSW, as depicted in Figures 5.9d, 5.9h, and 5.9l, exhibits characteristics almost identical to U as shown in Figures 5.9b, 5.9f, and 5.9j.

5.3.3.2. Evolution of V

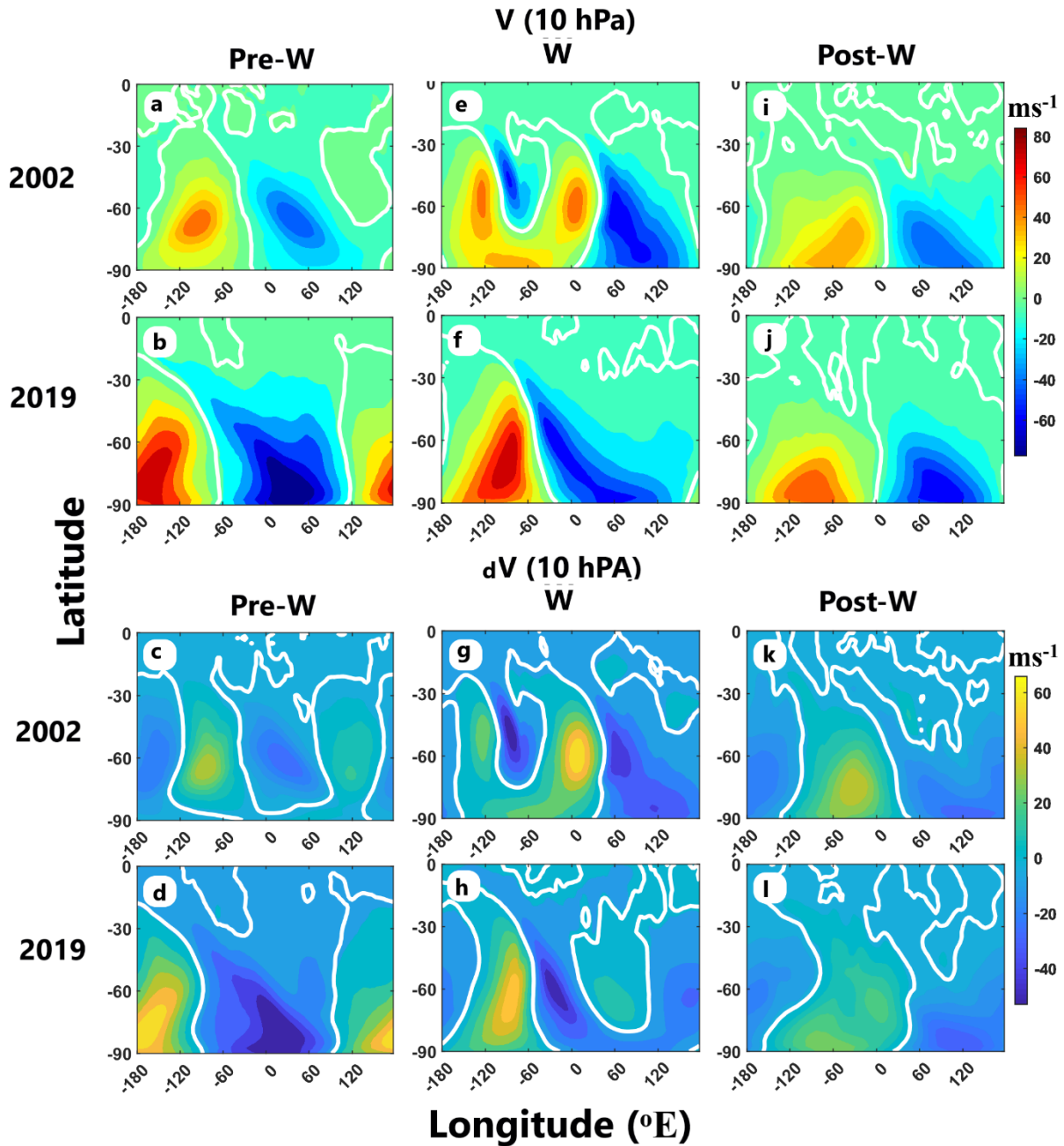


Figure 5. 10. Latitude-longitude section of V at 10 hPa during 2002 (a) Pre-W (e) W, and (i) Post-W and dV during 2002 (c) Pre-W (g) W, and (k) Post-W at 10 hPa. Same for V during 2019 (b) Pre-W (f) W, and (j) Post-W and dV during 2019 (d) Pre-W (h) W, and (l) Post-W. Please note the change of scale in the colorbars corresponding to each subplot while

comparing. Also, consider the difference in colorbar used to represent actual and deseasoned variability.

Figure 5.10 displays the latitude-longitude section of V at the 10 hPa level across various phases of SSW for both warming events. Figure 5.10a illustrates the V profile during the Pre-W phase of 2002, where zonal wavenumber 1 structures in V appear prominent at high latitudes. Similarly, the V profile during the 2019 Pre-W phase also indicates a dominant zonal wavenumber 1 signature at mid and high latitudes, noticeable from the alternating appearance of northerly and southerly winds across longitudes (Figure 5.10b). The dV profile during the 2002 Pre-W phase in Figure 5.10c reveals a dominant zonal wavenumber 2 component at mid latitudes, extending to high latitudes. Likewise, the dV profile during the 2019 Pre-W phase (Figure 5.10d) shows a clear zonal wavenumber 1 structure at mid and high latitudes.

Moving to the W phase, the V profile during the 2002 event (Figure 5.10e) exhibits a significant zonal wavenumber 2 structure at mid and high latitudes. In contrast, during the 2019 W phase, the zonal wavenumber 1 component in V continues to dominate, with a sharp change from southerly to northerly winds along 60° W at 30 - 60° S (Figure 5.10f). The latitude-longitude section of dV during the 2002 W stage (Figure 5.10g) shows features similar to Figure 5.10e. Interestingly, during the 2019 W days, there's an emergence of a zonal wavenumber 2 component in dV (Figure 5.10h) at mid and high latitudes, not previously evident in the V profile (Figure 5.10f).

Additionally, the zonal wavenumber 1 structure also appears to persist at mid and high latitudes during the 2002 (Figure 5.10i) and 2019 (Figure 5.10j) Post-W phase. The dV profiles during the 2002 (Figure 5.10k) and 2019 (Figure 5.10l) Post-W phase exhibit features similar to V (Figure 5.10i and 5.10j, respectively).

Figure 5.11 represents the same as Figure 5.10, but at the 1 hPa level. The zonal wavenumber 1 structure of V is prominently observed at mid and high latitudes during various phases of both the 2002 (Figure 5.11a, 5.11e, and 5.11i) and 2019 (Figure 5.11b, 5.11f, and 5.11j) events. However, there's a gradual decrease in wind magnitude during the W and Post-W phases. The dV profiles demonstrate the alternating presence of southerly and northerly deseasoned flow across the longitudinal domain in mid and high latitudes during the Pre-W,

W, and Post-W phases of both the 2002 (Figure 5.11c, 5.11g, and 5.11k) and 2019 (Figure 5.11d, 5.11h, and 5.11l) events, aligning with the variability observed in V.

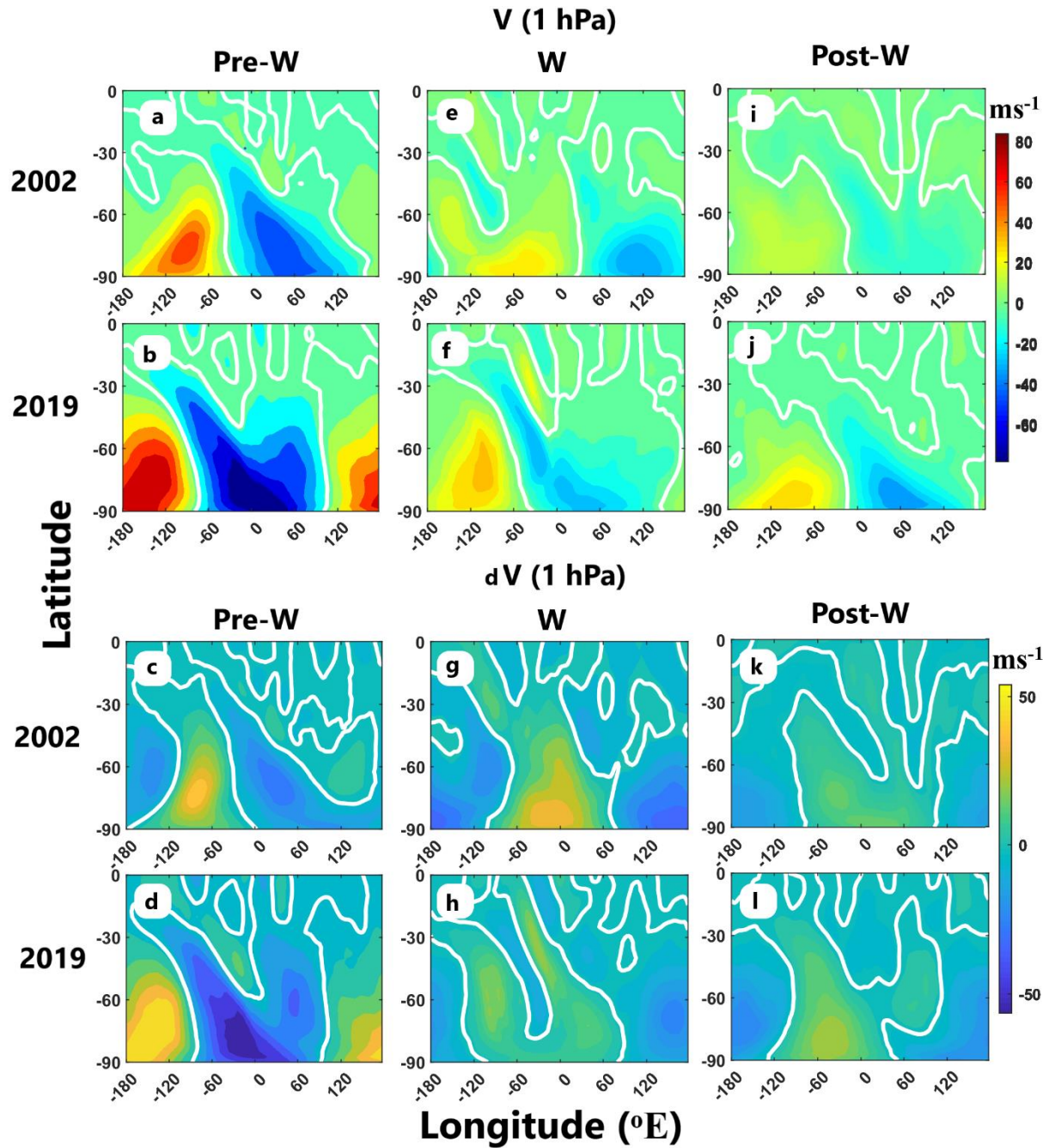


Figure 5. 11. Same as Figure 5.10, but at 1 hPa.

Figure 5.12 illustrates the same as Figure 5.10, albeit at the 0.01 hPa pressure level. At this level, the V profile showcases a notable zonal wavenumber 1 structure at mid and high latitudes during the 2002 Pre-W phase (Figure 5.12a), which decreases in intensity during the W (Figure 5.12e) and Post-W (Figure 5.12i) phases.

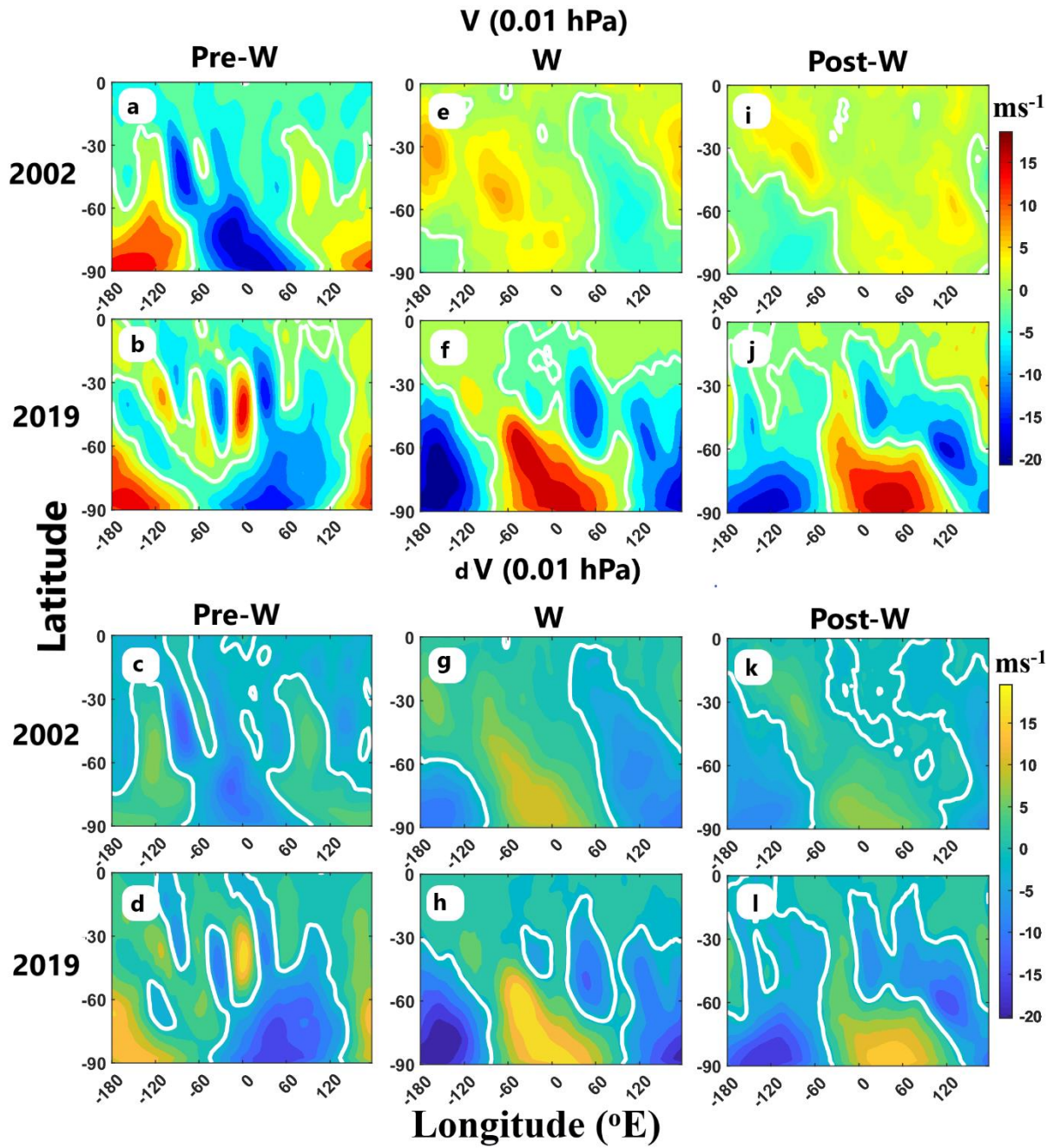


Figure 5. 12. Same as Figure 5.10, but at 0.01 hPa.

In contrast, during the 2019 Pre-W phase, there's an intermittent pattern of northerly and southerly winds around 30° S, hinting at potential modulation by higher zonal wavenumber waves. However, the dominance of the zonal wavenumber 1 structure is evident at high latitudes (Figure 5.12b). During the 2019 W phase, the zonal wavenumber 1 structure prevails at high latitudes (Figure 5.12f). Additionally, there's a noticeable shift in the longitudinal positioning of southerly and northerly winds during the W phase compared to the

Pre-W phase. The signature of the zonal wavenumber 1 structure remains prominent at high latitudes during the 2019 Post-W days (Figure 9j). The dV profiles at the 0.01 hPa level during the 2002 (Figures 5.12c, 5.12g, and 5.12k) and 2019 events (Figures 5.12d, 5.12h, and 5.12l) exhibit latitude-longitude features akin to V.

5.4. Discussion

The present study has highlighted several intriguing dynamic phenomena occurring during rare SSW events in the SH using the MERRA2 dataset. The primary objective of this study is to offer valuable insights into middle atmospheric dynamics concerning zonal mean flow and associated longitudinal variability in the global circulation during major (2002) and minor (2019) warming events through comparison.

Observations from the altitude-time variability of polar temperatures reveal the downward propagation of warming from the upper stratosphere to lower altitudes until the PWD in 2002 and 2019. However, this propagation appears more gradual in 2019 compared to 2002. In 2002, there is a sudden reversal of zonal mean westerlies at 60° S, extending to below 30 km altitude on the PWD (Figure 5.4e). Conversely, in 2019, the reversal of zonal mean westerlies at 60° S occurs much earlier in the mesosphere, continuing downward to as low as 35 km on the PWD (Figure 5.4f). Another significant difference is that in 2002, the actual wind in the upper mesosphere remains easterly for the rest of the observational days, unlike in 2019 (Figures 5.4e and 5.4f). This difference may be attributed to the late occurrence of the 2002 SSW event compared to 2019, where seasonal transition likely plays a dominant role. However, deseasoned variability clearly indicates the SSW impact at 60° S in terms of easterly (reversed state) forcing from the upper mesosphere to lower altitudes around the PWD in 2002 (Figure 5.4g). Interestingly, the deseasoned and easterly forcing appears to penetrate to much lower altitudes around the PWD in both events, which is not discernible from the actual wind. Moreover, the easterly forcing seemingly reaches tropospheric heights in 2002, unlike in 2019. Both the 2002 and 2019 SH SSW events exhibit extended spatio-temporal deseasoned poleward forcing after the PWD compared to the actual wind.

The early reversal to an easterly direction in the low latitude stratosphere from deseasoned variability, particularly in the extratropical region, further intensifies towards mid and high

latitudes around the PWD in both events. This poleward progression of the zero-wind line helps guiding planetary waves from the tropics to polar regions, leading to polar vortex disruption (Koushik et al., 2022). Notably, deseasoned zonal mean upper mesospheric meridional wind shows a northward (equatorward) wind flow tendency, particularly in lower latitudes on the PWD in 2002 and before the PWD in 2019, as depicted in Figures 5.6k and 5.6l, respectively. Removing seasonal variability from high-altitude meteorological analyses, as noted by Laskar et al. (2019), revealed similar equatorward wind anomalies during NH SSW events in 2010 and 2013 in the MLT altitudes. It is important to note that in the present study the seasonal transition feature is dominant in the upper mesospheric wind variability, but the deseasoned wind reveals a warming impact in terms of easterly and southerly forcing around the PWD. Studying meridional circulation in the middle atmosphere is crucial for understanding the spatiotemporal and altitudinal distribution of temperature, angular momentum of air masses, and chemical constituents during such warming events (Garcia, 1987). Overall, the zonal mean flow in the middle atmosphere significantly alters during SH SSW events.

The associated longitudinal variability in horizontal wind flow in the middle atmosphere during different phases of the 2002 and 2019 SH SSW events is evident in Figures 5.7, 5.8 and 5.9 for U and in Figures 5.10, 5.11 and 5.12 for V. The dominance of the zonal wavenumber 2 component in mid-stratospheric horizontal wind (Figures 5.7e and 5.10e) during the 2002 warming at mid latitudes may be linked with the observed polar vortex split (Charlton et al., 2005). The easterly forcing is apparent from deseasoned variability during the 2002 and 2019 warming phases (Figures 5.7g and 5.7h). However, such characteristics are not consistent across all longitudes globally, indicating asymmetry in longitudinal variability due to warming impacts. Interestingly, a clear enhancement in upper mesospheric U is observed during the 2019 warming (Figure 5.9f) and post-warming phases (Figure 5.9j) at mid latitudes between 60° E and 120° E. This feature remains consistent even after removing the SMS (Figures 5.9h and 5.9l), indicating the significant role of SSW on U enhancement. Moreover, a striking similarity in the U and V at 0.01 hPa during warming and post-warming phases suggests the prolonged impact of SSW on the upper mesosphere. The noticeable longitudinal interchange of the peak V between pre-warming and other phases at high latitudes in the upper mesosphere, especially in 2019, indicates a significant shift in meridional flow structure globally driven by warming-induced forcing.

The split feature observed in mid-stratospheric U during the 2002 warming is not found to extend to the upper stratosphere and above. Overall, upper stratospheric and mesospheric changes during both major and minor events do not necessarily correspond to changes in the mid-stratosphere. Smith et al. (2022) also suggested that upper stratospheric and mesospheric changes during SSWs weakly correlate with stratospheric changes. This study provides a detailed description of middle atmospheric circulation during two historically rare major and minor SSWs from the SH in terms of zonal mean flow and associated longitudinal variability. Notable differences in dynamical conditions between the 2002 and 2019 SH SSWs are also reported. It is worth mentioning that significant event-to-event variability in NH SSWs has been noted in past studies (Zülicke & Becker, 2013; Zülicke et al., 2018). The SH SSW occurs around the spring equinox, and variability during late winter to early spring is primarily due to seasonal transition controlled by solar radiation processes and wave-driven dynamical processes. This study is crucial as it aims to assess weak/fine-scale signatures of SSW in the middle atmosphere, isolating seasonal and interannual effects.

In essence, chapter 5 highlights several key findings on the dynamics of SH sudden stratospheric warmings (SSWs) and their broader atmospheric impacts. Through a deseasoning approach, we effectively isolated subtle warming effects, revealing weak dynamical signatures that would typically remain obscured. Notably, our analysis found that the 2002 SSW impacted the troposphere with easterly deseasoned forcing, unlike the 2019 event, thus adding a unique dimension to tropospheric influence. Chapter 5 also uncovered potential tropical stratospheric precursors, as indicated by earlier easterly forcing at extratropical latitudes, suggesting that SH SSWs may have a tropical connection. In the mesosphere, our approach identified distinctive easterly and southerly forcings, offering a more thorough view of middle atmospheric dynamics. Additionally, an uneven longitudinal response to warming events revealed varying horizontal wind patterns across longitudes. Together, these findings provide a nuanced understanding of how rare SH SSWs disturb middle atmospheric circulation and highlight differences between major and minor events, underscoring their distinct characteristics and broader implications.

5.5. Summary and conclusions

The current study delves into a comparative analysis of middle atmospheric circulation during two rare SH SSW events occurring in September 2002 and 2019, which had not been exclusively explored previously. Given that SH SSW events align with the spring equinox, we aim to isolate the effects of the warming event from seasonal contributions, allowing a focused investigation into the global circulation changes induced solely by these warming events. Our study offers a comprehensive and comparative examination of both actual and deseasoned parameters during these warming episodes.

The results reveal distinct features in the deseasoned flow, indicating notable easterly forcing around the PWD during both events. Particularly, the deseasoned variability shows an early onset of zonal mean easterly forcing in the stratosphere at extratropical latitudes, progressing toward mid and high latitudes around the PWD. This suggests a potential tropical precursor to SH SSW events. While seasonal transition dominates in the upper mesosphere, deseasoned winds highlight warming impacts characterized by easterly and southerly (equatorward) forcing around the PWD.

The remarkable similarity in the latitude-longitude variability of U and V during the warming and post-warming phases underscores the sustained impact of these warming events on the upper mesosphere. Notably, the minor SSW in 2019 demonstrates a significant influence, leading to a shift in the meridional circulation structure globally. This is evidenced by the appearance of longitudinal interchange of the upper mesospheric peak V at high latitudes between the pre-warming and other phases.

In essence, our study provides crucial insights into the perturbation of SH middle atmospheric flow caused by rare major and minor SSW events in the SH. These findings highlight the importance of such events, as they can significantly impact atmospheric circulation on a global scale.

Chapter 6

Nonlinear Interaction between Planetary-scale waves

6.1. Introduction

As discussed in Chapter 3, SSW is a dramatic meteorological event marked by intensified PWs, which include both stationary and traveling components. The SPWs, primarily active in the winter stratosphere (e.g., Pancheva et al., 2009a, 2009b; Mitra et al., 2022), can interact with the polar vortex, potentially causing its displacement or split. The traveling PWs (TPWs), with periods of up to about 30 days, play a crucial role in the latitudinal and vertical coupling during SSWs. Numerous studies have investigated the coupling between low and high latitudes in the middle atmosphere via SPWs and TPWs during SSWs in the NH (e.g., Pancheva et al., 2007; Guharay & Sekhar, 2012) and less frequent SSWs in the SH (e.g., Guharay et al., 2014a; Mitra et al., 2022). Previously, spectral analyses of satellite and reanalysis-derived U and T fields have shown zonally symmetric PW ($ZWN=0$) during the major 2003-04 NH SSW event (Pancheva et al., 2007, 2009a, 2009b), with the prevailing period same as the TPW. However, these zonally symmetric PWs are relatively underreported in the literature.

Prior research has noted significant variability in solar tides at mid and high latitudes (e.g., Chau et al., 2015; Conte et al., 2019) during SSWs in the MLT. Recent work by He et al. (2017, 2018) explained the observed semidiurnal tide (ST) variability at mid-latitudes during SSWs as a consequence of nonlinear interaction with TPWs. While there are some general studies on the nonlinear interaction between tides and PWs (e.g., Beard et al., 1999; Pancheva, 2001; Guharay et al., 2015), limited literature focuses on such interactions during transient events like SSWs.

Due to the significant amplitude of the ST in mid and high latitudes, this wave can sometimes engage in nonlinear interactions with other planetary-scale waves and tides in the middle atmosphere, leading to amplitude variability across various temporal scales. The suggestion is that the advection terms in the momentum equation contribute to nonlinear interactions among GWs, tides, and PWs in the middle atmosphere (Teitelbaum & Vial, 1991). As a result

of the nonlinear interaction between two primary waves, secondary waves of frequencies equal to the sum and difference of the frequencies of the primary waves are generated. If the difference between the frequencies of the primary waves is substantial, then the frequency of the secondary waves will be very close to the higher primary frequency. If the amplitude of these secondary waves is considerable, they will beat with the nearest primary frequency, causing modulation of the higher frequency primary wave at the frequency of the other primary component. Therefore, the interaction of the ST with sufficiently longer period planetary waves leads to a multitude of secondary wave components with frequencies close to the ST frequency.

The present study presents the first observational evidence of a two-step nonlinear interaction between planetary-scale waves during major SSW events associated with zonally symmetric PWs. The research focuses on the NH winters of 2008-09 and 2012-13, characterized by split-type major SSWs and strong polar night jet oscillations (Conte et al., 2019). Our observational data comprises wind measurements from the specular meteor radar (SMR) situated at Andenes (AN), northern Norway (69° N, 16° E). We also use a contemporaneous dataset from the MERRA-2 for ZWN diagnosis (Gelaro et al., 2017). We analyze U at 72 model pressure levels from 985 to 0.01 hPa (approximately 0 to 75 km) on a 2.5° x 2.5° latitude-longitude grid. The SPARC Reanalysis Intercomparison Project (S-RIP) Final Report has confirmed the suitability of MERRA2 for studying tides and PWs in the middle atmosphere (Harvey et al., 2022).

The chapter is organized into three sections: Section 6.2.1 discusses spectra of Semidiurnal Tides (ST) and PW in meteor radar winds, Section 6.2.2 examines the temporal evolution of interacting wave components, Section 6.2.3 investigates the dominant zonal wavenumber of primary waves, and Section 6.2.4 explores potential forcing mechanisms of the zonally symmetric PW in the two-step nonlinear interaction. Finally, Section 6.3 provides a summary and conclusions.

6.2. Results and Discussions

Our study period spans from November 1 to March 31. We define the SSW PWD as the date with the maximum positive temperature gradient between 90° N and 60° N at 10 hPa, which

typically aligns with the first wind reversal during major SSW events (e.g., Andrews et al., 1987). Note that we use the PWD solely to establish the onset of SSW, and our discussions are not sensitive to differing definitions of SSW onsets (Butler et al., 2015). In our analysis, January 23, 2009, and January 6, 2013, are identified as the PWDs, marked by vertical solid lines in all figures.

6.2.1. ST and PW spectra in the specular meteor radar winds

The Evolutionary Lomb Scargle (ELS) Periodogram has been calculated using the Lomb Scargle (LS) technique applied to hourly U with a shifting window of 21-day width across the entire observational interval (Schulz & Stattegger, 1997). The 21-day window size is mathematically the minimum required to distinguish between closely spaced periods, such as 11.7 and 12 hours and 12.3 and 12 hours. The ELS spectra reveal a sustained presence of a semidiurnal tide (ST) with a 12-hour period, exhibiting a sharp decline around the SSW PWD of the 2008-09 event, as depicted in Figure 6.1a. Interestingly, a transient increase is also noted at periods of 11.7 hours and 12.3 hours during this time.

Additionally, the wavelet amplitude spectra of hourly U demonstrate a notable rise in a quasi-20-day wave (Q20dw) around the SSW PWD (Figure 6.1b). Intriguingly, the appearance of upper sideband (USB) and lower sideband (LSB) corresponding to 11.7 hours and 12.3 hours periods, respectively, coincides with the occurrence of Q20dw. These USB and LSB could be secondary waves resulting from nonlinear interaction (Teitelbaum & Vial, 1991). The primary waves likely involved in this interaction are the ST and Q20dw, giving rise to secondary waves of LSB (~12.3 hours) and USB (~11.7 hours). Moreover, these USB/LSB, with frequencies closely aligned with the ST, undergo beat interactions, modulating the ST amplitude with a 20-day PW period. This modulation is corroborated by wavelet amplitude spectra of instantaneous ST amplitude, revealing a concurrent and significant quasi-20-day modulation around the SSW PWD (Figure 6.1c). The amplitude and phase of the ST are determined through least square fitting to time series data using a 4-day window shifted progressively by 1 day.

$$Y(t) = Y_o + \sum_{p=1}^3 A_p \cos \left[\frac{2\pi p}{24} (t - \varphi_p) \right] \quad (6.1)$$

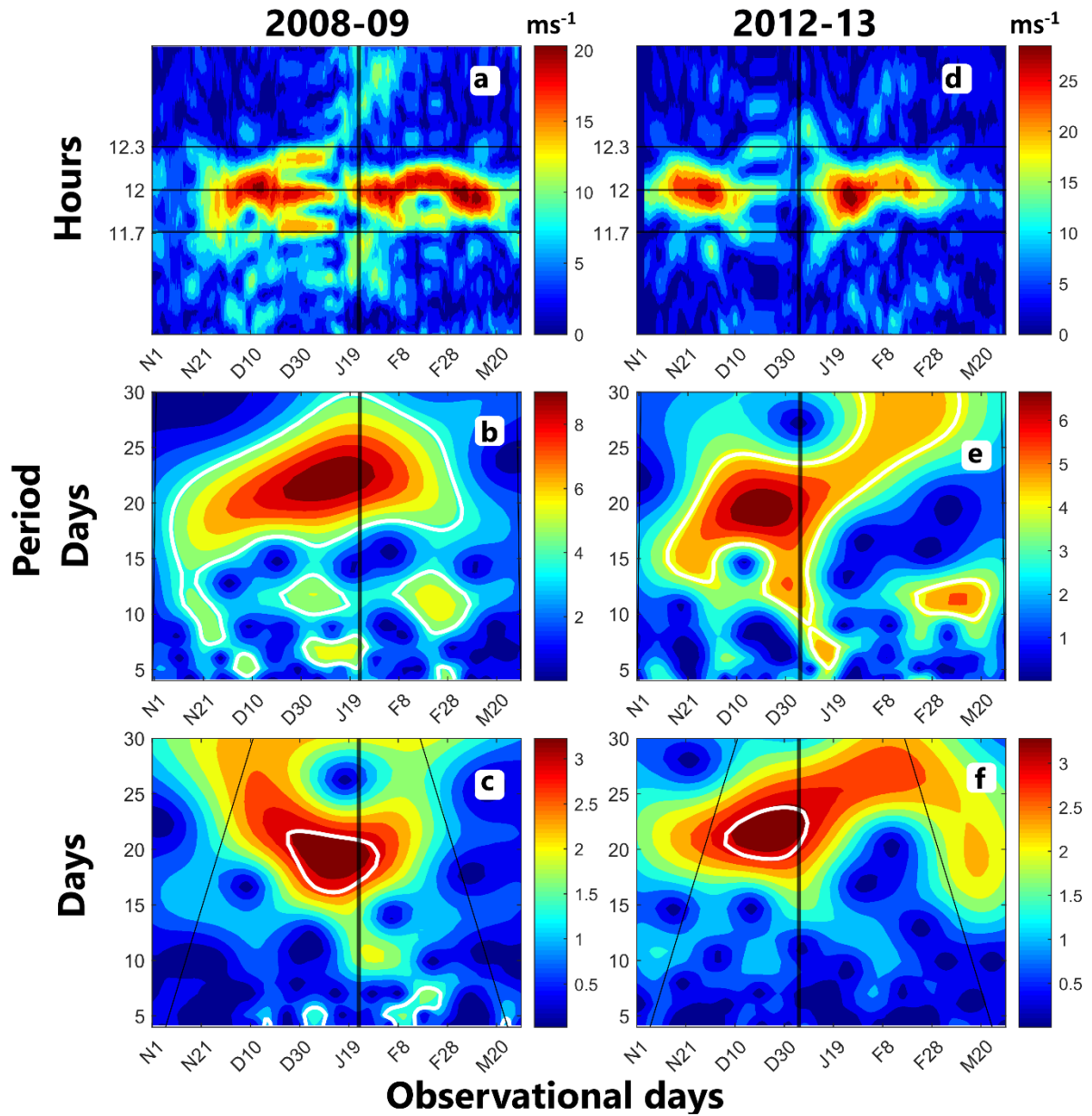


Figure 6. 1. (a) Evolutionary Lomb Scargle amplitude spectra (semidiurnal tide period range) and (b) wavelet amplitude spectra (PW period range) of the U at 90 km, and (c) wavelet spectra of the instantaneous ST amplitude at 90 km using meteor radar observations at Andenes (69.3° N, 16° E), from 1 November 2008 until 31 March 2009. (d, e, f) represent the same as (a, b, c) but during 2012-13. The solid vertical line represents the PWD and the thin tilted line represents the cone of influence (COI). The white curve in the wavelet spectra represents the 95 % confidence level. Please note the change of scale in the colorbars corresponding to each subplot while comparing. The letters N, D, J, F, and M in the x axis denote November, December, January, February, and March; the subsequent number indicates the day of the given month.

Similar features to Figures 6.1a-c are observed during the 2012-13 SSW event, as depicted in Figures 6.1d-f, respectively. Therefore, the ELS effectively identifies secondary waves in meteor radar winds resulting from nonlinear interactions between Q20dw and ST. The wavelet spectra highlight the presence of a significant Q20dw potentially involved in nonlinear interactions. These secondary waves modulate the ST amplitude with the PW period, evident from the wavelet spectra of instantaneous ST amplitude. The concurrent observations of secondary waves, significant Q20dw, and 20-day modulation of ST amplitude using ELS and wavelet methods on meteor radar winds provide compelling evidence of nonlinear interactions between ST and Q20dw. The novelty of the method lies in detecting transient occurrences of nonlinear interactions between planetary-scale waves during highly disturbed atmospheric conditions.

It's worth noting that in the 2008-09 case, observed USB or LSB periods appear slightly shifted from theoretical values towards 12 hours (Figure 6.1a), and the hourly wind wavelet spectrum (Figure 6.1b) shows a peak around 22 days. However, for uniformity and consistency, we consider Q20dw as the primary interacting wave and 11.7 and 12.3 hours as USB and LSB periods hereinafter.

6.2.2. Temporal evolution of interacting wave components

During both events, there's a notable burst of the 20dw lasting a few days in the altitude range of 80-90 km around the SSW PWD, as illustrated in Figures 6.2a and 6.2e. In the 2008-09 event, the 20d-like oscillation appears to descend from the upper MLT until it converges with a comparatively stronger counterpart from below. Generally, the pattern of the LSB doesn't seem to align with the primary wave, i.e., the ST, throughout the observation interval. Interestingly, the increase in the LSB component around the PWD, as shown in Figures 6.2b and 6.2f, coincides with a sudden weakening of the ST during both events, as depicted in Figures 6.2c and 6.2g. Conversely, regarding the USB, its relationship with the primary wave, i.e., the ST, appears consistent in terms of enhancement and weakening, as observed in Figures 6.2d and 6.2h. Such an outcome implies a dissimilar but evident relationship between the primary and secondary waves, due to the nonlinear interaction. Typically, the LSB, ST, and USB attain higher amplitudes above 90 km altitude.

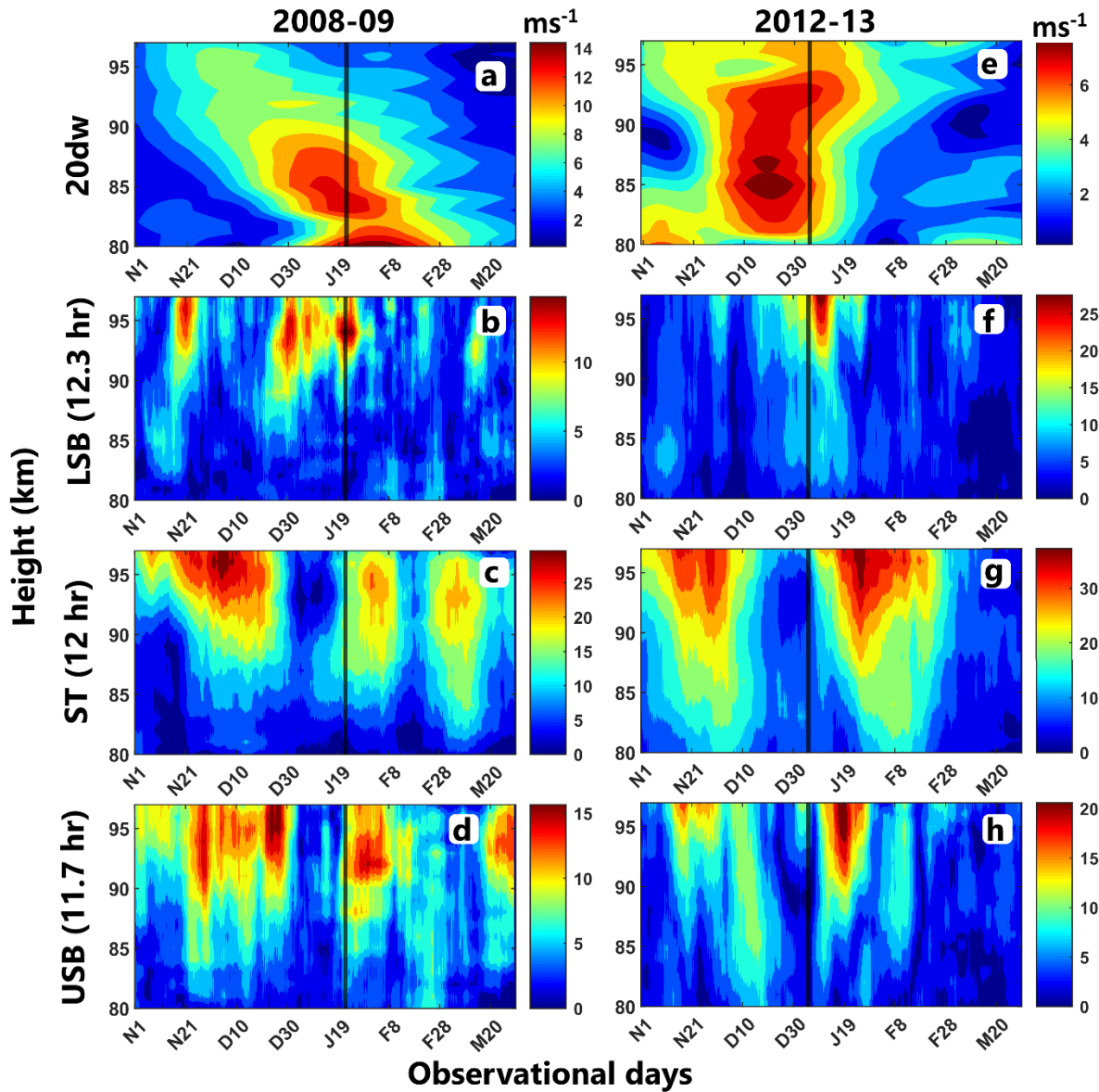
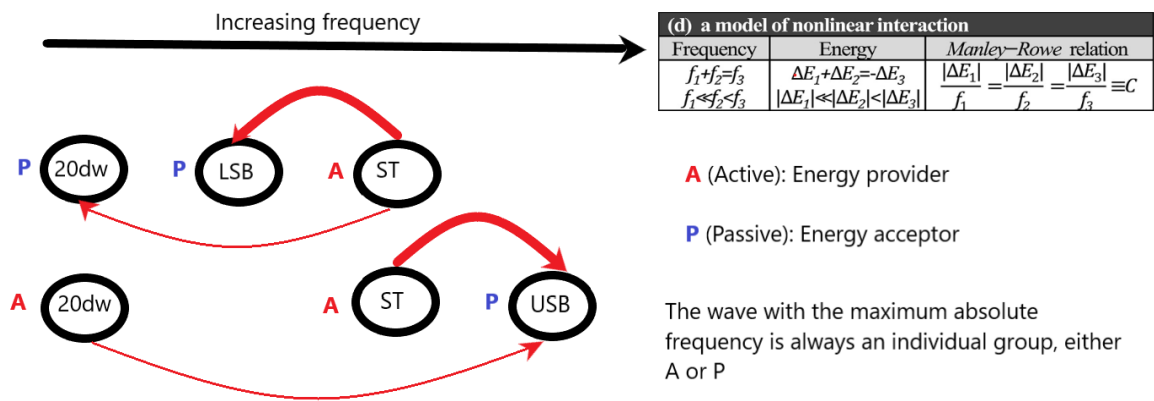


Figure 6. 2. (a) Altitude profile of the wavelet amplitude spectra of the 20dw, ELS amplitude spectra of (b) LSB, (c) ST, and (d) USB using meteor radar derived U at Andenes (69.3° N, 16° E) during the 2008-09 observational days. (e, f, g, h) represents the same as (a, b, c, d) but during 2012-13. Please note the change of scale in the colorbars for each subplot while comparing.

The Manley Rowe Relationship (MRR) can shed light on the energy exchange in the nonlinear interacting wave triad (He et al., 2017). According to the MRR, in this case, the ST component can be seen as supplying energy to the 20dw and LSB, following the Passive Passive Active (PPA) topology. In the interaction between the 20dw, ST, and USB triad, both the ST and the 20dw can supply energy to the USB, following the Active Active Passive (AAP) topology. Since the frequency of the 20dw is much lower than the ST, its energy

contribution in the interaction process can be considered negligible, as per the MRR relationship (Equation (1) in He et al., 2017). Therefore, the ST can practically be considered the primary energy source for both the USB and LSB components. This notion aligns with the observed high amplitude of the ST compared to the sidebands. The substantial amplitude of the LSB during warming indicates that it draws a significant amount of energy from the ST component, leading to a simultaneous decrease in ST amplitude. Further in-depth studies are required to understand the differing behaviors among sidebands due to interaction. Overall, warming-specific responses are noticeable in the LSB, while a consistent relationship with the parent wave can be observed in the case of USB. However, simultaneous enhancements in the USB and LSB around the warming at 90 km altitude in Figure 6.1a appear to be incidental.



The arrows orientate the energy flow, while their thickness denotes the amount.

Figure 6. 3. Schematic of the energy exchange among the nonlinear interacting triad (20dw, LSB, ST or 20dw, ST, USB) following the Manley Rowe energy exchange relationship (Details of the relationship can be found in He et al., 2017).

Moreover, the persistent relationship of the USB with the ST suggests its persistence reliance on the parent wave in terms of energy supply for sustenance. Although energy exchange through the 20dw can be considered negligible, the involvement of such PW component is crucial for nonlinear interaction. The limited energy exchange further indicates that the 20dw may be involved in other dynamic processes besides the studied nonlinear interaction. This aligns with the strong presence of the 20dw below 90 km altitude, where ST, USB, and LSB component amplitudes are minimal. External dynamics may influence such triad interactions by controlling the 20dw. Hence, investigating the potential forcing mechanism leading to enhanced 20dw during SSWs is crucial for a better understanding of underlying processes (details in section 6.2.4).

6.2.3. Dominant zonal wavenumber components of primary waves

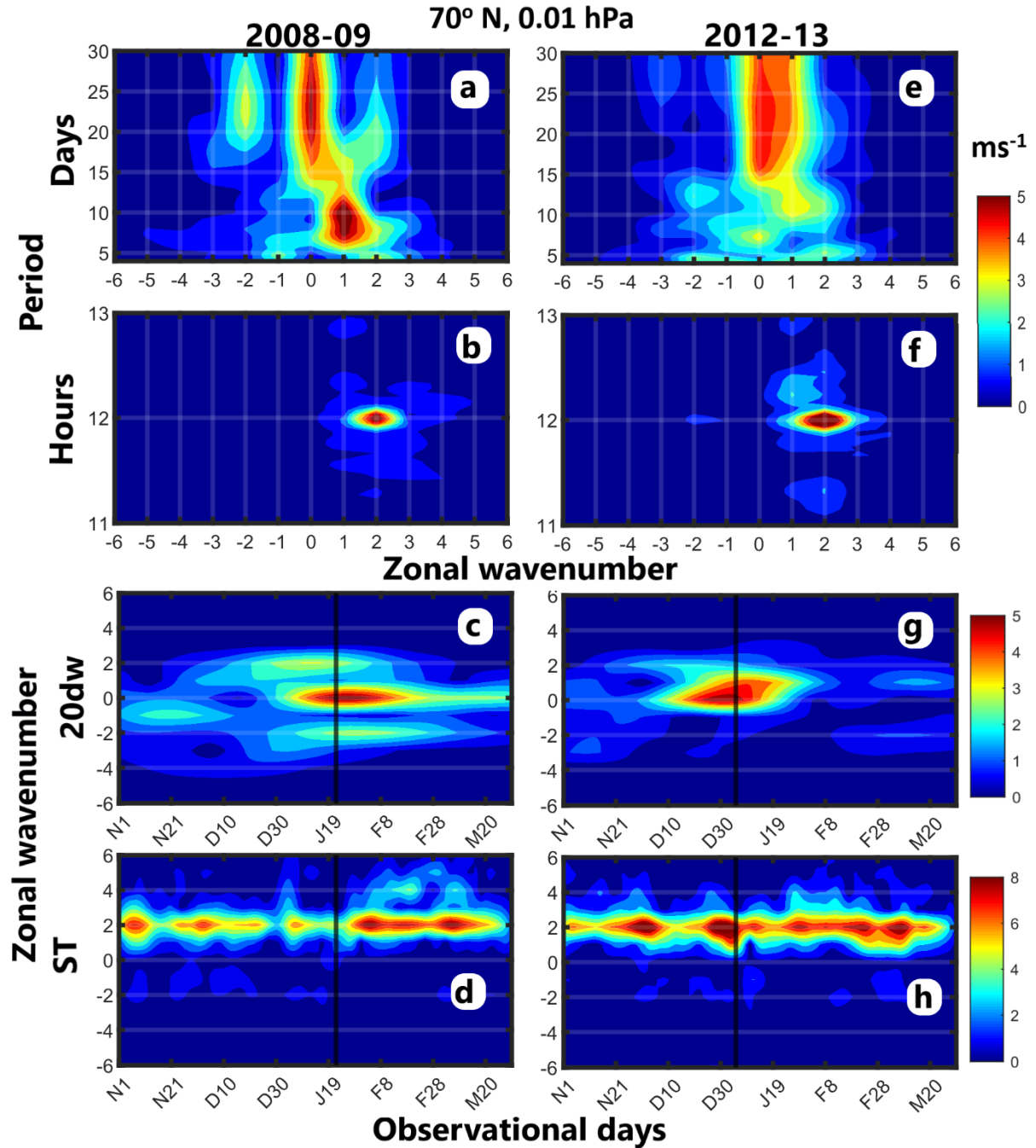


Figure 6. 4. Period versus zonal wavenumber spectra in the period range (a) 4 to 30 days, and (b) 11 to 13 hours utilizing U at 0.01 hPa, 70°N from MERRA-2 during 2008-09 SSW. (c) Temporal variability of different zonal wavenumber components of (c) 20dw, and (d) ST during the 2008-09 observational days. (e, f, g, h) represent the same as (a, b, c, d) but during 2012-13. Positive/ Negative zonal wavenumber denotes westward/ eastward propagation, and zero zonal wavenumber represents the zonally symmetric component.

The zonal wavenumber-period spectra are calculated using a Combined Fourier Wavelet (CFW) technique applied to 2-dimensional space-time MERRA-2 U data (Kikuchi, 2014; Yamazaki, 2022). This technique involves two steps. Firstly, the Fourier transform is applied to the longitudinal domain, yielding a time series of space Fourier coefficients. Secondly, the wavelet transform is performed on these time series to obtain wavelet coefficients, which are then used to calculate the CFW spectrum. The novelty of this method lies in its ability to identify the temporal occurrence of wave activity.

In this analysis, ZWN 0 corresponds to the zonally symmetric component, with positive/negative signs denoting westward (W)/eastward (E) propagation. The ZWN versus period spectra at 0.01 hPa (~ 75 km) and 70° N are shown in Figures 6.4a and 6.4b for PW and tidal period ranges, respectively, averaged over a 30-day interval centered around the 2008-09 SSW PWD. Similar spectra for the 2012-13 event are presented in Figures 6.4e and 6.4f. The pressure level 0.01 hPa in the MERRA-2 dataset is chosen as it is the closest to the meteor radar observational height. The nearest latitude to Andenes (AN) is selected as 70° N.

The ZWN-period spectra reveal a zonally symmetric 20dw corresponding to ZWN 0, hereafter referred to as 20dw0, and a westward traveling 10dw corresponding to ZWN 1 (10dwW1) during both events (Figures 6.4a and 6.4e). The dominance of the westward propagating migrating ST (zonal wavenumber 2 (SW2)) (Figures 6.4b and 6.4f) suggests its significance in the nonlinear interaction. The temporal evolution of the 20dw0 (Figures 6.4c and 6.4g) shows a strong enhancement around the PWD. Furthermore, the sustained feature of the SW2 component is evident during the 2008-09 (Figure 6.4d) and 2012-13 (Figure 6.4h) observational intervals.

The observations of the 20dw and the 10dw (Figures 6.4a and 6.4e) in the upper mesosphere (0.01 hPa) in the MERRA-2 wind are consistent with the meteor radar observations (Figures 6.1b and 6.1e). The enhancement of the 20dw0 around the PWD (Figures 6.4c and 6.4g) indicates its crucial role in the observed 20dw enhancement at meteor radar observational heights (Figures 6.2a and 6.2e). Hence, the 20dw0 and SW2 are likely the primary waves involved in nonlinear interaction, producing USB and LSB corresponding to ZWN 2. A schematic representation of the theoretical ZWN-period spectra involving 20dw0 and SW2 as

primary waves, producing USB and LSB as secondary waves corresponding to ZWN 2, is provided in Figure 6.5.

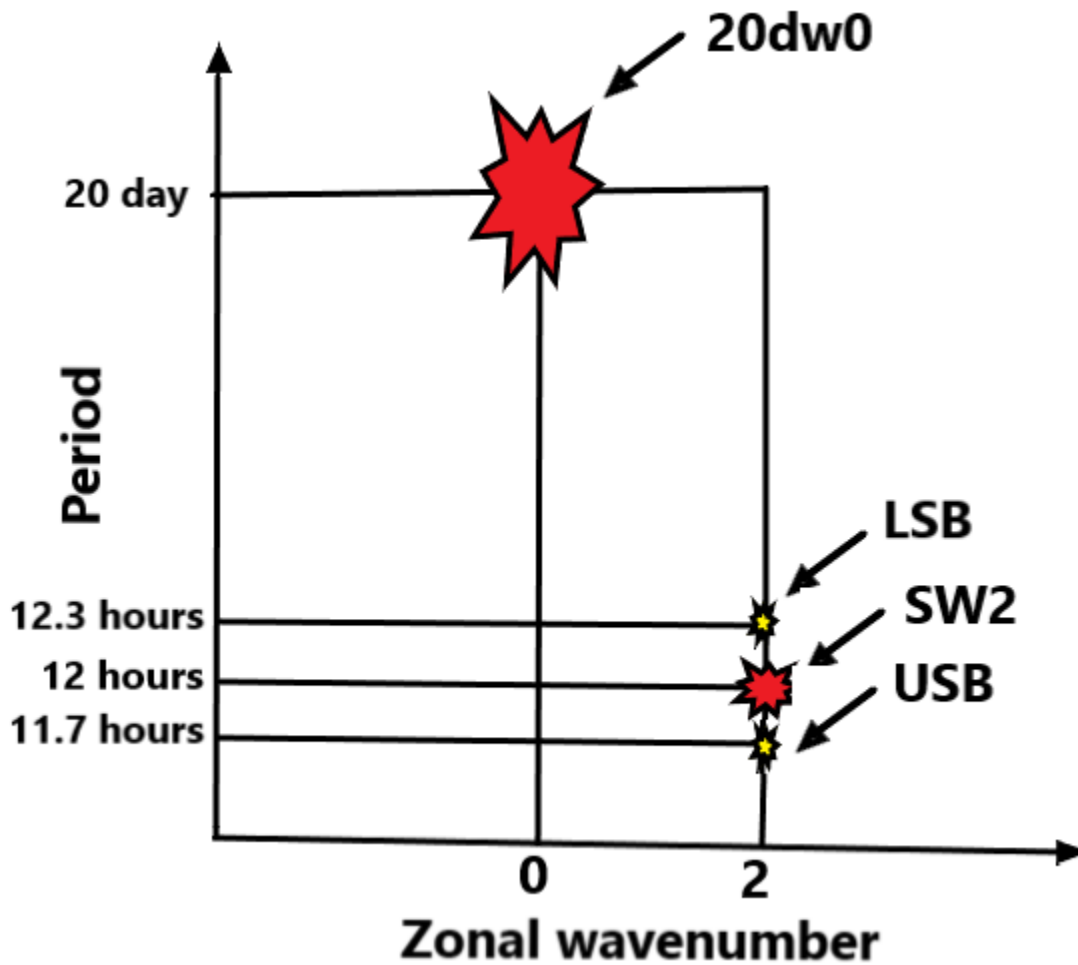


Figure 6. 5. Theoretical ZWN-period spectra of nonlinear interaction between primary waves SW2 and 20dw0, producing USB and LSB as secondary waves corresponding to ZWN 2.

Although faint features around strong SW2 are observed in the ZWN-period spectra (Figures 6.4b and 6.4f), the expected USB and LSB peaks corresponding to ZWN 2 seem unresolved in the MERRA-2 data, possibly due to inherent limitations of reanalysis datasets. However, USB and LSB components are clearly resolved in ground-based meteor radar observations.

6.2.4. Possible forcing mechanism of 20dw0

It is known that there are no zonally symmetric normal modes with PW periods (Longuet-Higgins, 1968). However, the zonally symmetric PW can arise from nonlinear interactions

between SPW and TPW (Pancheva et al., 2007). Mathematically, the nonlinear interaction between SPW with a frequency/ZWN pair $(0, s)$ and a TPW (ω, s) results in a zonally symmetric PW $(\omega, 0)$ and a TPW $(\omega, 2s)$ (Teitelbaum & Vial, 1991). Therefore, the observed 20dw0 in this study is likely generated primarily from nonlinear interactions between (i) SPW1 and 20dwW1/20dwE1 and/or (ii) SPW2 and 20dwW2/20dwE2. The altitude profile of the 20dw0 at 70° N shows a significant enhancement around the PWD (Figure 6.6a and 6.6c), suggesting a stratospheric origin near the 10 hPa (~ 30 km) pressure level. Additionally, since SPWs are predominantly active in the stratosphere, they may play a role in driving the 20dw0. Among the two most probable nonlinear interactions theoretically capable of producing the 20dw0, the second mechanism appears to be involved in this case, evidenced by concurrent enhancements of the primary waves (SPW2, 20dwW2) and secondary waves (20dw0, 20dwW4) in Figure 6.7.

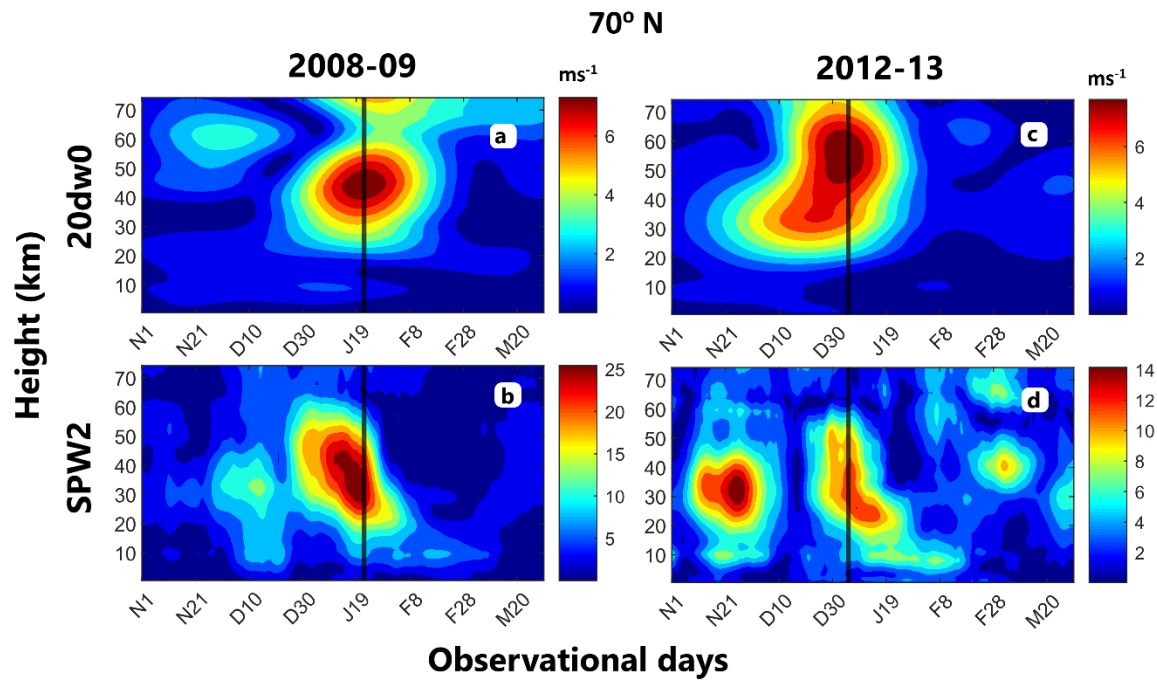


Figure 6. 6. Altitude profile of (a) 20dw0, and (b) SPW2 at 70° N during the 2008-09 observational days. (c, d) represent the same as (a, b), but during 2012-13. Please note the change of scale in the colorbars for each subplot while comparing.

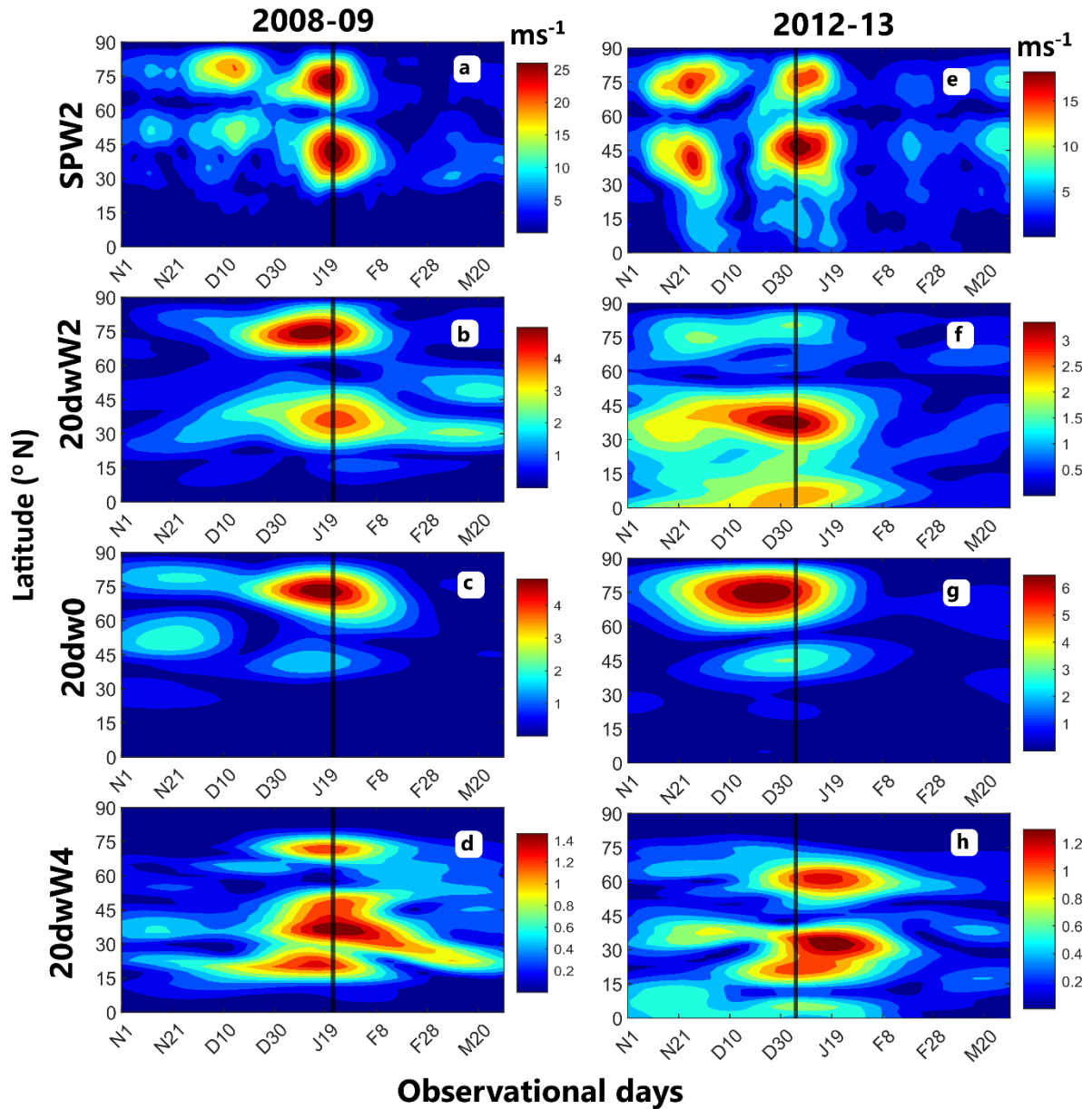


Figure 6. 7. Latitude profile at 10 hPa of (a) SPW2, (b) 20dwW2, (c) 20dw0, and (d) 20dwW4 during the 2008-09 observational days. (e, f, g, h) represent the same as (a, b, c, d), but during 2012-13.

The SPW2 is known to play a significant role in preconditioning the split of the polar vortex (Shepherd, 2000). The 2008-09 and 2012-13 SSW are both split types. The altitude profile of SPW2 at 70° N exhibits enhanced activity around the PWD in the stratosphere near 30 km altitude (Figure 6.6b and 6.6d). Figures 6.7a-d display the latitudinal profile of SPW2, 20dwW2, 20dw0, and 20dwW4, respectively, at 10 hPa during the 2008-09 observational days. Noticeable amplifications of the SPW2 are observed in two distinct branches at 65-80° N and 30-45° N around the 2008-09 PWD (Figure 6.7a), with similar enhancements in

20dwW2, 20dw0, and 20dwW4 seen in Figures 6.7b-d, respectively. The pattern of 20dwW2, 20dw0, and 20dwW4 suggests the significant role of nonlinear interactions between SPW2 and 20dwW2 in producing 20dw0 and 20dwW4 as secondary waves. However, the weak 20dwW4 is likely due to energy redistribution and dissipation. Similar features are noted during the 2012-13 observational period (Figures 6.7a-d). The main difference observed during the 2012-13 SSW is that the pattern of 20dw0 (Figure 6.7g) at high latitudes doesn't resemble that of 20dwW2 (Figure 6.7f) as expected from the interaction, possibly due to interactions with other waves and/or background conditions influencing 20dw0 behavior. Overall, the nonlinear interaction between SPW2 and 20dwW2 appears to be crucial in forcing 20dw0.

6.3. Summary and conclusions

The present study has provided compelling evidence of nonlinear interactions associated with a zonally symmetric wave during major SSWs. The ELS spectra derived from SMR data unveil secondary waves as the USB and LSB of the ST, while the wavelet spectra showcase the presence of a 20dw. Additionally, the wavelet spectra of the instantaneous ST amplitude confirm a 20-day modulation during the warming event, suggesting a nonlinear interaction between the ST and 20dw resulting in USB and LSB as secondary waves. The USB and LSB may beat with the ST, causing the tidal modulation with the 20-day PW period. The simultaneous and transient activity of the USB, LSB, and 20dw, as identified from the ELS and wavelet spectra of SMR-derived winds, provides strong evidence of nonlinear interaction between the ST and 20dw.

Interestingly, the LSB and USB exhibit dissimilar behaviors despite their association with the ST. The enhancement of the LSB in the MLT coincides with a decrease in ST amplitude around the PWD, suggesting its significant energy gain from the ST component, which aligns with previous studies (He et al., 2017; 2018). Conversely, the USB follows a similar pattern to the ST, substantiating its close relationship with the latter. The 20dw activity appears less affected by the nonlinear interaction involving ST, USB, or LSB, as minimal energy is exchanged through the 20dw according to the MRR. Nevertheless, the presence of the 20dw is crucial for the observed nonlinear interaction.

It is found that the zonally symmetric 20dw component, i.e., 20dw0, and the migrating ST component, i.e., SW2, are the primary waves involved in the nonlinear interaction, as ascertained from the ZWN-period spectra calculated using the MERRA-2 U. The enhanced 20dw observed in SMR data is linked to a concurrent enhancement in the 20dw0 component, which seems to originate from the stratosphere. The enhanced SPW2 is believed to interact non-linearly with 20dwW2 to generate 20dw0 in the stratosphere, potentially reaching MLT altitudes. As it is supported by the SMR observations, the 20dw0 further interacts non-linearly with SW2 to generate LSB and USB.

In essence, our study unveils the first observational evidence of a two-step nonlinear interaction between planetary-scale waves during split-type SSWs at boreal high latitudes. This interaction can be summarized as follows:

1. In the 1st step, nonlinear interaction between SPW2 and 20dwW2 produces the 20dw0.
2. In the 2nd step, nonlinear interaction between the dominant SW2 and previously generated 20dw0 gives rise to USB and LSB as secondary waves.

Chapter 7

Enhancement of zonally Symmetric Semidiurnal Tide during SSW

7.1. Introduction

As discussed in chapter 4, atmospheric tides are classified into migrating and non-migrating tides. Migrating tides, which travel westward in synchronization with the sun, are generated from the absorption of solar insolation by water molecules in the troposphere, ozone in the stratosphere, and N_2 and O_2 in the thermosphere. In contrast, non-migrating tides, which are non-sun-synchronous (traveling eastward, westward, or stationary), result from the absorption of solar insolation due to the non-uniform distribution of these absorbing species, the release of latent heat through tropical convection, tide-tide nonlinear interaction and the nonlinear interaction between tides and PWs (e.g., Forbes & Garrett, 1978; Hagan & Forbes, 2002; Huang et al., 2007; Xu et al., 2014; Truskowski et al., 2014). Although there exist studies on long-term and seasonal variability of migrating and non-migrating tides and the impact of the same on the ionosphere (Ramesh & Smith, 2014; Sridharan, 2019; Immel et al., 2006; Forbes et al., 2008), there are relatively fewer studies and limited understanding on tidal variability during SSW. Previously, Pedatella & Forbes (2010) reported evidence of coupling between SSWs and the ionosphere via non-migrating tides generated by the nonlinear interaction between planetary waves and the migrating semidiurnal tide. Overall, there is still a lack of adequate studies on the generation mechanism of specific tidal components during such an impactful transient event.

In this connection, the present study is the first exclusive observational study on the zonally symmetric semidiurnal tide (ST) component (S_0), with plausible generation mechanism during major SSWs. This study examines two events of the NH winter, i.e., 2008–2009 and 2012–2013, where an apparent enhancement in S_0 amplitude is observed around the PWD. Additionally, S_0 enhancement is also observed during the only rare major SSW event in the SH that occurred in September 2002, which is also included in the present work. The paper is divided into three sections. Section 7.2.1 describes the S_0 enhancement observed during

SSW. Section 7.2.2 depicts the total ozone variability. Section 7.2.3 discusses the vertical profile of S0 on peak amplitude days. Section 7.3 summarizes and concludes the result.

7.2. Results and Discussions

For the present investigation, we employ 3 hourly MERRA2 U data at 72 model pressure values from 985 to 0.01 hPa (0-75 km altitude) and is organized on a $2.5^\circ \times 2.5^\circ$ latitude-longitude grid. Additionally, we utilize the hourly total columnar ozone (TCO) data (single level) provided by MERRA-2 for the present investigation.

The amplitude of a wave with zonal wavenumber s and period T can be estimated by a nonlinear least-square fitting to 2-dimensional space-time MERRA-2 U data using the following equation.

$$A \cos \left[2\pi \left(\frac{t}{T} + \frac{s\lambda}{360} \right) - \varphi \right] \quad (7.1)$$

where A is the amplitude of the wave, t is the universal time, λ is the longitude, and φ is the phase of the wave (Pancheva & Mitchell, 2004). The positive, negative, and zero s values correspond to westward, eastward propagating, and zonally symmetric waves, respectively.

For tides, $T = \frac{24}{n}$; where $n = 1, 2$ denotes diurnal and semidiurnal component. For SPW, $\frac{1}{T} = 0$.

The time interval spans from 1 December to 28 February and 1 August to 31 October, centered around the NH and SH SSW, respectively. 23 January 2009, 6 January 2013, and 26 September 2002 are the PWDs marked by the vertical solid lines in all the figures.

7.2.1. Enhancement in S0 during SSW

Figure 7.1a represents the temporal variability of different ST ZWN (-4 to +4) components during the 2008-09 observational days at 70° N, 10 hPa (~ 30 km altitude). The migrating ST component (westward traveling) corresponding to ZWN 2, i.e., the SW2, shows sustained features but diminishes considerably for a few days around the PWD, with a concurrent short-term enhancement of the zonally symmetric ST component (ZWN 0), i.e., the S0. Interestingly, the S0 amplitude exceeds the usually dominant SW2 amplitude. The temporal

variability of different ZWN (1 to 4) components corresponding to SPW at 70° N, 10 hPa is shown in Figure 7.1b. SPW corresponding to ZWN1, i.e., the SPW1 seems to be active during the prewarming days, followed by a short-term substantial enhancement of SPW2 around the PWD. Simultaneous enhancement of S0 and SPW2 may indicate a possible nonlinear interaction between the SPW2 and SW2 primary waves, producing S0 as one of the secondary waves. Mathematically, a nonlinear interaction (in terms of frequency (hour^{-1}) /ZWN pair) between SPW2 (0, 2) and SW2 ($\frac{1}{12}$, 2) yields zonally symmetric S0 ($\frac{1}{12}$, 0) and SW4 ($\frac{1}{12}$, 4) as secondary waves (Teitelbaum & Vial, 1991). However, the SW4 amplitude seems too weak to be identified. In this context, Teitelbaum and Vial (1991) mentioned that one of the secondary waves produced due to nonlinear interaction may have a weak amplitude. As compared to the other, the small amplitude of one of the secondary waves is possibly due to energy redistribution and dissipation as discussed by Mitra et al., 2023b. Figure 7.1c exhibits the latitude profile of S0 variability at 10 hPa during the observational days. The S0 is found to enhance in the latitude band 60-80° N around the PWD. Further, the altitude profile of S0 temporal variability at 70° N (Figure 1d) reveals enhancement in the mid and upper stratosphere during the warming period.

Similarly, variability of the same parameters during the 2012-13 warming event has been shown in Figures 7.1e-h. It is interesting to note very similar features during the 2012-13 SSW. The decrease in SW2 amplitude and simultaneous increase in S0 amplitude around the PWD indicates significant energy transfer from the former to the latter. However, a relatively larger S0 component than the SW2 component implies that the SW2 is not the sole energy supplier to the S0. In this context, it is worth mentioning while migrating tides typically prevail in the middle atmosphere, non-migrating tides can occasionally reach comparable magnitude and even surpass migrating tides, as noted by Chang et al. (2009). Source of additional energy can be attributed to the most dominant SPW2 component. Therefore, both the primary waves are believed to supply energy to the S0. Overall, the enhanced S0 component during the two NH major SSW can be attributed to the nonlinear interaction between SW2 and SPW2.

Figures 7.1i-l represent the same as Figures 7.1a-d but during the 2002 SH major SSW. Enhancement in the S0 is noticeable around the PWD at 70° S, 10 hPa (Figure 7.1i). However, S0 enhancement is not simultaneous with SW2 decrement and doesn't coincide

with the SPW2 activity, which seems to be masked by the much stronger SPW1 during the prewarming days (Figure 7.1j). Such occurrence rules out the role of the nonlinear interaction in the generation of the S0 unlike the cases in the NH as depicted before. Moreover, the S0 enhancement seems confined within the latitude band 60-80° S in the middle and upper stratosphere, as seen from the corresponding latitude (Figure 7.1k) and altitude (Figure 7.1l) profiles. Such an interesting observation eliminates the role of nonlinear interaction and necessitates the quest for other plausible factors, such as variability in source species for the SH SSW event. Overall, the S0 seems to be the most dominant ST component, with an amplitude of about 3 ms^{-1} in the middle and upper stratosphere during all the major SSWs.

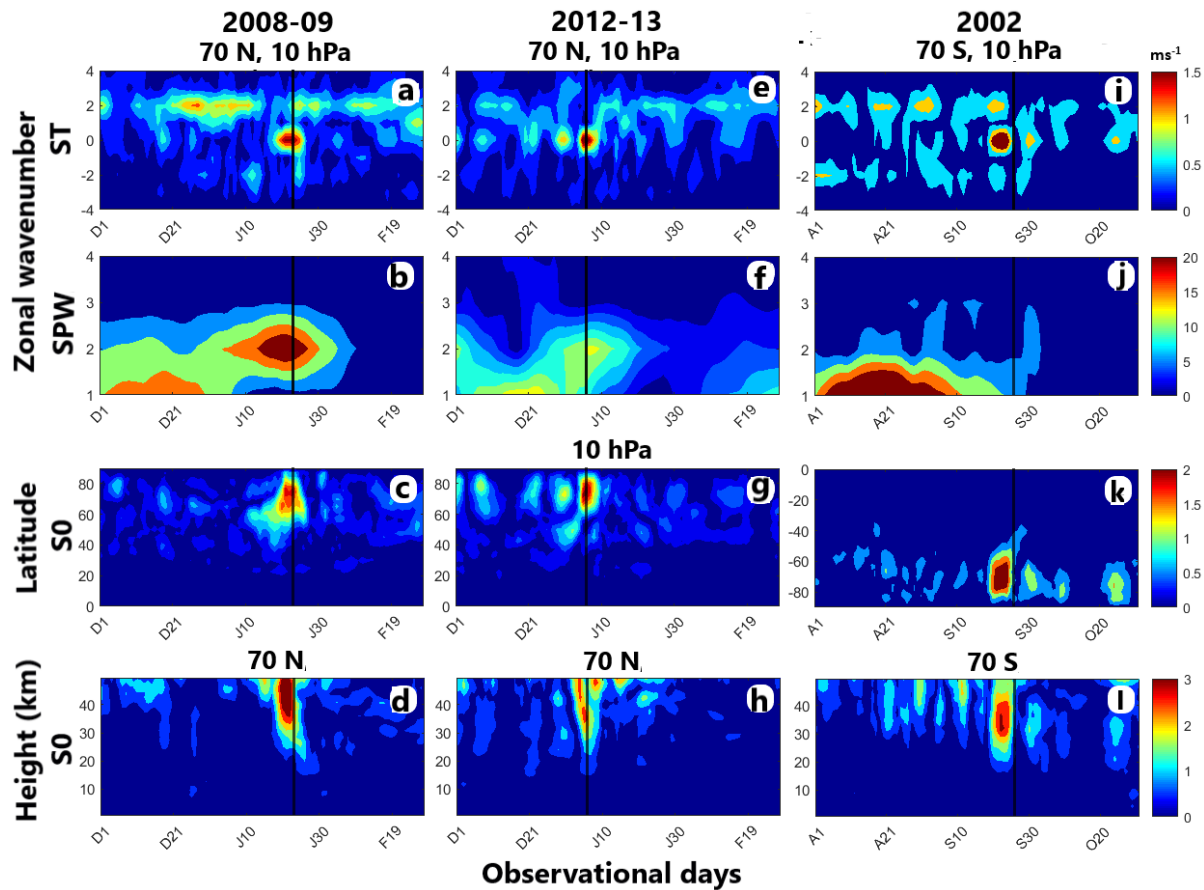


Figure 7. 1. Temporal variability of different ZWN components of (a) ST, (b) SPW utilizing U at 10 hPa, 70°N from MERRA 2 during 2008–2009 observational days (1 December–28 February). (c) Latitude profile at 10 hPa of S0. (d) Altitude profile at 70°N of S0. (e–h) The same as (a–d), but during 2012–2013. (i–l) The same as (a–d), but during 2002 (1 August–31 October). The solid vertical line represents the peak warming day. Please note the change of scale in the colorbars corresponding to each subplot while comparing. The letters D, J, F,

and A, S, O on the x axis denote December, January, February, and August, September, October; the subsequent number indicates the day of the given month.

7.2.2. S0 component in Ozone variability

Since no evident signature of non-linear interaction is found during 2002 SSW, the behavior of ozone is examined to understand its role (if any) in generating the S0 component for all the events. Figures 7.2a, 7.2c, and 7.2e represent the latitude distribution of zonal mean TCO during the 2008-09, 2012-13, and 2002 observational days. The seasonal transition can be clearly identified in the NH, as shown in Figures 7.2a and 7.2c, with temporal increase in TCO in arctic during winter. This is followed by a maximum in spring and decreasing values from summer to autumn in the NH (Figure 7.3). However, the abrupt increase in the TCO soon after the PWD may be ascribed to the possible role of PW in transporting ozone poleward from the mid-latitude during such large-scale disturbance, which may persist up to 2 months, as mentioned in previous studies (de La Cámara et al., 2018; Bahramvash Shams et al., 2022). It is interesting to note that the maximum TCO is observed between 45° and 60° S in the SH (Figure 7.2e), unlike in the NH, where TCO exhibits maximum at latitudes poleward of about 45° N. This may be attributed to weaker poleward transport of ozone in the SH due to relatively less PW activity and a stronger polar vortex than in the NH. Interestingly, there is a poleward transport of ozone-rich air from mid-latitudes around the PWD of the 2002 SH SSW, as seen in Figure 7.2e. Previous studies on the TCO during the 2002 austral SSW event attributed such an increased poleward ozone flux to enhanced tropospheric wave activity (Sinnhuber et al., 2003; Weber et al., 2003; Randall et al., 2005). Next, we attempt to find out the characteristics of S0 in the TCO variability in order to understand a plausible role of ozone in exciting the observed S0 in the selected SSW event/s.

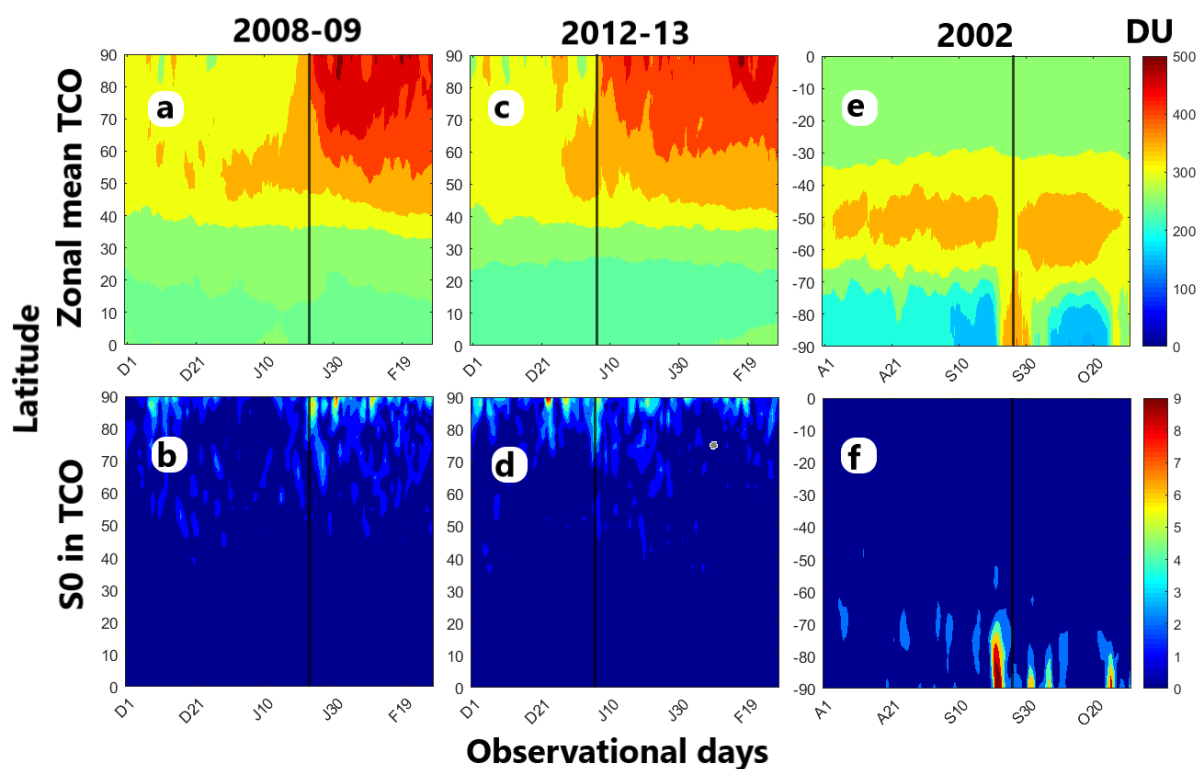


Figure 7. 2. The latitude profile of (a) TCO and (b) S0 (in TCO) in Dobson unit (DU) during 2008-09 observational days from MERRA-2 data. (c, d) represent the same as (a, b) but during 2012-13. (e, f) represent the same as (a,b), but during 2002.

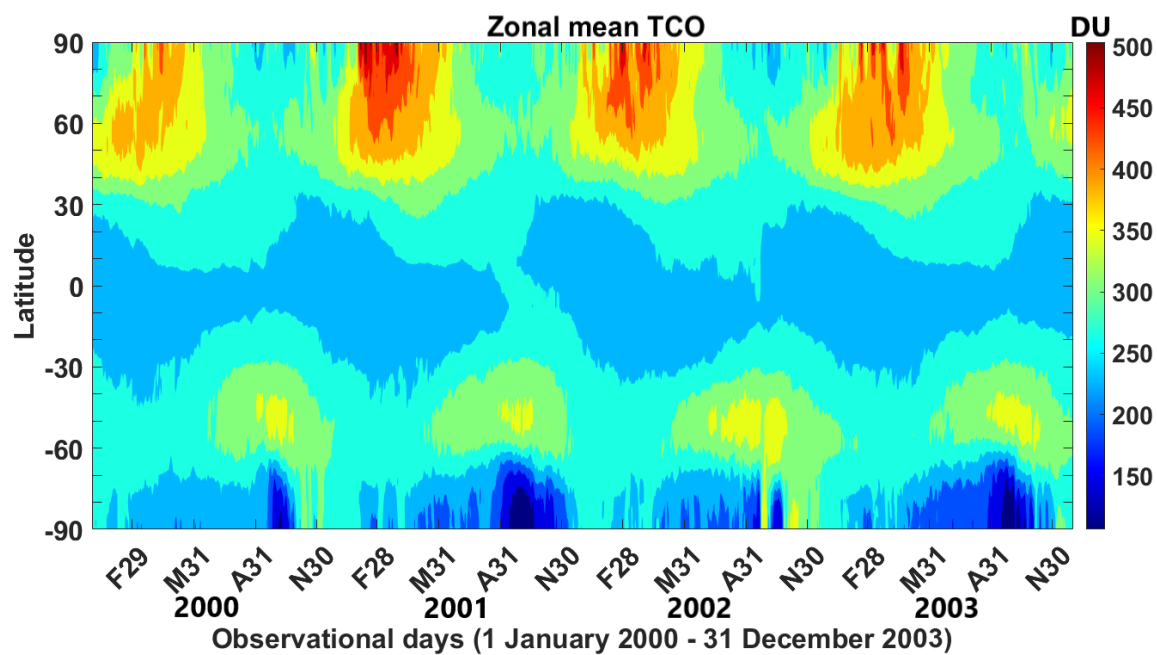


Figure 7. 3. Latitude-time variability of zonal mean total columnar ozone (TCO) in Dobson unit (DU) from 1 January 2000 to 31 December 2003. The letters F, M, A, and N on the x-

axis denote February, March, August, and November; the subsequent number indicates day of the month.

Figures 7.2b, 7.2d, and 7.2f represent the latitude profile of S0 in TCO during 2008-09, 2012-13, and 2002 observational days. It is interesting to note that the S0 in TCO is prominent around the PWD of the 2002 SH SSW (Figure 7.2f), unlike in the NH major SSWs. The noticeable S0 in the TCO is concurrent with the S0 enhancement in U around the 2002 PWD. This indicates the plausible role of ozone in thermally forcing the S0 tidal component during the 2002 SH SSW. It can be noted that the peak amplitude of the S0 in the TCO is found between 70° S and 90° S, and the same in the U is observed between 60° S and 80° S. To understand the finite difference in the observed peak latitudes of the S0 in the TCO and U we have looked into the latitudinal profile of the zonal mean U, amplitudes of the S0 in the TCO and U on 23 September 2002 when S0 amplitude maximizes (Figure 7.4). The peak S0 amplitude in the TCO is found near the pole followed by the same in the U and peak of the zonal mean U in the direction from high to low latitude. Since the zonal mean U (a measure of zonally symmetric structure) bears some imprint of the zonally symmetric waves, the S0 in the U in the present case can be deemed to be impacted by the structure of the zonal mean U to some extent. Therefore, the appearance of the S0 in the U is not only determined by the source, i.e., ozone but also influenced by the zonal mean U. Consequently, the peak S0 in the U can be expected to lie between the peak S0 in the TCO and peak zonal mean U resulting in a small difference in latitudes of the S0 peaks in the TCO and U in the present case. It is interesting to note the striking similarity of the S0 amplitude peak between TCO and U, further supporting their close relationship in this connection. The knowledge of spatial distribution and temporal variability of the stratospheric ozone is essential because it is an effective absorber of UV radiation, further altering the heating rate and temperature in the middle atmosphere (Pancheva et al., 2014). In this context it is relevant to mention that the change of circulation associated with enhanced PW activity during SSW can alter the ozone distribution, generating non-migrating tides (Goncharenko et al., 2012).

Therefore, the S0 enhancement during the 2002 SH major SSW is believed to be due to absorption of the solar UV radiation by the ozone distributed symmetrically over the globe.

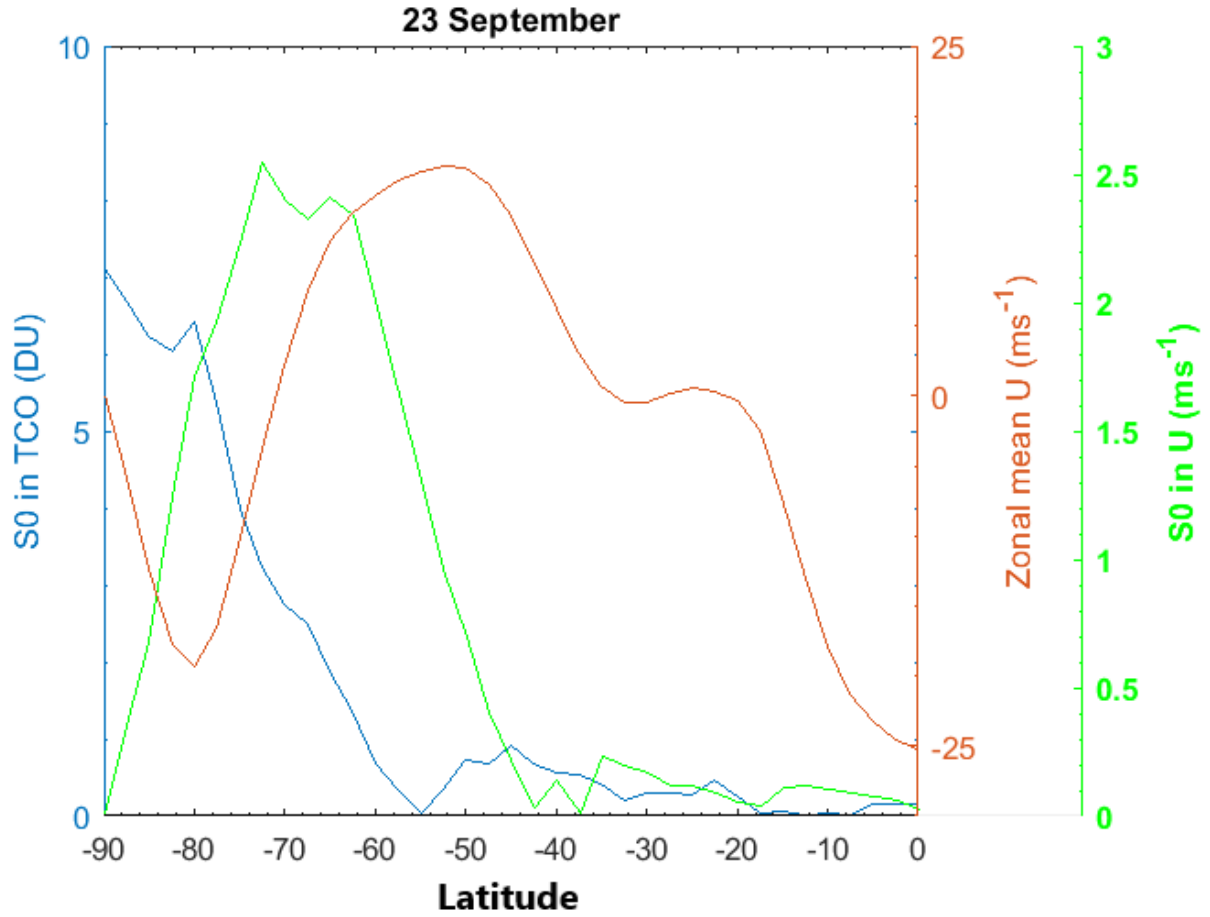


Figure 7. 4. The latitudinal profile of the zonal mean U (red curve) and amplitudes of the $S0$ in the TCO (blue curve) and U (green curve) on 23 September 2002.

7.2.3. Vertical profile of $S0$ at maximum

The peak in the $S0$ amplitude for the three warming events is observed on 20 January 2009, 6 January 2013, and 23 September 2002, as shown in Figure 7.5. In this section we consider only those events where $S0$ is found to be generated due to non-linear interaction. Figures 7.5a and 7.5c represent the height-latitude section of $S0$ amplitude on 20 January 2009 and 6 January 2013, respectively. The $S0$ enhancement seems to be primarily confined at high latitude middle and upper stratosphere (20-50 km). The growth of $S0$ starts around 20 km altitude and attains a maximum amplitude (3-4 ms^{-1}) in the upper stratosphere.

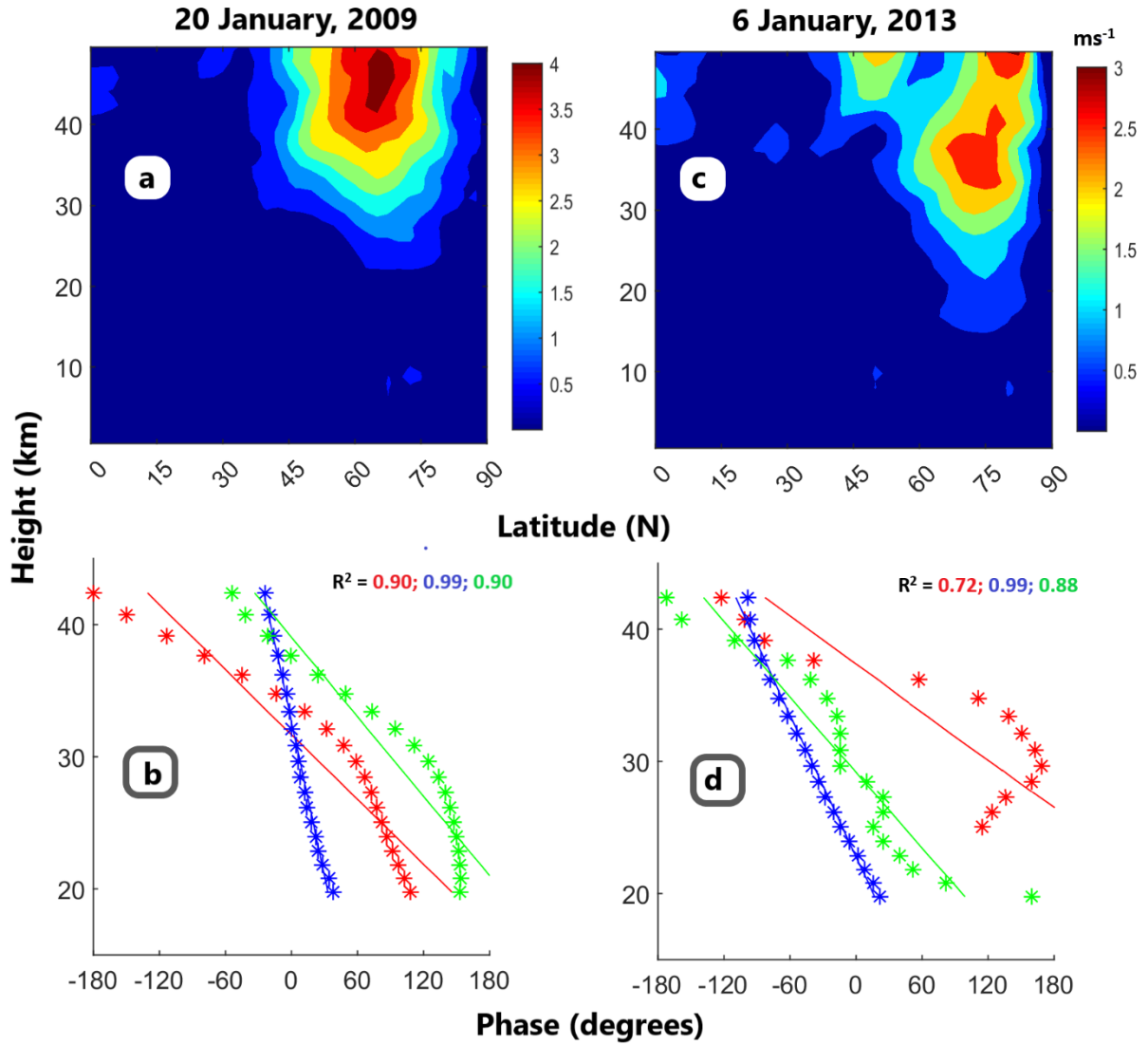


Figure 7. 5. (a) Height-latitude section of S0 amplitude in ms^{-1} , and (b) variation in SW2 (red curve), SPW2 (blue curve), and S0 (green curve) phase as a function of height at 70° N on 20 January 2009. (c, d) represent the same as (a, b) but on 6 January 2013. The straight line in (b, d) represents the linear fit. Coefficient of determination, R^2 , is highlighted with the same colour in plots b and d.

Figures 7.5b and 7.5d show the vertical phase for the SW2 (red curve), SPW2 (blue curve), and S0 (green curve) at 70° N on 20 January 2009 and 6 January 2013, respectively. Overall, the phase value decreases with height, indicating downward phase propagation and upward propagation of SW2, SPW2, and S0. Further, the vertical wavelength (λ) is calculated by linear least-square fits to the observed phases as a function of height (Davis et al., 2013).

λ is a function of slope (A), and the error in λ is calculated using uncertainty in A obtained from linear least square fit. The observed λ of SW2, SPW2, and S0 on 20 January, 2009, in the middle and upper stratosphere are 29.4 ± 2.4 km, 139.9 ± 3.7 km, and 36.0 ± 2.8 km, respectively. Similarly, on 6 January, 2013, the observed λ of SW2, SPW2, and S0 on 20 January, 2009, in the middle and upper stratosphere are 21.8 ± 3.8 km, 64.3 ± 1.5 km, and 34.2 ± 3.0 km, respectively.

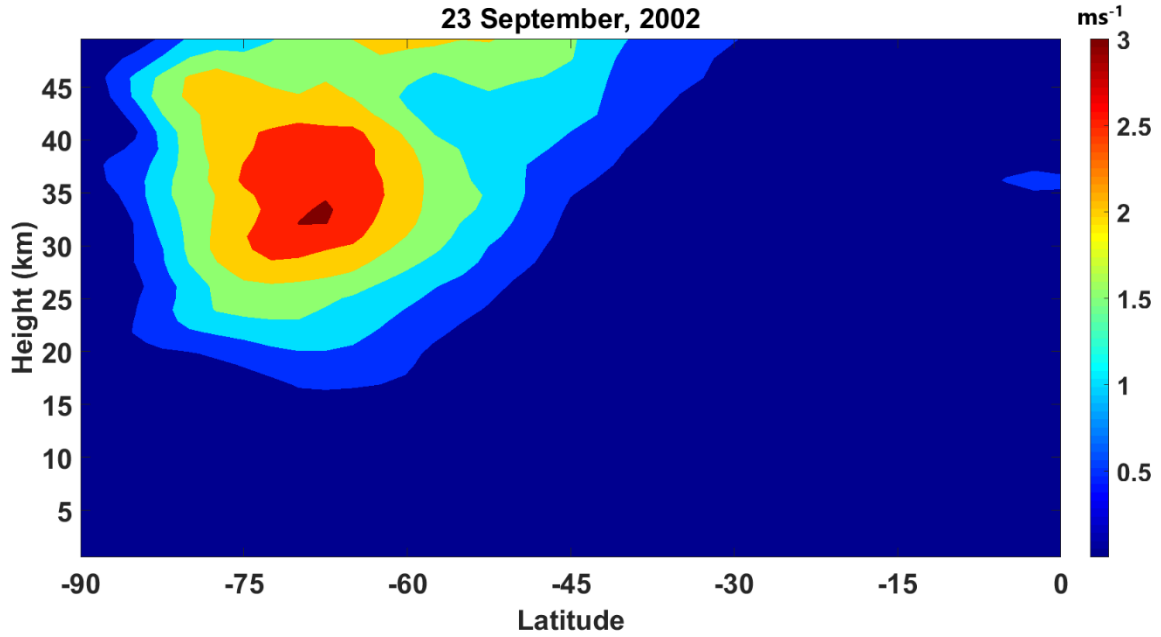


Figure 7. 6. Height-latitude section of S0 amplitude in ms^{-1} on 23 September 2002.

Theoretically, due to nonlinear interaction, the λ of S0 (λ_{S0}) is related to the same of primary waves (λ_{SW2} , λ_{SPW2}) as follows.

$$\frac{1}{\lambda_{S0}} = \frac{1}{\lambda_{SW2}} - \frac{1}{\lambda_{SPW2}} \quad (7.2)$$

The error in theoretical λ_{S0} is calculated from the error in the estimation of λ_{SW2} and λ_{SPW2} . The theoretical λ_{S0} estimated using equation (7.2), on 20 January, 2009, and 6 January, 2013, are 37.2 ± 3.8 km, and 32.9 ± 8.8 km, respectively. Interestingly, good agreement between the observed and theoretical λ_{S0} can be noted that further supports the proposition of nonlinear interaction in generating S0 during the 2008-09 and 2012-13 SSW in the NH.

Figure 7.6 illustrates the height-latitude structure of the S0 amplitude on 23 September 2002 (peak S0 amplitude day). Notably, the S0 amplitude appears confined within high latitude

mid and upper stratosphere (20–50 km) during the 2002 SH SSW, resembling the pattern observed during Northern Hemisphere SSWs (Figures 7.5a and 7.5c).

7.3. Summary and Conclusions

The present study provides interesting insight into the generation mechanisms involved in the S0 enhancement during SSW. The S0 amplitude seems to be active at mid and high latitude middle and upper stratosphere. The SW2 component of the ST shows weak but sustained features during the observational intervals. However, it diminishes considerably around the 2008-09 and 2012-13 PWD. The simultaneous enhancement of the SPW2 and S0 indicates a possible nonlinear interaction between the primary waves, i.e., SPW2 and SW2, in producing the S0 as a secondary wave. The S0 amplitude even exceeds the SW2 amplitude. Moreover, the decrease in SW2 is contemporaneous with S0 enhancement, indicating a transfer of significant energy of SW2 to S0. The other primary wave, i.e., SPW2 is also believed to feed energy to S0. Additionally, good agreement between the theoretical and observed λ of S0, further corroborates the role of nonlinear interaction between SW2 and SPW2 in producing the S0 during the 2008-09 and 2012-13 NH SSW.

However, nonlinear interaction process is not found to be involved in the observed S0 enhancement during the 2002 SH SSW. Interestingly, the S0-type zonally symmetric ozone distribution is unique around the PWD in the 2002 SH SSW. This is supported by the significant poleward transport of ozone-rich air from mid-latitudes around the 2002 PWD, resulting in the S0 enhancement. The latitudinal structure of the zonal mean U seems to cause a finite shift of the peak S0 in the U towards lower latitude.

In a nutshell, the two plausible generation mechanisms of S0 enhancement during the SSW events are:

- i. The SW2 and SPW2 non-linearly interact and produce S0 as a secondary wave as found in the two warming events in the NH.
- ii. On the other hand, the S0 is believed to be thermally excited in presence of a zonally symmetric ozone distribution during the 2002 SSW in the SH.

The present study delves into three captivating case studies that explore the enhancement of S0 during the SSW phenomenon in both hemispheres, accompanied by a discussion on plausible mechanisms. It is important to mention that various other factors contributing to S0

enhancement at various times over the year which remained unexplored need to be extensively studied from long-term data in future to achieve better understanding in this direction.

Chapter 8

Interhemispheric coupling via Q2DW modulation during pre-warming

8.1. Introduction

Following the previous investigation into the influence of SSW events on planetary wave and tidal dynamics, their nonlinear interactions, and the impact on middle atmospheric circulation, the present chapter is focused on examining the interhemispheric effects. The quasi-2-day wave (Q2DW) is a salient traveling PW (TPW) of the summer mesosphere, initially identified by Muller & Kingsley (1974) using meteor wind data. Since then, it has been extensively studied by several investigators from both hemispheres using ground-based, satellite-based observations and reanalysis datasets (e.g., Fritts et al., 1999; Tunbridge et al., 2011; Gu et al., 2018; Lieberman et al., 2021; He et al., 2021). The Q2DW is basically a Rossby-gravity normal mode sustained by barotropic/baroclinic instability of the summer mesospheric easterly jet, with peak activity typically in July-August in the NH and January-February in the SH (e.g., Plumb, 1983; Salby & Callaghan, 2001). The Q2DW significantly influences the MLT dynamics due to its fast phase speed and substantial amplification during propagation.

Moreover, the Q2DW influences upper atmospheric dynamics by interacting nonlinearly with tides, modulating neutral wind and dynamo electric fields (e.g., Gurubaran et al., 2001; Pancheva et al., 2006). Its dissipation also impacts polar mesospheric cloud occurrences by altering summer polar mesosphere temperatures (e.g., France et al., 2018; Lieberman et al., 2021). Recently, Yue and Gan (2021) highlighted the Q2DW modulation of daytime CO₂ mixing ratio in the MLT. Thus, comprehension of the underlying mechanisms governing the intermittency, propagation, and interaction of the Q2DW with other planetary-scale waves is crucial.

Another important long-period planetary wave is quasi-16-day wave (Q16DW) which exhibits slower propagation and typical occurrence during winter and inability to traverse the summer middle atmospheric easterlies (e.g., Manson et al., 1981; Jacobi et al., 1998b). However, past observations have detected Q16DW in the summer mid- and high-latitude mesosphere (see section 8.2.4). Initially identified by Kingsley et al. (1978) with periods of 12-20 days using meteor wind data, the Q16DW has since been extensively studied globally (e.g., Forbes et al., 1995; Pancheva et al., 2009a; McDonald et al., 2011; Guharay et al., 2016; Mitra et al., 2022). Although there are plenty of literatures that independently deals with the Q2DW and Q16DW, there is hardly any study that exclusively looks into the relationship between these two important wave components.

The present study provides an intriguing case of Q2DW modulation by quasi-16-day periods, shedding light on its potential role in carrying the Q16DW from the southern winter to the northern summer during prewarming of the 2019 SSW, an aspect that has remained untouched so far. The observational interval spans from 1 June to 3 October 2019, characterized by the 2019 SH SSW with a peak warming day (PWD) on 18 September 2019 (denoted by vertical lines in all the figures). The chapter is divided into three sections discussing the Q2DW activity in SMR winds (section 8.2.1), Quasi-16-day modulation in the summer MLT winds (section 8.2.2), dominant ZWN modes of the Q2DW and their coupling with Q16DW (section 8.2.3), modulation sources (section 8.2.4), and excitation sources of primary Q2DW and Q16DW ZWN components (section 8.2.5), concluding with a summary of findings (section 8.3).

8.2. Results and Discussions

Our observational data consist of wind (U, V) measurements from the specular meteor radar (SMR) located at São João do Cariri (CA) (7.4°S, 36.5°W), Wuhan (WU) (30.5° N, 114.6° E), and Juliusruh (JU) (54.6°N, 13.4°E). The diverse network of meteor radar observations used in the present study provides valuable insights into global Q2DW activity in the MLT (80-98 km).

Additionally, a global ERA5 data set provided by the ECMWF is utilized for ZWN diagnosis. We have used U and V at 137 model pressure levels within the 1,000–0.01 hPa (~0–80 km)

with a latitudinal and longitudinal grid of $2.5^\circ \times 2.5^\circ$. ERA5 data set complements the SMR observation, providing a comprehensive picture of dynamic variability below 80 km. Furthermore, it offers the opportunity to investigate the interhemispheric coupling associated with the planetary waves.

8.2.1. Q2DW activity in the MLT

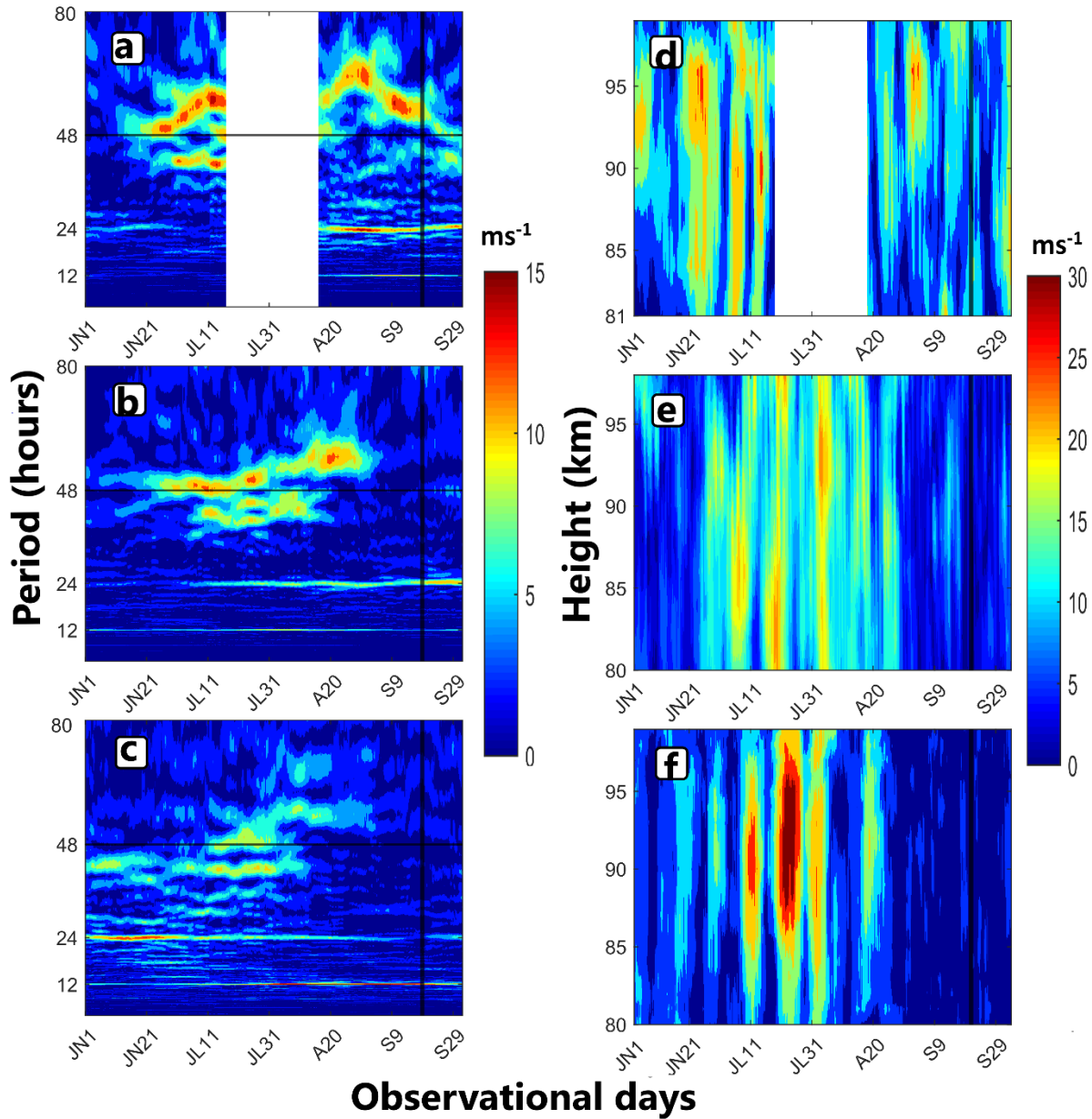


Figure 8. 1. ELS amplitude spectra (4-80 hours period range) in ms^{-1} using SMR-derived V at (a) 81 km, CA (7.4° S , 36.5° W), (b) 80 km, WU (30.5° N , 114.6° E), and (c) 80 km, JU (54.6° N , 13.4° E) from 1 June to 3 October 2019. Altitude profile of the Q2DW amplitude in ms^{-1} at (d) CA, (e) WU, and (f) JU. The solid black vertical line represents the peak warming

day. The letters JN, JL, A, and S in the x-axis denote June, July, August, and September; the subsequent number indicates the day of the given month.

The Evolutionary Lomb Scargle (ELS) Periodogram has been estimated using the Lomb Scargle technique applied to the hourly V using a 21-day window, progressively shifted by an hour over the entire observational interval (Schulz & Stattegger, 1997). This window size effectively resolves sidebands produced due to coupling with the PW periods (2-20 days). The Q2DW analysis has been exclusively limited to the V because of notably higher amplitude in V than in U (e.g., Pancheva et al., 2004; Guharay et al., 2013). Figure 8.1a-c represents ELS amplitude spectra of V at 80 km (height) at CA, WU, and JU, respectively, in the period range 4- 80 hours (encompassing dominant tide and Q2DW periods). Notably, a transient enhancement around the 48-hour period with prominent sidebands is observed across all radar sites from June to August, persisting longer at lower latitudes (Figure 8.1a) and diminishing towards higher latitudes (Figures 8.1b-c).

Closely-spaced sidebands near 48 hours may result from possible modulation of the Q2DW with longer-period planetary waves. In addition, the dominant ZWN modes of the Q2DW may also contribute to the periods close to 48 hours. It is important to mention here that appearance of such sidebands may imply secondary wave generation due to nonlinear interactions among primary waves. Since the theme of the present paper is to investigate modulation of a propagating wave component and consequent transmission of imprint of another wave, we have not studied details of secondary waves. In this regard it can be mentioned that even the modulating periodicity (longer period) is found to be absent in the background winds during the temporal span of interest as will be shown later, which further relieves the context of nonlinear interaction associated secondary waves in the present study.

Coupling between the Q2DW and longer period PWs using long term MLT winds is reported by previous studies (e.g., Jacobi et al., 1998a; Guharay et al., 2015). Utilizing a sliding six-day time window across the entire observational span, we assessed the ELS amplitude corresponding to the 48-hour period (representative of Q2DW) to understand short-term variability potentially induced by PW modulation. Figures 8.1d-f illustrate the temporal evolution of Q2DW activity at 80-98 km altitude at CA, WU, and JU, revealing distinct bursts of the Q2DW amplitude during July at all sites. The Q2DW peaks at higher altitudes at

mid-latitudes than at low latitudes in boreal summer (Figures 8.1d-f), indicating latitudinally upward Q2DW propagation. Unfortunately, due to data gaps at CA (indicated by white patches), further analysis is focused on WU and JU observations.

8.2.2. Quasi-16-day modulation in the summer MLT winds

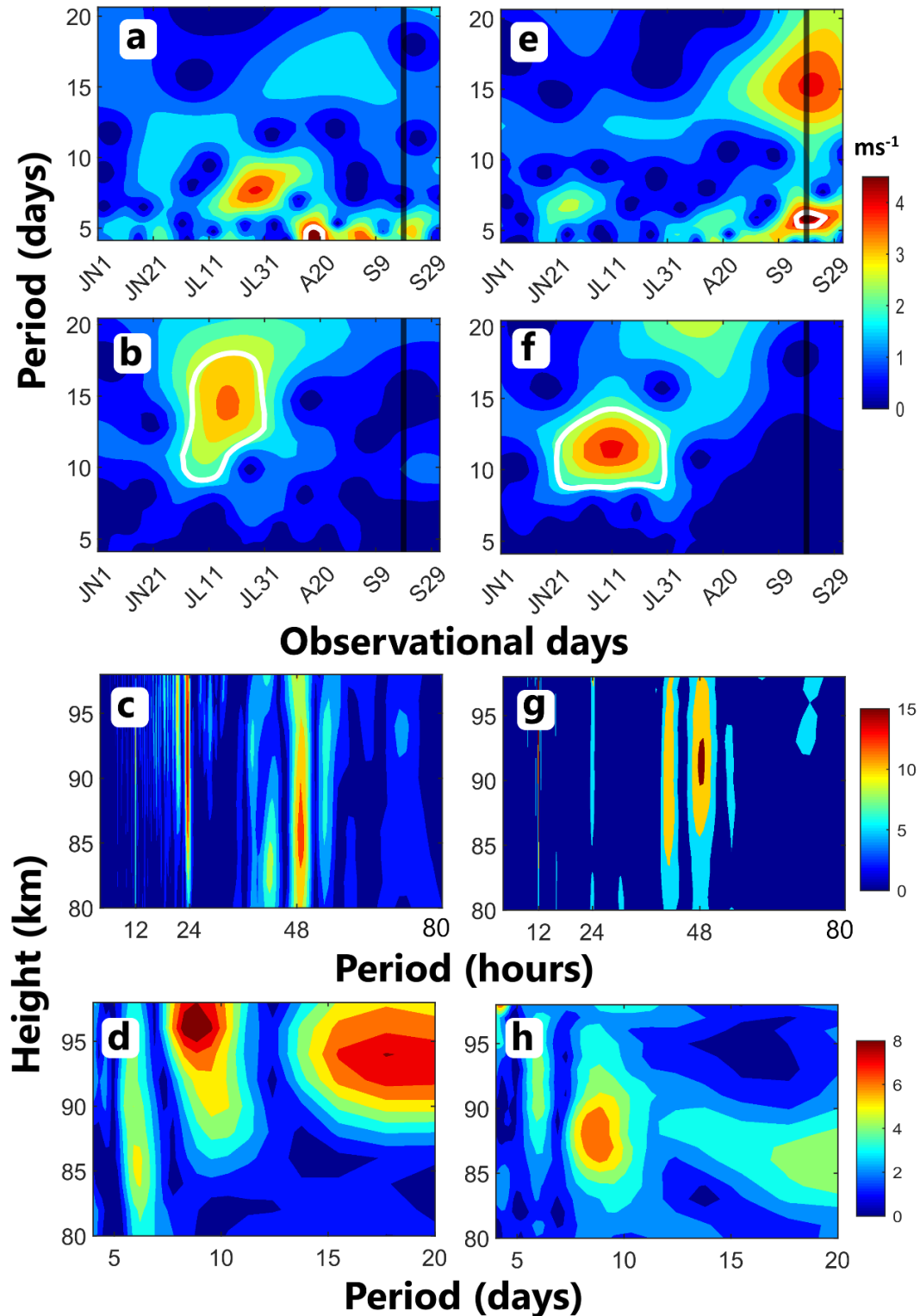


Figure 8. 2. Wavelet amplitude spectra (PW period range) of (a) *V*, and (b) Q2DW amplitude at 80 km during the observational days, and the vertical evolution (80-98 km) of dominant waves during July in the period range (c) 4-80 hours, and (d) 4-20 days using SMR-derived *V* at WU. (e, f, g, h) represents the same as (a, b, c, d) but at JU. The white curve in the wavelet spectra represents the 95% confidence level.

Figures 8.2a and 8.2e depict wavelet spectra of the hourly *V* at 80 km in the PW period range (2-20 days) at WU and JU, respectively. No simultaneous longer-period PW activity, along with the Q2DW enhancement, can be found, although they can be noted elsewhere. The wavelet spectra of *U* at 80 km also exhibit similar features, as shown in Figure 8.3. This finding negates the presence of any independently propagating PWs therein. Next, we investigate whether the Q2DW carries any signatures of long-period modulation. For this purpose, the daily amplitude of the Q2DW are estimated by employing the least square fit to the time series data using a 6-day window, progressively shifted by 1 day using the following equation.

$$Y(t) = Y_o + \sum_{p=1}^4 A_p \cos \left[\frac{2\pi}{T_p} (t - \varphi_p) \right] \quad (1)$$

where $p = 1, 2, 3, 4$ denotes Q2DW, diurnal, semidiurnal, and terdiurnal components, A_p is the amplitude, t is the universal time, and φ_p is the phase. T_p is the time period ($T_1 = 48$ hours; $T_2 = 24$ hours; $T_3 = 12$ hours; $T_4 = 8$ hours). $Y(t)$ is the hourly *V*, and Y_o is the mean wind over the fitting window. The resulting wavelet amplitude spectra estimated from the daily Q2DW amplitude at 80 km reveals a significant quasi-16-day (12-20 days) modulation at both WU (Figure 8.2b) and JU (Figure 8.2f). Therefore, even though the observed quasi-16-day period can't be attributed to an independent propagating wave in the lower MLT summer winds, the Q2DW appears crucial in carrying the Q16DW likely generated at lower altitudes similar to the propagation mechanism of intraseasonal oscillation (Eckermann et al., 1997).

To understand the vertical structure of the dominant wave within the Q2DW period range, ELS spectra of *V* during July at WU (Figure 8.2c) and JU (Figure 8.2g) are examined. At WU, the USB of the Q2DW is active within the 80-85 km altitude. The Q2DW amplitude peaks around 85 km and decreases at higher altitudes, while the LSB shows activity in the 85-95 km altitude (Figure 8.2c). Conversely, at JU above 85 km, both the Q2DW and its sidebands amplified (Figure 8.2g), with the Q2DW peaking at approximately 92 km. The USB looks stronger as compared to the LSB.

Figures 8.2d and 8.2h illustrate the same as Figures 8.2c and 8.2g, but within PW period range at WU and JU, respectively. In July, the dominant PWs included Q6DW, Q10DW, and Q16DW. Notably, Q16DW is observed in the upper MLT (above 90 km) (Figure 8.2d), coinciding with the Q2DW dissipation altitudes (Figure 8.2c) at WU, suggesting a possible link between Q2DW dissipation and Q16DW enhancement. While Q6DW and Q10DW are present at JU, no significant Q16DW is detected (Figure 8.2h), indicating that Q16DW probably appears at higher altitudes in concert with Q2DW dissipation altitudes at JU. The SMR observations imply that a Q16DW probably modulates the Q2DW. Initially, Q2DW serves as a carrier of Q16DW until dissipation, leading to Q16DW manifestation in the upper MLT summer winds. However, absence of the Q16DW in the background winds at altitudes where modulated Q2DW is observed prompts further investigation into potential modulation origin. Identifying primary zonal wavenumber modes of Q2DW is crucial for understanding modulation onset, which is explored using the ERA5 dataset in subsequent sections.

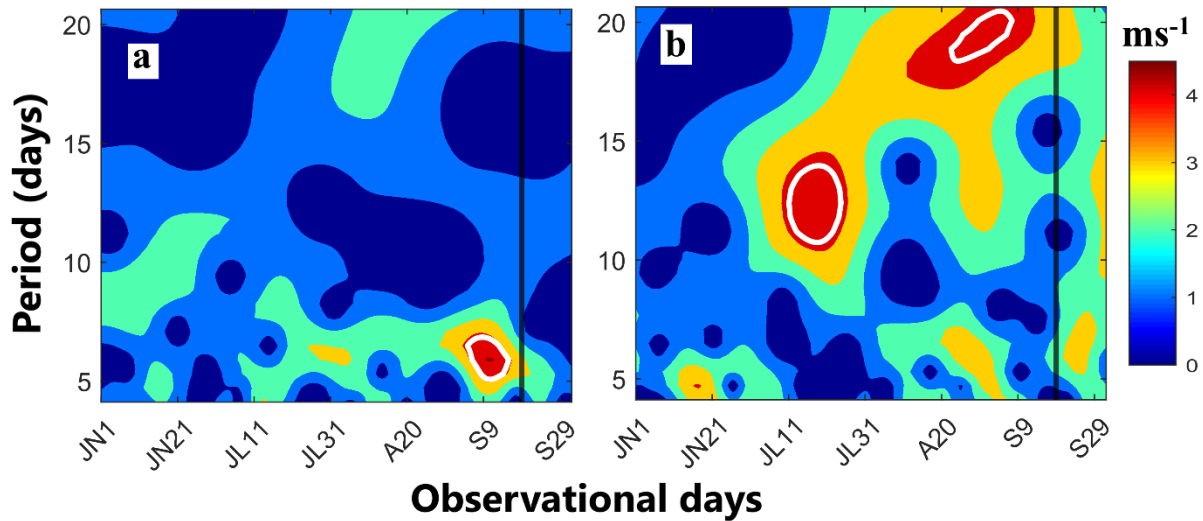


Figure 8. 3. Wavelet amplitude spectra (PW period range) of the U at 80 km using SMR observations at (a) WU (30.5° N, 114.6° E) and (b) JU (54.6° N, 13.4° E).

8.2.3. Zonal wavenumber diagnosis

The combined Fourier-Wavelet (CFW) technique is performed in the 2-dimensional space-time ERA5 V data to calculate the ZWN-period spectra. The novelty of the method lies in

identifying the temporal occurrence of wave activity. ZWN 0 signifies zonal symmetry, while positive/negative ZWN denotes westward (W)/eastward (E) propagation.

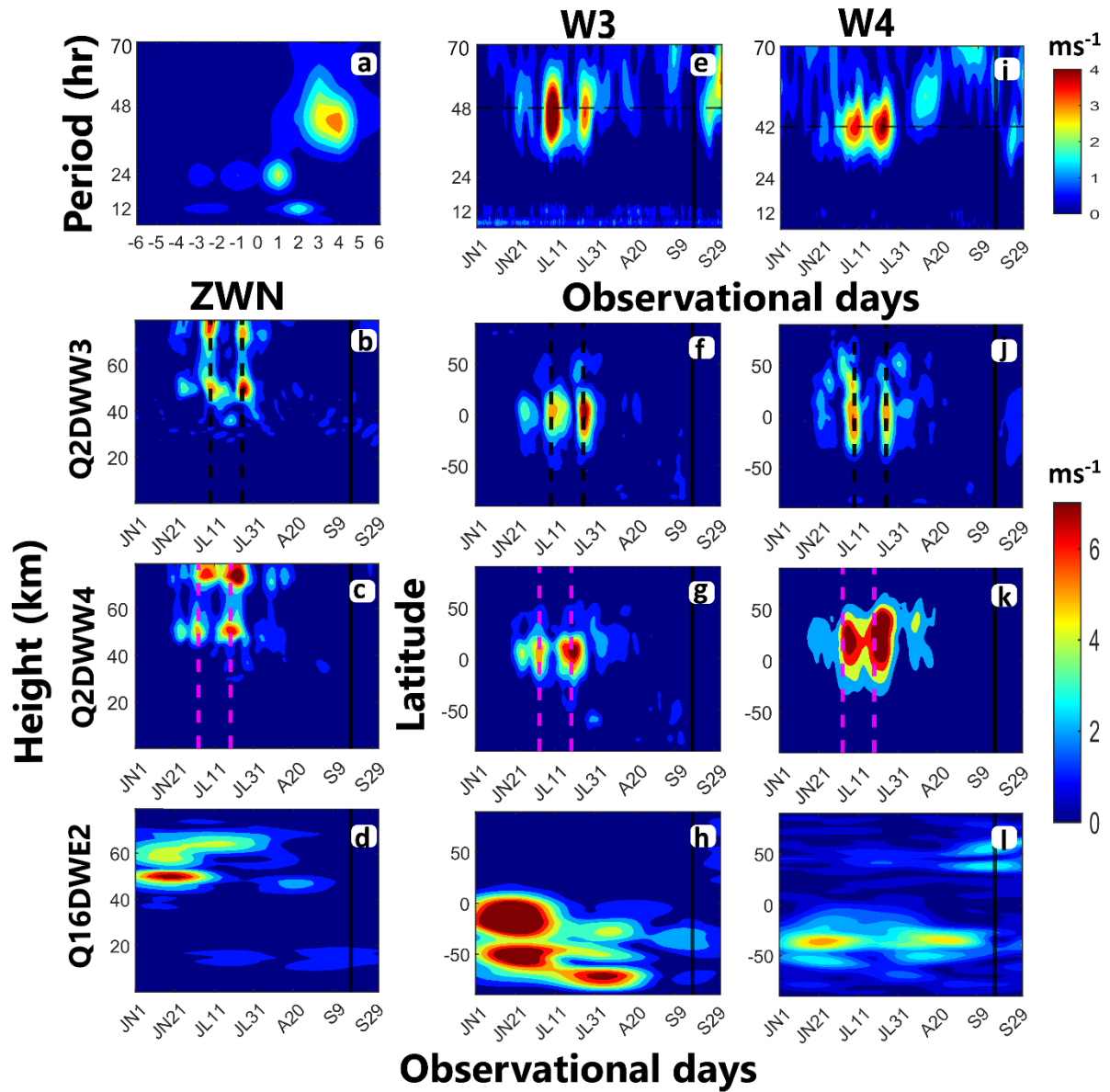


Figure 8. 4. (a) Period (4-70 hours) versus ZWN amplitude spectra at 80 km (0.01 hPa), 7.5° S during July. Height-time section of the (b) Q2DWW3, (c) Q2DWW4, and (d) Q16DWE2 amplitude at the equator. Temporal variability of (e) W3 in the 4-70 hours period. Latitude-time section of (f) Q2DWW3, (g) Q2DWW4, and (h) Q16DWE2 at 50 km. Temporal variability of (i) W4 in the 4-70 hours period. (j, k, l) represent the same as (f, g, h) but at 74 km. ERA5 V and U data are utilized for Q2DW and Q16DW analysis, respectively. Dashed vertical lines mark the peak amplitude day of Q2DWW3 (black) and Q2DWW4 (magenta).

Since at 80 km, the Q2DW amplitude exhibits a maximum at CA, the ZWN-period spectra is calculated at CA latitude, i.e., 7.5° S, and the nearest pressure level to 80 km, i.e., 0.01 hPa, available from ERA5. The ZWN versus period spectra at 0.01 hPa (~ 80 km), 7.5° S calculated by averaging the CFW spectra in July 2019 are shown in Figure 8.4a. The Q2DW is found to be westward (W) traveling corresponding to ZWN 3 and 4 (Figure 8.4a), hereafter referred to as Q2DWW3 and Q2DWW4, respectively. The time evolution of the dominant period of westward traveling ZWN 3 (W3) and 4 (W4) at 0.01 hPa, 7.5° S (Figures 8.4e and 8.4i), reveals two distinct peaks of enhancement, centered at periods 48 and 42 hours, respectively. Hence, the representative period of Q2DWW3 can be reasonably considered as 48 hours, and the same for Q2DWW4 is 42 hours for further analysis, which aligns with previous studies (e.g., Pancheva et al., 2004; Fritts et al., 1999; Lieberman, 1999).

Figure 8.4b represents the height-time profile of the Q2DWW3 amplitude at the equator. The Q2DWW3 has two distinct peaks on 9 July and 25 July (marked by dashed vertical black lines), showcasing 16-day modulation persisting above 50 km, with maxima at altitudes of 50 km and 74 km. The latitude-time sections of the Q2DWW3 reveal equatorial symmetry at 50 km (Figure 8.4f), and asymmetric extension to NH mid-latitudes at 74 km (Figure 8.4j), mirroring the 16-day modulation.

Figures 8.4c, 8.4g, and 8.4k represent the same as Figures 8.4b, 8.4f, and 8.4j, but for the Q2DWW4. The Q2DWW4 maximizes at altitudes of 50 km and 74 km, similar to the Q2DWW3 (Figure 8.4c). Two distinct peaks on 3 July and 19 July (marked by dashed vertical magenta lines) are apparent in the Q2DWW4 amplitude at 50 km. Therefore, there is a signature of 16-day modulation of the Q2DWW4 as well. However, at 74 km, the Q2DWW4 peaks appear a few days later with prominent 16-day modulation, possibly due to slower phase speed. The Q2DWW4 amplitude looks asymmetric about the equator with extension towards the summer NH (Figures 8.4g and 8.4k). The Q2DWW4 amplitude grows and shifts towards the NH mid-latitudes, as seen in Figure 8.4k. In general, the Q2DWW4 is likely to contribute more to carrying the Q16DW to NH mid-latitudes at higher altitudes due to its larger amplitudes than the Q2DWW3 (Tunbridge et al., 2011).

8.2.4. Origin of modulation

From the aforementioned observations, the modulation appears to originate near the equator at around 50 km altitude, suggesting a likelihood of finding the Q16DW nearby. To investigate this further, the dominant period of all ZWN modes ranging from -6 to +6 is examined using ERA5 U data (Figure 8.5). Generally, the Q16DW is more prominent in U than in V, so the analysis focuses on U only (e.g., Williams & Avery, 1992; Guharay et al., 2016; Huang et al., 2011). The eastward traveling Q16DW corresponding to ZWN 2 (Q16DWE2) is found to be dominant among all the traveling PWs of different ZWN at 50km, equator.

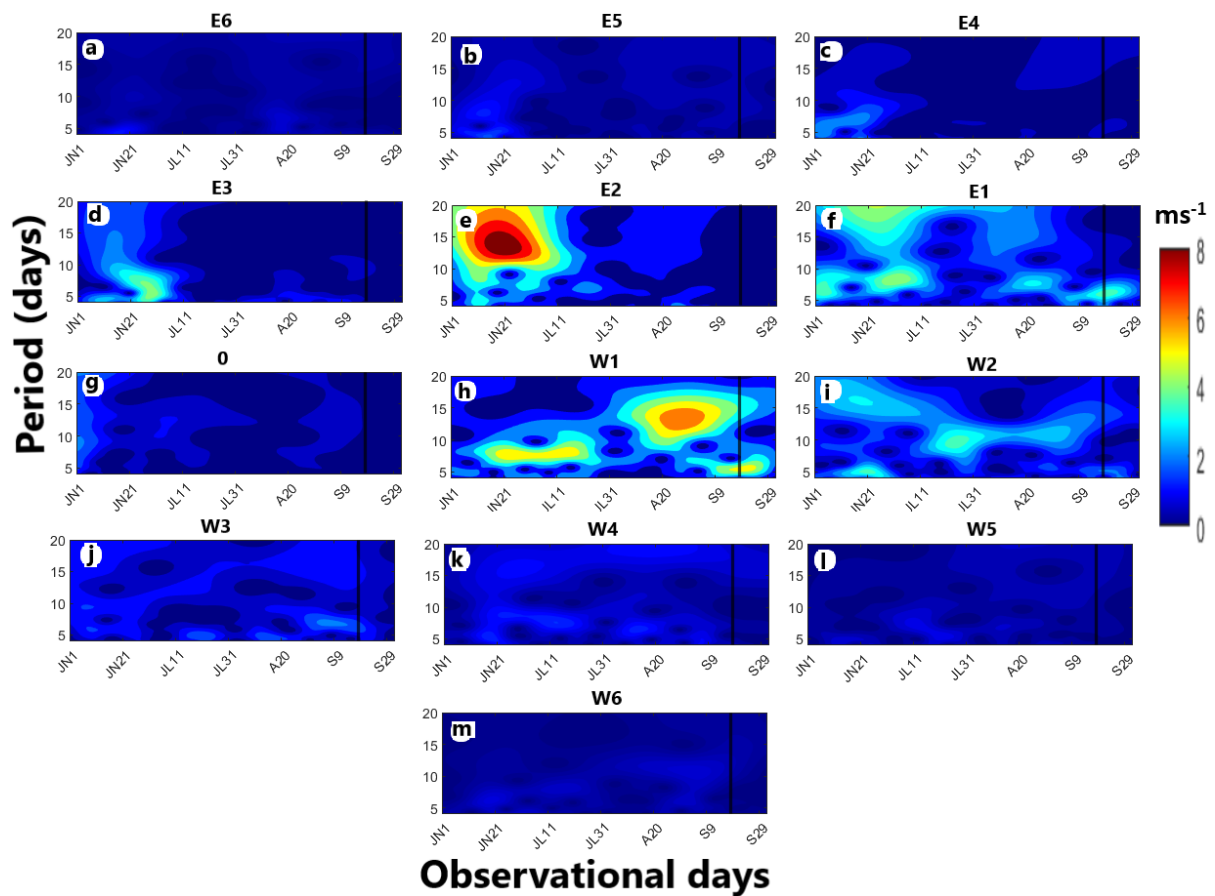


Figure 8. 5. The temporal variability of (a) Eastward traveling ZWN 6 (E6), (b) E5, (c) E4, (d) E3, (e) E2, (f) E1, (g) Zonally symmetric (ZWN=0), (h) Westward traveling ZWN 1 (W1), (i) W2, (j) W3, (k) W4, (l) W5, and (m) W6 in the period range 4-20 days at 50 km altitude at the equator using ERA5 U. Note the dominance of eastward traveling Q16DW corresponding to ZWN 2 (Q16DWE2) in (e).

Figures 8.4d, 8.4h, and 8.4l represent the same as Figures 8.4b, 8.4f, and 8.4j, but for the Q16DWE2. The altitude profile of the Q16DWE2 amplitude shows enhancement at 50 km

from 1 June to early July (Figure 8.4d). The latitude-time section of the Q16DWE2 at 50 km (Figure 8.4h) and 74 km (Figure 8.4l) indicates its activity only in the winter SH. McDonald et al. (2011) also observed a stronger amplitude of eastward propagating Q16DW in the winter SH compared to the westward propagating components. Interestingly, there is a decrease in amplitude and latitude spread of Q16DWE2 at higher altitudes (~ 74 km), suggesting a potential role of Q2DW in vertically carrying the signature of Q16DW to the summer hemisphere via modulation.

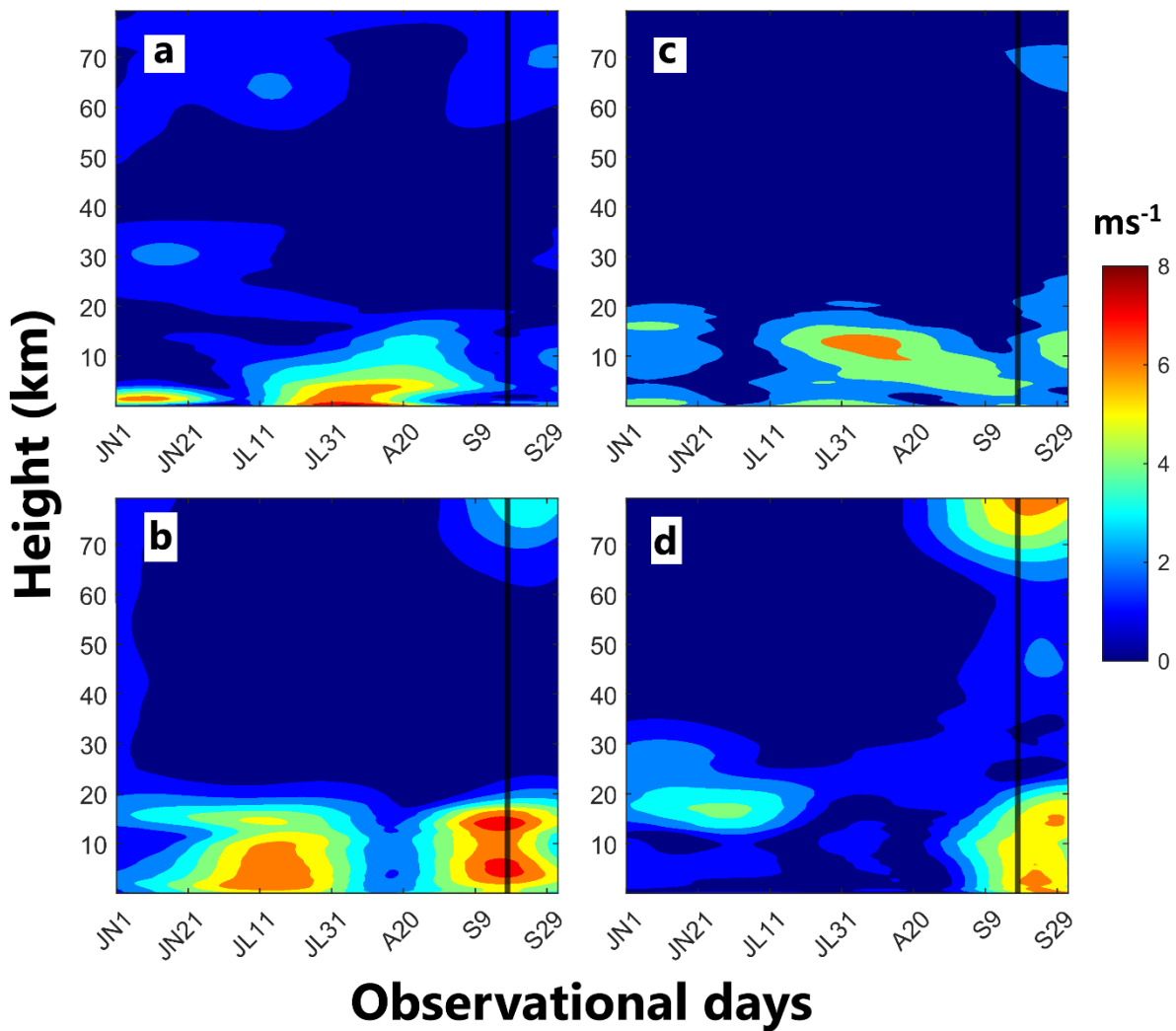


Figure 8. 6. Temporal variability of Q16DW at (a) WU and (b) JU in the altitude range of 0-80 km using ERA5 U. (c, d) represent the same as (a, b) but using ERA5 V.

The limitation of Q16DW activity within the troposphere at WU and JU is evident from vertical profiles (Figure 8.6), likely due to strong summer mesospheric easterlies impeding direct Q16DW propagation. Consequently, the highest probability of occurrence is observed

in winter. (Manson et al., 1981; Jacobi et al., 1998b). Nonetheless, the presence of the Q16DW in the summer mid-latitude upper MLT (Figure 8.2d) aligns with prior findings (Tsuda et al., 1988; Williams & Avery, 1992; Jacobi, 1998).

Two mechanisms proposed by the previous investigators attempted to explain how Q16DW reaches the summer mesosphere. One suggests it originates in the winter hemisphere and propagates along the zero wind line to the summer mesosphere (Dickinson et al., 1968; Miyahara et al., 1991; Forbes et al., 1995). The other theory suggests the Q16DW arises from oscillatory breaking of gravity waves modulated in the summer troposphere and lower stratosphere (Holton, 1984; Williams and Avery, 1992). The present study is significant in this context as it presents the first observational evidence of the potential role of Q2DW in carrying the Q16DW from the winter to summer hemisphere mesosphere through modulation.

8.2.5. Plausible excitation source

Analyzing Q16DWE2 amplitude variations at 50 km altitude at the equator reveals its peak on 19 June (Figure 8.7). Thus, the height-latitude section of the Q16DWE2 on 19 June is illustrated to understand its excitation location. Similarly, the initial peak amplitude of Q2DWW4 and Q2DWW3 is observed on 3 July and 9 July, respectively. Sustained high amplitude of the Q16DWE2 until the initiation of Q2DWW4 and Q2DWW3 modulation suggests its significant role in causing the modulation at 50 km altitude. Notably, alternate enhancement of Q2DWW3 and Q2DWW4 is consistent with Figure 8.4. The alternate wavenumber transition of the Q2DW activity between ZWN 4 and 3 is an interesting observation at 50 km altitude at the equator. Wavenumber transition of the Q2DW is reported in previous studies (e.g., Plumb, 1983; Norton & Thuburn, 1996; Tunbridge et al., 2011; Gu et al., 2023), which suggests a possible link to the selective amplification of various unstable wave modes, depending on the characteristics of the summer easterly jet. However, the underlying details of this interesting case of wavenumber transition is beyond the scope of the present work and will be explored next.

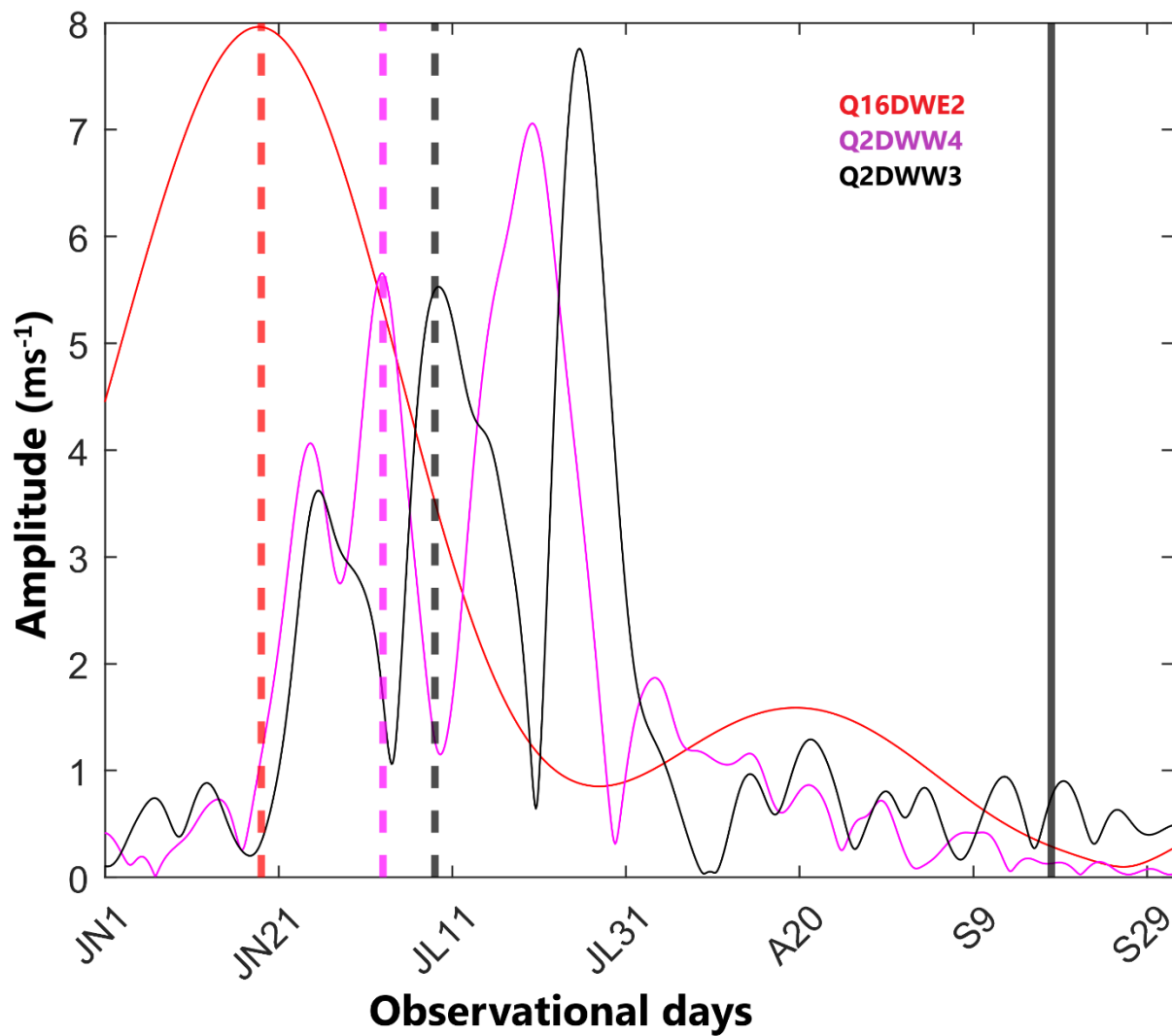


Figure 8. 7. Temporal variability of Q16DWE2 (red), Q2DWW4 (magenta), and Q2DWW3 (black) at an altitude of 50 km at the equator. The red dashed vertical line denotes the peak Q16DWE2 amplitude on 19 June. Similarly, magenta and black dashed vertical lines mark the initial peak amplitude of Q2DWW4 and Q2DWW3, respectively, on 3 July and 9 July.

Figures 8.8a and 8.8d illustrate the Q16DWE2 amplitude and the zonal mean U (ZMU) along the height-latitude section on 19 June. The black curve indicates the zero ZMU line, while the magenta curve represents the critical layer. The critical layer is the region where the zonal phase speed of the wave becomes equal to the ZMU. Although critical layers typically dampen waves, unstable flows can turn them into wave sources (e.g., Salby and Callaghan, 2001; Singh et al., 2024). The Q16DWE2 is primarily found between the critical layer and the zero wind line in the winter SH's upper stratosphere and lower mesosphere (30-70 km) (Figure 8.8a).

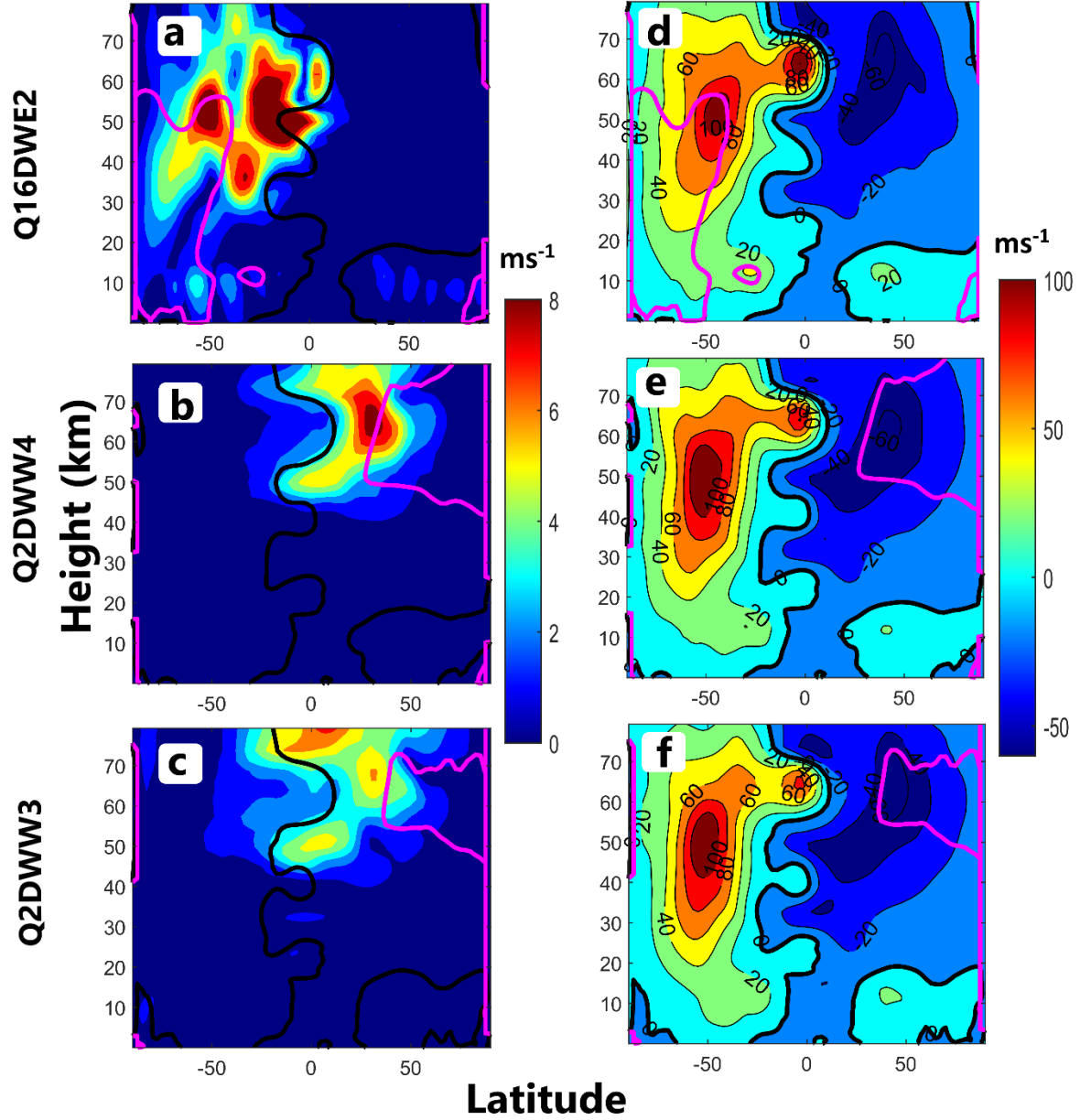


Figure 8. 8. Height latitude section of (a) Q16DWE2 amplitude on 19 June using ERA5 U, (b) Q2DWW4 amplitude on 3 July, and (c) Q2DWW3 amplitude on 9 July using ERA5 V. (d,e,f) represent the same as (a,b,c) but of the ZMU on 19 June, 3 July, and 9 July, respectively. The magenta curve represents the critical layer of the Q16DWE2 (a,d), Q2DWW4 (b,e), and Q2DWW3 (c,f). The black curve represents the zero ZMU line.

The Q16DWE2 extends beyond the zero wind line at 50 km, thriving within weak westerly flow between two westerly jets. Day-to-day variations in Q16DWE2 amplitude, critical layer, and ZMU are depicted in [Movie S1](#). Its amplification aligns with the intensification of winter westerly jet around 50 km altitude and 50° S, potentially drawing energy through baroclinic/barotropic instability. Upon closely monitoring the daily variability ([Movie S1](#)), it

seems the intensification and poleward shift of the westerly jet contribute to the poleward migration of the zero wind line, allowing Q16DWE2 presence across this line. This leakage across the zero wind line seems crucial for initiating the modulation process, as the Q16DWE2 approaches Q2DWW3 (Figure 8.8b) and Q2DWW4 (Figure 8.8c) amplification near 50 km. Wu et al. (1996) suggested that winter planetary waves (PWs) may trigger the summer Q2DW through their penetration into the summer stratosphere. In this connection, it can be comprehended that the observed long period modulation in the QTDW in the present study is due to proximity of the Q16DWE2 near the equator where the QTDW is excited.

Figures 8.8b and 8.8e represent the same as Figures 8.8a and 8.8d, but for the Q2DWW4 on 3 July. The Q2DWW4 is prevalent in the boreal summer between the zero wind line and the critical layer and lies equatorward of the boreal summer easterly jet around 60 km, 50° N (Figure 8.8b). The Q2DWW4 seems to derive energy from the easterly jet, showing enhancement near the jet intersected by the critical layer (Figure 8.8e). Figures 8.8c and 8.8f exhibit the same as Figures 8.8a and 8.8d, but of the Q2DWW3 on 9 July. The Q2DWW3 amplitude has a trimodal enhancement structure in the boreal summer (Figure 8.8c). Trimodal structure indicates three distinct regions of Q2DWW3 enhancement, located around 50 km and 74 km at the equator and at 60 km, 30° N. The Q2DWW3 also lies predominantly between the zero wind line and the critical layer, equatorward of the boreal summer easterly jet (Figure 8.8f). The Q2DWW3 mode at 60 km, 30° N seems to derive energy from the boreal summer easterly jet.

In comparison, the other two modes at the equator are potentially linked to the isolated small region of strong easterly at 74 km, equator, and the extension of the easterly jet near 50 km. Overall, the zero wind line decides the near-equator boundary of the Q2DWW4 (Figure 8.8b) and Q2DWW3 (Figure 8.8c). [Movies S2](#) and [S3](#) highlight daily variability in Q2DWW4 and Q2DWW3 amplitude, showcasing their interactions with the background ZMU. Both amplitudes increase as strong easterly jets shift poleward, along with the intersection of their critical layers.

Overall, the winter westerly jet in the Southern Hemisphere appears crucial in exciting the Q16DWE2, potentially through instability mechanisms. Similarly, the Q2DWW4 and

Q2DWW3 observed in the summer NH may be triggered by barotropic/baroclinic instability induced by the easterly jet, which aligns with previous studies (e.g., Randel, 1994; Salby & Callaghan, 2001). Modulation of the Q2DW initiates near the equator through the zero wind line due to the proximity of the winter hemispheric Q16DWE2.

8.3. Summary and Conclusions

In the present work, we have observed a modulation of the Q2DW amplitude with a quasi-16-day period using SMR observations. The source of this modulation is found to be located at an altitude of 50 km near the equator. The dominant Q16DWE2 wave in the winter hemisphere and its penetration across the zero-wind line likely initiates the modulation of the Q2DW in the summer hemisphere. The primary zonal wavenumber (ZWN) modes of the Q2DW show significant modulation with a quasi-16-day period.

No notable Q16DW is detected in the summer background winds, emphasizing the importance of Q2DWW3 and Q2DWW4 in carrying the Q16DW signature from the near equator to the boreal summer mesosphere. Interestingly, a Q16DW signature is observed in the upper MLT, coinciding with the altitude of Q2DW dissipation, further hinting at a potential link between the two phenomena.

In a nutshell, the present study provides a unique case of Q2DW modulation by a quasi-16-day period, highlighting its potential role in carrying the signature of the Q16DW from the winter to summer mesosphere.

Chapter 9

Summary and Future Plans

This chapter provides a summary of the key findings presented in the thesis and potential areas for future research based on that.

9.1. Summary

SSW is a dramatic wave-driven meteorological event in the winter hemisphere, in which the polar stratospheric temperature increases considerably by a few tens of kelvin within a few days. Such a robust event is also characterized by a substantial deceleration of the zonal mean westerly, near 60° latitude in the stratosphere. The event is called a major, if there is wind reversal from westerly to easterly at 10 hPa. Otherwise, it is classified as a minor event. The enhanced PW activity emanating from the troposphere provides the westward momentum to the westerly polar jet, hence the deceleration. The westerly polar jet supports the polar vortex and prevents cold air leakage from high to low latitudes. As the polar jet weakens, the polar vortex destabilizes and may either get displaced or split. Further, as the polar vortex weakens, the air in the vortex compresses downward, resulting in adiabatic warming.

SSW has far-reaching effects on Earth's atmospheric system. These events, characterized by rapid changes in stratospheric temperature and wind within days, trigger extensive alterations across the atmosphere. They impact surface weather, influencing storm tracks and increasing the likelihood of cold air outbreaks in certain regions like Europe and North America. SSW also affects ocean circulation patterns, creating sustained effects on surface winds.

Furthermore, SSW alters atmospheric wave dynamics, leading to fluctuations in temperature and winds in the middle atmosphere. These changes also influence atmospheric tides and TPWs, which are crucial for middle and upper atmospheric variability. Additionally, SSW induces variations in the Brewer-Dobson circulation, affecting the distribution of trace gas species such as ozone. Some SSW events facilitate the downwelling of NO_x-rich air into the stratosphere, impacting ozone chemistry.

The effects of SSW extend to the ionosphere, altering the equatorial ionization anomaly and causing substantial variability in electron density comparable to moderate geomagnetic storms. SSW also affects the equatorial electrojet and thermospheric neutral density, impacting satellite drag. In essence, although SSW is a phenomenon primarily observed in the polar winter stratosphere, its influence spans from the troposphere to the thermosphere and across both hemispheres, impacting global atmospheric system.

In this regard, the present thesis investigates the global impact of SSW in the middle atmosphere via planetary-scale waves. Special attention is given to the MLT region as it acts as a gateway between the electrically ionized ionosphere above and the bulk of the neutral atmosphere below. This is also the region where most of the atmospheric waves and tides dissipate and transfer their energy and momentum to the background atmosphere. Hence, the meteor radar observations of horizontal wind used in the present thesis are crucial in understanding the planetary-scale waves associated MLT variability during SSW. The reanalysis dataset provides global information on the atmospheric parameters in the middle and lower atmosphere, enabling us to investigate latitudinal and vertical coupling via waves. Moreover, the reanalysis dataset helps us understand the excitation mechanism of PWs and tides and trace the origin, propagation, and possible dissipation of these waves.

Therefore, the present thesis provides a comprehensive picture of the middle atmospheric wave dynamics during SSW. The major science outcomes of the thesis, described in chapters 3 to 8, are briefly discussed hereafter.

Chapter 3 focuses on PW dynamics during a rare Austral SSW event in September 2019, observed from the southern low-latitude stations. It addresses the impact of such events on the middle atmosphere at low latitudes. Here are the key findings and implications:

- **Contrasting Temperature Patterns:** The analysis reveals contrasting temperature patterns between tropical and high-latitude regions, with cooling in the tropical stratosphere during warming at high latitudes. Similarly, warming in the low-latitude mesosphere seems concurrent with high-latitude cooling. This disparity emphasizes the contrasting nature of thermodynamics during SSW events at low latitude with respect to high latitudes.

- Presence and behavior of TPWs: The study identifies a strong presence of the Q16DW in the stratosphere before the warming event, diminishing significantly afterward. Additionally, a significant and short-lived burst of the Q6DW is observed in the MLT post-warming, indicating rapid wave responses during SSW events at low latitudes.
- Zonal propagation direction of TPWs: Several TPW components, including Q16DW, Q10DW, Q6DW, and Q3DW, exhibit westward propagation with specific zonal wavenumbers (ZWN 1 and 2).
- Preconditioning by SPWs: The SPW1 and SPW2 seem to be active during the prewarming days in the mid and high latitude stratosphere and diminish considerably during post-warming days. The study emphasizes the significant role of SPW1 in preconditioning the 2019 minor SSW event owing to its substantial amplitude.
- Meridional airmass mixing and instability: Analysis of PV maps indicates notable meridional mixing of air masses, favoring instability during the warming period. The growth of the Q6DW during the warming period is attributed to baroclinic/barotropic instability processes, highlighting the role of dynamic processes in wave evolution during SSW events.
- Meridional propagation Patterns: EP flux analysis reveals propagation of the Q6DW and Q16DW from high and mid-latitudes to low latitudes associated with the SSW event, providing valuable insights into the wave source, propagation, and dissipation region.

Overall, these findings significantly contribute to our understanding of PW dynamics during rare SH SSW events, particularly in low-latitude regions. They also highlight the potential implications of dynamic PW processes on the middle atmosphere during such impactful and rare meteorological events in the SH.

Chapter 4 investigates atmospheric tidal dynamics in the MLT during the 2019 SH SSW event. The analysis is based on meteor radar observations from the equatorial, extratropical, middle, and high-latitude stations at CA, CP, KE, and RO. Moreover, MERRA2 dataset is utilized to understand the global tidal variability corresponding to different ZWN modes during the warming event. The major outcome of the study are as follows.

- Variability in local tides: The DT and ST amplitudes estimated using meteor radar V at a specific geographic location do not exhibit significant variability concerning the warming event.
- Variability in global tidal modes: Significant and consistent variability is observed in global tidal modes, particularly in the DW1, DE3, and SW2 components during the SSW event. The tidal ZWN modes are calculated using MERRA2 data. The broad variability is similar to the patterns seen in non-SSW years during the same season, indicating a link to seasonal tidal variability. Hence, the deseasoned tidal amplitudes are estimated to understand the changes solely due to SSW.
- Tidal sources: The broad seasonal variability in the DW1, DE3, and SW2 amplitudes can be attributed to various sources such as water vapor, convective activity, ozone, and the propagation conditions influenced by U.
- Distinct response to SSW event: Deseasoned tidal amplitudes show a significant increase in DW1 around PWD across all latitudes, indicating a clear response to the warming event. Deseasoned DE3 also exhibits a notable response, particularly at equatorial latitudes, while deseasoned SW2 shows enhancement around PWD.
- Complex processes at play: The study suggests that short-term variability in dominant tidal modes during SSW events cannot be fully explained by known sources alone, indicating the involvement of complex processes in these global disturbances. Further investigations are needed to better understand these dynamics.

The study highlights the response of global tidal modes in the SH MLT to the 2019 austral SSW, emphasizing the need for continued research in this area.

Chapter 5 provides a comparative analysis of the middle atmospheric circulation during a rare SH SSW events in September 2002 and 2019, which had not been extensively studied before. By focusing on the spring equinox period when these events occur, the research aims to differentiate the effects of the warming events from seasonal changes, allowing for a clearer examination of the global circulation alterations induced by these warmings. The study thoroughly compares actual and deseasoned atmospheric parameters during these events.

Key findings include:

- Deseasoned flow characteristics: Both events showed significant easterly forcing around the PWD. Specifically, there was an early onset of zonal mean easterly forcing in the stratosphere at extratropical latitudes, which then extended to mid and high latitudes around the PWD, hinting at a possible tropical precursor to these SSW events.
- Impact on upper mesosphere: Despite the dominant seasonal transition in the upper mesosphere, deseasoned winds revealed impacts of the warming events, characterized by easterly and southerly (equatorward) forcing around the PWD.
- Sustained effects on Upper Mesosphere: There was notable similarity in the latitude-longitude variability of U and V during and after the warming phases, indicating that the effects of these events persisted in the upper mesosphere.
- Influence of minor 2019 SSW: The minor SSW event in 2019 significantly altered the meridional circulation structure globally, as evidenced by the longitudinal interchange of the upper mesospheric peak V at high latitudes between different phases of the event.

In summary, the study provides useful insights into the disturbances in the Southern Hemisphere's middle atmospheric flow caused by major and minor SSW events. It emphasizes the importance of understanding and monitoring these events due to their substantial impact on global atmospheric circulation.

Chapter 6 presents significant evidence of nonlinear interactions involving a zonally symmetric wave during major NH SSWs. The analysis of ELS spectra from SMR data reveals secondary waves as the USB and LSB of the ST, while wavelet spectra indicate the presence of a 20dw. Furthermore, the wavelet spectra of the instantaneous ST amplitude show a 20-day modulation during the warming event, suggesting nonlinear interactions between the ST and 20dw, resulting in USB and LSB as secondary waves. These secondary waves appear to beat with the ST, causing tidal modulation with the 20-day PW period. The simultaneous and transient activities of USB, LSB, and 20dw provide robust evidence of nonlinear interactions between ST and 20dw.

Major findings include:

- **Dissimilar Behaviors of USB and LSB:** Despite their association with the ST, USB and LSB exhibit different behaviors. The enhancement of LSB in MLT coincides with a decrease in ST amplitude around the PWD, suggesting significant energy transfer from the ST to the LSB. Conversely, USB closely follows the ST pattern, indicating a strong relationship with the latter.
- **20dw Activity:** The 20dw shows minimal energy exchange with ST, USB, or LSB, indicating its lesser impact in the nonlinear interaction. However, its presence is crucial for these interactions.
- **Primary Waves in Nonlinear Interaction:** The study identifies the 20dw0 and SW2 as the primary waves involved in the nonlinear interaction. The enhanced 20dw observed in SMR data is linked to an enhancement in the 20dw0 component originating from the stratosphere. The nonlinear interaction between SPW2 and 20dwW2 generates 20dw0, which then interacts with SW2 to produce USB and LSB.

This study provides the first observational evidence of a two-step nonlinear interaction through zonally symmetric PWs during split-type SSWs at boreal high latitudes:

- I. First Step: Nonlinear interaction between SPW2 and 20dwW2 generates the 20dw0.
- II. Second Step: Nonlinear interaction between the dominant SW2 and the previously generated 20dw0 produces USB and LSB as secondary waves.

These findings highlight the complex and intricate nature of atmospheric wave interactions during SSW events. Understanding these interactions is crucial for improving various wave dynamical models.

Chapter 7 offers valuable insights into the mechanisms behind the enhancement of the S0 component during major SSWs in the NH and SH. Key findings are as follows:

- **Enhanced S0 amplitude:** The S0 remains notably active for a short term in the mid and high latitude middle and upper stratosphere during the PWD.

- The SW2 activity: The SW2 component shows weak but sustained features during the observation interval but diminishes significantly around the 2008-09 and 2012-13 PWDs.
- Role of nonlinear interactions: The simultaneous enhancement of the SPW2 and S0 suggests a possible nonlinear interaction between SPW2 and SW2, producing S0 as a secondary wave. S0 amplitude can exceed that of SW2, and the decrease in SW2 concurrent with S0 enhancement indicates significant energy transfer from SW2 to S0 during the interaction. SPW2 is also believed to contribute some energy to the S0.
- Supporting evidence favoring nonlinear interaction: The agreement between theoretical and observed wavelengths (λ) of S0 during the 2008-09 and 2012-13 NH SSWs further supports the role of nonlinear interactions in generating S0.
- Role of ozone distribution: However, during the 2002 SH SSW, the enhancement of S0 was not due to nonlinear interactions. Instead, a unique zonally symmetric ozone distribution around the PWD, supported by significant poleward transport of ozone-rich air from mid-latitudes, led to S0 enhancement.

Two Plausible Generation Mechanisms for S0 Enhancement:

- I. Nonlinear Interaction: The SW2 and SPW2 interact nonlinearly to produce S0 as a secondary wave as found in the 2008-09 and 2012-13 events.
- II. Thermal Excitation: S0 enhancement is believed to be thermally excited in the presence of a zonally symmetric ozone distribution, as observed during the 2002 SH SSW.

The study explores three case studies of S0 enhancement during SSW events in both hemispheres, highlighting different plausible mechanisms. The multifaceted nature of S0 enhancement observed from long-term analyses suggests a need for extensive future research to fully understand these complex processes. Understanding these mechanisms is required for improving our knowledge of atmospheric dynamics, as non-migrating tides may induce short-term significant variability of the middle atmosphere during such extreme events.

Chapter 8 portrays an interesting signature of interhemispheric coupling through PW modulation using a diverse location of meteor radar observations from low to high latitudes and the ERA5 dataset. The study highlights the potential role of the Q2DW as a carrier of the

Q16DW from the winter hemisphere to the summer hemisphere mesosphere through modulation.

The significant findings are as follows:

- Q2DW amplitude modulation: Meteor radar and ERA5 observations revealed a modulation of the Q2DW amplitude with a quasi-16-day period, originating near the equator at an altitude of 50 km. This modulation is likely triggered by the dominant Q16DWE2 wave from the winter hemisphere penetrating the zero-wind line, affecting Q2DW in the summer hemisphere. The ZWN modes of Q2DW also display significant 16-day modulation.
- Role of Q2DWW3 and Q2DWW4: No significant Q16DW was found in summer background winds, underscoring the importance of Q2DWW3 and Q2DWW4 in transporting the Q16DW signature from the equatorial region to the boreal summer mesosphere.
- Q16DW signature in the upper MLT: A notable Q16DW signature in the upper MLT coincides with the altitude where Q2DW dissipates, suggesting a potential link between these two dynamical entities.

This study is important as it unveils a unique case of Q2DW modulation over a quasi-16-day period, shedding light on its potential role in transporting Q16DW signatures across hemispheres. Understanding the mechanisms behind wave modulation and propagation will be helpful in the perspective of interhemispheric coupling via these PWs.

In conclusion, this thesis provides a comprehensive investigation of the global impact of the SSW on the middle atmospheric dynamics, focusing on planetary-scale waves. The study examines various aspects, including low latitude PW dynamics, global tidal variability, and nonlinear interactions between planetary-scale waves in both hemispheres during SSW events. The thesis also reveals the mechanisms behind the enhancement of zonally symmetric waves and the interhemispheric coupling processes through PW modulation. In a nutshell, the research underscores the complexity of atmospheric processes during SSW events and their far-reaching effects on the global middle atmospheric system (Figure 9.1), highlighting the importance of continued study to fully understand these processes.

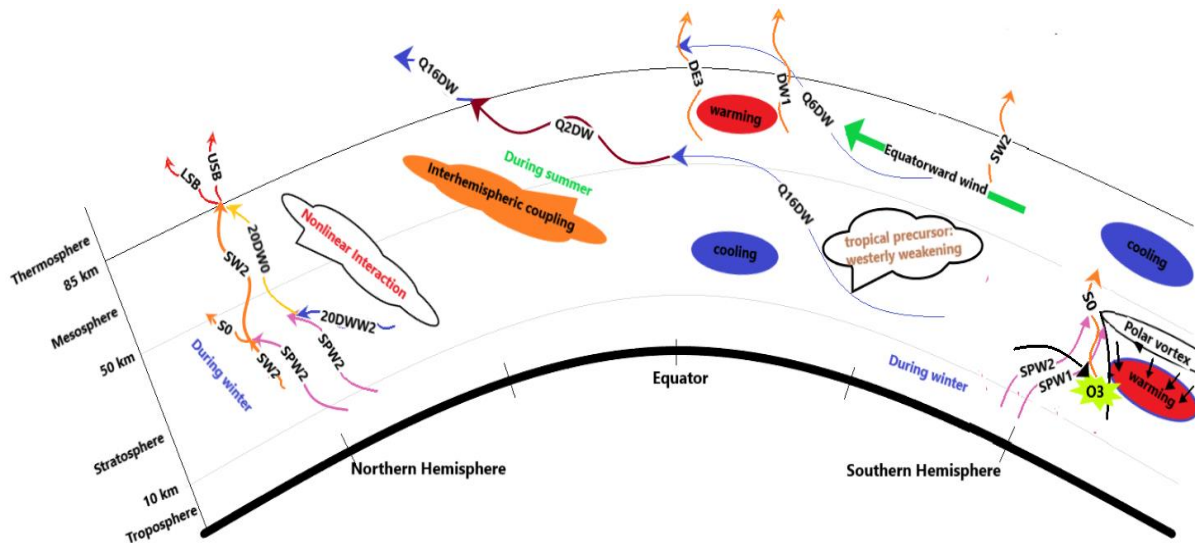


Figure 9. 1. A simplified diagram depicting global middle atmospheric dynamics during SSW events, influenced by planetary-scale waves, as explored in this thesis.

9.2. Broader Implication

The investigations conducted in this thesis have addressed several unresolved questions and provided novel observational evidence, highlighting critical gaps in our understanding of middle atmospheric dynamics during SSW events. These gaps need further exploration to enhance our comprehension of atmospheric processes during such extreme fluid dynamical events. The key implications of the results of this PhD thesis for the broader field of research include:

- **Enhanced Understanding of SSW Impacts:** The thesis provides novel insights into the global middle atmospheric dynamics during SSW events, especially rare Southern Hemisphere SSWs, improving our understanding of atmospheric responses to these phenomena.
- **Contribution to Planetary Wave and Tidal Dynamics:** The study advances the knowledge of planetary-scale waves, i.e., PWs and tides, focusing on their variability and interactions in the middle atmosphere, which are crucial for the accurate representation of atmospheric dynamics in whole atmosphere models.

- **New Mechanisms of Wave Interaction:** It identifies new mechanisms behind the non-linear interactions of PWs, including the first observational evidence of a multi-step coupling process via zonally symmetric waves, which has significant implications for understanding wave coupling and energy transfer between atmospheric layers.
- **Increased Focus on Interhemispheric Coupling:** The thesis highlights the modulation of waves like the quasi-2-day wave (Q2dw) by longer-period waves, shedding light on the processes that couple the Northern and Southern Hemispheres, essential for modeling interhemispheric influence.
- **Implications for Tidal Variability Studies:** The research provides a detailed examination of tidal responses to SSW events, showing how specific tidal components, like S0, are enhanced by non-linear interactions and unique source distributions, contributing to better forecasting and modeling of tidal dynamics in the MLT region.
- **Impact on Model Development:** The findings underscore the complexity of middle atmospheric processes during SSW events, suggesting the need for advanced dynamical models that can accurately reproduce the observed wave interactions and their effects on global atmospheric systems.
- **Global Middle Atmosphere Dynamics:** The thesis contributes to the broader understanding of wave dynamics in the middle atmosphere, emphasizing the role of PWs and tides in regulating thermospheric and ionospheric variability, critical for space weather and climate studies.

9.3. Future Scope

The results presented in this thesis have enhanced our understanding of global middle atmospheric dynamics during SSW, particularly planetary-scale waves. The results can be used as input into dynamic atmospheric models to improve its predictability under various scenarios. They offer new insights into middle atmospheric dynamical processes during SSW events and highlight several scientific issues that seek further investigations.

- **Relative Energy Exchange:** Conducting long-term statistical analyses to get an idea of relative energy exchange among primary and secondary waves is crucial for understanding the variability of planetary waves (PWs) and tides in connection with the nonlinear interactions. This will also help identifying secondary waves that may cause significant variability in the upper atmosphere and ionosphere.
- **Investigating the cause of Tidal Variability:** Further investigation is needed to understand the significant short-term changes in global tidal modes during SH SSW, as known tidal sources do not fully explain this variability. Unveiling the complex processes behind such changes is essential.
- **Wave Modulation Mechanisms:** Extensive research is required to understand the conditions that allow a higher-period wave to modulate a lower-period wave in the atmosphere. This will provide deeper insights into atmospheric wave dynamics.
- **Role of GWs, Tides, and Q2DW:** Understanding the roles of GWs, tides, and Q2DW in the observed transient TPWs in the MLT is necessary. TPWs may not directly propagate from the lower atmosphere but could appear in the MLT as lower-period waves (carrying TPW signature) dissipate.
- **Downward Influence of SH SSW:** Future work should explore the downward influence of SH SSW on altering convective activity and its impact on stratosphere-troposphere exchange processes and tropospheric weather patterns.
- **Ionospheric Impact of SH SSW:** Detailed investigation is required to understand the ionospheric impacts of SH SSW, including modulation of the equatorial electrojet, equatorial ionization anomaly, and equatorial spread F.

These research directions will further our understanding of atmospheric dynamics and improve predictive capabilities of atmosphere-ionosphere system.

References

- Abatzoglou, J. T., & Magnusdottir, G. (2006). Planetary wave breaking and nonlinear reflection: Seasonal cycle and interannual variability. *Journal of Climate*, 19(23), 6139-6152. <https://doi.org/10.1175/JCLI3968.1>
- Andrews, D. G., Holton, J. R., & Leovy, C. B. (1987). *Middle atmosphere dynamics* (No. 40). Academic press.
- Bahramvash Shams, S., Walden, V. P., Hannigan, J. W., Randel, W. J., Petropavlovskikh, I. V., Butler, A. H., & de la Cámara, A. (2022). Analyzing ozone variations and uncertainties at high latitudes during sudden stratospheric warming events using MERRA-2. *Atmospheric Chemistry and Physics*, 22(8), 5435-5458. <https://doi.org/10.5194/acp-22-5435-2022>
- Beard, A. G., Mitchell, N. J., Williams, P. J. S., & Kunitake, M. (1999). Non-linear interactions between tides and planetary waves resulting in periodic tidal variability. *Journal of Atmospheric and Solar-Terrestrial Physics*, 61(5), 363-376. [https://doi.org/10.1016/S1364-6826\(99\)00003-6](https://doi.org/10.1016/S1364-6826(99)00003-6)
- Becker, E. (2012). Dynamical control of the middle atmosphere. *Space Science Reviews*, 168, 283-314. <https://doi.org/10.1007/s11214-011-9841-5>
- Beer, T. (1974). *Atmospheric waves*. New York.
- Brasseur, G. P., & Solomon, S. (2005). *Aeronomy of the middle atmosphere Chemistry and physics of the stratosphere and mesosphere* (Vol. 32). Springer Science & Business Media.
- Butler, A. H., Seidel, D. J., Hardiman, S. C., Butchart, N., Birner, T., & Match, A. (2015). Defining sudden stratospheric warmings. *Bulletin of the American Meteorological Society*, 96(11), 1913-1928. <https://doi.org/10.1175/BAMS-D-13-00173.1>
- Chandran, A., Garcia, R. R., Collins, R. L., & Chang, L. C. (2013). Secondary planetary waves in the middle and upper atmosphere following the stratospheric sudden warming event of january 2012. *Geophysical Research Letters*, 40 (9), 1861-1867. <https://doi.org/10.1002/grl.50373>
- Chang, L. C., Palo, S. E., & Liu, H. L. (2009). Short-term variation of the $s = 1$ non-migrating semidiurnal tide during the 2002 stratospheric sudden warming. *Journal of Geophysical Research*, 114, D03109. <https://doi.org/10.1029/2008JD010886>
- Chapman, S., & Lindzen, R. S. (1970). *Atmospheric tides*, 200 pp. D. Reidel, Norwell, Mass.
- Charlton, A. J., O'Neill, A., Lahoz, W. A., & Berrisford, P. (2005). The splitting of the stratospheric polar vortex in the Southern Hemisphere, September 2002: Dynamical evolution. *Journal of the atmospheric sciences*, 62(3), 590-602. <https://doi.org/10.1175/JAS-3318.1>
- Charlton, A. J., & Polvani, L. M. (2007). A new look at stratospheric sudden warmings. Part I: Climatology and modeling benchmarks. *Journal of climate*, 20(3), 449-469. <https://doi.org/10.1175/JCLI3996.1>

- Charney, J. G., & Drazin, P. G. (1961). Propagation of planetary-scale disturbances from the lower into the upper atmosphere. *Journal of Geophysical Research*, 66(1), 83-109.
<https://doi.org/10.1029/JZ066i001p00083>
- Charney, J. G., & Stern, M. E. (1962). On the stability of internal baroclinic jets in a rotating atmosphere. *Journal of Atmospheric Sciences*, 19 (2), 159 - 172.
[https://doi.org/10.1175/1520-0469\(1962\)019h0159:OTSOIBi2.0.CO;2](https://doi.org/10.1175/1520-0469(1962)019h0159:OTSOIBi2.0.CO;2)
- Chau, J. L., Goncharenko, L. P., Fejer, B. G., & Liu, H. L. (2012). Equatorial and low latitude ionospheric effects during sudden stratospheric warming events: Ionospheric effects during SSW events. *Space Science Reviews*, 168, 385-417. <https://doi.org/10.1007/s11214-011-9797-5>
- Chau, J. L., Hoffmann, P., Pedatella, N. M., Matthias, V., & Stober, G. (2015). Upper mesospheric lunar tides over middle and high latitudes during sudden stratospheric warming events. *Journal of Geophysical Research: Space Physics*, 120(4), 3084-3096.
<https://doi.org/10.1002/2015JA020998>
- Conte, J. F., Chau, J. L., & Peters, D. H. (2019). Middle-and high-latitude mesosphere and lower thermosphere mean winds and tides in response to strong polar-night jet oscillations. *Journal of Geophysical Research: Atmospheres*, 124(16), 9262-9276.
<https://doi.org/10.1029/2019JD030828>
- Daubechies, I. (1988). Orthonormal bases of compactly supported wavelets. *Communications on pure and applied mathematics*, 41(7), 909-996. <https://doi.org/10.1002/cpa.3160410705>
- Davis, R. N., Du, J., Smith, A. K., Ward, W. E., & Mitchell, N. J. (2013). The diurnal and semidiurnal tides over Ascension Island (° S, 14° W) and their interaction with the stratospheric quasi-biennial oscillation: studies with meteor radar, eCMAM and WACCM. *Atmospheric Chemistry and Physics*, 13(18), 9543-9564. <https://doi.org/10.5194/acp-13-9543-2013>
- Dee, D. P., Uppala, S. M., Simmons, A. J., Berrisford, P., Poli, P., Kobayashi, S., ... & Vitart, F. (2011). The ERA-Interim reanalysis: Configuration and performance of the data assimilation system. *Quarterly Journal of the royal meteorological society*, 137(656), 553-597.
<https://doi.org/10.1002/qj.828>
- de La Cámara, A., Abalos, M., Hitchcock, P., Calvo, N., & Garcia, R. R. (2018). Response of Arctic ozone to sudden stratospheric warmings. *Atmospheric Chemistry and Physics*, 18(22), 16499-16513. <https://doi.org/10.5194/acp-18-16499-2018>
- Dickinson, R. E. (1968). Planetary Rossby waves propagating vertically through weak westerly wind wave guides. *Journal of the Atmospheric Sciences*, 25(6), 984-1002.
[https://doi.org/10.1175/1520-0469\(1968\)025<0984:PRWPVT>2.0.CO;2](https://doi.org/10.1175/1520-0469(1968)025<0984:PRWPVT>2.0.CO;2)
- Dole, R., Hoerling, M., & Schubert, S. (2008). CCSP, 2008: Reanalysis of Historical Climate Data for Key Atmospheric Features: Implications for Attribution of Causes of Observed Change. Asheville, NC.1
- Dowdy, A. J., Vincent, R. A., Murphy, D. J., Tsutsumi, M., Riggan, D. M., & Jarvis, M. J. (2004). The large-scale dynamics of the mesosphere–lower thermosphere during the southern hemisphere

- stratospheric warming of 2002. *Geophysical Research Letters*, 31(14).
<https://doi.org/10.1029/2004GL020282>
- Duck, T. J., Whiteway, J. A., & Carswell, A. I. (1998). Lidar observations of gravity wave activity and arctic stratospheric vortex core warming. *Geophysical Research Letters*, 25(15), 2813–2816. <https://doi.org/10.1029/98GL02113>
- Eckermann S. D., Rajopadhyaya D. K., Vincent R. A., (1997). Intraseasonal wind variability in the equatorial mesosphere and lower thermosphere: long-term observations from the central Pacific. *Journal of Atmospheric and Terrestrial Physics*, 59, 603–627.
[https://doi.org/10.1016/S1364-6826\(96\)00143-5](https://doi.org/10.1016/S1364-6826(96)00143-5)
- Eswaraiah, S., Kim, J. H., Lee, W., Hwang, J., Kumar, K. N., & Kim, Y. H. (2020). Unusual changes in the Antarctic middle atmosphere during the 2019 warming in the Southern Hemisphere. *Geophysical Research Letters*, 47(19), e2020GL089199.
<https://doi.org/10.1029/2020GL089199>
- Farge, M. (1992). Wavelet transforms and their applications to turbulence. *Annual review of fluid mechanics*, 24(1), 395–458. <https://doi.org/10.1146/annurev.fl.24.010192.002143>
- Forbes, J. M. (1995). Tidal and planetary waves. The upper mesosphere and lower thermosphere: A review of experiment and theory, 87, 67–87. <https://doi.org/10.1029/GM087>
- Forbes, J. M., Hagan, M. E., Miyahara, S., Vial, F., Manson, A. H., Meek, C. E., & Portnyagin, Y. I. (1995). Quasi 16-day oscillation in the mesosphere and lower thermosphere. *Journal of Geophysical Research: Atmospheres*, 100(D5), 9149–9163.
<https://doi.org/10.1029/90JA02006>
- Forbes, J. M., & Garrett, H. B. (1978). Thermal excitation of atmospheric tides due to insolation absorption by O₃ and H₂O. *Geophysical Research Letters*, 5(12), 1013–1016.
<https://doi.org/10.1029/GL005i012p01013>
- Forbes, J. M., Zhang, X., Palo, S., Russell, J., Mertens, C. J., & Mlynchak, M. (2008). Tidal variability in the ionospheric dynamo region. *Journal of Geophysical Research: Space Physics*, 113(A2).
<https://doi.org/10.1029/2007JA012737>
- France, J. A., Randall, C. E., Lieberman, R. S., Harvey, V. L., Eckermann, S. D., Siskind, D. E., ... & Russell III, J. M. (2018). Local and remote planetary wave effects on polar mesospheric clouds in the Northern Hemisphere in 2014. *Journal of Geophysical Research: Atmospheres*, 123(10), 5149–5162. <https://doi.org/10.1029/2017JD028224>
- Fritts, D. C., Isler, J. R., Lieberman, R. S., Burrage, M. D., Marsh, D. R., Nakamura, T., et al. (1999). Two-day wave structure and mean flow interactions observed by radar and High Resolution Doppler Imager. *Journal of Geophysical Research: Atmospheres*, 104(D4), 3953–3969.
<https://doi.org/10.1029/1998JD200024>
- Fritz, S., & Soules, S. (1970). Large-scale temperature changes in the stratosphere observed from nimbus iii. *Journal of Atmospheric Sciences*, 27 (7), 1091–1097.
[https://doi.org/10.1175/1520-0469\(1970\)027<1091:LSTCIT>2.0.CO;2](https://doi.org/10.1175/1520-0469(1970)027<1091:LSTCIT>2.0.CO;2)

- Gan, Q., Oberheide, J., & Pedatella, N. M. (2018). Sources, sinks, and propagation characteristics of the quasi 6-day wave and its impact on the residual mean circulation. *Journal of Geophysical Research: Atmospheres*, 123(17), 9152-9170. <https://doi.org/10.1029/2018JD028553>
- Garcia, R. R. (1987). On the mean meridional circulation of the middle atmosphere. *Journal of Atmospheric Sciences*, 44(24), 3599-3609. [https://doi.org/10.1175/1520-0469\(1987\)044<3599:OTMMCO>2.0.CO;2](https://doi.org/10.1175/1520-0469(1987)044<3599:OTMMCO>2.0.CO;2)
- Gelaro, R., McCarty, W., Suárez, M. J., Todling, R., Molod, A., Takacs, L., ... & Zhao, B. (2017). The modern-era retrospective analysis for research and applications, version 2 (MERRA-2). *Journal of climate*, 30(14), 5419-5454. <https://doi.org/10.1175/JCLI-D-16-0758.1>
- Goncharenko, L. P., Coster, A. J., Chau, J. L., & Valladares, C. E. (2010). Impact of sudden stratospheric warmings on equatorial ionization anomaly. *Journal of Geophysical Research: Space Physics*, 115(A10). <https://doi.org/10.1029/2010JA015400>
- Goncharenko, L. P., Coster, A. J., Plumb, R. A., & Domeisen, D. I. (2012). The potential role of stratospheric ozone in the stratosphere-ionosphere coupling during stratospheric warmings. *Geophysical Research Letters*, 39(8). <https://doi.org/10.1029/2012GL051261>
- Goncharenko, L. P., Harvey, V. L., Greer, K. R., Zhang, S.-R., & Coster, A. J. (2020). Longitudinally dependent low-latitude ionospheric disturbances linked to the antarctic sudden stratospheric warming of september 2019. *Journal of Geophysical Research: Space Physics*, 125 (8), e2020JA028199. <https://doi.org/10.1029/2020JA028199>
- Gu, S. Y., Dou, X., Pancheva, D., Yi, W., & Chen, T. (2018). Investigation of the abnormal quasi 2-day wave activities during the sudden stratospheric warming period of January 2006. *Journal of Geophysical Research: Space Physics*, 123(7), 6031-6041. <https://doi.org/10.1029/2018JA025596>
- Gu, S. Y., Wei, Y., Sha, X., Tang, L., & Li, N. (2023). A Case Study of the Wavenumber Transition between Westward Quasi-2 Day Wave $s=3$ and $s=4$ Modes in the Mesosphere. *Atmosphere*, 14(3), 442. <https://doi.org/10.3390/atmos14030442>
- Guharay, A., & Sekar, R. (2012). Signature of latitudinal coupling during a major sudden stratospheric warming in the tropics. *Journal of Atmospheric and Solar-Terrestrial physics*, 75, 122–126. <https://doi.org/10.1016/j.jastp.2011.06.010>
- Guharay, A., Batista, P. P., Clemesha, B. R., & Schuch, N. J. (2013). Study of the quasi-two-day wave during summer over Santa Maria, Brazil using meteor radar observations. *Journal of atmospheric and solar-terrestrial physics*, 92, 83-93. <http://dx.doi.org/10.1016/j.jastp.2012.10.005>
- Guharay, A., Batista, P. P., Clemesha, B. R., Sarkhel, S., & Buriti, R. A. (2013). On the variability of the terdiurnal tide over a Brazilian equatorial station using meteor radar observations. *Journal of Atmospheric and Solar-Terrestrial Physics*, 104, 87-95. <https://doi.org/10.1016/j.jastp.2013.08.021>

- Guharay, A., Batista, P., Clemesha, B., & Sarkhel, S. (2014). Response of the extratropical middle atmosphere to the september 2002 major stratospheric sudden warming. *Advances in Space Research*, 53 (2), 257–265. <https://doi.org/10.1016/j.asr.2013.11.002>
- Guharay, A., Batista, P. P., & Clemesha, B. R. (2015). Variability of the quasi-2-day wave and interaction with longer period planetary waves in the MLT at Cachoeira Paulista (22.7 S, 45 W). *Journal of Atmospheric and Solar-Terrestrial Physics*, 130, 57-67. <https://doi.org/10.1016/j.jastp.2015.05.010>
- Guharay, A., Batista, P. P., & Clemesha, B. R. (2015). On the variability of the diurnal tide and coupling with planetary waves in the MLT over Cachoeira Paulista (22.7 S, 45 W). *Journal of Atmospheric and Solar-Terrestrial Physics*, 133, 7-17. <http://dx.doi.org/10.1016/j.jastp.2015.07.016>
- Guharay, A., Batista, P. P., Clemesha, B. R., Buriti, R. A., & Schuch, N. J. (2016, April). Latitudinal variability of the quasi-16-day wave in the middle atmosphere over Brazilian stations. In *Annales Geophysicae* (Vol. 34, No. 4, pp. 411-419). Göttingen, Germany: Copernicus Publications. <https://doi.org/10.5194/angeo-34-411-2016>
- Guharay, A., & Batista, P. P. (2019). On the variability of tides during a major stratospheric sudden warming in September 2002 at Southern hemispheric extra-tropical latitude. *Advances in Space Research*, 63(8), 2337-2344. <https://doi.org/10.1016/j.asr.2018.12.037>
- Gurubaran, S., Ramkumar, T. K., Sridharan, S., & Rajaram, R. (2001). Signatures of quasi-2-day planetary waves in the equatorial electrojet: results from simultaneous observations of mesospheric winds and geomagnetic field variations at low latitudes. *Journal of Atmospheric and Solar-Terrestrial Physics*, 63(9), 813-821. [https://doi.org/10.1016/S1364-6826\(00\)00193-0](https://doi.org/10.1016/S1364-6826(00)00193-0)
- Hagan, M. E., & Forbes, J. M. (2002). Migrating and nonmigrating diurnal tides in the middle and upper atmosphere excited by tropospheric latent heat release. *Journal of Geophysical Research: Atmospheres*, 107(D24), ACL-6. <https://doi.org/10.1029/2001JD001236>
- Hagan, M. E., & Forbes, J. M. (2003). Migrating and nonmigrating semidiurnal tides in the upper atmosphere excited by tropospheric latent heat release. *Journal of Geophysical Research: Space Physics*, 108(A2). <https://doi.org/10.1029/2002JA009466>
- Hagan, M. E., Maute, A., Roble, R. G., Richmond, A. D., Immel, T. J., & England, S. L. (2007). Connections between deep tropical clouds and the Earth's ionosphere. *Geophysical Research Letters*, 34(20). <https://doi.org/10.1029/2007GL030142>
- Harvey, V.L., Knox, J., France, J., Fujiwara, M., Gray, L., Hirooka, T., Hitchcock, P., Hitchman, M., Kawatani, Y., Manney, G.L., McCormack, J., Orsolini, Y., Sakazaki, T., & Tomikawa, Y. (2022). Chapter 11: Upper Stratosphere Lower Mesosphere. In *SPARC Reanalysis Intercomparison Project (S-RIP) Final Report*, Fujiwara M., Manney G. L., Gray L. J., & Wright J. S. (Eds.), pp. 531-580. SPARC Report No. 10, WCRP-17/2020. <https://doi.org/10.17874/800dee57d13>

- Hauchecorne, A., & Chanin, M. L. (1988, August). Planetary waves-mean flow interaction in the middle atmosphere-Numerical modelling and lidar observations. In *Annales Geophysicae* (Vol. 6, pp. 409-415).
- He, M., Chau, J. L., Stober, G., Hall, C. M., Tsutsumi, M., & Hoffmann, P. (2017). Application of Manley-Rowe relation in analyzing non-linear interactions between planetary waves and the solar semidiurnal tide during 2009 sudden stratospheric warming event. *Journal of Geophysical Research: Space Physics*, 122(10), 10-783. <https://doi.org/10.1002/2017JA024630>
- He, M., Chau, J. L., Hall, C. M., Tsutsumi, M., Meek, C., & Hoffmann, P. (2018). The 16-Day planetary wave triggers the SW1-tidal-like signatures during 2009 sudden stratospheric warming. *Geophysical Research Letters*, 45, 12,631– 12,638. <https://doi.org/10.1029/2018GL079798>
- He, M., & Chau, J. L. (2019). Mesospheric semidiurnal tides and near-12 h waves through jointly analyzing observations of five specular meteor radars from three longitudinal sectors at boreal midlatitudes. *Atmospheric Chemistry and Physics*, 19(9), 5993-6006. <https://doi.org/10.5194/acp-19-5993-2019>
- He, M., Forbes, J. M., Chau, J. L., Li, G., Wan, W., & Korotyshkin, D. V. (2020). High-order solar migrating tides quench at SSW onsets. *Geophysical Research Letters*, 47(6), e2019GL086778. <https://doi.org/10.1029/2019GL086778>
- He, M., Chau, J. L., Forbes, J. M., Zhang, X., Englert, C. R., Harding, B. J., ... & Makela, J. J. (2021). Quasi-2-day wave in low-latitude atmospheric winds as viewed from the ground and space during January–March, 2020. *Geophysical Research Letters*, 48(13), e2021GL093466. <https://doi.org/10.1029/2021GL093466>
- Herlofson, N. (1948). The theory of meteor ionization. *Phys. Soc. Rep. Prog. Phys.*, 11, 444-454.
- Hersbach, H., Bell, B., Berrisford, P., Hirahara, S., Horányi, A., Muñoz-Sabater, J., ... & Thépaut, J. N. (2020). The ERA5 global reanalysis. *Quarterly Journal of the Royal Meteorological Society*, 146(730), 1999-2049. <https://doi.org/10.1002/qj.3803>
- Hibbins, R. E., Marsh, O. J., McDonald, A. J., & Jarvis, M. J. (2010). A new perspective on the longitudinal variability of the semidiurnal tide. *Geophysical research letters*, 37(14). <https://doi.org/10.1029/2010GL044015>
- Hibbins, R. E., Espy, P. J., Orsolini, Y. J., Limpasuvan, V., & Barnes, R. J. (2019). SuperDARN observations of semidiurnal tidal variability in the MLT and the response to sudden stratospheric warming events. *Journal of Geophysical Research: Atmospheres*, 124(9), 4862-4872. <https://doi.org/10.1029/2018JD030157>
- Hines, C. O. (1960). Internal atmospheric gravity waves at ionospheric heights. *Canadian Journal of Physics*, 38(11), 1441-1481. <https://doi.org/10.1139/p60-150>
- Hirota, I., & Hirooka, T. (1984). Normal mode rossby waves observed in the upper stratosphere. part i: First symmetric modes of zonal wavenumbers 1 and 2. *Journal of Atmospheric Sciences*, 41(8), 1253 - 1267. [https://doi.org/10.1175/1520-0469\(1984\)041<1253:NMRWOI>2.0.CO;2](https://doi.org/10.1175/1520-0469(1984)041<1253:NMRWOI>2.0.CO;2)

- Hitchman, M. H., Leovy, C. B., Gille, J. C., & Bailey, P. L. (1987). Quasi-stationary zonally asymmetric circulations in the equatorial lower mesosphere. *Journal of the atmospheric sciences*, 44(16), 2219-2236. [https://doi.org/10.1175/1520-0469\(1987\)044<2219:QSZACI>2.0.CO;2](https://doi.org/10.1175/1520-0469(1987)044<2219:QSZACI>2.0.CO;2)
- Hocking, W. K., Thayaparan, T., & Jones, J. (1997). Meteor decay times and their use in determining a diagnostic mesospheric temperature-pressure parameter: Methodology and one year of data. *Geophysical Research Letters*, 24(23), 2977-2980. <https://doi.org/10.1029/97GL03048>
- Hocking, W. K., Fuller, B., & Vandepeer, B. (2001). Real-time determination of meteor-related parameters utilizing modern digital technology. *Journal of Atmospheric and Solar-Terrestrial Physics*, 63(2-3), 155-169. [https://doi.org/10.1016/S1364-6826\(00\)00138-3](https://doi.org/10.1016/S1364-6826(00)00138-3)
- Hoffmann, P., Singer, W., & Keuer, D. (2002). Variability of the mesospheric wind field at middle and arctic latitudes in winter and its relation to stratospheric circulation disturbances. *Journal of Atmospheric and Solar-Terrestrial Physics*, 64 (8-11), 1229–1240. [https://doi.org/10.1016/S1364-6826\(02\)00071-8](https://doi.org/10.1016/S1364-6826(02)00071-8)
- Hoffmann, P., Becker, E., Singer, W., & Placke, M. (2010). Seasonal variation of mesospheric waves at northern middle and high latitudes. *Journal of Atmospheric and Solar-Terrestrial Physics*, 72(14–15), 1068–1079. <https://doi.org/10.1016/j.jastp.2010.07.002>
- Holton, J. R. (1984). The generation of mesospheric planetary waves by zonally asymmetric gravity wave breaking. *Journal of the atmospheric sciences*, 41(23), 3427-3430. [https://doi.org/10.1175/1520-0469\(1984\)041<3427:TGOMPW>2.0.CO;2](https://doi.org/10.1175/1520-0469(1984)041<3427:TGOMPW>2.0.CO;2)
- Huang CM, Zhang SD, Fan Y (2007) A numerical study on amplitude characteristics of the terdiurnal tide excited by nonlinear interaction between the diurnal and semidiurnal tides. *Earth Planets Space* 59:183–191. <https://doi.org/10.1186/BF03353094>
- Huang, X., Huang, K., Zhang, S., Huang, C., Gong, Y., & Cheng, H. (2022). Extraordinary quasi-16-day wave activity from October 2013 to January 2014 with radar observations at mid-latitudes and MERRA2 reanalysis data. *Earth, Planets and Space*, 74(1), 98. <https://doi.org/10.1186/s40623-022-01660-z>
- Immel, T. J., Sagawa, E., England, S. L., Henderson, S. B., Hagan, M. E., Mende, S. B., ... & Paxton, L. J. (2006). Control of equatorial ionospheric morphology by atmospheric tides. *Geophysical Research Letters*, 33(15). <https://doi.org/10.1029/2006GL026161>
- Jacobi, C., Schminder, R., & Kürschner, D. (1998a). Non-linear interaction of the quasi 2-day wave and long-term oscillations in the summer midlatitude mesopause region as seen from LF D1 wind measurements over Central Europe (Collm, 52° N, 15° E). *Journal of atmospheric and solar-terrestrial physics*, 60(12), 1175. [https://doi.org/10.1016/S1364-6826\(98\)00076-5](https://doi.org/10.1016/S1364-6826(98)00076-5)
- Jacobi, C., Schminder, R., & Kürschner, D. (1998b). Planetary wave activity obtained from long-period (2–18 days) variations of mesopause region winds over Central Europe (52° N, 15° E). *Journal of Atmospheric and Solar-Terrestrial Physics*, 60(1), 81-93. [https://doi.org/10.1016/S1364-6826\(97\)00117-X](https://doi.org/10.1016/S1364-6826(97)00117-X)

- Jacobi, C. (1998). The quasi 16-day wave in the summer midlatitude mesopause region and its dependence on the equatorial quasi-biennial oscillation. <https://nbn-resolving.org/urn:nbn:de:bsz:15-qucosa-213442>
- Jones, J., Webster, A. R., & Hocking, W. K. (1998). An improved interferometer design for use with meteor radars. *Radio Science*, 33(1), 55-65. <https://doi.org/10.1029/97RS03050>
- Kalnay, E., Kanamitsu, M., Kistler, R., Collins, W., Deaven, D., Gandin, L., ... & Joseph, D. (2018). The NCEP/NCAR 40-year reanalysis project. In *Renewable energy* (pp. Vol1_146-Vol1_194). Routledge. [https://doi.org/10.1175/1520-0477\(1996\)077<0437:TNYRP>2.0.CO;2](https://doi.org/10.1175/1520-0477(1996)077<0437:TNYRP>2.0.CO;2)
- Kanamitsu, M., Ebisuzaki, W., Woollen, J., Yang, S. K., Hnilo, J. J., Fiorino, M., & Potter, G. L. (2002). Ncep–doe amip-ii reanalysis (r-2). *Bulletin of the American Meteorological Society*, 83(11), 1631-1644. <https://doi.org/10.1175/BAMS-83-11-1631>
- Kanzawa, H. (1984). Four observed sudden warmings diagnosed by the eliasen-palm flux and refractive index. *Dynamics of the Middle Atmosphere*, 307.
- Kato, S., Tsuda, T. and Watanabe, F., 1982. Thermal excitation of non-migrating tides. *Journal of Atmospheric and Terrestrial Physics*, 44(2), pp.131-146. [https://doi.org/10.1016/0021-9169\(82\)90116-7](https://doi.org/10.1016/0021-9169(82)90116-7)
- Kidston, J., Scaife, A. A., Hardiman, S. C., Mitchell, D. M., Butchart, N., Baldwin, M. P., & Gray, L. J. (2015). Stratospheric influence on tropospheric jet streams, storm tracks and surface weather. *Nature Geoscience*, 8(6), 433-440. <https://doi.org/10.1038/ngeo2424>
- Kikuchi, K. (2014). An introduction to combined Fourier–wavelet transform and its application to convectively coupled equatorial waves. *Climate dynamics*, 43, 1339-1356. <https://doi.org/10.1007/s00382-013-1949-8>
- King, M. D., Kaufman, Y. J., Menzel, W. P., & Tanre, D. (1992). Remote sensing of cloud, aerosol, and water vapor properties from the moderate resolution imaging spectrometer(MODIS). *IEEE transactions on geoscience and remote sensing*, 30(1), 2-27. <https://doi.org/10.1109/36.124212>
- Kingsley, S. P., Muller, H. G., Nelson, L., & Scholefield, A. (1978). Meteor winds over Sheffield (53°N, 2°W). *Journal of Atmospheric and Terrestrial Physics*, 40(8), 917–922. [https://doi.org/10.1016/0021-9169\(78\)90143-5](https://doi.org/10.1016/0021-9169(78)90143-5)
- Kishore, P., Namboothiri, S., Igarashi, K., Gurubaran, S., Sridharan, S., Rajaram, R., & Ratnam, M. V. (2004). Mf radar observations of 6.5-day wave in the equatorial mesosphere and lower thermosphere. *Journal of Atmospheric and Solar-Terrestrial physics*, 66 (6-9), 507–515. <https://doi.org/10.1016/j.jastp.2004.01.026>
- Kodera, K. (2006). Influence of stratospheric sudden warming on the equatorial troposphere. *Geophysical Research Letters*, 33 (6). <https://doi.org/10.1029/2005GL024510>
- Körnig, H., & Becker, E. (2010). A simple model for the interhemispheric coupling of the middle atmosphere circulation. *Advances in Space Research*, 45(5), 661-668. <https://doi.org/10.1016/j.asr.2009.11.001>

- Koushik, N., Kumar, K.K., Ramkumar, G. et al. Planetary waves in the mesosphere lower thermosphere during stratospheric sudden warming: observations using a network of meteor radars from high to equatorial latitudes. *Climate Dynamics*, 54, 4059–4074 (2020). <https://doi.org/10.1007/s00382-020-05214-5>
- Koushik, N., Kumar, K. K., & Pramitha, M. (2022). A tropical stratopause precursor for sudden stratospheric warmings. *Scientific Reports*, 12(1), 2937. <https://doi.org/10.1038/s41598-022-06864-7>
- Labitzke, K. (1977). Interannual variability of the winter stratosphere in the Northern Hemisphere. *Monthly Weather Review*, 105(6), 762–770. [https://doi.org/10.1175/1520-0493\(1977\)105<0762:IVOTWS>2.0.CO;2](https://doi.org/10.1175/1520-0493(1977)105<0762:IVOTWS>2.0.CO;2)
- Labitzke, K. (1981). Stratospheric-mesospheric midwinter disturbances: A summary of observed characteristics. *Journal of Geophysical Research: Oceans*, 86(C10), 9665-9678. <https://doi.org/10.1029/JC086iC10p09665>
- Laskar, F. I., McCormack, J. P., Chau, J. L., Pallamraju, D., Hoffmann, P., & Singh, R. P. (2019). Interhemispheric meridional circulation during sudden stratospheric warming. *Journal of Geophysical Research: Space Physics*, 124(8), 7112-7122. <https://doi.org/10.1029/2018JA026424>
- Liebmann, B., & Smith, C. A. (1996). Description of a complete (interpolated) outgoing longwave radiation dataset. *Bulletin of the American Meteorological Society*, 77(6), 1275-1277. <http://www.jstor.org/stable/26233278>
- Lieberman, R. S., Riggins, D. M., Franke, S. J., Manson, A. H., Meek, C., Nakamura, T., . . . Reid, I. (2003). The 6.5-day wave in the mesosphere and lower thermosphere: Evidence for baroclinic/barotropic instability. *Journal of Geophysical Research: Atmospheres*, 108 (D20). <https://doi.org/10.1029/2002JD003349>
- Lieberman, R. S. (1999). Eliassen-Palm fluxes of the 2-day wave. *Journal of the Atmospheric Sciences*, 56(16), 2846–2861. [https://doi.org/10.1175/1520-0469\(1999\)056<2846:EPFOTD>2.0.CO;2](https://doi.org/10.1175/1520-0469(1999)056<2846:EPFOTD>2.0.CO;2)
- Lieberman, R. S., France, J., Ortland, D. A., & Eckermann, S. D. (2021). The role of inertial instability in cross-hemispheric coupling. *Journal of the Atmospheric Sciences*, 78(4), 1113-1127. <https://doi.org/10.1175/JAS-D-20-0119.1>
- Lima, L., Batista, P., Clemesha, B., & Takahashi, H. (2005). The 6.5-day oscillations observed in meteor winds over cachoeira paulista (22.7 s). *Advances in Space Research*, 36 (11), 2212–2217. <https://doi.org/10.1016/j.asr.2005.06.005>
- Lima, L. M., Medeiros, A. F., Buriti, R. A., Batista, P. P., Clemesha, B. R., & Takahashi, H. (2007). Mesospheric 2-Day waves observed simultaneously in the equatorial and low latitudes regions of Brazil. *Revista Brasileira de Geofísica*, 25, 43-48. <https://doi.org/10.1590/S0102-261X2007000600006>
- Lima, L. M., Alves, E. D. O., Batista, P. P., Clemesha, B. R., Medeiros, A. F. D., & Buriti, R. A. (2012). Sudden stratospheric warming effects on the mesospheric tides and 2-day wave

- dynamics at 7 S. *Journal of Atmospheric and Solar-Terrestrial Physics*, 78, 99-107.
<https://doi.org/10.1016/j.jastp.2011.02.013>
- Lim, E. P., Hendon, H. H., Butler, A. H., Garreaud, R. D., Polichtchouk, I., Shepherd, T. G., ... & Nakamura, H. (2020). The 2019 Antarctic sudden stratospheric warming. *SPARC newsletter*, 54, 10-13.
- Limpasuvan, V., Orsolini, Y. J., Chandran, A., Garcia, R. R., & Smith, A. K. (2016). On the composite response of the MLT to major sudden stratospheric warming events with elevated stratopause. *Journal of Geophysical Research: Atmospheres*, 121(9), 4518-4537.
<https://doi.org/10.1002/2015JD024401>
- Lin, Y. L. (2007). *Mesoscale dynamics* (Vol. 630). Cambridge: Cambridge University Press.
- Lindzen, R.S. and Chapman, S., 1969. Atmospheric tides. *Space science reviews*, 10(1), pp.3-188.
- Lindzen, R. S., & Hong, S. S. (1974). Effects of mean winds and horizontal temperature gradients on solar and lunar semidiurnal tides in the atmosphere. *Journal of the atmospheric sciences*, 31(5), 1421-1446. [https://doi.org/10.1175/1520-0469\(1974\)031<1421:EOMWAH>2.0.CO;2](https://doi.org/10.1175/1520-0469(1974)031<1421:EOMWAH>2.0.CO;2)
- Liu, H.-L., & Roble, R. G. (2002). A study of a self-generated stratospheric sudden warming and its mesospheric–lower thermospheric impacts using the coupled time-gcm/ccm3. *Journal of Geophysical Research: Atmospheres*, 107 (D23), ACL 15-1-ACL 15-18.
<https://doi.org/10.1029/2001JD001533>
- Liu, H., Miyoshi, Y., Miyahara, S., Jin, H., Fujiwara, H., & Shinagawa, H. (2014). Thermal and dynamical changes of the zonal mean state of the thermosphere during the 2009 SSW: GAIA simulations. *Journal of Geophysical Research: Space Physics*, 119, 6784–6791.
<https://doi.org/10.1002/2014JA020222>
- Liu, G., Hirooka, T., Eguchi, N., & Krüger, K. (2022). Dynamical evolution of a minor sudden stratospheric warming in the Southern Hemisphere in 2019. *Atmospheric Chemistry and Physics*, 22(5), 3493-3505. <https://doi.org/10.5194/acp-22-3493-2022>
- Lomb, N. R. (1976). Least-squares frequency analysis of unequally spaced data. *Astrophysics and space science*, 39, 447-462. <https://doi.org/10.1007/BF00648343>
- Longuet-Higgins, M. S. (1968). The eigenfunctions of Laplace's tidal equation over a sphere. *Philosophical Transactions of the Royal Society of London. Series A, Mathematical and Physical Sciences*, 262(1132), 511-607. <https://doi.org/10.1098/rsta.1968.0003>
- Manson, A. H., Gregory, J. B., & Meek, C. E. (1981). Atmospheric waves (≈ 10 min–30 days) in the mesosphere and thermosphere at saskatoon (52° N, 107° W), October 1978–September 1979. *Planetary and Space Science*, 29(6), 615-625. [https://doi.org/10.1016/0032-0633\(81\)90110-0](https://doi.org/10.1016/0032-0633(81)90110-0)
- Matsuno, T. (1971). A dynamical model of the stratospheric sudden warming. *Journal of Atmospheric Sciences*, 28(8), 1479-1494. [https://doi.org/10.1175/1520-0469\(1971\)028<1479:ADMOTS>2.0.CO;2](https://doi.org/10.1175/1520-0469(1971)028<1479:ADMOTS>2.0.CO;2)

- Maury, P., Claud, C., Manzini, E., Hauchecorne, A., & Keckhut, P. (2016). Characteristics of stratospheric warming events during Northern winter. *Journal of Geophysical Research: Atmospheres*, 121(10), 5368–5380. <https://doi.org/10.1002/2015JD024226>
- McDonald, A. J., Hibbins, R. E., & Jarvis, M. J. (2011). Properties of the quasi 16 day wave derived from EOS MLS observations. *Journal of Geophysical Research: Atmospheres*, 116(D6). <https://doi.org/10.1029/2010JD014719>
- McInturff, R. M. (1978). Stratospheric warmings: Synoptic, dynamic and general circulation aspects. NASA Reference Publ NASA-RP-1017:174. <http://ntrs.nasa.gov/archive/nasa/casi.ntrs.nasa.gov/19780010687.pdf>
- Meriwether, J. W., & Gerrard, A. J. (2004). Mesosphere inversion layers and stratosphere temperature enhancements. *Reviews of Geophysics*, 42(3). <https://doi.org/10.1029/2003RG000133>
- Mitchell, D. M., Charlton-Perez, A. J., & Gray, L. J. (2011). Characterizing the variability and extremes of the stratospheric polar vortices using 2D moment analysis. *Journal of the Atmospheric Sciences*, 68(6), 1194–1213. <https://doi.org/10.1175/2010JAS3555.1>
- Mitchell, N. J. (2015). Meteor Radar. <https://patarnott.com/atms411/pdf/class2019/radarMeteors.pdf>
- Mitchell, N. J. (2019). University of Bath: Rothera Skiymet Meteor Radar data (2005–present), Centre for Environmental Data Analysis. <https://catalogue.ceda.ac.uk/uuid/aa44e02718fd4ba49cefe36d884c6e50>
- Mitchell, N.J. (2021). University of Bath: King Edward Point Skiymet meteor radar data (2016–2020), Centre for Environmental Data Analysis. <https://doi.org/10.5285/061fc7fd1ca940e7ad685daf146db08f>
- Mitra, G., Guharay, A., Batista, P. P., & Buriti, R. A. (2022). Impact of the September 2019 Minor Sudden Stratospheric Warming on the Low-Latitude Middle Atmospheric Planetary Wave Dynamics. *Journal of Geophysical Research: Atmospheres*, 127(1), e2021JD035538. <https://doi.org/10.1029/2021JD035538>
- Mitra, G., Guharay, A., Batista, P. P., Buriti, R. A., & Moffat-Griffin, T. (2023a). Investigation on the MLT tidal variability during September 2019 minor sudden stratospheric warming. *Advances in Space Research*, 71(1), 869–882. <https://doi.org/10.1016/j.asr.2022.08.017>
- Mitra, G., Guharay, A., Conte, J. F., & Chau, J. L. (2023b). Signature of Two-Step Nonlinear Interactions Associated to Zonally Symmetric Waves During Major Sudden Stratospheric Warmings. *Geophysical Research Letters*, 50(19), e2023GL104756. <https://doi.org/10.1029/2023GL104756>
- Mitra, G., & Guharay, A. (2024). Impact of sudden stratospheric warming on middle atmospheric circulation in the southern hemisphere: A comparative study. *Journal of Atmospheric and Solar-Terrestrial Physics*, 254, 106173. <https://doi.org/10.1016/j.jastp.2024.106173>

- Mitra, G., Guharay, A., & Paulino, I. (2024). Signature of a zonally symmetric semidiurnal tide during major sudden stratospheric warmings and plausible mechanisms: a case study. *Scientific Reports*, 14(1), 23806. <https://doi.org/10.1038/s41598-024-72594-7>
- Miyahara, S. P. Y. I., Portnyagin, Y. I., Forbes, J. M., & Solovjeva, T. V. (1991). Mean zonal acceleration and heating of the 70-to 100-km region. *Journal of Geophysical Research: Space Physics*, 96(A2), 1225-1238. <https://doi.org/10.1029/90JA02006>
- Miyoshi, Y., & Yamazaki, Y. (2020). Excitation mechanism of ionospheric 6-day oscillation during the 2019 september sudden stratospheric warming event. *Journal of Geophysical Research: Space Physics*, 125 (9), e2020JA028283. <https://doi.org/10.1029/2020JA028283>
- Mukhtarov, P., Pancheva, D., Andonov, B., Mitchell, N. J., Merzlyakov, E., Singer, W., ... & Murayama, Y. (2007). Large-scale thermodynamics of the stratosphere and mesosphere during the major stratospheric warming in 2003/2004. *Journal of atmospheric and solar-terrestrial physics*, 69(17-18), 2338-2354. <https://doi.org/10.1016/j.jastp.2007.07.012>
- Muller, H. G., & Kingsley, S. P. (1974). Long period meteor wind oscillations. *Journal of Atmospheric and Terrestrial Physics*, 36(11), 1933-1943. [https://doi.org/10.1016/0021-9169\(74\)90180-9](https://doi.org/10.1016/0021-9169(74)90180-9)
- Nappo, C. J. (2013). *An introduction to atmospheric gravity waves* (Vol. 102). Academic press.
- Newman, P. A., & Nash, E. R. (2005). The unusual Southern Hemisphere stratosphere winter of 2002. *Journal of the atmospheric sciences*, 62(3), 614-628. <https://doi.org/10.1175/JAS-3323.1>
- Noguchi, S., Kuroda, Y., Kodera, K., & Watanabe, S. (2020). Robust enhancement of tropical convective activity by the 2019 antarctic sudden stratospheric warming. *Geophysical Research Letters*, 47 (15), e2020GL088743.1. <https://doi.org/10.1029/2020GL088743>
- Norton, W. A., & Thuburn, J. (1996). The two-day wave in a middle atmosphere GCM. *Geophysical Research Letters*, 23(16), 2113-2116. <https://doi.org/10.1029/96GL01956>
- Oberheide, J., Forbes, J. M., Häusler, K., Wu, Q., & Bruinsma, S. L. (2009). Tropospheric tides from 80 to 400 km: Propagation, interannual variability, and solar cycle effects. *Journal of Geophysical Research: Atmospheres*, 114(D1). <https://doi.org/10.1029/2009JD012388>
- Oberheide, J., Hagan, M. E., Richmond, A. D., & Forbes, J. M. (2015). Dynamical meteorology| atmospheric tides. *Encyclopedia of atmospheric sciences*, 287-297. <http://dx.doi.org/10.1016/B978-0-12-382225-3.00409-6>
- Pancheva, D. (2001). Non-linear interaction of tides and planetary waves in the mesosphere and lower thermosphere: observations over Europe. *Physics and Chemistry of the Earth, Part C: Solar, Terrestrial & Planetary Science*, 26(6), 411-418. [https://doi.org/10.1016/S1464-1917\(01\)00022-8](https://doi.org/10.1016/S1464-1917(01)00022-8)
- Pancheva, D., Mitchell, N. J., Younger, P. T., & Muller, H. G. (2003). Intra-seasonal oscillations observed in the MLT region above UK (52° N, 2° W) and ESRANGE (68° N, 21° E). *Geophysical research letters*, 30(21). <https://doi.org/10.1029/2003GL017809>

- Pancheva, D. V., & Mitchell, N. J. (2004). Planetary waves and variability of the semidiurnal tide in the mesosphere and lower thermosphere over Esrange (68 N, 21 E) during winter. *Journal of Geophysical Research: Space Physics*, 109(A8). <https://doi.org/10.1029/2004JA010433>
- Pancheva, D., Mitchell, N. J., Manson, A. H., Meek, C. E., Jacobi, C., Portnyagin, Y., ... & Muller, H. G. (2004). Variability of the quasi-2-day wave observed in the MLT region during the PSMOS campaign of June–August 1999. *Journal of atmospheric and solar-terrestrial physics*, 66(6-9), 539-565. <https://doi.org/10.1016/j.jastp.2004.01.008>
- Pancheva, D. V., Mukhtarov, P. J., Shepherd, M. G., Mitchell, N. J., Fritts, D. C., Riggin, D. M., ... & Kikuchi, T. (2006). Two-day wave coupling of the low-latitude atmosphere-ionosphere system. *Journal of Geophysical Research: Space Physics*, 111(A7). <https://doi.org/10.1029/2005JA011562>
- Pancheva, D. V., Mukhtarov, P. J., & Andonov, B. A. (2007). Zonally symmetric oscillations in the Northern Hemisphere stratosphere during the winter of 2003–2004. *Geophysical Research Letters*, 34(4). <https://doi.org/10.1029/2006GL028666>
- Pancheva, D., Mukhtarov, P., Mitchell, N. J., Merzlyakov, E., Smith, A. K., Andonov, B., ... & Murayama, Y. (2008a). Planetary waves in coupling the stratosphere and mesosphere during the major stratospheric warming in 2003/2004. *Journal of Geophysical Research: Atmospheres*, 113(D12). <https://doi.org/10.1029/2007JD009011>
- Pancheva, D. V., Mukhtarov, P. J., Mitchell, N. J., Fritts, D. C., Riggin, D. M., Takahashi, H., ... & Ramkumar, G. (2008b). Planetary wave coupling (5–6-day waves) in the low-latitude atmosphere–ionosphere system. *Journal of Atmospheric and Solar-Terrestrial Physics*, 70(1), 101-122. <https://doi.org/10.1016/j.jastp.2007.10.003>
- Pancheva, D., Mukhtarov, P., Andonov, B., Mitchell, N. J., & Forbes, J. M. (2009a). Planetary waves observed by TIMED/SABER in coupling the stratosphere–mesosphere–lower thermosphere during the winter of 2003/2004: part 1—comparison with the UKMO temperature results. *Journal of Atmospheric and Solar-Terrestrial Physics*, 71(1), 61-74. <https://doi.org/10.1016/j.jastp.2008.09.016>
- Pancheva, D., Mukhtarov, P., Andonov, B., Mitchell, N. J., & Forbes, J. M. (2009b). Planetary waves observed by TIMED/SABER in coupling the stratosphere–mesosphere–lower thermosphere during the winter of 2003/2004: Part 2—Altitude and latitude planetary wave structure. *Journal of Atmospheric and Solar-Terrestrial Physics*, 71(1), 75-87. <https://doi.org/10.1016/j.jastp.2008.09.027>
- Pancheva, D., Mukhtarov, P., & Smith, A. K. (2014). Non-migrating tidal variability in the SABER/TIMED mesospheric ozone. *Geophysical Research Letters*, 41(11), 4059-4067. <https://doi.org/10.1002/2014GL059844>
- Pancheva, D., Mukhtarov, P., & Siskind, D. E. (2018). The quasi-6-day waves in NOGAPS-ALPHA forecast model and their climatology in MLS/Aura measurements (2005–2014). *Journal of Atmospheric and Solar-Terrestrial Physics*, 181, 19-37. <https://doi.org/10.1016/j.jastp.2018.10.008>

- Pedatella, N. M., & Forbes, J. M. (2010). Evidence for stratosphere sudden warming-ionosphere coupling due to vertically propagating tides. *Geophysical Research Letters*, 37(11). <https://doi.org/10.1029/2010GL043560>
- Pedatella, N. M., & Liu, H. L. (2013). The influence of atmospheric tide and planetary wave variability during sudden stratosphere warmings on the low latitude ionosphere. *Journal of Geophysical Research: Space Physics*, 118(8), 5333-5347. <https://doi.org/10.1002/jgra.50492>
- Pedatella, N.M., Liu, H.L., Sassi, F., Lei, J., Chau, J.L. and Zhang, X., 2014. Ionosphere variability during the 2009 SSW: Influence of the lunar semidiurnal tide and mechanisms producing electron density variability. *J. Geophys. Res.* 119(5), pp.3828-3843. <https://doi.org/10.1002/2014JA019849>
- Pedatella, N. M., Chau, J. L., Schmidt, H., Goncharenko, L. P., Stolle, C., Hocke, K., ... & Siddiqui, T. A. (2018). How Sudden stratospheric warmings affect the whole atmosphere. <http://dx.doi.org/10.1029/2018EO092441>
- Pedlosky, J. (1964). The stability of currents in the atmosphere and the ocean: Part i. *Journal of Atmospheric Sciences*, 21 (2), 201–219. [https://doi.org/10.1175/1520-0469\(1964\)021<0201:TSOCIT>2.0.CO](https://doi.org/10.1175/1520-0469(1964)021<0201:TSOCIT>2.0.CO)
- Plumb, R. A. (1983). Baroclinic instability of the summer mesosphere: A mechanism for the quasi-two-day wave? *Journal of the Atmospheric Sciences*, 40(1), 262–270. [https://doi.org/10.1175/1520-0469\(1983\)040<0262:BIOTSM>2.0.CO;2](https://doi.org/10.1175/1520-0469(1983)040<0262:BIOTSM>2.0.CO;2)
- Press, W. H. (1996). *Numerical recipes in Fortran* (No. BOOK).
- Ramesh, K., & Smith, A. K. (2021). Long-term variability and tendencies in non-migrating diurnal tide from WACCM6 simulations during 1850–2014. *Journal of Geophysical Research: Space Physics*, 126, e2020JA028904. <https://doi.org/10.1029/2020JA028904>
- Randall, C. E., Manney, G. L., Allen, D. R., Bevilacqua, R. M., Hornstein, J., Treppe, C., ... & Bodeker, G. (2005). Reconstruction and simulation of stratospheric ozone distributions during the 2002 austral winter. *Journal of the atmospheric sciences*, 62(3), 748-764. <https://doi.org/10.1175/JAS-3336.1>
- Randel, W. J. (1994). Observations of the 2-day wave in NMC stratospheric analyses. *Journal of Atmospheric Sciences*, 51(2), 306-313. [https://doi.org/10.1175/1520-0469\(1994\)051<0306:OOTDWI>2.0.CO;2](https://doi.org/10.1175/1520-0469(1994)051<0306:OOTDWI>2.0.CO;2)
- Rao, J., Garfinkel, C. I., White, I. P., & Schwartz, C. (2020). The Southern Hemisphere minor sudden stratospheric warming in September 2019 and its predictions in S2S models. *Journal of Geophysical Research: Atmospheres*, 125(14), e2020JD032723. <https://doi.org/10.1029/2020JD032723>
- Rao, J., & Garfinkel, C. I. (2021). Projected changes of stratospheric final warmings in the Northern and Southern Hemispheres by CMIP5/6 models. *Climate Dynamics*, 56(9), 3353-3371. <https://doi.org/10.1007/s00382-021-05647-6>

- Reichler, T., Kim, J., Manzini, E., & Kröger, J. (2012). A stratospheric connection to Atlantic climate variability. *Nature Geoscience*, 5(11), 783-787. <https://doi.org/10.1038/ngeo1586>
- Rossby, C. G., Willett, H. C., Holmboe, M., Namias, J., Page, L., & Allen, R. (1939). Relation between variations in the intensity of the zonal circulation of the atmosphere and the displacements of the permanent centers of action atmosphere and the displacements of the permanent centers of action. https://elischolar.library.yale.edu/journal_of_marine_research/544
- Salby ML (1981). Rossby normal modes in nonuniform background configurations. Part II. Equinox and solstice conditions. *Journal of Atmospheric Sciences*, 38:1827–1840. [https://doi.org/10.1175/1520-0469\(1981\)038%3c1827:RNMINB%3e2.0.CO;2](https://doi.org/10.1175/1520-0469(1981)038%3c1827:RNMINB%3e2.0.CO;2)
- Salby, M. L., & Callaghan, P. F. (2001). Seasonal Amplification of the 2-Day Wave: Relationship between Normal Mode and Instability. *Journal of Atmospheric Sciences*, 58 (14), 1858-1869. [https://doi.org/10.1175/1520-0469\(2001\)058<1858:SAOTDW>2.0.CO;2](https://doi.org/10.1175/1520-0469(2001)058<1858:SAOTDW>2.0.CO;2)
- Sassi, F., Liu, H. L., Ma, J., & Garcia, R. R. (2013). The lower thermosphere during the Northern Hemisphere winter of 2009: A modeling study using high-altitude data assimilation products in WACCM-X. *Journal of Geophysical Research: Atmospheres*, 118(16), 8954-8968. <https://doi.org/10.1002/jgrd.50632>
- Savenkova, E. N., Gavrilov, N. M., & Pogoreltsev, A. I. (2017). On statistical irregularity of stratospheric warming occurrence during northern winters. *Journal of Atmospheric and Solar-Terrestrial Physics*, 163 , 14–22. <https://doi.org/10.1016/j.jastp.2017.06.007>
- Scargle, J. D. (1982). Studies in astronomical time series analysis. II-Statistical aspects of spectral analysis of unevenly spaced data. *Astrophysical Journal*, Part 1, vol. 263, Dec. 15, 1982, p. 835-853., 263, 835-853. <https://doi.org/10.1086/160554>
- Scherhag, R. (1952). Die explosionsartigen Stratosphärenenerwärmungen des Spätwinters 1951/52. *Berichte des Deutschen Wetterdienstes in der US-Zone*, 6(38), 51–63.
- Schoeberl, M. R. (1978). Stratospheric warmings: Observations and theory. *Reviews of Geophysics*, 16 (4), 521–538. <https://doi.org/10.1029/RG016i004p00521>
- Schulz, M., & Stattegger, K. (1997). SPECTRUM: Spectral analysis of unevenly spaced paleoclimatic time series. *Computers & Geosciences*, 23(9), 929-945. [https://doi.org/10.1016/S0098-3004\(97\)00087-3](https://doi.org/10.1016/S0098-3004(97)00087-3)
- Seviour, W. J. M., Mitchell, D. M., & Gray, L. J. (2013). A practical method to identify displaced and split stratospheric polar vortex events. *Geophysical Research Letters*, 40, 5268–5273. <https://doi.org/10.1002/grl.50927>
- Shaw, T. A., & Shepherd, T. G. (2008). Raising the roof. *Nature geoscience*, 1(1), 12-13. <https://doi.org/10.1038/ngeo.2007.53>
- Shepherd, T. G. (2000). The middle atmosphere. *Journal of Atmospheric and Solar-Terrestrial Physics*, 62(17-18), 1587-1601. [https://doi.org/10.1016/S1364-6826\(00\)00114-0](https://doi.org/10.1016/S1364-6826(00)00114-0)
- Siddiqui, T. A., Maute, A., Pedatella, N., Yamazaki, Y., Lühr, H., & Stolle, C. (2018, November). On the variability of the semidiurnal solar and lunar tides of the equatorial electrojet during

- sudden stratospheric warmings. In *Annales Geophysicae* (Vol. 36, No. 6, pp. 1545-1562). Copernicus GmbH. <https://doi.org/10.5194/angeo-36-1545-2018>
- Singh, D., Mitra, G., Guharay, A., Pallamraju, D., & Gurubaran, S. (2024). Quasi-two-day wave amplification through interhemispheric coupling during the 2010 austral summer. *Advances in Space Research*, 73(7), 3452-3463. <https://doi.org/10.1016/j.asr.2023.06.044>
- Sinnhuber, B. M., Weber, M., Amankwah, A., & Burrows, J. P. (2003). Total ozone during the unusual Antarctic winter of 2002. *Geophysical research letters*, 30(11). <https://doi.org/10.1029/2002GL016798>
- Sivakumar, V., Morel, B., Bencherif, H., Baray, J.-L., Baldy, S., Hauchecorne, A., & Rao, P. (2004). Rayleigh lidar observation of a warm stratopause over a tropical site, gadanki (13.5°N; 79.2°E). *Atmospheric Chemistry and Physics*, 4 (7), 1989–1996. <https://doi.org/10.5194/acp-4-1989-2004>
- Smith, A. K. (2003). The origin of stationary planetary waves in the upper mesosphere. *Journal of the atmospheric sciences*, 60(24), 3033-3041. [https://doi.org/10.1175/15200469\(2003\)060<3033:TOOSPW>2.0.CO;2](https://doi.org/10.1175/15200469(2003)060<3033:TOOSPW>2.0.CO;2)
- Smith, A. K. (2012). Interactions between the lower, middle and upper atmosphere. *Space science reviews*, 168, 1-21. <https://doi.org/10.1007/s11214-011-9791-y>
- Smith, A. K., Pedatella, N. M., & Mullen, Z. K. (2020). Interhemispheric coupling mechanisms in the middle atmosphere of WACCM6. *Journal of the Atmospheric Sciences*, 77(3), 1101-1118. <https://doi.org/10.1175/JAS-D-19-0253.1>
- Sridharan, S., Sathishkumar, S., & Gurubaran, S. (2012). Variabilities of mesospheric tides during sudden stratospheric warming events of 2006 and 2009 and their relationship with ozone and water vapour. *Journal of atmospheric and solar-terrestrial physics*, 78, 108-115. <https://doi.org/10.1016/j.jastp.2011.03.013>
- Sridharan, S. (2019). Seasonal variations of low-latitude migrating and non-migrating diurnal and semidiurnal tides in TIMED-SABER temperature and their relationship with source variations. *Journal of Geophysical Research: Space Physics*, 124, 3558–3572. <https://doi.org/10.1029/2018JA026190>
- Stober, G. (2009). Astrophysical studies on meteors using a SKiYMET all-sky meteor radar. Ph. D. Thesis.
- Sugar, G. R. (1964). Radio propagation by reflection from meteor trails. *Proceedings of the IEEE*, 52(2), 116-136. <https://doi.org/10.1109/PROC.1964.2801>
- Talaat, E. R., Yee, J.-H., & Zhu, X. (2002). The 6.5-day wave in the tropical stratosphere and mesosphere. *Journal of Geophysical Research: Atmospheres*, 107 (D12), ACL 1-1-ACL 1-5. <https://doi.org/10.1029/2001JD000822>
- Teitelbaum, H., & Vial, F. (1991). On tidal variability induced by non-linear interaction with planetary waves. *Journal of Geophysical Research*, 96(A8), 14,169–14,178. <https://doi.org/10.1029/91JA01019>

- Tomikawa, Y., Sato, K., Watanabe, S., Kawatani, Y., Miyazaki, K., & Takahashi, M. (2012). Growth of planetary waves and the formation of an elevated stratopause after a major stratospheric sudden warming in a T213L256 GCM. *Journal of Geophysical Research: Atmospheres*, 117(D16). <https://doi.org/10.1029/2011JD017243>
- Torrence, C., & Compo, G. P. (1998). A practical guide to wavelet analysis. *Bulletin of the American Meteorological society*, 79(1), 61-78. [https://doi.org/10.1175/1520-0477\(1998\)079<0061:APGTWA>2.0.CO;2](https://doi.org/10.1175/1520-0477(1998)079<0061:APGTWA>2.0.CO;2)
- Thiéblemont, R., Ayarzagüena, B., Matthes, K., Bekki, S., Abalichin, J., & Langematz, U. (2019). Drivers and surface signal of interannual variability of boreal stratospheric final warmings. *Journal of Geophysical Research: Atmospheres*, 124, 5400–5417. <https://doi.org/10.1029/2018JD029852>
- Tripathi, O. P., Baldwin, M., Charlton-Perez, A., Charron, M., Eckermann, S. D., Gerber, E., ... & Son, S. W. (2015). The predictability of the extratropical stratosphere on monthly time-scales and its impact on the skill of tropospheric forecasts. *Quarterly Journal of the Royal Meteorological Society*, 141(689), 987-1003. <https://doi.org/10.1002/qj.2432>
- Truskowski, A. O., Forbes, J. M., Zhang, X., & Palo, S. E. (2014). New perspectives on thermosphere tides: 1. Lower thermosphere spectra and seasonal-latitudinal structures. *Earth, Planets and Space*, 66, 1-17. <https://doi.org/10.1186/s40623-014-0136-4>
- Tsuda, T., Kato, S., & Vincent, R. (1988). Long period wind oscillations observed by the Kyoto meteor radar and comparison of the quasi-2-day wave with Adelaide HF radar observations. *Journal of Atmospheric and Terrestrial Physics*, 50(3), 225-230. [https://doi.org/10.1016/0021-9169\(88\)90071-2](https://doi.org/10.1016/0021-9169(88)90071-2)
- Tunbridge, V. M., Sandford, D. J., & Mitchell, N. J. (2011). Zonal wave numbers of the summertime 2 day planetary wave observed in the mesosphere by EOS Aura Microwave Limb Sounder. *Journal of Geophysical Research: Atmospheres*, 116(D11). <https://doi.org/10.1029/2010JD014567>
- Varotsos, C. (2002). The southern hemisphere ozone hole split in 2002. *Environmental Science and Pollution Research*, 9, 375-376. <https://doi.org/10.1007/BF02987584>
- Veenus, V., Das, S. S., & David, L. M. (2023). Ozone Changes Due To Sudden Stratospheric Warming-Induced Variations in the Intensity of Brewer-Dobson Circulation: A Composite Analysis Using Observations and Chemical-Transport Model. *Geophysical Research Letters*, 50(13), e2023GL103353. <https://doi.org/10.1029/2023GL103353>
- Verbeeck, C., & Wislez, J. M. (2006). Report on the second Radio Meteor School, September 10-14 2005, Oostmalle, Belgium. In *Proceedings of the International Meteor Conference, 24th IMC, Oostmalle, Belgium, 2005* (pp. 6-8).
- Vincent, R. A., Kovalam, S., Reid, I. M., Murphy, D. J., & Klekociuk, A. (2022). Southern Hemisphere Stratospheric Warmings and Coupling to the Mesosphere-Lower Thermosphere. *Journal of Geophysical Research: Atmospheres*, 127(15), e2022JD036558. <https://doi.org/10.1029/2022JD036558>

- Wan, W., Liu, L., Pi, X., Zhang, M. L., Ning, B., Xiong, J., & Ding, F. (2008). Wavenumber-4 patterns of the total electron content over the low latitude ionosphere. *Geophysical Research Letters*, 35(12). <https://doi.org/10.1029/2008GL033755>
- Weber, M., Dhomse, S., Wittrock, F., Richter, A., Sinnhuber, B. M., & Burrows, J. P. (2003). Dynamical control of NH and SH winter/spring total ozone from GOME observations in 1995–2002. *Geophysical Research Letters*, 30(11). <https://doi.org/10.1029/2002GL016799>
- Whiteway, J. A., & Carswell, A. I. (1994). Rayleigh lidar observations of thermal structure and gravity wave activity in the high arctic during a stratospheric warming. *Journal of Atmospheric Sciences*, 51 (21), 3122–3136. [https://doi.org/10.1175/1520-0469\(1994\)051<3122:RLOOTS>2.0.CO;2](https://doi.org/10.1175/1520-0469(1994)051<3122:RLOOTS>2.0.CO;2)
- Williams, C. R., & Avery, S. K. (1992). Analysis of long-period waves using the mesosphere-stratosphere-troposphere radar at Poker Flat, Alaska. *Journal of Geophysical Research: Atmospheres*, 97(D18), 20855–20861. <https://doi.org/10.1029/92JD02052>
- Wislez, J. M. (1996). Forward scattering of radio waves off meteor trails. In *Proceedings of the International Meteor Conference, 14th IMC, Brandenburg, Germany, 1995* (pp. 99–117).
- Wu, D. L., Fishbein, E. F., Read, W. G., & Waters, J. W. (1996). Excitation and evolution of the quasi-2-day wave observed in UARS/MLS temperature measurements. *Journal of Atmospheric Sciences*, 53(5), 728–738. [https://doi.org/10.1175/1520-0469\(1996\)053<0728:EAEOTQ>2.0.CO;2](https://doi.org/10.1175/1520-0469(1996)053<0728:EAEOTQ>2.0.CO;2)
- Xu, J., Smith, A. K., Liu, M., Liu, X., Gao, H., Jiang, G., & Yuan, W. (2014). Evidence for non-migrating tides produced by the interaction between tides and stationary planetary waves in the stratosphere and lower mesosphere. *Journal of Geophysical Research: Atmospheres*, 119, 471–489. <https://doi.org/10.1002/2013JD020150>
- Xu, F., & San Liang, X. (2017). On the generation and maintenance of the 2012/13 sudden stratospheric warming. *Journal of the Atmospheric Sciences*, 74(10), 3209–3228. <https://doi.org/10.1175/JAS-D-17-0002.1>
- Yamazaki, Y., Kosch, M. J., & Emmert, J. T. (2015). Evidence for stratospheric sudden warming effects on the upper thermosphere derived from satellite orbital decay data during 1967–2013. *Geophysical Research Letters*, 42(15), 6180–6188. <https://doi.org/10.1002/2015GL065395>
- Yamazaki, Y., Matthias, V., Miyoshi, Y., Stolle, C., Siddiqui, T., Kervalishvili, G., . . . others (2020). September 2019 antarctic sudden stratospheric warming: Quasi-6-day wave burst and ionospheric effects. *Geophysical Research Letters*, 47 (1), e2019GL086577. <https://doi.org/10.1029/2019GL086577>
- Yamazaki, Y. (2023). A method to derive Fourier–wavelet spectra for the characterization of global-scale waves in the mesosphere and lower thermosphere and its MATLAB and Python software (fourierwavelet v1. 1). *Geoscientific Model Development*, 16(16), 4749–4766. <https://doi.org/10.5194/gmd-16-4749-2023>
- Yue, J., & Gan, Q. (2021). Quasi-two-day wave modulation of carbon dioxide in the mesosphere and lower thermosphere. *Journal of Atmospheric and Solar-Terrestrial Physics*, 224, 105750. <https://doi.org/10.1016/j.jastp.2021.105750>

- Zhang, X., & Forbes, J. M. (2014). Lunar tide in the thermosphere and weakening of the northern polar vortex. *Geophysical Research Letters*, 41(23), 8201-8207. <https://doi.org/10.1002/2014GL062103>
- Zhao, G., Liu, L., Wan, W., Ning, B., & Xiong, J. (2005). Seasonal behavior of meteor radar winds over Wuhan. *Earth, planets and space*, 57(1), 61-70. <https://doi.org/10.1186/BF03351806>
- Zülicke, C., & Becker, E. (2013). The structure of the mesosphere during sudden stratospheric warmings in a global circulation model. *Journal of Geophysical Research: Atmospheres*, 118(5), 2255-2271. <https://doi.org/10.1002/jgrd.50219>
- Zülicke, C., Becker, E., Matthias, V., Peters, D. H., Schmidt, H., Liu, H. L., ... & Mitchell, D. M. (2018). Coupling of stratospheric warmings with mesospheric coolings in observations and simulations. *Journal of Climate*, 31(3), 1107-1133. <https://doi.org/10.1175/JCLI-D-17-0047.1>

List of Publications Included in Thesis

Publications In Refereed Journals

1. **Mitra, G.**, Guharay, A., Batista, P. P., & Buriti, R. A. (2022). Impact of the September 2019 minor sudden stratospheric warming on the low-latitude middle atmospheric planetary wave dynamics. *Journal of Geophysical Research: Atmospheres*, e2021JD035538. <https://doi.org/10.1029/2021JD035538>
2. **Mitra, G.**, Guharay, A., Batista, P. P., Buriti, R. A., & T. Moffat-Griffin (2023). Investigation on the MLT tidal variability during September 2019 minor sudden stratospheric warming. *Advances in Space Research*, 71(1), 869-882. <https://doi.org/10.1016/j.asr.2022.08.017>
3. **Mitra, G.**, Guharay, A., Conte, J. F., & Chau, J. L. (2023). Signature of two-step non-linear interactions associated to zonally symmetric waves during major sudden stratospheric warmings. *Geophysical Research Letters*, 50, e2023GL104756. <https://doi.org/10.1029/2023GL104756>
4. **Mitra, G.**, & Guharay, A. (2024). Impact of sudden stratospheric warming on middle atmospheric circulation in the southern hemisphere: A comparative study. *Journal of Atmospheric and Solar-Terrestrial Physics*, 254, 106173. <https://doi.org/10.1016/j.jastp.2024.106173>
5. **Mitra, G.**, Guharay, A., & Paulino, I. (2024). Signature of a zonally symmetric semidiurnal tide during major sudden stratospheric warmings and plausible mechanisms: a case study. *Scientific Reports*, 14(1), 23806. <https://doi.org/10.1038/s41598-024-72594-7>

Under preparation

6. **Mitra, G.**, Guharay, A., Batista, P. P., Buriti, R. A., Renkwitz, T., & Conte J. F. (2024). Imprint of quasi-16-day period in boreal summer through modulation of quasi-2-day wave: A signature of interhemispheric coupling.

List of Publications Outside Thesis

Publications In Refereed Journals

7. Singh, D., **Mitra, G.**, Guharay, A., Pallamraju, D., & Gurubaran, S. (2024). Quasi-two-day wave amplification through interhemispheric coupling during the 2010 austral summer. *Advances in Space Research*, 73(7), 3452-3463.
<https://doi.org/10.1016/j.asr.2023.06.044>

Under Review

8. Fontes, P. A., Muella, M. T. A. H., Resende, L. C. A., Jesus, R. D., Fagundes, P. R., **Mitra, G.**, Pillat, V. G., Batista, P. P., Buriti, R. A., Correia, E., Peter, T. M. (2024). Effect of the Planetary Wave Oscillation in the E-Sporadic (Es) Layers during a Rare Antarctic Sudden Stratospheric Warming in 2019.

JGR Atmospheres

RESEARCH ARTICLE

10.1029/2021JD035538

Key Points:

- Both traveling and stationary planetary waves with zonal wavenumber 1 seem to play a salient role in preconditioning the warming event
- Existing instability is believed to support the growth of the quasi-6-day wave (Q6DW) in post warming interval
- The Q6DW and Q16DW are found to propagate from high and mid latitudes to low latitudes during the warming

Correspondence to:

G. Mitra,
reachmitragourav@gmail.com

Citation:




Mitra, G., Guharay, A., Batista, P. P., & Buriti, R. A. (2022). Impact of the September 2019 minor sudden stratospheric warming on the low-latitude middle atmospheric planetary wave dynamics. *Journal of Geophysical Research: Atmospheres*, 127, e2021JD035538. <https://doi.org/10.1029/2021JD035538>

Received 7 JUL 2021
Accepted 14 DEC 2021

Author Contributions:

Conceptualization: G. Mitra, A. Guharay
Data curation: R. A. Buriti
Formal analysis: G. Mitra
Resources: P. P. Batista
Supervision: A. Guharay
Writing – review & editing: P. P. Batista, R. A. Buriti

Impact of the September 2019 Minor Sudden Stratospheric Warming on the Low-Latitude Middle Atmospheric Planetary Wave Dynamics

G. Mitra^{1,2} , A. Guharay¹ , P. P. Batista³ , and R. A. Buriti⁴

¹Space and Atmospheric Sciences Division, Physical Research Laboratory, Ahmedabad, India, ²Department of Physics, Indian Institute of Technology, Gandhinagar, India, ³Heliophysics, Planetary Sciences and Aeronomy Division, National Institute for Space Research, INPE, São José Dos Campos, Brazil, ⁴Department of Physics, Federal University of Campina Grande, Campina Grande, Brazil

Abstract Planetary wave (PW) associated dynamical variability in the equatorial and extratropical middle atmosphere during the September 2019 Southern hemisphere minor sudden stratospheric warming (SSW) is investigated utilizing meteor radar wind observations from São João do Cariri (7.4°S, 36.5°W) and Cachoeira Paulista (22.7°S, 45°W) and reanalysis data. Signature of the mesospheric warming in conjunction with the stratospheric cooling is found at low latitudes. The strong westerly wind at low latitudes decelerates notably near 65 km at the onset of the warming episode, although no wind reversal is observed. The wind spectra reveal a prevalent quasi-16-day wave (Q16DW) prior to the SSW and existence of a quasi-6-day wave (Q6DW) after the warming event. Possible existence of barotropic/baroclinic instability in the low and mid latitude middle atmosphere may be responsible for exciting the Q6DW. Both traveling and stationary waves exhibit notable activities during the warming event. Although involvement of both zonal wavenumbers 1 and 2 PWs are found in the event, PW with zonal wavenumber 1 seems to play a vital role in preconditioning the same. Furthermore, significant latitudinal mixing of air mass between the tropics and high latitudes is evident in the potential vorticity map. The Eliassen-Palm flux diagnosis shows the propagation of the Q6DW and Q16DW from mid to low latitudes during the warming event.

Plain Language Summary A minor but impactful sudden stratospheric warming event occurred in the Southern hemisphere during September 2019. This event is characterized by a marked deceleration of the zonal mean westerlies at polar stratosphere although no wind reversal is observed. Simultaneously, stratospheric temperature at high latitudes increases sharply by more than 25 K within a few days. During the same warming event, stratospheric cooling and mesospheric warming is found at the present low latitude stations. The wind spectra reveal a long period wave of about 16 days prior to the warming event in the stratosphere followed by a relatively shorter period wave (~6 days) in the mesosphere. The 6-day wave component is possibly excited due to the instability in the middle atmosphere at low and middle latitudes during the warming episodes. Both traveling and stationary large-scale waves are supposed to play a vital role in preconditioning the warming event. There is also significant meridional air mass mixing during the warming days owing to possible planetary wave (PW) driven weakening of the zonal mean westerlies. The PW fluxes for both the aforementioned components are observed to propagate from high and mid to low latitudes during the warming event.

1. Introduction

Sudden stratospheric warming (SSW) is a dramatic episode in the winter stratosphere, which involves an abrupt increase in polar stratospheric temperature by a few tens of kelvin in several days (Andrews et al., 1987). The SSW was first reported by Scherhag (1952) using radiosonde observations. Major and minor warmings are two main categories of the SSW event. Reversal of temperature gradient poleward of 60° is a signature of both major and minor events, but the reversal of zonal mean zonal wind at 60° latitude and 10 hPa pressure level is the characteristics of a major warming (Labitzke et al., 2005). The occurrence of SSW is more frequent in the Northern hemisphere (NH) than the Southern hemisphere (SH) because of higher planetary wave (PW) activity due to topographic difference and land-sea contrast. Also, the cumulative wave flux requirement to cause SSW

in SH is supposed to be much larger because of stronger SH polar jet as compared to the NH counterpart (Rao et al., 2019).

It is well known that the abnormal change in the stratospheric temperature and the zonal wind due to anomalous PW activity during the SSW has a significant effect on the dynamical variability of the middle atmosphere (Pedatella et al., 2018). Impact of the SSW on the mesosphere and lower thermosphere (MLT) from the NH mid and high latitudes is reported by a handful of previous literatures (Whiteway & Carswell, 1994; Hoffmann et al., 2002). However, a very few studies from the SH mid and high latitudes are available to date (Dowdy et al., 2004). Fritz and Soules (1970) were the first to report the influence of the polar disturbances caused by the SSW on the tropical atmosphere. Past studies found stratospheric cooling in the tropics during the SSW event (Andrews et al., 1987; Guharay & Batista, 2019). There are quite a few investigations on the coupling between low and high latitude middle atmosphere during the SSW event in the NH (Guharay & Sekar, 2012; Kodera, 2006; Sivakumar et al., 2004).

Until now, in the SH, one major SSW occurred in 2002 (Dowdy et al., 2004). Furthermore, observational studies on the response of the tropical middle atmosphere during major SSW from the SH are insufficient (Guharay et al., 2014; Guharay & Batista, 2019) and hence more investigations from low latitudes are required to understand low and high latitudes coupling during such dramatic event. Recently, a minor but impactful SSW event occurred in the SH in September 2019 (Lim et al., 2020; Yamazaki et al., 2020). Interestingly, Noguchi et al. (2020) reported substantial enhancement of convective activity in the tropics of the summer hemisphere during the 2019 SH minor warming episode. The 2019 SSW event offered a suitable condition to study the ionospheric variability due to forcing from the lower and middle atmosphere owing to its occurrence during a period of low solar activity (Goncharenko et al., 2020).

Most recently, Yamazaki et al. (2020) observed a quasi-6-day wave (Q6DW) forcing from the middle atmosphere to cause ionospheric variability during the 2019 September warming event. Miyoshi and Yamazaki (2020) concluded that the non-linear interaction between the Q6DW and migrating semidiurnal tide as the excitation mechanism of the 6-day oscillation in the ionosphere during the same event. Unfortunately, the features of the dynamical variability in the middle atmosphere, especially at low latitude during the same event is not yet explored.

Therefore, in our present study, we aim to investigate the PW associated dynamical variability in the equatorial and extratropical middle atmosphere during the September 2019 minor SSW event utilizing meteor radar wind observations from São João do Cariri (7.4°S, 36.5°W) (CA) and Cachoeira Paulista (22.7°S, 45°W) (CP) and global reanalysis data set. Our present study is important in view of the lack of adequate understanding related to the impact of the SSW on the SH low latitude middle atmosphere dynamics.

2. Observational Database

For the present study, we have utilized two databases during the period centered around the minor warming episode ~ from 1 August to 31 October (2019), as described below.

2.1. Meteor Radar

The radar systems at CA and CP are all-sky interferometric meteor radars which operate at a frequency of 35.24 MHz, with pulse width of 13 μ s, pulse repetition frequency of 2 kHz and peak power of 12 kW. It consists of a single three-element Yagi antenna for transmission and five phase-coherent two-element Yagi receiving antennas. The receiving antennas are aligned along two orthogonal baselines with the central one common to both for detecting the echo signal from the meteors. Details of the derivation of the horizontal winds from the meteor trail echoes can be found in the available literature (Hocking et al., 2001). For the present work, we have utilized horizontal wind values within the altitude range 81–99 km with a vertical resolution of 3 km and a temporal resolution of 1 hr.

2.2. ERA5 Database

The ERA5 database provides reanalysis data of various atmospheric parameters available from 1979 to the present time provided by the European Center for Medium-range Weather Forecasts (ECMWF) (Hersbach et al., 2020).

For the present investigation, we have used temperature, zonal wind and meridional wind at 137 model pressure levels within the range 1,000–0.01 hPa (~0–80 km) with a latitudinal and longitudinal grid of $0.1^\circ \times 0.1^\circ$. The closest grid points to CP and CA are chosen as (22.7°S, 45°W) and (7.4°S, 36.5°W) respectively. Thus, the analysis of ERA5 data set is aimed to complement the meteor radar observation for providing a holistic picture of the dynamical variability in the lower and middle atmosphere. Furthermore, the ERA5 global database offers the opportunity to investigate the latitudinal coupling between high and low latitude during such a dynamical event.

3. Results

To identify heating/cooling in a qualitative manner the differences between the zonal mean temperature and temporal mean (August–October 2019) of zonal mean temperature at 10 hPa pressure level in the SH, using the ERA5 data set, are plotted during the interval 1 August to 31 October 2019 (Day of year [DOY] 213 = 1 August) in Figure 1a. At high latitude ($>75^\circ\text{S}$), the temperature difference is mostly negative from DOY 213 to DOY 248. It becomes positive with the maximum warming on 18 September (DOY 261), and the warming persists for the remaining period of study. Noticeable warming greater than 25 K exists between DOY 253 and DOY 263, which is considered as the warming period (SSW event) in our present study as per the criteria defined by McInturff (1978), that is, a temperature increase of at least 25 K in a week or less at any stratospheric altitudes in any region of winter hemisphere. Such warming at mid and high latitudes corresponds to cooling during the period between DOY 243 and DOY 263 in the tropical area, which is the topic of interest in this paper. Relative cooling between DOY 243 and DOY 263 at 10 hPa at low latitudes ($<30^\circ\text{S}$) can be noted from Figure 1a. Figure 1b shows the zonal mean zonal wind during the above-mentioned period at 10 hPa. The strong eastward wind at 10 hPa, 60°S decelerates monotonously by 70 m s^{-1} (approx.) till the end of warming, that is, DOY 263, although there is no wind reversal. The altitudinal profiles of difference between zonal mean temperature and temporal mean of zonal mean temperature at 60°S , 22.7°S (CP latitude) and 7.4°S (CA latitude) are shown in Figures 1c, 1e and 1g, respectively. Similarly, the altitudinal profiles of the zonal mean zonal wind at 60°S , 22.7°S (CP latitude) and 7.4°S (CA latitude) are shown in Figures 1d, 1f, and 1h, respectively. Following observations are noteworthy.

1. At 60°S (Figure 1c), remarkable increase of temperature can be noted in the mid-stratosphere (20–40 km) during the warming period that continues for the remaining period of observations, whereas there is significant cooling at mesospheric altitudes concurrent with the stratospheric warming
2. Westerly wind at 60°S (Figure 1d) diminishes in magnitude at the advent of the warming event in the middle atmosphere with a reversal in the zonal wind at altitudes in the upper stratosphere as prominent during the SSW event. Therefore, the present minor warming episode can be termed high stratospheric warming (Savenkova et al., 2017)
3. However, the low latitude middle atmosphere (Figures 1e and 1g) shows contrasting behavior with respect to high latitude, that is, cooling in the stratosphere coincident with the high latitude warming and warming in the mesosphere concurrent with the high latitude cooling
4. The zonal wind at low latitude (Figures 1f and 1h), especially, at CP near 50–70 km altitude shows noticeable weakening with the advent of the warming. However, at lower latitude (CA) such effect is very weak and exists over narrow altitude region near 65 km

To determine the involvement of traveling PWs (if any) over the present locations, a wavelet analysis using Morlet as a mother wavelet is carried out for the observational interval. Figures 2a–2c and 2d show the wavelet power spectra for zonal wind at 90 km, 0.02 hPa (~80 km), 1 hPa (~48 km) and 10 hPa (~32 km), respectively at CP. Bold white curves in each plot represent 95% confidence level. It is clear from Figure 2a that a Q6DW (also observed by Yamazaki et al. (2020) in the ionosphere) with periods 5–7 days becomes prominent in mid-MLT (90 km) just after the warming, that exists for a few days. At 0.02 hPa (near mesopause), zonal wind wavelet spectrum at CP shows a strong quasi-10-day wave (Q10DW) with periods 9–12 days before the warming event and a relatively weaker Q6DW which exists during and after the warming event as seen in Figure 2b. A quasi-16-day wave (Q16DW) with periodicity in the range 14–20 days exists in the prewarming condition in the mesopause region (0.02 hPa) with lesser strength. Wavelet power spectra for the zonal wind exhibits the Q16DW at 1 hPa (upper stratosphere) before the warming event and weakens in the following interval (Figure 2c). Almost similar feature is observed at 10 hPa, as seen in Figure 2d. The strength of the Q16DW is greater at 1 hPa than that at 10 hPa. Figures 2e–2g and 2h show the meridional wind wavelet spectra at CP at 90 km, 0.02 hPa, 1 hPa and

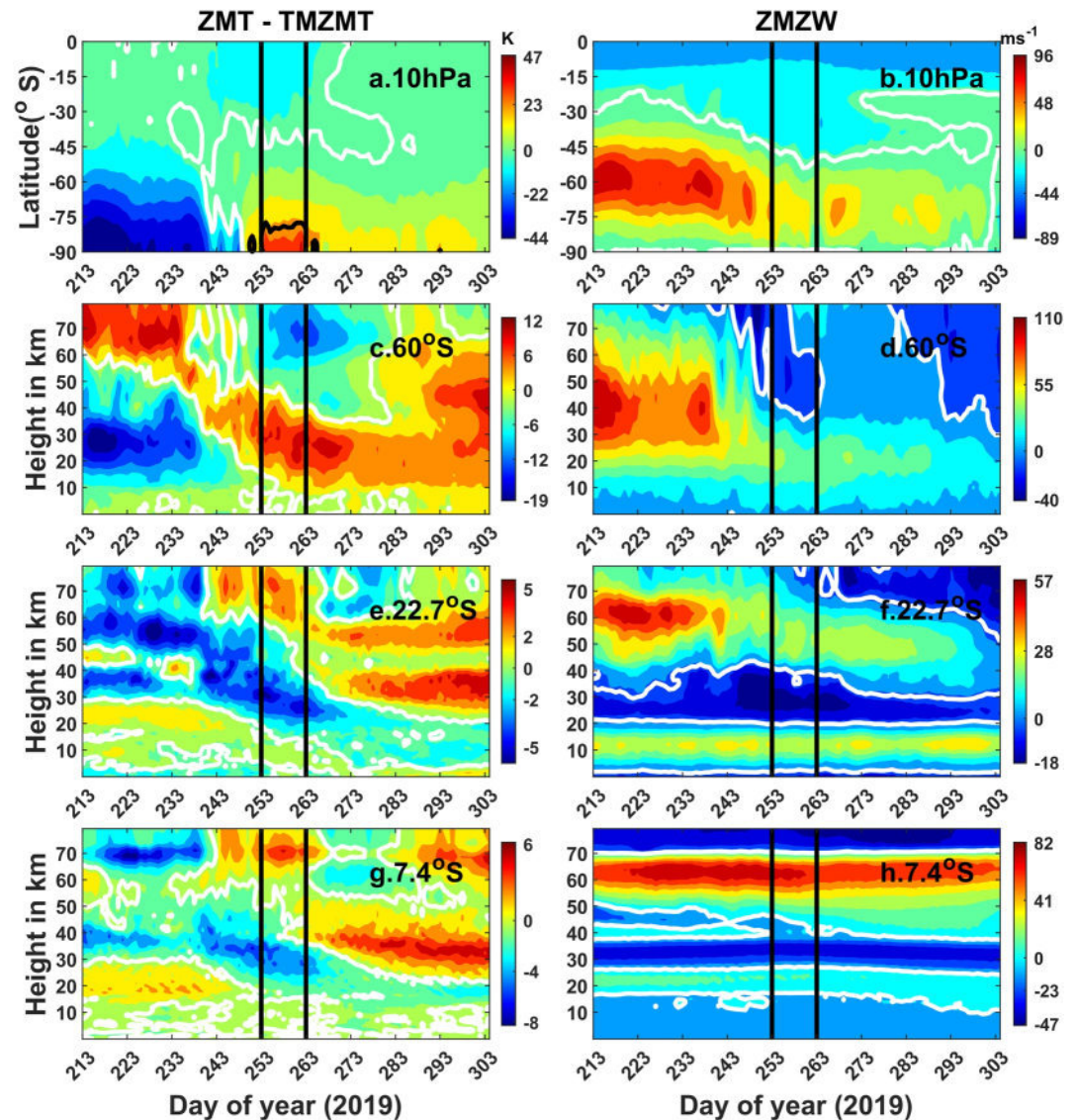


Figure 1. (a) Difference between the zonal mean temperature and temporal mean of zonal mean temperature (ZMT–TMZMT) during August–October 2019 (DOY 213–1 August) and (b) zonal mean zonal wind (ZMWZ) plotted during the same period at 10 hPa pressure level using ERA5. Altitudinal profiles (~0–80 km) of difference between the zonal mean temperature and temporal mean of zonal mean temperature are shown at (c) 60°S, (e) 22.7°S (CP latitude) and (g) 7.4°S (CA latitude). Similarly, altitudinal profiles (~0–80 km) of zonal mean zonal wind are shown at (d) 60°S, (f) 22.7°S (CP latitude) and (h) 7.4°S (CA latitude). The white bold curves represent zero value in all the plots, and the bold black curve represents a value of 25 K in Figure 1a. Region between two vertical lines shows warming period for the present and all the following figures. Please note the change of scale in the colorbars corresponding to each subplot while comparing.

10 hPa, respectively. The Q6DW is observed to be well distributed around the warming days in the mid-MLT region, as seen in Figure 2e. At 0.02 hPa pressure level near the mesopause (Figure 2f), there is a Q10DW during the pre-warming interval, followed by the appearance of a Q6DW which intensifies at the end of warming and continues till DOY 273. In the upper stratosphere at 1 hPa pressure level (Figure 2g), the meridional wind wavelet spectrum exhibits a strong Q16DW before the warming episodes, which weakens by the end of the warming. At 10 hPa (Figure 2h), the Q6DW is found to be dominant for a few days during the pre-warming time and again reappears with comparatively lesser intensity during the warming days, and, the Q16DW appears during the warming days. Additionally, there exists a weak quasi-3-day wave (Q3DW) with periodicity of 3–4 days after the warming event for a short while. Overall, the zonal wind wavelet spectra show robust wave activity in terms of power as compared to the meridional wind wavelet spectra.

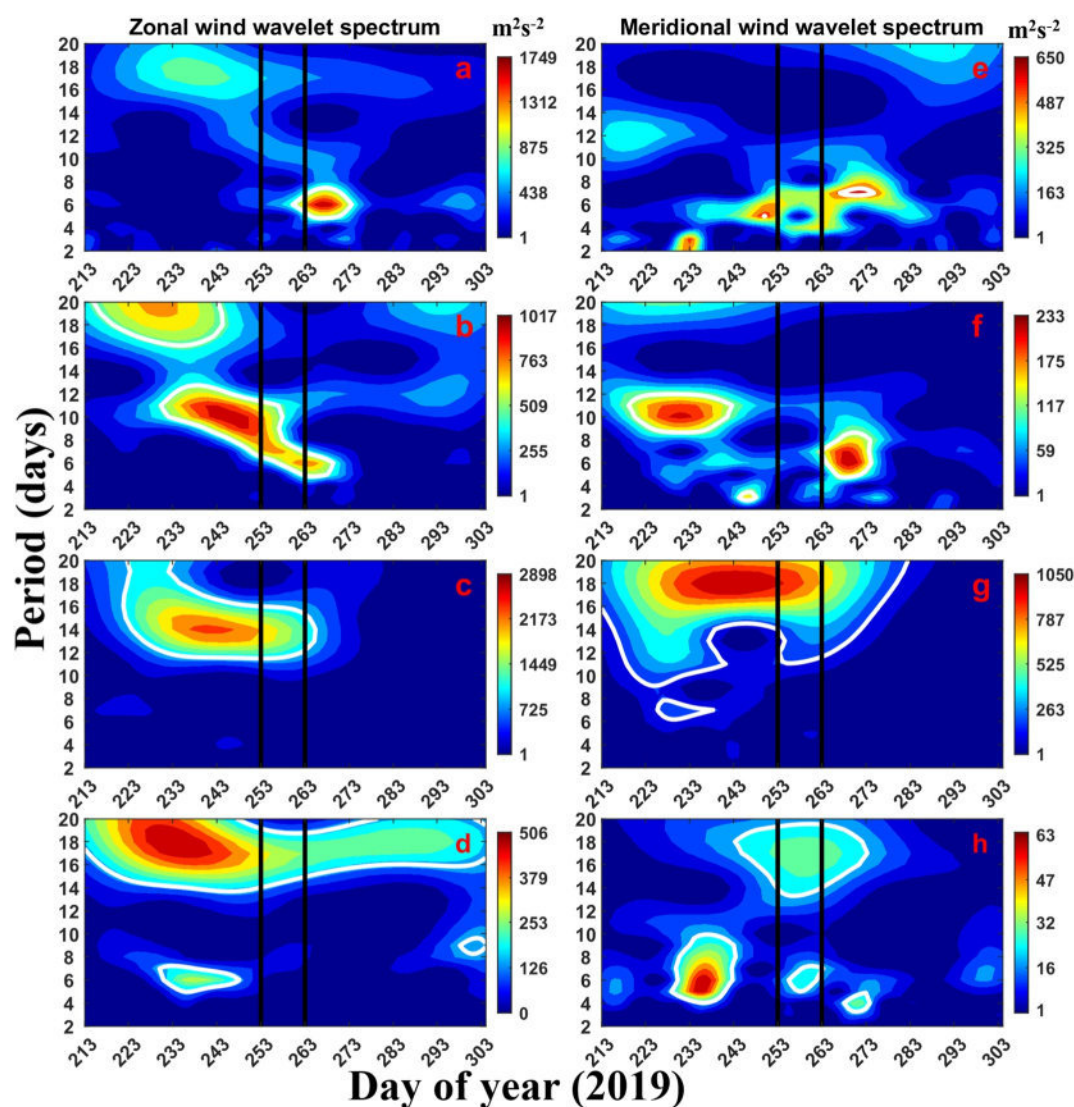


Figure 2. Wavelet power spectra at 90 km for (a) zonal wind, (e) meridional wind using meteor radar. Wavelet spectra in the zonal wind at (b) 0.02 hPa, (c) 1 hPa, (d) 10 hPa and meridional wind at (f) 0.02 hPa, (g) 1 hPa, (h) 10 hPa at CP using ERA5. Bold white curves in each plot represent 95% confidence level. Please note the change of scale in the colorbars corresponding to each subplot while comparing.

Similarly, Figures 3a–3c and 3d represent the zonal wind wavelet spectra for CA at 90 km, 0.02 hPa, 1 hPa and 10 hPa, respectively. The Q10DW feature is significant at 90 km (Figure 3a) during warming days, but its magnitude is lesser as compared to the Q6DW which is present during a short interval following the warming. Enhancement of the Q6DW in the zonal wind wavelet spectrum in the mesopause (0.02 hPa) during a short interval after the warming days is evident from Figure 3b. The Q16DW activity is dominant in the upper stratosphere (1 hPa) before warming days and vanishes at the onset of the warming event (Figure 3c). In the mid-stratosphere (10 hPa) the Q10DW is present throughout the observational period except an interval of around 10 days before the warming onset. On the other hand, the Q16DW enhances during warming days and weakens after the warming, as seen in Figure 3d. Figures 3e–3g and 3h illustrate the PW features in the meridional wind over CA at 90 km, 0.02, 1 and 10 hPa, respectively. There are weak traces of the Q6DW around the warming days at 90 km (Figure 3e). The Q3DW is present before the onset of warming at 0.02 hPa pressure level (Figure 3f). In the upper stratosphere at 1 hPa, the Q16DW is present before the warming days. At the same altitude, the Q3DW becomes significant between DOY 233 and DOY 243, as shown in Figure 3g. The Q3DW is found to be significant before, during and after the warming event at 10 hPa pressure level (Figure 3h).

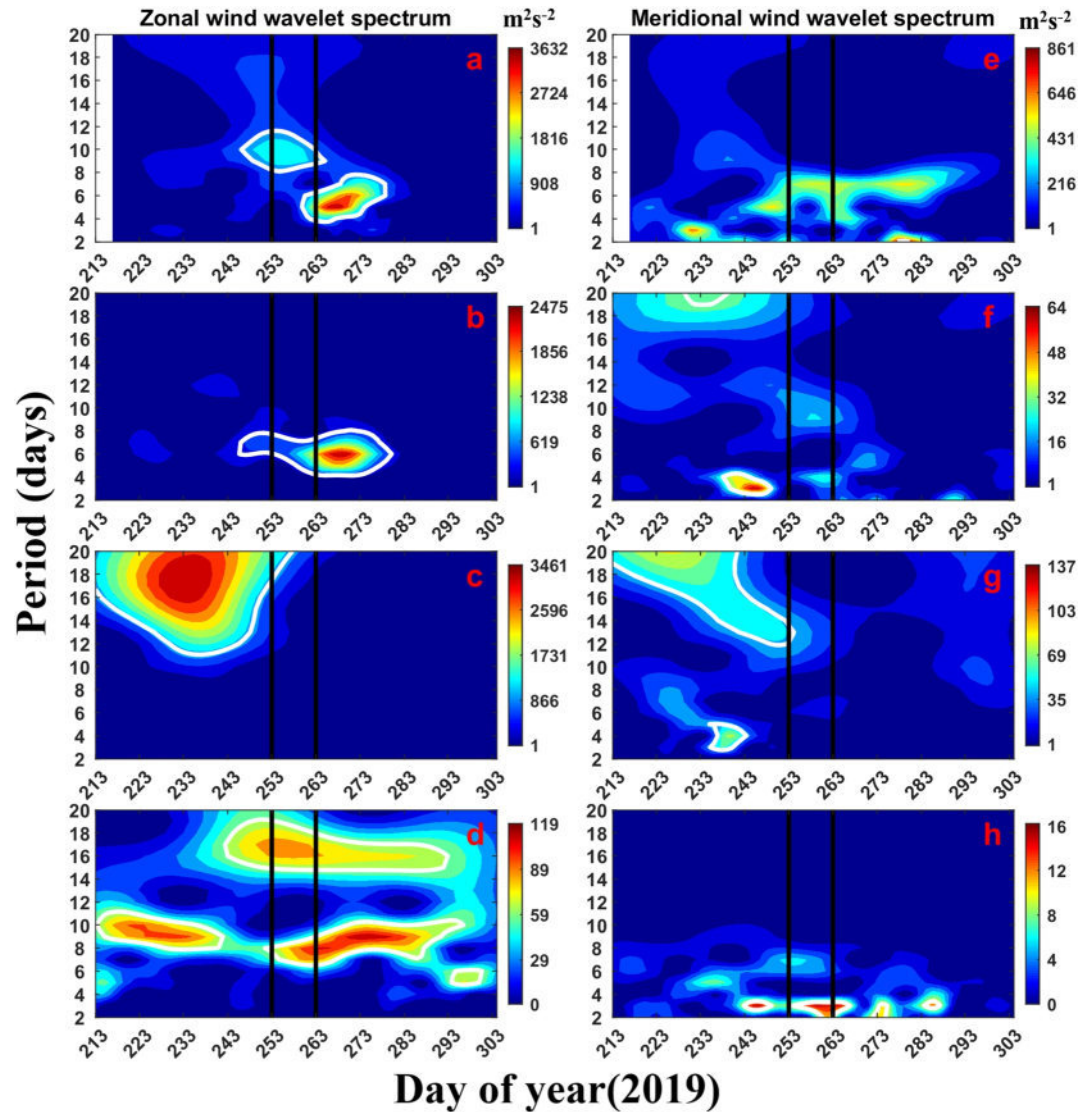


Figure 3. Similar to Figure 2, but shown for CA.

As the wavelet spectra at both observational locations reveal the most dominant periodicities around 6 and 16 days, we further looked into the vertical structure of the two wave components in both wind components in the MLT region as shown in Figure 4. For this purpose, the representative amplitudes of the waves are calculated by using non-linear cosine fit with periods of 6 and 16 days, respectively (Pancheva et al., 2018). As we are interested in looking into the pattern of spatiotemporal variability of the two wave components, consideration of specific periods in the representative amplitude estimation does not affect the interpretation. Figure 4a shows a prominent signature of the Q6DW in the zonal wind during the warming days at CP. The Q16DW in the zonal wind at CP is most active during the pre-warming interval in the MLT region (Figure 4b) although another enhancement is found near top of the MLT during post warming. At CA strong feature of the high Q6DW activity during the late warming phase spread throughout the MLT range can be observed in the zonal wind (Figure 4c). Prominent activity of the Q16DW mostly during the pre-warming interval in the zonal wind at CA is discernible from Figure 4d, although an isolated patch of the wave amplitude can be noted at the lower MLT in the post warming interval. On the other hand, the peak representative amplitude of the Q6DW at CP generally reveals a much weaker signature in the meridional wind as compared to the zonal counterpart as visible at various times in the observational span (Figure 4e). The activity of the Q16DW at CP is found to be notable during pre-warming interval mostly at higher MLT altitudes in the meridional wind as evident in Figure 4f and weaker signature of the

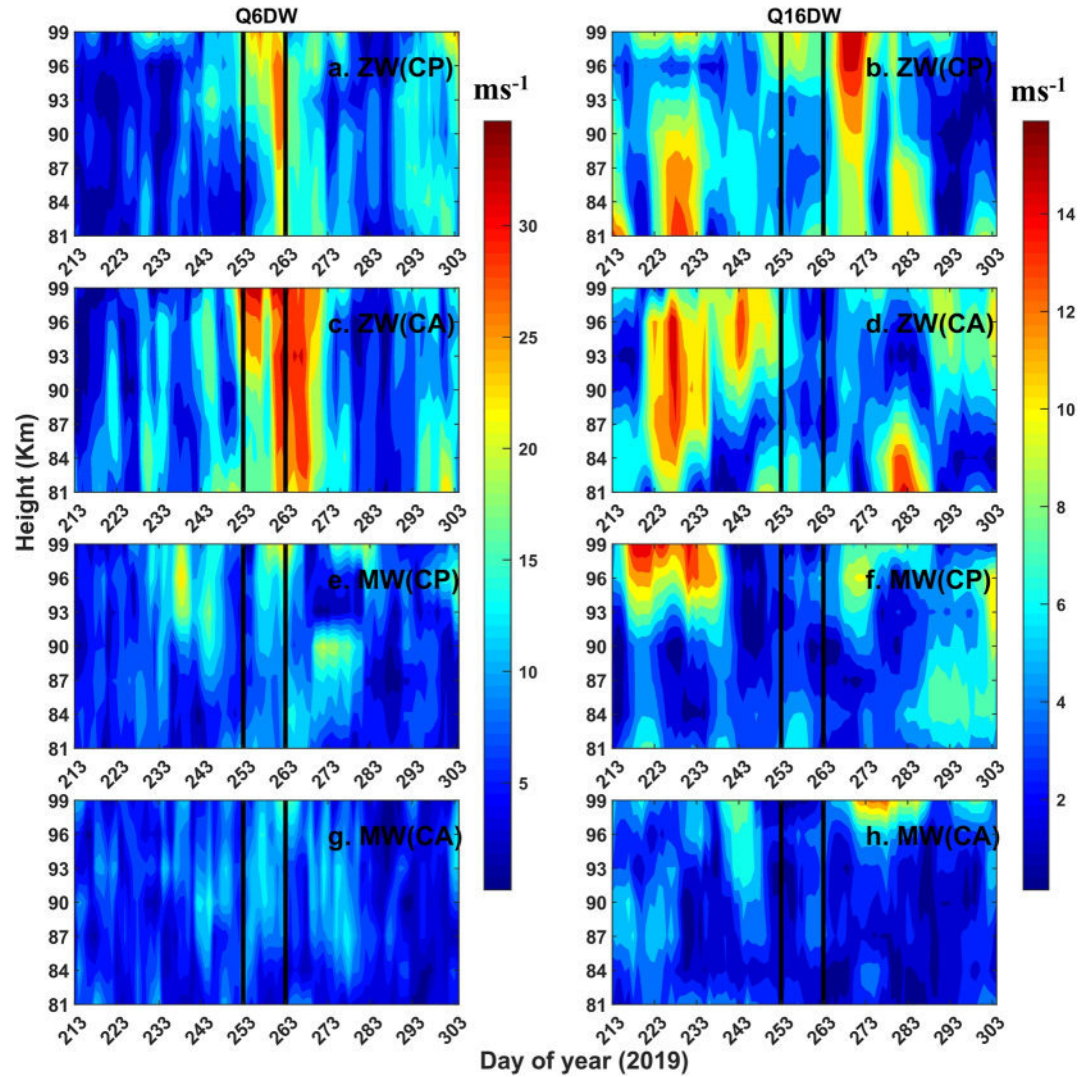


Figure 4. The meteor radar derived representative amplitude of the (a) Q6DW and (b) Q16DW in the zonal wind (ZW) at CP. The same for the (c) Q6DW and (d) Q16DW in the zonal wind at CA. The same for the (e) Q6DW and (f) Q16DW in the meridional wind (MW) at CP. The same for the (g) Q6DW and (h) Q16DW in the meridional wind at CA. Please note the change of scale in the colorbars while comparing.

same is also visible in post warming period. The meridional wind at CA exhibits traces of weak 6-day periodicity around the warming days (Figure 4g). The weak feature of the Q16DW in the meridional wind at CA is mainly observed during pre-warming interval and at higher MLT in post warming span, as seen in Figure 4h. Overall, the representative amplitude of the Q6DW is found to be greater as compared to that of the Q16DW in the MLT region. In general, the Q16DW is observed to be more prominent in pre-warming interval and the Q6DW dominates during post-warming interval consistent with the previous results (Figures 2 and 3) from various altitudes in the middle atmosphere.

To identify the direction of propagation of the traveling PWs around the warming episode, we have utilized the zonal and meridional wind data at 0.02, 1 and 10 hPa at both CP and CA latitude during September 2019 using ERA5 data set. The amplitude of a wave with zonal wavenumber s and period T can be estimated by the non-linear least-square fitting using the following equation.

$$A \cos \left[2\pi \left(\frac{t}{T} + s \frac{\lambda}{360} \right) - \phi \right] \quad (1)$$

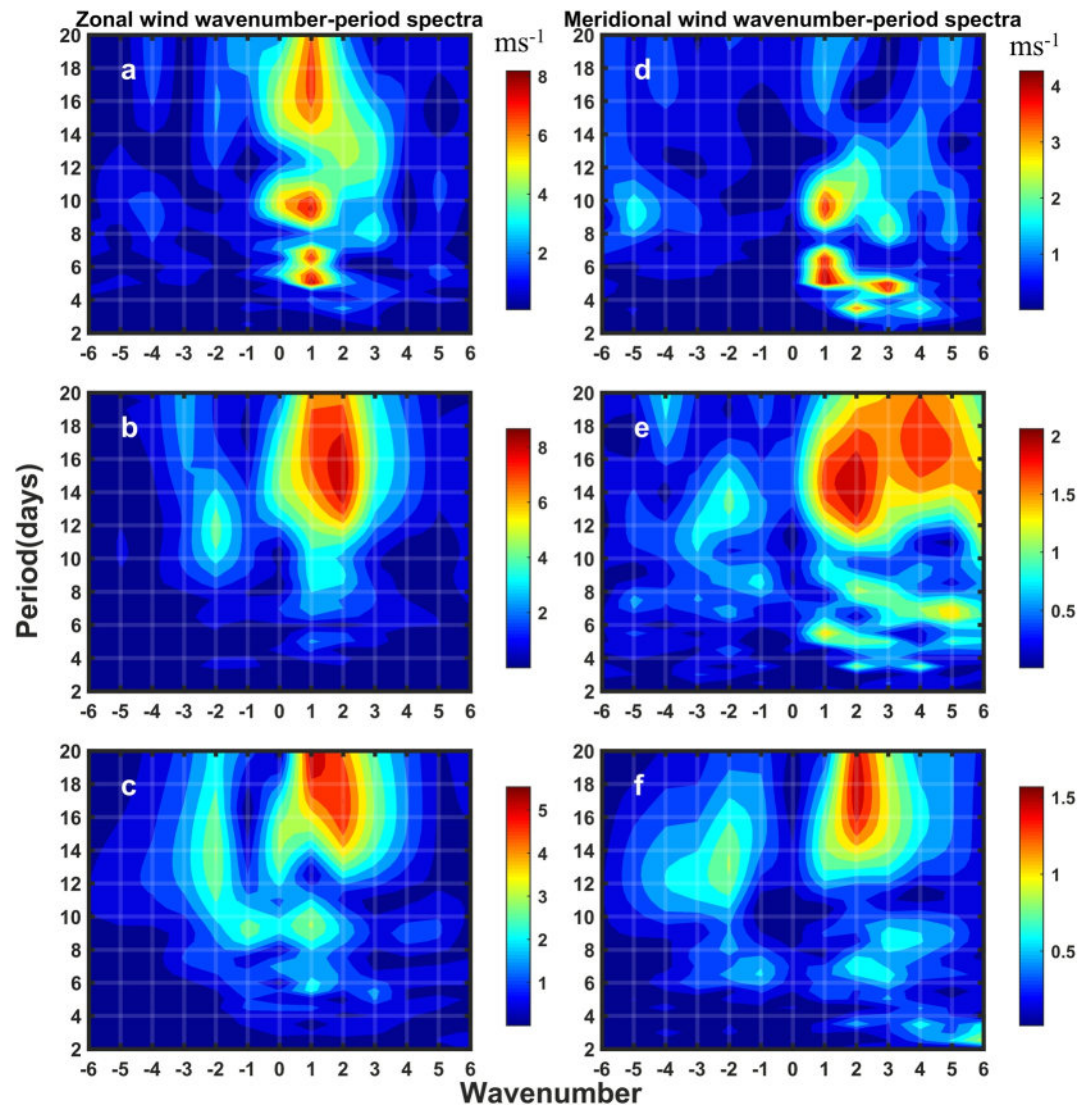


Figure 5. Period versus wavenumber spectra in the zonal wind at (a) 0.02 hPa (b) 1 hPa, (c) 10 hPa and meridional wind at (d) 0.02 hPa (e) 1 hPa, (f) 10 hPa at CP latitude (22.7°S) using ERA5. Please note the change of scale in the colorbars corresponding to each subplot while comparing.

where A is the amplitude of the wave, t is the universal time, λ is the longitude, and ϕ is the phase of the wave. The positive and negative values of s correspond to westward and eastward propagating waves, respectively. The wavenumber-period spectra for the zonal wind over CP at 0.02, 1 and 10 hPa are shown in Figures 5a–5c, respectively. The following features are notable in the wavenumber-period spectra of zonal wind over CP: (a) The zonal wavenumber 1 is the primary westward component of the Q16DW, Q10DW and Q6DW in the mesopause region (0.02 hPa), as observed in Figure 5a. (b) The westward propagating Q16DW with zonal wavenumber 2 is dominant in the zonal wind at 1 hPa pressure level (Figure 5b). (c) In the mid-stratosphere (10 hPa), the Q16DW exhibits a strong westward zonal wavenumber 1 component and a relatively weaker westward zonal wavenumber 2 component as noted from Figure 5c. Similarly, the wavenumber-period spectra of the meridional wind over CP calculated at 0.02, 1 and 10 hPa pressure levels are shown in Figures 5d–5f, respectively. The meridional wind wavenumber-period spectra exhibit following features: (a) The Q10DW mainly consists of westward zonal wavenumber 1, whereas the Q6DW contains both westward zonal wavenumber 1 and 3 in the mesopause (0.02 hPa). Additionally, a weak feature of the Q3DW is found to contain westward zonal wavenumber 2 as seen in Figure 5d. (b) The Q16DW is primarily composed of westward zonal wavenumber 2 in the upper stratosphere (Figure 5e). (c) The Q16DW has a strong westward zonal wavenumber 2 component at 10 hPa (Figure 5f).

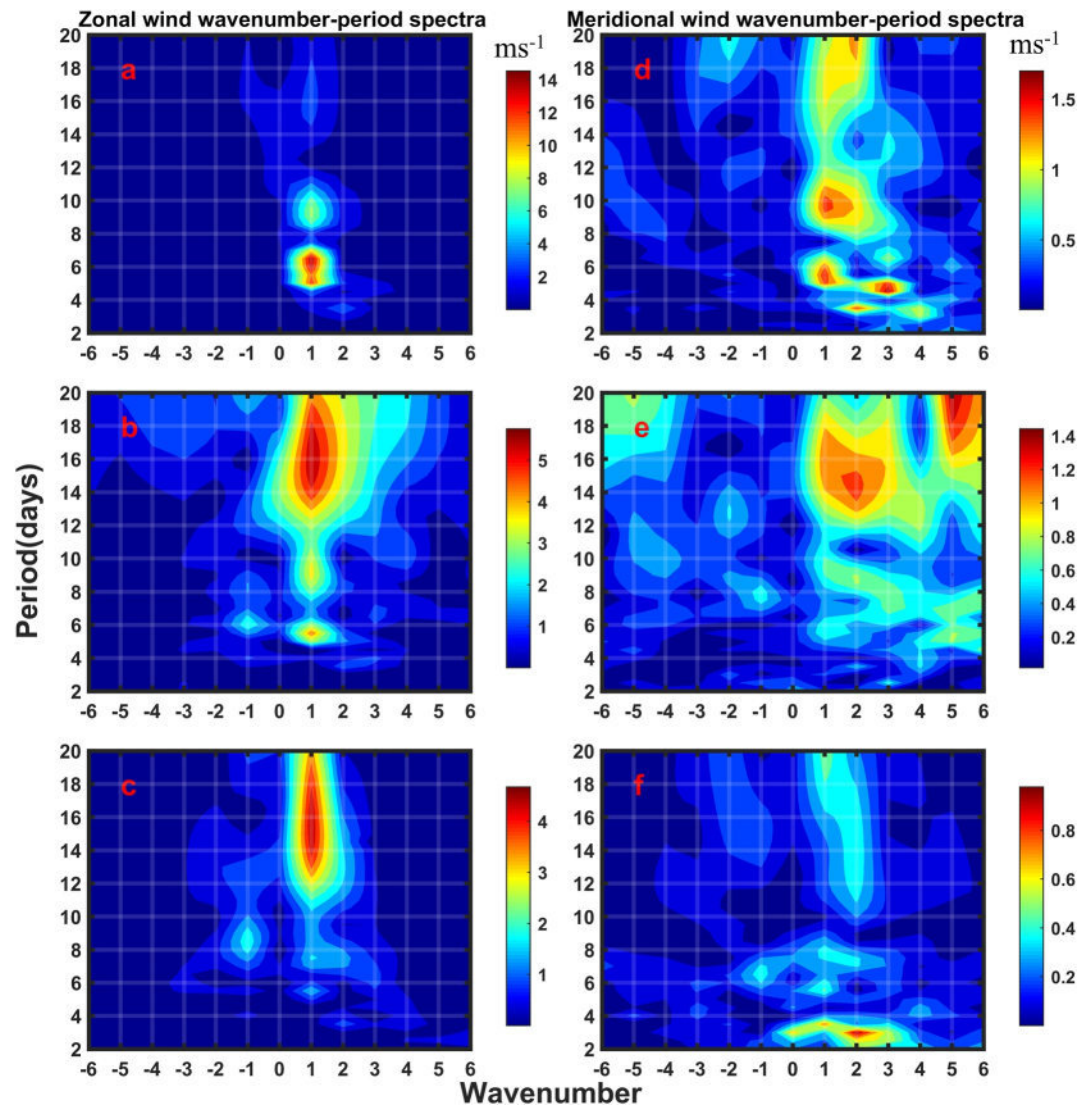


Figure 6. Similar to Figure 5, but at CA latitude (7.4°S).

Similarly, the wavenumber-period spectra of the zonal wind over CA at 0.02, 1 and 10 hPa is illustrated in Figures 6a–6c, respectively. Following features are interesting to note. (a) The Q6DW observed in the zonal wind wavelet spectra at 0.02 hPa travels westward with zonal wavenumber 1, in Figure 6a. A weak signature of the Q10DW with westward zonal wavenumber 1 can be found at 0.02 hPa. (b) The westward propagating zonal wavenumber 1 component is prominent in the Q16DW at 1 hPa (upper stratosphere) as seen in Figure 6b. (c) In the mid-stratosphere (10 hPa), the Q16DW propagates westward with zonal wavenumber 1 (Figure 6c). Figures 6d–6f show the wavenumber-period spectra of meridional wind over CA at 0.02, 1 and 10 hPa respectively. The key features are (a) The primary component of the Q10DW is westward zonal wavenumber 1, and that of the Q6DW is westward zonal wavenumber 1 and 3 in the mesopause (0.02 hPa). Additionally, the Q3DW contains westward zonal wavenumber 2 as seen in Figure 6d. (b) The Q16DW is found to consists of westward zonal wavenumber 2 (Figure 6e). (cg) The Q3DW is primarily westward with zonal wavenumber 2 in the mid-stratosphere at 10 hPa (Figure 6f). Overall, the amplitude of the wavenumber-period spectra for the meridional wind is significantly less than that of the zonal wind over both CP and CA. Hence, zonal wind will be considered for further analysis.

The Q6DW and Q16DW is found to be primarily westward with zonal wavenumber 1 component as revealed in the wavenumber-period spectra. Hence, we looked into the temporal variability of the westward zonal wavenumber 1 component of the Q6DW (Q6DW1) and Q16DW (Q16DW1) in the zonal wind during the observational

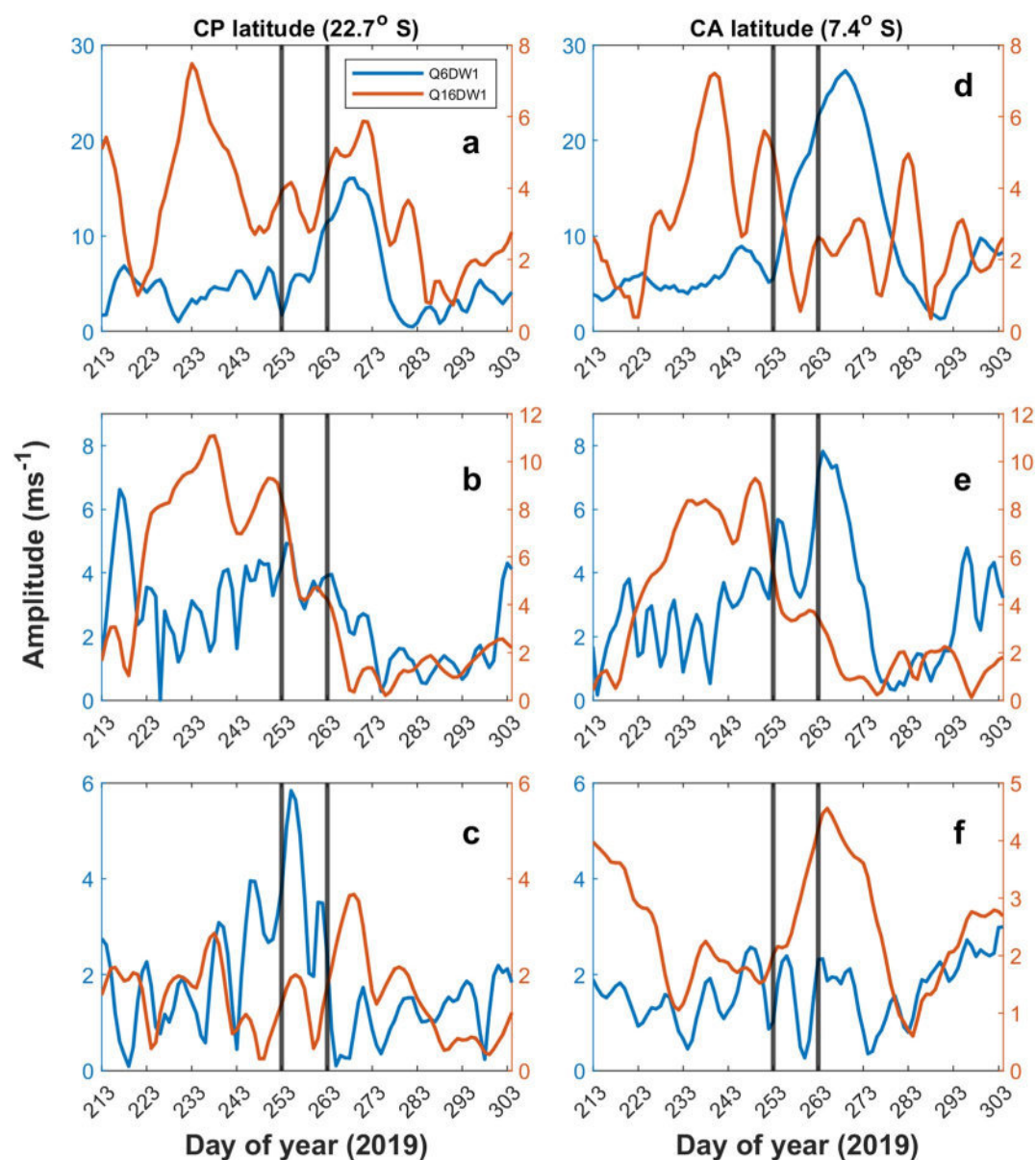


Figure 7. The representative amplitude of the Q6DW1 (blue curve) and Q16DW1 (red curve) in the zonal wind at (a) 0.02 hPa, (b) 1 hPa and (c) 10 hPa at CP latitude (22.7°S). The same at (e) 0.02 hPa, (f) 1 hPa and (h) 10 hPa, but at CA latitude (7.4°S).

interval, as shown in Figure 7. The representative amplitudes of the Q6DW1 and Q16DW1 are derived using Equation 1 considering periods 6 and 16 days and marked by blue and red color, respectively. Figures 7a–7c show the representative amplitude of the Q6DW1 and Q16DW1 at CP latitude at 0.02, 1 and 10 hPa, respectively. Similarly, Figures 7d–7f show the representative amplitude of the Q6DW1 and Q16DW1 in CA latitude at 0.02, 1 and 10 hPa, respectively. At 0.02 hPa, the Q16DW1 shows almost simultaneous enhancement with similar amplitude before warming around DOY 233–243 at both locations. Another peak in postwarming interval is also visible around DOY 273 at CP and DOY 283 at CA with smaller amplitude. The Q6DW1 wave shows simultaneous amplification around DOY-268 at both locations with almost twice amplitude at CA as compared to CP. Overall, the Q6DW1 is found to be significantly higher in amplitude as compared to the Q16DW1.

At 1 hPa broad enhancement peak is found in the Q16DW1 amplitude at both locations during prewarming interval and subsequent weak feature in postwarming interval. The Q6DW1 does not show any consistent enhancement

except a sharp peak on DOY 217 at CP. However, at CA a prominent enhancement is found in the Q6DW1 on DOY 263. It can be noted that the Q6DW1 activity reduces significantly, whereas the Q16DW1 enhances at 1 hPa as compared to that at higher altitude (0.02 hPa).

At 10 hPa the Q16DW1 does not show any notable behavior in response to the warming at CP although it shows warming time enhancement at CA. On the other hand, the Q6DW1 shows amplification during warming at CP and no evident increase at CA unlike the Q16DW1. It can be mentioned that both the wave components are found to be much weaker at 10 hPa as compared to the higher altitudes. Therefore, the Q16DW1 is found to be mainly dominant during prewarming interval and the Q6DW1 enhances during postwarming interval at both tropical and extratropical upper stratosphere and MLT, which is consistent with the wavelet spectra (Figures 2 and 3).

In addition to traveling PWs, characteristics of the stationary planetary waves (SPW) dynamics during the observational span is also investigated. To assess the variability of the dominant wave components in the middle atmosphere, the amplitudes of the SPW corresponding to zonal wavenumbers 1 and 2 in the zonal wind are estimated following the method same as Pancheva, Mukhtarov, Mitchell, Merzlyakov, et al. (2008) and shown in Figure 8. The temporal variation of stationary planetary wavenumber 1 (SPW1) in the SH at 0.02, 1 and 10 hPa is illustrated in Figures 8a–8c. There is evident amplification of the SPW1 at mid latitudes (30–60°S) during the warming and post warming phase near mesopause (0.02 hPa), as seen in Figure 8a. In the upper stratosphere at 1 hPa pressure level (Figure 8b), the SPW1 enhances before the warming at high latitudes. It decays abruptly at the onset of the warming event and remains weaker for the rest of the observational period. At mid latitude, the SPW1 is observed to be active until the warming onset and drastically weakens hereafter. At 10 hPa, the SPW1 exhibits high amplitude at polar latitudes during the warming days and becomes sufficiently weaker after the warming. At mid latitudes, the SPW1 weakens as the warming begins, as seen in Figure 8c. The stationary planetary wavenumber 2 (SPW2) obtained from the daily zonal wind data at 0.02, 1 and 10 hPa are plotted in Figures 8d–8f, respectively. At 0.02 hPa, there is no notable feature in the activity of SPW2 in response to SSW event (Figure 8d). The SPW2 is observed to be active until the end of the warming at 1 hPa in mid latitudes as evident from Figure 8e. The amplitude of the SPW2 is higher at mid latitudes than high latitudes at 1 hPa. The SPW2 remains active before and during warming days but weakens in post warming time at 10 hPa pressure level (Figure 8f). Overall, both components exhibit evident variability in connection with the warming episode with stronger SPW1 as compared to the SPW2, as illustrated in Figure 8.

Breaking of PW causes mixing of air masses between the low and high latitudes (Abatzoglou & Magnusdotir, 2006). As per the availability of the Ertel's potential vorticity (PV) in ERA5 database we show the results of PV up to 1 hPa from the ground. Figures 9a and 9b show the temporal variation of PV averaged over 35–45°W longitudes (considering CP and CA) at 1 hPa and 10 hPa respectively. Such PV maps can give important insights into the temporal dynamics of the meridional air mass mixing. Figure 9a shows a well-stratified layer of increasing absolute PV (APV) value with latitude preceding the warming event at 1 hPa. There is a noticeable intrusion of low APV value across high latitudes during warming days and continues for the remaining period of observation. Few patches of high APV value spread to low latitudes, possibly due to large scale mixing during the warming event (DOY 253–263). Stratified layers of increasing APV value with latitude also exists at 10 hPa (Figure 9b). At this level, notable variability of the APV is observed at high latitude (>70°S) during warming, although at low latitude such effect is not evident.

We further investigate the existence of the baroclinic/barotropic instability during the observational period, as shown in Figures 9c and 9d. According to Charney-Stern-Pedlosky criteria (Pedlosky, 1964), a reversal in the sign of the meridional gradient of PV of the background flow is a necessary but not sufficient condition for the growth of waves. Therefore, an extremum in the latitudinal variability of the PV may indicate barotropic/baroclinic instability. Hence, the meridional gradient of PV averaged over 35–45°W longitudes (covering both locations, CP and CA) at 1 hPa and 10 hPa is calculated. Figures 9c and 9d show only the negative PV gradient at 1 hPa and 10 hPa, respectively to identify the regions of instability. There are several patches of negative PV gradient across all latitudes throughout the observational period at 1 hPa. A dense patch of the same is prominent within the latitudinal domain of 20–40°S during DOY 233 and DOY 263 in Figure 9c may indicate considerable instability. Almost similar features are also observed in the mid-stratosphere at 10 hPa (Figure 9d).

For further investigation the possible source, dissipation and propagation of the dominant wave components, that is, Q6DW or Q16DW are represented by the Eliassen-Palm flux or EP flux (F) and divergence of the EP flux,

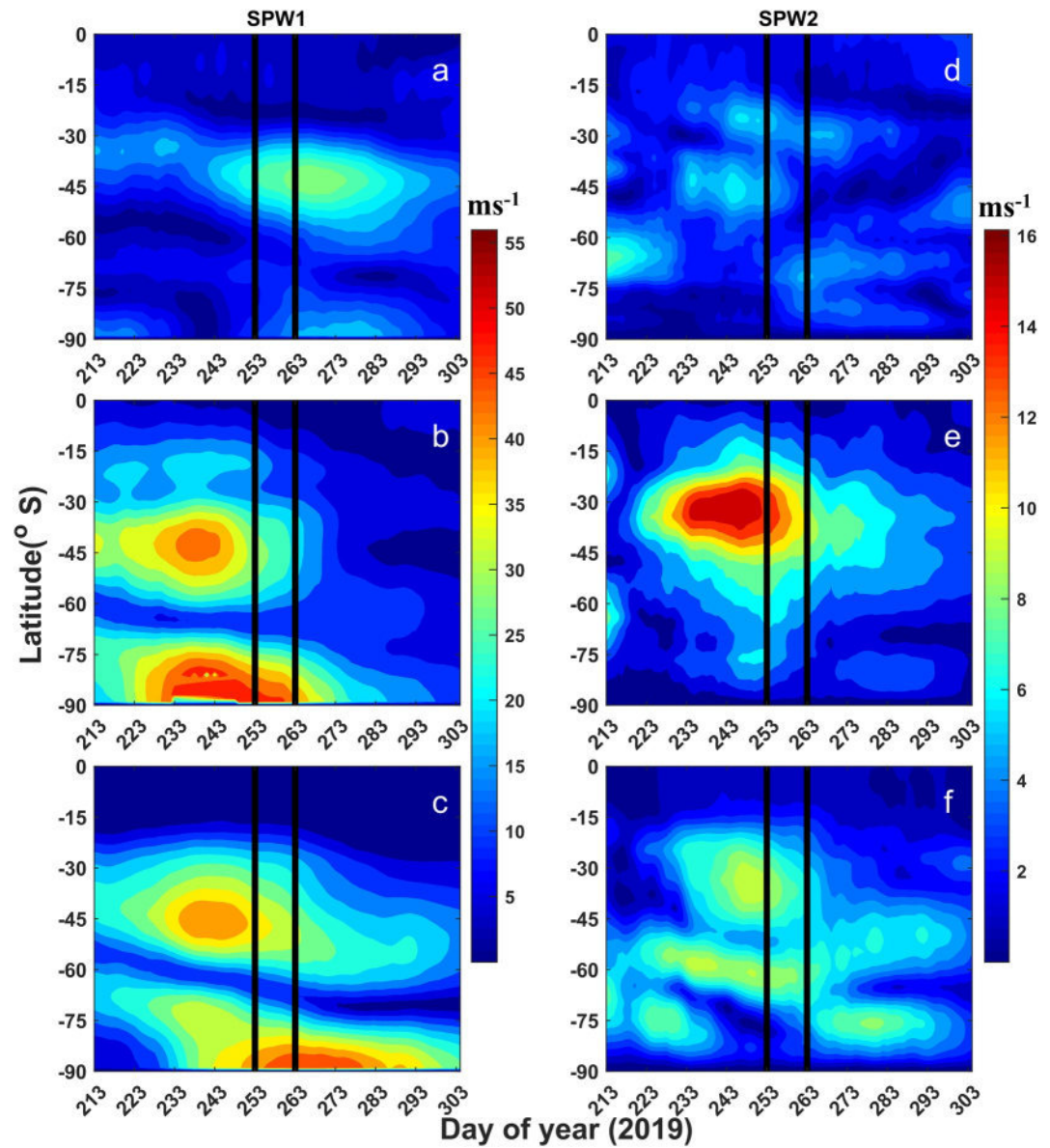


Figure 8. Latitudinal-temporal variation of SPW1 at (a) 0.02 hPa (b) 1 hPa, (c) 10 hPa and SPW2 at (d) 0.02 hPa (e) 1 hPa, (f) 10 hPa estimated from the zonal wind using ERA5 data set. Please note the change of scale in the colorbars while comparing.

$\nabla \cdot \mathbf{F}$ (Andrews et al., 1987; Sivakumar et al., 2004), which are expressed in spherical geometry under quasi-geostrophic approximation as:

$$F = \{f_{(\theta)}, F(z)\} = \left\{ -\rho_o a \cos \phi \left(\overline{v'u'} \right), f \rho_o a \cos \phi \left(\frac{\overline{v'\theta'}}{\theta_z} \right) \right\} \quad (2)$$

$$\nabla \cdot \mathbf{F} = \frac{1}{a \cos \phi} \left(F_{(\phi)} \cos \phi \right)_{\phi} + (F(z))_z \quad (3)$$

In Equations 2 and 3, overbar denotes zonal mean and prime indicates perturbation due to the Q6DW or Q16DW with all other symbols being as in Andrews et al. (1987). The perturbations due to the Q6DW and Q16DW are calculated by using a band pass filter with passbands of 5–7 days and 14–20 days, respectively in the zonal wind

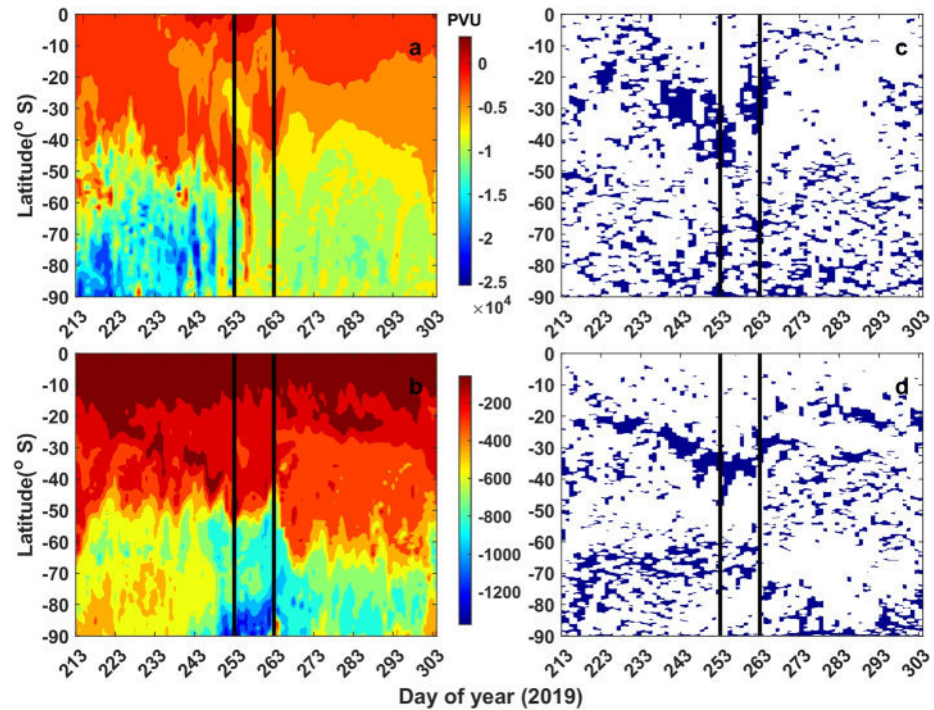


Figure 9. Temporal evolution of PV averaged within 35–45°W with latitudes using ERA5 at (a) 1 hPa and (b) 10 hPa in Potential vorticity unit PVU ($1 \text{ PVU} = 10^{-6} \text{ K m}^2 \text{ kg}^{-1} \text{ s}^{-1}$). The blue contour represents negative value of meridional gradient of PV averaged within 35–45°W at (c) 1 hPa and (d) 10 hPa in PVU per degree latitude. Please note the change of scale in the colorbars while comparing.

(u), meridional wind (v) and potential temperature (θ). Wave driving D is proportional to divergence of EP flux ($\nabla \cdot \mathbf{F}$) as explained in Sivakumar et al., 2004.

$$D = \frac{1}{\rho_0 a \cos \phi} \nabla \cdot \mathbf{F} \quad (4)$$

F points in the direction of PW propagation (Kanzawa, 1984). Negative D value signifies strong EP flux convergence. The convergence of EP flux vectors indicates the possibility of PW breaking and dissipation of wave energy to the mean flow. Positive D value indicates the source region. We have selected individual days as cases like pre-warming (1 and 6 September), warming (11 and 18 September) and post warming (24 and 30 September) to illustrate the dynamical evolution of wave propagation and zonal wave forcing. Figures 10a–10f shows latitude-height cross-sections of F (arrow) (both components are scaled appropriately for visibility) and wave driving, D (in contours) corresponding to the Q6DW for prior, during and post warming periods. During the prewarming and warming interval (1–18 September), strong wave convergence is found at polar latitude within 30–60 km and weak wave divergence can be noted at higher altitude, that is, 70–80 km. The wave flux (F) is found to be predominantly equatorward in the stratosphere (20–40 km) at mid latitudes (30–50°S) during prewarming span (1–11 September). It is noteworthy to mention that concurrent divergence and equatorward wave flux starts enhancing from the peak warming time (18 September) at 70–80 km near 30–50°S. Another zone of equatorward wave flux is prominent in the troposphere, mainly during warming and post warming time (18–30 September) which is limited within 20–50°S although it is not found to be supported by the coincident divergence. Additionally, the wave convergence/divergence at low and mid latitudes is relatively less up to 70 km after the warming (24–30 September). Therefore, the notable point here is the significant equatorward propagation of the Q6DW during post warming period in the upper mesosphere favored by a plausible source in the mid latitude.

Similarly, Figures 11a–11f shows latitude-height cross-sections of wave flux (F) (arrow) and wave driving, D corresponding to the Q16DW for prior, during and post warming periods. The wave activity in terms of convergence/divergence is high near polar region within 20–60 km vertical range. At mid latitude (50–60°S) the convergence zone near 50 km weakens with time and ultimately changes to a divergence zone from where prominent

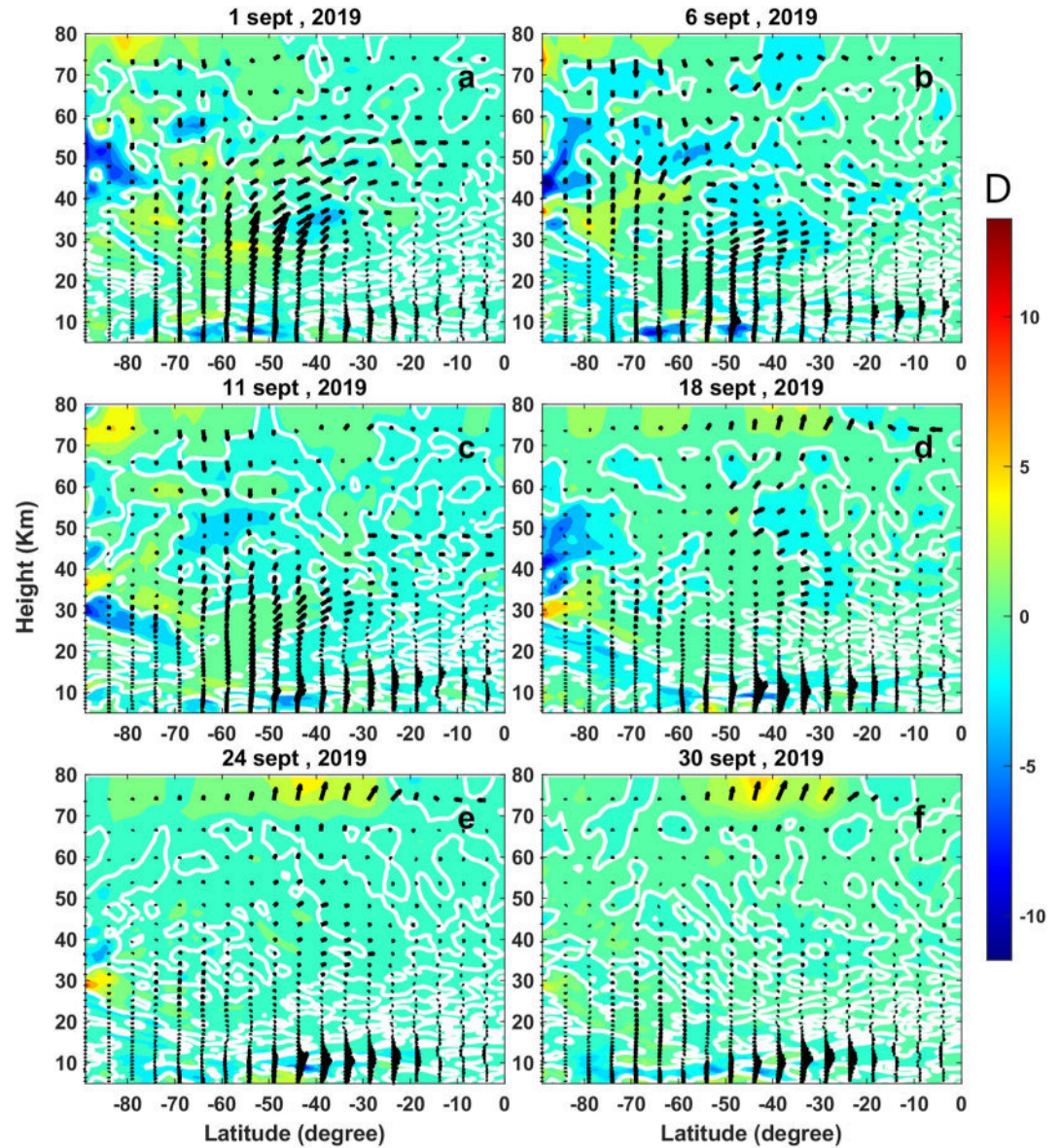


Figure 10. EP flux cross-section of the Q6DW in the meridional plane for prior, during and post warming periods shown for various days. The contour value represents wave driving, D in $\text{m s}^{-1} \text{ day}^{-1}$. The white bold curve represents zero value of D .

equatorward wave flux is found to exist until 24 September and hereafter it weakens significantly. Another zone of temporally increasing wave flux is found to maximize near 10–12 km within the latitude range 20–50°S although no supportive concurrent divergence can be identified. Therefore, the most consistent signature in this plot is the gradually increasing Q16DW flux in the stratosphere from mid to low latitudes during the warming period.

4. Discussion

Our present study has illustrated some essential dynamical aspects of a minor SSW event from the SH during September 2019 with meteor radar wind observations from two low latitude Brazilian stations and ERA5 reanalysis data set. The 2019 minor SSW is only the second most robust warming event in the SH reported so far (Noguchi et al., 2020). The current study aims at providing valuable insights into the middle atmospheric dynamics in terms of PWs activity, especially at low latitudes during such a rare event. In the present study, the warming event involves mesospheric cooling at 60°S from DOY 213 until DOY 263 (end of warming). Mesospheric cooling

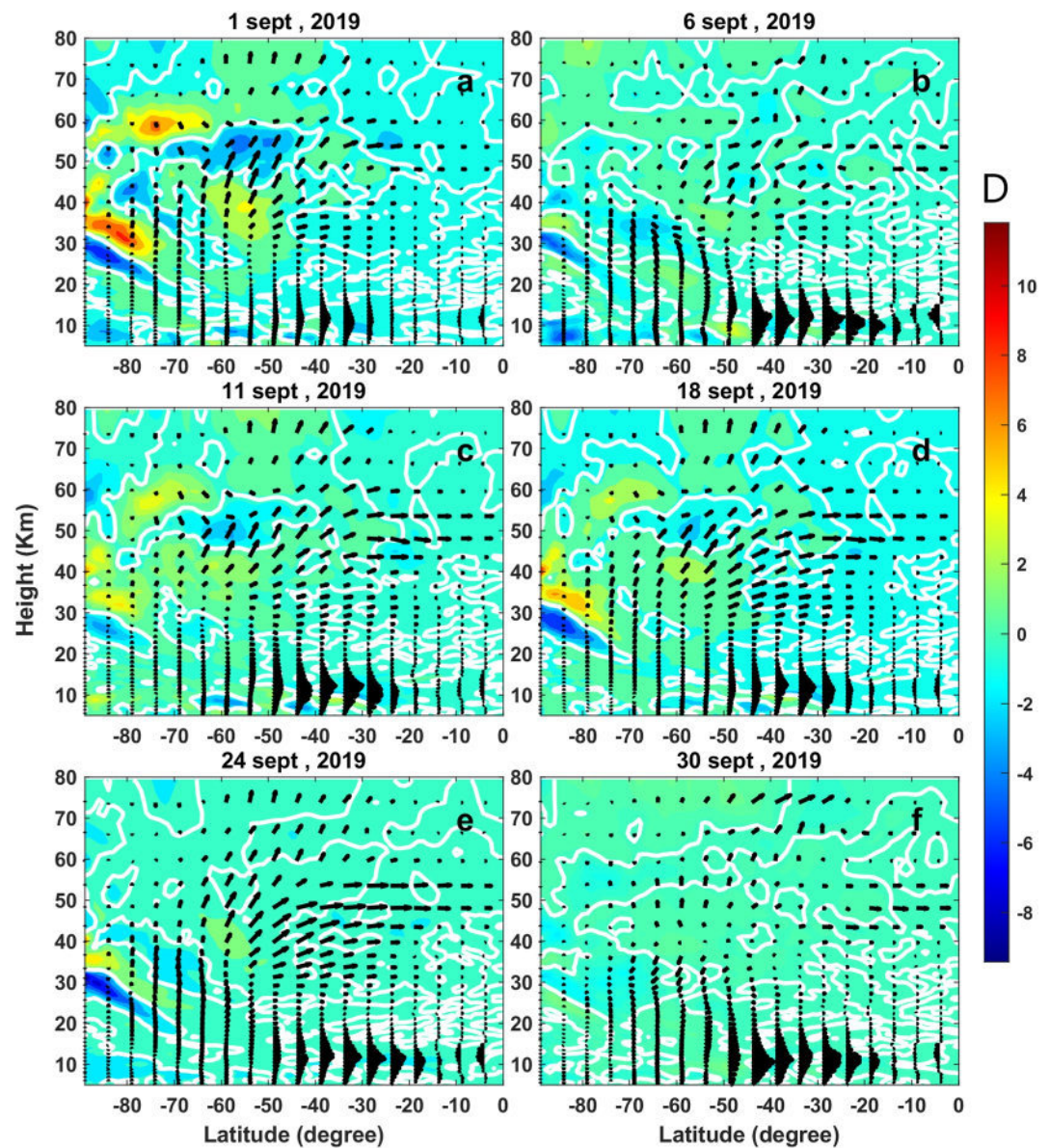


Figure 11. Similar to Figure 10, but for the Q16DW.

during the warming event was reported in the past studies (Duck et al., 1998; Mukhtarov et al., 2007; Schoeberl, 1978). The adiabatic cooling in the polar mesosphere is due to the upward flow of mean residual circulation (Liu & Roble, 2002; Matsuno, 1971). Polar stratospheric warming is concurrent with stratospheric cooling at the present observing tropical latitudes. Tropical stratospheric cooling coincident with stratospheric warming at high latitudes was reported in past studies (Fritz & Soules, 1970; Guharay et al., 2014). Fritz and Soules (1970), with NIMBUS III satellite observations over the NH, inferred that cooling at the tropical latitudes is due to eddy heat transport from high to low latitudes caused by a change in meridional circulation. Noguchi et al., (2020) studied the 2019 SH minor warming event and concluded that the tropical cooling is due to enhanced Brewer-Dobson (BD) circulation. Furthermore, the present minor warming event involves mesospheric warming at low latitudes which is concurrent with mesospheric cooling at high latitudes.

The 2019 SH minor SSW event is characterized by the sudden deceleration of westerly zonal-mean zonal wind from 90 to 10 m s⁻¹ at 60°S, 10 hPa (Lim et al., 2020; Yamazaki et al., 2020). Such a reduction in magnitude from late August to mid-September 2019 is comparable to that of 2002 SH major SSW event accompanying a change

from about 60 to -20 m s^{-1} in late September (Guharay et al., 2014; Lim et al., 2020). In the present event, the reversal of westerly zonal mean zonal wind at high latitude (60°S) initially occurred in the upper mesosphere on 2 September (DOY 245), followed by a descend to the lower altitude reaching 36 km height on 18 September (DOY 261) which is consistent with recent studies by Yamazaki et al. (2020) and Miyoshi and Yamazaki (2020). Since the wind reversal at high latitudes does not occur at 10 hPa, the present event is classified as a minor event in the SH. The zonal mean zonal wind at the present observing latitudes is also affected due to the polar warming in terms of weakening of the eastward wind. Such a feature is prominent around 65 km (mesosphere) over both latitudes of CA and CP. The reduction in the magnitude of westerly zonal wind at around 65 km in low latitudes (Figures 1f and 1h) may be possibly due to the induction of westward momentum to the mean flow by the dissipation of PW at mesospheric altitudes during the warming period.

The observed strong westerly wind before warming as seen in Figures 1d–1h possibly supports and enhances the activity of PW. PW propagates upward provided the background wind speed is below the Rossby critical velocity (Charney & Drazin, 1961). The wavelet spectra at both low latitude locations exhibit almost similar responses in planetary waves pertained to the warming event. The enhanced Q16DW activity at mid and upper stratosphere weakens after the warming days, followed by appearance of the Q6DW in the upper mesosphere (0.02 hPa) and MLT region after the end of warming and remains active for a week (Figures 2 and 3). The Q6DW is generally an equinoctial phenomenon in the MLT region over equatorial and tropical regions when the background wind is moderately westward during April/May and Sept/Oct months (Lima et al., 2005; Kishore et al., 2004). Furthermore, the Q6DW is generally found to be strong in the zonal wind in the MLT region. Additionally, the Q6DW's appearance does not appear to be consistent in the meridional wind with smaller amplitude as compared to the zonal wind counterpart in keeping with previous study (Kishore et al., 2004). The appearance of the Q6DW in the zonal wind after the warming days at the tropical mesosphere may be due to the weakening of westerly zonal mean wind at around 65 km altitude, as seen in Figures 1g and 1h. Although there is a signature of the Q6DW in the meridional wind at CP, it is relatively weak and insignificant at CA. Miyoshi and Yamazaki (2020) studied the behavior of the Q6DW using simulation from Ground-to-topside model of Atmosphere and Ionosphere for Aeronomy (GAIA) during the same warming event and found similar features of the Q6DW supporting the present findings. It is interesting to note that the Q16DW is mainly active in the stratosphere during prewarming conditions, followed by the dominance of the Q6DW in the upper mesosphere during and after the warming. These observations suggest a possibility of dissipation of the Q16DW and subsequent generation of secondary waves in the form of the Q6DW at mesospheric altitudes and MLT region. Occurrence of the secondary PWs in the mesosphere after the 2012 minor SSW event was observed by Chandran et al. (2013). According to the past study, the secondary wave in the MLT after the SSW is due to in situ generation of instabilities in presence of large temperature and wind gradients. In the present study, the reversal of eastward zonal mean zonal wind at 60°S , above 10 hPa (Figure 1f) may be responsible for the enhancement of the Q6DW. In this context, Koushik et al. (2020) suggested that significant wind reversals in the stratosphere following SSWs (2008–2009, 2009–2010 and 2011–2012) in the NH may favor the instability mechanism for the generation of secondary planetary waves. The presence of PW with period 6.5 and 16 days during the same time may suggest some relationship between them (Talaat et al., 2002). The mesospheric warming anomaly during the SSW event at low latitudes as seen in Figures 1c and 1d, is possibly due to the dissipation of the Q16DW, which is mainly active during pre-warming conditions in the stratosphere. Additionally, there exist Q10DW and Q3DW at various times during the observational period. However, they do not seem to offer a striking response to the present minor SSW event. Overall, there is a finite difference in the periodicity of traveling waves observed in the meridional wind than in the zonal wind. This may be because of doppler shift in the frequency of traveling waves due to variation in the background winds (Pancheva, Mukhtarov, Mitchell, Fritts, et al., 2008; Salby, 1981).

The present analysis of propagation direction of the traveling PW (Q16DW, Q10DW and Q3DW) over both CP and CA as seen in Figures 5 and 6 reveals westward PW with zonal wavenumber 1 and 2 as the dominating component. The Q16DW is primarily westward flowing with zonal wavenumber 1 component. Since the Q16DW is mainly active before the initiation of warming event, it may be deemed to play a role in preconditioning the warming event. Additionally, the Q6DW observed primarily at the end of warming is also westward propagating with zonal wavenumber 1. In this context, it should be mentioned that the Q6DW in the atmosphere is basically Rossby wave with zonal wavenumber 1 (Hirota & Hirooka, 1984) which is a robust feature in the middle and upper atmosphere (Hirota & Hirooka, 1984; Lieberman et al., 2003; Pancheva et al., 2018; Talaat et al., 2002). We also observe a strong SPW1 in the stratosphere (10 hPa and 1 hPa) of middle and high latitudes preceding the

warming event that reduces drastically during post-warming conditions, which is in agreement with the previous finding by Yamazaki et al., 2020. Similar features of the SPW2 are observed at 10 hPa (Figure 8f) and 1 hPa (Figure 8e), but with remarkably lower amplitude than that of the SPW1. This indicates salient role of the PWs, predominantly zonal wavenumber 1 (stationary and westward traveling) in preconditioning the SH 2019 minor SSW event.

The barotropic/baroclinic instability is believed to be present at the onset of the warming as evident from the negative meridional gradient at low and mid latitudes (Figures 9c and 9d). The instability diminishes considerably after the warming episode. Such instability helps in the growth of PW activity by extracting energy out of the horizontal/vertical shear of the background flow or equivalently from horizontal temperature gradients (Charney & Stern, 1962). In connection with the generation and maintenance of the 2012/13 SSW, Xu and San Liang (2017) argued that the instability was characterized by the extraction of available potential energy from the vertical or meridional unstable wind structure leading to a reversal of the polar jet. In the present study the existence of instability is also prominent in the zonal mean zonal wind, where the strong westerly jet decelerates at the onset of warming days, as observed in Figures 1d–1h. Furthermore, Tomikawa et al. (2012) indicated the possibility of barotropic/baroclinic growth of PW just after the SSW from the reversed PV gradient in connection with the formation of anomalous westward jet. Theoretical studies of Salby and Callaghan (2001) reported amplification of the 6.5-day wave in an unstable background condition. Lieberman et al. (2003) and Gan et al. (2018) suggested growth of the Q6DW due to baroclinic and barotropic instability during equinoxes. Limpasuvan et al. (2016) reported the generation of westward propagating secondary PWs during SSW through the occurrence of barotropic/baroclinic jet instability. Therefore, consistency of the present findings with the aforesaid previous investigations further corroborates a possible link between the Q6DW and instability of the middle atmosphere. Furthermore, the concurrence of zero wind line at low latitude in Figure 1b and negative PV gradient patch in Figure 8d at 10 hPa during DOY 213–263, suggests a possible link between instability and reversal of zonal mean zonal wind.

The EP flux diagnosis reveals the propagation of the Q6DW and Q16DW from mid and high latitudes to equator in the stratosphere and lower mesosphere. Existence of an intensifying divergence zone with the equatorward Q6DW flux around 70–80 km altitude within the latitudinal range of 30–50°S on the warmest day, that is, 18 September and subsequent interval may indicate a possible source of Q6DW at CP and CA in keeping with the signatures found in Figures 2 and 3 at 0.02 hPa and 90 km altitude. The prominent equatorward Q16DW flux seems to be active until the end of warming days and diminishes during post-warming days. Furthermore, the presence of divergence zone at mid and high latitudes may indicate plausible source region of the Q16DW. Overall, the equatorward Q6DW/Q16DW activity is found to be prominent up to a latitude as low as 20°S (near CP location). Additionally, the impact of the warming is found to be weaker at equatorial latitude (near CA) as compared to the extratropics, which is consistent with the past studies (Hauchecorne & Chanin, 1988; Whiteway & Carswell, 1994).

5. Summary and Conclusions

The present work portrays the PW dynamics in the middle atmosphere during a minor but impactful SSW event in September 2019 observed from two low latitude stations in the Brazilian sector. Although there are studies on convective activity and ionospheric variability during this event, there is hardly any literature related to the impact on the middle atmosphere at low latitudes. Based on the observed features the present warming event can also be termed as high stratospheric warming. The low latitude middle atmosphere shows contrasting character with respect to the high latitude, that is, cooling in the stratosphere coincident with the high latitude warming and warming in the mesosphere concurrent with the high latitude cooling. A strong Q16DW is mostly found to be present before the warming interval and weakens considerably after the warming episode. Another PW component, that is, Q6DW is found in the mesosphere and MLT during the initial days of post warming phase. A handful of traveling PW components, that is, Q16DW, Q10DW, Q6DW and Q3DW are found during the observational period primarily correspond to the westward zonal wavenumber 1 and 2. Furthermore, the current study points out the dominant role of SPWs with zonal wavenumber 1 in preconditioning the 2019 minor SSW event. PV maps in the stratosphere shows significant latitudinal mixing of the air mass. The growth of the Q6DW during the warming is probably associated with baroclinic/barotropic instability. The EP flux reveals propagation of the Q6DW and Q16DW from high and mid to low latitudes associated to the SSW event.

Data Availability Statement

ERA5 data set utilized in the current study is available at <https://www.ecmwf.int/en/forecasts/datasets>. The meteor radar datasets analyzed for the current study are available at <https://figshare.com/s/9eeb223a6429d7e436b4>.

Acknowledgments

The authors acknowledge C. Torrence and G. Compo for the wavelet tool, available at URL: <http://paos.colorado.edu/research/wavelets/>. The present work is supported by the Department of Space (Government of India), National Institute for Space Research, Federal University of Campina Grande, National Council for Scientific and Technological Development (Government of Brazil) and Sao Paulo Research Foundation (Sao Paulo, Brazil). Authors would like to thank Dora Pancheva and three anonymous reviewers for their valuable comments and suggestions.

References

- Abatzoglou, J. T., & Magnusdottir, G. (2006). Planetary wave breaking and non linear reflection: Seasonal cycle and interannual variability. *Journal of Climate*, 19(23), 6139–6152.
- Andrews, D. G., Holton, J. R., & Leovy, C. B. (1987). *Middle atmosphere dynamics* (No. 40). Academic Press.
- Chandran, A., Garcia, R. R., Collins, R. L., & Chang, L. C. (2013). Secondary planetary waves in the middle and upper atmosphere following the stratospheric sudden warming event of January 2012. *Geophysical Research Letters*, 40(9), 1861–1867. <https://doi.org/10.1002/grl.50373>
- Charney, J. G., & Drazin, P. G. (1961). Propagation of planetary-scale disturbances from the lower into the upper atmosphere. *Journal of Geophysical Research*, 66(1), 83–109. <https://doi.org/10.1029/JZ066i001p00083>
- Charney, J. G., & Stern, M. E. (1962). On the stability of internal baroclinic jets in a rotating atmosphere. *Journal of the Atmospheric Sciences*, 19(2), 1592–1612. [https://doi.org/10.1175/1520-0469\(1962\)019<1592:OTSOIB2.0](https://doi.org/10.1175/1520-0469(1962)019<1592:OTSOIB2.0)
- Dowdy, A. J., Vincent, R. A., Murphy, D. J., Tsutsumi, M., Riggins, D. M., & Jarvis, M. J. (2004). The large-scale dynamics of the mesosphere–Lower thermosphere during the southern hemisphere stratospheric warming of 2002. *Geophysical Research Letters*, 31(14). <https://doi.org/10.1029/2004GL020282>
- Duck, T. J., Whiteway, J. A., & Carswell, A. I. (1998). Lidar observations of gravity wave activity and arctic stratospheric vortex core warming. *Geophysical Research Letters*, 25(15), 2813–2816. <https://doi.org/10.1029/98GL02113>
- Fritz, S., & Soules, S. (1970). Large-scale temperature changes in the stratosphere observed from nimbus iii. *Journal of the Atmospheric Sciences*, 27(7), 10912–11097. [https://doi.org/10.1175/1520-0469\(1970\)027<10912:LSTCIT>2.0.CO](https://doi.org/10.1175/1520-0469(1970)027<10912:LSTCIT>2.0.CO)
- Gan, Q., Oberheide, J., & Pedatella, N. M. (2018). Sources, sinks, and propagation characteristics of the quasi 6-day wave and its impact on the residual mean circulation. *Journal of Geophysical Research: Atmospheres*, 123(17), 9152–9170. <https://doi.org/10.1029/2018JD028553>
- Goncharenko, L. P., Harvey, V. L., Greer, K. R., Zhang, S.-R., & Coster, A. J. (2020). Longitudinally dependent low-latitude ionospheric disturbances linked to the Antarctic sudden stratospheric warming of September 2019. *Journal of Geophysical Research: Space Physics*, 125(8), e2020JA028199. <https://doi.org/10.1029/2020JA028199>
- Guharay, A., Batista, P., Clemesha, B., & Sarkhel, S. (2014). Response of the extratropical middle atmosphere to the September 2002 major stratospheric sudden warming. *Advances in Space Research*, 53(2), 257–265. <https://doi.org/10.1016/j.asr.2013.11.002>
- Guharay, A., & Batista, P. P. (2019). On the variability of tides during a major stratospheric sudden warming in September 2002 at Southern hemispheric extra-tropical latitude. *Advances in Space Research*, 63(8), 2337–2344. <https://doi.org/10.1016/j.asr.2018.12.037>
- Guharay, A., & Sekar, R. (2012). Signature of latitudinal coupling during a major sudden stratospheric warming in the tropics. *Journal of Atmospheric and Solar-Terrestrial Physics*, 75, 122–126. <https://doi.org/10.1016/j.jastp.2011.06.010>
- Hauchecorne, A., & Chanin, M. L. (1988). Planetary waves-mean flow interaction in the middle atmosphere: Modelisation and comparison with lidar observations. *Annales Geophysicae*, 6, 409–416.
- Hersbach, H., Bell, B., Berrisford, P., Hirahara, S., Horányi, A., Muñoz-Sabater, J., et al. (2020). The ERA5 global reanalysis. *Quarterly Journal of the Royal Meteorological Society*, 146(730), 1999–2049. <https://doi.org/10.1002/qj.3803>
- Hirota, I., & Hirooka, T. (1984). Normal mode Rossby waves observed in the up495 per stratosphere. part i: First symmetric modes of zonal wavenumbers 1 and 2. *Journal of the Atmospheric Sciences*, 41(8), 12532–12167. [https://doi.org/10.1175/1520-0469\(1984\)041<1253:499NMRWOI2.0.CO](https://doi.org/10.1175/1520-0469(1984)041<1253:499NMRWOI2.0.CO)
- Hocking, W. K., Fuller, B., & Vandepier, B. (2001). Real-time determination of meteor related parameters utilizing modern digital technology. *Journal of Atmospheric and Solar-Terrestrial Physics*, 63, 155–169. [https://doi.org/10.1016/S1364-6826\(00\)00138-3](https://doi.org/10.1016/S1364-6826(00)00138-3)
- Hoffmann, P., Singer, W., & Keuer, D. (2002). Variability of the mesospheric wind field at middle and arctic latitudes in winter and its relation to stratospheric circulation disturbances. *Journal of Atmospheric and Solar-Terrestrial Physics*, 64(8–11), 1229–1240. [https://doi.org/10.1016/S1364-6826\(02\)00071-8](https://doi.org/10.1016/S1364-6826(02)00071-8)
- Kanzawa, H. (1984). Four observed sudden warmings diagnosed by the Eliassen-Palm flux and refractive index. *Dynamics of the Middle Atmosphere*, 307.
- Kishore, P., Namboothiri, S., Igarashi, K., Gurubaran, S., Sridharan, S., Rajaram, R., & Ratnam, M. V. (2004). Mf radar observations of 6.5-day wave in the equatorial mesosphere and lower thermosphere. *Journal of Atmospheric and Solar-Terrestrial Physics*, 66(6–9), 507–515. <https://doi.org/10.1016/j.jastp.2004.01.026>
- Kodera, K. (2006). Influence of stratospheric sudden warming on the equatorial troposphere. *Geophysical Research Letters*, 33(6). <https://doi.org/10.1029/2005GL024510>
- Koushik, N., Kumar, K. K., Ramkumar, G., Subrahmanyam, V., Kishore Kumar, G., Hocking, W. K., et al. (2020). Planetary waves in the mesosphere lower thermosphere during stratospheric sudden warming: Observations using a network of meteor radars from high to equatorial latitudes. *Climate Dynamics*, 54, 4059–4074. <https://doi.org/10.1007/s00382-020-05214-5>
- Labitzke, K., Naujokat, B., & Kunze, M. (2005). The lower arctic stratosphere in winter since 1952: An update. *Sparc Newsletter*, 24, 27–28.
- Lieberman, R. S., Riggins, D. M., Franke, S. J., Manson, A. H., Meek, C., Nakamura, T., et al. (2003). The 6.5-day wave in the mesosphere and lower thermosphere: Evidence for baroclinic/barotropic instability. *Journal of Geophysical Research: Atmospheres*, 108(D20). <https://doi.org/10.1029/2002JD003349>
- Lim, E.-P., Hendon, H. H., Butler, A. H., Garreaud, R. D., Polichtchouk, I., & Shepherd, T. G. (2020). The 2019 antarctic sudden stratospheric warming. *Sparc Newsletter*, 54, 10–13.
- Lima, L., Batista, P., Clemesha, B., & Takahashi, H. (2005). The 6.5-day oscillations observed in meteor winds over Cachoeira paulista (22.7 s). *Advances in Space Research*, 36(11), 2212–2217. <https://doi.org/10.1016/j.asr.2005.06.005>
- Limpasuvan, V., Orsolini, Y. J., Chandran, A., Garcia, R. R., & Smith, A. K. (2016). On the composite response of the MLT to major sudden stratospheric warming events with elevated stratopause. *Journal of Geophysical Research: Atmospheres*, 121(9), 4518–4537. <https://doi.org/10.1002/2015JD024401>
- Liu, H.-L., & Roble, R. G. (2002). A study of a self-generated stratospheric sudden warming and its mesospheric–lower thermospheric impacts using the coupled TIME-GCM/CCM3. *Journal of Geophysical Research: Atmospheres*, 107(D23). <https://doi.org/10.1029/2001JD001533>

- Matsuno, T. (1971). A dynamical model of the stratospheric sudden warming. *Journal of the Atmospheric Sciences*, 28(8), 14792–21494. [https://doi.org/10.1175/1520-0469\(1971\)028<1479:ADMOTS>2.0](https://doi.org/10.1175/1520-0469(1971)028<1479:ADMOTS>2.0)
- McInturff, R. M. (1978). Stratospheric warmings: Synoptic, dynamic and general circulation aspects. *NASA Reference Publ* NASA-RP-1017:174. Retrieved from <http://ntrs.nasa.gov/archive/nasa/casi.ntrs.nasa.gov/19780010687.pdf>
- Miyoshi, Y., & Yamazaki, Y. (2020). Excitation mechanism of ionospheric 6-day oscillation during the 2019 September sudden stratospheric warming event. *Journal of Geophysical Research: Space Physics*, 125(9), e2020JA028283. <https://doi.org/10.1029/2020JA028283>
- Mukhtarov, P., Pancheva, D., Andonov, B., Mitchell, N. J., Merzlyakov, E., Singer, W., & Murayama, Y. (2007). Large-scale thermodynamics of the stratosphere and mesosphere during the major stratospheric warming in 2003/2004. *Journal of Atmospheric and Solar-Terrestrial Physics*, 69(17–18), 2338–2354. <https://doi.org/10.1016/j.jastp.2007.07.012>
- Noguchi, S., Kuroda, Y., Kodera, K., & Watanabe, S. (2020). Robust enhancement of tropical convective activity by the 2019 Antarctic sudden stratospheric warming. *Geophysical Research Letters*, 47(15), e2020GL088743.
- Pancheva, D., Mukhtarov, P., Mitchell, N. J., Merzlyakov, E., Smith, A. K., Andonov, B., & Murayama, Y. (2008). Planetary waves in coupling the stratosphere and mesosphere during the major stratospheric warming in 2003/2004. *Journal of Geophysical Research: Atmospheres*, 113(D12). <https://doi.org/10.1029/2007JD009011>
- Pancheva, D., Mukhtarov, P., & Siskind, D. E. (2018). The quasi-6-day waves in NOGAPS- ALPHA forecast model and their climatology in MLS/Aura measurements (2005–2014). *Journal of Atmospheric and Solar-Terrestrial Physics*, 181, 19–37. <https://doi.org/10.1016/j.jastp.2018.10.008>
- Pancheva, D. V., Mukhtarov, P. J., Mitchell, N. J., Fritts, D. C., Riggins, D. M., Takahashi, H., & Ramkumar, G. (2008). Planetary wave coupling (5–6-day waves) in the low-latitude atmosphere–ionosphere system. *Journal of Atmospheric and Solar-Terrestrial Physics*, 70(1), 101–122. <https://doi.org/10.1016/j.jastp.2007.10.003>
- Pedatella, N., Chau, J., Schmidt, H., Goncharenko, L., Stolle, C., Hocke, K., et al. (2018). How sudden stratospheric warmings affect the whole atmosphere. *Eos Transactions American Geophysical Union*, 99, 35–38.
- Pedlosky, J. (1964). The stability of currents in the atmosphere and the ocean: Part i. *Journal of the Atmospheric Sciences*, 21(2), 2012–2219. [https://doi.org/10.1175/1520-0469\(1964\)021<2012:TSOCIT>2.0.CO](https://doi.org/10.1175/1520-0469(1964)021<2012:TSOCIT>2.0.CO)
- Rao, J., Garfinkel, C. L., Chen, H., & White, I. P. (2019). The 2019 new year stratospheric sudden warming and its real-time predictions in multiple S2S models. *Journal of Geophysical Research: Atmospheres*, 124(21), 11155–11174. <https://doi.org/10.1029/2019JD030826>
- Salby, M. L. (1981). Rossby normal modes in nonuniform. *Journal of the Atmospheric Sciences*, 38, 18272–21840. [https://doi.org/10.1175/1520-0469\(1981\)038%3c1827:RNMINB%3e2.0.CO](https://doi.org/10.1175/1520-0469(1981)038%3c1827:RNMINB%3e2.0.CO)
- Salby, M. L., & Callaghan, P. F. (2001). Seasonal amplification of the 2- day wave: Relationship between normal mode and instability. *Journal of the Atmospheric Sciences*, 58(14), 18582–21869. [https://doi.org/10.1175/1520-0469\(2001\)058h1858:557SAOTDWi2.0.CO](https://doi.org/10.1175/1520-0469(2001)058h1858:557SAOTDWi2.0.CO)
- Savenkova, E. N., Gavrilov, N. M., & Pogoreltsev, A. I. (2017). On statistical irregularity of stratospheric warming occurrence during northern winters. *Journal of Atmospheric and Solar-Terrestrial Physics*, 163, 14–22. <https://doi.org/10.1016/j.jastp.2017.06.007>
- Scherhag, R. (1952). Die explosionsartigen stratosphärenwärmungen des spatwinters 1951-1952. *Ber. Deut. Wetterd.*, 6, 51–63.
- Schoeberl, M. R. (1978). Stratospheric warmings: Observations and theory. *Reviews of Geophysics*, 16(4), 521–538. <https://doi.org/10.1029/RG016i004p00521>
- Sivakumar, V., Morel, B., Bencherif, H., Baray, J.-L., Baldy, S., Hauchecorne, A., & Rao, P. (2004). Rayleigh lidar observation of a warm stratopause over a tropical site, gadanki (13.5°N; 79.2°E). *Atmospheric Chemistry and Physics*, 4(7), 1989–1996. <https://doi.org/10.5194/acp-4-1989-2004>
- Talaat, E. R., Yee, J.-H., & Zhu, X. (2002). The 6.5-day wave in the tropical stratosphere and mesosphere. *Journal of Geophysical Research: Atmospheres*, 107(D12). <https://doi.org/10.1029/2001JD000822>
- Tomikawa, Y., Sato, K., Watanabe, S., Kawatani, Y., Miyazaki, K., & Takahashi, M. (2012). Growth of planetary waves and the formation of an elevated stratopause after a major stratospheric sudden warming in a T213L256 GCM. *Journal of Geophysical Research: Atmospheres*, 117(D16). <https://doi.org/10.1029/2011JD017243>
- Whiteway, J. A., & Carswell, A. I. (1994). Rayleigh lidar observations of thermal structure and gravity wave activity in the high arctic during a stratospheric warming. *Journal of Atmospheric Sciences*, 51(21), 31222–33136. [https://doi.org/10.1175/1520-0469\(1994\)051<3122:R-LOOTS>2.0.CO;2](https://doi.org/10.1175/1520-0469(1994)051<3122:R-LOOTS>2.0.CO;2)
- Xu, F., & San Liang, X. (2017). On the generation and maintenance of the 2012/13 sudden stratospheric warming. *Journal of the Atmospheric Sciences*, 74(10), 3209–3228. <https://doi.org/10.1175/JAS-D-17-0002.1>
- Yamazaki, Y., Matthias, V., Miyoshi, Y., Stolle, C., Siddiqui, T., & Kervalishvili, G. (2020). September 2019 antarctic sudden stratospheric warming: Quasi-6-day wave burst and ionospheric effects. *Geophysical Research Letters*, 47(1), e2019GL086577. <https://doi.org/10.1029/2019GL086577>

Investigation on the MLT tidal variability during September 2019 minor sudden stratospheric warming

G. Mitra^{a,b,*}, A. Guharay^{a,*}, P.P. Batista^c, R.A. Buriti^d, T. Moffat-Griffin^e

^a Space and Atmospheric Sciences Division, Physical Research Laboratory, Ahmedabad, GJ, India

^b Department of Physics, Indian Institute of Technology, Gandhinagar, GJ, India

^c Heliophysics, Planetary Sciences and Aeronomy Division, National Institute for Space Research, INPE, São José dos Campos, SP, Brazil

^d Department of Physics, Federal University of Campina Grande, Campina Grande, PB, Brazil

^e British Antarctic Survey, High Cross, Madingley Rd, Cambridge CB3 0ET, UK

Received 11 March 2022; received in revised form 4 August 2022; accepted 6 August 2022

Available online 10 August 2022

Abstract

Tidal variability in the mesosphere and lower thermosphere (MLT) during September 2019 Southern hemisphere minor sudden stratospheric warming (SSW) is investigated utilizing ground-based meteor radar wind observations from the equatorial, extratropical, middle, and high latitude stations and global reanalysis dataset. The polar warming is found to move from the mesosphere to the stratosphere until the peak warming day (PWD) of the SSW. The diurnal and semidiurnal tides at individual observational sites do not exhibit any consistent response during the observational interval, but a notable and consistent variability in some specific zonal wavenumber components, i. e., DW1 (migrating diurnal tide), DE3 (nonmigrating eastward wavenumber 3 diurnal tide), and SW2 (migrating semidiurnal tide) is found in the global reanalysis dataset. Incidentally, the warming event occurs during Spring equinox when a dominant seasonal change in the tidal activities generally takes place and hence seasonal variability is also looked into while identifying the SSW impact during the observational interval. It is found that the seasonal broad changes in the DW1, DE3, and SW2 amplitudes can be explained by the variability in the tidal sources, i.e., water vapor, convective activity, ozone, etc during the observational period. However, the extracted short-term variability in the global tidal modes on removing seasonal trend reveals noticeable response in connection with the warming event. The deseasoned amplitude of the DW1 significantly enhances around the PWD at most of the present latitudes. The deseasoned DE3 amplitude responds significantly in the middle atmosphere at low latitudes during the warming phase. The deseasoned SW2 exhibit clear enhancement around the PWD at all the latitudes. However, the deseasoned tidal features do not seem to correlate well with that of the source species unlike the seasonal ones that imply involvement of complex processes during the warming event, seeking further future investigations in this regard.

© 2022 COSPAR. Published by Elsevier B.V. All rights reserved.

Keywords: MLT dynamics; Sudden stratospheric warming; Atmospheric tides

1. Introduction

One of the wave-driven major disturbances in the middle atmosphere is the Sudden Stratospheric Warming (SSW). Occasionally, the circulation becomes highly disturbed during winter, accompanied by a marked amplification of planetary waves (Matsuno, 1971). The disturbed motion is characterized by a significant deceleration of

* Corresponding authors at: Space and Atmospheric Sciences Division, Physical Research Laboratory, Ahmedabad, GJ, India (G. Mitra).

E-mail addresses: gourav@prl.res.in (G. Mitra), guharay@prl.res.in (A. Guharay), paolo.batista@inpe.br (P.P. Batista), tmof@bas.ac.uk (T. Moffat-Griffin).

zonal mean westerlies or even a reversal into zonal mean easterlies. Simultaneously, stratospheric temperature over high latitudes increases sharply by a few tens of Kelvins in just a few days (Andrews et al., 1987). Major and minor warmings are two main categories of SSW. Reversal of the zonal mean temperature gradient poleward of 60° is a signature of both major and minor events, but the reversal of zonal mean zonal wind at 60° latitude and 10 hPa pressure level is the characteristics of a major warming (Labitzke et al., 2005). Interestingly the occurrence of SSW is more frequent in the Northern hemisphere (NH) than the Southern hemisphere (SH) because of higher planetary wave (PW) activity due to topographic difference and land-sea contrast. Also, the cumulative wave flux requirement to cause SSW in SH is supposed to be much larger because of the stronger SH polar jet than the NH counterpart (Rao et al., 2020; Guharay et al., 2014).

Atmospheric tides are large-scale global oscillations of the atmosphere primarily excited by diurnal heating of the atmosphere due to solar near-infrared (NIR) absorption by the water vapor in the troposphere, solar ultraviolet (UV) absorption by the ozone in the stratosphere, and far-ultraviolet (FUV) and extreme ultraviolet (EUV) radiation absorption by the molecular oxygen in the thermosphere (Chapman & Lindzen, 1970; Forbes & Garrett, 1978). At any given height, the day-night variation in the absorbed radiation due to differential heating gives rise to periods that are integral subharmonics of a solar day, such as 24 h (diurnal tide (DT)), 12 h (semidiurnal tide (ST)), 8 h (terdiurnal tide (TT)), 6 h (quarterdiurnal tide (QT)) and so on. The atmospheric tides are further classified into migrating and nonmigrating tides. Migrating tides are sun-synchronous and travel westward, whereas the nonmigrating tides do not follow the apparent motion of the sun and travel eastward, westward, or remain stationary (Kato et al., 1982).

Previous studies reported a significant influence on the atmospheric tides during NH SSW (Goncharenko et al., 2012; Lima et al., 2012) and SH SSW (Guharay and Batista, 2019). Sridharan et al. (2012) observed a decrease of ST amplitude in the zonal wind at 88 km over a tropical site before the onset of a 2011 NH minor SSW. Sassi et al. (2013) mentioned the decrease in the amplitude of the migrating ST due to the increase in the westward meridional shear in the MLT during the 2009 SSW event. Guharay and Batista (2014) found a dominant signature of the migrating DT during 2002 SH major SSW which has the potential to give rise to other nonmigrating components due to nonlinear interactions with the planetary waves. Recently He et al., 2020 reported quenching of higher-order migrating tides such as TT, QT, and so on at SSW onsets. Of late, a multi-station study by He and Chau, 2019 with zonal wavenumber constraints method found a weakening of the migrating ST component during SSW.

Until now, in the SH, one major SSW occurred in 2002 (Dowdy et al., 2004; Guharay et al., 2014; Guharay &

Batista, 2019). Recently, a minor but impactful SSW event occurred in the SH in September 2019 (Yamazaki et al., 2020; Mitra et al., 2022). Although there have been studies on the convective activity (Noguchi et al., 2020), ionospheric variability (Miyoshi and Yamazaki, 2020), and planetary wave activity (Mitra et al., 2022) concerning this event, there is hardly any literature related to the variability of the atmospheric tides. Therefore, in our present study, we aim to investigate the atmospheric tide associated dynamical variability in the SH middle atmosphere during the September 2019 minor SSW event. For this purpose, we have utilized meteor radar wind observations from São João do Cariri (7.4°S , 36.5°W) (CA), Cachoeira Paulista (22.7°S , 45°W) (CP), King Edward Point (54.3°S , 36.5°W) (KE), and Rothera (67.6°S , 68.1°W) (RO), which are equatorial, extratropical, middle and high latitude stations respectively. Additionally, we employ a longitudinally spread contemporaneous global reanalysis dataset to extract and study the behavior of different zonal wavenumber modes of atmospheric tides during the warming event. Our present study is important because of the lack of adequate understanding related to the impact of the SSW on the SH middle atmospheric tidal wave dynamics.

2. Observational database

For the present study, we have utilized three databases during the period centered around the minor warming episode \sim from 1 August to 31 December (2019), as described below.

2.1. Meteor radar

The radar systems at CA and CP are all-sky interferometric meteor radars operating at a frequency of 35.24 MHz, with a pulse repetition frequency of 2 kHz and peak power of 12 kW. The all-sky interferometric meteor radars at KE and RO operate at a frequency of 32.5 MHz, pulse repetition frequency of 2144 Hz, and peak power of 6 kW (Mitchell, 2019, 2021). It consists of a single three-element Yagi antenna for transmission and five phase-coherent two-element Yagi receiving antennas. The receiving antennas are aligned along two orthogonal baselines, with the central one common to both for detecting the echo signal from the meteors. Details of the derivation of the horizontal winds from the meteor trail echoes can be found in the available literature (Hocking et al., 2001). The meteor radar systems measure horizontal wind values within the altitude range of 80–100 km with a vertical resolution of 3 km and a temporal resolution of 1 hr.

2.2. MERRA-2 database

Modern-Era Retrospective analysis for Research and Applications version 2 (MERRA-2) is the latest version of global atmospheric reanalysis for the satellite era produced by the NASA Global Modeling and Assimilation

Office (GMAO) using the Goddard Earth Observing System Model (GEOS) version 5.12.4 (Gelaro et al. 2017). The dataset covers the period of 1980-present with the latency of ~ 3 weeks after the end of a month.

M2I3NVASM (or inst3_3d_asm_Nv) is an instantaneous 3-dimensional 3-hourly data collection in MERRA-2. For the present investigation, we have used temperature, zonal wind, and meridional wind at 72 model pressure levels within the range 985–0.01 hPa (~ 0 –75 km) with a latitude-longitude grid of $0.5^\circ \times 0.625^\circ$.

M2I1NXASM (or inst1_2d_asm_Nx) is an instantaneous 2-dimensional hourly data collection in MERRA-2. We have utilized the total precipitable water vapor (TPWV) and the total columnar ozone (TCO) for the present study. Since the database has a spatial resolution of $0.5^\circ \times 0.625^\circ$, the closest latitude points to CA, CP, KE, and RO are chosen as 7.5°S , 22.5°S , 54.5°S , and 67.5°S respectively.

2.3. Outgoing longwave radiation (OLR)

OLR data obtained from the National Center for Environmental Prediction (NCEP) is used as a proxy for convective activity. The OLR data available on a latitude-longitude grid of $2.5^\circ \times 2.5^\circ$ is chosen at the closest latitude of the observational sites to calculate the zonal mean of daily OLR. The nearest latitudes (available at OLR data) to CA, CP, KE, and RO are selected as 7.5°S , 22.5°S , 55°S , and 67.5°S , respectively, for studying the convective activity.

3. Results

3.1. Background state

A minor SH SSW event is defined if the zonal mean temperature gradient between 60°S and the south pole reverses at 10 hPa pressure level, accompanied by no wind reversal at 60°S , (Labitzke et al., 2005). A study on the 2019 SH minor SSW event by Eswaraiah et al., 2020 reported the onset day on 30 August 2019 (Day of year [DOY] 242) characterized by a sudden rise in the zonal mean polar stratospheric temperature with a peak value on 17 September 2019 (DOY 260). In the current study, a black solid and dashed vertical line marks the onset and peak warming day (PWD), respectively in all the Figures. The altitudinal profile of the difference between the zonal mean temperature at 90°S and 60°S is plotted using the MERRA-2 dataset during the interval 1 August to 31 October 2019 (DOY 213 = 1 August) in Fig. 1a, to identify the relative latitudinal warming and cooling in the atmosphere up to 0.01 hPa (~ 75 km). The bold white lines represent zero value in all the plots, and the bold black curve represents a value of 20 K in Fig. 1a. The zonal mean temperature difference between 90°S and 60°S exceeding 20 K is considered as high polar warming in the present study. The zonal mean temperature difference reverses and becomes positive from

30 August (DOY 242) onwards at upper stratosphere (30–45 km altitude), which signifies polar stratospheric warming relative to midlatitude. Noticeable polar stratospheric warming greater than 20 K is observed within the altitude range 30–45 km between DOY 242 and DOY 263. Simultaneously, a negative zonal mean temperature gradient in the altitudinal band 60–75 km indicates polar mesospheric cooling with respect to midlatitude, coincident with polar stratospheric warming. An interesting observation is the apparent downward propagation of the high poleward warming from the mesosphere to the stratosphere until the PWD.

Fig. 1b shows the latitudinal profile of the zonal mean zonal wind during the above-mentioned period at 10 hPa. The strong eastward wind at 10 hPa, 60°S decelerates monotonously by 70 ms^{-1} (approx.) until the PWD, i.e., DOY 260, although there is no wind reversal. The latitudinal profile of the difference between the zonal mean temperature and the temporal mean (August - October 2019) of zonal mean temperature at 0.01 hPa is shown in Fig. 1c. Relative mesospheric cooling at 0.01 hPa at high and mid-latitudes is observed between the onset and PWD. However, the low latitude mesosphere offers contrasting behavior as compared to the high latitude, i.e., warming in the mesosphere concurrent with high latitude cooling, as shown before. The zonal mean zonal wind at 0.01 hPa is shown in Fig. 1d. There is a considerable deceleration in the zonal mean westerly wind at the advent of the warming event, particularly in the latitudinal band 20 – 40°S . Interestingly, a wind reversal is observed at mid and high latitudes at 0.01 hPa, for a few days between the onset and PWD. However, the zonal wind in the equatorial ($<7^\circ\text{S}$) mesosphere does not exhibit any noteworthy variability in connection with the SSW.

3.2. Local tidal variability

Such significant changes in the background dynamical condition during the warming event further motivated us to investigate the possible response in the principal harmonics of atmospheric tides in the MLT concerning the warming event. For this purpose, the amplitude of the dominant atmospheric tides, i.e., Diurnal tide (DT) and semidiurnal tide (ST) is derived utilizing zonal and meridional wind data at RO, KE, CP, and CA. The horizontal wind data from the meteor radar and MERRA-2 are utilized to provide a holistic picture of the dynamical variability of the DT and ST in the MLT region from 50 km up to 100 km. The tidal amplitude can be estimated by the non-linear least-squares fitting using the following wave equation.

$$Y(t) = Y_o + A_n \cos\left[\frac{2\pi n}{24}(t - \varphi_n)\right] \quad (1)$$
 where $n = 1, 2$ denotes diurnal and semidiurnal components, A_n is the amplitude, t is the universal time and φ_n is the phase. $Y(t)$ is the hourly meridional/ zonal wind, and Y_o is the mean wind over the fitting window, i.e., 48 h. The window is

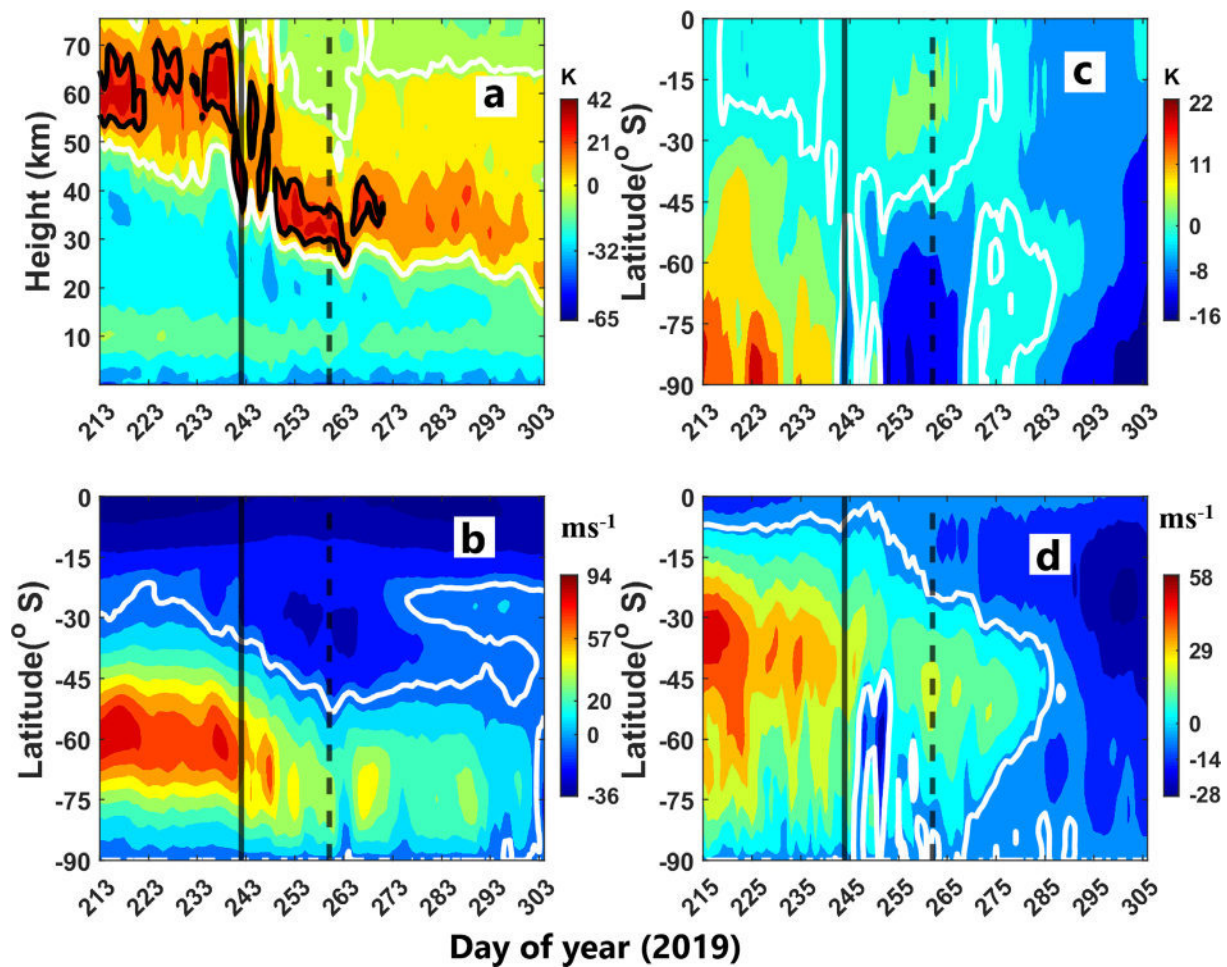


Fig. 1. (a) Altitudinal profile of difference between the zonal mean temperature at 90°S and 60°S during August–October 2019 (DOY 213 ~ 1 August). (b) Latitudinal profile of the zonal mean zonal wind at 10 hPa during the same period. (c) Latitudinal profile of the difference between zonal mean temperature and the temporal mean of zonal mean temperature at 0.01 hPa. (d) Latitudinal profile of the zonal mean zonal wind at 0.01 hPa. The bold white line represents zero value in the present figure and all the following figures, and the bold black curve represents a value of 20 K in Fig. 1a. The vertical black solid line and the dashed line represent the SSW onset date and the PWD, respectively for the present and all the following figures. Please note the change of scale in the color bars while comparing.

shifted progressively by 1 day (24 h) to derive the daily amplitudes of the tide, as illustrated in Fig. 2.

Overall, the DT and ST amplitude in the zonal wind is significantly less than that of the meridional wind over RO, KE, CP, and CA. Moreover, the DT and ST amplitude derived from the meridional and zonal wind exhibits similar features during the observational period (Figures not shown). Hence, we consider only the meridional wind for further analysis to avoid redundancy. The temporal variation in the DT amplitude in the MLT (~50–100 km) over RO, KE, CP, and CA are shown in Fig. 2a–d, respectively. The top and bottom contour plots of each subplot in Fig. 2 show the DT/ST amplitude derived from meteor radar (~80–100 km) and MERRA-2 (~50–75 km), respectively. The white vertical patches in the contour plot indicate missing observational data in the meteor radar. One may note appreciable difference in tidal amplitudes between radar and reanalysis datasets. Since we emphasize on the pattern of the variability of the derived tidal ampli-

tude, the absolute magnitude of the same does not affect our inferences. Amplitude of DT at RO appears to show an overall decreasing trend in the mesosphere (50–75 km) at the SSW onset, without any conspicuous response to the warming in the LT (80–100 km) (Fig. 2a). Also, the DT amplitude at KE doesn't exhibit any notable features concerning the warming event in the LT but a discernible decrease in amplitude is observed in the mesosphere until the onset date, as shown in Fig. 2b. Fig. 2c illustrates the variability in the DT amplitude at CP, where a sudden burst in amplitude is apparently observed around the SSW onset date. Furthermore, the DT amplitude does not seem to reveal any striking signature at CA around the warming interval, as evident in Fig. 2d.

Similarly, Fig. 2e–h show the variability in the ST amplitude in the MLT over RO, KE, CP, and CA, respectively. The ST amplitude at RO exhibits no apparent variability concerning the warming event in the LT although a gradual drop in amplitude is noticeable in the mesosphere at

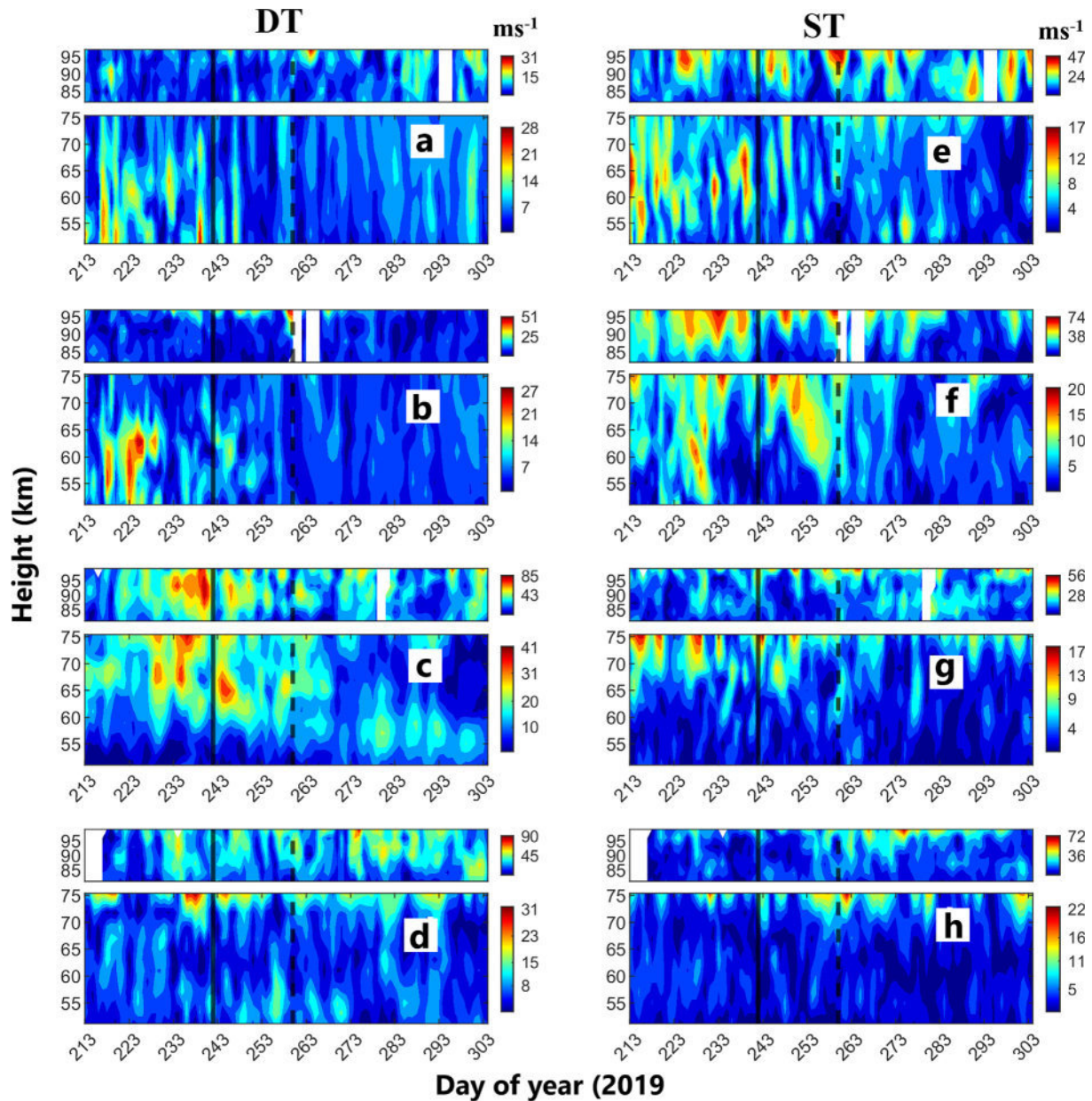


Fig. 2. Temporal variation in the DT amplitude in ms^{-1} at (a) RO (67.6°S, 68.1°W), (b) KE (54.3°S, 36.5°W), (c) CP (22.7°S, 45°W), and (d) CA (7.4°S, 36.5°W) using meteor radar-derived meridional wind (80–100 km altitude) and MERRA2 reanalysis dataset (50–75 km) altitude. Same for the ST amplitude in ms^{-1} at (e) RO, (f) KE, (g) CP, and (h) CA. Please note the change of scale in the color bars while comparing.

the SSW onset (Fig. 2e). At KE, the ST seems to be active during the prewarming phase and diminishes after PWD (Fig. 2f). There is no apparent variability in the ST amplitude at CP concerning the SSW event in the LT. Nevertheless, an identifiable decrement in ST amplitude is observed in the mesosphere after the PWD as shown in Fig. 2g. The ST amplitude is found to be significant for a few days around the PWD at CA (Fig. 2h). Overall, although some variability is noted at certain region and location in connection with the warming event, no consistent response in the local DT and ST amplitudes is found in this regard. Next, we look into the variability in the dominant global DT and ST modes corresponding to different zonal

wavenumbers to find any variability during the warming event.

3.3. Variability of global tidal modes

The tidal amplitude corresponding to different zonal wavenumbers is estimated utilizing the meridional wind in the mesosphere (~ 50 –75 km) from the MERRA-2 reanalysis dataset. The amplitude of a wave with zonal wavenumber s and period T can be estimated by the non-linear least-square fitting using the following wave equation.

$$A_{n,s} \cos[2\pi(n\frac{t}{24} + s\frac{\lambda}{360}) - \varphi_{n,s}] \quad (2)$$

where $n = 1, 2$ denotes diurnal and semidiurnal components, $A_{n,s}$ is the wave's amplitude, t is the universal time and $\varphi_{n,s}$ is the wave's phase. The periodicity in longitude λ is given by the zonal wavenumber s . We use the abbreviation DWs/DEs to denote a westward/eastward propagating DT, respectively. In the case of ST, 'D' in the above-mentioned abbreviations is replaced by 'S'. The positive and negative values of s correspond to westward and eastward propagating waves. Since the MERRA-2 data resolution is 3 h, the daily amplitude is derived using 48 data points, i.e., 6-day window, which is progressively shifted by a day. After analyzing the principal zonal wavenumbers ($s = -4$ to $+4$) corresponding to DT and ST, we find a notable response during the observational interval of the warming event in the amplitude only in the case of DW1 (migrating), DE3 (nonmigrating), and SW2 (migrating), which are shown in Fig. 3. To derive the tidal parameters in the MERRA-2 reanalysis dataset utilizing Eq. (2) we have chosen the latitude closest to the meteor radar observational site. Thus, the chosen latitudes are 67.5°S for RO, 54.5°S for KE, 22.5°S for CP, and 7.5°S for CA.

Fig. 3a–d show the temporal variability of the DW1 at 67.5°S, 54.5°S, 22.5°S, and 7.5°S latitude, respectively. The readers are requested to note the change in the scale of the color bars in each subplot while comparing. The DW1 seems to exhibit a gradual increase in amplitude starting a few days before the PWD and remains active during the post-warming phase at 67.5°S (Fig. 3a). Fig. 3b appears to show the enhanced DW1 amplitude after the PWD at 54.5°S similar to Fig. 3a. At 22.5°S a small decrement in the DW1 amplitude is observed in the upper mesosphere (65–75 km altitude) for a few days between the SSW onset and PWD. Moreover, relative enhancement in the DW1 amplitude is observed at lower altitudes (50–60 km) in the mesosphere after the PWD (Fig. 3c). Fig. 3d shows the enhanced activity of the DW1 after the PWD at 7.5°S.

Fig. 3e–h show the temporal variability of the DE3 at 67.5°S, 54.5°S, 22.5°S, and 7.5°S latitude, respectively. The DE3 component shows significant enhancement during the pre-warming period and diminishes considerably at SSW onset and continues to remain weak in the warming and post-warming interval at 67.5°S (Fig. 3e). At 54.5°S (Fig. 3f), the DE3 also seems to behave in the same manner as Fig. 3e. A slight enhancement in the DE3 activity is noticeable around the warming onset till the PWD at 22.5°S (Fig. 3g). Another notable enhancement in the DE3 amplitude is observed in the upper mesosphere starting a week after the PWD. The DE3 amplitude at 7.5°S (Fig. 3h) exhibits similar observational features as Fig. 3g.

Overall, the DW1 amplitude is apparently dominant during the post-warming phase at RO, KE, CA and CP latitude. Therefore, the DW1 amplitude seems to evince con-

sistent characteristics at the above-mentioned representative locations in the SH. The DE3 amplitude apparently enhances during the pre-warming interval and diminishes at the SSW onset at high latitudes, i.e., at RO and KE latitudes. However, the DE3 amplitude at low latitudes (CA and CP) seems to increase primarily during the post-warming phase. Hence, the behavior of the DE3 at low latitudes shows a contrasting character with respect to high latitudes.

Fig. 3i–l show the SW2 amplitude variability during the observational interval in the MLT at 67.5°S, 54.5°S, 22.5°S, and 7.5°S latitude, respectively. The SW2 amplitude appears to diminish considerably after the PWD at 67.5°S (Fig. 3i). At 54.5°S, the SW2 seems to remain relatively higher before the warming onset and exhibits a decrement in its activity after the PWD as shown in Fig. 3j. At 22.5°S, the SW2 activity remains weak during most of the pre-warming period. However, it enhances in the upper mesosphere just around the PWD and continues during the post-warming interval (Fig. 3k). Fig. 3l exhibits enhancement in the SW2 amplitude around the PWD which continues during the rest of the observational interval, similar to Fig. 3k. Altogether, the SW2 amplitude shows weakening after the PWD at high latitudes i.e., at RO and KE. However, there is a noticeable increase in the SW2 amplitude after the PWD in the low latitude upper mesosphere (CP and CA). Hence, the SW2 activity at low latitudes shows contrasting behavior with respect to the high latitudes during the observational period.

3.4. Tidal sources

The role of possible sources in the variability of the DW1, DE3, and SW2 amplitude is to be looked into next. The DW1 is excited primarily by absorption of solar near-infrared (NIR) radiation by water vapor in the lower atmosphere (Lieberman et al., 2007; Sridharan et al., 2012). The nonmigrating DE3 is excited by the latent heat release associated with convective activity (Hagan & Forbes, 2002; Hagan et al., 2007). Therefore, we investigated the variability in total precipitable water vapor (TPWV) utilizing the MERRA-2 data and outgoing longwave radiation (OLR) provided by the NCEP to understand the response of the DW1 and DE3 during the observational period. TPWV is defined as the total atmospheric water vapor contained in a vertical column of the cross-section unit (King et al., 1992). OLR is the measure of energy emitted from Earth and its atmosphere out to space in the form of infrared thermal radiation. The greater (lesser) OLR values indicate suppressed (enhanced) convection. Hence, the current study utilizes the OLR value as a proxy for convection. Fig. 4a–d show the variability of zonal mean TPWV (blue curve) and zonal mean OLR (red curve) at 67.5°S, 54.5°S, 22.5°S, and 7.5°S, respectively. The thin curve represents the daily amplitude, and the bold curve indicates the moving average of the amplitudes in all the figures. The moving

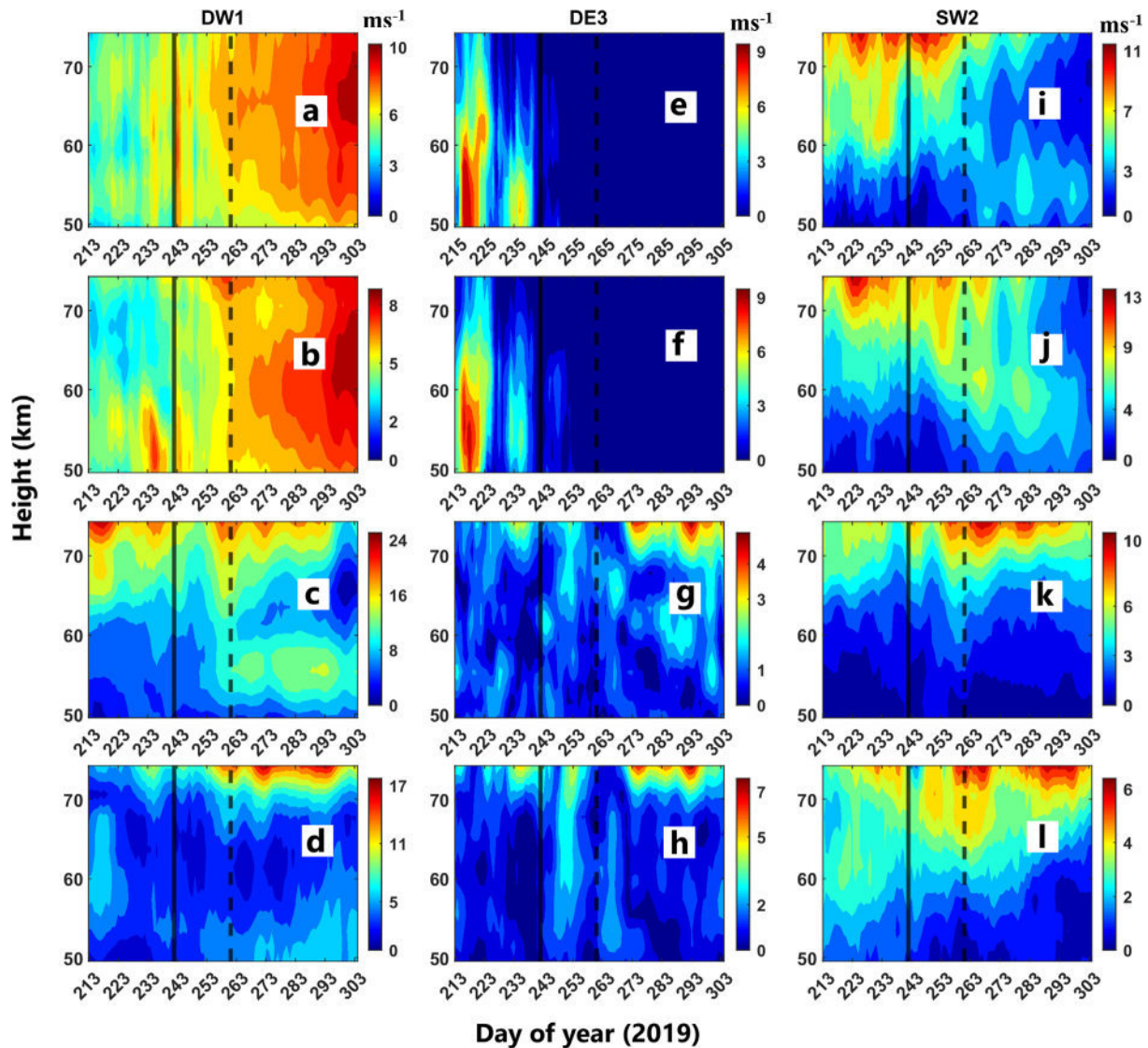


Fig. 3. Temporal variation in the DW1 amplitude in ms^{-1} in the mesosphere (50–75 km altitude) at (a) 67.5°S (RO latitude), (b) 54.5°S (KE latitude), (c) 22.5°S (CP latitude) and (d) 7.5°S (CA latitude) estimated using meridional wind data from MERRA-2. Same for the DE3 amplitude in ms^{-1} at (e) 67.5°S (RO latitude), (f) 54.5°S (KE latitude), (g) 22.5°S (CP latitude) and (h) 7.5°S (CA latitude), and for the SW2 amplitude in ms^{-1} at (i) 67.5°S (RO latitude), (j) 54.5°S (KE latitude), (k) 22.5°S (CP latitude) and (l) 7.5°S (CA latitude). Please note the change of scale in the color bars while comparing.

average is calculated over a sliding window of length 11 days to delineate the broad variability.

At 67.5°S, the OLR shows an apparent increase at the onset of the warming event. The TPWV does not indicate evident variability apart from a noticeable peak around the onset date (Fig. 4 a). At 54.5°S both the OLR and TPWV exhibit gradual increment during the observational span (Fig. 4b). The OLR at 22.5°S does not show any notable change concerning the warming event. However, there is an increasing trend in the TPWV at the SSW onset which continues during the rest of the observational period, as depicted in Fig. 4c. At 7.5°S the OLR value seems to drop after the PWD and remains low for the rest of the observational interval. On the other hand, the TPWV shows significant continuous enhancement following the PWD (Fig. 4d).

Overall, the TPWV shows an increasing trend at all the present latitudes except at the high latitude (67.5°S) where TPWV is remarkably small as compared to the other latitudes. The OLR seems to decrease at low latitude (7.5°S) and increase at mid and high latitudes (54.5°S and 67.5°S) at the SSW onset and during the post-warming interval. The OLR is observed to be greater at mid and high latitudes than at low latitudes, and the TPWV is found to be more significant at low latitudes than at high latitudes. Such variability has important implications related to the dynamical condition of the ambient atmosphere, which will be discussed in the next section.

Several past studies attributed the SW2 amplitude variability to the change in forcing due to stratospheric ozone variability (Goncharenko et al., 2012; Sridharan et al., 2012). Change in the tidal propagation related to the zonal

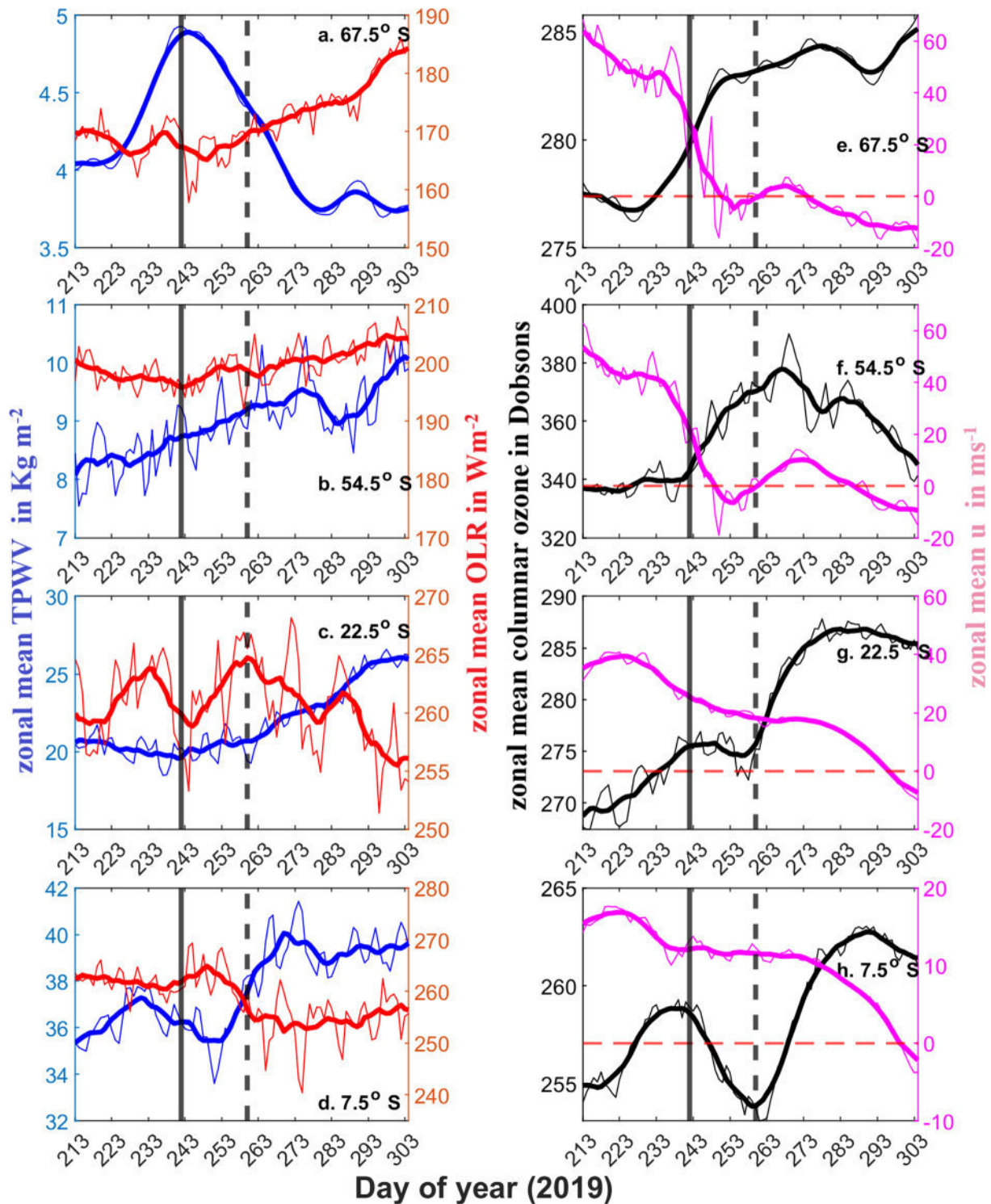


Fig. 4. Temporal variation in the zonal mean TPWV (blue curve) in Kg m^{-2} and zonal mean OLR in Wm^{-2} (red curve) at (a) 67.5°S (RO latitude), (b) 54.5°S (KE latitude), (c) 22.5°S (CP latitude) and (d) 7.5°S (CA latitude). Temporal variation in the zonal mean columnar ozone (black curve) in Dobsons and zonal mean u (averaged over 50–75 km altitude) in ms^{-1} (magenta curve) at (a) 67.5°S (RO latitude), (b) 54.5°S (KE latitude), (c) 22.5°S (CP latitude) and (d) 7.5°S (CA latitude). The thin curve represents the daily value, and the bold curve indicates the moving average.

mean atmospheric conditions was also reported by the past studies (e.g., [Pedatella & Liu, 2013](#)). The heating by the solar UV radiation due to absorption through ozone in the stratosphere and mesosphere is a primary excitation source for SW2 tide (e.g., [Lindzen and Chapman, 1969](#)).

Previous studies showed that the meridional temperature gradient and associated zonal wind affect tidal propagation ([Lindzen and Hong, 1974](#); [Aso et al., 1981](#)). These studies instigate us to look into the role of the zonal mean columnar ozone (O_3) and zonal mean zonal wind (u) (averaged

over the altitude region 50–75 km) in the MLT towards the variability of the SW2 during the observational interval. Fig. 4e–h show the temporal variability in the ozone (black curve) in Dobsons and u (magenta curve) in m s^{-1} at 67.5°S, 54.5°S, 22.5°S, and 7.5°S, respectively. The dashed red horizontal line in Fig. 4e–h represents zero wind. The westerly u at 67.5°S decelerates considerably from $\sim 20 \text{ m s}^{-1}$ at the SSW onset to 0 m s^{-1} before the PWD and hereafter reverses to the easterly wind for a few days. The ozone starts increasing few days before the onset of the warming event at 67.5°S (Fig. 4e). The u at 54.5°S behaves very similarly to that at 67.5°S.

The ozone is found to increase at warming onset and peaking just after the PWD at 54.5°S. A similar weakening trend of the westerly u is observed at 22.5°S, as shown in Fig. 4g. However, here reversal of the westerly to the easterly takes place a month after the PWD. The ozone also behaves in a similar fashion at 54.5°S although it peaks after a month of the warming onset at 7.5°S. At 7.5°S (Fig. 4h), the u exhibits variability similar to Fig. 4g. The ozone seems to peak around the SSW onset followed by a minimum near the PWD. Another rise in the ozone is observed almost a month later at 7.5°S. Overall, significant deceleration of the westerly wind in the mesosphere (averaged over 50–75 km altitude) is observed at all observational latitudes. In general, the ozone is found to be maximum at mid latitude (54.5°S) and minimum at equatorial latitude (7.5°S). The relationship of the ozone and zonal wind with the observed tidal variability will be discussed later.

3.5. Deseasoned tidal variability

So far, we have attempted to characterize tidal variability in September (spring equinox) 2019. However, since the tidal activities respond significantly to the seasonal transition (equinox), it is important to find the general seasonal behavior with the help of the other non-SSW years around the same temporal interval in order to isolate the seasonal contribution from the SSW effect taking place at the same time interval. For that purpose, we have chosen the same observational interval (1 August–31 October) of 2017, 2018, 2020, and 2021 (adjacent non-SSW years) to further analyze the seasonal behavior of the tidal components. Surprisingly, the broad variability of the DW1, DE3, and SW2 amplitudes in the non-SSW years (Figure not shown) are found to exhibit almost similar behavior with the year 2019. Therefore, the broad variability observed around the present warming event is most probably due to the seasonal effect. Therefore, to identify the signatures of the tidal variability solely associated with the SSW, the composite seasonal mean amplitudes corresponding to the non-SSW years of all the major tidal modes have been subtracted from the instantaneous tidal amplitudes. This method can be termed as deseasoning of the tides as mentioned in the rest of the paper. The deseasoned tidal amplitude during the observational period of the 2019 warming

event are shown in Fig. 5. The deseasoned amplitudes of the respective tides are mentioned with a “d” suffix in the rest of the paper.

Therefore, a positive or negative DW1d value represents an increment or decrement in the DW1 amplitude during the 2019 SSW observational interval with respect to the considered non-SSW years. DE3d and SW2d represent the deseasoned amplitude as mentioned above in the case of DE3 and SW2, respectively. The bold white line in Fig. 5 represents 2 sigma deviation from the composite seasonal mean amplitude and the area enclosed by this curve is considered to be statistically significant. The readers are requested to note the change in the scale of the color bars in each subplot while comparing. The DW1d shows consistent positive patch in the upper mesosphere around the PWD all the locations except RO. Furthermore, consecutive bursts of positive DW1d near 50–60 km altitude can be noted during the postwarming period at CP. The DE3d does not exhibit any distinct patches concerning the 2019 warming event at 67.5°S, 54.5°S, and 22.5°S, as shown in Fig. 5e–g. However, DE3d is found to be significantly negative before the onset date at 7.5°S, and later switches to positive for a few days around the PWD (Fig. 5h). The SW2d is found to be significantly positive at the SSW onset for a few days at 67.5°S and 54.5°S, as shown in Fig. 5i and 5j, respectively. Fig. 5k and 5l exhibit the positive SW2d observed on and after the PWD at 22.5°S and 7.5°S, respectively. Overall, mainly the DW1d and SW2d show substantial enhancement (positive patches) in response to the 2019 minor warming event with respect to the non-SSW years.

We also attempt to investigate the relationship between the deseasoned tidal amplitudes and the deseasoned source parameters (TPWV, ozone, OLR etc.). However, no correlation among the tides and source parameters are found and hence details are not included in the paper. The implication of this finding will be discussed later.

To obtain a holistic picture of the tidal dynamics associated around the warming we further looked into the latitudinal-temporal variability of the amplitude of the DW1, DE3, and SW2 at a representative altitude in the MLT, i. e. 0.01 hPa in the SH. Fig. 6a–c show the latitudinal-temporal section of the DW1, DE3, and SW2 amplitude, respectively at 0.01 hPa. The readers are requested to note the change in the scale of the color bars in each subplot while comparing. At 0.01 hPa, the DW1 is apparently dominant in the latitudinal band (15–35°S) during the pre-warming interval, followed by a shift in the enhancement structure towards equatorial latitude as it weakens during the post-warming phase. A slight enhancement in the DW1 amplitude at mid and high latitudes (60–90°S) during the post-warming interval is also observed (Fig. 6a). The DE3 amplitude starts growing at the onset of the warming event at low latitudes. There is a relative decrement in the DE3 activity at mid and high latitudes at the SSW onset (Fig. 6b). Fig. 6c shows the dominant activity of the SW2 at mid-latitudes until the PWD. At

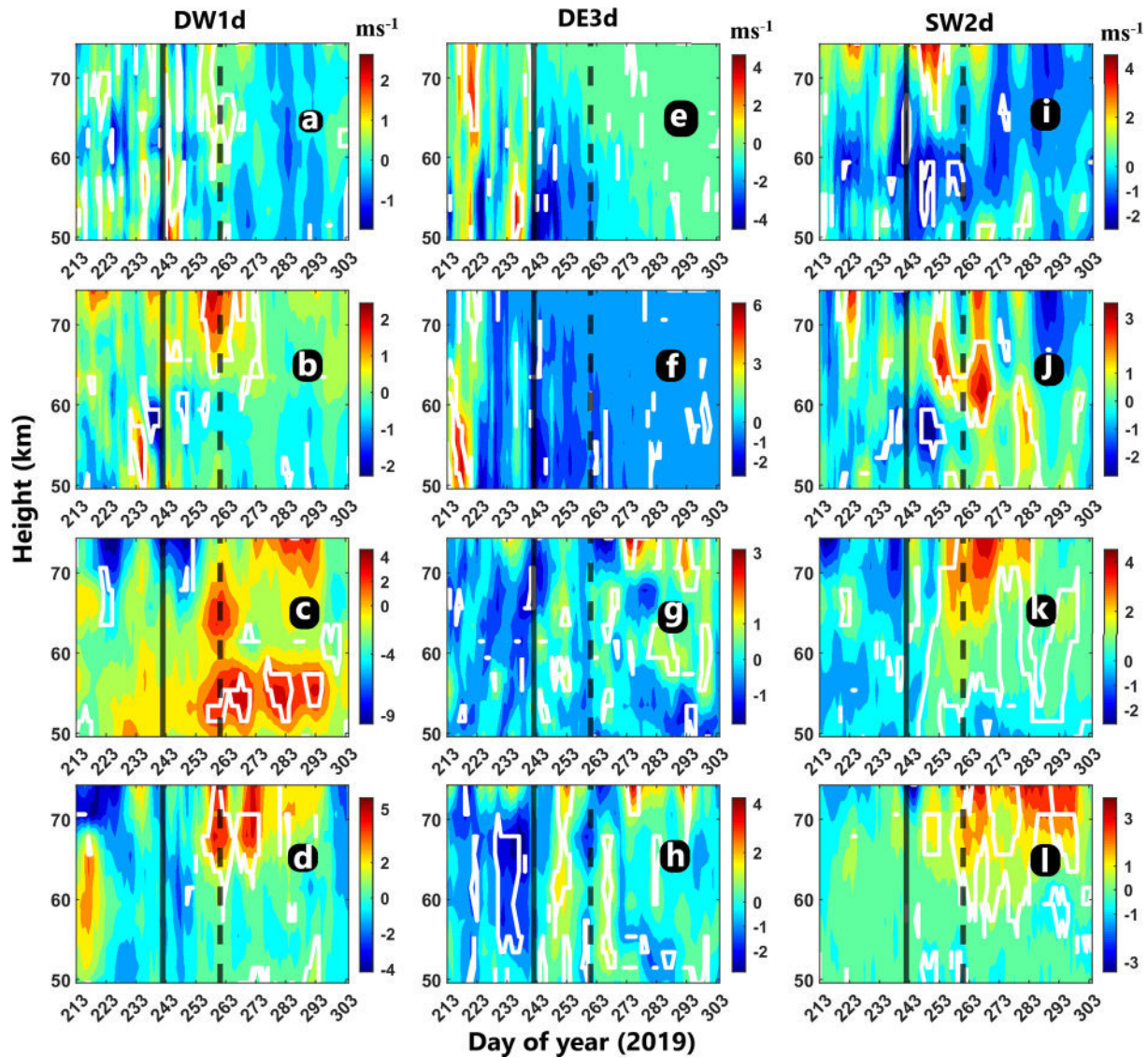


Fig. 5. Temporal variation in the DW1d in ms^{-1} in the mesosphere (50–75 km altitude) at (a) 67.5°S (RO latitude), (b) 54.5°S (KE latitude), (c) 22.5°S (CP latitude) and (d) 7.5°S (CA latitude) estimated from MERRA-2 data. Same for the DE3d in ms^{-1} at (e) 67.5°S (RO latitude), (f) 54.5°S (KE latitude), (g) 22.5°S (CP latitude) and (h) 7.5°S (CA latitude), and for the SW2d amplitude in ms^{-1} at (i) 67.5°S (RO latitude), (j) 54.5°S (KE latitude), (k) 22.5°S (CP latitude) and (l) 7.5°S (CA latitude). The white contour line denotes statistically significant region. Please note the change of scale in the color bars while comparing.

low latitude (15–30°S) there also exists an enhancement in the SW2 amplitude that maximizes around the PWD. It should be mentioned that the similar broad variability features in the DW1, DE3, and SW2 amplitudes are found during the non-SSW years as well (not shown here), hence such broad variability may not be attributed solely to the 2019 SH SSW as also found before.

To identify the SSW associated impact the temporal variability of the DW1d, DE3d, and SW2d at 0.01 hPa in the SH are also shown in Fig. 6d, e, f, respectively. The white contour line represents statistically significant region as mentioned before. The DW1d is found to be positive around the PWD at equatorial, mid, and high latitudes (Fig. 6d). However, at extratropical latitudes, the DW1d has a negative value at the SSW onset which continues till the PWD. Fig. 6e shows significant activity of the DE3 par-

ticularly at equatorial latitudes in terms of a positive DE3d patch between the onset and PWD followed by a negative patch soon after the PWD for a few days. The SW2 shows significant enhancement which is identified by the positive SW2d value observed at the SSW onset until the PWD, especially at high latitudes (Fig. 6f). At low latitude significant positive SW2d can be noted around the PWD. Overall, the SW2d exhibits the most significant response with enhancement to the warming event, followed by the DW1 and DE3 during the observational span.

4. Discussion

Our present study has illustrated some interesting and unique dynamical aspects of a minor SSW event from the SH during September 2019 with meteor radar wind

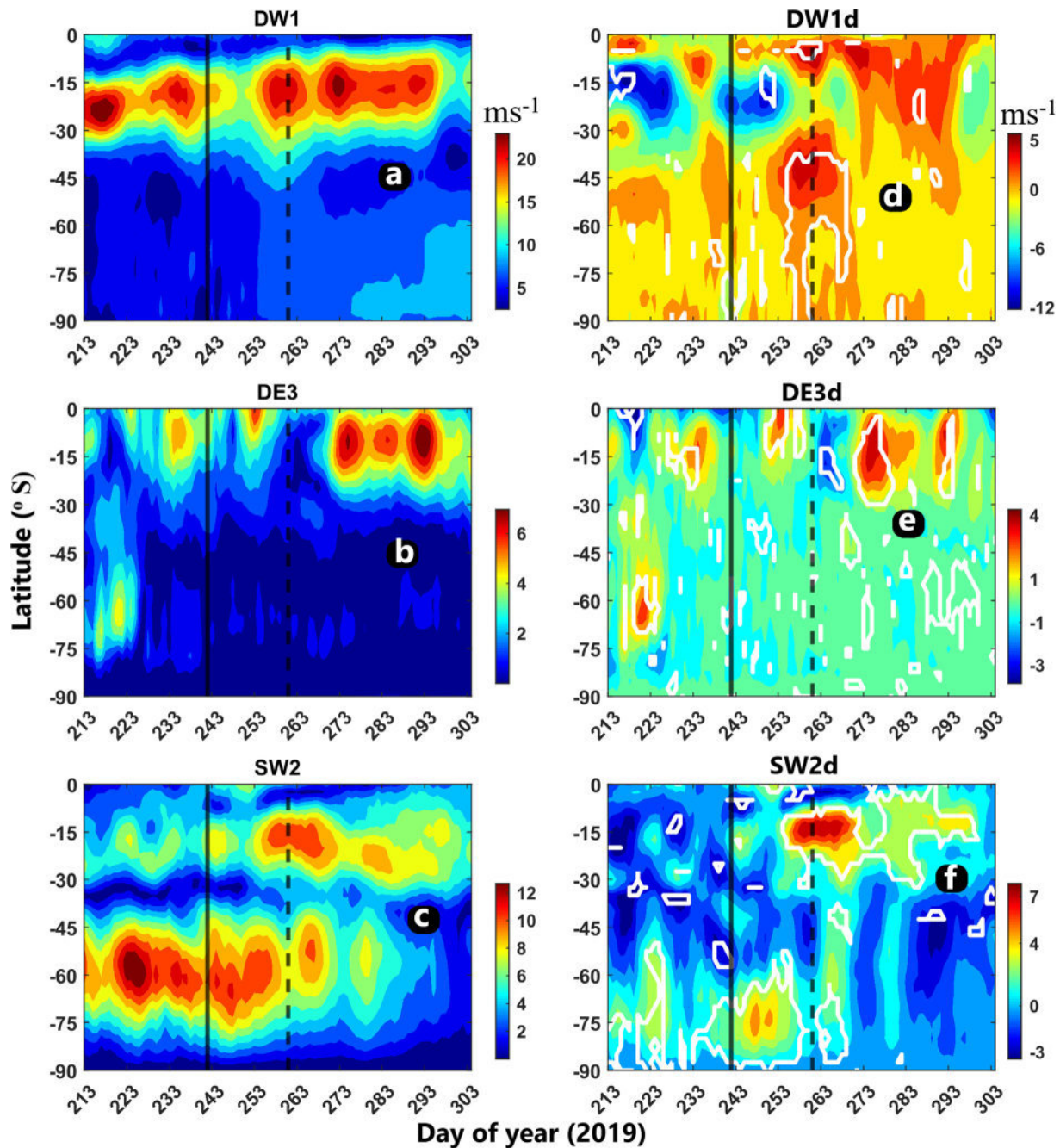


Fig. 6. Latitudinal-temporal variation of the (a) DW1, (b) DE3, and (c) SW2 amplitude at 0.01 hPa estimated from the MERRA-2 data set. Same for the (d) DW1d, (e) DE3d, and (f) SW2d at 0.01 hPa. The white contour line denotes statistically significant region. Please note the change of scale in the color bars while comparing.

observations and the MERRA-2 reanalysis dataset. The 2019 minor SSW is only the second most robust warming event in the SH reported so far. The current study aims at providing valuable insights into the MLT dynamics in terms of tidal activity during such a rare event.

The present minor warming event reveals movement of high polar warming from the mesosphere to the stratosphere before the SSW onset, as shown in Fig. 1a. According to Pedatella et al. (2018), the mesospheric anomalies often, although not always, initially appear a week or more before the peak stratospheric disturbances. The low lati-

tude MLT (0.01 hPa) shows contrasting behavior with respect to high latitudes, i.e., warming in the mesosphere concurrent with high latitude cooling. Polar mesospheric cooling during the warming event was reported in past studies (Schoeberl, 1978; Mukhtarov et al., 2007; Mitra et al., 2022). The adiabatic cooling in the polar mesosphere is due to the upward flow of mean residual circulation (Matsuno, 1971; Liu and Roble, 2002). The zonal mean zonal wind is also affected at 0.01 hPa in terms of weakening of the westerly wind and reversal to easterly wind at mid and high latitudes before the SSW onset (Fig. 1d)

(Limpasuvan et al., 2016; Pedatella et al., 2014). Such reduction in the magnitude of the westerly wind may be due to the induction of the westward momentum to the mean flow by the dissipation of westward traveling PW at mesospheric altitudes during the warming period (Mitra et al. 2022).

Therefore, a noticeable and significant change in the background dynamical condition is found during the September 2019 SH minor SSW event. However, such changes are not accompanied by a consistent variability in the local DT and ST amplitude in the MLT region during the observational interval, as observed from the individual meteor radar observational sites, i.e., RO, KE, CP, and CA (Fig. 2). Furthermore, the global tidal modes in terms of various wavenumber components seem to reveal noticeable variability during the observational period (Fig. 3).

The ground-based method from a single geographic location has a disadvantage in distinguishing between global and local signatures. The constructive and destructive interference between different zonal wavenumbers can itself drive longitudinal and temporal variations in the locally measured tidal wind variability (Hibbins et al., 2010). Any discussion on the drivers of tidal variability needs to address each mode separately (Hibbins et al., 2019). To address this issue in the present work the zonal wavenumber diagnosis utilizing the MERRA-2 global reanalysis dataset is employed for elucidating the global tidal propagation response concerning the observational interval.

Interestingly, in the present study, there is a significant global scale tidal variability during the observational period, as found in the DW1, DE3, and SW2 amplitude in the MLT. We have found a consistent variability in the DW1 amplitude in terms of increased amplitude around the PWD at all the present latitudes (Fig. 3). Furthermore, the observed broad-scale variability in the DW1 amplitude during the observational period is consistent with the TPWV at all the locations (except at RO where water vapor is generally very less), as seen in Fig. 4a–d. Chapman and Lindzen (1970) described the most significant forcing of the DW1 as solar near-infrared absorption by water vapor in the troposphere. In this context, it can be mentioned that Lieberman et al. (2007) reported a substantial enhancement of the DW1 due to increased water vapor concentration. However, since the DW1 amplitude varies in similar manner during the spring equinox in non-SSW years as well, such variability may be attributed to the seasonal changes. Interestingly, the deseasoned component of the DW1, i.e., DW1d is found to increase significantly for a few days around the PWD at all the present latitudes as noted by the positive patches (Fig. 5a–d) indicating a plausible response of the DW1 to the warming event.

We observed contrasting behavior of the DE3 amplitude at mid and high latitudes (decrease) with respect to low latitudes (increase), after the 2019 SSW onset. Such reduction in the DE3 amplitude at mid and high latitudes may be due to decreased convective activity at a similar latitude. Sup-

pressed (enhanced) convective activity can be identified from the increased (decreased) OLR value particularly from DOY 233 onwards, as illustrated in Fig. 4a–d. Similarly, increased convective activity at low latitudes may explain the rise in the DE3 amplitude. Such contrasting behavior of DE3 amplitudes between low and high latitudes is also visible in the global tidal map at 0.01 hPa from Fig. 6b. The previous study by Hagan and Forbes (2003) mentioned about the convectively forced DE3 which is in line with the present interpretation. However, the DE3 amplitude in the SSW year is found to have similar trends in the non-SSW years as well, hence such broad-scale variability due to convective activity may be dominated by seasonal changes. Interestingly, the deseasoned component of the DE3 (DE3d) amplitude exhibits a prominent response to the SSW at CA latitude as found by the significant negative patch before onset and changes to positive hereafter around the PWD and postwarming interval (Fig. 5h). It can be mentioned that, the DE3 has potential to propagate directly into the thermosphere to modulate the E region dynamo and imprinting the tropospheric convective variability into the ionospheric plasma (Oberheide et al., 2009; Chang et al., 2013). Furthermore, the prominent role of the DE3 in causing wavenumber 4 structure of the equatorial ionization anomaly in global scale was also reported by the previous studies (Immel et al., 2006; Wan et al., 2008). Therefore, changes in the DE3 amplitude at low latitudes in connection with the SSW, as found in the present study may bear important implications on the ionospheric variability.

The SW2 amplitude is found to decrease considerably from the PWD onwards at mid and high latitudes, i.e. at KE and RO (Fig. 3i, 3j). However, at low latitudes, i.e. at CP and CA the SW2 amplitude is found to increase in the upper mesosphere around the PWD (Fig. 3k, 3l). According to the past studies, when the background winds are strongly westward, conditions become less favorable for the propagation of the SW2 from the stratosphere into the MLT (Lindzen and Hong, 1974; Aso et al., 1981; Pedatella & Liu, 2013; Limpasuvan et al., 2016). In this context, it is relevant to mention that the eastward wind reversal had also been referred to explain the SW2 weakening after SSW onset in the past studies (Hibbins et al., 2019; Sassi et al., 2013). Furthermore, the ozone also shows an increasing trend after PWD (Fig. 4f–h) similar to the SW2 activity at low latitudes i.e. at CP and CA implying the plausible influence of the ozone on the SW2 activity. However, such broad variability in the SW2 amplitude in the SSW year is most probably due to the seasonal change as similar behavior in the SW2 activity is found in the non-SSW years. It should be mentioned that the deseasoned component of the SW2, i.e., SW2d is found to enhance significantly between the onset and PWD at high latitudes (Fig. 5i and 5j). Additionally, we observe a significant enhancement in the SW2d amplitude in the low latitude MLT which maximizes after the PWD (Fig. 5k and 5l). Such significant response in the SW2d to the SSW is further supported by Fig. 6c and 6f.

As mentioned before that no clear relationship between the deseasoned tidal amplitudes and the deseasoned source parameters (TPWV, ozone, OLR etc.) unlike the seasonal trend are found in the present study. This indicates that the short-term temporal variability in the global tidal modes due to the SSW during the seasonal transition are not governed directly by the sources, rather it implies the involvement of some complex processes in connection with such global-scale atmospheric disturbances. Understanding the underlying physical mechanisms of such short-term variability in the tidal components during the SSW requires further extensive investigations.

5. Summary and conclusions

The present work portrays the atmospheric tidal wave dynamics in the MLT during a minor but impactful SSW event in September 2019 observed in the SH from equatorial, extratropical, mid, and high latitudes. Although there have been studies on the convective activity, ionospheric variability, and planetary wave activity during this event, there is hardly any literature related to the variability of the atmospheric tides. The DT and ST amplitude derived from location-specific meteor radar meridional wind does not reveal any consistent variability in the MLT during the observational interval. However, we observe substantial and consistent variability in the global tidal modes at similar latitudes, particularly in the DW1, DE3, and SW2 components during the observational period. Surprisingly, similar behavior in the DW1, DE3, and SW2 amplitude is also found in non-SSW years during the same season. Hence such a behavior is attributed to the seasonal variability of the tides. The broad variability in the DW1, DE3, and SW2 amplitude can be linked to the respective sources, i. e., water vapor, convective activity, ozone, and zonal wind.

To delineate the exclusive response of the global tidal modes to the present warming event, the deseasoned tidal amplitudes are estimated. Interestingly, the deseasoned DW1 is found to increase significantly for a few days around the PWD at all the latitudes showing a clear response to the warming. The deseasoned DE3 is also found to respond significantly pertaining to the warming event at equatorial latitudes. The deseasoned SW2 exhibits notable enhancement around the PWD. The short-term (deseasoned) variability in the dominant tidal modes in connection with the SSW can't be explained through sources as complex processes are deemed to be involved in such global disturbances and hence further investigations are being sought in this regard.

Declaration of Competing Interest

The authors declare that they have no known competing financial interests or personal relationships that could have appeared to influence the work reported in this paper.

Acknowledgements

The present work is supported by the Department of Space (Government of India), National Institute for Space Research, Federal University of Campina Grande, National Council for Scientific and Technological Development (Government of Brazil), Sao Paulo Research Foundation (Sao Paulo, Brazil) and Natural Environment Research Council (NERC), UK. The radars at KE and RO were supported by NERC grant numbers NE/R001391/1 and NE/R001235/1. The authors would like to thank the reviewers for useful comments.

References

- Andrews, D.G., Holton, J.R., Leovy, C.B., 1987. Middle atmosphere dynamics (No. 40). Academic Press.
- Aso, T., Nonoyama, T., Kato, S., 1987. Numerical simulation of semidiurnal atmospheric tides. *J. Geophys. Res.* **92** (A13), 11388–11400. <https://doi.org/10.1029/JA086iA13p11388>.
- Chang, L.C., Lin, C.H., Yue, J., Liu, J.Y., Lin, J.T., 2013. Stationary planetary wave and nonmigrating tidal signatures in ionospheric wave 3 and wave 4 variations in 2007–2011 FORMOSAT-3/COSMIC observations. *J. Geophys. Res.* **118** (10), 6651–6665. <https://doi.org/10.1002/jgra.50583>.
- Chapman, S., Lindzen, R.S., 1970. *Atmospheric Tides*. D. Reidel, Norwell, Mass, 200 pp.
- Dowdy, A.J., Vincent, R.A., Murphy, D.J., Tsutsumi, M., Riggan, D.M., Jarvis, M.J., 2004. The large-scale dynamics of the mesosphere–lower thermosphere during the Southern Hemisphere stratospheric warming of 2002. *Geophys. Res. Lett.* **31** (14). <https://doi.org/10.1029/2004GL020282>.
- Eswaraiah, S., Kim, J.H., Lee, W., Hwang, J., Kumar, K.N., Kim, Y.H., 2020. Unusual changes in the Antarctic middle atmosphere during the 2019 warming in the Southern Hemisphere. *Geophys. Res. Lett.* **47** (19), e2020GL089199.
- Forbes, J.M., Garrett, H.B., 1978. Thermal excitation of atmospheric tides due to insolation absorption by O₃ and H₂O. *Geophys. Res. Lett.* **5** (12), 1013–1016. <https://doi.org/10.1029/GL005i012p01013>.
- Gelaro, R., McCarty, W., Suárez, M.J., Todling, R., Molod, A., Takacs, L., Randles, C.A., Darmenov, A., Bosilovich, M.G., Reichle, R., Wargan, K., 2017. The modern-era retrospective analysis for research and applications, version 2 (MERRA-2). *J. Clim.* **30** (14), 5419–5454. <https://doi.org/10.1175/JCLI-D-16-0758.1>.
- Goncharenko, L.P., Coster, A.J., Plumb, R.A., Domeisen, D.I., 2012. The potential role of stratospheric ozone in the stratosphere–ionosphere coupling during stratospheric warmings. *Geophys. Res. Lett.* **39** (8). <https://doi.org/10.1029/2012GL051261>.
- Guharay, A., Batista, P.P., Clemesha, B.R., Sarkhel, S., 2014. Response of the extratropical middle atmosphere to the September 2002 major stratospheric sudden warming. *Adv. Space Res.* **53** (2), 257–265. <https://doi.org/10.1016/j.asr.2013.11.002>.
- Guharay, A., Batista, P.P., 2019. On the variability of tides during a major stratospheric sudden warming in September 2002 at Southern hemispheric extra-tropical latitude. *Adv. Space Res.* **63** (8), 2337–2344. <https://doi.org/10.1016/j.asr.2018.12.037>.
- Hagan, M.E., Forbes, J.M., 2002. Migrating and nonmigrating diurnal tides in the middle and upper atmosphere excited by tropospheric latent heat release. *J. Geophys. Res.* **107** (D24), ACL-6. <https://doi.org/10.1029/2001JD001236>.
- Hagan, M.E., Forbes, J.M., 2003. Migrating and nonmigrating semidiurnal tides in the upper atmosphere excited by tropospheric latent heat release. *J. Geophys. Res.* **108** (A2). <https://doi.org/10.1029/2002JA009466>.
- Hagan, M.E., Maute, A., Roble, R.G., Richmond, A.D., Immel, T.J., England, S.L., 2007. Connections between deep tropical clouds and the

- Earth's ionosphere. *Geophys. Res. Lett.* 34 (20). <https://doi.org/10.1029/2007GL030142>.
- He, M., Chau, J.L., 2019. Mesospheric semidiurnal tides and near-12 h waves through jointly analyzing observations of five specular meteor radars from three longitudinal sectors at boreal midlatitudes. *Atmospheric Chem. Phys.* 19 (9), 5993–6006. <https://doi.org/10.5194/acp-19-5993-2019>.
- He, M., Forbes, J.M., Chau, J.L., Li, G., Wan, W., Korotyskhin, D.V., 2020. High-order solar migrating tides quench at SSW onsets e2019GL086778. *Geophys. Res. Lett.* 47 (6). <https://doi.org/10.1029/2019GL086778>.
- Hibbins, R.E., Espy, P.J., Orsolini, Y.J., Limpasuvan, V., Barnes, R.J., 2019. SuperDARN observations of semidiurnal tidal variability in the MLT and the response to sudden stratospheric warming events. *J. Geophys. Res.* 124 (9), 4862–4872. <https://doi.org/10.1029/2018JD030157>.
- Hibbins, R.E., Marsh, O.J., McDonald, A.J., Jarvis, M.J., 2010. A new perspective on the longitudinal variability of the semidiurnal tide. *Geophys. Res. Lett.* 37 (14). <https://doi.org/10.1029/2010GL044015>.
- Hocking, W.K., Fuller, B., Vandepeer, B., 2001. Real-time determination of meteor-related parameters utilizing modern digital technology. *J. Atmos. Sol. Terr. Phys.* 63 (2–3), 155–169. [https://doi.org/10.1016/S1364-6826\(00\)00138-3](https://doi.org/10.1016/S1364-6826(00)00138-3).
- Immel, T.J., Sagawa, E., England, S.L., Henderson, S.B., Hagan, M.E., Mende, S.B., Frey, H.U., Swenson, C.M., Paxton, L.J., 2006. Control of equatorial ionospheric morphology by atmospheric tides. *Geophys. Res. Lett.* 33 (15). <https://doi.org/10.1029/2006GL026161>.
- Kato, S., Tsuda, T., Watanabe, F., 1982. Thermal excitation of non-migrating tides. *J. Atmos. Terr. Phys.* 44 (2), 131–146. [https://doi.org/10.1016/0021-9169\(82\)90116-7](https://doi.org/10.1016/0021-9169(82)90116-7).
- King, M.D., Kaufman, Y.J., Menzel, W.P., Tanre, D., 1992. Remote sensing of cloud, aerosol, and water vapor properties from the moderate resolution imaging spectrometer (MODIS). *IEEE Trans. Geosci. Remote Sens.* 30 (1), 2–27. <https://doi.org/10.1109/36.124212>.
- Labitzke, K., Naujokat, B., Kunze, M., 2005. The lower Arctic stratosphere in winter since 1952: an update. *Sparc. Newslett.* 24, 27–28.
- Lieberman, R.S., Riggins, D.M., Ortland, D.A., Nesbitt, S.W., Vincent, R.A., 2007. Variability of mesospheric diurnal tides and tropospheric diurnal heating during 1997–1998. *J. Geophys. Res.* 112 (D20). <https://doi.org/10.1029/2007JD008578>.
- Lima, L.M., Alves, E.O., Batista, P.P., Clemesha, B.R., Medeiros, A.F., Buriti, R.A., 2012. Sudden stratospheric warming effects on the mesospheric tides and 2-day wave dynamics at 7 S. *J. Atmos. Sol. Terr. Phys.* 78, 99–107. <https://doi.org/10.1016/j.jastp.2011.02.013>.
- Limpasuvan, V., Orsolini, Y.J., Chandran, A., Garcia, R.R., Smith, A.K., 2016. On the composite response of the MLT to major sudden stratospheric warming events with elevated stratopause. *J. Geophys. Res.* 121 (9), 4518–4537. <https://doi.org/10.1002/2015JD024401>.
- Lindzen, R.S., Chapman, S., 1969. Atmospheric tides. *Space Sci. Rev.* 10 (1), 3–188.
- Lindzen, R.S., Hong, S.S., 1974. Effects of mean winds and horizontal temperature gradients on solar and lunar semidiurnal tides in the atmosphere. *J. Atmos. Sci.* 31 (5), 1421–1446.
- Liu, H.L., Roble, R.G., 2002. A study of a self-generated stratospheric sudden warming and its mesospheric-lower thermospheric impacts using the coupled TIME-GCM/CCM3. *J. Geophys. Res.* 107 (D23), ACL-15. <https://doi.org/10.1029/2001JD001533>.
- Matsuno, T., 1971. A dynamical model of the stratospheric sudden warming. *J. Atmos. Sci.* 28 (8), 1479–1494. [https://doi.org/10.1175/1520-0469\(1971\)028<1479:ADMOTS>2.0.CO;2](https://doi.org/10.1175/1520-0469(1971)028<1479:ADMOTS>2.0.CO;2).
- Mitchell, N.J., 2019. University of Bath: Rothera Skiyet Meteor Radar data (2005–present), Centre for Environmental Data Analysis. <https://catalogue.ceda.ac.uk/uuid/aa44e02718fd4ba49cfe36d884c6e50>.
- Mitchell, N.J., 2021. University of Bath: King Edward Point Skiyet meteor radar data (2016–2020), Centre for Environmental Data Analysis. <https://doi.org/10.5285/061fc7fd1ca940e7ad685daf146db08f>.
- Mitra, G., Guharay, A., Batista, P.P., Buriti, R.A., 2022. Impact of the September 2019 minor sudden stratospheric warming on the low-latitude middle atmospheric planetary wave dynamics e2021JD035538. *J. Geophys. Res.*
- Miyoshi, Y., Yamazaki, Y., 2020. Excitation mechanism of ionospheric 6-day oscillation during the 2019 September sudden stratospheric warming event e2020JA028283. *J. Geophys. Res.* 125 (9).
- Mukhtarov, P., Pancheva, D., Andonov, B., Mitchell, N.J., Merzlyakov, E., Singer, W., Hocking, W., Meek, C., Manson, A., Murayama, Y., 2007. Large-scale thermodynamics of the stratosphere and mesosphere during the major stratospheric warming in 2003/2004. *J. Atmos. Sol. Terr. Phys.* 69 (17–18), 2338–2354.
- Noguchi, S., Kuroda, Y., Koder, K., Watanabe, S., 2020. Robust enhancement of tropical convective activity by the 2019 Antarctic sudden stratospheric warming e2020GL088743. *Geophys. Res. Lett.* 47 (15). <https://doi.org/10.1029/2020GL088743>.
- Oberheide, J., Forbes, J.M., Häusler, K., Wu, Q., Bruinsma, S.L., 2009. Tropospheric tides from 80 to 400 km: Propagation, interannual variability, and solar cycle effects. *J. Geophys. Res.* 114 (D1). <https://doi.org/10.1029/2009JD012388>.
- Pedatella, N.M., Liu, H.L., 2013. The influence of atmospheric tide and planetary wave variability during sudden stratosphere warmings on the low latitude ionosphere. *J. Geophys. Res.* 118 (8), 5333–5347. <https://doi.org/10.1002/jgra.50492>.
- Pedatella, N.M., Liu, H.L., Sassi, F., Lei, J., Chau, J.L., Zhang, X., 2014. Ionosphere variability during the 2009 SSW: Influence of the lunar semidiurnal tide and mechanisms producing electron density variability. *J. Geophys. Res.* 119 (5), 3828–3843.
- Pedatella, N.M., Chau, J.L., Schmidt, H., Goncharenko, L.P., Stolle, C., Hocke, K., Harvey, V.L., Funke, B., Siddiqui, T.A. How Sudden stratospheric warmings affect the whole atmosphere. <https://doi.org/10.1029/2018EO092441>.
- Rao, J., Garfinkel, C.I., White, I.P., Schwartz, C., 2020. The Southern Hemisphere minor sudden stratospheric warming in September 2019 and its predictions in S2S models e2020JD032723. *J. Geophys. Res.: Atmos.* 125 (14). <https://doi.org/10.1029/2020JD032723>.
- Sassi, F., Liu, H.L., Ma, J., Garcia, R.R., 2013. The lower thermosphere during the Northern Hemisphere winter of 2009: A modeling study using high-altitude data assimilation products in WACCM-X. *J. Geophys. Res.* 118 (16), 8954–8968. <https://doi.org/10.1002/jgrd.50632>.
- Schoeberl, M.R., 1978. Stratospheric warmings: Observations and theory. *Rev. Geophys.* 16 (4), 521–538. <https://doi.org/10.1029/RG016i004p00521>.
- Sridharan, S., Sathishkumar, S., Gurubaran, S., 2012. Variabilities of mesospheric tides during sudden stratospheric warming events of 2006 and 2009 and their relationship with ozone and water vapour. *J. Atmos. Sol. Terr. Phys.* 78, 108–115.
- Wan, W., Liu, L., Pi, X., Zhang, M.L., Ning, B., Xiong, J., Ding, F., 2008. Wavenumber-4 patterns of the total electron content over the low latitude ionosphere. *Geophys. Res. Lett.* 35 (12).
- Yamazaki, Y., Matthias, V., Miyoshi, Y., Stolle, C., Siddiqui, T., Kervlishvili, G., Laštovička, J., Kozubek, M., Ward, W., Themens, D.R., Kristoffersen, S., 2020. September 2019 Antarctic sudden stratospheric warming: Quasi-6-day wave burst and ionospheric effects e2019GL086577. *Geophys. Res. Lett.* 47 (1).

Geophysical Research Letters®



RESEARCH LETTER

10.1029/2023GL104756

Key Points:

- Spectral analysis on meteor radar winds provides evidence of non-linear interaction between semidiurnal tide and quasi-20-day wave
- Possible role of zonal wavenumber 2 stationary planetary wave in forcing zonally symmetric 20-day wave in the stratosphere
- First observational evidence of two-step non-linear interaction associated with zonally symmetric planetary waves during major sudden stratospheric warmings

Supporting Information:

Supporting Information may be found in the online version of this article.

Correspondence to:

J. F. Conte and G. Mitra,
conte@iap-kborn.de;
reachmitragourav@gmail.com

Citation:

Mitra, G., Guharay, A., Conte, J. F., & Chau, J. L. (2023). Signature of two-step non-linear interactions associated to zonally symmetric waves during major sudden stratospheric warmings. *Geophysical Research Letters*, 50, e2023GL104756. <https://doi.org/10.1029/2023GL104756>

Received 31 MAY 2023

Accepted 20 SEP 2023

Author Contributions:

Conceptualization: G. Mitra

Data curation: J. F. Conte

Formal analysis: G. Mitra

Investigation: G. Mitra

Methodology: G. Mitra

Resources: J. L. Chau

Supervision: A. Guharay

Writing – original draft: G. Mitra

Writing – review & editing: A. Guharay,
J. F. Conte, J. L. Chau

© 2023. The Authors.

This is an open access article under the terms of the [Creative Commons Attribution-NonCommercial-NoDerivs License](#), which permits use and distribution in any medium, provided the original work is properly cited, the use is non-commercial and no modifications or adaptations are made.

Signature of Two-Step Non-Linear Interactions Associated to Zonally Symmetric Waves During Major Sudden Stratospheric Warmings

G. Mitra^{1,2} , A. Guharay¹ , J. F. Conte³ , and J. L. Chau³ 

¹Space and Atmospheric Sciences Division, Physical Research Laboratory, Ahmedabad, GJ, India, ²Department of Physics, Indian Institute of Technology, Gandhinagar, GJ, India, ³Leibniz-Institute of Atmospheric Physics at the University of Rostock, Kühlungsborn, Germany

Abstract Atmospheric tides and associated dynamics during two major boreal sudden stratospheric warmings (SSWs) have been investigated. The evolutionary Lomb Scargle and wavelet spectral analysis of specular meteor radar (SMR)-derived hourly winds reveal evidence of non-linear interactions between the semidiurnal solar tide and the quasi-20-day wave (Q20dw) during SSWs. The zonal wavenumber (ZWN) diagnosis indicates possible non-linear interaction between the dominant semidiurnal migrating tide (SW2) and zonally symmetric 20-day wave (20dw0) component, producing the secondary waves. The non-linear interaction between the ZWN 2 component of stationary planetary wave (SPW2) and westward propagating 20-day wave (20dwW2) in the stratosphere seems crucial to produce the 20dw0. As observed in the SMR-derived wind spectra, the excited 20dw0 possibly interacts non-linearly with SW2 to generate secondary waves. Therefore, the present study provides the first observational evidence of a two-step non-linear interaction associated with zonally symmetric planetary waves during major SSWs.

Plain Language Summary The sun-synchronous semidiurnal tide (SW2) is a major wave in the middle and high latitude mesosphere and lower thermosphere (MLT). Sudden stratospheric warming (SSW) is a polar winter hemispheric event characterized by enhanced planetary wave (PW) activity. Non-linear interaction between the two waves produces secondary waves whose frequencies are sum and difference of the primary waves. Further, the secondary waves, having a frequency closely spaced to the tidal frequency, beat with the tide, resulting in modulation of the tidal amplitude by the PW's period due to the non-linear interaction. The spectral analysis of specular meteor radar-derived hourly winds supports this notion, and hence provides evidence for non-linear interactions in the MLT. The dominant PW involved in the interaction is found to be zonally symmetric. The non-linear interaction between the stationary PW and propagating PW in the stratosphere plays an important role in forcing the zonally symmetric component, that can reach MLT altitudes. Furthermore, non-linear interaction between SW2 and the zonally symmetric PW produces the observed secondary waves in the MLT in the form of side bands in radar spectra. Overall, the present study provides the first observational evidence of a two-step non-linear interaction during SSWs.

1. Introduction

Sudden Stratospheric warming (SSW) is a dramatic meteorological event in the polar region of the winter hemisphere, in which the stratospheric temperature increases by a few tens of Kelvin within a few days, affecting atmospheric dynamics on a global scale (Andrews et al., 1987). Such a large-scale disturbance is accompanied by enhanced planetary waves (PWs) consisting of stationary and traveling components. The stationary planetary waves (SPWs) are predominantly active in the winter stratosphere (e.g., Mitra et al., 2022; Pancheva et al., 2009a, 2009b). The interaction between the SPW ZWN 1 (SPW1) or the SPW2 and the polar vortex can result in displacement or split of the polar vortex. The traveling planetary waves (TPW), with periods up to ~30 days, are crucial in the latitudinal and altitudinal coupling during SSWs. There are quite a few investigations on the coupling between low and high latitudes in the middle atmosphere via SPW and TPW during SSWs in the northern hemisphere (NH) (e.g., Guharay & Sekar, 2012; Pancheva et al., 2007) and infrequent SSWs in the southern hemisphere (e.g., Guharay et al., 2014a; Mitra et al., 2022). Previously, spectral analysis of satellite and reanalysis derived zonal wind and temperature fields revealed zonally symmetric PW (ZWN = 0) during the

major 2003–2004 NH SSW event (Pancheva et al., 2007, 2009a, 2009b), with prevailing period same as the TPW. Unfortunately, the zonally symmetric PW are least reported in the available literature.

Past studies reported significant variability in the solar tides at mid and high latitudes (e.g., Chau et al., 2015; Conte et al., 2019), and low latitudes (e.g., Guharay & Batista, 2019; Mitra et al., 2023) during SSWs in the mesosphere and lower thermosphere (MLT). He et al. (2017, 2018) recently explained the observed semidiurnal tide (ST) variability at mid latitudes during SSWs as a result of non-linear interaction with TPWs. Although there have been several general studies on non-linear interaction between tides and PWs (e.g., Beard et al., 1999; Guharay et al., 2015; Pancheva, 2001), there are comparatively less literature on the same during a transient event like SSW.

The present study provides the first observational evidence of a two-step non-linear interaction between planetary-scale waves during major SSWs associated with zonally symmetric PWs. The 2008–2009 and 2012–2013 NH winters are investigated in this study. Both winters are characterized by a major SSW of split type, and are associated with strong polar night jet oscillations (Conte et al., 2019). The paper is divided into four sections. Section 2 discusses the data set used in this study. Section 3.1 describes the ST and PW spectra in the specular meteor radar (SMR) winds. Section 3.2 discusses the temporal evolution of the interacting wave components. Section 3.3 discusses the dominant ZWN component of the primary waves. Section 3.4 discusses the possible forcing mechanism of the zonally symmetric PW component involved in the two-step non-linear interaction. Section 4 summarizes and concludes the results.

2. Observations

Our observational data consist of wind measurements made with the SMR located at Andenes, northern Norway (69°N, 16°E). Technical details of this instrument are summarized in Hoffmann et al. (2010). The current study uses hourly zonal winds (U) derived at a vertical resolution of 2 km following the procedure introduced by Hocking et al. (2001).

Additionally, a longitudinally spread contemporaneous data set provided by the Modern-Era Retrospective Analysis for Research and Applications, version 2 (MERRA-2) is utilized for ZWN diagnosis (Gelaro et al., 2017). We have used U at 72 model pressure levels between 985 and 0.01 hPa (approx. 0–75 km), with a latitude-longitude grid of $2.5^\circ \times 2.5^\circ$. The SPARC Reanalysis Intercomparison Project Final Report demonstrated the suitability of MERRA2 for tide and PW studies in the middle atmosphere (Harvey et al., 2022).

The time interval spans from 1 November to 31 March. The date with the maximum positive temperature gradient between 90° and 60°N at 10 hPa, is defined as the SSW peak warming day (PWD). The latter is obtained around the date of the first wind reversal during each major event (e.g., Andrews et al., 1987). Note that in the present study, the PWD is used only to determine the commencement of the SSW, and our discussions are not sensitive to the equivocal definitions of SSW onsets (Butler et al., 2015). 23 January 2009 and 6 January 2013 are considered the PWDs, as marked by the vertical solid lines in all the figures.

3. Results and Discussions

3.1. ST and PW Spectra in the Specular Meteor Radar Winds

The evolutionary Lomb Scargle (ELS) Periodogram has been estimated using the Lomb Scargle technic applied to the hourly U using a (1-day) shifting window of 21-day width over the entire observational interval (Schulz & Statterger, 1997). Mathematically, the 21-day is the minimum (integer) window size to resolve two closely spaced periods, such as 11.7 and 12 and 12.3 and 12 hr. The ELS spectra show a sustained feature of a ST corresponding to a period of 12 hr, with a sharp decrease around the PWD of the 2008–2009 SSW, as shown in Figure 1a. Interestingly, a transient enhancement at the periods 11.7 and 12.3 hr is observed at the same time.

Further, wavelet amplitude spectra of the hourly U reveal a significant enhancement of a quasi-20-day wave (Q20dw) around the PWD (Figure 1b). Interestingly, the appearance of the upper sideband (USB) and lower sideband (LSB) corresponding to the periods 11.7 and 12.3 hr, respectively, is concurrent with the occurrence of the Q20dw. Such USB and LSB can be generated as secondary waves due to non-linear interaction (Teitelbaum & Vial, 1991). The plausible primary waves involved in the interaction are the ST and the Q20dw, and the resulting secondary waves are LSB (~12.3) hours and USB (~11.7 hr). Moreover, the USB/LSB, having a frequency

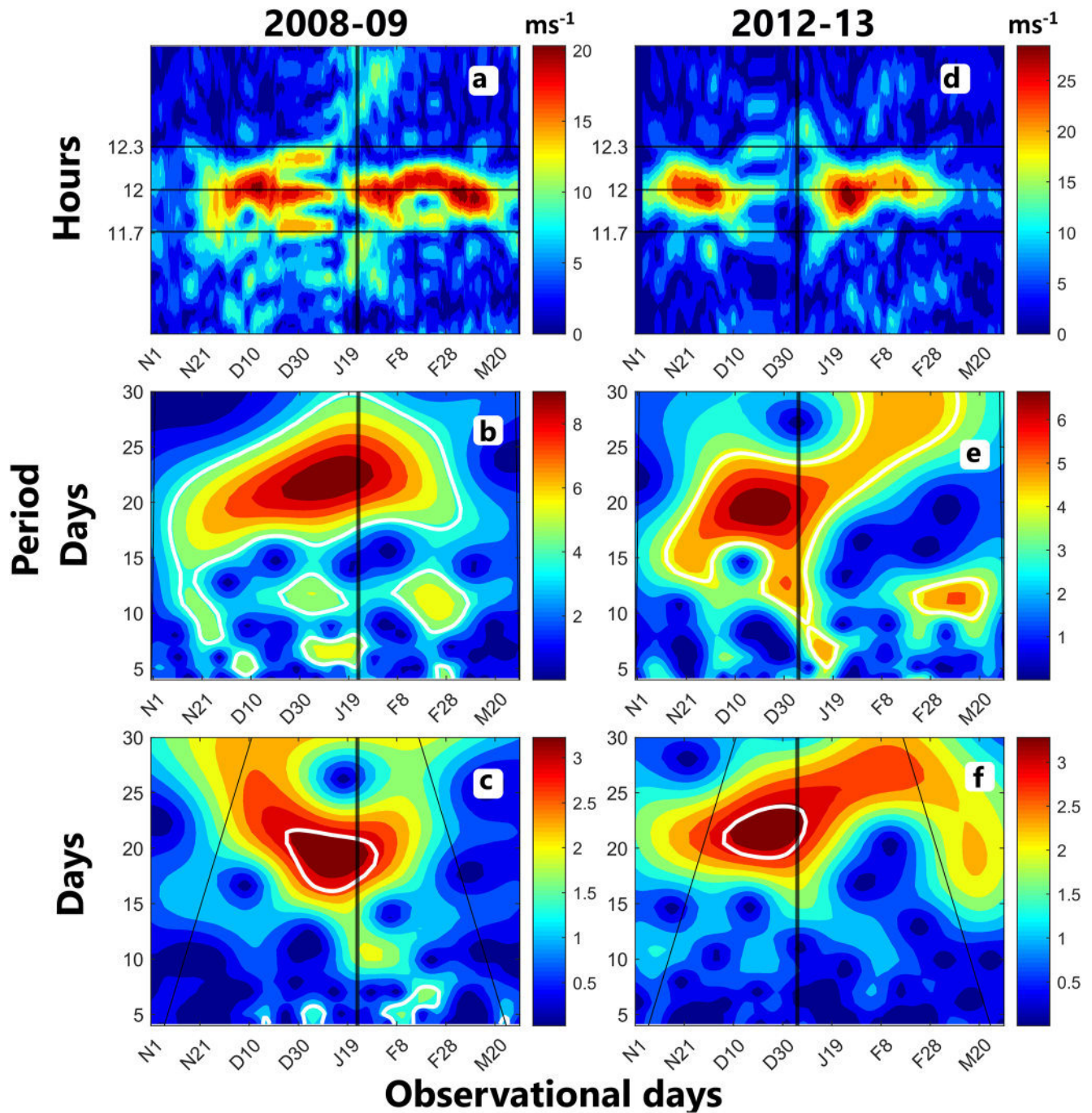


Figure 1. (a) Evolutionary Lomb Scargle amplitude spectra (semidiurnal tide [ST] period range) and (b) wavelet amplitude spectra (planetary wave period range) of the U at 90 km, and (c) wavelet spectra of the instantaneous ST amplitude at 90 km using meteor radar observations at Andenes (69.3°N, 16°E), from 1 November 2008 to 31 March 2009. (d–f) Represent the same as (a–c) but during 2012–2013. The solid vertical line represents the peak warming day and the thin tilted line represents the cone of influence. The white curve in the wavelet spectra represents the 95% confidence level. Please note the change of scale in the colorbars corresponding to each subplot while comparing. The letters N, D, J, F, and M in the x axis denote November, December, January, February, and March; the subsequent number indicates the day of the given month.

closely spaced to that of the ST, beat with the ST, resulting in modulation of the ST amplitude with the 20-day PW period. This is confirmed by the wavelet amplitude spectra of instantaneous ST amplitude, which show a contemporaneous and significant quasi-20-day modulation around the PWD (Figure 1c). The amplitude and phase of the ST are estimated by a least squares fitting to the time series data using a 4-day window, progressively shifted by 1 day using the following equation.

$$Y(t) = Y_o + \sum_{p=1}^3 A_p \cos \left[\frac{2\pi p}{24} (t - \varphi_p) \right] \quad (1)$$

where $p = 1, 2, 3$ denotes diurnal, semidiurnal, and terdiurnal components, A_p is the amplitude, t is the universal time, and φ_p is the phase. $Y(t)$ is the hourly U, and Y_o is the mean wind over the fitting window, that is, 4 days (Hoffmann et al., 2010).

Features similar to Figures 1a–1c, are also observed during the 2012–2013 SSW event, as seen in Figures 1d–1f, respectively. Hence, the ELS successfully identifies the secondary waves in the radar winds that are produced by the non-linear interaction between the 20dw and the ST. The wavelet spectra indicate the presence of a significant Q20dw, allegedly involved in the non-linear interaction. The secondary waves beat with the ST, modulating its amplitude with the PW period, as it can be identified from the wavelet spectra of the instantaneous ST amplitude. Concurrent observations of the secondary waves, significant Q20dw, and 20-day modulation of the ST amplitude around the SSW using the ELS and wavelet method on meteor radar winds provide strong evidence of non-linear interaction between the ST and the Q20dw. The novelty of the present method lies in identifying the transient occurrence of the non-linear interaction between planetary-scale waves under a strongly disturbed atmospheric condition. One may note that in the case of 2008–2009, the observed periods of the USB or LSB seem to be slightly shifted from the theoretical values toward the 12 hr (Figure 1a), and the hourly wind wavelet spectrum (Figure 1b) shows the peak around 22 days. However, one can note that the rest of the spectra in Figure 1 show a prominent period around the 20-day period. Therefore, for uniformity and consistency, we will consider 20dw as a primary interacting wave and 11.7 and 12.3 hr as the USB and LSB periods hereinafter.

3.2. Temporal Evolution of Interacting Wave Components

A noticeable burst of the 20dw for a few days in the altitude region 80–90 km around the PWD is evident during both events (Figures 2a and 2e). In 2008–2009, the 20d like oscillation seems to extend downward from the upper MLT until it meets the other relatively stronger counterpart from below (details in Text S1 in Supporting Information S1). Overall, the pattern of the LSB does not seem to follow the primary wave, that is, the ST over the observational intervals. Interestingly, the enhancement in the LSB component around the PWD (Figures 2b and 2f) is concurrent with the sudden weakening of the ST during both events (Figures 2c and 2g). On the contrary, in case of the USB, the relationship with the primary wave, that is, the ST, looks consistent in terms of enhancement and weakening, as seen in Figures 2d and 2h. Such an outcome implies a dissimilar but evident relationship between the primary and secondary waves, due to the non-linear interaction. Generally, LSB, ST, and USB attain higher amplitudes above 90 km of altitude. The corresponding phase and vertical wavelength are described in Text S2 and Figures S1–S3 in Supporting Information S1.

The Manley Rowe relationship (MRR) can be used to understand the energy exchange in the non-linear interacting wave triad (He et al., 2017). According to the MRR, in the present case the ST component can be considered to feed energy to the 20dw and LSB, following the Passive Passive Active topology. In the case of the 20dw, ST, and USB triad interaction, both the ST and the 20dw can feed energy to the USB, following the Active Active Passive topology. Since the frequency of the 20dw is much smaller than the ST, the energy contribution from the 20dw in the interaction process can be deemed negligible, as per the MRR relationship between energy exchange and frequency (Equation 1 in He et al. (2017)). Therefore, practically, the ST can be assumed to be the major energy source that feeds both the USB and LSB components. This assumption is consistent with the observed high amplitude of the ST as compared to the sidebands. The large amplitude of the LSB during the warming indicates that the LSB takes a significant amount of energy from the ST component, as evidenced by the simultaneous decrease of the ST amplitude. Further detailed studies in future are needed to understand the disparate behavior among sidebands due to the interaction. Overall, warming specific response can be found in the LSB, and consistent relationship with the parent wave can be noticed in the case of USB. However, one may note simultaneous enhancement features in the USB and LSB around the warming in Figure 1a at 90 km, which seem to be incidental.

Furthermore, the consistent relationship of the USB with the ST also implies its persistent dependence on the parent wave, in terms of energy feeding for its sustenance. Although the energy exchange through the 20dw can be considered negligible, the involvement of such PW component is essential for the non-linear interaction. The insignificant energy exchange further implies that the 20dw may be involved in other dynamical processes in addition to the non-linear interaction here studied. This is in line with the occurrence of a strong 20dw below 90 km altitude, where the amplitudes of the ST, USB, and LSB components are minimal. The external dynamics may influence

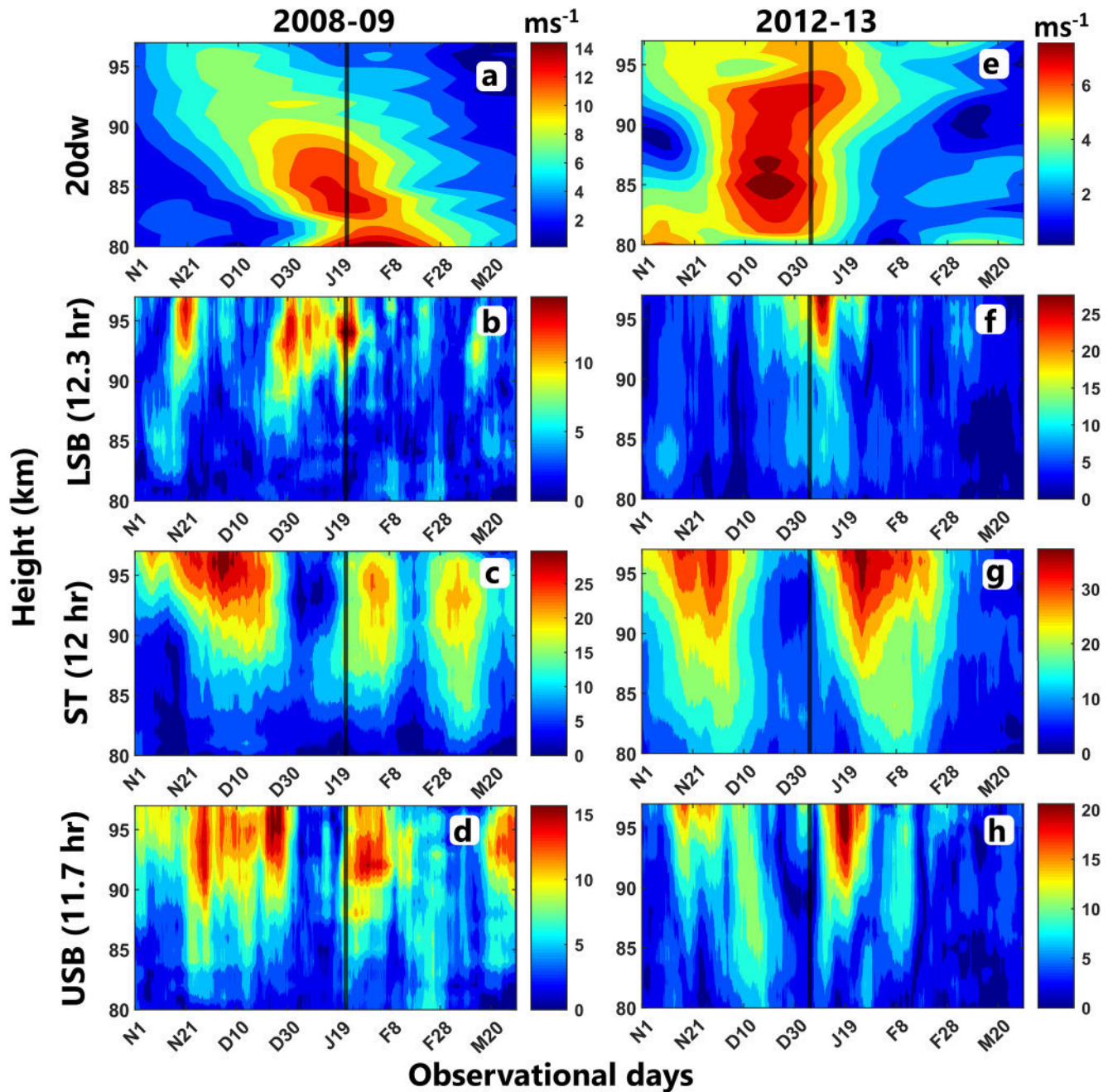


Figure 2. (a) Altitude profile of the wavelet amplitude spectra of the 20dw, evolutionary Lomb Scargle amplitude spectra of (b) lower sideband, (c) semidiurnal tide, and (d) upper sideband using meteor radar derived U at Andenes (69.3°N, 16°E) during the 2008–2009 observational days. (e–h) Represents the same as (a–d) but during 2012–2013. Please note the change of scale in the colorbars for each subplot while comparing.

such triad interactions by controlling the 20dw. Hence, the possible forcing mechanism leading to the enhanced 20dw during the SSW is worth investigating for better understanding of the underlying processes (see Section 4).

3.3. Dominant Zonal Wavenumber Components of Primary Waves

A combined Fourier Wavelet (CFW) technique (Kikuchi, 2014; Yamazaki, 2022) is performed in the 2-dimensional space time MERRA-2 U data to calculate the ZWN-period spectra. The CFW is a two-step method. In the first step, the Fourier transform is applied to the longitudinal domain, and the time series of the space Fourier

coefficients are obtained. The wavelet transform is performed on these time series in the second step, and the wavelet coefficients are derived. The wavelet coefficients are used to calculate the CFW spectrum. The novelty of the method lies in identifying the temporal occurrence of wave activity.

The ZWN 0 corresponds to the zonally symmetric component. The positive/negative sign of ZWN corresponds to the westward (W)/eastward (E) propagation. The ZWN versus period spectra at 0.01 hPa (~ 75 km), 70°N calculated by averaging the CFW spectra over a 30-day interval centered around the 2008–2009 SSW PWD are shown in Figures 3a and 3b, for the PW and tidal period ranges, respectively. Figures 3e and 3f are similar to Figures 3a and 3b, but for the 2012–2013 event. The pressure level 0.01 hPa in the MERRA-2 data set is chosen as it is the closest to the meteor radar observational height. The nearest latitude to Andenes (AN) is selected as 70°N . The ZWN-period spectra reveal a zonally symmetric 20dw corresponding to ZWN 0, hereafter referred to as 20dw0, and a westward traveling 10dw corresponding to ZWN 1 (10dwW1) during both events (Figures 3a and 3e). The dominance of westward propagating migrating ST (ZWN 2 (SW2)) (Figures 3b and 3f), indicates its relevance in the non-linear interaction. The temporal evolution of the 20dw (Figures 3c and 3g) shows a strong enhancement in the 20dw0 component around the PWD. Furthermore, the sustained feature of the SW2 component is evident during the 2008–2009 (Figure 3d) and 2012–2013 (Figure 3h) observational intervals.

The observations of the 20dw and the 10dw (Figures 3a and 3e) in the upper mesosphere (0.01 hPa) in the MERRA-2 wind are consistent with the meteor radar observations (Figures 1b and 1e). Also, enhancement of the 20dw0 (Figures 3c and 3g) around the PWD further indicates the salient role of the zonally symmetric 20dw0 component for the 20dw enhancement observed in the meteor radar observational heights (Figures 2a and 2e). Hence, the 20dw0 and the SW2 are most possibly the primary waves involved in non-linear interaction producing the USB and LSB in the radar wind spectra. Mathematically, the dominant primary waves, that is, the 20dw0 and the SW2 non-linearly interact to produce USB and LSB corresponding to ZWN 2. Please refer to Figure S4 in Supporting Information S1, which is a schematic representation of the theoretical ZWN-period spectra involving 20dw0 and SW2 as the primary waves producing USB and LSB as secondary waves corresponding to ZWN 2. Although faint patches around the strong SW2 feature are observed in the ZWN-period spectra (Figures 3b and 3f), the expected USB and LSB peaks in the period corresponding to the ZWN 2 seem to remain unresolved in the MERRA-2 data probably due to the inherent limitations of the reanalysis data set (Text S3 in Supporting Information S1). However, the USB and LSB components are clearly resolved from the ground-based meteor radar observations as depicted before.

3.4. Possible Forcing Mechanism of 20dw0

It is known that there are no zonally symmetric normal modes with PW periods (Longuet-Higgins, 1968). However, the zonally symmetric PW may be generated due to non-linear interaction between SPW and TPW (Pancheva et al., 2007). Mathematically, a non-linear interaction between a SPW with frequency/ZWN pair (0, s) and a TPW (ω , s) yields a zonally symmetric PW (ω , 0) and a TPW (ω , 2s) (Teitelbaum & Vial, 1991). Hence, the observed 20dw0 in the present study can be considered to be generated mainly due to non-linear interactions between (a) SPW1 and 20dwW1/20dwE1 and/or (b) SPW2 and 20dwW2/20dwE2. Also, the altitude profile of the 20dw0 at 70°N shows a substantial enhancement around the PWD (please refer to Figures S5a and S5c in Supporting Information S1), which may point to a stratospheric origin close to the 10 hPa (~ 30 km) pressure level. Furthermore, the SPWs are mostly active in the stratosphere, indicating their possible role in forcing the 20dw0. From the above-mentioned two most probable non-linear interactions that can theoretically produce the 20dw0, the second mechanism is found to be involved in the present case. One can observe coincident and consistent enhancements of the primary waves (SPW2, 20dwW2) and secondary waves (20dw0, 20dwW4) in Figure 4.

It is well known that SPW2 plays a salient role in preconditioning the split of the polar vortex (Shepherd, 2000). The 2008–2009 and 2012–2013 SSW are both split types. The altitudinal profile of the SPW2 at 70°N shows intense activity around the PWD in the stratosphere around 30 km altitude (Figures S5b and S5d in Supporting Information S1). Figures 4a–4d show the latitudinal profile of the SPW2, 20dwW2, 20dw0, and 20dwW4, respectively, at 10 hPa during the 2008–2009 observational days. Two distinct branches of SPW2 amplification at 65° – 80°N and 30° – 45°N are noticeable around the 2008–2009 PWD (Figure 4a). Similar enhancements are also observed in the 20dwW2, 20dw0, and 20dwW4, as seen in Figure 4b–4d, respectively. The pattern of the 20dwW2, 20dw0, and 20dwW4 indicates the salient role of non-linear interactions between SPW2 and 20dwW2, to produce the 20dw0 and 20dwW4 as secondary waves. However, the weak 20dwW4 is possibly due to energy redistribution and dissipation (Text S4 in Supporting Information S1). Similar features are also observed during

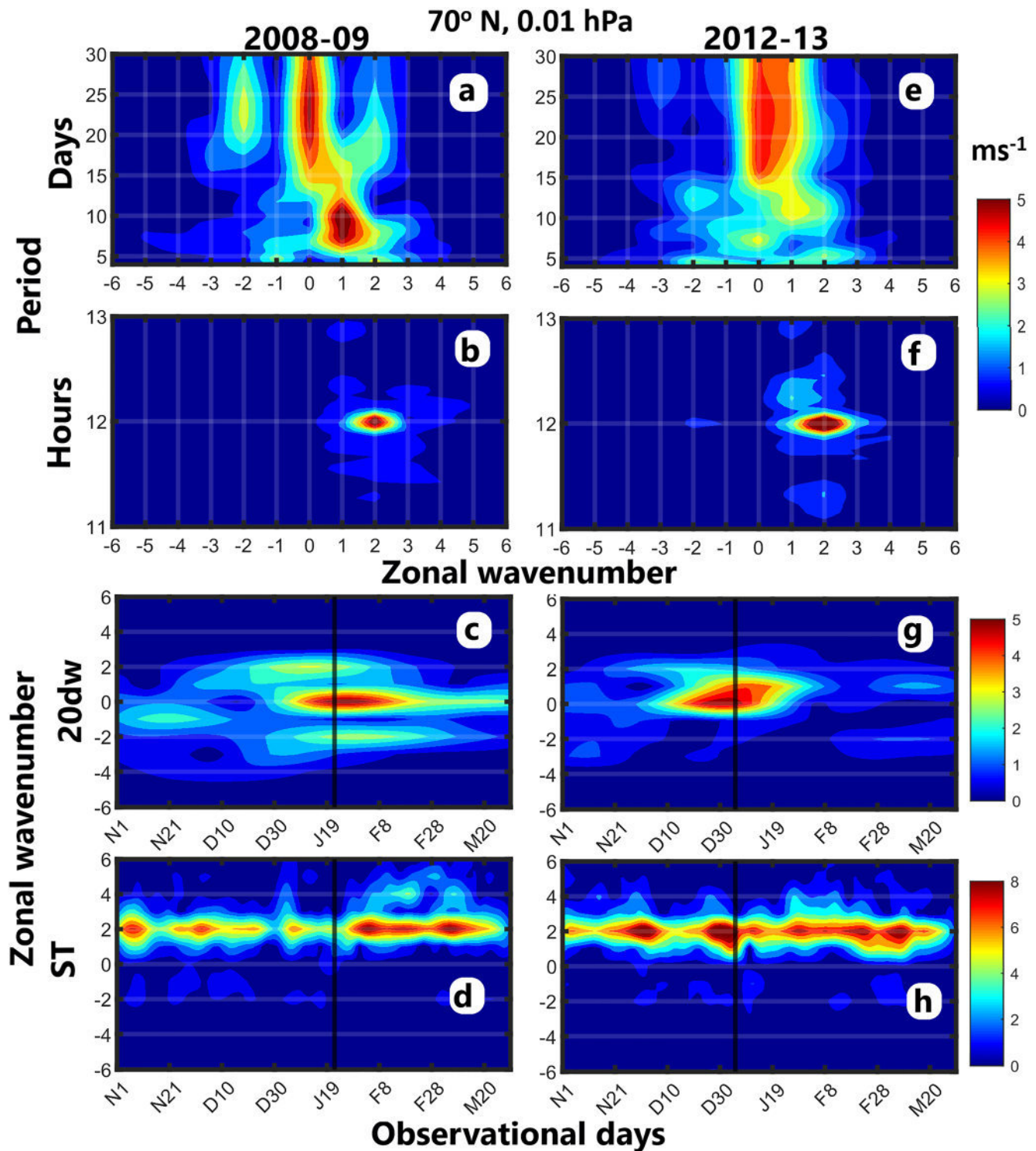


Figure 3. Period versus zonal wavenumber (ZWN) spectra in the period range (a) 4–30 days and (b) 11–13 hr utilizing U at 0.01 hPa, 70°N from Modern-Era Retrospective Analysis for Research and Applications, version 2 during 2008–2009 sudden stratospheric warming. (c) Temporal variability of different ZWN components of (c) 20dw and (d) semidiurnal tide during the 2008–2009 observational days. (e–h) Represent the same as (a–d) but during 2012–2013. Positive/Negative ZWN denotes westward/eastward propagation and zero ZWN represents the zonally symmetric component.

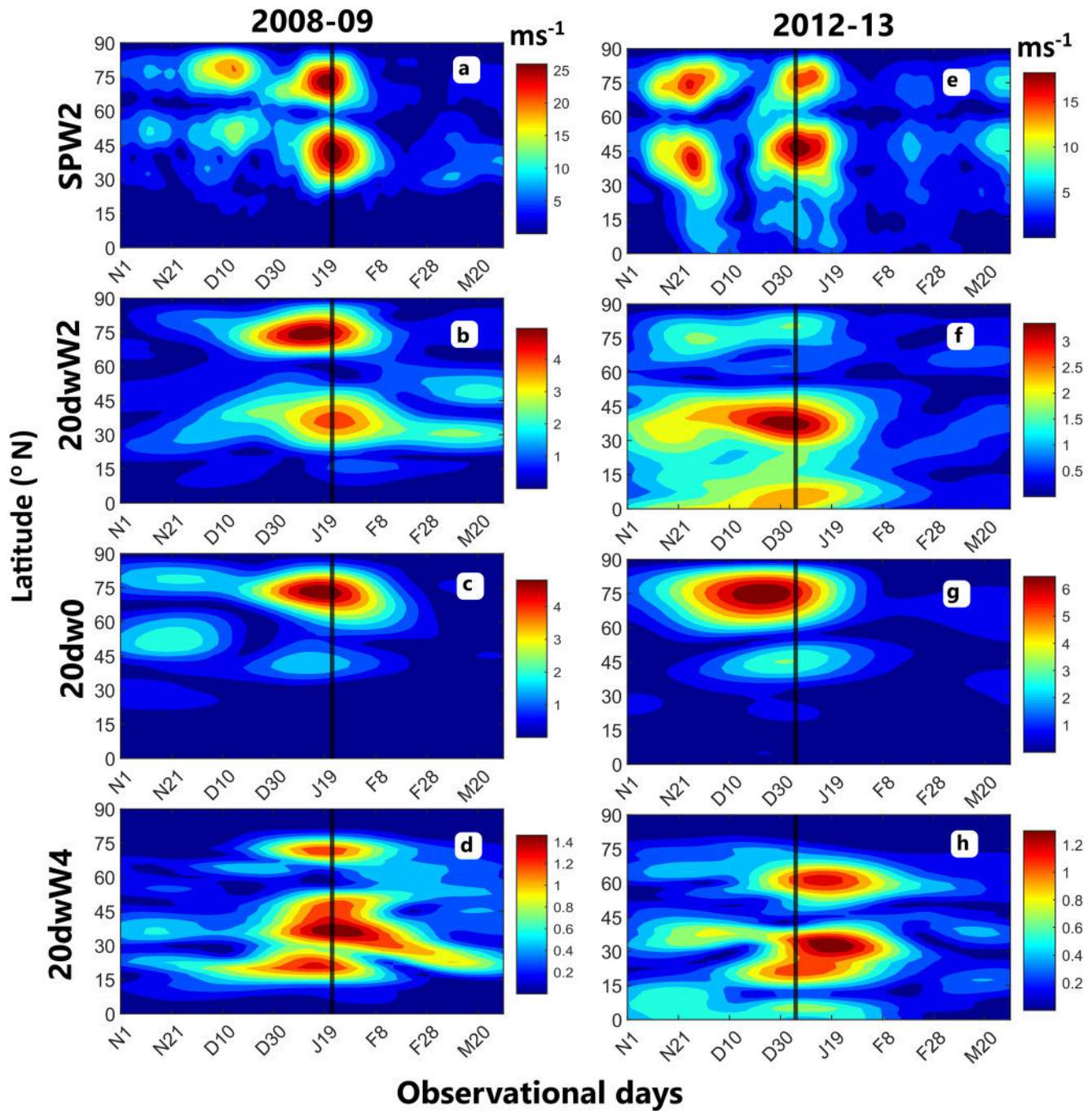


Figure 4. Latitude profile at 10 hPa of (a) SPW2, (b) 20dwW2, (c) 20dw0, and (d) 20dwW4 during the 2008–2009 observational days. (e–h) Represent the same as (a–d), but during 2012–2013.

the 2012–2013 observational interval (Figures 4a–4d). The only noticeable difference observed during the 2012–2013 SSW is that the pattern of the 20dw0 (Figure 4g) at high latitudes does not resemble that of the 20dwW2 (Figure 4f), as expected due to the interaction. The discrepancy in this case may be ascribed to interactions with other waves and/or background conditions that affect the 20dw0 behavior. Overall, the non-linear interaction between SPW2 and 20dwW2 seems to play a crucial role in forcing the 20dw0.

4. Summary and Conclusions

In the present work we have found signature of non-linear interaction in connection with a zonally symmetric wave during major SSWs. The ELS spectra of SMR-derived hourly U identify the secondary waves as USB and LSB of the ST. The wavelet spectra of hourly U reveal the presence of a 20dw. Furthermore, wavelet spectra of the instantaneous ST amplitude confirm a modulation of 20 days on the same during the warming event. Therefore, non-linear interaction between the ST and 20dw can be deemed to produce USB and LSB as the secondary waves. The USB and LSB may beat with the ST, causing the tidal modulation in the 20-day PW period. The simultaneous and transient activity of the USB, LSB and 20dw, as identified from the ELS and wavelet spectra of SMR-derived winds, provides strong evidence of non-linear interaction between the ST and 20dw.

It is interesting to note the dissimilar behaviors of the LSB and USB, although both of them are found to be associated to the ST. The enhancement of the LSB in the MLT is concurrent with the decrease of the ST amplitude around the PWD. Hence, according to recent studies, the LSB can be considered to obtain most of its energy from the ST component (He et al., 2017, 2018). However, the USB exhibits a similar pattern with the parent wave, i.e., the ST, substantiating its close relationship with the latter. The 20dw activity is less affected by the non-linear interaction involving the 20dw, ST and USB or LSB, as minimal energy is exchanged through the 20dw as per the MRR. However, at the same time, the presence of the 20dw is essential for the observed non-linear interaction.

It is found that the zonally symmetric 20dw component, that is, 20dw0, and the migrating ST component, that is, SW2, are the primary waves involved in the non-linear interaction, as ascertained from the ZWN-period spectra calculated using the MERRA-2 U. The enhancement of the 20dw, as seen from the SMR observations, is linked to the concurrent enhanced 20dw0 component, which seems to have a stratospheric origin. The enhanced SPW2 is believed to interact non-linearly with the 20dwW2 to produce the 20dw0 in the stratosphere, which could reach MLT altitudes. As it is supported by the SMR observations, the 20dw0 further interacts non-linearly with SW2 to generate LSB and USB.

In a nutshell, the present study provides the first observational evidence of a two-step non-linear interaction between planetary-scale waves during two split-type SSWs at boreal high latitudes. The observed two-step non-linear interaction can be summarized as follows.

1. In the first step, non-linear interaction between SPW2 and 20dwW2 produces the 20dw0.
2. In the second step, non-linear interaction between the dominant SW2 and previously generated 20dw0 gives rise to the USB and LSB as secondary waves.

Data Availability Statement

The specular meteor radar winds used in this work are available in HDF5 format at <https://doi.org/10.22000/1026>. The MERRA-2 data set utilized in the current study is available at <https://gmao.gsfc.nasa.gov/reanalysis/MERRA-2/>.

Acknowledgments

Authors GM and AG are supported by the Department of Space (Government of India). GM is thankful to SCOSTEP and the Leibniz-Institute of Atmospheric Physics for the support under the SCOSTEP visiting scholar program. Authors would like to thank the reviewers for useful comments. Open Access funding enabled and organized by Projekt DEAL.

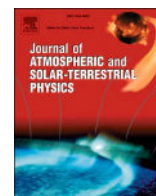
References

- Andrews, D. G., Holton, J. R., & Leovy, C. B. (1987). *Middle atmosphere dynamics* (No. 40). Academic Press.
- Beard, A. G., Mitchell, N. J., Williams, P. J. S., & Kunitake, M. (1999). Non-linear interactions between tides and planetary waves resulting in periodic tidal variability. *Journal of Atmospheric and Solar-Terrestrial Physics*, 61(5), 363–376. [https://doi.org/10.1016/S1364-6826\(99\)00003-6](https://doi.org/10.1016/S1364-6826(99)00003-6)
- Butler, A. H., Seidel, D. J., Hardiman, S. C., Butchart, N., Birner, T., & Match, A. (2015). Defining sudden stratospheric warmings. *Bulletin of the American Meteorological Society*, 96(11), 1913–1928. <https://doi.org/10.1175/BAMS-D-13-00173.1>
- Chau, J. L., Hoffmann, P., Pedatella, N. M., Matthias, V., & Stober, G. (2015). Upper mesospheric lunar tides over middle and high latitudes during sudden stratospheric warming events. *Journal of Geophysical Research: Space Physics*, 120(4), 3084–3096. <https://doi.org/10.1002/2015JA020998>
- Conte, J. F., Chau, J. L., & Peters, D. H. (2019). Middle- and high-latitude mesosphere and lower thermosphere mean winds and tides in response to strong polar-night jet oscillations. *Journal of Geophysical Research: Atmospheres*, 124(16), 9262–9276. <https://doi.org/10.1029/2019JD030828>
- Gelaro, R., McCarty, W., Suárez, M. J., Todling, R., Molod, A., Takacs, L., et al. (2017). The modern-era retrospective analysis for research and applications, version 2 (MERRA-2). *Journal of Climate*, 30(14), 5419–5454. <https://doi.org/10.1175/JCLI-D-16-0758.1>
- Guharay, A., Batista, P., Clemesha, B., & Sarkhel, S. (2014a). Response of the extratropical middle atmosphere to the September 2002 major stratospheric sudden warming. *Advances in Space Research*, 53(2), 257–265. <https://doi.org/10.1016/j.asr.2013.11.002>
- Guharay, A., & Batista, P. P. (2019). On the variability of tides during a major stratospheric sudden warming in September 2002 at Southern Hemispheric extra-tropical latitude. *Advances in Space Research*, 63(8), 2337–2344. <https://doi.org/10.1016/j.asr.2018.12.037>
- Guharay, A., Batista, P. P., & Clemesha, B. R. (2015). On the variability of the diurnal tide and coupling with planetary waves in the MLT over Cachoeira Paulista (22.7 S, 45 W). *Journal of Atmospheric and Solar-Terrestrial Physics*, 133, 7–17. <https://doi.org/10.1016/j.jastp.2015.07.016>

- Guharay, A., & Sekar, R. (2012). Signature of latitudinal coupling during a major sudden stratospheric warming in the tropics. *Journal of Atmospheric and Solar-Terrestrial Physics*, 75, 122–126. <https://doi.org/10.1016/j.jastp.2011.06.010>
- Harvey, V. L., Knox, J., France, J., Fujiwara, M., Gray, L., Hirooka, T., et al. (2022). Chapter 11: Upper stratosphere lower mesosphere. In M. Fujiwara, G. L. Manney, L. J. Gray, & J. S. Wright (Eds.) *SPARC reanalysis Intercomparison Project (S-RIP) final Report*. SPARC Report No. 10, WCRP-17/2020 (pp. 531–580). <https://doi.org/10.17874/800dee57d13>
- He, M., Chau, J. L., Hall, C. M., Tsutsumi, M., Meek, C., & Hoffmann, P. (2018). The 16-day planetary wave triggers the SW1-tidal-like signatures during 2009 sudden stratospheric warming. *Geophysical Research Letters*, 45(22), 12631–12638. <https://doi.org/10.1029/2018GL079798>
- He, M., Chau, J. L., Stober, G., Hall, C. M., Tsutsumi, M., & Hoffmann, P. (2017). Application of Manley-Rowe relation in analyzing non-linear interactions between planetary waves and the solar semidiurnal tide during 2009 sudden stratospheric warming event. *Journal of Geophysical Research: Space Physics*, 122(10), 10–783. <https://doi.org/10.1002/2017JA024630>
- Hocking, W. K., Fuller, B., & Vandepeer, B. (2001). Real-time determination of meteor related parameters utilizing modern digital technology. *Journal of Atmospheric and Solar-Terrestrial Physics*, 63(2–3), 155–169. [https://doi.org/10.1016/S1364-6826\(00\)00138-3](https://doi.org/10.1016/S1364-6826(00)00138-3)
- Hoffmann, P., Becker, E., Singer, W., & Placke, M. (2010). Seasonal variation of mesospheric waves at northern middle and high latitudes. *Journal of Atmospheric and Solar-Terrestrial Physics*, 72(14–15), 1068–1079. <https://doi.org/10.1016/j.jastp.2010.07.002>
- Kikuchi, K. (2014). An introduction to combined Fourier–wavelet transform and its application to convectively coupled equatorial waves. *Climate Dynamics*, 43(5–6), 1339–1356. <https://doi.org/10.1007/s00382-013-1949-8>
- Longuet-Higgins, M. S. (1968). The eigenfunctions of Laplace's tidal equation over a sphere. *Philosophical Transactions of the Royal Society of London. Series A, Mathematical and Physical Sciences*, 262(1132), 511–607. <https://doi.org/10.1098/rsta.1968.0003>
- Mitra, G., Guharay, A., Batista, P. P., & Buriti, R. A. (2022). Impact of the September 2019 minor sudden stratospheric warming on the low-latitude middle atmospheric planetary wave dynamics. *Journal of Geophysical Research: Atmospheres*, 127(1), e2021JD035538. <https://doi.org/10.1029/2021JD035538>
- Mitra, G., Guharay, A., Batista, P. P., Buriti, R. A., & Moffat-Griffin, T. (2023). Investigation on the MLT tidal variability during September 2019 minor sudden stratospheric warming. *Advances in Space Research*, 71(1), 869–882. <https://doi.org/10.1016/j.asr.2022.08.017>
- Pancheva, D. V. (2001). Non-linear interaction of tides and planetary waves in the mesosphere and lower thermosphere: Observations over Europe. *Physics and Chemistry of the Earth - Part C: Solar, Terrestrial & Planetary Science*, 26(6), 411–418. [https://doi.org/10.1016/S1464-1917\(01\)00022-8](https://doi.org/10.1016/S1464-1917(01)00022-8)
- Pancheva, D. V., Mukhtarov, P., Andonov, B., Mitchell, N. J., & Forbes, J. M. (2009a). Planetary waves observed by TIMED/SABER in coupling the stratosphere–mesosphere–lower thermosphere during the winter of 2003/2004: Part 1—Comparison with the UKMO temperature results. *Journal of Atmospheric and Solar-Terrestrial Physics*, 71(1), 61–74. <https://doi.org/10.1016/j.jastp.2008.09.016>
- Pancheva, D. V., Mukhtarov, P., Andonov, B., Mitchell, N. J., & Forbes, J. M. (2009b). Planetary waves observed by TIMED/SABER in coupling the stratosphere–mesosphere–lower thermosphere during the winter of 2003/2004: Part 2—Altitude and latitude planetary wave structure. *Journal of Atmospheric and Solar-Terrestrial Physics*, 71(1), 75–87. <https://doi.org/10.1016/j.jastp.2008.09.027>
- Pancheva, D. V., Mukhtarov, P. J., & Andonov, B. A. (2007). Zonally symmetric oscillations in the Northern Hemisphere stratosphere during the winter of 2003–2004. *Geophysical Research Letters*, 34(4), L04807. <https://doi.org/10.1029/2006GL028666>
- Schulz, M., & Stattegger, K. (1997). SPECTRUM: Spectral analysis of unevenly spaced paleoclimatic time series. *Computers & Geosciences*, 23(9), 929–945. [https://doi.org/10.1016/S0098-3004\(97\)00087-3](https://doi.org/10.1016/S0098-3004(97)00087-3)
- Shepherd, T. G. (2000). The middle atmosphere. *Journal of Atmospheric and Solar-Terrestrial Physics*, 62(17–18), 1587–1601. [https://doi.org/10.1016/S1364-6826\(00\)00114-0](https://doi.org/10.1016/S1364-6826(00)00114-0)
- Teitelbaum, H., & Vial, F. (1991). On tidal variability induced by non-linear interaction with planetary waves. *Journal of Geophysical Research*, 96(A8), 14169–14178. <https://doi.org/10.1029/91JA01019>
- Yamazaki, Y. (2022). A two-step method to derive combined Fourier-wavelet spectra from space-time data for studying planetary-scale waves, and its Matlab and Python software (cfw v1. 0) (pp. 1–28). EGU sphere. <https://doi.org/10.5194/egusphere-2022-1275>

References From the Supporting Information

- Davis, R. N., Du, J., Smith, A. K., Ward, W. E., & Mitchell, N. J. (2013). The diurnal and semidiurnal tides over Ascension Island (°S, 14°W) and their interaction with the stratospheric quasi-biennial oscillation: Studies with meteor radar, eCMAM and WACCM. *Atmospheric Chemistry and Physics*, 13(18), 9543–9564. <https://doi.org/10.5194/acp-13-9543-2013>
- Eckermann, S. D., Rajopadhyaya, D. K., & Vincent, R. A. (1997). Intraseasonal wind variability in the equatorial mesosphere and lower thermosphere: Long-term observations from the central Pacific. *Journal of Atmospheric and Solar-Terrestrial Physics*, 59(6), 603–627. [https://doi.org/10.1016/S1364-6826\(96\)00143-5](https://doi.org/10.1016/S1364-6826(96)00143-5)
- Guharay, A., Batista, P. P., Clemesha, B. R., Sarkhel, S., & Buriti, R. A. (2014b). Investigation of the intraseasonal oscillations over a Brazilian equatorial station: A case study. *Earth Planets and Space*, 66, 1–13. <https://doi.org/10.1186/s40623-014-0145-3>
- Hoffmann, P., & Jacobi, C. (2012). Planetary wave characteristics of gravity wave modulation from 30–130 km. *Advances in Radio Science*, 10, 271–277. <https://doi.org/10.5194/ars-10-271-2012>
- Pancheva, D., Mitchell, N. J., Younger, P. T., & Muller, H. G. (2003). Intra-seasonal oscillations observed in the MLT region above UK (52°N, 2°W) and ESRANGE (68°N, 21°E). *Geophysical Research Letters*, 30(21), 2084. <https://doi.org/10.1029/2003GL017809>
- Smith, A. K. (2003). The origin of stationary planetary waves in the upper mesosphere. *Journal of the Atmospheric Sciences*, 60(24), 3033–3041. [https://doi.org/10.1175/15200469\(2003\)060<3033:TOOSPW>2.0.CO;2](https://doi.org/10.1175/15200469(2003)060<3033:TOOSPW>2.0.CO;2)



Research Paper

Impact of sudden stratospheric warming on middle atmospheric circulation in the southern hemisphere: A comparative study

G. Mitra^{a,b,*}, A. Guharay^{a,**}^a Space and Atmospheric Sciences Division, Physical Research Laboratory, Ahmedabad, GJ, India^b Department of Physics, Indian Institute of Technology, Gandhinagar, GJ, India

ARTICLE INFO

Handling Editor: Dora Pancheva

Keywords:

Middle atmospheric circulation
Southern sudden stratospheric warming
Atmospheric coupling

ABSTRACT

A comparative study on the impact of rare Southern Hemisphere (SH) Sudden Stratospheric Warmings (SSW) on the middle atmospheric circulation is investigated using a global reanalysis dataset. Since the SH SSW generally occur around spring equinox marking the seasonal transition, so an attempt has been made to isolate the seasonal transition effect from the actual data by carrying out deseasoning to delineate the effects mainly due to the warming. The deseasoned winds are able to extract relatively weak dynamical signatures of SSW at lower altitudes in terms of prominent zonal mean easterly forcing around the peak warming day (PWD) which are not evident from the actual winds. The influence of 2002 SSW seems to reach the troposphere in terms of easterly deseasoned forcing, which is not the case in 2019. Also the deseasoned winds in the stratosphere reveals earlier occurrence of easterly forcing in the extratropical latitudes, which progresses poleward around the PWD indicating a possible tropical precursor to the SH SSW. In general, the actual upper mesospheric wind is dominated by seasonal transition but the deseasoned winds reveal easterly and southerly forcing due to the SSW. Interestingly, the horizontal flow is found to be very different or even opposite in direction at different longitudes indicating uneven longitudinal response of the atmosphere to the warming events across the globe. Overall, the present study provides a detailed and comparative overview of the middle atmospheric circulation in terms of zonal mean flow and concomitant zonal variability during two rare major and minor SSW events in the SH.

1. Introduction

Occasionally during winter, the global atmospheric circulation becomes highly perturbed, accompanied by a marked amplification of planetary waves (Matsuno, 1971). Simultaneously the polar stratospheric temperature increases considerably by a few tens of Kelvin within a few days (Andrews et al., 1987). Such a dramatic warming event is called Sudden Stratospheric Warming (SSW). Major and minor warmings are the two main categories of the SSW. The reversal of the zonal mean temperature gradient poleward of 60° is a signature of both major and minor events. Additionally, the reversal of the zonal mean zonal wind at 60° latitude and 10 hPa pressure level is a characteristic of major SSW (Labitzke et al., 2005). Moreover, based on the polar vortex structure, SSW can be further classified into ‘vortex-displacement’ or ‘vortex-split’ type event (Charlton and Polvani, 2007).

Although SSW is a polar stratospheric phenomenon, it has the potential to impact the global atmospheric system from the troposphere to

the thermosphere and across both hemispheres (Pedatella et al., 2018). There are a handful of interesting studies on the Southern Hemisphere (SH) SSW affecting the global atmospheric system, such as the impact on the convective activity in the tropics (Eguchi and Kadera, 2007; Noguchi et al., 2020), ionospheric variability (Yamazaki et al., 2020), planetary waves (Guharay et al., 2014; Mitra et al., 2022) and tidal dynamics (Guharay and Batista, 2019; Mitra et al., 2023) in the low-latitude middle atmosphere, and interhemispheric coupling (He et al., 2020; Pedatella et al., 2021). SSW is more frequent in the Northern Hemisphere (NH) than in the Southern Hemisphere (SH). On average, major SSW in the NH occur once every two years. The only major warming observed in the SH occurred in September 2002 (Varotsos 2002, 2004), leading to an ozone hole nearly 40% smaller than the average observed in the six preceding years. Another minor but robust Antarctic SSW happened in September 2019. Such hemispheric asymmetry in the occurrence of the SSW is primarily due to higher planetary wave activity in the NH owing to higher orographic difference and land-sea contrast,

* Corresponding author. Space and Atmospheric Sciences Division, Physical Research Laboratory, Ahmedabad, GJ, India.

** Corresponding author. Space and Atmospheric Sciences Division, Physical Research Laboratory, Ahmedabad, GJ, India.

E-mail addresses: gourav@prl.res.in, reachmitragourav@gmail.com (G. Mitra), guharay@prl.res.in (A. Guharay).

and secondly, because of stronger SH polar jets (Newman and Nash, 2005; Rao et al., 2020).

So far, the SH SSW occurred around the spring equinox, marking the seasonal transition from late winter to early spring. During the transition period, the seasonal changes due to the solar radiative process and the dynamical process mainly driven by enhanced planetary wave activity play a crucial role in weakening the polar vortex (Rao and Garfinkel, 2021) and finally resulting in easterly wind. The transition from westerly to easterly circulation, called Stratospheric Final Warming (SFW), may be late and very smooth, controlled mainly by radiative processes, or abrupt, dynamically driven by enhanced planetary waves (Butler et al., 2015; Maury et al., 2016). Considering this aspect, the present study aims to isolate the seasonal mean background state from the actual winds to understand the dynamical features of the middle atmospheric circulation solely due to such rare SH SSW. Recently, Veenus et al. (2023) indicate the influence of 2019 SH SSW on the stratospheric circulation which in turn affects the ozone and water vapor transport from the tropics to the pole. Although on the same warming events, there have been studies on the planetary wave forcing in the mesosphere and lower thermosphere (Vincent et al., 2022) and also the role of planetary wave activity in the evolution of the 2019 minor event (Liu et al., 2022), detailed and comparative aspects on the middle atmospheric circulation during the SH SSW has remained untouched so far. Hence, the current study attempts to compare the characteristics of the middle atmospheric circulation during two prominent major and minor events from the SH. For that purpose, a global reanalysis dataset is utilized to understand the latitudinal, altitudinal and associated longitudinal variability in the middle atmospheric circulation during such unusual and dramatic SH SSWs.

2. Data and analysis method

For the present study we have utilized a global reanalysis database during the period centered around the 2002 major and 2019 SH minor warming episodes ~ from 1 August to 31 October of the year 2002 and 2019, respectively, as described below.

2.1. MERRA-2 database

Modern-Era Retrospective analysis for Research and Applications version 2 (MERRA-2) is the latest version of global atmospheric reanalysis for the satellite era produced by the NASA Global Modeling and Assimilation Office (GMAO) using the Goddard Earth Observing System Model (GEOS) version 5.12.4 (Gelaro et al., 2017). The dataset covers the period of 1980-present with the latency of ~3 weeks after the end of a month.

M2I3NVASM (or inst3_3d_asm_Nv) is an instantaneous 3-dimensional 3-hourly data collection in MERRA-2. For the present investigation, we have used temperature (T), zonal wind (U), and meridional wind (V) at 72 model pressure levels within the range 985–0.01 hPa (~0–75 km) with a latitude-longitude grid of $0.5^\circ \times 0.625^\circ$.

2.2. Analysis method

In general, the SSW event in the SH occurs around the September equinox. However, the seasonal transition also takes place during the same time. Therefore, in the SSW years the atmospheric dynamics is affected by both the aforementioned factors. Hence, to determine the SSW impact it is essential to isolate the seasonal contribution taking place at the same time interval.

The objective of the present study is to isolate and analyze the impact of sudden stratospheric warming (SSW) events in the Southern Hemisphere (SH) by separating the seasonal contribution during the September equinox, aiming to discern the specific influence of SSW on atmospheric dynamics.

For that purpose, deseasoned values of the atmospheric parameters

(T, U, and V) are estimated by subtracting the seasonal mean state (SMS) from the instantaneous values. The SMS is represented by the 90-day central moving average during the concerned SH SSW year. The deseasoned value of the respective parameters are mentioned with a “d” prefix in the rest of the paper. Detailed explanation provided in the supplementary material elaborates on the reasons and advantages of estimating the SMS and determining the corresponding window width.

The purpose of deseasoning is to understand the relatively weak dynamical features of the middle atmosphere solely due to the SSW that might not be apparent in actual parameters. Additionally, the analysis method eliminate interannual variability of the SMS during observational periods.

3. Results

3.1. Altitude-time variability of the zonal mean background conditions

The time-height section-of the temperature (T) at 90° S during the observational period for the years 2002 and 2019 are shown in Fig. 1a and b, respectively. Maximum polar warming at 10 hPa is observed on 27 September (DOY 271) 2002, considered as the peak warming day (PWD) for the 2002 SH major SSW. Similarly, for the 2019 SH minor SSW, 19 September (DOY 263) is identified as the PWD. In the current study, a black solid line represents the PWD for the 2002 and 2019 SH SSW events. The white contour curve represents zero value in the present and all the following figures. Intermittent enhancement in the polar T characterized by three distinct warming bursts can be identified around 40 km altitude before the 2002 PWD, as shown in Fig. 1a. Rapid downward propagation of the warming up to 15 km altitude is noticeable on the 2002 PWD. Fig. 1b reveals the gradual propagation of the warming to lower altitudes up to 20 km until the 2019 PWD.

The time-height section of the deseasoned polar T (dT) for the 2002 and the 2019 SH SSW are shown in Fig. 1c and d. The warming bursts near 40 km altitude, as observed in Fig. 1a, become more prominent in Fig. 1c. Interestingly, there is a noticeable polar mesospheric cooling above 40 km concurrent with polar stratospheric warming. Similarly, Fig. 1d exhibits discernible stratospheric warming features during the 2019 SSW event. As evident from the dT variability, the warming seems to start early in the upper stratosphere and extend to lower altitudes around the 2002 and 2019 PWD. However, in 2019, the downward propagation of warming is more gradual as compared to the 2002 event.

Fig. 1e and f represent the time-height section of the zonal mean zonal wind (ZMU) at 60° S during the observational intervals of the years 2002 and 2019, respectively. Intermittent weakening of the zonal mean westerlies concurrent with the warming pulses (Fig. 1a) is found before the 2002 PWD in the altitude region of 30–60 km, followed by a sudden reversal to easterlies near the PWD, as seen in Fig. 1e. However, the wind reversal persists for the rest of the observational interval in the upper mesosphere. In the case of the 2019 SSW, the reversal of westerly wind to easterly takes place before the PWD in the upper mesosphere and gradually reaches an altitude as low as 37 km on the PWD (Fig. 1f). The easterly wind reverses to the westerly wind soon after the PWD. The zonal mean westerly is found to reverse again after some days from the PWD in the altitude region above 35 km with an earlier reversal in the mesosphere. Therefore, the reversed state of the ZMU (easterly) in the mesosphere and stratosphere for a few days around the 2019 PWD is discernible from the actual variability, unlike 2002, where the upper mesospheric westerly turns to easterly.

The time-height section of the deseasoned ZMU (dZMU) at 60° S for the 2002 and the 2019 SH SSW are shown in Fig. 1g and h. The dZMU diminishes considerably around the 2002 PWD in the observed altitude region (0–75 km) and reinstates to former values a few days after the PWD (Fig. 1g). During the 2019 event, the dZMU shows easterly from late August (~ DOY 233) to early October (DOY 283) in the stratosphere and mesosphere above 20 km centered around the PWD, as evident in Fig. 1h. It can be noted that the influence of the SSW is found to extend

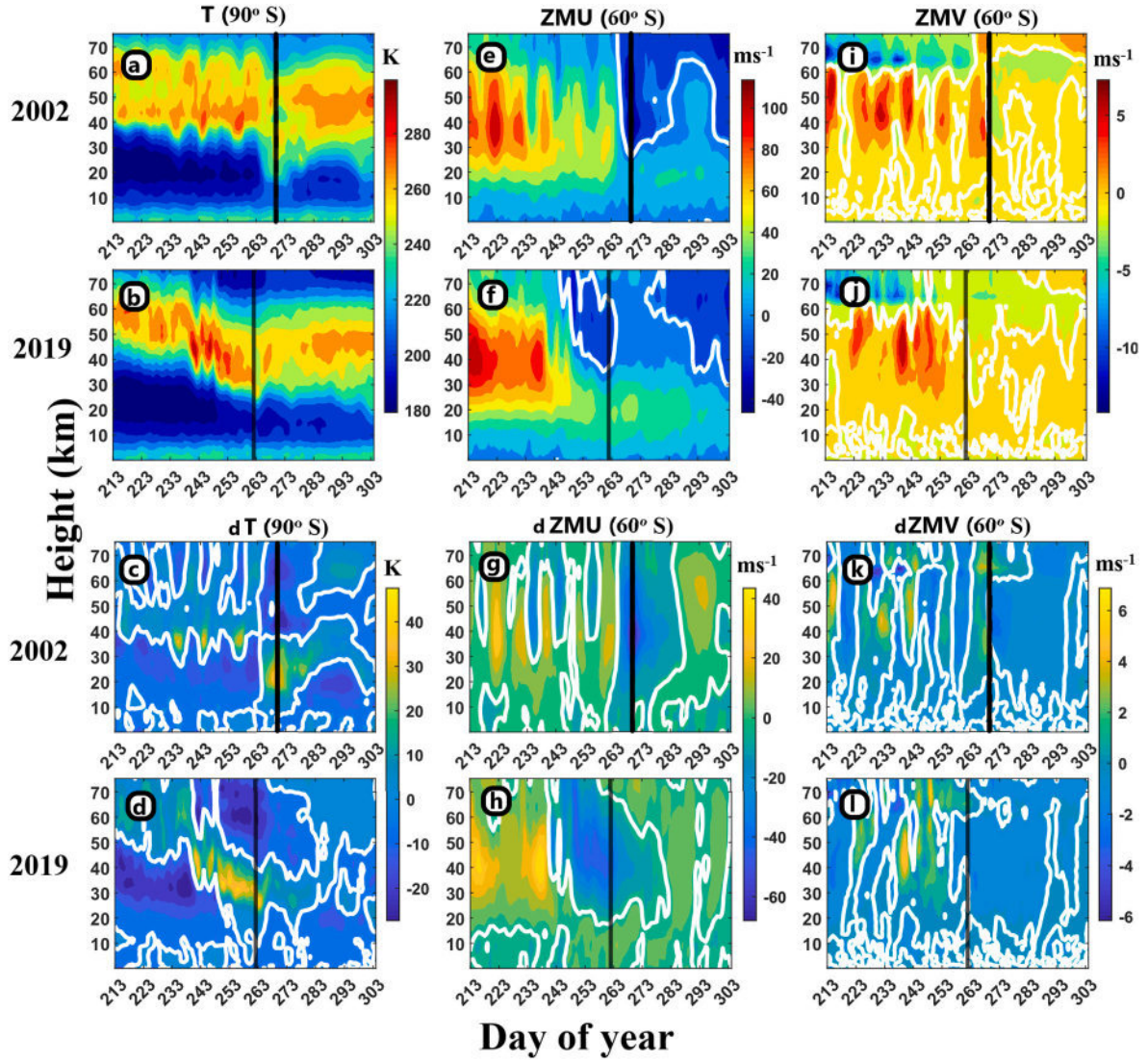


Fig. 1. Time-height section of (a) T at 90° S, (e) ZMU at 60° S, and (i) ZMV at 60° S during 2002 observational days and (b) T at 90° S, (f) ZMU at 60° S, and (j) ZMV at 60° S during 2019 observational days. Same for (c) dT at 90° S, (g) dZMU at 60° S, and (k) dZMV at 60° S during 2002 observational days and (d) dT at 90° S, (h) dZMU at 60° S, and (l) dZMV at 60° S during 2019 observational days. The solid vertical line represents the PWD. The white bold curves represent zero values in all the plots. Please note the change of scale in the colorbars corresponding to each subplot while comparing. Also, consider the difference in colorbar used to represent actual and deseasoned variability.

further towards lower altitudes in dZMU as compared to the ZMU. Interestingly, SSW's effect seems to penetrate the troposphere during 2002 unlike in 2019, as visible from the negative dZMU around the PWD. This further emphasizes the need to look into the deseasoned variability to delineate the influence of SSW on lower altitudes. Moreover, the upper mesospheric dZMU in 2002 shows a prominent effect of SSW, which seems to be overshadowed by the seasonal transition in the ZMU profile.

The time-height section of the zonal mean meridional wind (ZMV) at 60° S during the observational period for the years 2002 and 2019 are shown in Fig. 1i and j, respectively. Alternative weakening and strengthening of zonal mean southerlies is observed until the PWD of the 2002 SSW in the upper stratosphere and lower mesosphere (40–60 km) (Fig. 1i). In the case of 2019 SSW, the southerly wind seems to enhance for few days before the PWD, as seen in Fig. 1j. The deseasoned ZMV (dZMV) for the 2002 (Figs. 1k) and 2019 (Fig. 1l) SH SSW interestingly exhibit much extended spatio-temporal reversed (northerly) wind condition after the PWD as compared to the ZMV.

3.2. Latitude-time distribution of zonal mean flow

To understand the characteristics of the zonal mean circulation in the middle atmosphere during the SH SSW, we have looked into the latitude-time section of the ZMU and ZMV at three representative altitudes in the SH. The representative pressure levels are 10 hPa (~30 km), 1 hPa (~45 km), and 0.01 hPa (~75 km).

3.2.1. ZMU

The latitude-time section of the ZMU at 10 hPa (mid stratosphere) during two warming events are shown in Fig. 2a and b, respectively. During the 2002 SSW, the strong westerly ZMU near 60° S, exhibits intermittent weakening before reversing into the easterly wind around the PWD (Fig. 2a). In the case of 2019 SSW, there is a considerable deceleration of the westerly ZMU near 60° S, until the PWD with no wind reversal (Fig. 2b). Fig. 2c and d represent the latitudinal profile of the dZMU at 10 hPa during the observational intervals of 2002 and 2019, respectively. A conspicuous deceleration is apparent in the westerly wind which seems to start early in extratropical latitudes (30–45° S) and advances to mid and high latitudes during both the

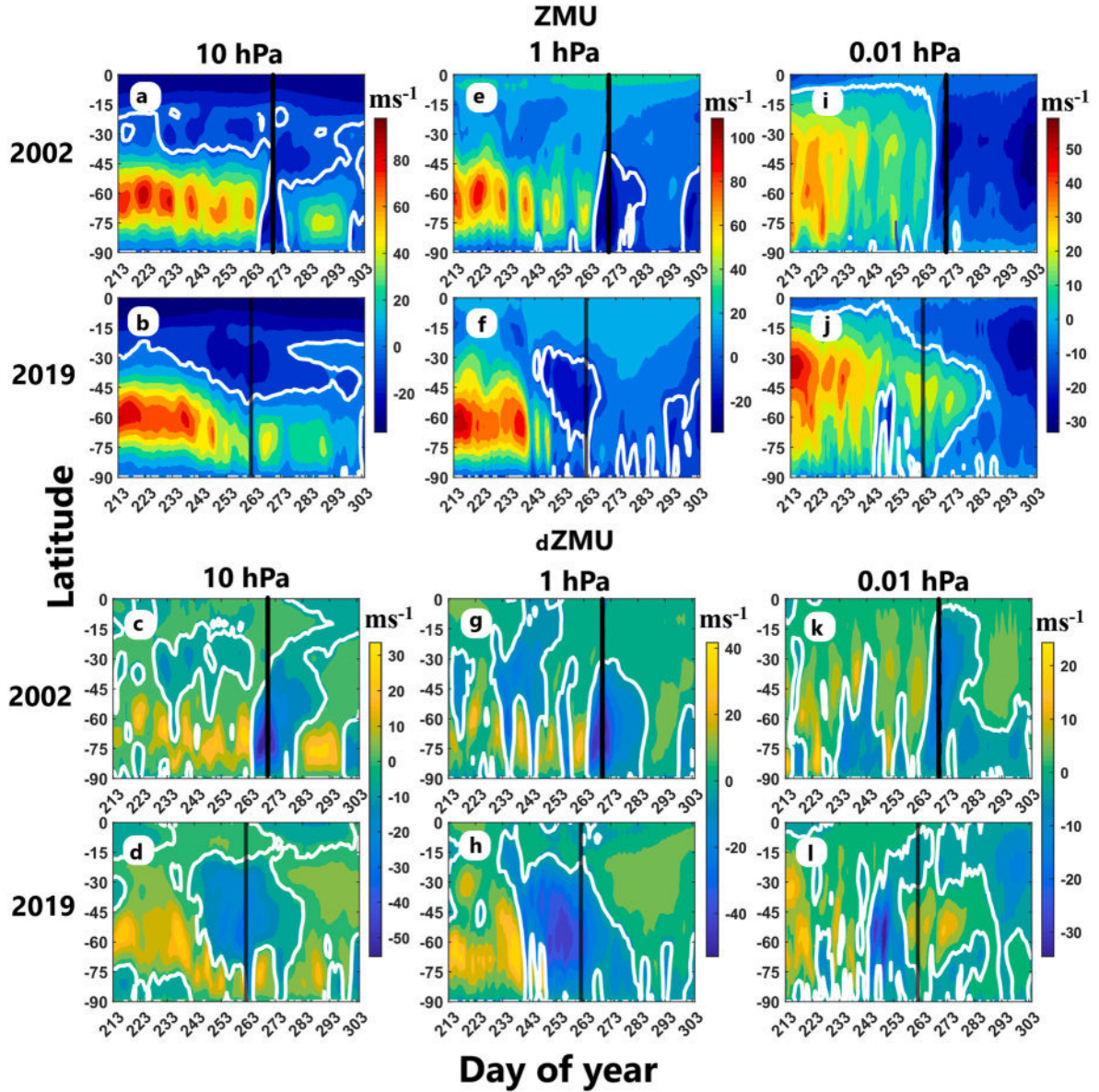


Fig. 2. Latitudinal-time section of ZMU at (a) 10 hPa, (e) 1 hPa, and (i) 0.01 hPa and dZMU at (c) 10 hPa, (g) 1 hPa, and (k) 0.01 hPa during 2002 observational days. Same during 2019 observational days for ZMU at (b) 10 hPa, (f) 1 hPa, and (j) 0.01 hPa and dZMU at (d) 10 hPa, (h) 1 hPa, and (l) 0.01 hPa. Please note the change of scale in the colorbars corresponding to each subplot while comparing. Also, consider the difference in colorbar used to represent actual and deseasoned variability.

events as ascertained from the distinct negative values of dZMU (Fig. 2c and d). It can be further noted that the weakening of the westerly wind during the minor SSW can be clearly identified in the corresponding dZMU profile (Fig. 2d), which seems masked in the actual variability.

Fig. 2e–h represent the same as Fig. 2a–d but at 1 hPa (upper stratosphere). The westerly ZMU reverses into easterly for a few days around the 2002 PWD (Fig. 2e) and the 2019 PWD (Fig. 2f) in the middle and high latitudes. The reversal in the westerly ZMU during 2019 warming starts early in 30° S, as seen in Fig. 2f. Interestingly, the poleward progression of zero wind line starts early at low latitude stratosphere, as clearly evident from the dZMU profile of both the events (Fig. 2g and h), although finite discontinuity in 2002 event can be noted.

Fig. 2i and j represent the latitudinal-time section of the ZMU at 0.01 hPa (upper mesosphere) during 2002 and 2019, respectively. The zonal mean westerly wind starts weakening and reverses into the easterly wind a few days before the 2002 PWD, which persists for the rest of the observational days (Fig. 2i). In the case of the 2019 event, the westerly ZMU reversal to easterly is observed for a short duration a few days

before the PWD. Another almost permanent westerly to easterly reversal of the ZMU, possibly owing to the seasonal transition, is noticeable (Fig. 2j). Therefore, no clear response to the warming episodes of the ZMU at 0.01 hPa can be found out. The latitudinal-temporal variability in the dZMU at 0.01 hPa during 2002 and 2019 are shown in Fig. 2k and l, respectively. The dZMU is found to exhibit a distinct occurrence of easterly forcing lasting for a few days around the PWD expanding over whole SH (Fig. 2k). For the 2019 SSW, the existence of an easterly forcing a few days before the PWD can be found in Fig. 2l. It should be noted that noticeable difference between the ZMU (Fig. 2i and j) and dZMU (Fig. 2k and l) profiles is observed at upper mesosphere during both the events.

3.2.2. ZMV

Similarly, we looked into the latitudinal-temporal variability of the ZMV at the aforementioned representative altitudes for the two warming events. Fig. 3a and b illustrate the latitudinal profile of the ZMV at 10 hPa for the 2002 and 2019 SSW events, respectively. During the 2002 event, the prominent band of southerly wind, centered at 60° S, shows

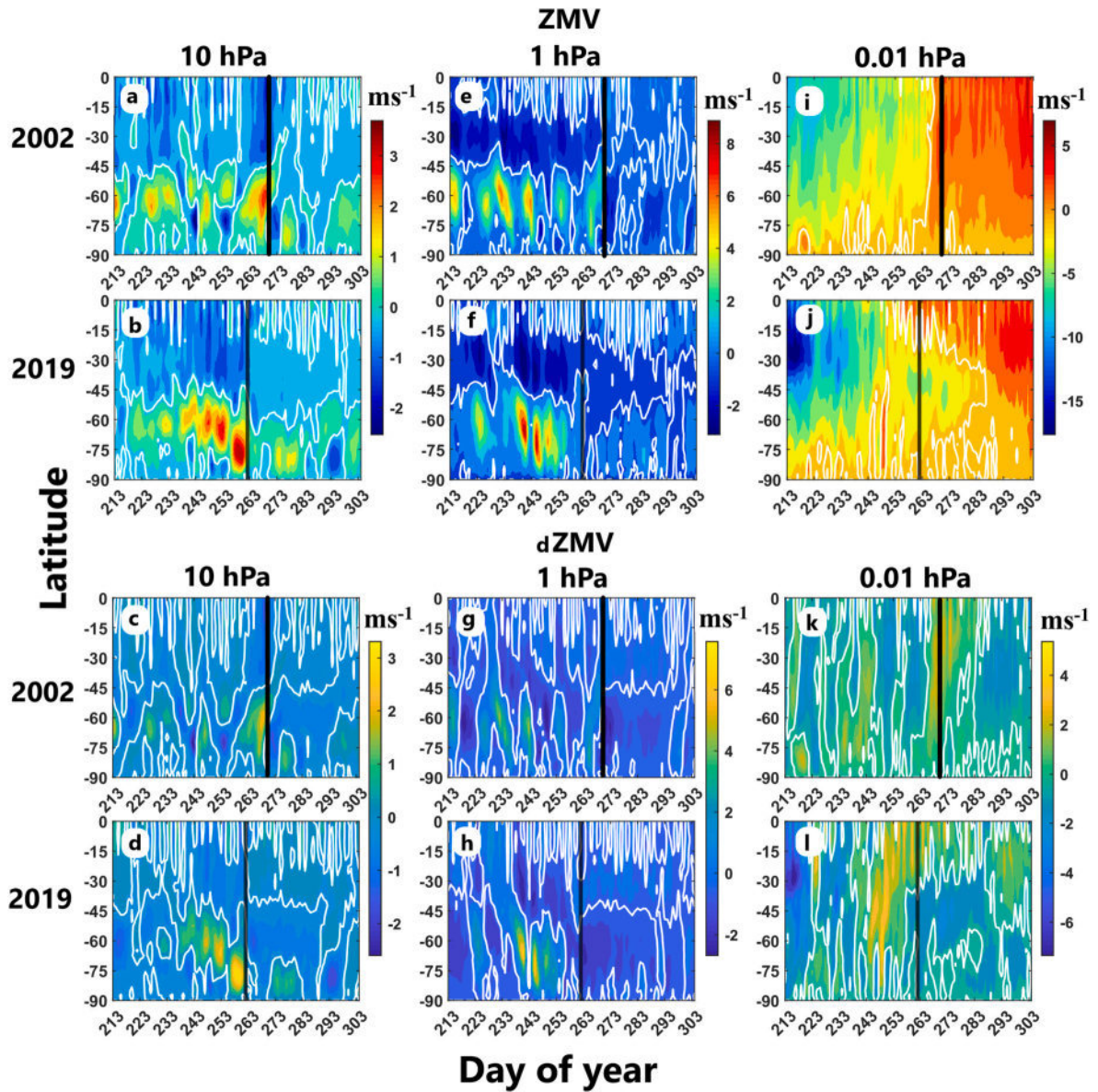


Fig. 3. Latitude-time section of ZMV at (a) 10 hPa, (e) 1 hPa, and (i) 0.01 hPa and dZMV at (c) 10 hPa, (g) 1 hPa, and (k) 0.01 hPa during 2002 observational days. Same during 2019 observational days for ZMV at (b) 10 hPa, (f) 1 hPa, and (j) 0.01 hPa and dZMV at (d) 10 hPa, (h) 1 hPa, and (l) 0.01 hPa. Please note the change of scale in the colorbars corresponding to each subplot while comparing. Also, consider the difference in colorbar used to represent actual and deseasoned variability.

intermittent strengthening before the PWD and diminishes suddenly thereafter (Fig. 3a). During 2019 a poleward movement of the southerly ZMV patches from midlatitude (60° S) can be found until the PWD (Fig. 3b). The latitude-time variability of the dZMV at 10 hPa during these events are shown in Fig. 2c and d. An evident southerly deseasoned forcing can be found around the 2002 PWD at midlatitude (Fig. 2c). Fig. 2d illustrates the conspicuous poleward movement of the southerly dZMV, which seems to intensify around the PWD in 2019 similar to the corresponding ZMV profile.

Fig. 3e and f illustrate the latitudinal-temporal variability in ZMV at 1 hPa during the 2002 and 2019 events. In 2002 intermittent strengthening in the southerly ZMV centered at 60° S is observed until the PWD (Fig. 3e). In 2019 the enhanced southerly ZMV can be found a few days before the PWD (Fig. 3f). The dZMV profiles (Fig. 3g and h) seem to show very similar behavior to the ZMV at 1 hPa.

The latitudinal profile of the ZMV at 0.01 hPa during the two events are shown in Fig. 3i and j. The northerly ZMV turns southerly around the 2002 PWD and persists for the rest of the observational days (Fig. 3i). As

seen in Fig. 3i, similar features are observed during the 2019 event (Fig. 3j). The only difference is the late reversal of northerly ZMV to southerly after the 2019 PWD in the middle latitudes. The overall pattern is very similar to the ZMU at 0.01 hPa (Fig. 2i and j). Fig. 3k and l shows the latitudinal-temporal variability of the dZMV at 0.01 hPa during the 2002 and 2019 events, respectively. In 2002 an evident southerly deseasoned forcing can be noted around the PWD especially at low latitude (Fig. 3k). Fig. 3l exhibits southerly deseasoned forcing that started a few days before the PWD mainly at low latitude in 2019.

Overall, notable differences are observed between actual and deseasoned zonal mean flow particularly in the upper mesosphere. Hence the deseasoned flow is able to provide important insight into the characteristics of the zonal mean horizontal wind circulation caused by the sudden global scale disturbance, i. e., SSW.

3.3. Global distribution of winds at various phases of SSW

To understand the evolution of the horizontal wind flow and the

associated zonal variability concerning the SH SSW, we have looked into the latitude-longitude section of both U and V in three different phases, i. e., pre-warming (pre-W), warming (W), and post-warming (post-W) with respect to the SSW PWD. Here, the pre-W, W and post-W phases are identified with respect to the PWD. For each phase we have carried out a 5-day average to illustrate the dynamic state of the horizontal wind. In the case of the 2002 event, the temporal average of U/V during 15–19 September, 25–29 September, and 5–9 October are estimated to illustrate the evolution of the U/V at three phases of 2002 SSW. A 5-day separation is selected between two consecutive phases, such as pre-W and W or W and post-W. Similarly, we have chosen 7–11 September, 17–21 September, and 27 September–1 October as time intervals representing the Pre-W, W, and Post-W phases for the 2019 SSW.

3.3.1. Evolution of U

To investigate the evolution of the U during Pre-W, W, and Post-W phases, we have chosen 10 hPa, 1 hPa and 0.01 hPa as the representative altitudes in the middle atmosphere. Fig. 4a and b represent the latitude-longitude section of the U at 10 hPa during the pre-W phase of 2002 and 2019, respectively. Fig. 4c and d illustrate the deseasoned U (dU) at 10 hPa during the 2002 and 2019 pre-W phase, respectively. Fig. 4e–h and 4i–l represent the same as Fig. 4a–d but for the W and post-W phases, respectively. The white bold curve represents the zero value. At 10 hPa, a strong westerly is found to meander in the mid and high latitudes across all longitudes over the globe during the 2002 (Figs. 4a) and 2019 Pre-W (Fig. 4b) phases. The features exhibited in Fig. 4a and b appear more prominent in the dU profiles during the Pre-W phases of 2002 (Figs. 4c) and 2019 (Fig. 4d). Two distinct patches of westerly wind sandwiched between easterly zones signifying the dominance of

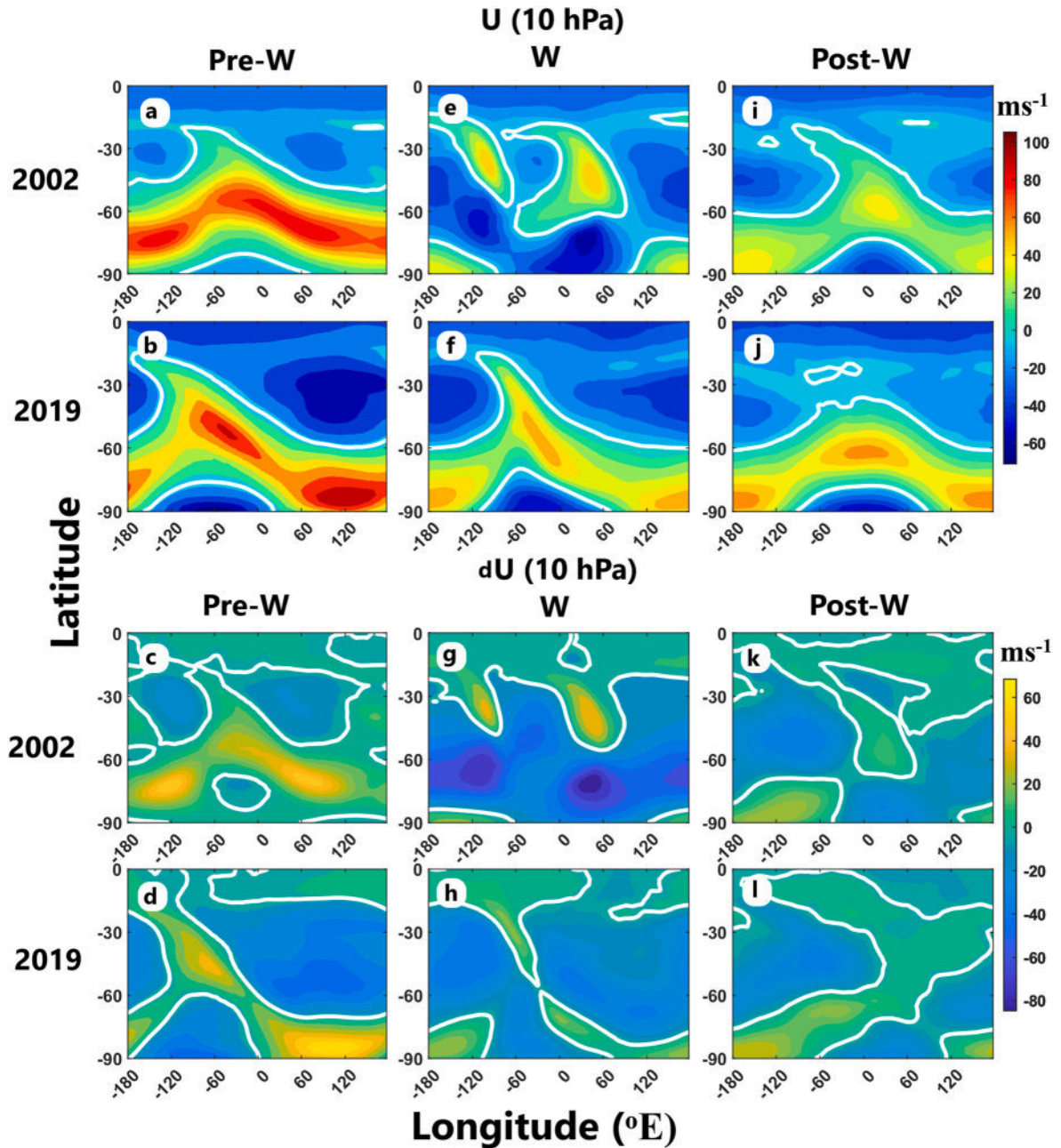


Fig. 4. Latitude-longitude section of U at 10 hPa during 2002 (a) Pre-W (e) W, and (i) Post-W and dU during 2002 (c) Pre-W (g) W, and (k) Post-W at 10 hPa. Same for U during 2019 (b) Pre-W (f) W, and (j) Post-W and dU during 2019 (d) Pre-W (h) W, and (l) Post-W. Please note the change of scale in the colorbars corresponding to each subplot while comparing. Also, consider the difference in colorbar used to represent actual and deseasoned variability.

zonal wavenumber 2 structure can be found in the midlatitudes during the W phase of the 2002 SSW (Fig. 4e). In the case of the 2019 event, the pattern of U looks very similar to the pre-W phase with reduced magnitude along with an eastward shift of the same at low latitude ($\sim 30^\circ\text{S}$) (Fig. 4f). The reversal in the westerly wind at high latitude and appearance of the zonal wavenumber 2 feature in the U at midlatitudes become conspicuous in the dU profile during the 2002 W phase (Fig. 4g). Fig. 4h shows a noticeable weakening in the westerly wind during the 2019 W phase, as visible from the negative dU values at mid and high-latitudes. The U is found to reinstate the westerly trend at mid and high-latitudes during the 2002 post-W phase with smaller overall magnitude as compared to the pre-W phase (Fig. 4i). In the case of the 2019 event, the westerly wind at high latitudes remains weak during the post-W phase (Fig. 4j). As per the dU profiles during the post-W phase, the easterly zones are suppressed by the westerly ones for both 2002 (Figs. 4k) and 2019 (Fig. 4l), although the patterns don't look similar to

the pre-W phase unlike the behavior of the U.

Fig. 5 shows the same as Fig. 4, but at 1 hPa level. The prominent structure of westerly wind is seen during the 2002 pre-W across all the longitudes centered about 60°S (Fig. 5a). This is followed by a reversal of westerly to easterly at mid and high latitudes during the 2002 W phase (Fig. 5e), and the westerly wind seems to partially recover during the 2002 post-W days (Fig. 5i). During the 2019 pre-W days, the U appears to vary in opposite fashion at mid and high latitudes. Interestingly, a dominant zonal wavenumber 1 structure of U in the midlatitudes is found to be in the opposite phase to the same at high latitudes, i.e., the easterly and westerly patches seem to interchange their location among the mid and high latitudes with longitude (Fig. 5b). Similar features are observed during the 2019 W days but with smaller magnitude (Fig. 5f). The westerly wind dominates during the 2019 post-W days (Fig. 5j) although magnitude is much smaller than the previous two phases. Fig. 5c, g, and 5k exhibit prominent features of the evolution of dU

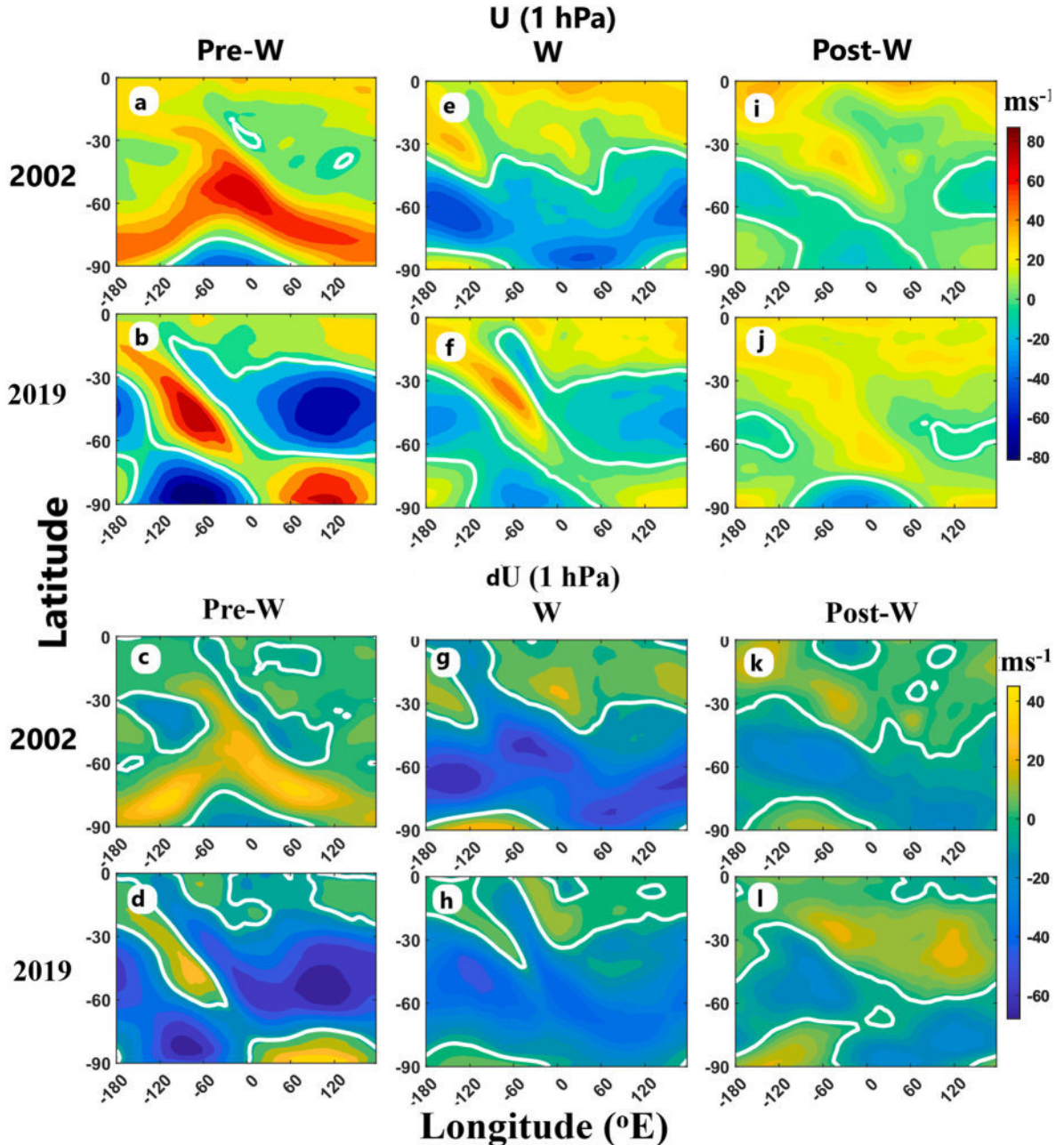


Fig. 5. Same as Fig. 4, but at 1 hPa.

concerning the 2002 event, which behave almost similar to Fig. 5a, e, and 5i, respectively. During the 2019 pre-W phase, the dU shows significant easterly at mid and high latitudes at different longitudes (Fig. 5d), followed by weakening of overall magnitude during the W phase (Fig. 5h), and post-W phase (Fig. 5l). During the 2019 post-W phase, the westerly flow persists at lower latitude and easterly wind can be found at higher latitude over most of the longitudes.

Fig. 6 shows the same as Fig. 4, but at 0.01 hPa. The dominant westerly wind during the 2002 pre-W phase can be noted in Fig. 6a. It is interesting to note the reversal of the westerly to the easterly during the W and post-W phases, as seen in Fig. 6e and 6i, respectively. However, in the case of the 2019 event, the westerly wind generally dominates during the pre-W days (Fig. 6b). The westerly seems to intensify during W phase in the eastern longitude sector at mid latitudes (Fig. 6f), which persists during the post-W phase as well (Fig. 6j). Fig. 6c, g, and 6k show dU which is very similar to U, as seen in Fig. 6a, e, and 6i during the 2002 event. The variability of dU during different phases of the 2019

SSW, as shown in Fig. 6d, h, and 6l, exhibits characteristics almost similar to U as seen in Fig. 6b, f, and 6j.

3.3.2. Evolution of V

Fig. 7 show the latitude-longitude section of V at 10 hPa level at various phases of the SSW for both warming events. Fig. 7a shows the profile of the V during the 2002 Pre-W phase. The zonal wavenumber 1 structures in the V seem to dominate at high latitudes. The profile of V during the 2019 pre-W phase also reveals the dominant signature of zonal wavenumber 1 at mid and high latitudes, as can be identified from the alternate appearance of northerly and southerly wind across the longitude (Fig. 7b). The dV profile during the 2002 pre-W phase as plotted in Fig. 7c reveals dominant zonal wavenumber 2 component in the V at mid latitude that seems to extend to high latitudes. The dV profile during the 2019 pre-W phase (Fig. 7d) shows evident zonal wavenumber 1 structure at mid and high latitudes. The V profile during 2002 W phase (Fig. 7e) shows prominent zonal wavenumber 2 structure

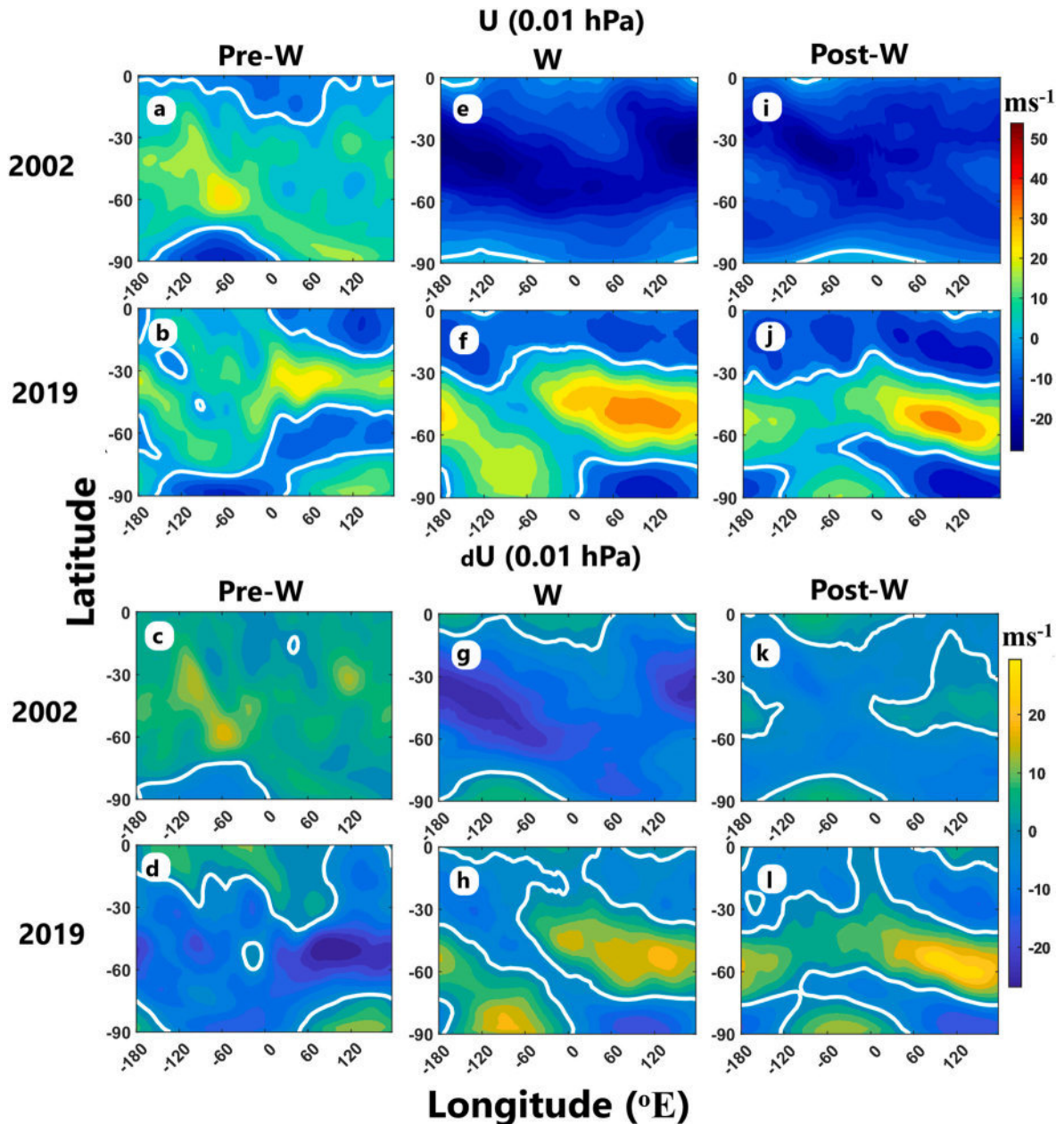


Fig. 6. Same as Fig. 4, but at 0.01 hPa.

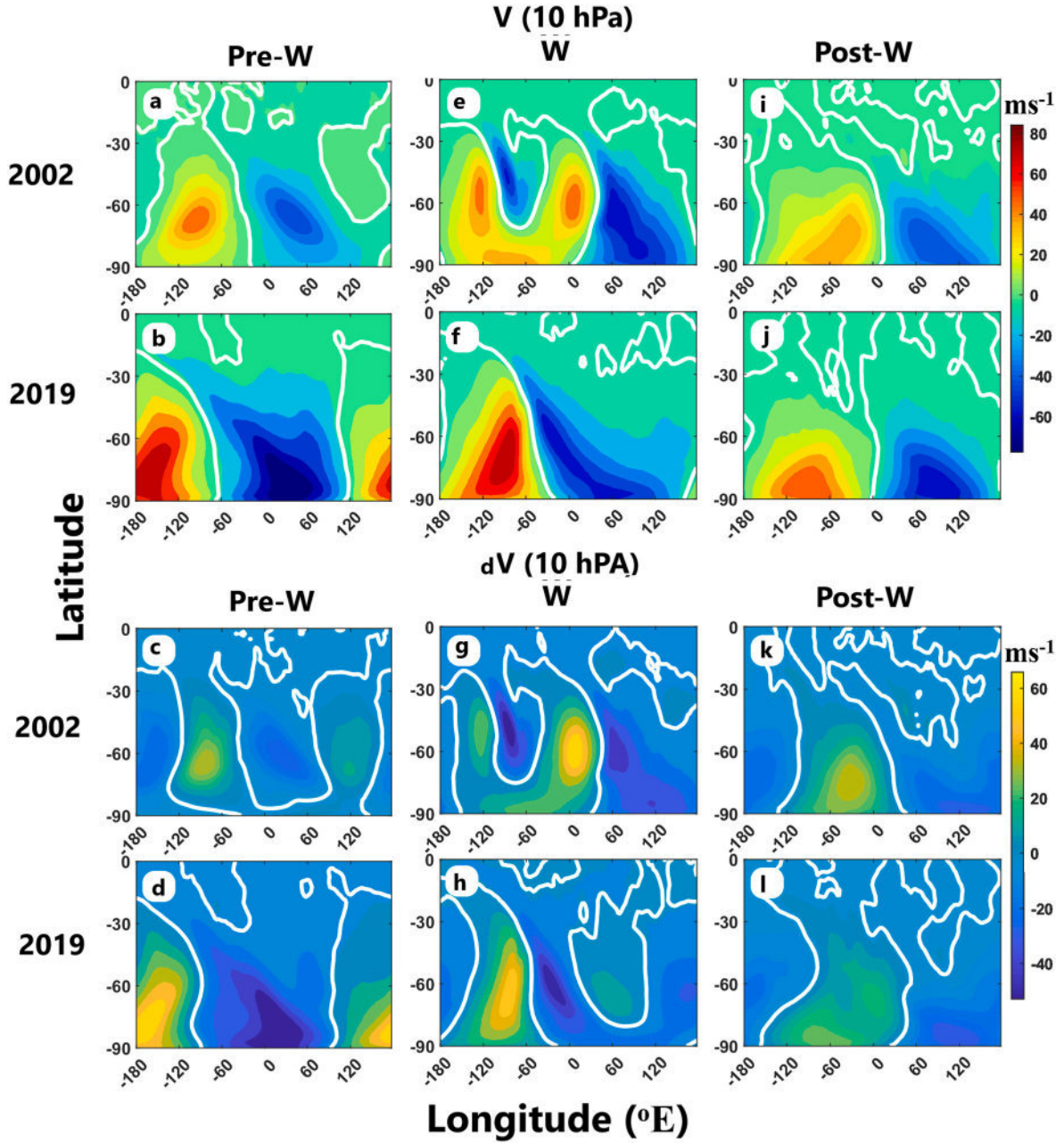


Fig. 7. Latitude-longitude section of V at 10 hPa during 2002 (a) Pre-W (e) W, and (i) Post-W and dV during 2002 (c) Pre-W (g) W, and (k) Post-W at 10 hPa. Same for V during 2019 (b) Pre-W (f) W, and (j) Post-W and dV during 2019 (d) Pre-W (h) W, and (l) Post-W. Please note the change of scale in the colorbars corresponding to each subplot while comparing. Also, consider the difference in colorbar used to represent actual and deseasoned variability.

at mid and high latitudes. The zonal wavenumber 1 component in V continues to dominate during the 2019 W phase and a sharp change from the southerly to the northerly wind is seen along 60° W at 30–60° S. The latitude-longitude section of dV during the 2002 W stage (Fig. 7g) exhibits features similar to Fig. 7e. Interestingly, there is an appearance of zonal wavenumber 2 component in dV (Fig. 7g) at mid and high latitudes during the 2019 W days, which was not evident in the profile of the V (Fig. 7f). The zonal wavenumber 1 structure also seems to be present at mid and high latitudes during the 2002 (Figs. 7i) and 2019 (Fig. 7j) post-W phases. The profiles of the dV during the 2002 (Figs. 7k) and 2019 (Fig. 7l) post-W days reveals features similar to V (Fig. 7i and j, respectively).

Fig. 8 shows the same as Fig. 7, but at 1 hPa level. The zonal wavenumber 1 structure of V appears dominant at mid and high latitudes during the different phases of 2002 (Fig. 8a, e, and 8i) and 2019

(Fig. 8b, f, and 8j) events. However, the wind magnitude diminishes as it progresses to W and post-W phases. The dV profiles exhibit alternate presence of southerly and northerly deseasoned flow along the longitudinal domain in the middle and high latitudes during the pre-W, W, and post-W phases of the 2002 (Fig. 8c, g, and 8k) and 2019 (Fig. 8d, h, and 8l) events which are consistent with the variability of V.

Fig. 9 represents the same as Fig. 7, but at 0.01 hPa. At 0.01 hPa, the profile of the V exhibits prominent zonal wavenumber 1 structure at mid and high latitudes during the 2002 pre-W phase (Fig. 9a) that diminishes in magnitude during the W (Fig. 9e) and post-W (Fig. 9i) phases. During the 2019 pre-W phase, there is an alternate and intermittent structure of northerly and southerly winds about 30° S, implying the possible modulation by higher zonal wavenumber waves. However, the zonal wavenumber 1 structure looks dominant at high latitudes (Fig. 9b). The zonal wavenumber 1 structure is found to prevail during the 2019 W

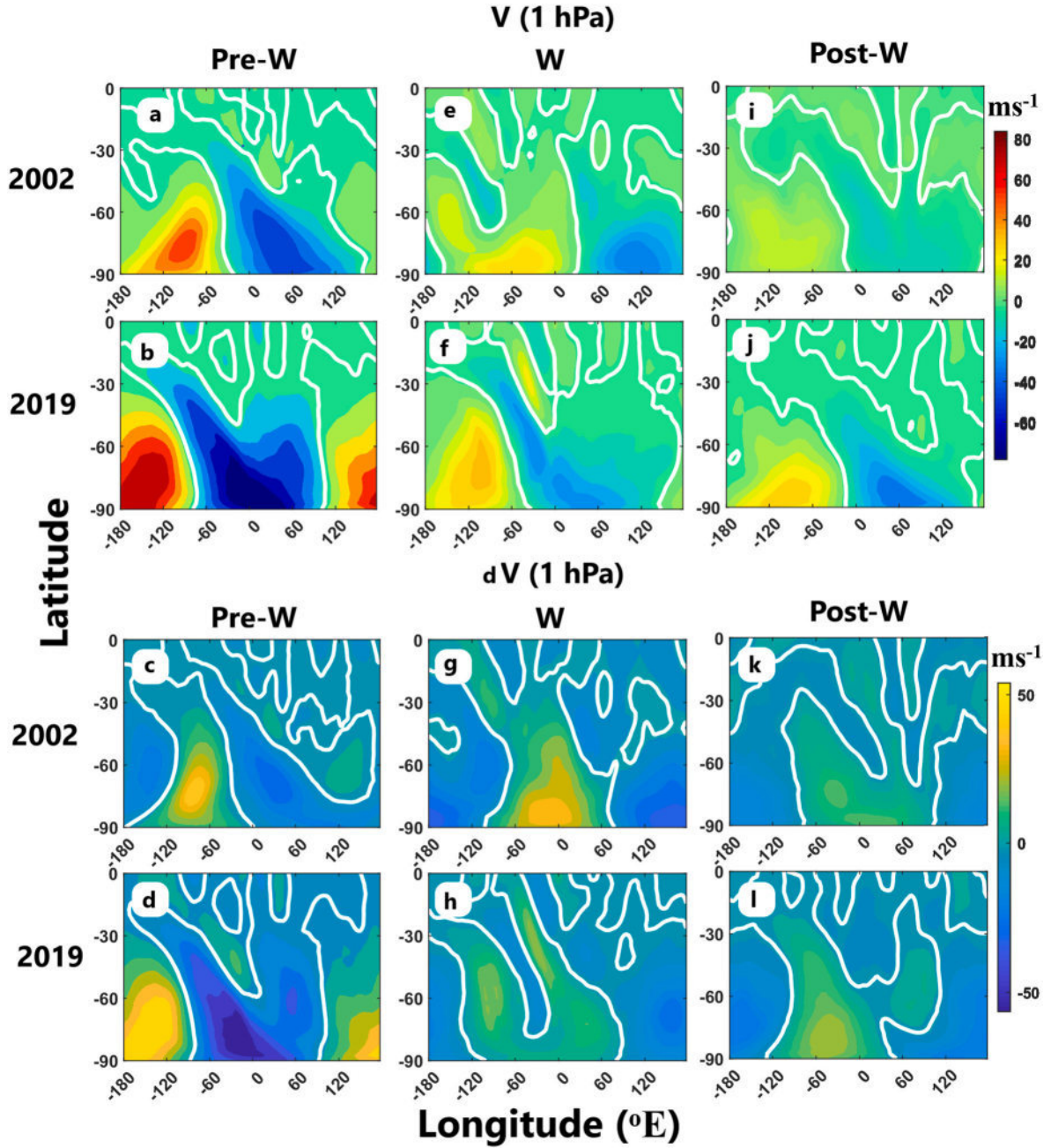


Fig. 8. Same as Fig. 7, but at 1 hPa.

phase at high latitudes (Fig. 9f). Also, the southerly and northerly winds seem to interchange their longitudinal location during the W phase as compared to the pre-W phase. The signature of the zonal wavenumber 1 structure remains prominent at high latitudes during the 2019 post-W days (Fig. 9j). The dV profiles at 0.01 hPa exhibits latitude-longitude features similar to V for both events.

4. Discussions

Our present study has illustrated a handful of interesting dynamical aspects during rare SSW events in the SH using the MERRA2 dataset. The current study aims at providing valuable insights into the middle atmospheric dynamics in terms of zonal mean flow and associated zonal variability in global distribution of flow during a major (2002) and minor (2019) warming events. Moreover, the present work also portrays a comparative study of the middle atmospheric circulation between

major and minor SSW events in the SH.

Observations from the altitude-time variability of the polar temperature reveal the downward propagation of the warming from the upper stratosphere to lower altitudes until the PWD in 2002 and 2019. However, such propagation seems to be more gradual in 2019 than 2002. There is a sudden reversal of the zonal mean westerlies at 60° S which extends to an altitude below 30 km on the PWD in 2002 (Fig. 1e). However, in 2019 the zonal mean westerlies at 60° S reverse much early in the mesosphere, which continues downward as low as 35 km on the PWD (Fig. 1f) unlike the former event. Another key difference between both the events is the actual wind in the upper mesosphere remains easterly for the rest of the observational days in 2002, unlike in 2019 (Fig. 1e and f). This may be attributed to the late occurrence of the 2002 SSW event as compared to the 2019 one, where seasonal transition might play a dominant role. However, the deseasoned variability clearly delineates the SSW impact at 60° S in terms of easterly (reversed state)

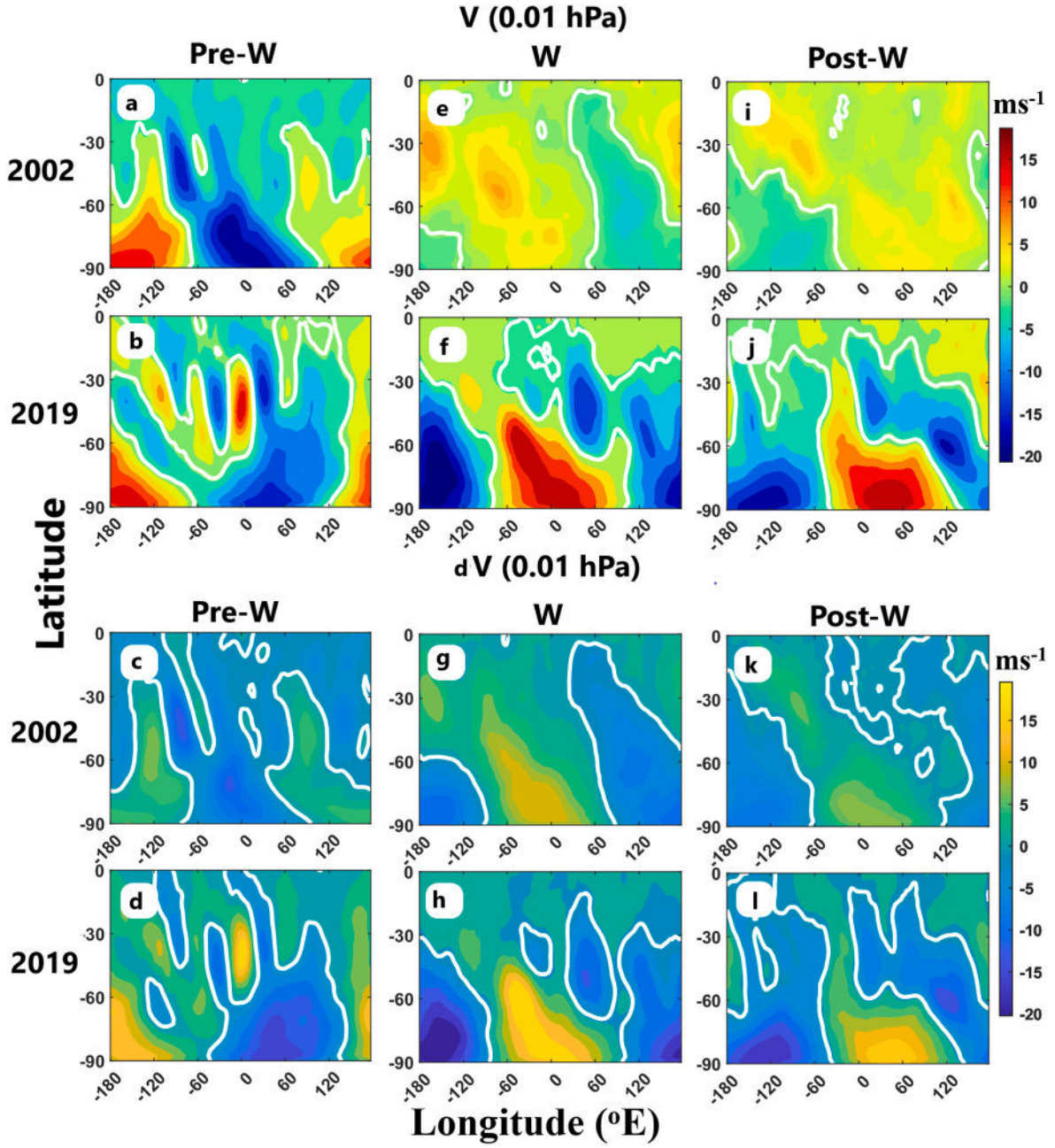


Fig. 9. Same as Fig. 7, but at 0.01 hPa.

forcing from the upper mesosphere to lower altitudes around the PWD in 2002 (Fig. 1g). Interestingly, the deseasoned and easterly forcing seems to penetrate to much lower altitude around the PWD on both events, which is not identifiable from the actual wind. Moreover, the easterly forcing apparently reaches tropospheric heights in 2002, which is not the case in 2019. Both the 2002 and 2019 SH SSW interestingly exhibit much extended spatio-temporal deseasoned poleward forcing after the PWD as compared to the actual wind.

The reversal to easterly direction is observed early in the low latitude stratosphere from the deseasoned variability, particularly in the extratropical region, and further strengthens towards mid and high latitudes around the PWD on both the events. Such poleward progression of zero wind line helps efficiently focus planetary waves from tropical to polar regions, leading to the polar vortex disruption (Koushik et al., 2022). Interestingly, the deseasoned zonal mean upper mesospheric meridional wind shows a northward (equatorward) wind flow tendency,

particularly in the lower latitudes on the PWD in 2002 and before the PWD in 2019, as seen in Fig. 3k and l, respectively. On removing seasonal variability from the high-altitude meteorological analyses, Laskar et al. (2019) reported similar equatorward wind anomalies during the 2010 and 2013 SSW Northern hemisphere (NH) SSW in the mesosphere and lower thermosphere altitudes. It is important to note that in the present study the seasonal transition feature is dominant in the upper mesospheric wind variability, but the deseasoned wind reveals a warming impact in terms of westerly and southerly forcing around the PWD. The study of meridional circulation in the middle atmosphere is important to understand the spatio-temporal and altitudinal distribution of temperature, angular momentum of airmass, and chemical constituents (Garcia, 1987) during such warming events. Overall, the zonal mean flow in the middle atmosphere is found to be affected significantly during the SH SSW.

The associated zonal variability in the horizontal wind flow in the

middle atmosphere during different phases of the 2002 and 2019 SH SSW are evident for U in Figs. 4–6 and, V in Figs. 7–9. The prominence of the zonal wavenumber 2 component in the mid stratospheric horizontal wind (Figs. 4e and 7e) during the 2002 W at mid latitudes is possibly linked with the split of polar vortex observed by Charlton et al. (2005). The westerly forcing is apparent from the deseasoned variability during the 2002 and 2019 W phases (Fig. 4g and h). However, such characteristics are not uniform at all longitudes over the globe, further signifying the asymmetry in the longitudinal variability due to such warming impact. Interestingly, a clear enhancement in the upper mesospheric U is observed during the 2019 W (Fig. 6f) and post-W phases (Fig. 6j) at mid latitudes within the longitudinal range 60° E and 120° E. The same feature remains intact upon removing the SMS (Fig. 6h and i) indicating prominent role of SSW on the enhancement structure of U. Moreover, striking similarity in U and V at 0.01 hPa during the W and post-W phases indicates the prolonged/sustained impact of the SSW on the upper mesosphere. The apparent longitudinal interchange of the peak V between pre-W and other 2 phases at high latitude in the upper mesosphere, especially in 2019 indicates significant shift of the meridional flow structure across the globe driven by the forcing due to the warming.

Also, the split feature as observed in the mid-stratosphere (10 hPa) U during the 2002 W (Fig. 4e) is not found to extend to the upper stratosphere (Fig. 5e) and above (Fig. 6e). Overall, the upper stratospheric and mesospheric changes during both events (major and minor) do not necessarily correspond to changes in the mid-stratosphere. In this context, Smith et al., (2020) also suggested the upper stratosphere and mesosphere changes that occur during SSWs are only weakly correlated with the stratospheric changes. The current study provides detailed description on the middle atmospheric circulation during two historically rare major (2002) and minor (2019) SSWs from the SH in terms of zonal mean flow and concomitant zonal variability. The present study also reports notable differences in the dynamical conditions between the 2002 and 2019 SH SSWs. In this context it can be mentioned that, significant event-to-event variability in the case of the NH SSWs was mentioned in the past studies (Zülicke and Becker, 2013; Zülicke et al., 2018). As mentioned earlier, the SH SSW occurs around the spring equinox. The variability during the late winter to early spring period is primarily due to seasonal transition controlled by solar radiative process and wave driven dynamical process. The current study is important as it attempts to assess the weak/fine-scale signatures of the SSW in the middle atmosphere on isolating the seasonal as well as interannual effects.

5. Summary and conclusions

The present study portrays a comparative study on the characteristics of the middle atmospheric circulation during two rare SH SSWs in September 2002 and 2019 which remained unexplored so far. Since the SH SSW occurs around the spring equinox, an attempt is made to remove the seasonal contribution to delineate the effects on the global circulation solely due to the warming event. A detailed and comparative study on the variability of the actual and deseasoned parameters during the warming is presented. The weak features due to influence of SSW to lower altitudes seems evident from the deseasoned flow in terms of prominent easterly forcing around the PWD of both events. Also from the deseasoned variability, the zonal mean easterly forcing is observed early in the stratosphere in extratropical latitudes and progress towards mid and high latitudes around the PWD indicating a possible tropical precursor to the southern SSW. The seasonal transition feature is dominant in the upper mesosphere but the deseasoned winds reveal warming impact in terms of easterly and southerly (equatorward) forcing around the PWD. Striking similarity in the latitude-longitude variability of the U and V during the W and post-W phases signifies sustained impact of the warming on the upper mesosphere. Significant influence of the 2019 minor SSW seems to cause a shift in the meridional circulation structure across the globe as evident from the appearance of

the longitudinal interchange of the upper mesospheric peak V at high latitude between pre-W and other two phases. Overall, the current study provides important insights into the SH middle atmospheric flow perturbation due to the rare SSW by comparing major and minor events.

CRedit authorship contribution statement

G. Mitra: Conceptualization, Formal analysis, Investigation, Methodology, Writing – original draft, Writing – review & editing. **A. Guharay:** Conceptualization, Methodology, Supervision, Writing – review & editing.

Declaration of competing interest

The authors declare that they have no known competing financial interests or personal relationships that could have appeared to influence the work reported in this paper.

Data availability

No data was used for the research described in the article.

Acknowledgements

The present work is supported by the Department of Space (Government of India). Authors would like to thank the MERRA-2 team for providing the access to the database available at <https://gmao.gsfc.nasa.gov/reanalysis/MERRA-2/>. Authors would like to thank the reviewers for useful comments.

Appendix A. Supplementary data

Supplementary data to this article can be found online at <https://doi.org/10.1016/j.jastp.2024.106173>.

References

- Andrews, D.G., Holton, J.R., Leovy, C.B., 1987. *Middle Atmosphere Dynamics* (No. 40). Academic press.
- Butler, A.H., Seidel, D.J., Hardiman, S.C., Butchart, N., Birner, T., Match, A., 2015. Defining sudden stratospheric warmings. *Bull. Amer. Meteor.* 96 (11), 1913–1928. <https://doi.org/10.1175/BAMS-D-13-00173.1>.
- Charlton, A.J., O'Neill, A., Lahoz, W.A., Berrisford, P., 2005. The splitting of the stratospheric polar vortex in the Southern Hemisphere, September 2002: dynamical evolution. *J. Atmos. Sci.* 62 (3), 590–602. <https://doi.org/10.1175/JAS-3318.1>.
- Charlton, A.J., Polvani, L.M., 2007. A new look at stratospheric sudden warmings. Part I: climatology and modeling benchmarks. *J. Clim.* 20 (3), 449–469. <https://doi.org/10.1175/JCLI3996.1>.
- Eguchi, N., Kodera, K., 2007. Impact of the 2002, Southern Hemisphere, stratospheric warming on the tropical cirrus clouds and convective activity. *Geophys. Res. Lett.* 34, L05819 <https://doi.org/10.1029/2006GL028744>.
- Garcia, R.R., 1987. On the mean meridional circulation of the middle atmosphere. *J. Atmos. Sci.* 44 (24), 3599–3609. [https://doi.org/10.1175/1520-0469\(1987\)044<3599:OTMMCO>2.0.CO;2](https://doi.org/10.1175/1520-0469(1987)044<3599:OTMMCO>2.0.CO;2).
- Gelaro, R., McCarty, W., Suárez, M.J., Todling, R., Molod, A., Takacs, L., et al., 2017. The modern-era retrospective analysis for research and applications, version 2 (MERRA-2). *J. Clim.* 30 (14), 5419–5454. <https://doi.org/10.1175/JCLI-D-16-0758.1>.
- Guharay, A., Batista, P.P., Clemesha, B.R., Sarkhel, S., 2014. Response of the extratropical middle atmosphere to the September 2002 major stratospheric sudden warming. *Adv. Space Res.* 53 (2), 257–265. <https://doi.org/10.1016/j.asr.2013.11.002>.
- Guharay, A., Batista, P.P., 2019. On the variability of tides during a major stratospheric sudden warming in September 2002 at Southern hemispheric extra-tropical latitude. *Adv. Space Res.* 63 (8), 2337–2344. <https://doi.org/10.1016/j.asr.2018.12.037>.
- He, M., Chau, J.L., Forbes, J.M., Thorsen, D., Li, G., Siddiqui, T.A., et al., 2020. Quasi-10-day wave and semidiurnal tide nonlinear interactions during the Southern Hemisphere SSW 2019 observed in the Northern Hemispheric mesosphere. *Geophys. Res. Lett.* 47 (23), e2020GL091453 <https://doi.org/10.1029/2020GL091453>.
- Koushik, N., Kumar, K.K., Pramitha, M., 2022. A tropical stratopause precursor for sudden stratospheric warmings. *Sci. Rep.* 12 (1), 2937. <https://doi.org/10.1038/s41598-022-06864-7>.
- Laskar, F.I., McCormack, J.P., Chau, J.L., Pallamraju, D., Hoffmann, P., Singh, R.P., 2019. Interhemispheric meridional circulation during sudden stratospheric

- warming. *J. Geophys. Res. Space Phys.* 124 (8), 7112–7122. <https://doi.org/10.1029/2018JA026424>.
- Labitzke, K., Naujokat, B., Kunze, M., 2005. The lower Arctic stratosphere in winter since 1952: an update. *Sparc Newsletter* 24, 27–28.
- Liu, G., Hirooka, T., Eguchi, N., Krüger, K., 2022. Dynamical evolution of a minor sudden stratospheric warming in the Southern Hemisphere in 2019. *Atmos. Chem. Phys.* 22 (5), 3493–3505. <https://doi.org/10.5194/acp-22-3493-2022>.
- Matsuno, T., 1971. A dynamical model of the stratospheric sudden warming. *J. Atmos. Sci.* 28 (8), 14792–21494. [https://doi.org/10.1175/1520-0469\(1971\)028<1479:ADMOTS>2.0](https://doi.org/10.1175/1520-0469(1971)028<1479:ADMOTS>2.0).
- Maury, P., Claud, C., Manzini, E., Hauchecorne, A., Keckhut, P., 2016. Characteristics of stratospheric warming events during Northern winter. *J. Geophys. Res. Atmos.* 121 (10), 5368–5380. <https://doi.org/10.1002/2015JD024226>.
- Mitra, G., Guharay, A., Batista, P.P., Buriti, R.A., 2022. Impact of the september 2019 minor sudden stratospheric warming on the low-latitude middle atmospheric planetary wave dynamics. *J. Geophys. Res. Atmos.* 127 (1), e2021JD035538 <https://doi.org/10.1029/2021JD035538>.
- Mitra, G., Guharay, A., Batista, P.P., Buriti, R.A., Moffat-Griffin, T., 2023. Investigation on the MLT tidal variability during September 2019 minor sudden stratospheric warming. *Adv. Space Res.* 71 (1), 869–882. <https://doi.org/10.1016/j.asr.2022.08.017>.
- Newman, P.A., Nash, E.R., 2005. The unusual Southern Hemisphere stratosphere winter of 2002. *J. Atmos. Sci.* 62 (3), 614–628. <https://doi.org/10.1175/JAS-3323.1>.
- Noguchi, S., Kuroda, Y., Kodera, K., Watanabe, S., 2020. Robust enhancement of tropical convective activity by the 2019 Antarctic sudden stratospheric warming. *Geophys. Res. Lett.* 47 (15) e2020GL088743. <https://doi.org/10.1029/2020GL088743>.
- Pedatella, N., Chau, J., Schmidt, H., Goncharenko, L., Stolle, C., Hocke, K., et al., 2018. How sudden stratospheric warmings affect the whole atmosphere. *Eos* 99. <https://doi.org/10.1029/2018EO092441>.
- Pedatella, N.M., Liu, H.L., Conte, J.F., Chau, J.L., Hall, C., Jacobi, C., et al., 2021. Migrating semidiurnal tide during the September equinox transition in the Northern Hemisphere. *J. Geophys. Res. Atmos.* 126 (3) <https://doi.org/10.1029/2020JD033822> e2020JD033822.
- Rao, J., Garfinkel, C.I., White, I.P., Schwartz, C., 2020. The Southern Hemisphere minor sudden stratospheric warming in September 2019 and its predictions in S2S models. *J. Geophys. Res. Atmos.* 125 (14) <https://doi.org/10.1029/2020JD032723> e2020JD032723.
- Rao, J., Garfinkel, C.I., 2021. Projected changes of stratospheric final warmings in the Northern and Southern Hemispheres by CMIP5/6 models. *Clim. Dynam.* 56 (9–10), 3353–3371. <https://doi.org/10.1007/s00382-021-05647-6>.
- Smith, A.K., Pedatella, N.M., Mullen, Z.K., 2020. Interhemispheric coupling mechanisms in the middle atmosphere of WACCM6. *J. Atmos. Sci.* 77 (3), 1101–1118. <https://doi.org/10.1175/JAS-D-19-0253.1>.
- Varotsos, C., 2002. The southern hemisphere ozone hole split in 2002. *Environ. Sci. Pollut. Control Ser.* 9, 375–376. <https://doi.org/10.1007/BF02987584>.
- Varotsos, C., 2004. The extraordinary events of the major, sudden stratospheric warming, the diminutive Antarctic ozone hole, and its split in 2002. *Environ. Sci. Pollut. Control Ser.* 11, 405–411. <https://doi.org/10.1007/BF02979661>.
- Veenus, V., Das, S.S., 2023. Role of southern hemisphere sudden stratospheric warming in altering the intensity of brewer-dobson circulation and its impact on stratospheric ozone and water vapor. *Advances in Space Research.* <https://doi.org/10.1016/j.asr.2023.12.012>.
- Vincent, R.A., Kovalam, S., Reid, I.M., Murphy, D.J., Klekociuk, A., 2022. Southern hemisphere stratospheric warmings and coupling to the mesosphere-lower thermosphere. *J. Geophys. Res. Atmos.* 127 (15), e2022JD036558 <https://doi.org/10.1029/2022JD036558>.
- Yamazaki, Y., Matthias, V., Miyoshi, Y., Stolle, C., Siddiqui, T., Kervalishvili, G., et al., 2020. September 2019 Antarctic sudden stratospheric warming: quasi-6-day wave burst and ionospheric effects. *Geophys. Res. Lett.* 47 (1), e2019GL086577 <https://doi.org/10.1029/2019GL086577>.
- Zülicke, C., Becker, E., 2013. The structure of the mesosphere during sudden stratospheric warmings in a global circulation model. *J. Geophys. Res. Atmos.* 118 (5), 2255–2271. <https://doi.org/10.1002/jgrd.50219>.
- Zülicke, C., Becker, E., Matthias, V., Peters, D.H., Schmidt, H., Liu, H.L., et al., 2018. Coupling of stratospheric warmings with mesospheric coolings in observations and simulations. *J. Clim.* 31 (3), 1107–1133. <https://doi.org/10.1175/JCLI-D-17-0047.1>.



OPEN

Signature of a zonally symmetric semidiurnal tide during major sudden stratospheric warmings and plausible mechanisms: a case study

G. Mitra^{1,2}, A. Guharay¹ & I. Paulino³✉

Sudden Stratospheric Warming (SSW) is a winter phenomenon initiated primarily by the enhanced stationary planetary waves (SPWs), characterized by an increase in polar stratospheric temperature by a few tens of kelvin for a few days. Wave-wave non-linear interaction can produce secondary waves, with sum and difference frequencies of the primary wave frequencies. The sun-synchronous semidiurnal tide is a major component at mid and high latitude middle atmosphere, which non-linearly interacts with the dominant SPW in the stratosphere to produce the zonally symmetric semidiurnal tide component (S0), as observed during two boreal SSWs. The zonally symmetric distribution of ozone has also potential to excite the S0 component by absorption of solar ultraviolet radiation as evident during a rare Austral SSW. Overall, the present study sheds light on the dominant generation mechanisms involved in the S0 enhancement during the SSW.

Sudden Stratospheric Warmings (SSWs) are meteorological phenomena driven by enhanced planetary wave (PW) activity in winter, in which the polar stratospheric temperature increases considerably by a few tens of Kelvin¹. Such an extreme event can have far-reaching effects on the Earth's atmosphere, from the troposphere to the thermosphere and across both the hemispheres². The predominantly active stationary planetary waves (SPW) in the winter stratosphere are crucial in preconditioning the SSW^{3–5}. The interaction between SPW1 (zonal wavenumber 1) or SPW2 and the polar vortex can lead to displacement or split of the polar vortex⁶.

Atmospheric thermal tides are global-scale oscillations with periods of subharmonics of a solar day, such as 24 h (diurnal tide), 12 h (semidiurnal tide (ST)), 8 h (terdiurnal tide), 6 h (quarterdiurnal tide) and so on⁷. They can be further classified into migrating and non-migrating tides. Migrating tides, which travel westward in synchronization with the sun, are generated from the absorption of solar insolation by water molecules in the troposphere, ozone in the stratosphere, and N₂ and O₂ in the thermosphere. In contrast, non-migrating tides, which are non-sun-synchronous (traveling eastward, westward, or maintaining zonal symmetry), result from the absorption of solar insolation due to the non-uniform distribution of these absorbing species, the release of latent heat through tropical convection, tide-tide non-linear interaction and the non-linear interaction between tides and PWs^{8–12}. Although there exist studies on long-term and seasonal variability of migrating and non-migrating tides and the impact of the same on the ionosphere^{13–16}, there are relatively fewer studies and limited understanding on tidal variability during SSW. Past studies reported significant variability in thermal tides during SSW in the mesosphere and lower thermosphere (MLT) in the NH^{17–19} as well as observations from the SH^{20,21}. Previously, Pedatella & Forbes²² reported evidence of coupling between SSWs and the ionosphere via non-migrating tides generated by the non-linear interaction between planetary waves and the migrating semidiurnal tide. Overall, there is still a lack of adequate studies on the generation mechanism of specific tidal components during such an impactful transient event.

In this connection, the present work is the first exclusive observational case study on the zonally symmetric ST component (S0), with plausible generation mechanisms during three major SSWs. This study examines all the

¹Space and Atmospheric Sciences Division, Physical Research Laboratory, Ahmedabad, GJ, India. ²Department of Physics, Indian Institute of Technology, Gandhinagar, GJ, India. ³Unidade Acadêmica de Física, Universidade Federal de Campina Grande, Avenida Aprígio Veloso, 882 Bloco CY2, 58429900 Campina Grande, PB, Brazil. ✉email: igo.paulino@df.ufcg.edu.br

SSW events in the last two decades to find out the signature of S0 and finally concentrates on two events of the northern hemisphere (NH) winter, i.e., 2008–2009 and 2012–2013, and an event from the southern hemisphere (SH), i.e., September 2002, where the signature of the S0 enhancement can be explained in the light of probable excitation mechanisms. It should be mentioned that the S0 signatures are also found in some other years (Fig. 1) although their source mechanisms remain elusive as per present understanding. However, the present study is important as it attempts to investigate the least explored feature of S0 and probable generation mechanisms for the first time. The paper is divided into four sections. Section "Dataset and methodology" discusses the dataset and methodology used in the present study. Section "Enhancement in S0 during SSW" describes the S0 enhancement observed during SSW. Section "S0 component in Ozone variability" depicts the total ozone variability.

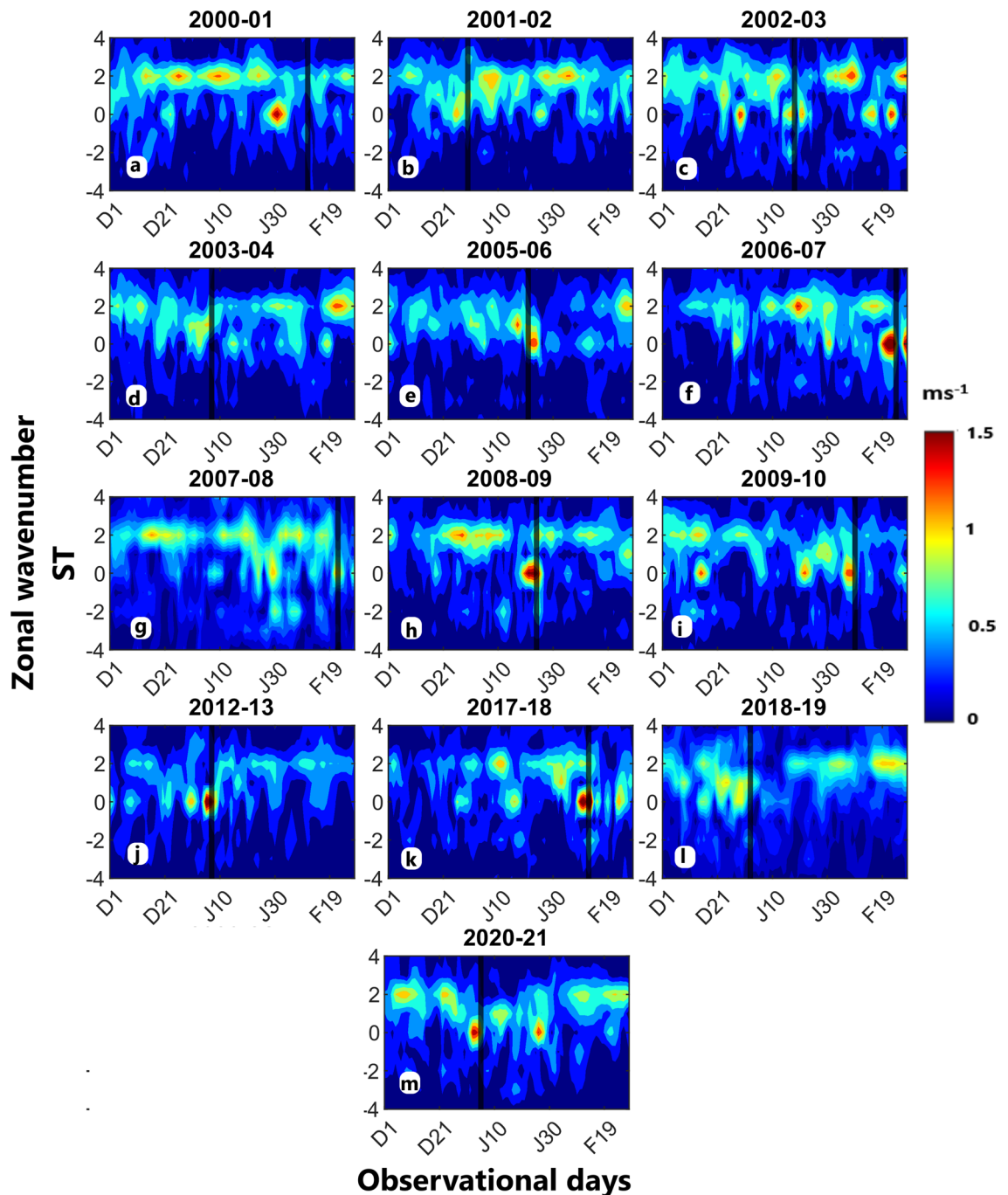


Fig. 1. Variability in the semidiurnal tide (ST) components in the stratosphere during major SSW. Temporal variability of different ZWN components of ST utilizing U at 10 hPa, 70°N from MERRA 2 during (a) 2000–2001, (b) 2001–2002, (c) 2002–2003, (d) 2003–2004, (e) 2005–2006, (f) 2006–2007, (g) 2007–2008, (h) 2008–2009, (i) 2009–2010, (j) 2012–2013, (k) 2017–2018, (l) 2018–2019, and (m) 2020–2021 observational days (December 1–February 28). The solid vertical line represents the peak warming day. The letters D, J, F on the x axis denote December, January, and February; the subsequent number indicates the day of the given month.

Section "Vertical profile of S0 at maximum" discusses the vertical profile of S0 on peak amplitude days. Section "Summary and Conclusions" summarizes and concludes the result.

Dataset and methodology

We employ a longitudinally spread contemporaneous data set from the Modern-Era Retrospective Analysis for Research and Applications, version 2 (MERRA-2) for zonal wavenumber (ZWN) diagnosis²³. This dataset includes 3 hourly zonal wind (U) values at 72 model pressure levels from 985 to 0.01 hPa, corresponding to approximately 0–75 km altitude, and is organized on a $2.5^\circ \times 2.5^\circ$ latitude–longitude grid. Furthermore, the suitability of MERRA-2 for studying tides and PW in the middle atmosphere was demonstrated in the SPARC Reanalysis Intercomparison Project (SRIP) Final Report²⁴.

Additionally, we utilize the hourly total columnar ozone (TCO) data (single level) provided by MERRA-2 for our current purpose. The MERRA2 dataset incorporates ozone information obtained by assimilating partial columns and total ozone measurements. These measurements are derived from a series of Solar Backscatter Ultraviolet (SBUV) instruments deployed on different platforms by the National Oceanic and Atmospheric Administration (NOAA)²⁵. Beginning in October 2004, the SBUV data was replaced by a combination of TCO data from the Aura Ozone Monitoring Instrument (OMI)²⁶, and stratospheric ozone profiles from the Aura Microwave Limb Sounder (MLS)²⁷. Moreover, Davis et al.²⁸ evaluated the accuracy of TCO in MERRA2 against both assimilated and independent observations and demonstrated the suitability in TCO variability studies, as reported in the SRIP. Bahramvash Shams et al.²⁹ validated the TCO data from MERRA2 against independent observations from ozonesondes and Fourier Transform Infrared (FTIR) retrievals. Further, they encouraged the usage of the same at high latitudes during highly disturbed dynamical events such as SSW.

The amplitude of a wave with zonal wavenumber s and period T can be estimated by a non-linear least-square fitting to 2-dimensional space–time MERRA-2 U data using the following equation.

$$A \cos \left[2\pi \left(\frac{t}{T} + \frac{s\lambda}{360} \right) - \varphi \right] \quad (1)$$

where A is the amplitude of the wave, t is the universal time, λ is the longitude, and φ is the phase of the wave³⁰. The positive, negative, and zero s values correspond to westward, eastward propagating, and zonally symmetric waves, respectively. For tides, $T = \frac{24}{n}$; where $n = 1, 2$ denotes diurnal and semidiurnal component. For SPW, $\frac{1}{T} = 0$.

The time interval spans from 1 December to 28 February and 1 August to 31 October, centered around the NH and SH SSW, respectively. The SSW peak warming day (PWD) is when the maximum temperature gradient occurs between 90° and 60° N/S at 10 hPa. This date typically aligns with the initial wind reversal at 10 hPa, 60° N/S during each major event³¹. It is important to note that, in our current study, we use the PWD solely to determine the start of the SSW, and any ambiguities in the definitions of SSW onsets³² do not affect our discussions.

Results and discussions

Enhancement in S0 during SSW

Figure 1 illustrates the variability in amplitudes of different dominant ZWN components (-4 to $+4$) of the semidiurnal tide (ST) during SSW years since 2000 at 10 hPa (~ 30 km altitude) and 70° N. The analysis includes all the major SSWs between 2000 and 2021, where the PWD falls within the observational interval (1 December to 28 February).

The migrating semidiurnal tide (westward-traveling) corresponding to ZWN 2, i.e., the SW2 shows dominant and consistent features during the observational interval, as observed in most SSW years. A notable observation is the short-term and sporadic enhancement in the zonally symmetric ST component corresponding to ZWN 0, i.e., the S0, particularly around the PWD in several SSW years, such as 2001–02, 2003–04, 2005–06, 2006–07, 2008–09, 2012–13, 2017–18, and 2020–21. The PWD of respective SSW years are marked by the vertical solid lines in Fig. 1. It is interesting to note that the S0 enhancement appears to coincide with a decrease in SW2 indicating a plausible relationship between SW2 and S0. Therefore, based on such finding, we can guess a probable generation mechanism of the S0 in connection with the SW2, which may primarily indicate a nonlinear interaction between SW2 and stationary planetary wave 2 (SPW2) for its excitation. Next, based on the common intuition, another potential mechanism to excite the S0 may be the variability of the source of the semidiurnal tide, i.e., ozone. In the following part of the manuscript, we will discuss the S0 excitation sources in the light of these two probable generation mechanisms.

In view of the above discussion, only the SSW events of 2008–09, 2012–13 in the NH, and 2002 in the SH are investigated in detail because the S0 enhancement can be clearly explained by the the most probable mechanisms for these cases. The remaining S0 enhancement events cannot be explained by means of plausible mechanisms at present (please see the "summary and conclusions" section for details). 23 January 2009, 6 January 2013, and 26 September 2002 are the PWDs marked by the vertical solid lines in all the figures.

Now, we concentrate on the three selected events where any of the two mechanisms, as discussed before, can be responsible for the amplification of the S0. Figure 2a represents the temporal variability of different ZWN (-4 to $+4$) components of the ST during the 2008–09 observational days at 70° N, 10 hPa. The SW2 amplitude, shows sustained features but diminishes considerably for a few days around the PWD, with a concurrent short-term enhancement of the S0 component. Interestingly, the S0 amplitude exceeds the usually dominant SW2 amplitude. The temporal variability of different ZWN (1 to 4) components corresponding to SPW at 70° N, 10 hPa is shown in Fig. 2b. SPW corresponding to ZWN1, i.e., the SPW1 seems to be active during the prewarming days, followed by a short-term substantial enhancement of SPW2 around the PWD. Simultaneous enhancement of S0 and SPW2 may indicate a possible non-linear interaction between the SPW2 and SW2 primary waves, producing S0 as one

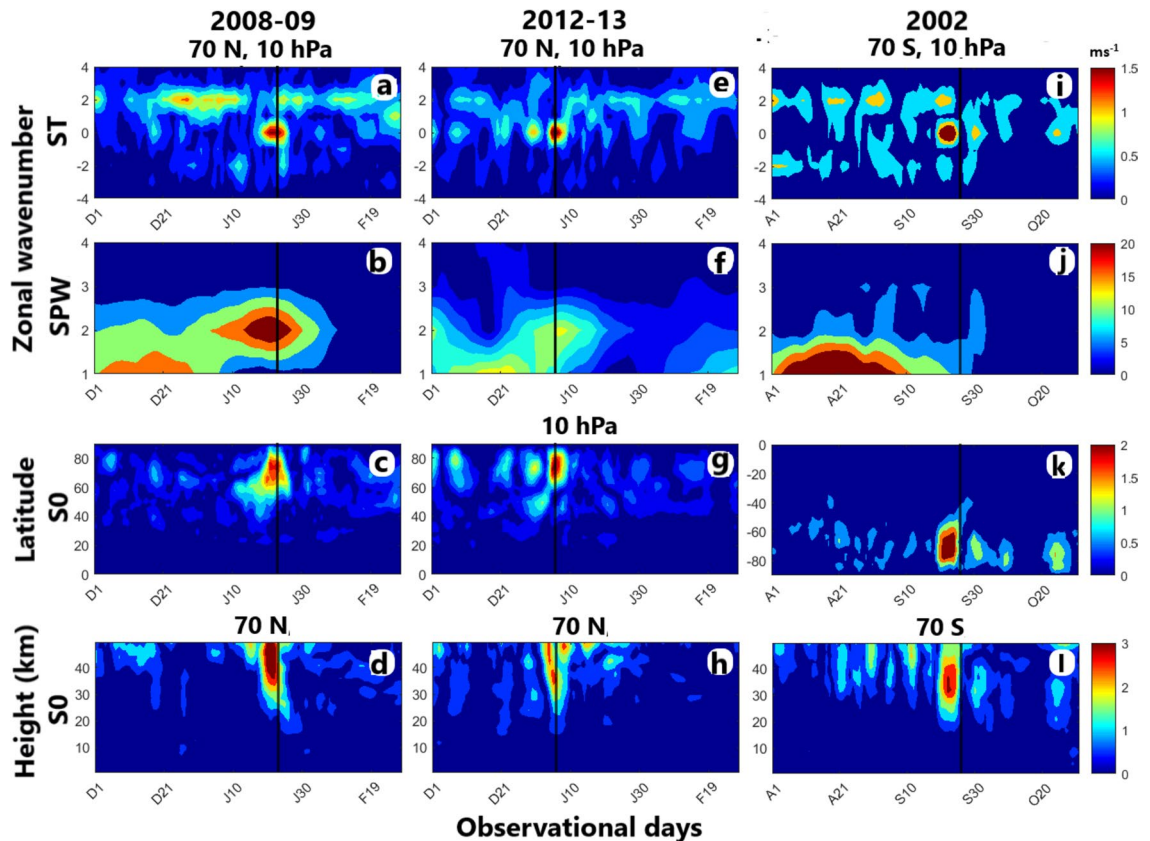


Fig. 2. Enhancement in S0 during SSW. Temporal variability of different ZWN components of (a) ST, (b) SPW utilizing U at 10 hPa, 70°N from MERRA 2 during 2008–2009 observational days (December 1–February 28). (c) Latitude profile at 10 hPa of S0. (d) Altitude profile at 70°N of S0. (e–h) The same as (a–d), but during 2012–2013. (i–l) The same as (a–d), but during 2002 (August 1–October 31). The solid vertical line represents the peak warming day. Please note the change of scale in the colorbars corresponding to each subplot while comparing. The letters D, J, F, and A, S, O on the x axis denote December, January, February, and August, September, October; the subsequent number indicates the day of the given month.

of the secondary waves. Mathematically, a non-linear interaction (in terms of frequency (hour^{-1}) /ZWN pair) between SPW2 (0, 2) and SW2 ($\frac{1}{12}$, 2) yields zonally symmetric S0 ($\frac{1}{12}$, 0) and SW4 ($\frac{1}{12}$, 4) as secondary waves³³. However, the SW4 amplitude seems too weak to be identified. In this context, Teitelbaum and Vial (1991)³³ mentioned that one of the secondary waves produced due to non-linear interaction may have a weak amplitude. As compared to the other, the small amplitude of one of the secondary waves is possibly due to energy redistribution and dissipation³⁴. Figure 2c exhibits the latitude profile of S0 variability at 10 hPa during the observational days. The S0 is found to enhance in the latitude band 60–80° N around the PWD. Further, the altitude profile of S0 temporal variability at 70° N (Fig. 2d) reveals enhancement in the mid and upper stratosphere during the warming period. Please note that the tidal amplitudes (e.g., S0, SW2) and SPW amplitudes (e.g., SPW1, SPW2) are statistically significant and lie within the 95% confidence interval.

Similarly, variability of the same parameters during the 2012–13 warming event has been shown in Figs. 2e–h. It is interesting to note very similar features during the 2012–13 SSW. The decrease in SW2 amplitude and simultaneous increase in S0 amplitude around the PWD indicates significant energy transfer from the former to the latter. However, a relatively larger S0 component than the SW2 component implies that the SW2 is not the sole energy supplier to the S0. In this context, it is worth mentioning that while migrating tides typically prevail in the middle atmosphere, non-migrating tides can occasionally reach comparable magnitude and even surpass the migrating tides³⁵. The source of additional energy can be attributed to the most dominant SPW2 component. Therefore, both the primary waves are believed to supply energy to the S0. Overall, the enhanced S0 component during the two NH major SSW can be attributed to the non-linear interaction between the SW2 and SPW2.

Figure 2i–l represent the same as Fig. 2a–d but during the 2002 SH major SSW. Enhancement in the S0 is noticeable around the PWD at 70° S, 10 hPa (Fig. 2i). However, S0 enhancement is not simultaneous with the SW2 decrement and doesn't coincide with contemporaneous SPW2 activity, which seems to be masked by the much stronger SPW1 during the prewarming days (Fig. 2j). Such occurrence rules out the role of the non-linear interaction in the generation of the S0 unlike the previous cases. Moreover, the S0 enhancement seems confined within the latitude band 60–80° S in the middle and upper stratosphere, as seen from the corresponding latitude (Fig. 2k) and altitude (Fig. 2l) profiles. Such an interesting observation eliminates the role of non-linear interaction and necessitates the quest for other plausible factors, such as variability in source species for this event.

Overall, the S0 seems to be the most dominant ST component, with an amplitude of about 3 ms^{-1} in the middle and upper stratosphere during all the selected major SSWs.

S0 component in Ozone variability

Since no evident signature of non-linear interaction is found during 2002 SSW, behavior of the ozone is examined to understand its role (if any) in generating the S0 component for all the events. Figure 3a, c, and e represent the latitude distribution of zonal mean TCO during the 2008–09, 2012–13, and 2002 observational days. The seasonal transition can be clearly identified in 2008–09 and 2012–13, as shown in Fig. 3a and c, with a temporal increase in TCO during winter. This is followed by a maximum in spring and decreasing values from summer to autumn in the NH (Figure S1 in Supporting Information S1). However, the abrupt increase in the TCO soon after the PWD at high latitude may be ascribed to the weakened vortex driven by dissipating PW and subsequent enhanced poleward transport of ozone from the mid-latitude owing to such large-scale disturbances, which may persist up to 2 months, as mentioned in the previous studies^{29,36}. It is interesting to note that the maximum TCO is observed between 45° and 60° S in 2002 (Fig. 3e), unlike the other two NH events, where TCO exhibits maximum at latitudes poleward of about 45° N. This may be attributed to weaker poleward transport of ozone in the SH due to relatively less PW activity and a stronger polar vortex than in the NH. On the contrary, there is a poleward transport of ozone-rich air from mid-latitudes around the PWD of the 2002 SH SSW due to strong polar disturbances, as seen in Fig. 3e. Previous studies on TCO during the 2002 austral SSW event attributed such an increased poleward ozone flux to enhanced tropospheric wave activity^{37–39}. Next, we attempt to find out the characteristics of S0 in the TCO variability in order to understand a plausible role of ozone in exciting the observed S0 in the selected SSW events.

Figure 3b, d, and f represent the latitude profile of S0 in TCO during 2008–09, 2012–13, and 2002 observational days. It is interesting to note that the S0 in TCO is prominent around the PWD of the 2002 SSW (Fig. 3f), unlike the other two events. The noticeable S0 in the TCO is concurrent with the S0 enhancement in U around the 2002 PWD. This indicates the plausible role of ozone in thermally forcing the S0 tidal component during the 2002 SSW. It can be noted that the peak amplitude of the S0 in the TCO is found between 70° S and 90° S, and the same in the U is observed between 60° S and 80° S. To understand the finite difference in the observed peak latitudes of the S0 in the TCO and U we have looked into the latitudinal profile of the zonal mean U, amplitudes of the S0 in the TCO and U on 23 September 2002 when S0 amplitude maximizes (Figure S2 in Supporting Information S1). The peak S0 amplitude in the TCO is found near the pole followed by the same in the U and peak of the zonal mean U in a sequence from high to low latitude. Since the zonal mean U (a measure of zonally symmetric structure) bears some imprint of the zonally symmetric waves⁴⁰, the S0 in the U in the present case can be deemed to be impacted by the structure of the zonal mean U to some extent. Therefore, the appearance of the S0 in the U is not only determined by the source, i.e., ozone but also influenced by the zonal mean U. Reasonably, the peak S0 in the U can be expected to lie between the peak S0 in the TCO and peak zonal mean U resulting in a small

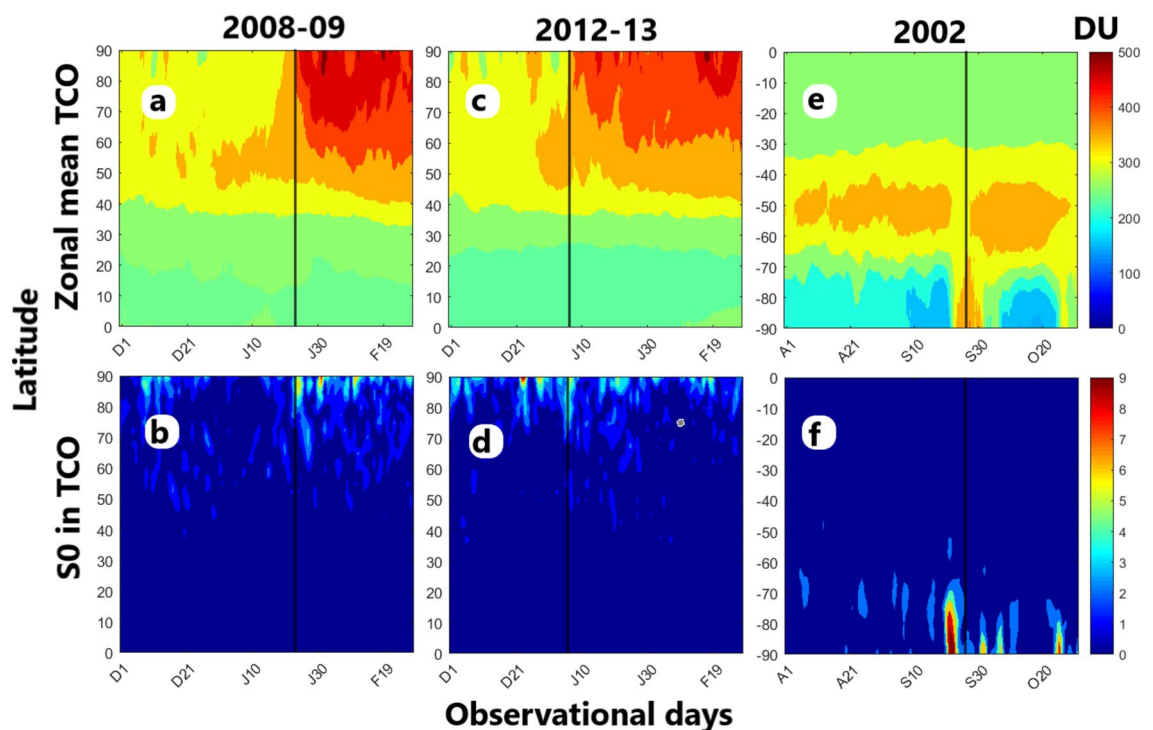


Fig. 3. Ozone variability during SSW. The latitude profile of (a) TCO and (b) S0 (in TCO) in Dobson unit (DU) during 2008–09 observational days from MERRA-2 data. (c, d) represent the same as (a, b) but during 2012–13. (e, f) represent the same as (a, b), but during 2002.

difference in latitudes of the S0 peaks in the TCO and U in the present case. In other words, the zonal mean U at a particular latitude, which is independent of longitude, represents a zonally symmetric structure that influences the location of the peak of the S0 amplitude in U in combination with the source structure (S0 in TCO). Therefore, the zonal mean U influences the latitudinal distribution of the S0 component in U in addition to the source (ozone). It is interesting to note the striking similarity of the S0 amplitude peak between TCO and U, further supporting their close relationship in this connection. Additionally, a secondary yet mild enhancement in the S0 tide is observed at the end of October 2002 (Fig. 2i, k, and l). This could be linked to the increased poleward transport of ozone (Fig. 3e) and the corresponding concurrent increase in S0 in TCO (Fig. 3f). The underlying reason for this second enhancement might be related to the delayed response of the 2002 SH SSW, similar to the 2019 SH SSW as noted by Yang et al.⁴¹. However, further future investigation is needed to confirm this.

The knowledge of spatial distribution and temporal variability of the stratospheric ozone is essential because it is an effective absorber of UV radiation, further altering the heating rate and temperature in the middle atmosphere⁴². In this context it is relevant to mention that the change of circulation associated with enhanced PW activity during SSW can alter the ozone distribution, generating non-migrating tides⁴³.

Therefore, the S0 enhancement during the 2002 SH major SSW is believed to be due to the absorption of the solar UV radiation by the ozone distributed symmetrically over the globe.

Vertical profile of S0 at maximum

The peak in the S0 amplitude for the three selected warming events is observed on 20 January 2009, 6 January 2013, and 23 September 2002, as shown in Fig. 2. In this section we consider only those two events where S0 is found to be generated due to non-linear interaction. Figure 4a and c represent the height-latitude section of S0 amplitude on 20 January 2009 and 6 January 2013, respectively. The S0 enhancement seems to be primarily confined at high latitude middle and upper stratosphere (20–50 km). The growth of S0 starts around 20–30 km altitude and attains a maximum amplitude ($3\text{--}4\text{ ms}^{-1}$) in the upper stratosphere. A similar height-latitude structure of the S0 amplitude is observed on 23 September 2002 (peak S0 amplitude day), as shown in Figure S3 in Supporting Information S1.

Figure 4b and d show the vertical phase for the SW2 (red curve), SPW2 (blue curve), and S0 (green curve) at 70° N on 20 January 2009 and 6 January 2013, respectively. Overall, the phase value decreases with height, indicating downward phase propagation and upward propagation of SW2, SPW2, and S0. Further, the vertical wavelength (λ) is calculated by linear least-square fits to the observed phases as a function of height⁴⁴.

λ is a function of slope (A), and the error in λ is calculated using uncertainty in A obtained from linear least square fit. The observed λ of SW2, SPW2, and S0 on 20 January, 2009, in the middle and upper stratosphere are $29.4 \pm 2.4\text{ km}$, $139.9 \pm 3.7\text{ km}$, and $36.0 \pm 2.8\text{ km}$, respectively. Similarly, on 6 January, 2013, the observed λ of SW2, SPW2, and S0 on 20 January, 2009, in the middle and upper stratosphere are $21.8 \pm 3.8\text{ km}$, $64.3 \pm 1.5\text{ km}$, and $34.2 \pm 3.0\text{ km}$, respectively.

Theoretically, due to non-linear interaction, the λ of S0 (λ_{S0}) is related to the same of primary waves (λ_{SW2} , λ_{SPW2}) as follows.

$$\frac{1}{\lambda_{S0}} = \frac{1}{\lambda_{SW2}} - \frac{1}{\lambda_{SPW2}} \quad (2)$$

The error in theoretical λ_{S0} is calculated from the error in the estimation of λ_{SW2} and λ_{SPW2} . The theoretical λ_{S0} estimated using Eq. (2), on 20 January, 2009, and 6 January, 2013, are $37.2 \pm 3.8\text{ km}$, and $32.9 \pm 8.8\text{ km}$, respectively. Interestingly, good agreement between the observed and theoretical λ_{S0} can be noted that further supports the proposition of non-linear interaction in generating S0 during the 2008–09 and 2012–13 SSW in the NH.

Summary and conclusions

The present study provides interesting insight into the S0 enhancement during SSW and the plausible generation mechanisms for some of the cases for the first time. The S0 amplitude is found to be active at mid and high latitude middle and upper stratosphere. The SW2 shows weak but sustained features during the observational intervals. However, it diminishes considerably around PWD of a few major SSWs (Fig. 1). The simultaneous enhancement of the SPW2 and S0 during the 2008–09 and 2012–13 NH SSW indicates a possible non-linear interaction between the primary waves, i.e., SPW2 and SW2, in producing the S0 as a secondary wave. The S0 amplitude even exceeds the SW2 amplitude. Moreover, the decrease in SW2 is contemporaneous with S0 enhancement, indicating a transfer of significant energy of SW2 to S0. The other primary wave, i.e., the SPW2, is also believed to feed energy to the S0. Additionally, good agreement between the theoretical and observed λ of S0, further corroborates the role of non-linear interaction between SW2 and SPW2 in producing the S0 during the 2008–09 and 2012–13 SSW.

Interestingly, the S0 excitation during the 2002 SSW seems to be linked with the zonally symmetric ozone distribution. This is supported by the significant poleward transport of ozone-rich air from mid-latitudes around the 2002 PWD, resulting in the S0 enhancement. The latitudinal structure of the zonal mean U seems to cause a finite shift of the peak S0 derived in the U towards lower latitude.

In a nutshell, the two most plausible generation mechanisms of S0 enhancement during the three selected SSW events are verified:

- i. The SW2 and SPW2 non-linearly interact and produce S0 as a secondary wave as found in the 2008–09 and 2012–13 warming events.

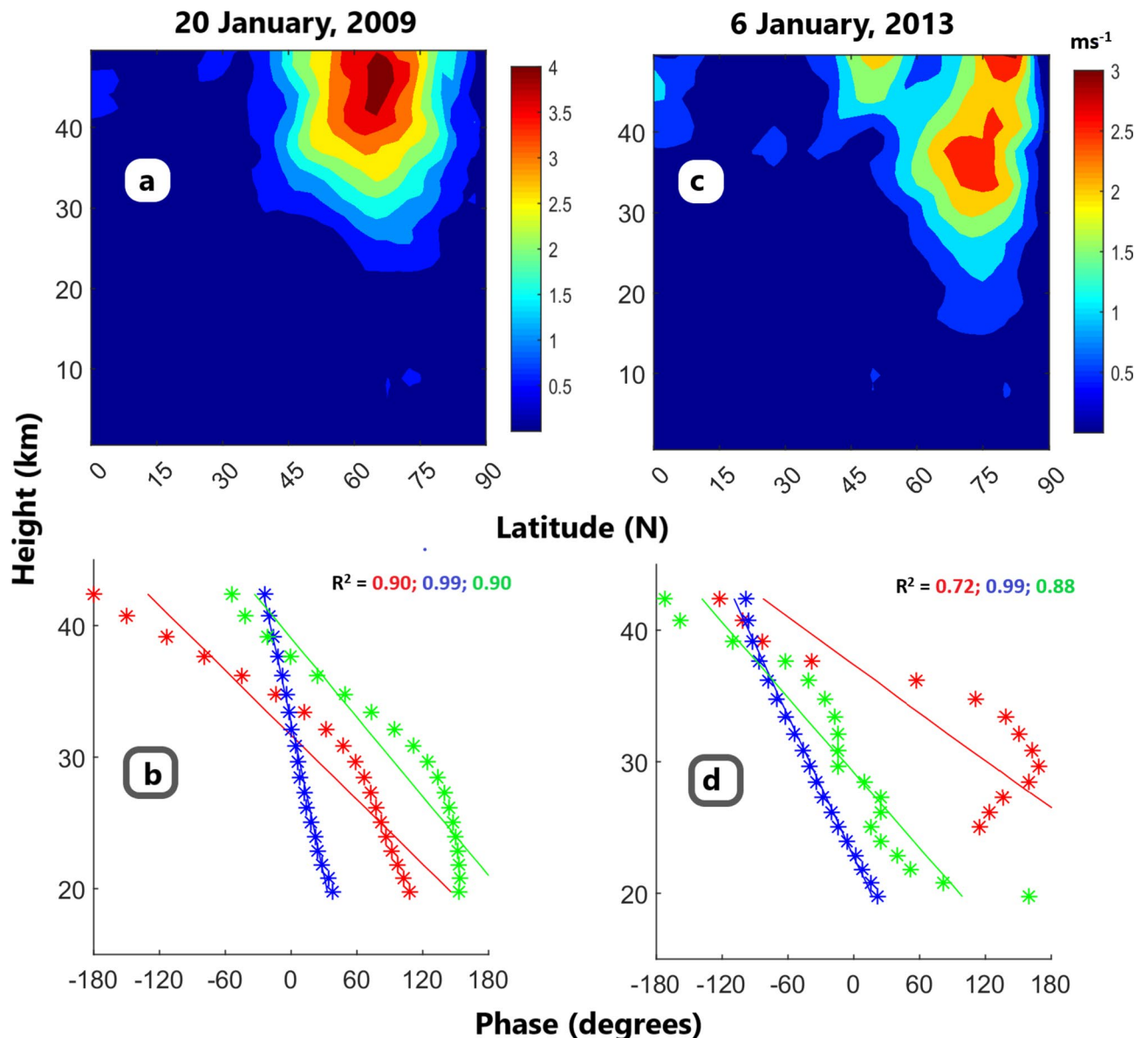


Fig. 4. Vertical profile of S0 at maximum. (a) Height-latitude section of S0 amplitude in ms^{-1} , and (b) variation in SW2 (red curve), SPW2 (blue curve), and S0 (green curve) phase as a function of height at 70° N on 20 January 2009. (c, d) represent the same as (a, b) but on 6 January 2013. The straight line in (b, d) represents the linear fit. Coefficient of determination R^2 , is highlighted with the same colour in plots b and d.

- ii. On the other hand, the S0 is believed to be thermally excited in presence of a zonally symmetric ozone distribution during the 2002 SSW.

However, based on the above findings we cannot reach to a general conclusion that nonlinear interaction play role in NH and ozone is responsible in SH for exciting the S0 as the present case study deals with merely three events. Any firm inference in this regard is only possible based on investigating a large number of events which may be pursued in future. The present study delves into the captivating cases of S0 enhancement using two decades of observations during the SSW in both hemispheres, accompanied by a discussion on the plausible generation mechanisms for the three prominent cases. However, the S0 signatures during other SSW years do not show any conspicuous link with the most probable generation mechanisms of S0 as discussed in the present study. In addition to the described specific interacting wave pairs, possible alternative generation mechanisms of S0 may involve non-linear interactions between (i) SPW1 and SW1/SE1, (ii) SPW2 and SE2, (iii) DW1 and DE1, (iv) DW2 and DE2. However, on carefully verifying the results of all the years, none of these primary wave pairs are found to exhibit their involvement in the nonlinear interactions precluding us to conclude on the excitation of the S0. Furthermore, the role of ozone is also not found in any SSW events except in 2002 (not shown). Then the important question arises in the mind about the actual mechanisms behind the unexplained S0 enhancements in other SSW years except the selected three events. At present we are not sure whether some

of the primary interacting waves are suppressed/undetected in the results due to some unknown reasons. All these concerns indicate the pressing need of future comprehensive investigations to unveil the unknown details of those unexplained events as those are beyond the scope of the present work. Nevertheless, the present study carries its importance as it is the first exclusive observational study on the amplification and plausible generation mechanism of the least explored S0 tide during major SSW.

Data availability

The MERRA-2 data set utilized in the current study is available at <https://gmao.gsfc.nasa.gov/reanalysis/MERRA-2/>.

Received: 15 May 2024; Accepted: 9 September 2024

Published online: 11 October 2024

References

- Matsuno, T. A dynamical model of the stratospheric sudden warming. *J. Atmos. Sci.* **28**(8), 14792–21494. [https://doi.org/10.1175/1520-0469\(1971\)028%3c1479:ADMOTS%3e2.0](https://doi.org/10.1175/1520-0469(1971)028%3c1479:ADMOTS%3e2.0) (1971).
- Pedatella, N. M., J. L. Chau, Hauke Schmidt, L. P. Goncharenko, Claudia Stolle, K. Hocke, V. L. Harvey, Bernd Funke, and T. A. Siddiqui. "How Sudden stratospheric warmings affect the whole atmosphere." <https://doi.org/10.1029/2018EO092441> (2018).
- Pancheva, D. V., Mukhtarov, P., Andonov, B., Mitchell, N. J. & Forbes, J. M. Planetary waves observed by TIMED/SABER in coupling the stratosphere–mesosphere–lower thermosphere during the winter of 2003/2004: Part 1—Comparison with the UKMO temperature results. *J. Atmos. Sol.-Terr. Phys.* **71**(1), 61–74. <https://doi.org/10.1016/j.jastp.2008.09.016> (2009).
- Guharay, A., Batista, P., Clemesha, B. & Sarkhel, S. Response of the extratropical middle atmosphere to the September 2002 major stratospheric sudden warming. *Adv. Space Res.* **53**(2), 257–265. <https://doi.org/10.1016/j.asr.2013.11.002> (2014).
- Mitra, G., Guharay, A., Batista, P. P. & Buriti, R. A. Impact of the September 2019 minor sudden stratospheric warming on the low-latitude middle atmospheric planetary wave dynamics. *J. Geophys. Res. Atmos.* **127**(1), e2021JD035538. <https://doi.org/10.1029/2021JD035538> (2022).
- Shepherd, T. G. The middle atmosphere. *J. Atmos. Sol.-Terr. Phys.* **62**(17–18), 1587–1601. [https://doi.org/10.1016/S1364-6826\(00\)00114-0](https://doi.org/10.1016/S1364-6826(00)00114-0) (2000).
- Chapman, S., & Lindzen, R. S. (1970). Atmospheric tides, 200 pp. D. Reidel, Norwell, Mass.
- Forbes, J. M. & Garrett, H. B. Thermal excitation of atmospheric tides due to insolation absorption by O₃ and H₂O. *Geophys. Res. Lett.* **5**(12), 1013–1016. <https://doi.org/10.1029/GL005i012p01013> (1978).
- Hagan, M. E. & Forbes, J. M. Migrating and non-migrating diurnal tides in the middle and upper atmosphere excited by tropospheric latent heat release. *J. Geophys. Res. Space Phys.* **107**(D24), 4754. <https://doi.org/10.1029/2001JD001236> (2002).
- Huang, C. M., Zhang, S. D. & Fan, Y. A numerical study on amplitude characteristics of the terdiurnal tide excited by non-linear interaction between the diurnal and semidiurnal tides. *Earth Planet Sp* **59**, 183–191. <https://doi.org/10.1186/BF03353094> (2007).
- Xu, J. *et al.* Evidence for non-migrating tides produced by the interaction between tides and stationary planetary waves in the stratosphere and lower mesosphere. *J. Geophys. Res. Atmos.* **119**, 471–489. <https://doi.org/10.1002/2013JD020150> (2014).
- Truskowski, A. O., Forbes, J. M., Zhang, X. & Palo, S. E. New perspectives on thermosphere tides: 1 Lower thermosphere spectra and seasonal-latitudinal structures. *Earth Planet Sp* **66**, 1–17. <https://doi.org/10.1186/s40623-014-0136-4> (2014).
- Ramesh, K. & Smith, A. K. Long-term variability and tendencies in non-migrating diurnal tide from WACCM6 simulations during 1850–2014. *J. Geophys. Res. Space Phys.* **126**, e2020JA028904. <https://doi.org/10.1029/2020JA028904> (2021).
- Sridharan, S. Seasonal variations of low-latitude migrating and non-migrating diurnal and semidiurnal tides in TIMED-SABER temperature and their relationship with source variations. *J. Geophys. Res. Space Phys.* **124**, 3558–3572. <https://doi.org/10.1029/2018JA026190> (2019).
- Immel, T. J. *et al.* Control of equatorial ionospheric morphology by atmospheric tides. *Geophys. Res. Lett.* <https://doi.org/10.1029/2006GL026161> (2006).
- Forbes, J. M. *et al.* Tidal variability in the ionospheric dynamo region. *J. Geophys. Res. Space Phys.* <https://doi.org/10.1029/2007JA012737> (2008).
- Chau, J. L., Hoffmann, P., Pedatella, N. M., Matthias, V. & Stober, G. Upper mesospheric lunar tides over middle and high latitudes during sudden stratospheric warming events. *J. Geophys. Res. Space Phys.* **120**(4), 3084–3096. <https://doi.org/10.1002/2015JA020998> (2015).
- Conte, J. F., Chau, J. L. & Peters, D. H. Middle-and high-latitude mesosphere and lower thermosphere mean winds and tides in response to strong polar-night jet oscillations. *J. Geophys. Res. Atmos.* **124**(16), 9262–9276. <https://doi.org/10.1029/2019JD030828> (2019).
- He, M. *et al.* High-order solar migrating tides quench at SSW onsets. *Geophys. Res. Lett.* **47**(6), e2019GL086778. <https://doi.org/10.1029/2019GL086778> (2020).
- Guharay, A. & Batista, P. P. On the variability of tides during a major stratospheric sudden warming in September 2002 at Southern Hemispheric extra-tropical latitude. *Adv. Space Res.* **63**(8), 2337–2344. <https://doi.org/10.1016/j.asr.2018.12.037> (2019).
- Mitra, G., Guharay, A., Batista, P. P., Buriti, R. A. & Moffat-Griffin, T. Investigation on the MLT tidal variability during September 2019 minor sudden stratospheric warming. *Adv. Space Res.* **71**(1), 869–882. <https://doi.org/10.1016/j.asr.2022.08.017> (2023).
- Pedatella, N. M. & Forbes, J. M. Evidence for stratosphere sudden warming-ionosphere coupling due to vertically propagating tides. *Geophys. Res. Lett.* <https://doi.org/10.1029/2010GL043560> (2010).
- Gelaro, R. *et al.* The modern-era retrospective analysis for research and applications, version 2 (MERRA-2). *J. Clim.* **30**(14), 5419–5454. <https://doi.org/10.1175/JCLI-D-16-0758.1> (2017).
- Harvey, V. L., Knox, J., France, J., Fujiwara, M., Gray, L., Hirooka, T., *et al.* Chapter 11: Upper stratosphere lower mesosphere. In M. Fujiwara, G. L. Manney, L. J. Gray, & J. S. Wright (Eds.) *SPARC reanalysis Intercomparison Project (S-RIP) final Report*. SPARC Report No. 10, WCRP-17/2020 (pp. 531–580). <https://doi.org/10.17874/800dee57d13> (2022).
- Flynn, L. E. *et al.* Measurements and products from the solar backscatter ultraviolet (SBUV/2) and ozone mapping and profiler suite (OMPS) instruments. *Int. J. Remote Sens.* **30**(15–16), 4259–4272. <https://doi.org/10.1080/01431160902825040> (2009).
- Levelt, P. F. *et al.* Science objectives of the ozone monitoring instrument. *IEEE Trans. Geosci. Remote Sens.* **44**(5), 1199–1208. <https://doi.org/10.1109/TGRS.2006.872336> (2006).
- Waters, J. W. *et al.* The earth observing system microwave limb sounder (EOS MLS) on the Aura satellite. *IEEE Trans. Geosci. Remote Sens.* **44**(5), 1075–1092. <https://doi.org/10.1109/TGRS.2006.873771> (2006).
- Davis, S. M., Hegglin, M. I., Dragani, R., Fujiwara, M., Harada, Y., Kobayashi, C., *et al.* Chapter 4: Overview of Ozone and Water Vapour. In M. Fujiwara, G. L. Manney, L. J. Gray, & J. S. Wright (Eds.) *SPARC reanalysis Intercomparison Project (S-RIP) final Report*. SPARC Report No. 10, WCRP-17/2020 (pp. 531–580). <https://doi.org/10.17874/800dee57d13> (2022).
- Bahramvash Shams, S. *et al.* Analyzing ozone variations and uncertainties at high latitudes during sudden stratospheric warming events using MERRA-2. *Atmos. Chem. Phys.* **22**(8), 5435–5458. <https://doi.org/10.5194/acp-22-5435-2022> (2022).

30. Pancheva, D. V. & Mitchell, N. J. Planetary waves and variability of the semidiurnal tide in the mesosphere and lower thermosphere over Esrange (68°N, 21°E) during winter. *J. Geophys. Res. Space Phys.* <https://doi.org/10.1029/2004JA010433> (2004).
31. Andrews, D. G., Holton, J. R. & Leovy, C. B. *Middle atmosphere dynamics* No. 40 (Academic Press, London, 1987).
32. Butler, A. H. *et al.* Defining sudden stratospheric warmings. *Bull. Amer. Meteor. Soc.* **96**(11), 1913–1928. <https://doi.org/10.1175/BAMS-D-13-00173.1> (2015).
33. Teitelbaum, H. & Vial, F. On tidal variability induced by non-linear interaction with planetary waves. *J. Geophys. Res. Space Phys.* **96**(A8), 14169–14178. <https://doi.org/10.1029/91JA01019> (1991).
34. Mitra, G., Guharay, A., Conte, J. F. & Chau, J. L. Signature of two-step non-linear interactions associated to zonally symmetric waves during major sudden stratospheric warmings. *Geophys. Res. Lett.* **50**(19), e2023GL104756. <https://doi.org/10.1029/2023GL104756> (2023).
35. Chang, L. C., Palo, S. E. & Liu, H. L. Short-term variation of the $s = 1$ non-migrating semidiurnal tide during the 2002 stratospheric sudden warming. *J. Geophys. Res. Atmos.* **114**, D03109. <https://doi.org/10.1029/2008JD010886> (2009).
36. de La Cámara, A., Abalos, M., Hitchcock, P., Calvo, N. & Garcia, R. R. Response of Arctic ozone to sudden stratospheric warmings. *Atmos. Chem. Phys.* **18**(22), 16499–16513. <https://doi.org/10.5194/acp-18-16499-2018> (2018).
37. Sinnhuber, B. M., Weber, M., Amankwah, A. & Burrows, J. P. Total ozone during the unusual Antarctic winter of 2002. *Geophys. Res. Lett.* <https://doi.org/10.1029/2002GL016798> (2003).
38. Weber, M. *et al.* Dynamical control of NH and SH winter/spring total ozone from GOME observations in 1995–2002. *Geophys. Res. Lett.* <https://doi.org/10.1029/2002GL016799> (2003).
39. Randall, C. E. *et al.* Reconstruction and simulation of stratospheric ozone distributions during the 2002 austral winter. *J. Atmos. Sci.* **62**(3), 748–764. <https://doi.org/10.1175/JAS-3336.1> (2005).
40. Pancheva, D. V., Mukhtarov, P. J. & Andonov, B. A. Zonally symmetric oscillations in the Northern Hemisphere stratosphere during the winter of 2003–2004. *Geophys. Res. Lett.* <https://doi.org/10.1029/2006GL028666> (2007).
41. Yang, C. *et al.* The delayed response of the troposphere-stratosphere-mesosphere coupling to the 2019 Southern SSW. *Geophys. Res. Lett.* **49**(23), e2022GL101759. <https://doi.org/10.1029/2022GL101759> (2022).
42. Pancheva, D., Mukhtarov, P. & Smith, A. K. Non-migrating tidal variability in the SABER/TIMED mesospheric ozone. *Geophys. Res. Lett.* **41**(11), 4059–4067. <https://doi.org/10.1002/2014GL059844> (2014).
43. Goncharenko, L. P., Coster, A. J., Plumb, R. A. & Domeisen, D. I. The potential role of stratospheric ozone in the stratosphere-ionosphere coupling during stratospheric warmings. *Geophys. Res. Lett.* <https://doi.org/10.1029/2012GL051261> (2012).
44. Davis, R. N., Du, J., Smith, A. K., Ward, W. E. & Mitchell, N. J. The diurnal and semidiurnal tides over Ascension Island (°S, 14°W) and their interaction with the stratospheric quasi-biennial oscillation: Studies with meteor radar, eCMAM and WACCM. *Atmos. Chem. Phys.* **13**(18), 9543–9564. <https://doi.org/10.5194/acp-13-9543-2013> (2013).

Acknowledgements

The present work is supported by the Department of Space, Government of India. IP thanks to CNPq (309981/2023-9) and UFCG (23096.061009/2024-56) for supporting the research. The authors would like to thank the MERRA-2 team for providing access to the database. Authors are thankful to two anonymous reviewers for their useful comments to improve the manuscript.

Author contributions

GM and AG conceptualized the research. GM performed the analyses and prepared the manuscript. AG supervised the study, reviewed and edited the manuscript. IP reviewed and edited the manuscript.

Competing interests

The authors declare no competing interests.

Additional information

Supplementary Information The online version contains supplementary material available at <https://doi.org/10.1038/s41598-024-72594-7>.

Correspondence and requests for materials should be addressed to I.P.

Reprints and permissions information is available at www.nature.com/reprints.

Publisher's note Springer Nature remains neutral with regard to jurisdictional claims in published maps and institutional affiliations.

Open Access This article is licensed under a Creative Commons Attribution-NonCommercial-NoDerivatives 4.0 International License, which permits any non-commercial use, sharing, distribution and reproduction in any medium or format, as long as you give appropriate credit to the original author(s) and the source, provide a link to the Creative Commons licence, and indicate if you modified the licensed material. You do not have permission under this licence to share adapted material derived from this article or parts of it. The images or other third party material in this article are included in the article's Creative Commons licence, unless indicated otherwise in a credit line to the material. If material is not included in the article's Creative Commons licence and your intended use is not permitted by statutory regulation or exceeds the permitted use, you will need to obtain permission directly from the copyright holder. To view a copy of this licence, visit <http://creativecommons.org/licenses/by-nc-nd/4.0/>.

© The Author(s) 2024